CHEMICAL DYNAMICS AND PHOTOCHEMISTRY

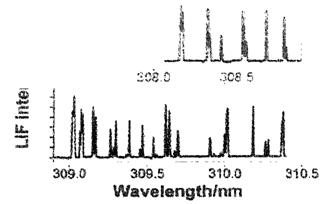

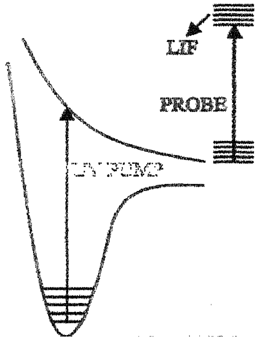

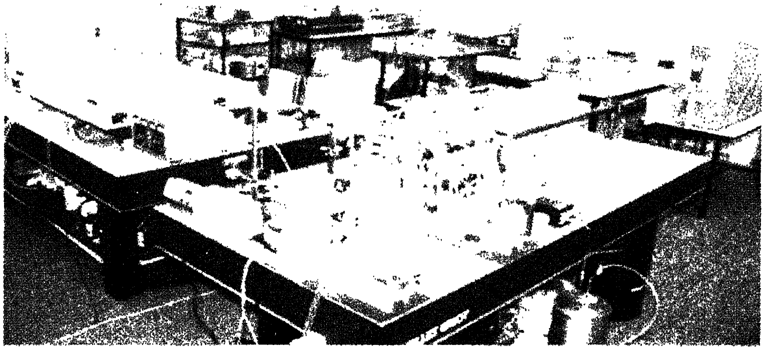

Edited by
J P MITTAL

INDIAN NATIONAL SCIENCE ACADEMY
NEW DELHI

CHEMICAL DYNAMICS AND PHOTOCHEMISTRY

CHEMICAL DYNAMICS
AND
PHOTOCHEMISTRY

Guest Editor

Dr. J P Mittal, FNA

INDIAN NATIONAL SCIENCE ACADEMY
BAHADUR SHAH ZAFAR MARG, NEW DELHI – 110 002

ATIONAL SCIENCE ACADEMY

– *A*
thyamurthy, FNA

sistant Executive Secretary – I
, Section Officer – I

US $ 100/-

000

---

ahni, Executive Secretary, Indian National Science Academy, Bahadur Shah Zafar Marg, New Delhi – 110 002 and
Institute of Science Communication (CSIR), Dr. K S Krishnan Marg, New Delhi – 110 012

EDITOR'S REMARKS

Chemists have a long cherished desire to synthesize new molecules/compounds and establish their structure and also study the dynamics of chemical reactions taking place in these processes. Using a variety of spectroscopic tools, it has been possible, over the years, to widen the horizon of the frontiers of knowledge. The availability of newer instrumental tools such as ultrafast tunable lasers, electron accelerators and other detectors like CCD has paved the way for tremendous advancement in the areas of Chemical Dynamics and Photochemistry.

The present volume gives an extensive account of the work carried out in these important areas by different researchers, of whom four are from abroad and nine are from within the country. We are thankful to the individual authors who have put in their efforts in writing these articles for this special issue. We are grateful to Dr J P Mittal who, in addition to making his own contribution, has taken great pains to persuade others into contributing and has acted as the Guest Editor for this special issue. We are indebted to Prof S K Malik, Editor, IJPAM who, during his tenure as Editor, PINSA-A conceived the idea of producing such a special issue and invited Dr J P Mittal to shoulder the responsibility of putting it together. Lastly, our editorial staff, Shri A K Tagore and Shri M Ranganathan need to be appreciated for their meticulous editorial and production assistance in bringing out this volume.

N Sathyamurthy
Editor, PINSA – A

15 June 2000

PREFACE

Overall the science of chemistry encompasses three broad areas of activity: (1) synthesis of molecules; (2) determination of their structure; and (3) study of the dynamics of chemical reactions. Since the days of alchemy, a few centuries ago, synthesis of new molecules was and still is the main activity of chemists. In the 20th century, new instrumental techniques like X-ray crystallography, spectroscopic techniques like UV-Visible, IR and NMR became available so that synthesized molecules could be unequivocally characterized and their structure elucidated. This, in turn, encouraged the synthesis activity so that preconceived structures could be synthesized. However, the past few decades have witnessed tremendous growth in understanding the progress of a chemical reaction itself, i.e., the dynamics of chemical reaction. Usually, chemical reactions are carried out under macroscopic/bulk conditions and thus only the gross features are observed. However, to understand how and why a chemical reaction occurs, an understanding of elementary chemical reactions at molecular/microscopic level is essential. How fast is a given chemical reaction? What are the reaction intermediates? Does the activated complex or transition postulated in every chemical reaction really exist? Can one detect and influence it? How do initial conditions, e.g. reagents in preselected internal energy states, affect the outcome of a given chemical reaction? How does the exoergicity of a chemical reaction appear in various internal energy states of products? How does reagent orientation/steric factor affect the product formation? Can one observe the progress of a chemical reaction like in a slow motion video film? Can the outcome of a chemical reaction with specified internal energy conditions be predicted in advance? Can the chemical reaction be controlled? Will the dream of `bond selective chemistry' be realised?

In the past few decades, new instrumental techniques like ultrafast and tunable lasers, electron accelerators, molecular beams, optical techniques like fluorescence with single photon counting and upconversion, resonance Raman, detectors like CCD, have opened vast avenues of advanced research in Chemical Dynamics. Lasers have become an inseparable part of this endeavour. Photons have been used (1) to select reagents in predetermined internal energy states, (2) to bring out photocatalysed transformations of reactions and (3) to detect reaction products in their nascent internal energy states. This shows a great overlap between the areas of chemical dynamics and photochemistry. In this context, we are pleased to bring out a special issue on "Chemical Dynamics and Photochemistry".

In India, all the major funding agencies like DST, UGC, CSIR and DAE have regarded these two topics as thrust areas for funding R & D. India has a long tradition of excellent work in the area of photochemistry. The field has matured now, with good experimental facilities being available at many centres. Many synthetic chemists use photochemical techniques to shorten synthetic routes in some advanced synthetic procedures. Even in industry, photochemistry has made a mark owing to commercial applications like photocuring.

Chemical dynamics is a new area demanding both sophisticated experimental as well as intense theoretical inputs. Theoretical research in India is at a quite advanced stage. Facilities for experimental work, however, need a further boost, although facilities for studying fast and ultrafast processes like laser flash photolysis, electron pulse radiolysis exist in this country. Chemistry Group at the Bhabha Atomic Research Centre (BARC) and Tata Institute of Fundamenal Research (TIFR) have made pioneering contributions in these areas in the past decade or so. Recently, a National Centre for Ultrafast Processes has been set up in the University of Madras which will cater to the needs of researchers from the universities. Many other agencies are planning to set up facilities with ultrafast lasers. Another area that requires attention is related to molecular beam techniques. Only a limited number of centres like BARC, TIFR, Indian Association for the Cultivation of Science have ventured into such technologically difficult area. New facilities like resonance Raman, resonance enhanced multiphoton ionization, free electron lasers are poised to give a boost to the photochemistry and chemical dynamics research. Synchrotron radiation facility at the Centre for Advanced Technology (CAT), Indore should be welcome for the scientists working in these twin areas. It is hoped that the present special issue provides inspiration for sustaining and initiating new programmes in these areas.

We have been fortunate to have some outstanding researchers from India and abroad who have contributed 13 excellent articles on contemporary problems to the special issue. As a Guest Editor, it is my privilege to thank the contributors for the great pains they have taken to write the reviews and to the Editorial Board of the Review Journal, PINSA-A, for giving me this opportunity. I hope that the readers will appreciate these articles.

J P Mittal
Chemistry Group
Bhabha Atomic Research Centre
Mumbai 400 085
Guest Editor
Special Volume on
"Chemical Dynamics & Photochemistry"

CONTENTS

Page

The Dynamics of the $H+X_2O$ ($X = H,D$) Gas-Phase Isotope Reactions: Comparison between Experiment and Quantum Theory
Hans-Robert Volpp 1

Investigation and Control of Photodissociation Dynamics: An Overview
Vandana K and Manoj K Mishra 29

Dynamics of (He, H_2^+) Collisions
B Maiti and N Sathyamurthy 59

Free Electron Laser Photochemistry: Current Developments and Future Prospects
Sisir K Sarkar 71

Laser Gas-Phase Photolysis of Organosilicon Compounds: Approach to Formation of Hydrogenated Si/C, Si/C/F, Si/C/O, Si/O Phases
Josef Pola 107

Resonance Raman Intensity Analysis Applied to Photodissociation Reactions of Polyatomic Molecules
David Lee Phillips 137

Ultrafast Electron Transfer Dynamics in Sensitised TiO_2 Nanoparticles
Hirendra N Ghosh, John B Asbury and Tianquan Lian 177

Photophysical Processes in Organised Assemblies
Kankan Bhattacharyya 199

Dynamics of Photosynthetic Excitation Transfer
Villy Sundström and Tõnu Pullerits 219

Photo and Radiation Chemistry of Quinones
Tulsi Mukherjee 239

Magnetic Field Effect in Chemistry - The Indian Scenario
Samita Basu, Mintu Halder and Mihir Chowdhury 267

Photoionization Studies in Aqueous Micellar Solutions
A V Sapre 289

Photophysical Properties of Two Infrared Laser Dyes - IR144 and IR140: A Picosecond Laser Flash Photolysis Study
Jyotirmayee Mohanty, Dipak K Palit and Jai P Mittal 303

THE DYNAMICS OF THE H + X_2O (X=H,D) GAS-PHASE ISOTOPE REACTIONS: COMPARISON BETWEEN EXPERIMENT AND QUANTUM THEORY*

HANS-ROBERT VOLPP

Physikalisch-Chemisches Institut der Universität Heidelberg, Im Neuenheimer Feld 253,
D-69120 Heidelberg, (Germany)

The gas-phase reaction of hydrogen atoms with water has become a prototypical benchmark system for comparison between results of experimental reaction dynamics studies and quasiclassical as well as with approximate and exact four-atom quantum mechanical reactive scattering calculations. The present article is an attempt to review the advances achieved in recent experimental and theoretical dynamics studies with a particular focus on the partially isotopically substituted H + D_2O reaction system for which besides OH and OD radical formation channels also the hydrogen-atom abstraction channel has been investigated in detail recently using pulsed laser "pump-probe" methods.

Keywords: Molecular Reaction Dynamics; Isotope Exchange Reactions; Hot Atom Chemistry

1 Introduction

Following the impressive progress made in the quantum treatment of the adiabatic atom-diatom reactive scattering problem[1], the gas-phase reaction of hydrogen atoms with water

$$H(^2S) + H_2O(\tilde{X}\,^1A_1) \rightarrow OH(X^2\Pi) + H_2(X^1\Sigma_g^+) \qquad \ldots (1)$$

and its reverse reaction

$$OH(X^2\Pi) + H_2(X^1\Sigma_g^+) \rightarrow H(^2S) + H_2O(\tilde{X}\,^1A_1) \qquad \ldots (-1)$$

together with their different isotopic variants have recently attracted extensive interest among experimentalists[1] and theoreticians[2] working in the field of molecular reaction dynamics. Being some of the most "simplest" four-atom reactions they have become benchmark systems towards the development of rigorous quantum mechanical atom-triatom[3] and diatom-diatom reactive scattering methods[5].

Besides their fundamental interest, reactions (1) and (-1) are also of practical importance in combustion, in atmospheric and in interstellar chemistry[6]. As a consequence, thermal rate coefficients for both reactions have been measured over a wide range of temperatures[7]. The enthalpy of reaction (1) is $\Delta H_r(298\ K) = 0.66$ eV and the activation energy is 0.84 eV[8]. The recommended expression for the thermal rate coefficient of reaction (1) and (-1) in the temperature range T = 300–2000 K is $k_1(T) = 7.51 \times 10^{-16}\ T^{1.6} \exp(-9720\ K/T)\ cm^3/s$ and $k_{-1}(T) = 1.70 \times 10^{-16}\ T^{1.6} \exp(-1660\ K/T)\ cm^3/s$, respectively[8]. Direct experimental investigations of the kinetics of the fully deuterated version of reaction (1) were also carried out which indicated a kinetic isotope effect of unity in the temperature range T = 1285–2261 K[9] More recent kinetics studies of the OH + $HD/D_2/H_2$ isotopic reactions down to T = 250 K revealed a very large isotopic effect on the rate constant suggesting a strong increase in the importance of tunneling at low temperatures[10]. In these studies H/D atom product branching ratios of $\Gamma_{H/D} = 0.21$ and $\Gamma_{H/D} = 0.35$ were determined for the OH + HD reaction at T = 250 K and 298 K, respectively. H/D product branching ratios considerably smaller than unity can be attributed to quantum mechanical tunneling, which favours at collision energies below the

*Paper dedicated by the author to Professor Jürgen Wolfrum on the occasion of his 60th birthday.

reaction threshold abstraction of H atoms (via OH + HD → D + HOH) over D atom abstraction (via OH + HD → H + HOD). On the other hand, for the reaction of HD with translationally energetic OH radicals with an average center-of-mass collision energy of $E_{c.m.} = 0.24$ eV a value of $\Gamma_{H/D} = 1.2 \pm 0.2$ was reported[11] The preference for the D atom abstraction channel observed in the latter study is an experimental indication that for translational energies above the reaction threshold the dynamics of the OH + HD reactive collision might be influenced by reagents′ steric effects as suggested by time-dependent quantum wavepacket (TD-QWP) calculations of the OH + HD reaction[12].

In addition to the thermal kinetics studies a number of experiments were carried out in which the effects of the reagent internal energies on the reaction rate has been investigated. For reaction (1) the influence of selective $H_2O(|ab>^{\pm}|c>)$ reagent[a] vibrational excitation[13] on the relative room-temperature reaction rate has been extensively studied by Crim and co-workers[14]. These experiments in which high overtones, e.g. $|02>^-$, $|02>^-|2>$, $|03>^-$, $|13>^-$, $|04>^-$, of the water molecule were selectively excited, revealed significant mode- and state-specific propensities[14,15]. These studies showed that the rate coefficient for the H + $H_2O(|04>^-)$ reaction was about twice that for the H + $H_2O(|03>^-)$ reaction and about a factor of ten greater than the value for H + $H_2O(|02>^-)$[16]. Only recently an absolute state-specific room-temperature rate constant of 4.9×10^{-10} cm^3/s could be measured for the removal of $H_2O(|04>^-)$ molecules in collisions with H atoms[17]. Although the observation of OH product radical formation in the latter experiments demonstrated that reaction occurs, the actual branching ratio between reaction of $H_2O(|04>^-)$ molecules and vibrational relaxation by H atoms could not be determined experimentally. Theoretical studies using vibrational coupled-channel infinite-order-sudden (VCC-IOS) quantum mechanical nonreactive scattering calculations[18] on a model potential energy surface (PES) based on the spectroscopic intramolecular force field of H_2O[19] and the accurate H + HF → H_2 + F reaction 6SEC-PES[20] yielded a value of 4.47×10^{-10} cm^3/s for the room-temperature H + $H_2O(|04>^-)$ vibrational deactivation rate constant[21]. While the latter result suggests that the measured rate constant is dominated by vibrational deactivation, most recent VCC-IOS quantum mechanical nonreactive scattering calculations on a realistic H + H_2O PES[22] indicated that vibrational deactivation and reaction are of comparable importance[23]. For reaction (-1), the effect of initial vibrational excitation of the OH radical and the H_2 molecule on the reaction rate was studied in state-selected kinetics experiments. In these experiments it was observed that the room-temperature rate of reaction (-1) is enhanced by a factor of <1.5 by vibrational excitation of OH[24] whereas if H_2 is excited to $v = 1$ the rate increases by a factor of (120 ± 40)[25] and (155 ± 38)[26]. A detailed comparison of the experimentally observed rate enhancements with the results of calculations based on vibrationally adiabatic transition-state theory (VA-TST)[27] can be found in the article by Smith[28].

The prototypical nature of reactions (1) and (−1) has stimulated a variety of reaction dynamics experiments in recent years. The first dynamics experiment of reaction (1) in which an absolute reaction cross section could be determined was reported in 1984 by Kleinermanns and Wolfrum[29]. In these experiments, pulsed laser photolysis (LP) for the generation of translationally energetic H atoms was combined with time-resolved laser-induced fluorescence (LIF) in the ultra-violet spectral (UV) region for the detection of nascent OH product radicals[30]. In a number of subsequent experiments the LP/LIF "pump-probe" technique was employed to measure scalar and vectorial dynamical quantities of reaction (1), for example nascent OH fine-structure state distributions[31], OH energy partitioning[32], OH product angular momentum alignment parameters[33], state-resolved differential cross sections[34], and absolute reaction cross sections in the collision energy range $E_{c.m.} = 1.0$–2.5 eV[35-37]. The collisonal excitation of H_2O by translationally excited H atoms was investigated at $E_{c.m.} = 2.2$ eV using time-resolved Fourier-transform infrared emission spectroscopy for the detection of the rotationally and vibrationally excited H_2O molecules[38]. Most recently results from collision-induced ionization experiments of the H + H_2O reaction were reported in which a beam of high-energetic H atoms with well-defined collision energies in the range $E_{c.m.}$ = 10–170 eV was produced by the laser-photodetachment technique[39].

---

[a] The notation $(|ab>^{\pm}|c>)$ for the water molecule vibrational states is a local mode notation where a and b denote the numbers of *O*-H stretch quanta in each bond and c, which is only given if it is nonzero, designates the number of bending quanta. The superscript describes the symmetric (+) or antisymmetric (−) combination of a quanta and b quanta in the two OH bonds (ref. [13]).

Chemical dynamic studies have been reported where the influence of reagent translational excitation on the reactivity of reaction (-1) was investigated[40]. In these studies, absolute reaction cross sections for reaction (-1) and the isotopic variant OH + D_2 were measured employing a "pump-probe" technique in which translationally excited OH radicals were produced by pulsed laser photolysis and the H and D product atoms were detected by vacuum-UV LIF. In the same study, H/D product branching ratio measurements for the OH + D_2 reaction were reported for collision energies of $E_{c.m.}$ = 0.28 eV and 0.37 eV which demonstrated that D + HOD is the dominant reaction pathway. In crossed-molecular-beams studies of the OH + D_2 → D + HOD reaction at $E_{c.m.}$ = 0.27 eV a strongly backward-scattered (with respect to the OH direction) HOD angular distribution was observed[41] suggesting direct rebound dynamics. The results of ref. [40] and [41] indicate that the OH + H_2 gas-phase reaction proceeds via a simple and direct hydrogen abstraction mechanism through a tightly constrained transition state, in which the formation of the new HH-OH bond occurs simultaneously with the cleavage of the old H-HOH bond. Studies focussing on a direct investigation of the transition state region of reaction (-1) were carried out using photoelectron spectroscopy of the H_3O^- anion[42], Ref. [43] reports on recent experiments in which OH and H_2/D_2 reactants could be stabilized as weakly bound $OH(X^2\Pi)\cdots H_2$ and $OH(X^2\Pi)\cdots D_2$ binary complexes by photolytically generating OH radicals within a supersonic expansion of H_2 and D_2, respectively. Spectroscopic investigation of these "prereactive" complexes[44] allowed the examination of the topology of the attractive well region in the entrance channel to the hydrogen abstraction reaction (−1)[45]. In order to probe inelastic energy transfer processes between the different $OH(X^2\Pi)$ rotational spin-orbit and Λ-doublet fine-structure states[46], which are believed to be responsible for the H_2 collisional pumping[47] of interstellar OH masers[48], state-specific collision studies of OH radicals with H_2 and D_2 were carried out at energies ($E_{c.m.}$ = 0.083 eV[49] and 0.074 eV[50]) below the reaction threshold[b]. Studies of state-to-state inelastic OH + H_2 scattering processes under restricted initial conditions were performed recently by vibrational state-selective infrared excitation of OH overtone transitions in an $OH(X^2\Pi)\cdots$*ortho*-H_2 binary complex[51].

In 1972 Bibler and Firestone studied the temperature dependence of the ionizing (β-particle) radiation induced isotope exchange between H_2 and D_2O which can be described by the overall exchange reactions $H_2 + D_2O = HD + HOD$ and $H_2 + D_2O = D_2 + H_2O$[52]. These experiments showed that in the temperature range T = 491–654 K HD is formed by a chain reaction mechanism propagated by the gas-phase elementary reactions

$$H + D_2O \rightarrow HD + OD \qquad \ldots (2a)$$

$$H + D_2O \rightarrow HOD + D \qquad \ldots (2b)$$

at comparable rates, while D_2 formation *via*

$$H + D_2O \rightarrow D_2 + OH \qquad \ldots (2c)$$

takes place at a much slower rate. In the same study Arrhenius activation energies and relative frequency factors for the reactions (2a-c) and the fully deuterated version of reaction (1) were estimated[53]. Fig. 1 shows a correlation diagram of the H + D_2O reaction system on the basis of symmetry. Energies of the minimas, the transition states T(2a), T(2b) and the stationary point T*(2c) for the three reaction channels (2a-c) were taken from refs. [54] and [55].

Molecular dynamics studies of the H + D_2O reaction which allowed the investigation of reaction product channels which could not be distinguished experimentally in the case of the protonated reaction have recently provided detailed information about the underlying reaction mechanism of reaction (1). Absolute reaction cross section measurements for the two reaction pathways (2a) and (2c)[40] confirmed that the $H + H_2O \rightarrow H_2 + OH$ reaction proceeds almost exclusively by a direct H atom abstraction mechanism *via* a H–H-O-H transition state (denoted as T(2a) in Fig. 1) rather than *via* the formation of an oxonium radical (H_3O) intermediate followed by a decomposition to $H_2 + OH$ products. In addition, studies in which the rotational excitation of the nascent OD product radicals was determined at different collision energies allowed — by comparison with the corresponding results obtained for reaction (1) — the elucidation of how mass effects and reagents' zero-point energies affect the collision dynamics of the abstraction pathway[31,40,56]. Vibrational and rotational state distributions of HD products formed in reaction (2a) were measured by Zare and co-workers[57] at a collision energy of approximately 2.7 eV using (2+1) resonance-enhanced multi-photon ionization (REMPI) for HD detection[c]. The dynamics studies showed that the OD products are almost exclusively in their vibrational ground state with very low rotational excitation, while excitation of the HD internal degrees of freedom accounts for about 35% of the available energy. State-to-state dynamics experiments of reaction (2a) were also performed to examine the influence of reagent translational *versus* selective D_2O (0, 0, 1) and (0, 1, 1) vibrational excitation[d] on the reactivity[40,58].

---

[b] Kinetics studies in the low temperature range (250<T/K<470) of the OH+H_2 and OH+D_2 reactions yielded Arrhenius activation energies of E_A=0.18 eV (ref. [5j]) and E_A=0.23 eV (ref. [7d]) respectively.

The article is organized as follows. In Section 2 a brief overview about the recent achievements made in the theoretical treatment of the reactions (1), (-1) and (2a-c) will be given. The focus will be on reactive scattering calculations on *ab initio* based PESs which provide dynamical quantities (e.g. reaction cross sections, reaction product state distributions) which allow for direct comparison with the results of experimental dynamics studies employing laser based photochemical techniques. As an example the pulsed laser photolysis-laser induced fluorescence "pump-and-probe" method and its application for the measurement of absolute reaction cross sections will be described in Section 3. Results of dynamics studies of reaction (1), (2a) and (2c) employing photolytically generated translationally excited H atoms and state-resolved

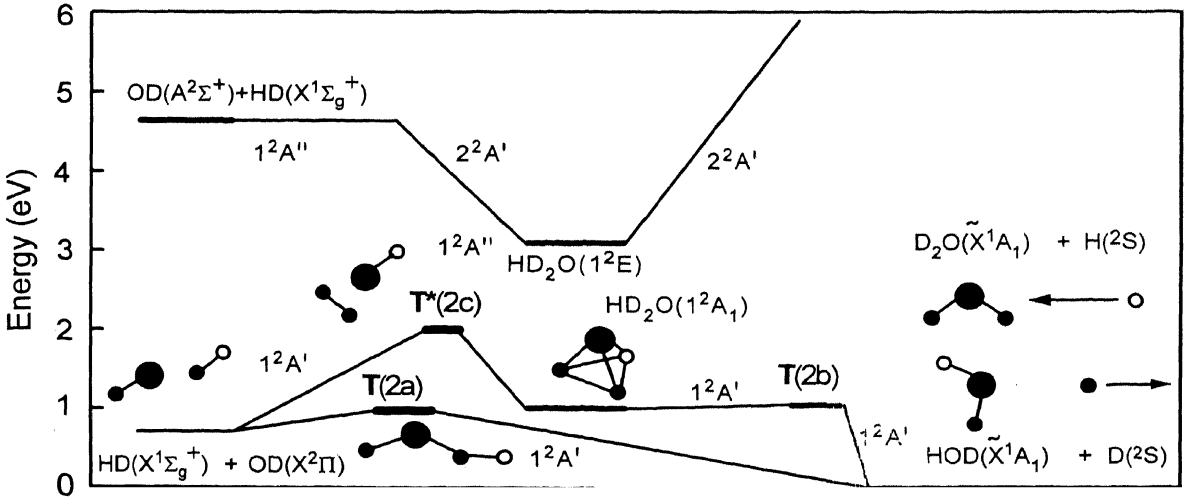
Energy (eV)
0
1
2
3
4
5
6
$OD(A^2\Sigma^+)+HD(X^1\Sigma_g^+)$
$1^2A''$
$2^2A'$
$2^2A'$
$1^2A''$
$HD_2O(1^2E)$
$T^*(2c)$
$HD_2O(1^2A_1)$
$D_2O(\tilde{X}^1A_1)$ + $H(^2S)$
$1^2A'$
T(2a)
$1^2A'$
T(2b)
$1^2A'$
$HD(X^1\Sigma_g^+)$ + $OD(X^2\Pi)$
$1^2A'$
$HOD(\tilde{X}^1A_1)$ + $D(^2S)$

Fig. 1 Correlation diagram for the $H + D_2O$ reaction system. T(2a), T(2b) denote the transition states for the reaction pathways (2a), (2b), respectively. The energy and structure of the abstraction reaction transition state, T(2a), were taken from Ref. 67. Energies of the HD_2O minimum, the transition state T(2b) and stationary point T*(2c) are from ref. [54].

---

[c] In these experiments a single UV laser tunable in the wavelength region 202-221 nm was used to initiate the $H+D_2O$ reaction by HI photolysis and to measure (within the 5 ns duration of the laser pulse) the HD rotational and vibrational product quantum state distribution via (2+1) REMPI. As a consequence the H atom collision energy varied with the HD quantum state detected between E_{cm}=3.0 eV (for HD, v=0) and E_{cm}=2.4 eV (for HD, v=2)

[d] (0,0,1) and (0,1,1) denote the asymmetric stretch fundamental state and the asymmetric bend stretch combination state of the D_2O molecule

OH/OD and HD product detection will be reviewed in Sections 4.1 and 4.2 and compared with QCT and quantum mechanical scattering (QMS) calculations. Finally recent results of H + D_2O reaction dynamics and non-equilibrium kinetics experiments[59,60], which allowed for the first time the direct study of the hydrogen atom exchange channel (2b), will be presented in Section 4.3 and compared with most recent QMS calculations. The article ends with drawing some conclusions about the current status in the understanding of the multi-channel nature of the H + D_2O reaction system.

2 Potential Energy Surfaces, Direct *ab initio* Dynamics Studies and Reactive Scattering Calculations

The quantum mechanical treatment of "slow" elementary molecular collisions[e] is mostly based on the Born-Oppenheimer separation of electronic and nuclear motion which allows to solve the electronic and nuclear parts of the Schrödinger equation separately. The consequence of this separation ansatz is the concept of a potential energy surfaces (PES) representing the solution of the electronic Schrödinger equation for different geometrical configurations of the fixed nuclei.

As a consequence, the construction of a reliable global analytical PES for the use in dynamical studies requires (i) that *ab initio* electronic structure calculations are carried out for a representative sample of nuclear configurations and (ii) that afterwards an appropriate model function is chosen for fitting the *ab initio* data. In the alternative direct *ab initio* dynamics approach task (ii) is removed because the electronic potential energies are calculated as they are needed[61]. In ref. [62] direct *ab initio* dynamics calculations of thermal rate constants and kinetic isotope effects for reaction (1) and (-1) were reported. However, most of the molecular dynamics studies for the reactions (1) and (-1) were carried out employing analytical PESs. The most widely used PES in these calculations is the one made by Schatz and Elgersma (in the following denoted as SE-PES)[63] which represents an empirical fit to the *ab initio* points of Walch *et al.*[64] The SE-PES has several known defects: (1) several features of the geometry of transition state for the H atom abstraction pathway (denoted a T(2a) in Fig. 1) are inaccurate, (2) it does not describe well the potential and the vibrational energy levels for H_2O, (3) it has spurious wells in the OH + H_2 channel[65], (4) only one of the H atoms in the H_2O molecule is capable to react with the incident H atom (therefore reaction pathway (2c) is not possible), (5) the transition state for the H atom exchange channel (denoted a T(2b) in Fig. 1) might be seriously in error because, due to lack of *ab initio* data, the properties of the PES in that region were not optimized during the fit[66]. A series of PESs (denoted as I1-I5) were developed by Isaacson[67] some of which are based on (partly unpublished) *ab initio* data obtained by Kraka and Dunning[68] around the saddle point T(2a) and along the abstraction reaction path. As in the case of the SE-PES no *ab initio* information characterizing the H_3O region was included in the fit. Therefore it can be expected that even the latest version (I5) provides a "global" PES that accurately represents (only) the abstraction reaction pathway[69]. Although the I5-PES allows reaction for either of the H atoms in the H_2O molecule it does not treat the two H atoms equivalently. Therefore two different abstraction pathways exist on the I5-PES which have different barriers and hence exhibit a different reactivity. In ref. [70], Jordan and Collins presented an "automated procedure" in which an *ab initio* quantum chemical calculation package was merged with a PES interpolation and iteration scheme[71] for the construction of a global PES for reaction (-1). In these calculations, it was demonstrated that with this procedure it is possible to generate, starting from a set of minimum energy path *ab initio* points of the abstraction pathway, a global PES which includes reaction channels (for example an H atom exchange pathway) that were not considered initially. However, the PES obtained in this studies does not have chemical accuracy because of the low level of the electronic structure calculation method used. More recently another PES was developed by Kliesch, Werner, and Clary (KWC-PES) which is based on high level *ab initio* data points[72]. Although this PES fits the *ab initio* frequencies and geometries of the abstraction transition state, it was found to be inappropriate for out-of-plane geometries away from the transition state region. In addition, the KWC-PES does not describe the full symmetry of the reaction system. Most recently a global PES was constructed by Ochoa de Aspuru and Clary (OC-PES)[22]. which describes the full symmetry of the H + H_2O reaction system and which is also a much better fit to the *ab initio* data points of ref. [72] than the KWC-PES. However, also in the construction of the OC-PES, which can be regarded at present as the most accurate PES for the H + H_2O reaction system, no H_3O *ab initio* data was included.

---

[e] In a "slow" elementary molecular collision process the speed of the nuclear motion is very much less compared to the velocity of the electrons.

Due to the considerable experimental and theoretical interest in the existence of a stable or metastable H_3O radical[73] a number of studies were performed which provided detailed H_3O structural information. The effect of different basis set functions on the H_3O structure was investigated by Niblaeus, Roos and Siegbahn, who found that because of the Rydberg character of the H_3O ground state the inclusion of diffusion functions on the O atom is essential for the prediction of a symmetric geometry with three equivalent H atoms as a local minimum on the global ground-state PES[74]. They further noted that d-type polarization functions on the O atom are required in order to predict a pyramidal local $H_3O(1^2A_1)$ minimum in C_{3v} geometry schematically shown in Fig. 1 which otherwise would be planar (D_{3h}). The local C_{3v} minimum was found to be located about 0.89 eV above the H + H_2O asymptote with dissociation barrier of 0.15 eV. Talbi and Saxon investigated the transition states for dissociation of the (1^2A_1) H_3O ground state ($1^2A'$ using C_s designation) to H + H_2O and OH + H_2 ground state products[54]. They found that the dissociation pathway $H_3O(1^2A') \rightarrow$ H + H_2O can be described by a conventional transition state with one imaginary frequency with a transition state geometry between that of the $H_3O(1^2A')$ minimum and that of H_2O with the dissociation coordinate being a O-H stretch type motion. On the other hand, in the same study it was not possible to locate the transition state for the $H_3O(1^2A') \rightarrow OH + H_2$ dissociation channel.

A stationary point (denoted as T*(2c) in Fig. 1) with two imaginary frequencies was found at an energy 1.10 eV above the $H_3O(1^2A')$ minimum (corresponding to an energy of 1.99 eV relative to H + H_2O) indicating that stability of the $H_3O(1^2A')$ state depends on the barrier of the $H_3O(1^2A') \rightarrow$ H + H_2O dissociation channel. Recently *ab initio* studies of the interaction of H_2 with ground state $OH(X^2\Pi)$ and electronically excited $OH(A^2\Sigma^+)$ radicals were performed for T-shaped HO–H_2 configurations[75]. In these calculations a conical intersection of the ground- and excited-state potentials was found for the T-shaped HO—H_2 configuration with an intermolecular distance of 2.6 a_0 at an energy of about 3.12 eV above the H + H_2O reagents′ asymptote. Through this conical intersection it would in principle be possible that a H_3O intermediate formed during a H + H_2O collision decomposes to $OH(X^2\Pi) + H_2$ products. In case of the reaction H + D_2O such a mechanism could result in $OH(X^2\Pi)$ + D_2 products via reaction (2c). In addition, the existence of the conical intersection, although in most of the experimental ground state reaction dynamics studies it might not be energetically accessible[f], could influence the dynamics through the geometric phase effect[76,77].

Extensive QCT studies of the reaction (1) and (-1) were carried out by Schatz and co-workers[63,78,79] in the early 1980s employing the SE-PES. This pioneering work revealed numerous valuable details of the molecular reaction dynamics, for example, the existence of mode and bond selectivity in reaction (1)[80]. Several subsequent QCT studies of the reactions (1) and (−1) were performed on the SE-PES[65,66,81], and the results have been reviewed in ref. [82]. In more recent QCT studies the I5-PES[83] and the OC-PES[84] were also used. The QCT studies have provided an extensive set of dynamical data which allowed for a detailed comparison with results from various state-resolved reaction dynamics experiments of reaction (1)[34,37,57] and (-1)[40,41]. The comparison with experiment has highlighted several problems which occur when QCT calculations are performed on reactions involving polyatomic reagents[2]. Among the more severe problems to be mentioned is the inability of the QCT method to conserve quantum mechanical zero point energy and to account for the quantum mechanical tunneling effect. The first tends to make QCT cross sections larger than the corresponding quantum mechanical ones while the second tends to make the QCT cross section smaller than the quantum mechanical ones. This can lead, however, in some cases to the fortuitous cancellation of the two effects resulting in an accidentally good agreement between the QCT and rigorous QMS calculations. Nevertheless, the QCT method is a very useful concept as it offers the possibility by using trajectory animation to visualize molecular collision events. An alternative approach proposed by Billing is the use of a mixed quantal/classical (QC) scheme in which the degrees of freedom where quantum effects dominate are treated quantum mechanically by employing an effective Hamiltonian approach for coupling the quantal and classical part of the scattering problem[85].

---

[f] The highest translational energy employed so far in H+D_2O chemical dynamics experiments .was approximately 3.0 eV (see foot note c).

QMS studies for reactions (1) and (-1) were reported by Clary in 1991 which represent the first quantum mechanical calculations on a state-selected four-atom reaction system with nonlinear geometry[86]. In this work and in the subsequent studies of the same reactions[87] a rotating bond approximation (RBA) was applied. Similar calculations were reported by Bowman and co-workers who used the adiabatic bend approximation (ABA)[88]. In the RBA-QMS studies of reaction (1) all H_2O, and the H_2 and OH vibrations as well as the OH rotation were treated explicitly while the H_2O and H_2 rotational motions are not treated explicitly. The latter motions have to be approximated, however, in order to derive OH rotational state distributions and absolute reaction cross sections which can be compared with experimental results. It was found that the absolute reaction cross sections derived from RBA-QMS depend strongly on the approximation method applied to correct for the degrees of freedom not explicitly treated in the scattering calculations.

Three different ways of approximation were tested and discussed in detail in ref. [87b]. The ABA approach involves the explicit treatment of the H_2O stretching, and the H_2, OH vibrations while all other degrees of freedom are treated adiabatically. As a consequence this approach can not yield cross sections that are OH and H_2 rotational state resolved. To obtain OH, H_2 and OD, HD rotational sate distribution for reactions (1) and (2a), Bowman and Wang developed an adiabatic-bend Franck-Condon (AB-FC) model which they applied to examine the influence of H-HOH and H-DOD transition-state bending excitation on the final product rotational state distributions[89]. At the same time, Baer and collaborators have adapted their method of negative imaginary potentials (NIPs)[90] to study reactions (1) and (-1)[91]. In all these QMS studies the number of degrees of freedom was restricted to three (3D)[92]. The full-dimensional treatment of the reactive atom-triatom scattering problem, however, requires the inclusion of six degrees of freedom as depicted in Fig. 2. QMS calculations with increasingly higher dimensionality were reported by Echave and Clary for reaction (1)[93] and for reaction (-1) by Baer *et al.* (4D)[94] and for the reaction OH + HD → H + HOD, D + H_2O by Zhang *et al.* (5D)[95]. Finally a number of full-dimensional (6D) QMS studies of reaction (-1) and its isotopic substituted versions were reported by Zhang and co-workers[12,96], Miller and co-workers[97], and by Neuhauser[98]. The latter studies yielded accurate reaction probabilities which represent important benchmarks to test the validity of the QCT and the approximate QMS methods. In addition, absolute reaction cross sections and thermal rate constants obtained in the 6D studies for reaction (-1) allow for the most rigorous comparison with available experimental data[10,11,99] and hence allow to access the accuracy of the SE-PES which was employed in these calculations. Among the other available PESs only the KWC-PES was used so far in a RBA-QMS (3D) study in which the differential cross section and the product energy disposal for the OH + D_2 → D + HOD

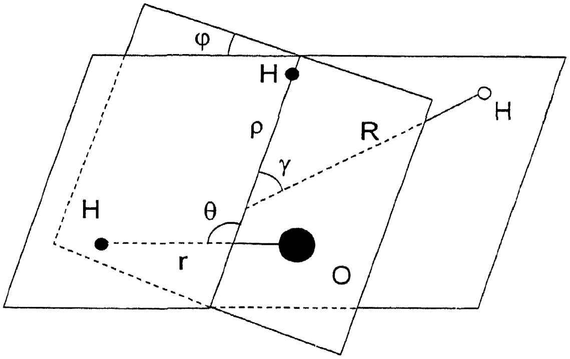

Fig. 2 The six Jacobi coordinates for the H + H_2O reaction system.

reaction were calculated. A comparison with experimental result of Casavecchia and co-workers[41] and with earlier RBA-QMS calculations on the SE-PES revealed that the KWC-PES yields results which are in somewhat better agreement with the experiment.

Compared to the large number of 6D QMS studies of the diatom-diatom reaction (-1) there are only two studies reported for the atom-triatom reaction (1) which yielded dynamical quantities for comparison with experiments. The calculations were performed by Zhang and Light by means of a time-dependent quantum wave packet (TD-QWP) method employing the SE-PES. In these calculations, absolute reaction cross sections[100] and OH rotational product state distributions[101] were obtained for collision energies up to 1.8 eV. Although, as noted in ref. [100], reaction probabilities for the H atom exchange pathway ($H' + H_2O \rightarrow H'OH + H$) were obtained in these calculations, the exchange dynamics were not considered.

Recently QMS calculations (employing the SE-PES) were reported for reaction (1) and for the H + D_2O reaction which also included the exchange pathway (2a)[102]. In these calculation three degrees of freedom were explicitly treated, namely: **r**, the distance of the non-reactive O-H (O-D) bond of the $H_2O(D_2O)$ molecule; ρ, the distance between the "reactive" H (D) atom and the center-of-mass of the OH (OD) moiety of the $H_2O(D_2O)$ molecule; **R**, the distance between the "reactive" H (D) atom and the center-of-mass of the $H_2O(D_2O)$ molecule. The three Jacobi angles were treated in the following way: the angle θ was held fixed during the calculations and assumed to be equal to θ_e the equilibrium bending angle of the $H_2O(D_2O)$ molecule; the angle γ was held fixed during a single calculation and is then varied from one calculation to the other. The coordinate system used in the 3D QMS calculations is shown in Fig. 3a. Fig. 3b depicts H + D_2O reaction cross section obtained for different values of γ at collision energies of 1.25 and 2.2 eV, respectively. γ-fixed cross sections are then used to calculate absolute reaction cross sections by a ($\sin\gamma$)-weighted integration over γ. The out-of-plane angle φ was taken into account by employing a φ-averaged potential (see Fig. 2) which was obtained for each set of coordinates (**r**, **R**, ρ, θ, γ) during the scattering calculations. In the calculations NIPs were used to decouple the hydrogen atom abstraction (2a) and hydrogen atom exchange (2b) product arrangement channels. The application of NIPs in the product channels actually converts the reactive scattering problem into an elastic scattering problem which allows that the numerical treatment can be carried out in the reagents arrangement channel only and hence avoids the need to treat the Schrödinger equation in the different product channels. As a consequence, the calculated reaction cross sections represent the

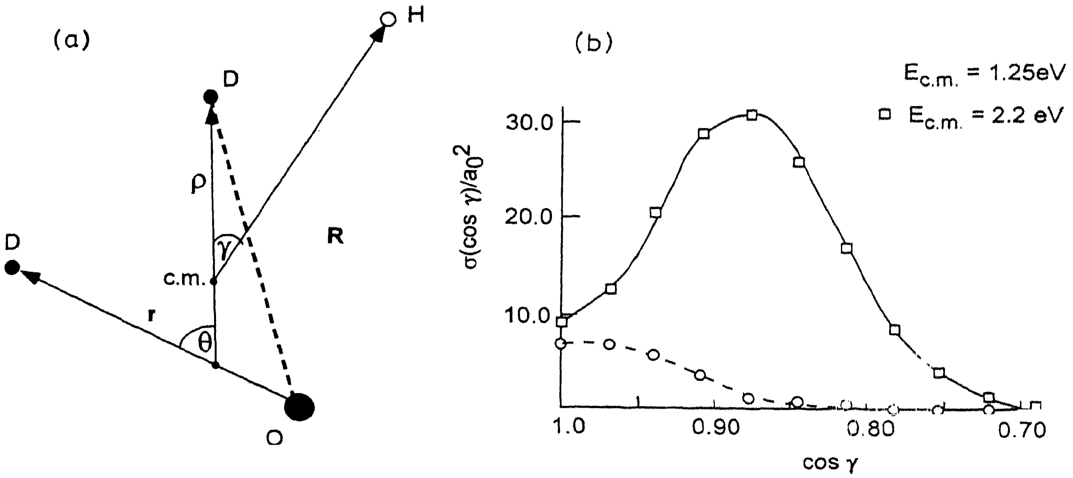

Fig. 3 (a) Coordinates treated in the reduced dimensional 3D QMS calculations of the H + D_2O reaction (ref. [102]), (b) 3D QMS angular dependent integral reaction cross sections for the H + D_2O reaction.

integral value for the sum of all possible reaction products channels. Because the SE-PES does not allow for reaction (2c) the theoretical H + $D_2O \rightarrow$ products reaction cross sections correspond to the sum of the reaction cross sections of abstraction (2a) and the H atom exchange reaction (2b). The results of these calculations allow for the first time a direct comparison with the experimental absolute reaction cross section recently measured for the abstraction and the hydrogen atom exchange channel. The latter results will be presented in Section 4.2 and 4.3, respectively.

3 The Pulsed Laser Photolysis / Laser Induced Fluorescence (LP/LIF) "pump-probe" Technique

Besides "hot" atom chemistry experiments in which highly translationally energetic reactants with broad, continuous energy distributions are generated by nuclear reactions[103], photolytic sources provide an alternative means of generating translationally excited atoms and free radicals for gas phase chemical reaction studies. Monochromatic UV photolysis of HX-type (X = Br, Cl, SH) precursor molecules, for example, can be employed to generate very fast H atoms with almost monoenergetic translational energy distributions which can, in principle, be used to probe the energy dependence of reactions. Although this method has been available for at least 3 decades its use in dynamics studies has been hampered by the fact that the experimental data such as product yields particularly when measured employing stable product analysis have to be corrected for effects of reagent moderating non-reactive collisions[104] and, depending on the reaction system under investigation, also for secondary chemical reactions. These problems can be avoided by the use of pulsed laser "pump-probe" techniques[105] in which a first UV photolysis laser "pump" pulse generates the translationally excited reagent by photolysis of an appropriate precursor compound and a briefly delayed second "probe" laser pulse monitors the reaction products. If optical detection techniques, like tunable dye laser induced fluorescence, are used for product detection high levels of internal quantum state resolution and, by employing polarized laser light, even a state-selective probe of product rotational alignment can be achieved[106]. A schematic description of the pulsed LP/LIF "pump-probe" method for dynamics studies of reaction (2a) is shown in Fig. 4 where H atoms are produced by UV photodissociation of HBr and the OD reaction products are detected by UV LIF with quantum-state resolution. With short "pump-probe" delay times (< 200 ns) and appropriately selected partial pressure conditions (p(HX) + p(H_2O) < 200mTorr) the dynamics of reactive collisions can be studied under effectively "single collision" conditions by avoiding significant moderation of the initial H atom translational energy distribution as well as the relaxation of the nascent internal vibrational

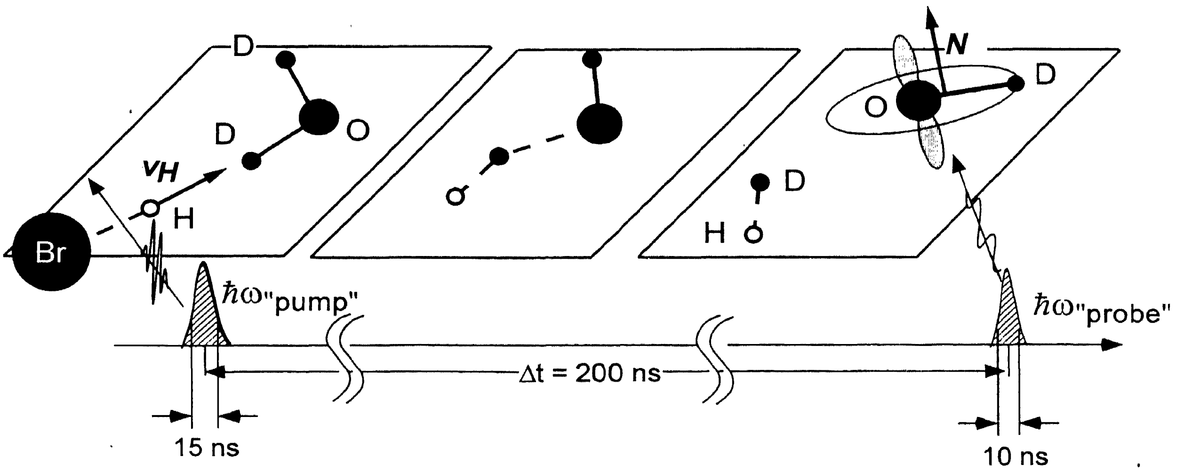

Fig. 4 Schematic description of the pulsed LP/LIF "pump-probe" method for state resolved molecular dynamics studies of the H + $D_2O \rightarrow OD(v, N) + HD$ abstraction reaction under single collision conditions.

and rotational fine-structure state distribution of the OD products.

3.1 *Experimental: H + H_2O/D_2O Reaction Dynamics Studies Employing OH/OD Product Detection*

A typical experimental arrangement for LP/LIF chemical dynamics studies of elementary gas-phase reactions under low-pressure laminar flow conditions is schematically depicted in Fig. 5[107]. In the dynamics studies reported in refs [37] and [40], translationally excited H atoms were generated by pulsed UV laser photolysis of HX-type precursors (X = HS, Cl, Br, I) which were flowed through the reactor together with the stable reagent (H_2O and D_2O, respectively) in order to avoid accumulation of reaction products. These experiments were carried out with room temperature H_2O and D_2O, at a total pressure of typically 40-120 mTorr with an HX:$H_2O(D_2O)$ reagent ratio between 1:5 and 1:10. With the precursor/photolysis wavelength combinations, H_2S/248 nm, HI/266 nm, HI/248 nm, H_2S/193 nm, HBr/193 nm, H atoms with well defined H–$H_2O(D_2O)$ center-of-mass frame collision energies ranging from $E_{c.m.} = 1.0$ eV up to $E_{c.m.} = 2.5$ eV could be obtained. Details about the dynamics experiments employing translationally excited H atoms in combination with vibrationally excited D_2O can be found in ref. [58].

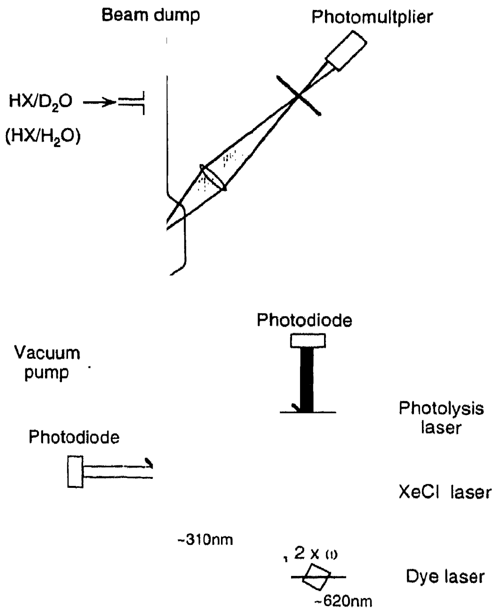

Fig. 5 Experimental apparatus used for molecular dynamics studies of the H + H_2O/D_2O reactions employing photolytically generated H atoms and quantum state resolved OH/OD product radical detection using LIF.

As depicted in Fig. 4, typically 60-150 ns after the photodissociation pulse (with a pulse duration of about 15 ns), nascent OH and OD product radicals were probed by a second copropagating UV laser beam by LIF using the 0-0 and 1-1 diagonal bands of the $A^2\Sigma^+ \leftarrow X^2\Pi$ system. The probe beam was provided by a frequency-doubled dye laser, pumped by a XeCl excimer laser and was tunable in the wavelength region 305–320 nm in order to scan OH and OD LIF excitation spectra. In Fig. 6, a LIF excitation spectrum of OD radicals produced in the reaction of energetic H atoms ($E_{c.m.} = 2.5$ eV) with D_2O is depicted. Each point in the LIF spectrum was obtained by averaging over 40 laser shots. By means of a computer program it was possible to divide the scanning region of the probe laser into "slow" and "fast" scanning regions. In the fast scanning region between the OD/OH transitions the probe laser was scanned with a wavelength tuning step size ten times larger than the step size in the region were transitions are located. From the LIF spectra OD/OH vibrational and rotational fine-structure state distributions were then obtained by numerical integration of the spectral lines and normalization with respect to the corresponding Einstein coefficients of absorption[109-110].

In order to derive absolute cross sections for the reaction under investigation the OH/OD LIF signals of the unknown OH/OD number densities produced in the reactive collision have to be calibrated against the LIF signals of well-known number densities of a reference reaction. In the original method introduced by Kleinermanns and Wolfrum[111], HNO_3 laser photolysis was utilized as a OH radical calibration source[36]. However, in subsequent studies[37] the better characterized UV photodissociation of H_2O_2 was employed. A detailed description of the actual calibration procedure for the measurement of absolute reactive cross sections for the reactions (1, 2a, 2c) is given in ref. [37].

3.2 *Experimental: H + D_2O → HOD + D Reaction Dynamics and Non-Equilibrium Kinetics Studies Employing H and D Atom Detection*

The H + D_2O reaction experiments employing

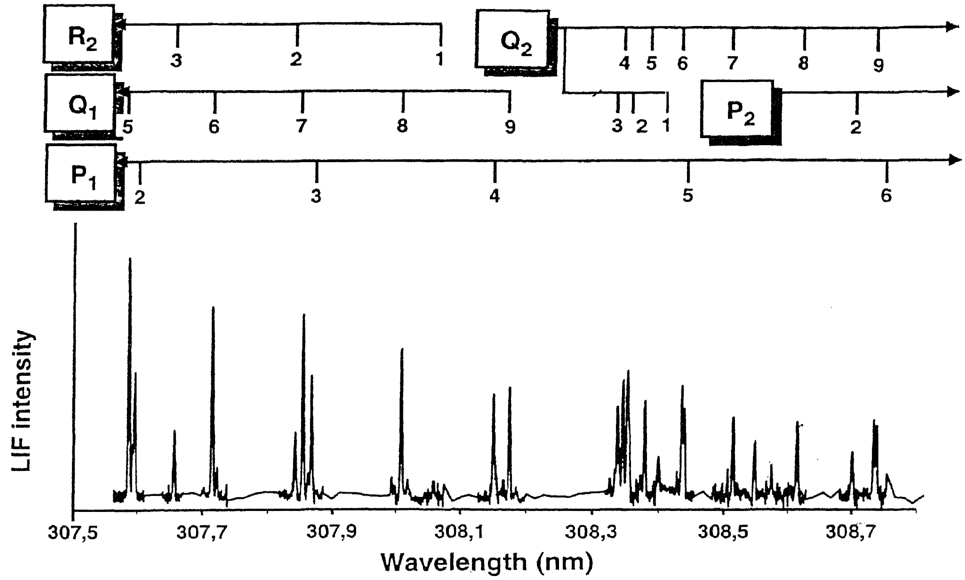

Fig. 6 Part of a LIF excitation spectrum recorded in the wavelength region 307.6-308.8 nm of the OD($A^2\Sigma^+$; v=0 ← $X^2\Pi$; v=0) transition recorded 150 ns after the pulsed laser photolysis of a flowing mixture of HBr and D_2O (HBr/D_2O ratio 1:5) at a total pressure of 120 mTorr. Only the main lines of the OD(A-X) transition are indicated.

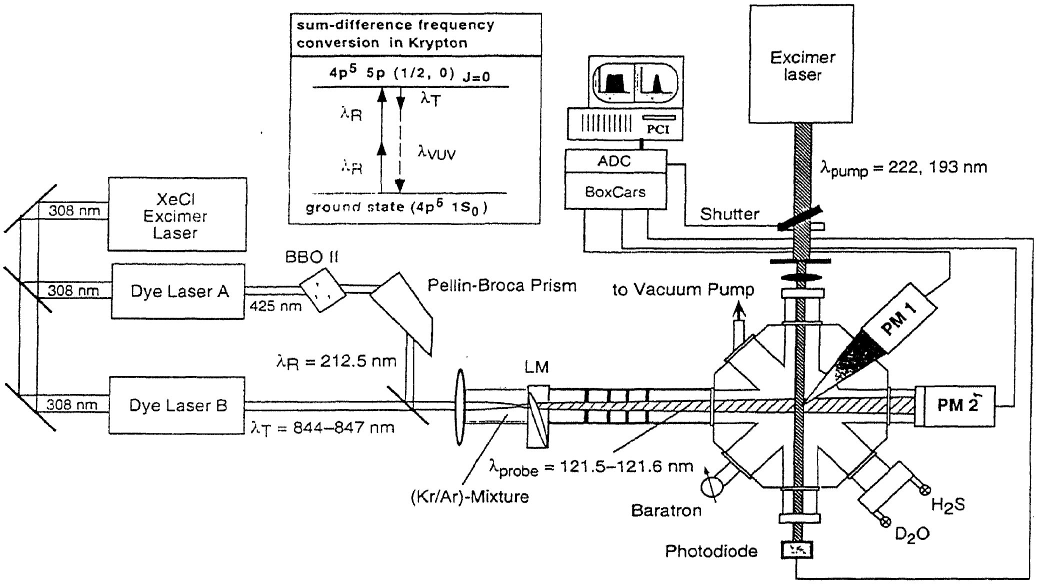

Fig. 7 Schematic description of the experimental apparatus used in the molecular dynamics and non-equilibrium kinetics studies of the H + D_2O → D + HOD exchange reaction. (LM: lens monochromator, PM: photomultiplier). The four-wave mixing scheme for generation of tunable VUV laser radiation in Kr for H and D atom LIF detection is shown in the inset.

H/D atom detection were carried out in a flow reactor with a modified design. Because of the need to directly connect the VUV generation cell to the flow reactor a crossed laser beams setup was chosen which is schematically shown in Fig. 7. During the measurements, H_2S/D_2O precursor/reagent mixtures (if necessary together with the moderator gas Ar) were continuously pumped through the reactor with a flow rate high enough to ensure renewal of the gas mixture between two successive photolysis laser shots. The flow rate of H_2S was regulated by a calibrated mass flow controller, the D_2O flow was regulated with a glass valve. The cell pressure was measured by a MKS Baratron. Translationally energetic H atoms with H-D_2O center-of-mass collision energies of $E_{c.m.}$ = 1.5 eV and 2.2 eV were generated by pulsed laser photolysis of H_2S at excimer laser wavelengths of 222 nm and 193 nm, respectively. H and D atoms were detected with sub-Doppler resolution via one-photon ($2p^2P \leftarrow 1s^2S$) VUV laser-induced fluorescence. Therefore, narrow-band ($\Delta\nu_{VUV} = 0.4$ cm^{-1}) VUV laser radiation, tunable around the H (121.567 nm) and D (121.534 nm) atom Lyman-α transitions, was generated using resonant third-order sum-difference frequency conversion ($\omega_{VUV} = 2\omega_R - \omega_T$) of pulsed dye laser radiation (pulse duration ~15 ns) in a phase-matched Kr-Ar mixture[112]. The fixed frequency ω_R ($\lambda_R = 212.55$ nm) was two-photon resonant with the Kr 4p-5p (1/2, 0) transitions and ω_T could be tuned from 844 nm to 848 nm in order to cover the H and D atom Lyman-α transitions. The generated Lyman-α light was carefully separated from unconverted laser radiation by a lens monochromator (LM in Fig. 7). The VUV probe beam was aligned to overlap the photolysis beam in the viewing region of a LIF detector. H and D atom LIF signals were measured through a band pass filter by a solar blind photomultiplier positioned at right angles to both the photolysis and probe lasers. Details about the background subtraction method used to remove small D atom signal contributions originating from D_2O photolysis by the probe laser are given in ref. [59]. The probe beam intensity was monitored behind the reaction cell with an additional photomultiplier. LIF signals, probe beam intensity and photolysis laser intensities were recorded and the LIF signal was normalized to both laser intensities.

(i) Single Collision Dynamics Studies of H + $D_2O \rightarrow HOD + D$

In the single collision absolute reaction cross section measurements, no moderator gas was used. Values for the H_2S:D_2O ratios were typically between 1:5 and 1:30. The experiments were carried out at a low total pressure of p_{tot} = 50–120 mTorr and at short pump-probe delay times of Δt = 80–180 ns to avoid translational relaxation of the energetic H atoms. For the reaction cross section measurements at energies $E_{c.m.}$ = 1.5 eV and 2.2 eV a method introduced by Bersohn and co-workers[113] for the measurement of absolute reaction cross sections for the H + $D_2 \rightarrow$ D + HD hydrogen exchange reaction was adapted. The absolute reactive cross section σ_R for the H + $D_2O \rightarrow$ D + HOD reaction can be determined using the following expression:

$$\sigma_R(E_{c.m.}) = S_D / (S_H\, \nu_{rel}\, [D_2O]\, \Delta t) \qquad \ldots (3)$$

ν_{rel} is the relative velocity which can be calculated from the corresponding center-of-mass collision energy ($E_{c.m.} = 1/2\ \mu\, \nu_{rel}^2$) of the reactants. μ represents the reduced mass of the H-D_2O collision pair. $E_{c.m.}$ and hence ν_{rel} can be calculated from the photolysis laser wavelength, the H–SH bond dissociation energy and the internal state distribution of the SH fragment[114]. Δt is the time delay between pump and probe laser pulses. [D_2O] denotes the gas-phase concentration of the D_2O reagent present in excess, which is therefore essentially constant. S_D and S_H are the integrated areas of the D and H atom Doppler profiles (see Fig. 8) which are a measure of the relative concentrations of the photolytically generated H atom reagent $[H]_{\Delta t=0}$ and the D atom reaction products $[D]_{\Delta t}$. Furthermore, the analysis of the measured D atom product Doppler profiles allows the determination of the fraction of the available energy released as D—HOD product translational energy.

(ii) Non-Equilibrium Kinetics Studies of H + $D_2O \rightarrow HOD + D$

The non-equilibrium experiments were carried out in an excess of Ar buffer gas which acts as a moderator of the energetic H atoms. In these experiments the total pressure was typically 1–5 Torr with a H_2S/D_2O partial pressure between 50 and 150 mTorr. The H_2S partial pressure was determined from the flow rates, while the D_2O partial pressure was measured using a photolytic calibration method similar to that used in ref. [115]. A number of test measurements were performed in order to find the most appropriate experimental conditions such as type of moderator gas, H_2S/D_2O ratios, and total pressure.

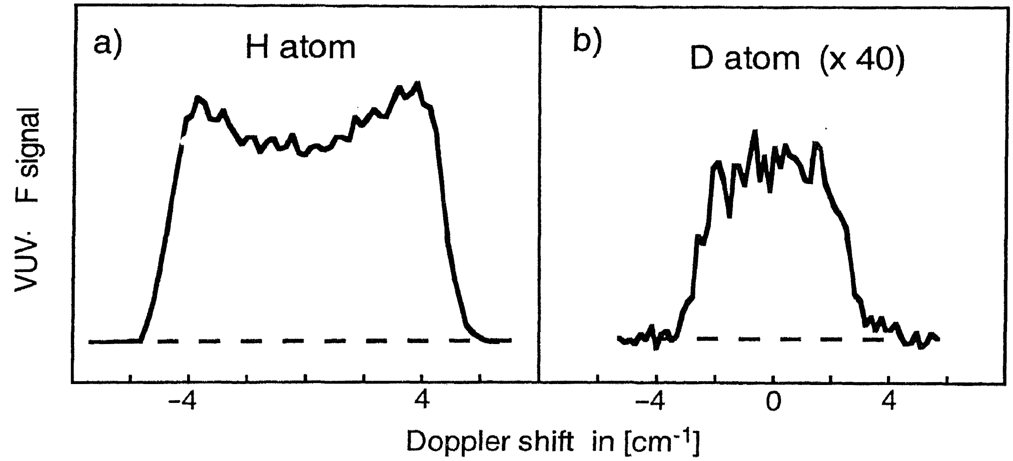

Fig. 8 H atom reagent and D atom product Doppler profiles as obtained in the single collision studies of the H + D$_2$O → D + HOD reaction. H atoms are generated via linearly polarized H$_2$S photolysis at 222 nm in the presence of 63 m Torr D$_2$O. The D atom products are probed at a delay time of 130 ns. The centers of the LIF spectra correspond to the Lyman-α transition of the H (82259.1cm^{-1}) and D atom (82281.4 cm^{-1}), respectively

When translationally hot H atoms are generated by pulsed laser photolysis of the H$_2$S precursor molecule in a large excess of a moderator gas, the initially present nascent non-equilibrium H atom velocity distribution evolves towards the thermal equilibrium distribution determined by the temperature of the moderator gas. In this case the velocity distribution of the H atoms has to be described by a time-dependent distribution function for which the time evolution is given by a linearized Boltzmann equation[116]. When, in addition, a reagent is present, reactive collisions occur in competition with the translational relaxation. The non-equilibrium kinetics of the formation of D atoms in the moderated hot H atom reaction H + D$_2$O → D + HOD are then described by the rate equation:

$$\frac{d[\mathrm{D}]_t}{dt} = \left\{ \int_0^{\infty} \sigma(v_{\mathrm{rel}}) v_{\mathrm{rel}} f(v_{\mathrm{rel}}, t) dv_{\mathrm{rel}} \right\} [H]_t [\mathrm{D_2O}] \qquad \dots (4)$$

Here it has been assumed that D$_2$O is present in excess over H atoms so that the D$_2$O concentration remains constant in time. The term in {...} braces represents the reaction rate constant which, under the translationally non-equilibrium conditions of the present experiments, is time-dependent. After replacing $[H]_t$ by $[H]_{t=0} - [D]_t$ and introducing the new variable $\chi_D(t) = [D]_t / [H]_{t=0}$, which represents the fractional yield of D atoms produced, eq. (5) can be obtained as a solution of eq. 4 for the initial condition $\chi_D(t = 0) = 0$.

$$\chi_{\mathrm{D}}(\Delta t) = [\mathrm{D_2O}] \times \int_0^{\Delta t} \left\{ \int_0^{\infty} \sigma_{\mathrm{R}}(v_{\mathrm{rel}}) v_{\mathrm{rel}} f(v_{\mathrm{rel}}, t) dv_{\mathrm{rel}} \right. \times (1 - \chi_{\mathrm{D}}(t)) dt \qquad \dots (5)$$

The delay time Δt between the pump laser pulse, which generates the H atom reagents, and the probe laser pulse, which detects the D atom products, corresponds to the reaction time. In order to perform the integration in eq. 5, one has to know the excitation function, i.e. the reaction cross section σ_R as a function of the relative velocity, as well as the time-dependence of the relative velocity distribution function $f(v_{rel},t)$. However, when $\chi_D(\Delta t)$ and $f(v_{rel},t)$ can be measured, information about the form of the excitation function can be obtained.

Using the LP/LIF technique described above allows the direct determination of both the D atom product yield $\chi_D(\Delta t)$ and the time dependent relative velocity distribution function $f(v_{rel},t)$. $\chi_D(\Delta t)$ is given by the ratio of the integrated areas of the D atom product measured at reaction time Δt (see e.g. Fig. 9c) and the nascent H atom reagent Doppler profile measured at a reaction time close

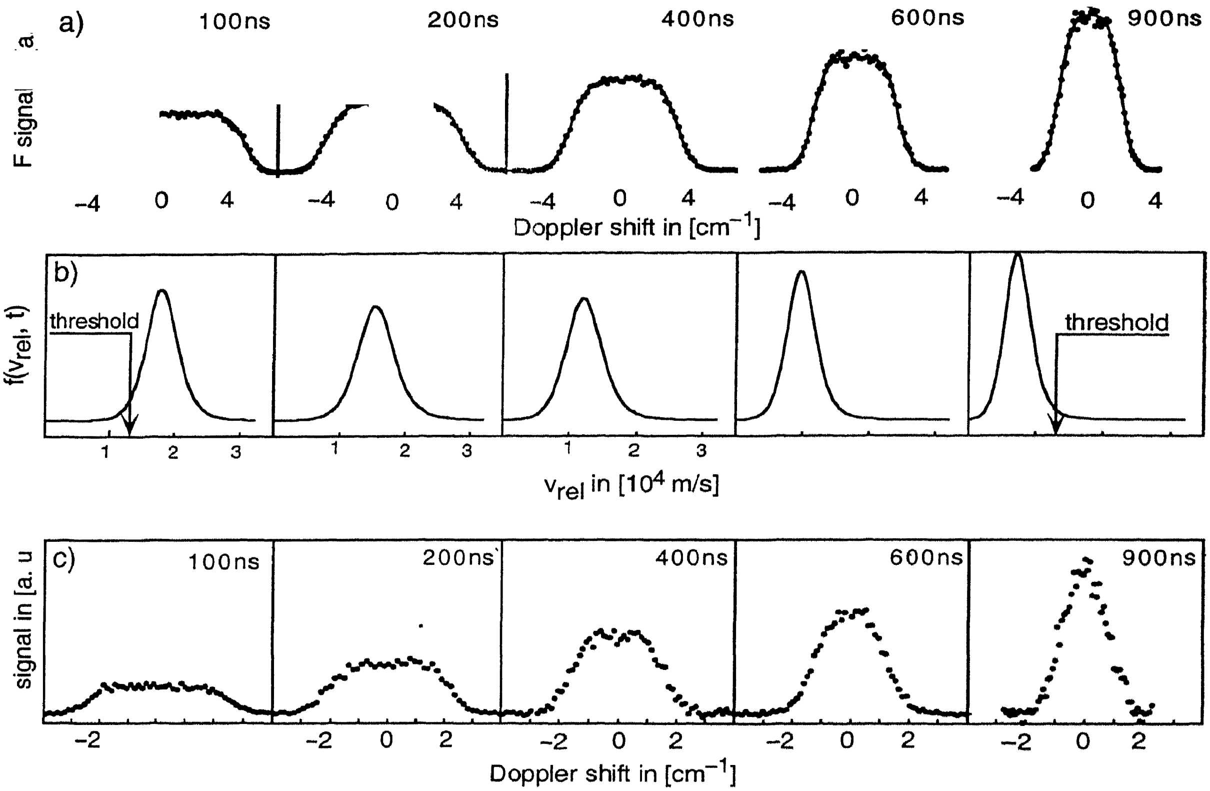

Fig. 9 (a) H atom Doppler profiles measured at different pump/probe delay times between 100 and 900 ns after 193 nm photolysis of H_2S in a flowing mixture of 120 mTorr D_2O and 1.4 Torr Ar. Solid lines are results of a fit to the time evolution of H atom laboratory velocity distribution $f(v_z,t)$ as described in the text. (B) Time evolution of the corresponding distribution function $f(v_{rel},t)$ of the H + D_2O reagents' relative velocity. The arrows mark the threshold for the H + D_2O → D + HOD reaction. (C) Doppler profiles of D atoms produced in the H + D_2O reaction.

to zero (before significant reaction could occur). Each H atom Doppler profile measured at a given time t (see Fig. 9a) reflects, *via* the linear Doppler shift $\nu - \nu_0 = v_z \nu_0 / c$, the laboratory frame distribution $f_H(v_z,t)$ of the velocity component v_z. Therefore the evaluation of H atom Doppler line shapes measured at different pump/probe delay times allows the time evolution of the v_z velocity component $f_H(v_z,t)$ to be derived. The time-dependent relative velocity distribution function $f(v_{rel},t)$ (shown in Fig. 9b) was obtained by differentiation of $f(v_z,t)$ followed by a laboratory to center-of-mass transformation[117]. Measured D atom product yields, $\chi_D(\Delta t)$, are shown in Fig. 10. The experimental data were analyzed by assuming for the excitation function the "line-of-centers"(LOC) function[1a].

$$\sigma_R(E+_{\text{c.m.}}) = \begin{cases} \sigma_0\left(1-\dfrac{E_0}{E_{\text{c.m.}}}\right) & \text{for } E_{\text{c.m.}} \geq E_0 \\ 0 & \text{for } E_{\text{c.m.}} < E_0 \end{cases} \quad \ldots (6)$$

The LOC function described by eq. (6) contains two parameters, the reaction threshold energy E_0 and σ_0 which represents the asymptotic value of the excitation function for $E_{\text{c.n}} \rightarrow \infty$. Using the time-dependent parameterization of the H atom speed distribution $f(v_{rel},t)$, D atom yields predicted by the LOC excitation function were calculated *via* eq. (5) for the conditions corresponding to each measured data point $\chi_D(\Delta t)$. In the data evaluation the integration of eq. (5) was performed using a fourth-order Runge-Kutta algorithm[118]. A measure

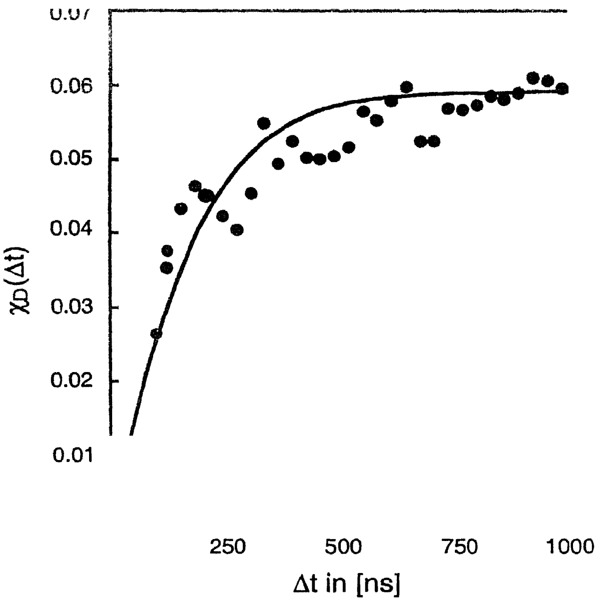

Fig. 10 Plot of the measured D atom product yield χ_D versus reaction time. Filled circles represent experimental data The solid line is the result of a simulation of the experimental moderation conditions using a "line-of-centers" LOC excitation functions $\sigma_R(E_{c.m.})$ for the H + $D_2O \rightarrow D + HOD$ reaction and the measured velocity distributions $f(v_{rel}, t)$. Details of the numerical modeling are given in the text.

of the quality of the two parameters E_0 and σ_0 could be obtained by computing the global mean squared deviation of the non-equilibrium kinetics data sets and the single collision cross sections from the corresponding values calculated from the LOC function. Optimization of the two LOC function parameters was performed by a non-linear least-squares fit procedure. With this method, optimized parameters $E_0 = 0.88 \pm 0.11$ eV and $\sigma_0 = 2.2 \pm 0.3$ a_0^2 (a_0 = 1 bohr = 0.529×10^{-10} m) were obtained (errors represent one standard deviation). The dashed line in Fig. 10 represents $\chi_D(\Delta t)$ calculated with the optimized LOC parameters.

4 Results and Discussion

4.1 *The Dynamics of the H + $H_2O \rightarrow OH + H_2$ Reaction*

The dependence of the rotational and vibrational excitation of the OH product formed in the reaction of H atoms with H_2O in the vibrational ground state has been studied in detail at different collision energies between 1.0 eV and 2.5 eV[31-33]. In these studies, it was found that even at the highest collision energies the OH products are formed almost exclusively in the vibrational ground state OH(ν = 0) with low rotational excitation (only between 12 and 4% of the total available energy appears as OH rotation).

The absence of OH product vibrational excitation was attributed to special features of the transition state geometry of the H atom abstraction reaction pathway (2a). Comparison of the OH bond length of the non-reaction OH bond at the H-HOH-transition state with the equilibrium values in the H_2O and OH molecules shows that the OH bond length is almost constant in going from the reagents through the transition state to the products[67]. As a result, the OH bond acts as a spectator during the reactive collision. In state selected experiments of reaction (1), Crim and co-workers could demonstrate that the vibrational excitation in the H_2O spectator bond is conserved as OH vibrational excitation. They found that the reaction H + $H_2O(|13\rangle^-)$ yields primarily OH in the (v=1)-state[14].

A number of different models have been proposed to rationalize the small rotational excitation of the OH product and the fact that the measured rotational distributions are rather insensitive to the collision energy. An impulsive model was suggested in ref. [29], in which the recoil of the H_2 product from the O atom *via* a bent transition-state configuration produces the torque leading to OH product rotational excitation. Within this model, the degree of OH rotational excitation is actually limited by the small mass of the departing H_2 fragment and the small "lever arm" given by the distance between the center of mass of the OH molecule and the O atom. In ref. [56], a stripping model was described, where OH rotational excitation is produced by simply mapping H_2O reagent zero-point bend excitation onto the OH product rotation. Calculations employing the more sophisticated AB-FC model of Bowman and Wang revealed that H-HOH transition state bending excitation of up to five quanta leads to generally cold OH rotational state distributions, as observed in the experiments for collision energies up to 2.5 eV, suggesting that only a small number of low-lying H-HOH bending states are excited during the reaction[89].

OH rotational and vibrational excitation observed in full-dimensional QCT calculations on the SE-PES was found to be in good agreement with the experimental results while the same calculations on the I5-PES lead to a considerable lower OH rotational excitation (in particular at low collision energies around 1 eV) than observed in the experiments[83]. Also, as far as the amount of energy released into OH + H_2 product translation is concerned, the QCT results for the SE-PES are closer to the experimental values than the results for the I5-PES[83]. At the lowest collision energy of the experiments ($E_{c.m.}$ = 1.0 eV), QMS calculations on the SE-PES employing the RBA approximation gave an OH rotational distribution in very good agreement with the experimental one[87a]. At higher collision energies (1.5 and 2.2 eV), however, the RBA-QMS calculations predict OH rotational distributions somewhat "colder" than the experimental ones (see Fig. 5-10 of ref. [87a]). On the other hand, recent 6D QMS calculations on the SE-PES gave OH distributions which are in good agreement with the experiments at higher energies[101]. In Fig. 11, the results of the 6D QMS calculations are compared with an experimental OH rotational distribution obtained at $E_{c.m.}$ = 1.8 eV. At this point it should be noted that so far both in the QCT and in the QMS studies the electronic orbital and the spin angular momentum of the OH($^2\Pi$) product radical has not been treated. Because of the interaction between the spin of the unpaired electron and the electronic angular momentum, every rotational state of the OH($^2\Pi$) radical is split into two spin-orbit states, $\Pi_{1/2}$ and $\Pi_{3/2}$. In the rotating molecule, due to the interaction of the electronic angular momentum and the rotational angular momentum, every spin-orbit state is further split into two Λ-components, $\Pi(A')$ and $\Pi(A'')$[46] Therefore for a given rotational angular momentum quantum number N the measured OH rotational fine-structure distribution was averaged over the two OH spin-orbit and the two Λ-components in order to allow for comparison with the QMS results as shown in Fig. 11. The OH(A′) states can be characterized by the π molecular orbital (which corresponds to the bond broken during reaction) being located in the plane of rotation. The electronic wavefunction of the $\Pi(A')$-states is symmetric with respect to the plane of rotation, while the electronic wavefunction of the $\Pi(A'')$-states is antisymmetric. Fig. 12 shows that the $\Pi(A')/\Pi(A'')$ population ratio derived from the fine-structure distribution measured at $E_{c.m.}$ = 1.5, 1.8 and 2.2 eV increases with increasing rotational quantum number as OH undergoes transition from Hund's coupling case (a) to coupling case (b). The orientation and symmetry of the OH π-orbital (as defined in the high-*J* limit) with respect to the plane of rotation is also depicted schematically for the two different Λ-components. As noted by Honda *et al.*[31], the preference population of the $\Pi(A')$ states at higher

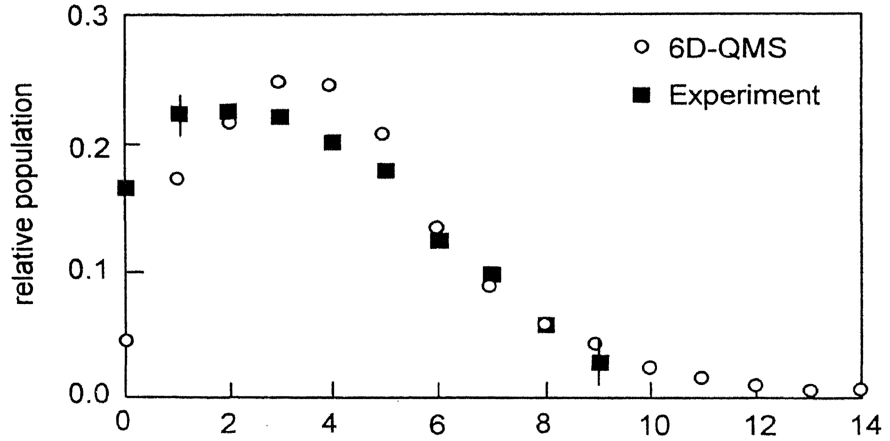

Fig. 11 Product rotational state distribution of OH(v=0) from the reaction H + $H_2O \rightarrow OH + H_2$ at a collision energy of 1.8 eV. Filled squares are experimental results from Ref. 37. The open circles are results from a full-dimensional (6D) quantum scattering calculation (ref. [100]).

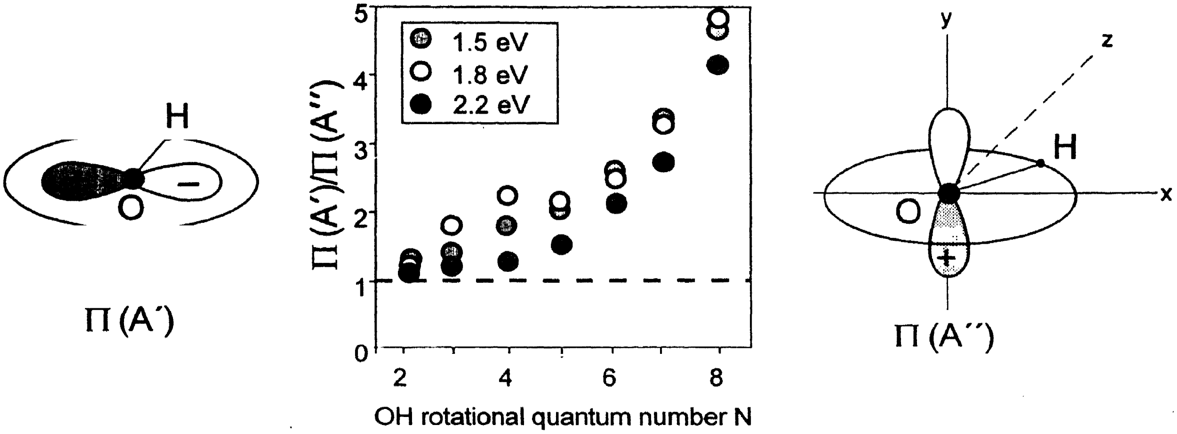

Fig. 12 Population ratio of the two Λ-components of OH radicals formed in the reaction H + $H_2O \rightarrow OH + H_2$ at different collision energies.

rotational quantum numbers is the result of a slightly higher rotational "temperature" of the Π(A′) Λ-component compared to that of the Π(A″) Λ-component[37] In addition, integration of the observed Π(A′)/Π(A″) ratio over the rotational states populated in the reaction indicates that the relative cross section for producing OH in the (A′)-state is significantly larger than the one for producing OH in the (A″)-state. This was explained in the framework of a classical model based on the analysis of the normal mode eigenvector of the imaginary frequency of the transition state of reaction (1) which shows that this mode is mainly an OH stretch[88]. In this picture the preference population of the OH(A′)-states in the reaction simply reflects that a perpendicular collision of H with H_2O (which would lead to OH in the A″-state) has less chance to couple with the O-H stretching in the transition state, which moves the system along the reaction coordinate. On the other hand, a planar approach has more chance to couple with the O-H stretching, leading to the higher cross section for OH formation with the unpaired orbital lobes in the plane of reagent approach (see Fig. 12). This interpretation is supported by the results of recent QCT calculations on the SE- and the I5-PES in which it was observed that in the energy region 1.0-2.2 eV two different types of collision mechanisms are operating[83]. One mechanism leads to backward scattered products arising from a "rebound" mechanism in which the incident H atom collides nearly collinearly with the H-O bond of the H_2O resulting in backward scattered H_2 products. Because of the almost collinear H-H-O approach, the transition state is nearly planar, the subsequent energy release to the OH products leads to rotational excitation in the plane of approach. In the second mechanism which leads to forward scattered products the incident H atom encounters one of the H atoms of the H_2O molecule and "drags" it into the forward direction. For the latter mechanism nonplanar geometries were found to be more important[83]. The results of the QCT calculations on the SE-PES indicate that at 1.4 eV the reactive cross section for planar collisions is about a factor of two higher than the cross section for the nonplanar ones[83]. This result is in reasonable agreement with the experimental results obtained at a slightly higher collision energy of 1.5 eV. At a collision energy of 2.2 eV, however, the QCT calculations predict that the planar and nonplanar reaction cross sections are about the same while the experiments at that energy (see Fig. 12) still show a clear preference for planar collisions.

Absolute reaction cross sections have been obtained in a number of QCT, RBA-QMS and exact QMS studies. A comparison between the experimental absolute reaction cross sections and QCT results obtained using the SE-[66,83], I5-[83], and the OC-surface[23] are depicted in Fig. 13. The theoretical cross sections denoted as QCT1(SE) in Fig. 13 were determined without any constrains

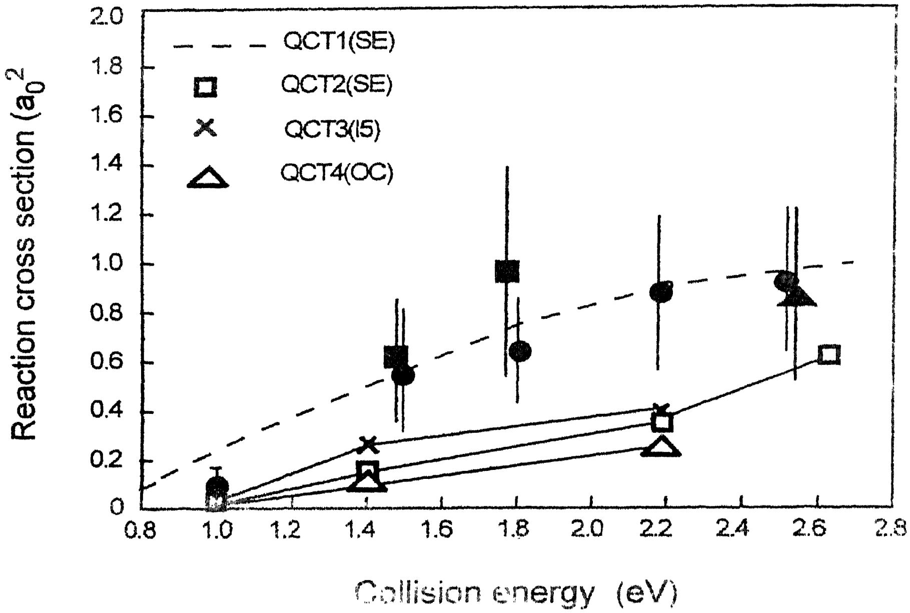

Fig. 13 Comparison of measured absolute reaction cross sections for the reaction $H + H_2O \rightarrow OH + H_2$ with results from QCT studies on different PESs as described in detail in the text. The filled triangle, squares, and circles are measured cross sections from refs. [29, 36 and 37].

regarding the zero point energy conservation[66]. The other QCT cross sections were obtained by putting an energy constrain on the H_2 product by rejecting in the calculation trajectories in which the H_2 molecule is formed with less than zero point energy. The OH product zero point energy was not constrained in these calculations, since OH is considered as a spectator during the reaction. Because the SE-PES allows reaction only for one of the H atoms in the H_2O molecule all cross section obtained on the SE-PES were multiplied by two. The I5-PES allows for reaction with either H atom of the H_2O molecule, however, it does not treat the H atoms "democratically". As a consequence two reaction pathways for reaction (1) exist with different barriers. In the calculation of the QCT3(I5) values only those trajectories associated with the reaction pathway which has the correct barrier were analyzed, and then the resulting cross sections were multiplied by two for comparison with experiment[83]. Finally most recent QCT results obtained using the OC-PES are included and denoted as QCT4(OC)[23]. The OC-PES describes the full symmetry of the reaction system and allows reaction with both H atoms of the H_2O molecule. As it can be seen in Fig. 13, the QCT results for the three different PESs are in reasonable agreement with each other when a zero point energy constrain is put on the H_2 product. However, this leads to absolute reaction cross sections which are markedly lower than the experimental ones. As noted in ref. [119], QCT calculations (on the SE-PES) in which trajectories are omitted when either product has less than zero point energy result in absolute cross sections which are a factor of 10 smaller than the experimental cross sections.

In Fig. 14, the experimental absolute reaction cross sections are compared with results of different quantum mechanical calculations. The values denoted as QMS-RBA (dashed lines in Fig. 14) are the results of scattering calculations on the SE-PES employing the RBA approximation[87b]. The index 1-3 refers to the three different methods applied to convert RBA cross sections into absolute reaction cross sections by taking into account *a posteriori* the degrees of freedom which are not treated explicitly in the scattering calculations. As it can be seen the values of the absolute reaction cross sections QMS-RBA (1-3) are quite sensitive to the assumed dynamics of the degrees of freedom not treated explicitly in the

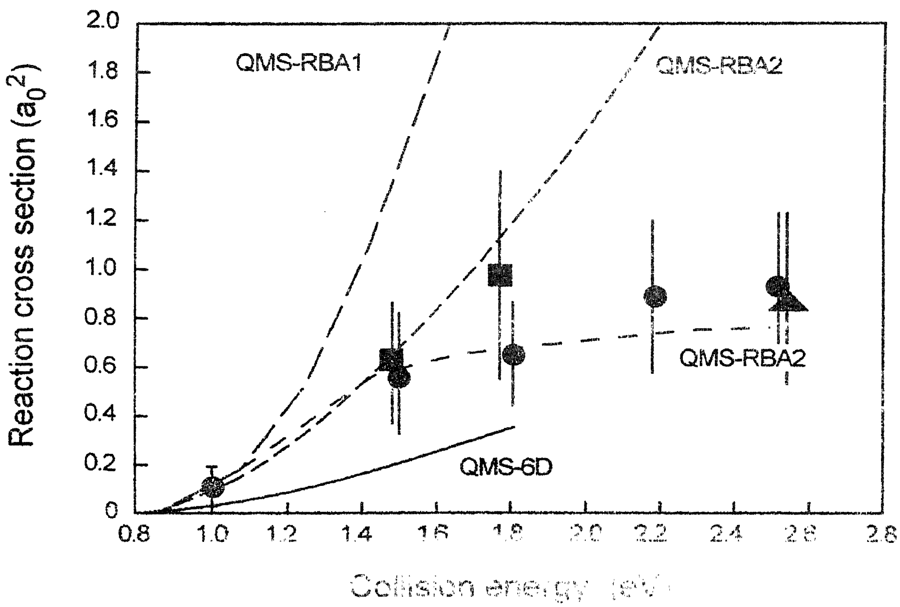

Fig. 14 Comparison of measured absolute reaction cross sections for the reaction H + $H_2O \rightarrow OH + H_2$ with results from QMS studies on the SE-PES. QMS-RBA(1-3) values were obtained employing the RBA approximation in combination with three different methods to correct for the degrees of freedom not explicitly treated in the scattering calculations (for details see text and Ref. 92b). QMS-6D are the results of a full-dimentional (6D) quantum mechanical calculation (ref. [100]). The filled triangle, squares, and circles are measured cross sections from refs. [29, 36 and 37].

RBA approximation (for details see ref. [87b]). The values denoted as QMS-6D represent absolute reaction cross section calculated in a full dimensional (6D) scattering calculation using the SE-PES[100]. The results of the accurate 6D calculations overlap with the experimental value at $E_{c.m.} = 1.0$ eV. At intermediate energies (around 1.5 eV) they are substantially lower than the experimental values. However, if extrapolated to higher energies agreement with experiment might be achieved at around 2.2 eV.

4.2 *The Dynamics of the H + $D_2O \rightarrow OD + HD$ ($OH + D_2$) reaction*

For the protonated reaction (1) the H atom abstraction pathway (H + $H_2O \rightarrow [H\text{-}HOH]^\ddagger \rightarrow OH + H_2$) cannot be directly distinguished from a H_3O complex forming (H + $H_2O \rightarrow [H_3O]^\ddagger \rightarrow OH + H_2$) mechanism. On the other hand, for the H + D_2O reaction the abstraction (H + $D_2O \rightarrow [H\text{-}DOD]^\ddagger \rightarrow OD + HD$) and complex forming pathway (H + $D_2O \rightarrow [HD_2O]^\ddagger \rightarrow OH + D$) can be investigated separately by detecting OD or OH product radicals.

For the abstraction reaction (2a), OD($^2\Pi$) product rotational state distribution were measured in the translational energy range $E_{c.m.} = 1.5\text{-}2.5$ eV by different groups[31,40,56,58]. As in case of reaction (1) within the experimental detection limit no vibrational excited OD radicals are formed in the reaction with vibrational ground state D_2O and the produced OD(v = 0) radicals exhibit little rotational excitation; only about 7-2% of the total available energy is actually channeled into the OD rotational degree of freedom. The analysis of the OD reaction product fine structure distributions revealed a similar preference for the population of the symmetric $\Pi(A')$ Λ-component as observed in reaction (1). Comparison of the OH and the OD rotational state distribution obtained in reaction (1) and (2a) indicates that at collision energies ≤ 2.2 eV OD radicals produced via (2a) are more rotationally excited than the OH radicals formed in reaction (1) (see Fig. 15)[32,58] At $E_{c.m.} = 2.2$ eV a value of $E_{rot}(OH)/E_{rot}(OD) = 0.7 \pm 0.2$ was obtained[40,32] while the opposite behavior, $E_{rot}(OH) > E_{rot}(OD)$, was observed at $E_{c.m.} = 2.5$ eV where a value of $E_{rot}(OH)/E_{rot}(OD) = 1.7 \pm 0.7$ was found[56]

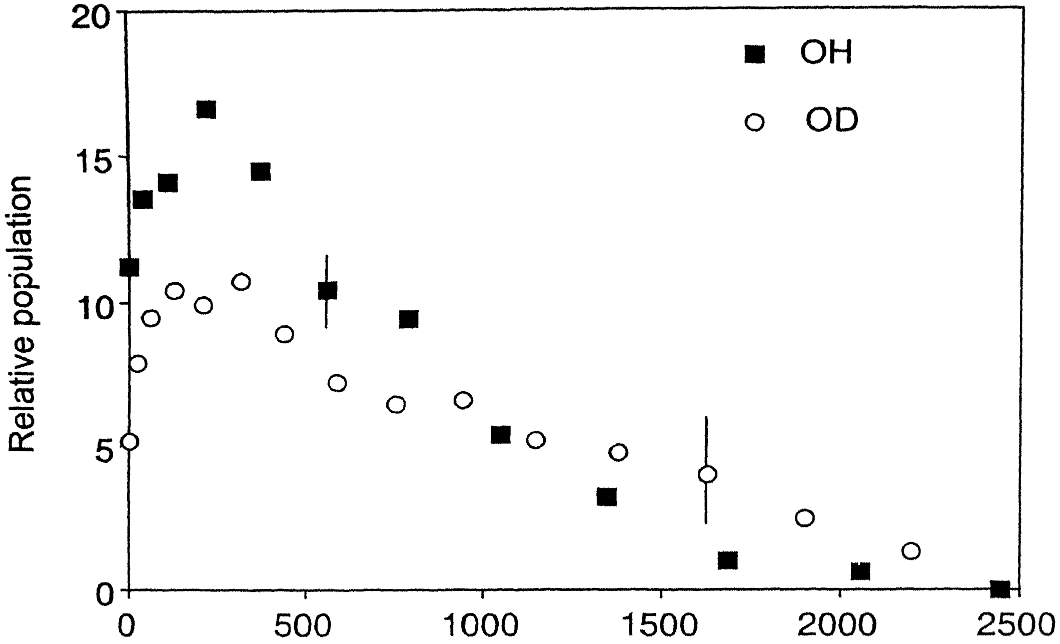

Fig. 15 Comparison between the measured OH (v=0) and OD(v=0) rotational state distributions from reaction (1) and reaction (2a) at a collision energy of 2.2 eV.

The experimental results are in line with results of QCT calculations on the SE-PES, which gave values of $E_{rot}(OH)/E_{rot}(OD) = 1.1$ and $E_{rot}(OH)/E_{rot}(OD) = 1.3$ for $E_{c.m.} = 2.5$ eV and $E_{c.m.} = 2.7$ eV, respectively[66]. As an explanation it was suggested that the reaction mechanism for the abstraction reaction pathway changes from an impulsive "rebound" mechanism at lower collision energies to a "stripping" mechanism at higher energies[40]. For the impulsive mechanism the torque produced by the H_2/HD molecule recoiling from the O atom determines the degree of OH/OD rotational excitation. Therefore one would expect — because the center of mass of the OD is about twice as far from the O atom as in case of OH — that the OD radicals from reaction (2a) have a higher degree of rotational excitation than the OH radicals from reaction (1) resulting in $E_{rot}(OH)/E_{rot}(OD) < 1$ as experimentally observed at lower energies. In a simple adiabatic stripping model OH/OD product rotational excitation is produced by mapping H_2O/D_2O reagent zero-point bend excitation onto OH/OD rotation and resulting in a collision energy independent value of $E_{rot}(OH)/E_{rot}(OD) = 1.4$ (corresponding to the ratio of the H_2O/D_2O reagent zero-point bending frequencies)[56]. Further evidence that the initial bending excitation of the H_2O/D_2O reagent determines the OH/OD product rotational energy was also found in vibrationally state-selected experiments of Crim and co-worker and Zare and co-workers who observed that H_2O/D_2O reagent bending excitation results in additional OH/OD product rotational excitation[14,15,,58]. Experimental studies focusing on the detection of the HD co-product carried out in the Zare group at a collision energy of approximately $E_{c.m.} = 2.7$ eV revealed that excitation of the HD internal degrees of freedom accounts for about 35% of the available energy[c] In these studies the rotational and vibrational state distributions of the HD products were determined and it was found that 25% of the available energy appears at HD rotational energy and 13% as HD vibrational energy. Based on the OD rotational excitation observed at $E_{c.m.} = 2.5$ eV (2%) it was estimated that 63% of the available energy is channeled into OD + HD product translational energy. An energy-constrained surprisal analysis of the HD internal state distributions indicated that the data cannot be reproduced by a statistical model as it is the case for the OD product state distributions, which could be described by rotational temperature[37]. The experimental results can be compared with results of QCT calculations on the SE-PES which predict 33% and 12% of the available energy to appear as HD rotational and vibrational energy, respectively (and 3% as OD rotational energy)[66]. However, a more detailed comparison based on the individual HD rotational state distributions of the probed HD (v = 0, 1, 2) vibrational states revealed significant discrepancies between the experiment and the QCT calculations[66].

Absolute reaction cross section measurement and OD/OH branching ratio measurements were carried out for reaction (2a) and (2c) in the collision energy range 1.0-2.5 ev[40]. From the measured OD/OH branching ratios an upper limit of 2×10^{-3} a_0^2 can be derived for the absolute reaction cross section of reaction (2c) which indicates that in H + D_2O the OH formation is only of minor importance. The latter results are in agreement with the results of the *ab initio* studies described in section (2) and earlier experimental studies of D_2 and HD formation rates, in which it was estimated that the room temperature rate of reaction (2c) is about 250 times lower than the rate of reaction (2a)[52].

The measured absolute reaction cross sections for the abstraction reaction (2a) are depicted in Fig. 16 and compared with results of QCT and QMS-RBA2 calculations on the SE-PES. As first noted by Honda *et al.*[30] at the same collision energy, the reaction cross section for reaction (2a) is considerably, smaller (about a factor of 2-2.5 in the range $E_{\text{c.m.}}$ = 1.5-2.5 eV) than the corresponding cross section for the protonated reaction (1). As can be seen in Fig. 16, the observed isotope effect on the reactivity could be qualitatively reproduced by the QCT and QMS-RBA2 calculations, although, it can be expected that the agreement between the absolute values of the QCT and the experimental cross sections would be much worth if the QCT calculations would have been analyzed with a product zero point energy constrain (see Fig. 13). As it has been observed for reaction (1) the inclusion of product zero point energy constrains in the QCT method

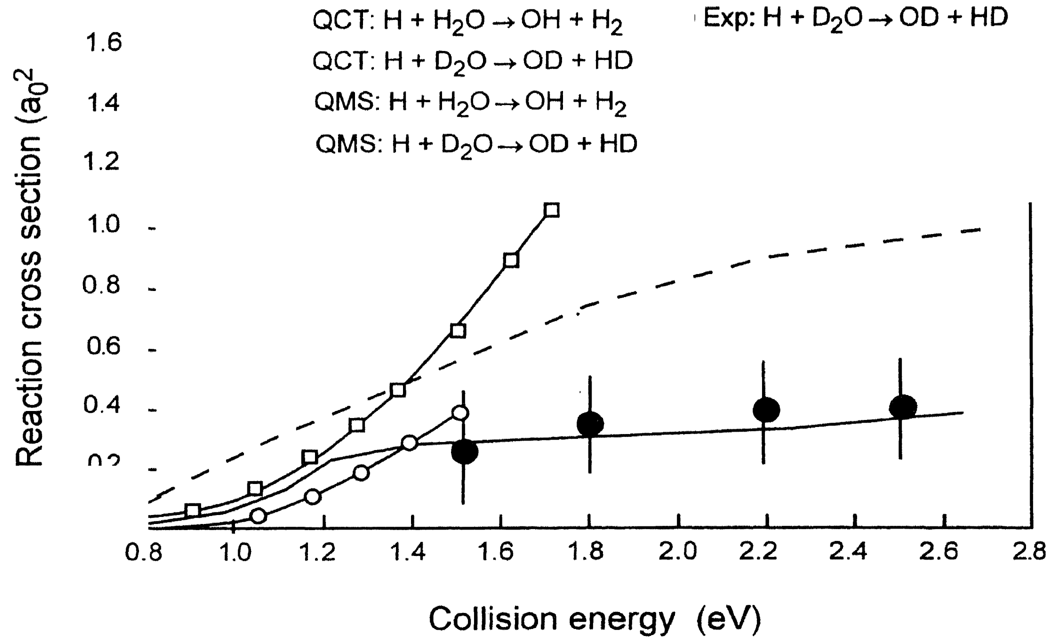

Fig. 16 Comparison of measured absolute reaction cross sections for the H + $D_2O \rightarrow$ OH + HD reaction with the results of QCT and QMS-RBA2 studies on the SE-PES. To illustrate the H/D isotope effect observed in the calculations, the corresponding QCT and QMS-RBA2 results obtained for the H + $H_2O \rightarrow$ OH + H_2 reaction (see Fig.14) are also depicted.

leads to a considerably smaller cross section which would bring the QCT results closer to the QMS-RBA2 values at energies below 1.2 eV. The QMS-RBA2 reaction cross section at $E_{\mathrm{c.m.}}$ = 1.5 eV agrees within the experimental error bar with the measured value. However, it can be expected that if the QMS-RBA2 calculations would be extended to higher collision energies the resulting cross section would be markedly higher than the experimental value as it is the case (see Fig. 14) for reaction (1).

State-to-state dynamics experiments carried out at $E_{\mathrm{c.m.}}$ = 1.5 eV showed that excitation of the asymmetric stretch fundamental (0,0,1) of the D_2O molecule[d] dramatically enhances the reactivity of the abstraction reaction compared to the vibrational ground state reaction[58]. This observation is in line with the model suggested in section 4.1 to explain the preferential population of the symmetric $\Pi(A')$ Λ-component in reaction (1). Stretch vibration channels energy into the motion along the reaction coordinate of the abstraction reaction pathway which, as a consequence, promotes this type of reaction. The excitation of the D_2O asymmetric stretch fundamental (0,0,1) corresponds to an energy increase of 0.35 eV which results in a 400% increase of the reaction cross section. In contrary, a comparison of the ground vibrational state cross sections at $E_{\mathrm{c.m.}}$ = 1.5 eV and $E_{\mathrm{c.m.}}$ = 1.8 eV (see Fig. 16) indicates that putting about the same amount of energy into the H + D_2O reagents relative translational coordinate increases the cross section only by about 40%. This behaviour is consistent with the general principle established by Polanyi and co-workers for the effects of translational versus vibrational excitation on the reaction cross section of endothermic atom-diatom reactions with a "late" reaction barrier[120].

4.3 *The Dynamics of the H + $D_2O \rightarrow$ D + HOD exchange reaction*

The first dynamics studies of the hydrogen atom exchange channel (2b) were carried out in our group at a collision energy of $E_{\mathrm{c.m.}}$ = 2.2 eV[59] These studies revealed that the exchange cross section, 1.3 ± 0.3 a_0^2, is markedly higher than the abstraction cross section of 0.4 ± 0.1 a_0^2 measured at the same collision energy[40]. The experimental observation is in qualitative agreement with results of QCT calculations on the SE-PES which yielded for the $H' + H_2O \rightarrow H + HOH'$ exchange reaction and the corresponding abstraction reaction (1) values of 2.3 a_0^2 and 0.9 a_0^2, respectively[66].

Further measurements of the excitation function and the reaction threshold were performed for reaction (2a) employing the moderated "hot" H atom technique described in section 3.2[60]. The experimentally obtained excitation function $\sigma_R(E_{\mathrm{c.m.}})$, together with absolute reaction cross section measured at two single-collision energies of 1.5 eV and 2.2 eV are depicted in Fig. 17. The reaction threshold energy, E_0 = 0.88 ± 0.11 eV, determined in these experiments is consistent with the activation energy of 0.83 ± 0.02 eV proposed by Bibler and Firestone[52]. Both experimental values are markedly higher than the barrier height of 0.406 eV associated with the exchange channel on the SE-PES[66]. The H_3O *ab initio* calculations described in section 2, on the other hand, yielded for the H atom exchange reaction barrier a value of 1.04 eV which is close to the upper limit of experimental value obtained in the non-equilibrium

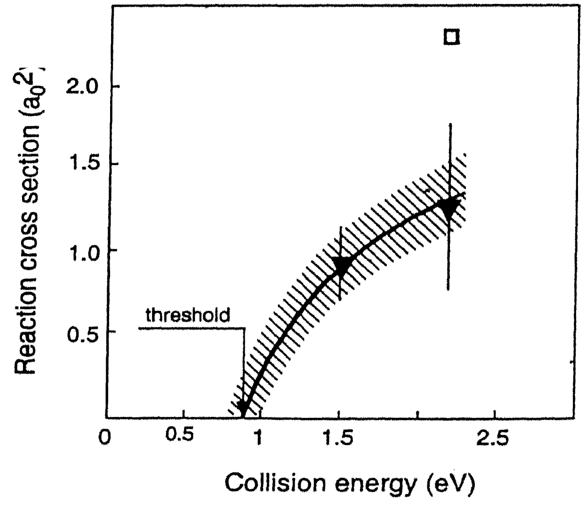

Fig. 17 Absolute reaction cross sections for the H + $D_2O \rightarrow$ D + HOD exchange reaction. Filled triangles are experimental single collision reaction cross sections reported in refs. [58 and 59]. The solid line is the excitation function $\sigma_R(E_{\mathrm{c.m.}})$ as derived in the non-equilibrium kinetics studies. The shaded area reflects the statistical uncertainty (1σ) of the global least squares-fit procedure used to determine the optimum excitation function (for details see text). For comparison the result of a QCT study on the SE-PES for the protonated exchange reaction $H' + H_2O \rightarrow H + HOH'$ is also depicted as an open square (ref. [66]).

kinetics measurements and only slightly higher than the barrier of the abstraction reaction on the SE-PES (0.923 eV).

In the single-collision reaction dynamics studies carried out at $E_{c.m.}$ = 1.5 eV and $E_{c.m.}$ = 2.2 eV it was found that 69 ± 11 % and 58 ± 9 % of the available energy appears as relative translational energy of the D + HOD products[59,60]. Both values are considerably higher than the statistical "prior" value[121] of about 30% calculated according to ref. [122]. This might indicate that the exchange reaction occurs by a direct mechanism rather than *via* formation of a long-lived HD_2O intermediate. Again it is possible to compare the experimental results with QCT calculations for the protonated exchange reaction $H' + H_2O \rightarrow H + HOH'$ on the SE-PES[66]. In the latter studies it was observed that at $E_{c.m.}$ = 2.2 eV, the H_2O internal excitation accounts for about 40% of the available energy leaving 60% for translational excitation of the H + HOH′ products. Although no properties of the H_3O exchange reaction region of the SE-PES were based on *ab initio* results (see section 2), comparison with the present experimental results (abstraction *versus* exchange cross section ratio and product translational energy release) suggests that the PES properties in the hydrogen exchange region might describe the dynamics, at least at high collision energies, reasonably well. Furthermore it can be expected that after adjusting the exchange reaction barrier to the higher *ab initio* value the QCT exchange reaction cross section will decrease, eventually leading to a more quantitative agreement with the measured exchange reaction cross section.

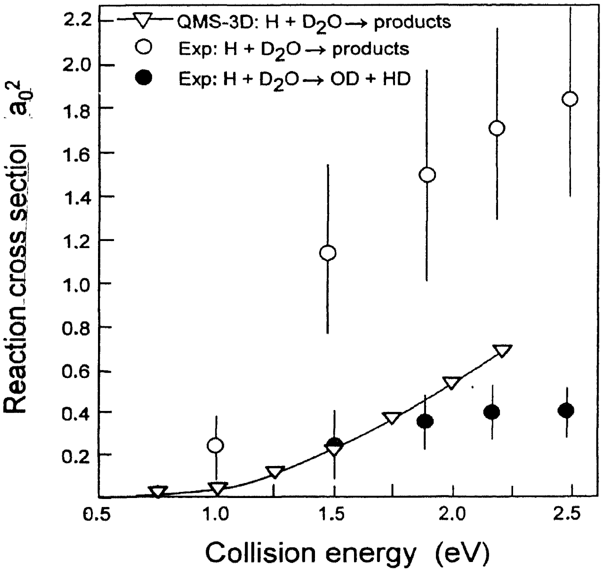

Fig. 18 Integral reaction cross sections (open triangles) for the H + $D_2O \rightarrow$ products reaction obtained in 3D QMS studies on the SE-PES (ref. [102]). For comparison the experimental values for the abstraction reaction (2a) are depicted as solid circles. The open circles correspond to the sum of the experimental cross sections of the abstraction reaction (2a) and the hydrogen exchange reaction (2b).

As described in section (2), most recently 3D QMS studies were performed employing the SE-PES in which integral cross sections, representing the sum of the reaction cross sections of the H atom abstraction and exchange reaction channels, were calculated for the H + H_2O and H + D_2O reactions. The theoretical results for the H + D_2O reaction are depicted in Fig. 18 and compared with experimental values obtained by summing up the measured reaction cross sections of reaction (2a) and (2b). In contradiction to what one would expect from the fact that the exchange reaction barrier on the SE-PES is much too low, the 3D QMS integral cross section are considerably smaller than the corresponding experimental integral cross section over the whole range of collision energies. A further comparison can be made between the 3D QMS integral cross sections of the H + $H_2O \rightarrow$ products reaction and the cross sections obtained in the 6D QMS studies for the H + $H_2O \rightarrow OH + H_2$ reaction[100]. As shown in Fig. 19 the 3D integral cross section are similar to the cross sections of the 6D abstraction cross section at energies below 1.5 eV indicating that in this energy region the 3D cross sections are dominated by the abstraction process. Only at energies above 1.2 eV contributions from the exchange reaction are clearly noticeable in the 3D calculations suggesting that the threshold for the exchange reaction is markedly higher than the threshold for the abstraction channel. Such a conclusion, however, would be in disagreement with the well-known topological properties of the SE-PES. On the other hand, there exists also the possibility that one of the approximations applied in the 3D QMS calculations could result in an artificially high exchange reaction threshold[102].

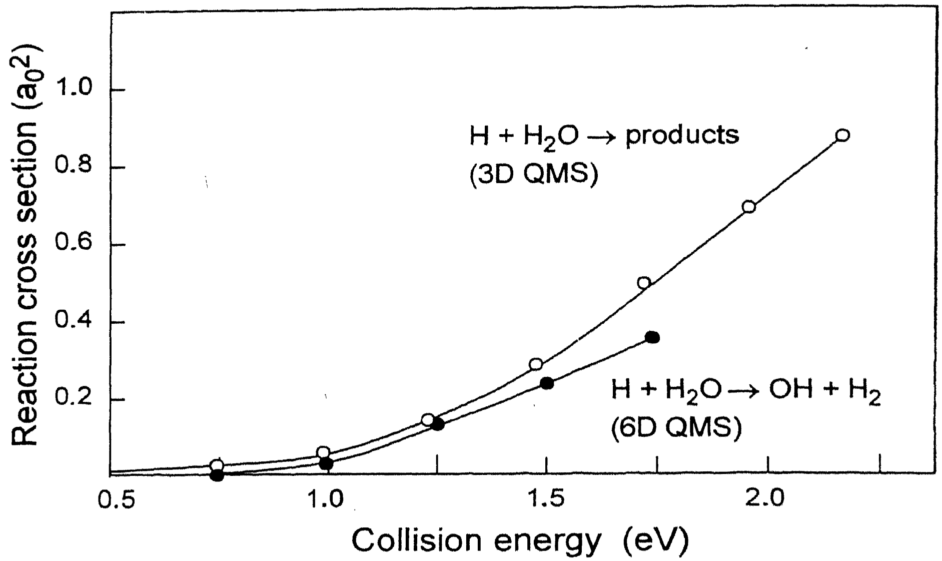

Fig. 19 Comparison between the 3D QMS integral reaction cross sections (ref. [102]) and 6D QMS cross sections for the H atom abstraction reaction (ref. [100]).

Fig. 20a-c describes schematically a typical planar H + D_2O collision leading to hydrogen atom exchange[102]. In the reagent approach geometry depicted in Fig. 20a the value of γ, the angle between the H atom velocity vector and the direction of the "reactive" D atom, corresponds approximately to the value for which the 3D QMS calculations suggest the highest reaction probability for hydrogen atom exchange at a collision energy of 2.2 eV (see Fig. 3b). Fig. 20b illustrates the structure of the exchange reaction transition state of the SE-PES[123]. Fig. 20c shows the geometry of the departing products taking into account that on the SE-PES only the $D^{(1)}$ atom can react. As can be inferred from Fig. 20 a-c the hydrogen exchange reactions requires considerable bending of the D_2O reagent on the way to the $[HD_2O]^{\ddagger}$ transitions state. As a consequence one can expect that fixing the D-O-D bending angle to the equilibrium value of the D_2O reagent (θ_e = 104°) as it has been done in the 3D QMS calculations would force the reaction system to take higher energies routes on the PES during the reactive collision. This in turn could result in an artificially high reaction threshold for the exchange pathway. At this point, it should be noted that it can be expected that the same approximation of fixing the D-O-D bending angle to the D_2O reagent

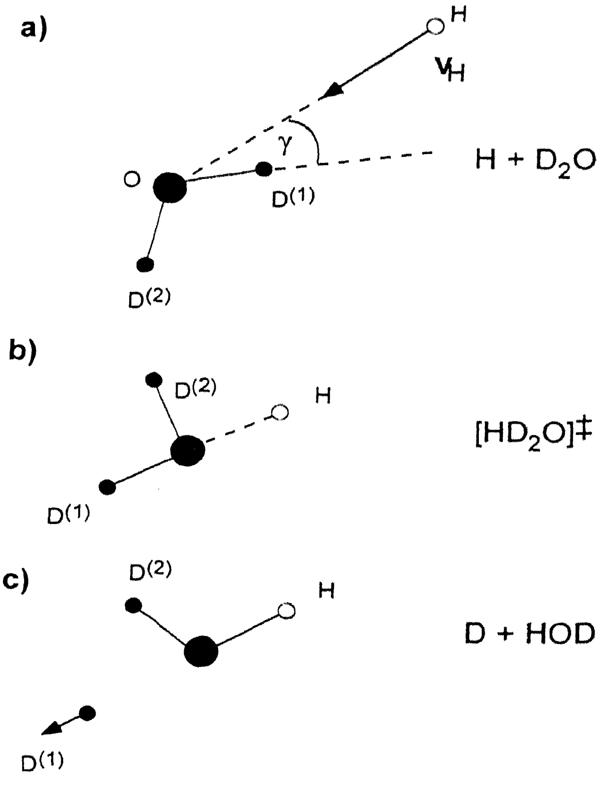

Fig. 20 Schematic description of H + D_2O reactive collision leading to hydrogen atom exchange (ref. [102]). Details are discussed in the text.

equilibrium value does not affect the abstraction reaction pathway, as this pathway does not involve major D-O-D bending motion in going from the reagents to the $[H\text{-}DOD]^{\ddagger}$ transition state. This in fact would explain the good agreement between the results of the 3D QMS and the 6D QMS calculations for the H + H_2O reaction at collision energies below 1.5 eV (see Fig. 19). However, for a more rigorous test of the global accuracy of the SE-PES and the approximations applied in the 3D QMS method[102] further full-dimensional QMS calculations preferably for the experimentally well-characterized H + D_2O reaction system are clearly needed.

5 Conclusions

This paper has reviewed and discussed recent results of experimental and theoretical molecular dynamics studies of the prototypical four-atom reactions H + H_2O and H + D_2O. On the experimental side the discussion has been confined to reaction dynamics studies carried out employing the pulsed LP/LIF "pump-probe" technique with a focus on recent results obtained for the H + D_2O reaction and its different product channels (2a-c). On the theoretical side, an attempt has been made to review recent work which has provided dynamical quantities for direct comparison with the H + D_2O experiments. The most noticeable result of this attempt seems to be that the multichannel nature of the H + H_2O and H + D_2O reactions has been largely neglected in the theoretical dynamics studies[g]. Although the necessary *ab initio* data for the hydrogen atom exchange pathway is available, no efforts were made so far to include this data into a global PES. Therefore the accuracy of the existing PESs reflects to a large extent the chemical intuition of the PES-designers rather than the achievements made in quantum chemistry. However, considering the exceptional role this reaction plays in the development of full-dimensional four-atom quantum scattering methods the necessity of a most accurate *ab initio* based multiple-product channel PES is obvious. The results of accurate full-dimensional QMS studies obtained on a carefully validated globally accurate PES can then serve as benchmarks for the development and test of approximate quantum scattering methods for the treatment of polyatomic reaction systems with multiple product channels.

6 Acknowledgements

Financial support of the Deutsche Forschungs gemeinschaft and the Sonderforschungsbereich 359 "Reaktive Strömung, Diffusion und Transport" is gratefully acknowledged. Thanks are due to R A Brownsword, T Laurent, M Hillenkamp, P Schmiechen, H P Upadhyaya, R K Vatsa, H-Y Yoo for their enthusiastic work in the laboratory. Discussions and communications with G.C. Schatz were very helpful. M Cameron and O Ohana are thanked for their help in the preparation of the manuscript.

Collaboration with M Baer and H Szichman (Soreq-Nuclear Research Centre, Yavne, Israel) and J P Mittal (Bhabha-Atomic Research Centre, Bombay, India) was supported by grant No. E1447 of the Bundesministerium für Bildung und Forschung (Germany) and by KFA Jülich and DLR Bonn under the Indo-German bilateral agreement (project No. INI-207), respectively. This article is dedicated to Professor Jürgen Wolfrum on the occasion of his 60th birthday and the author would like to thank Professor Jürgen Wolfrum in particular for his continuous support.

---

[g] One noticeable exception is the article by Marcus who discussed the dynamics of the $H+H_2O$ reaction system and its multiple arrangement channels employing global two-dimensional potential energy plots. (For details see ref. [124]).

References

1 R D Levine and R B Bernstein *Molecular Reaction Dynamics and Chemical Reactivity* Oxford University Press Oxford (1987); (b) G C Schatz *Annu Rev Phys Chem* **39** (1988) 317; (c) W H Miller *Annu Rev Phys Chem* **41** (1990) 245; (d) (Ed. J M Bowman) *Advances in Molecular Vibrations and Collision Dynamics* JAI Press Greenwich Conn **I, II** (1994); (e) Chemical Reaction Theory *Faraday Discussion* **110** (1998); (f) Chemical Reaction Theory *Phys Chem Chem Phys* **1** (1999) and references therein

2 F F Crim *J Phys Chem* **100** (1996) 12725; (b) M Alagia, N Balucani, P Casavecchia, D Stranges, G G Volpi, D C Clary, A Kliesch and H J Werner *Chem Phys* **207** (1996) 389 and references therein

3 J M Bowman and G C Schatz *Annu Rev Phys Chem* **46** (1985) 169 and references therein

4 D H Zhang and J C Light *J Chem Phys* **104** (1996) 4544

5 D Neuhauseer *J Chem Phys* **100** (1994) 9272; D H Zhang and J Z H Zhang *J Chem Phys* **101** (1994) 1146

6 J Warnatz, U Maas, R W Dibble *Combustion: Physical Chemical Fundamentals, Modeling and Simulation, Experiments, Pollutant Formation* Springer Heidelberg (1996); R P Wayne *Chemistry of Atmospheres* (2nd ed) Oxford University Press Oxford (1991), *Rate Coefficients in Astrochemistry* (Eds. T J Millar and D A Williams) Kluwer Dordrecht (1998); P Andresen *Astron Astrophys* **154** (1986) 42 and references therein

7 A A Westenberg and N DeHaas *J Chem Phys* **58** (1973) 4061; (b) R Zellner *J Phys Chem* **83** (1979) 18; (c) F P Tully and A R Ravishankara *J Phys Chem* **84** (1980) 3126; (d) A R Ravishankara, J M Nicovich, R L Thompson and F P Tully *J Phys Chem* **85** (1981) 2498; (e) P Frank and Th Just *Ber Bunsenges Phys Chem* **89** (1985) 181; (f) V Schmidt, G Y Zhu, K H Becker and E H Fink *Ber Bunsenges Phys Chem* **89** (1985) 321; (g) J V Michael and J W Sutherland *J Phys Chem* **92** (1988) 3853; (h) J V Michael *Advances in Chemical kinetics and dynamics* (Ed. J R Barker) JAI Press Inc Greenwich (1992); (i) R Atkinson, D L Baulch, R A Cox, R F Hampson, Jr., J A Ken and J Troe *J Phys Chem Ref Data* **21** (1992) 1125; (j) R C Oldenburg, G W Loge, D M Harradine, K R Winn *J Phys Chem* **96** (1992) 8426; (k) G Dixon-Lewis and D J Williams *Comprehensive Chemical Kinetics* **17** (1997) Elsevier Amsterdam and references therein

8 D L Baulch, C J Cobos, R A Cox, C Esser, P Frank, Th Just, J A Kerr, M J Pilling, J Troe, R W Walker and J Warnatz *J Phys Chem Ref Data* **21** (1992) 411

9 J R Fisher and J V Michael *J Phys Chem* 94 (1990) 2465; J V Michael *Isotope Effects in Gas-Phase Chemistry* (Ed. J A Kaye) Am Chem Soc Washington DC (1992)

10 R K Talukdar, T Gierczak, L Goldfarb, Y Rudich, B S Madhava Rao and A R Ravishankara *J Phys Chem* **100** (1996) 3037

11 R A Brownsword, M Hillenkamp, P Schmiechen, H R Volpp and J Wolfrum *Chem Phys Lett* **275** (1997) 325

12 D H Zhang and J Z H Zhang *Chem Phys Lett* **232** (1995) 370

13 M S Child and R T Lawton *Chem Phys Lett* **87** (1982) 217

14 A Sinha, M C Hsiao and F F Crim *J Chem Phys* **92** (1990) 6333; A Sinha *J Chem Phys* **94** (1990) 4391; F F Crim, A Sinha, M C Hsiao and J D Thoemke *Mode Selective Chemistry* **24** (Eds J Jortner, R D Levine and B Pulman) **24** Kluwer Academic Publishers **24** (1991) and references therein

15 M J Bronikowksi, W R Simpson, B Girard and R N Zare *J Chem Phys* **95** (1991) 8647; M J Bronikowski, W R Simpson and R N Zare *J Phys Chem* **97** (1993) 2194

16 A Sinha, M C Hsiao and F F Crim *J Chem Phys* **94** (1991) 4928; A Sinha, J D Thoemke and F F Crim *J Chem Phys* **96** (1992) 372; J M Pfeiffer, J D Thoemke, R B Metz, A Sinha, M C Hsiao, E Woods and F F Crim *Gas Phase Chemical Reaction Systems: Experiments and Models 100 Years after Max Bodenstein* Springer Series Chem Phys **61** (Eds. J Wolfrum, H R Volpp, R Rannacher, J Warnatz) Springer Heidelberg (1996) and references therein

17 G Hawthorne, P Sharkey and I W M Smith *J Chem Phys* **108** (1998) 4693

18 G C Schatz and G Lendvay *J Chem Phys* **106** (1997) 3548

19 L Polyansky, P Jensen and J Tennyson *J Chem Phys* **105** (1996) 6490

20 R Steckler, D G Truhlar and B C Garret *J Chem Phys* **82** (1985) 5499; G C Lynch, R Steckler, D W Schwenke, A J C Varandas and D G Truhlar *J Chem Phys* **94** (1991) 7136; S L Mielke, G C Lynch, D G Truhlar and D W Schwenke *Chem Phys Lett* **213** (1993) 10; *ibid.* **217** (1994) 173

21 G Lendway, K S Bradley and G C Schatz *J Chem Phys* **110** (1999) 2963

22 G Ochoa de Aspuru and D C Clary *J Phys Chem* **A102** (1998) 9631

23 G C Schatz, G Wu, G Lendvay, De-Cai Fang and L B Harding *Faraday Discussion* **113** (1999) (in press)

24 J E Spencer, H Endo and G P Glass *16th Intern Symp Combustion* The Combustion Institute Pittsburg PA (1977) 289

25 R Zellner and W Steinert *Chem Phys Lett* **81** (1981) 568

26 G P Glass and B K Chaturvedi *J Chem Phys* **75** (1981) 2749

27 E Pollak *Theory of Chemical Reaction Dynamics* (Ed. M Baer) CRC Press Boca Raton **3 (2)** (1985); D G Truhlar, A D Isaacson and B C Garrett *Theory of Chemical Reaction Dynamics* (Ed. M Baer) CRC Press Boca Raton **4 (2)** (1985)

28 I W M Smith *Advances in Gas-Phase Photochemistry and Kinetics: Bimolecular Collisions* (Eds. M N R Ashfold and J E Baggot) The Royal Society of Chemistry London (1989)

29 K Kleinermanns and J Wolfrum *Appl Phys* **B 34** (1984) 5

30 A Eckbreth *Laser Diagnostics for Combustion Temperature and Species* (2nd Ed) Gordon & Breach Amsterdam (1996), W Demtröder *Laser Spectroscopy - Basic Concepts and Instrumentation* (2nd Ed) Springer New York (1997)

31 K Honda, M Takayanagi, T Nishiya, H Ohoyama and I Hanazaki *Chem Phys Lett* **180** (1991) 321

32 A Jacobs, H -R Volpp and J Wolfrum *Chem Phys Lett* **218** (1994) 51

33 H -R Volpp and J Wolfrum *Workshop on Imaging Methods in Molecular Structure and Dynamics* The Weizmann Institute of Science Israel (1994)

34 M Brouard, I Burak, G A J Markillie, K McGrath and C Vallance *Chem Phys Lett* **281** (1997) 97

35 A Jacobs, H -R Volpp, J Wolfrum *24th Intern Symp on Combustion* The Combustion Institute Pittsburg PA (1992) 605

36 K Kessler and K Kleinermanns *Chem Phys Lett* **190** (1992) 145

37 A Jacobs, H -R Volpp and J Wolfrum *J Chem Phys* **100** (1994) 1936

38 C M Lovejoy, L Goldfarb and S R Leone *J Chem Phys* **96** (1992) 7180

39 P Wilhelms and B Brehm *Verhandl DPG (VI)* **34** (1999) 297

40 S Koppe, T Laurent, P D Naik, H -R Volpp and J Wolfrum *Can J Chem* **72** (1994) 615 (Special Issue honouring Prof. J C Polanyi)

41 M Alagia, N Balucani, P Casavecchia, D Stranges and G G Volpi *J Chem Phys* **98** (1993) 2459; *J Chem Soc Faraday Trans* **91** (1995) 575

42 D M Neumark *Robert A Welch Foundation 38th Conference on Chemical Research* (1994); E de Beer, E H Kim, D M Neumark, R F Gunion and W C Lineberger *J Chem Phys* **99** (1994) 13627

43 R A Loomis and M I Lester *J Chem Phys* **103** (1995) 4371

44 R A Loomis, R L Schwartz and M I Lester *J Chem Phys* **104** (1996) 6984

45 S M Miller, D C Clary, A Kliesch and H J Werner *Mol Phys* **83** (1994) 405

46 G Herzberg *Molecular Spectra and Molecular Structure* **1** Van Nostrand Princeton (1950)

47 M Shapiro and H Kaplan *J Chem Phys* **71** (1979) 2182; D P Dewangan and D R Flower *J Phys* **B14** (1981) 2179; *ibid.* **16** (1983) 2157

48 H Weaver, D R Williams, N H Dieter and W T Lim *Nature* **208** (1965) 29; M M Litvak *Ann Rev Astron Astrophys* **12** (1974) 97

49 P Andersen, D Häusler and H W Lülf *J Chem Phys* **81** (1984) 571; P Andresen, N Aristov, V Beushausen, D Häusler and H W Lülf *J Chem Phys* **95** (1991) 5763

50 K Schreel and J J ter Meulen *J Chem Phys* **105** (1996) 4522

51 J M Hossenlopp, D T Anderson, M W Todd and M I Lester *J Chem Phys* **109** (1998) 10707

52 N E Bibler and R F Firestone *J Phys Chem* **76** (1972) 621

53 E. Ratajczak and A F Trotman-Dickenson *Supplementary Tables of Bimolecular Gas Reactions* Office of Scientific and Technological Information University of Wales London (1970)

54 D Talbi and R Saxon *J Chem Phys* **91** (1989) 2376

55 G C Schatz and S P Walch *J Chem Phys* **72** (1980) 776

56 A Jacobs, H -R Volpp and J Wolfrum *Chem Phys Lett* **196** (1992) 249

57 D E Adelman, S V Filset and R N Zare *J Chem Phys* **98** (1993) 4636

58 M J Bronikowski, W R Simpson and R N Zare *J Phys Chem* **97** (1993) 2204

59 R A Brownsword, M Hillenkamp, T Laurent, R K Vatsa, H -R Volpp and J Wolfrum *Chem Phys Lett* **259** (1996) 375

60 R A Brownsword, M Hillenkamp, T Laurent, H -R Volpp, J Wolfrum, R K Vatsa and H-S Yoo *J Phys Chem* **A101 36** (1997) 6448 (*Special issue honouring Prof Y T Lee*)

61 T N Truong *J Chem Phys* **100** (1994) 8014; R Steckler, G M Thurman, J D Watss and R J Bartlett *J Chem Phys* **106** (1997) 3926 and references therein

62 T N Truong and T J Evans *J Phys Chem* **98** (1994) 9558

63 G C Schatz and H Elgersma *Chem Phys Lett* **73** (1980) 21

64 S P Walch and T H Dunning *J Chem Phys* **72** (1980) 1303

65 O Rashed and N J Brown *J Chem Phys* **82** (1985) 5506; (b) J A Harrison and H R Mayne *J Chem Phys* **88** (1988) 7424; (c) D C Clary *J Chem Phys* **95** (1991) 7298

66 K Kudla and G C Schatz *J Chem Phys* **98** (1993) 4644

67 A D Isaacson *J Phys Chem* **96** (1992) 531; A D Isaacson and S -H Hung *J Chem Phys* **101** (1994) 3928

68 E Kraka and T H Dunning (unpublished results); T H Dunnin, L B Harding and E Kraka *Supercomputer Algorithms for Reactivity, Dynamics and Kinetics of Small Molecules* (Ed. A Laganà) Kluver Dordrecht (1989)

69 A D Isaacson, *J Chem Phys* **107** (1997) 3832

70 M J T Jordan and M A Collins *J Chem Phys* **104** (1994) 460

71 J Ischtwan and M A Collins *J Chem Phys* **100** (1996) 8080

72 A Kliesch, H -J Werner and D C Clary (unpublished results) quoted in ref 2(b)

73 W J Griffiths, F M Harris and J H Beynon *Int J Mass Spectrum Ion Processes* **77** (1987) 233

74 K S E Niblacus, B O Roos and P E M Siegbahn *Chem Phys* **25** (1977) 207

75 M I Lester, R A Loomis, R L Schwartz and S P Walch *J Phys Chem* **101** (1997) 9195

76 A Kuppermann, Y M Wu *Chem Phys Lett* **205** (1993) 577; G D Billing and A Kuppermann *Chem Phys Lett* **294** (1998) 26

77 D R Yarkony *J Phys Chem* **100** (1996) 18612 and references therein

78 G C Schatz *J Chem Phys* **74** (1981) 1133; G C Schatz *J Chem Phys* **79** (1983) 5386

79 H Elgersma and G C Schatz *Int J Quant Chem Symp* **15** (1981) 611; G C Schatz, J L Colton and M C Grant *J Phys Chem* **88** (1984) 2971

80 T H Dunning, L B Harding, A F Wagner, G C Schatz and J Bowman *Science* **240** (1988) 453

81 K Kudla and G C Schatz *Chem Phys Lett* **193** (1992) 507; K S Bradley and George Schatz *J Phys Chem* **98** (1994) 3788

82 G C Schatz *J Phys Chem* **98** (1995) 10678

83 G C Bradley and G C Schatz *J Chem Phys* **108** (1998) 7994

84 G C Schatz, G Wu, G Lendvay, D -C Fang and L B Harding *Faraday Discussions* **113** (1999) (in press)

85 N Balakrishnan and G Billing *Chem Phys Lett* **233** (1994) 145

86 D C Clary *J Chem Phys* **95** (1991) 7298

87 D C Clary *J Chem Phys* **96** (1992) 3656; (b) G Nyman and D C Clary *J Chem Phys* **99** (1993) 7774

88 J Bowman and D Wang *J Chem Phys* **96** (1992) 7852; (b) D Wang and J Bowman *J Chem Phys* **96** (1992) 8906; (c) D Wang and J Bowman *J Chem Phys* **98** (1993) 6235

89 D Wang and J M Bowman *Chem Phys Lett* **207** (1993) 227

90 D Neuhauser and M Baer *J Chem Phys* **90** (1989) 4351

91 H Szichman, I Last, A Baram and M Baer *J Phys Chem* **97** (1993) 6436; H Szichman, E Last and M Baer *J Phys Chem* **98** (1994) 828

92 D C Clary *J Phys Chem* **98** (1994) 10678

93 J Echave and D C Clary *J Chem Phys* **100** (1994) 402

94 M Baer, H Szichman, E Rosenman, S Hochman-Kowal and A Persky *Gas Phase Chemical Reaction Systems: Experiments and Models 100 Years after Max Bodenstein* (Eds. J Wolfrum, H -R Volpp, R Rannacher and J Warnatz) Springer Series in Chemical Physics Springer Heidelberg **61** (1996)

95 D H Zhang and J Z H Zhang *J Chem Phys* **99** (1993) 5615

96 D H Zhang and J Z H Zhang *J Chem Phys* **100** (1994) 2679; *ibid. J Chem Phys* **101** (1994) 1146; W Zhu, J Dai, J Z H Zhang and D H Zhang *J Chem Phys* **105** (1996) 4881; D H Zhang and S Y Lee *J Chem Phys* **109** (1998) 2708

97 U Manthe, T Seideman and W H Miller *J Chem Phys* **99** (1993) 10078; U Manthe, T Seideman and W H Miller *J Chem Phys* **101** (1994) 4759

98 D Neuhauser *J Chem Phys* **100** (1994) 9272

99 D H Zhang, J C Light and S Y lee *J Chem Phys* **109** (1998) 79 and references therein

100 D H Zhang, J C Light *J Chem Phys* **104** (1996) 4544

101 D H Zhang, J C Light *J Chem Phys* **105** (1996) 1291

102 H Szichman, M Baer, H-R Volpp and J Wolfrum *J Chem Phys* **111** (1999) 567

103 L Szilard, T A Chalmers *Nature* **134** (1934) 462; H A Schwartz, R R Williams and W H Hamill *J Am Chem Soc* **74** (1952) 6007; R M Martin and J E Willard *J Chem Phys* **40** (1964) 3007

104 A Kuppermann *Isr J Chem* **7** (1969) 303

105 K Kleinermanns and J Wolfrum *Laser Chem* **2** (1983) 339

106 J P Simons *J Phys Chem* **91** (1987) 5378

107 J G Pruett and R N Zare *J Chem Phys* **64** (1976) 1774

108 G H Dieke and H M Crosswhite *J Quant Spectr Rad Transf* 2 (1962) 97

109 I L Chidsey, D R Crosley *J Quant Spectr Rad Transf* **23** (1980) 23

110 W L Dimfl and J L Kinsey *J Quant Spectr Rad Transf* **21** (1979) 233

111 K Kleinermanns and J Wolfrum *Chem Phys* **80** (1984) 1446

112 G Hilber, A Lago and R Wallenstein *J Opt Soc Am* **B4** (1987) 1753

113 G W Johnston, B Katz, K Tsukiyama and R Bersohn *J Phys Chem* **91** (1987) 5445

114 G N A van Veen, K A Mohamed, T Baller and A E de Vries *Chem Phys* **74** (1983) 261

115 R A Brownsword, M Hillenkamp, T Laurent, R K Vatsa and H -R Volpp *J Chem Phys* **106** (1997) 9563

116 J Park, N Shafer, R Bersohn *J Chem Phys* **91** (1989) 7861

117 W J v D Zande, R Zhang, R N Zare, K G McKendrick and J J Valentini *J Phys Chem* **95** (1991) 8205

118 C W H Press, B P Flannery, S A Teukolsky and W T Vetterling *Numerical Recipes in C* Cambridge University Press Cambridge (1988)

119 K Kudla and G C Schatz *Chem Phys* **175** (1993) 71

120 J C Polanyi and W H Wong *J Chem Phys* **51** (1969) 1439; M H Mok and J C Polanyi *J Chem Phys* **51** (1969) 1451; M H Mok and J C Polanyi *J Chem Phys* **53** (1970) 4588

121 R D Levine and J L Kinsey *Atom-Molecule Collision Theory - A Guide for the Experimentalist* (Ed. R B Bernstein) Plenum Press New York (1979)

122 J T Muckermann *J Phys Chem* **93** (1989) 180

123 G C Schatz (Private communication)

124 R A Marcus *J Phys Chem* **95** (1991) 8236

INVESTIGATION AND CONTROL OF PHOTODISSOCIATION DYNAMICS: AN OVERVIEW

VANDANA K† AND MANOJ K MISHRA

Department of Chemistry, Indian Institute of Technology Bombay, Powai, Mumbai 400 076 (India)

This review summarizes recent progress in development of theoretical and experimental approaches towards the use of lasers for selective and controlled dissociation of bonds. The Field Optimized Initial State (FOIST) based approach developed recently provides a syncretistic advance allowing for an optimal interplay between the field parameters and molecular initial state and serves as the principal source of illustrative examples in this review. Application of FOIST to IBr and HI photodissociation reveals that the dream of harnessing lasers for selective control of photodissociation may be pursued in a new and promising manner, permitting selective control without recourse to high intensity ultrafast lasers. The Raman Excitation Profiles (REP) are shown to offer a very detailed description of photodissociation dynamics.

Key Words: Photodissociation; Selective Control; Flux Maximization; Branching Ratio; Raman Excitation Profile

1 Introduction

Photodissociation involves breaking of a bound molecule by the absorption of photons. The energy absorbed is converted into internal energy of the molecule and if the energy exceeds the binding energy of the weakest bond, then the bond breaks irreversibly. Photodissociation being at the core of photochemistry, is a vehicle for some of the most critical chain reactions, and new technologies like the ozone cycle and chemical lasers respectively. Detailed discussion of these established aspects appear in many text books[1]. Apart from these crucial roles, photodissociation of small polyatomic molecules provides information on state to state molecular dynamics involving energy transfer between various molecular modes, breaking and creation of chemical bonds and transition between different electronic states. A comprehensive description of these features has been presented in an excellent textbook by Schinke[2]. Analysis of photodissociation dynamics has also led to an attempt to use photons to alter the underlying quantum effects[3-20] to selectively control the product formation in photodissociation reactions and a review of the recent trends in this exciting new area is the basic purpose of this review.

Initial attempts to steer the reaction path towards the desired product were based on manipulation of macroscopic thermodynamic parameters such as temperature, pressure and concentration or use of appropriate catalysts. However, in most cases, this has not afforded the desired selectivity. It has been realized that in almost all reactions except those involving some small molecules, the locally deposited energy rapidly redistributes itself throughout the molecule, destroying the selectivity of bond cleavage. The rate of intramolecular vibrational redistribution is often greater than the reaction rates and the energy reshuffles statistically within the molecular bonds[21]. In molecules such as CF_3Br for example, dissociation of the C-Br bond using laser tuned to this frequency is possible but the cleavage of the C-F bond by a laser in tune with the frequency is not possible due to the coupling of C-F stretch with other vibrational modes; dissociation occurs in a statistical manner and the weaker C-Br bond is cleaved first[22].

Recent advances in laser chemistry have initiated the dream of using ultrashort high intensity laser pulses as molecular scissors for cleaving bonds selectively and has received considerable attention as a potent route for achieving product selectivity in chemical reactions[21-24]. Recognition of the fact that the short and intense laser pulses could be used for product selectivity in chemical reactions has contributed quite substantially to the development of lasers and vice-versa. The possibility that the unique characteristics of the laser radiation can be exploited to improve the selectivity of product formation in a chemical reaction has stimulated the implementation and testing of many schemes[3-20]. Theoretical and experimental work in this area has burgeoned in many different directions and offers the possibility of selective product formation by controlling the underlying quantum dynamics through the use of appropriately designed lasers. Experimental success using these approaches have also begun to appear recently[25-28].

---

†CSIR Senior Research Fellow

In keeping with the experimental advances, theoretical treatments have kept pace by advocating novel approaches which explicitly incorporate optimization of various filed parameters and the initial states involved. The pump and dump[6-7], coherent control[8-14,26-29] and optimal control[12] methods emphasize field design to achieve the desired control objectives and have been reviewed extensively[3,7,9-12]. The product yield has also been shown to depend critically on the molecular initial state[15] and a new scheme based on shaping a Field Optimized Initial State (FOIST)[16-20] for the chosen field and desired photodissociation objective has been pursued in our group. Examples from our use of FOIST will anchor discussions illustrating salient features of investigation and control of photodissociation dynamics and shall be the principal focus of this review.

Rest of this review is organized as follows. Selective control as flux maximization in the desired channel is considered in Section 2. It will be seen that the selective control of photodissociation may be achieved by altering the field parameters or by optimizing the initial state. The control schemes utilizing field design are discussed first and since these have been reviewed extensively only recently[3] our presentation of these schemes will be skeletal and we follow the chronology of developments in this area with Pump and Dump, Coherent Control and Optimal Control being reviewed in this order in section 3. In Section 4, we shall present our FOIST based control scheme and a detailed analysis of its results. Raman Excitation Profiles (REP) provide a very detailed and sensitive probe of photodissociation dynamics and their use to probe IBr photodissociation and validation of the three state IBr model will be taken up in Section 5. Finally, a summary of main results in Section 6 concludes this review.

2 Product Yield as Time Integrated Flux

At its simplest, selective control of photodissociation involving a single bond may be presented schematically as

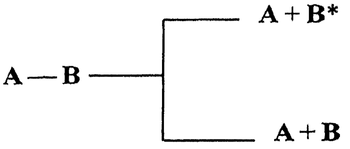

and the underlying photodynamics is portrayed in Fig. 1.

Provided the transition dipole moment μ_{01} between the ground (0) and the first excited (1) electronic states is nonzero, using a laser of sufficient power and appropriate frequency, the molecule AB in the ground vibrational level of the ground electronic state can be excited to the electronic state 1, whereby, the probability density begins to flow down the repulsive potential energy curve 1 and on encountering the crossing point between curves 1 and 2 will flow into both the A+B and the A+B* channels. This flow of probability density ρ is governed by the continuity equation.

$$\frac{\partial \rho}{\partial t} + \bar{\nabla}.\bar{j} = 0$$

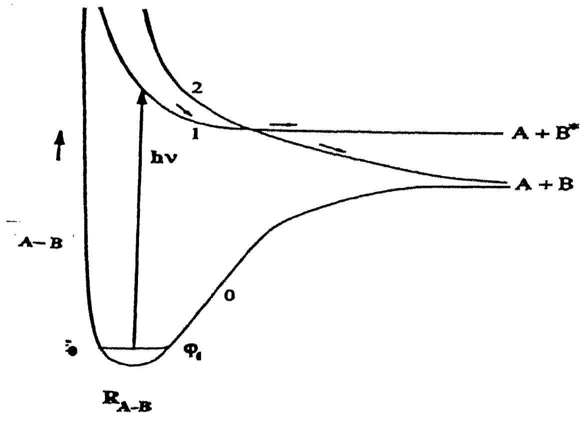

Fig. 1 Multiproduct photodissociation in simple curve crossing reactions. ϕ_0 represents the ground vibrational level and ε_0, the corresponding energy.

and is monitored by measuring the flux $\vec{j}$ in these channels at a suitable asymptotic point in the dissociative limit of the potential energy curves 1 and 2. Selective control of products **A+B** or **A+B*** may therefore be achieved by designing techniques to selectively maximize time integrated flux in these competing channels.

Defining the time integrated flux operator $\hat{F}$ as

$$\hat{F} = \int_0^T dt U^{\dagger} \hat{j} \hat{U}(t,0), \quad \hat{j} = \frac{1}{2m} [\hat{p}\delta(r - r_d) + \delta(r - r_d)\hat{p}] \quad \dots (1)$$

with m as the reduced mass, $\hat{p}$ the momentum operator along the reaction coordinate and r_d the grid point in the asymptotic region where the flux is evaluated, the time-integrated flux,

$$\int_0^T dt < \hat{j} >_t = \int_0^T dt < \psi(t) | \hat{j} | \psi(t)$$

$$= \int_0^T dt < \psi(0) | \hat{U}^{\dagger}(t,0) \hat{j} \hat{U}(t,0) | \psi(0) > \dots (2)$$

$$\text{or} \quad \int_0^T dt < \hat{j} >_t = < \psi(0) | \hat{F} | \psi(0) >, \quad \dots (3)$$

represents the product yield and as seen in eq. (3) may be controlled by altering the field dependent part $\hat{U}(t,0)$ of $\hat{F}$ where $U(t,0) \approx e^{-iHt/\hbar}; H = H_0 + \vec{\mu}.\vec{E}(t)$ with $\vec{E}(t)$ representing the oscillatory electromagnetic field or by altering the field free initial state $\psi(0)$. In the case of more than one possible dissociation channel, the operator $\hat{j}$ is channel specific and in a discrete representation of the electronic curves on a spatial grid, r_d denotes the grid point appropriate to the desired channel. The more established control schemes like the Pump and Dump, Coherent Control and the Optimal Control are based on altering F i.e field design and are presented briefly in the following section.

3 Selective Control Using Field Design

As can be seen from eq. (2) the product yield in different channels may be controlled by manipulating the initial state evolution through alteration in field attributes which affect $\hat{F}$ or by altering the initial state $\psi(0)$. The earlier schemes for selective control were based on optimizing field attributes to achieve the desired photodissociation objective and are discussed below.

3.1 Pump and Dump Scheme

Tannor and Rice[6] showed that the selectivity of product formation can be induced by shaping and spacing pump and dump laser pulses. A first laser pulse transfers amplitude from the ground state to the excited potential energy surface. The wavepacket formed on the excited potential energy surface is a linear combination of vibrational states and evolves spatially and temporally. The wave packet on the repulsive excited state being non-stationary, a part of it will evolve on the surface and the rest of it may be dumped back to the ground state in such a way that amplitude preferentially emerges, eventually in the particular desired channel.

This scheme utilizes the excited electronic state to mediate the reaction on the ground electronic state potential energy surface. The stereoscopic view of the ground and excited state potential energy surfaces are shown in Fig. 2 where the arrows show, the amplitude transfers associated with the pump and the dump pulses. As an illustration of this scheme, we may consider a molecule ABC which undergoes fragmentation to produce ABC→BC + A and ABC→AB+C on the ground state potential energy surface. At $t=0$, the system is assumed to be in the ground state. The solution of the Schrödinger equation can be represented by two coupled integral equations for the amplitudes in the ground and the excited state potential energy surfaces and to second order in perturbation[6].

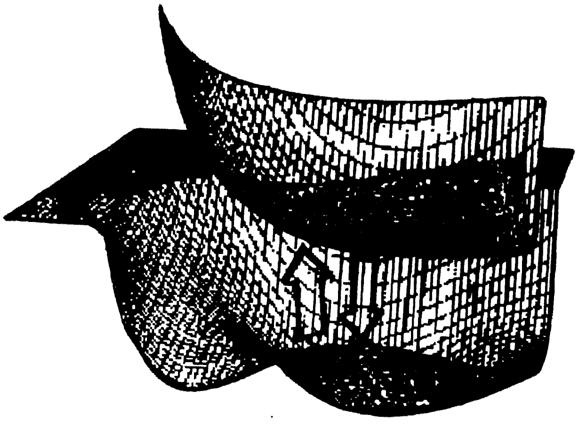

Fig. 2 A schematic representation of Pump and Dump scheme.

$$\psi_g^{(2)}(t) = -(\frac{i}{\hbar^2} \int_{-\infty}^{t}\int_{-\infty}^{t_2} dt_1 dt_2 e^{-i\hat{H}_g(t_2-t_1)/\hbar} \times \hat{\mu}.E\,(t_2) e^{-i\hat{H}_e(t_2-t_1)/\hbar} \mu.E(t_1)\psi_g(0)e^{-i\omega_g t} \quad \ldots (4)$$

$$\psi_e^{(2)}(t_2) = -\frac{i}{\hbar^2} \int_{-\infty}^{t_2} dt_1 e^{-i\hat{H}_e(t_2-t_1)/\hbar} \hat{\mu}.E(t_1)\psi_g(0)e^{-i\omega_g t_1} \quad \ldots (5)$$

where labels g and e represent the ground and the excited potential energy surfaces respectively. The amplitude $\psi_g(0)$ evolving on the ground state potential energy surface from $t=0$ to $t=t_1$ is transferred to excited potential energy surface through vertical transition at time t_1. It is then allowed to propagate till time t_2 and is then dumped back to the ground state surface on which it evolves till time t.

The sequence of the light pulses that optimizes the desired product selectivity has to be determined. The variationally optimized temporal profile of the dump pulse is given by

$$b^*(t_2) \propto \int_{-\infty}^{t_2} \langle \phi_e | e^{iH(t_2-t_1)/\hbar} | \phi_g \rangle a(t_1) dt_1 \quad \ldots (6)$$

where $a(t_1)$ and $b(t_2)$ are the first and the second electromagnetic field pulse form, H is the Hamiltonian for propagation of the molecule coupled with radiation field. Although, the wavepacket shape and the width changes as it evolves on the potential energy surfaces, only the time interval between the pump and the dump pulses is used to modify the product selectivity. The evolving wavepacket on the excited potential energy surface effectuates a very complicated amplitude distribution $b(t)$ and an efficient transfer of amplitude to the exit channel by a simple dump pulse is unattainable[3].

For a system with multiple electronic surfaces in which the various product channels are not well separated, the extent of selectivity cannot be controlled at all. The difficulty associated with generating laser pulses of few femtoseconds duration in the lab is another major disadvantage of the method[7]. An interesting application of this scheme is seen in the work of Chakrabarti *et al.*[30] where the pump and dump scheme has been utilized to control photo-induced desorption of NO from Pt(111) surface.

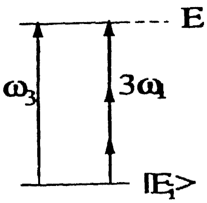

Fig. 3 Coherent control through interface between the 1 photon and 3 photon pathways.

3.2 *Coherent Control*

In this approach developed by Brumer and Shapiro[10], the control of the product selectivity is achieved by making two degenerate exit channel wavefunctions interfere constructively or destructively by simultaneous generation of two or more coherent excitation routes to the final state as shown in Fig. 3.

Various scenarios exploiting the consequences of interference between excitation pathways have been studied by Brumer and Shapiro[9]. Here we have focussed on interference involving one and three photon pathways between the bound initial state of the molecule and specific product state in the continuum as it is the case that has been subjected to experimental verification.

Let $\hat{H}_g$ and $\hat{H}_e$ be the Born-Oppenheimer Hamiltonians representing ground and the excited states respectively. The molecule is assumed to be initially in an eigenstate of $\hat{H}_g$ with energy E_i and the final state is in the continuum with energy E. The continuum state of energy E is represented by $|E,n,q^- >$ where n denotes all the quantum numbers of the system excluding energy, and q^- denotes particular product channel with the superscript representing the incoming boundary conditions. Suppose the molecule, in its initial state is irradiated with an electromagnetic field consisting of two colour lasers.

$$E(t) = E_1 \cos(\omega_1 t + \vec{k}_1.\vec{R} + \theta_1) + E_3 \cos(\omega_3 t + \vec{k}_3.\vec{R} + \theta_3)$$

with $\omega_3 = 3\omega_1$, $E_a = |E_a|\hat{\varepsilon}_a$ with $a = 1,3$, $|E_a|$ the magnitude and $\hat{\varepsilon}_a$ its polarization plane. Let $k_3 = 3k_1$, corresponding to parallel incident fields. The probability of forming a product molecule in exit channel q with energy E is[9].

$$W(E,q;E_i) = W_3(E,q;E_i) + W_{13}(E,q;E_i)$$

where $W_\alpha(E,q;E_i), \alpha = 3,1$, are the probabilities of fragmentation arising from absorption of one and three photons respectively and $W_{13}(E,q;E_i)$ represents the interference between the two fragmentation pathways. In the weak field, the branching ratio for the products in channel q and q' is given by[9].

$$R_{qq'} = \frac{\dfrac{|E_3|^2 F_3^{(q)} - 2|E_3||E_1|^3 \cos(\theta_3 - 3\theta_1 + \delta_{13}^{(q)})}{\left|F_{13}^{(q)}\right| + |E_1|^6 F_1^{(q)}}}{\dfrac{|E_3|^2 F_3^{(q')} - 2|E_3||E_1|^3 \cos(\theta_3 - 3\theta_1 + \delta_{13}^{(q')})}{\left|F_{13}^{(q')}\right| + |E_1|^6 F_1^{(q')}}}$$

where,

$$F_3^{(q)} = \left(\frac{\hbar}{\pi|E_3|}\right)^2 W_3(E,q;E_i),$$

$$F_1^{(q)} = \left(\frac{\hbar}{\pi|E_1|^3}\right)^2 W_1(E,q;E_i),$$

and similarly for q'. It can be seen that both numerator and denominator contain sum of the contributions from one and three photon pathways and an interference term. Since the interference term could be altered by changing the relative phases of one and three photon pathways $(\theta_3 - \theta_1)$ and their relative amplitudes, control of the product ratios can be attained very often over a wide range of field attributes. In principle, the ratio of the products in different channels could be controlled over a considerable range by varying the intensities and relative polarization of the one and three photofragmentation pathways.

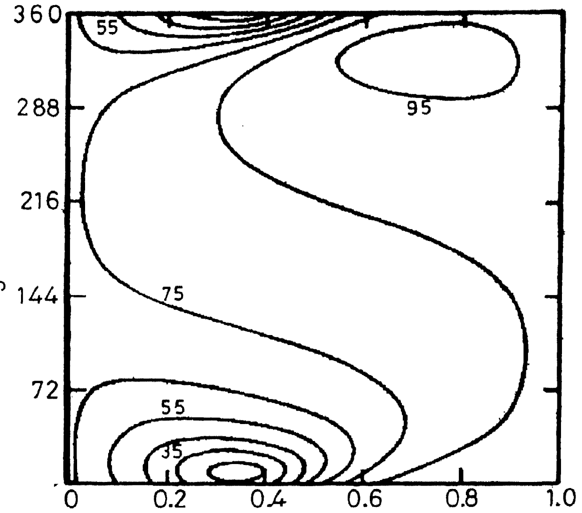

Fig. 4 The Br* in I-Br → I + Br/I + Br* dissociation using 1 photon – 3 photon coherent control.

An example of the effectiveness of this approach is shown in Fig. 4 where the yield of $Br^*(^2P_{1/2})$ is seen to range from 25-95% as a function of phase difference $(\theta_3 - \theta_1)$ and field intensity between the one photon and the three photon lasers.

To the degree that simple systems with a small number of isolated intermediate and final states can be found, this approach is quite attractive for practical implementation. It has the advantage of intuitive simplicity and ease of experimental actuation. This is the only scheme which has been tested experimentally and control of photodissociation of DI[3] using the 1 photon - 3 photon scenario outlined earlier is clearly seen in Fig. 5.

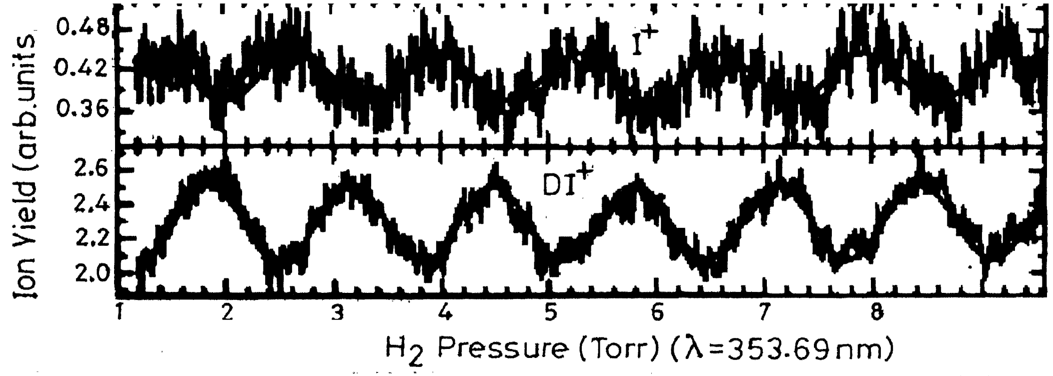

Fig. 5 Control of DI dissociation and autoionization by changing the H_2 pressure in cells through which the lasers pass to change the phase between 1 photon-3 photon pathways to effect interference based coherent control.

There are many variations of the Brumer Shapiro control scheme. We have dealt with only one of these schemes and we refer the reader to the original publications for further details[10].

3.3 The general Field Design using Optimal Control

Optimal Control theory is a non-linear theory applicable to fields of arbitrary strength. It attempts to find the best solution to a given control problem under the stated curcumstances and constraints. In this most general approach, a mathematical cost functional is constructed whose minimization produces the desired field $\varepsilon(t)$. The optimizing functional $\bar{J}(\varepsilon)$ comprises of two components.

$$\bar{J}(\varepsilon) = J_0 + J_p \qquad \dots (7)$$

where J_0 is the physical objective and J_p represents the penalty terms.

The physical objective involved in a molecular control problem may include localization of energy, dissociation of a particular bond etc. If an objective must be satisfied in time *T*, the goal is that the expectation values $\langle \psi(T)|\hat{O}|\psi(T)\rangle$ must be a particular value $\bar{O}$ where $|\psi(T)\rangle$ is the state of the quantum mechanical system at time *T* and $\hat{O}$, operator corresponding to the observable, i.e. the appropriate objective functional is

$$J_0 = (\langle \psi(T)|\hat{O}|\psi(T)\rangle - \bar{O})^2$$

and attainment of the expectation value equal to $\bar{O}$, is the desired target to be reached by minimizing J_0 The state of the system at a target time T will depend functionally on the field $\varepsilon(t)$ for all $0 \le t \le T$ and this dependence is assumed to be tacitly included in $\psi(t)$. Often it is also the case that, while trying to evaluate the physical objective, there could be some parameters that should be avoided. For example, in attempting to dissociate a particular bond, it may be desired that the remaining part of the molecule remain intact or suffer minimal disturbances. Such terms are called penalty terms and define J_p. All the terms involved are explicitly or implicitly dependent on $\mathcal{E}$, and extremization of $J(\varepsilon)$ setting,

$$\frac{\delta \bar{J}(\varepsilon)}{\delta \varepsilon} = 0 \qquad \dots (8)$$

coupled with canonical requirement of fulfillment of time dependent Schrödinger equation at all times implemented using Lagrangian constraint functional[13] determines the optimal $\varepsilon(t)$ required to attain the desired objective. This technique has been applied to various problems[14] and to assist in a comparative assessment of optimal and coherent control schemes control of IBr → I + Br/I + Br* dissociation using this method[15] will be used to illustrate its strengths and weaknesses. In this case, the cost functional to be minimized is

$$J = \left(1 - \int_0^T dtj_m(t, x_d)\right)^2 + \left(\int_0^T dtj_n(t, x_d)\right)^2 \qquad \dots (9)$$

where; $\int_0^T dtj_i(t, x_d), i = m, n,$ is the time-integrated flux of probability across appropriately chosen asymptotic point x_d on the potential curves for channels *m/n*. The product selectivity and maximization for m_{th} channel and the minimization of the product in the n_{th} channel is achieved by minimizing the objective functional of eq. (9). The optimal field obtained by minimizing eq. (9) for the Br^* channel is shown in Fig. 6.

While the field form in Fig. 6 does achieve 99% selectivity with 80% dissociation, the field intensity and form cannot be effected easily in realistic laboratory conditions and additional simplifications become necessary[15]. The mechanism by which the field induces selective photodissociation can be in part determined from the plots of the power spectrum and the position expectation value on the ground electronic state is plotted in Figs. 8 and 7 respectively.

The solid line in Fig. 7 which shows the position expectation value on the ground electronic state indicates that a non-stationary state is formed since the wavepacket continues to oscillate after the field is turned off. The position expectation value span corresponds to bond stretch in highly excited vibrational states and represents a mixing of many vibrational levels under the influence of $\varepsilon(t)$. This is also indicated in the power spectrum (Fig. 8) where spacing between the peaks is roughly the spacing between vibrational energy levels of the ground electronic state. Apparently, the optimal pulse $\varepsilon(t)$ of Fig. 6 forms a coherent superposition of vibrational states on the ground electronic surface through optical pumping and subsequently uses this to produce the desired wavepacket which then exits out of the desired channel. The principal

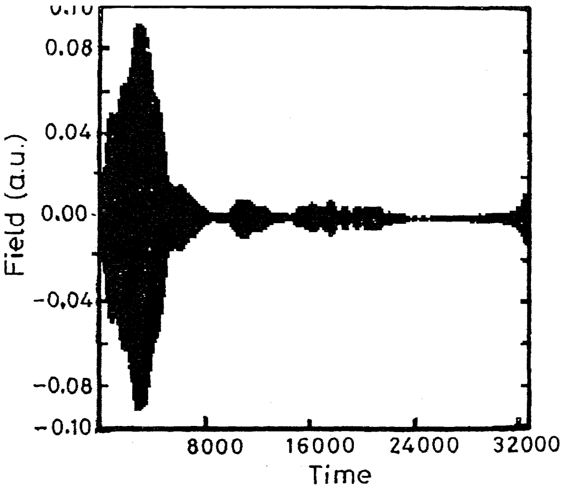

Fig. 6 The optimal field obtained for maximizing the Br yield in the photodissociation of IBr.

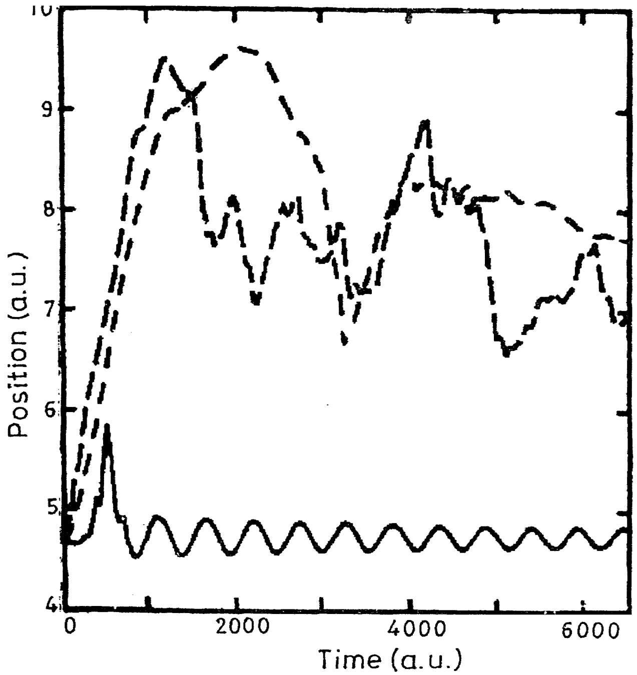

Fig. 7 Variation of position expectation values with time on each potential energy surface.

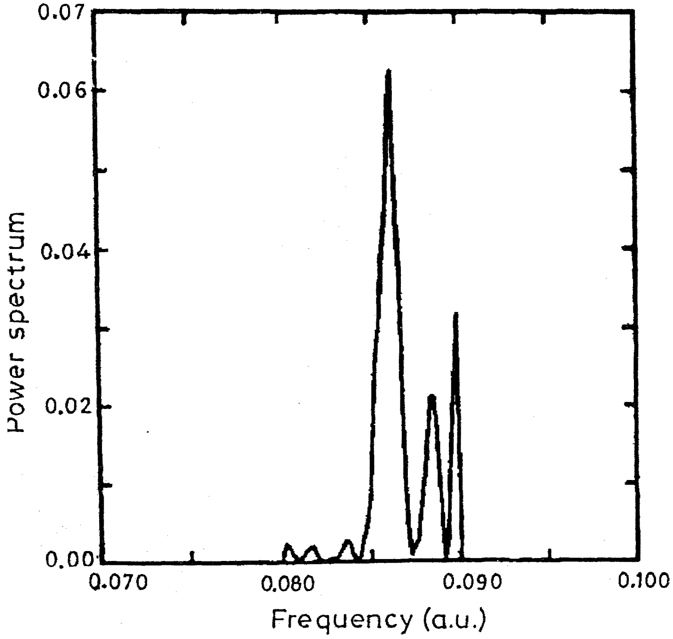

Fig. 8 Power spectrum corresponding to the field obtained for maximizing Br* yield in the photodissociation of IBr.

role of the optimal field at its maximum intensity seems to be to produce a suitably altered initial state.

The optimal pulse shape and the requisite field intensity is difficult to reproduce in normal laboratory conditions, it is desirable to formulate methods which can deliver substantive yield and requisite selectivity for photolysis pulses with inbuilt ease of laboratory reproducibility and a new method pursuing these objectives is discussed in the following section.

4 Field Optimized Initial State (FOIST)

The focus of the theoretical approaches discussed so far has been on field design, whereas, we have shown earlier (eq. 3) that the photodissociation yield depends also on the initial vibrational state from which photolysis is induced. This dependence has been found to be fairly acute and examples include the photodissociation of H_2^+[31], D^+[32] HI[33,34], HOD[4,35,36] and HCl[37] in each of which the product yield has been found to be quite sensitive to the initial vibrational state of the molecule. Since the initial vibrational state which is subjected to photolysis is critical in determining the photodissociation products, it is reasonable to expect an appropriately optimized linear superposition of these vibrational eigenstates to serve as a better initial condition for selective maximiziation of the desired product.

Towards this end, a scheme to establish the optimal linear mix of the field free vibrational eigenstates for the given photolysis pulse and chosen photodissociation objective has been pursued in our group[16,17] whereby, the emphasis is shifted from control through design of an appropriate field, to control through the design of an appropriate field, to control through the design of an optimal linear combination of the field free vibrational eigenstates for the chosen photolysis pulse. Applications of Field Optimized Initial State (FOIST) based selective control to HI[16] and IBr[17] have successfully identified the optimal linear combinations for multicolour cw and Gaussian fields of different intensities, frequencies and phase differences and considerable enhancement in selectivity and product yield using these field optimized initial states has been demonstrated[16,17]. The optimal combinations depend on the choice of the photdissociation objective, i.e., the linear combination which will maximize flux out of the $I + Br(^2P_{3/2})$ in the IBr differs markedly from that which will maximize flux out of the excited $I+Br^*(^2P_{1/2})$ channel[17]. Similar considerations hold in the photodissociation of HI as well[16].

The FOIST scheme achieves selective flux maximization by altering the spatial profile of the initial state to be subjected to the photolysis pulse and since changes in flux are due to the flow of probability density, the probability density profiles of the optimal superpositions have been examined to try and isolate the mechanistic features which may be responsible for selective control. These optimal linear combinations being field specific, a comprehensive analysis will require the optimizations to be carried out and the structural features of the optimal initial state to be analysed for sufficiently large number of field parameters. Instead, the Time Dependent Wave Packet (TDWP) method pioneered by Heller[38-40] permits the evaluation of branching ratios for a large number of frequencies from a single calculation[41], where, in this analysis, the initial wavepacket to be promoted to the excited electronic states is the optimal superposition of the field free eigenstates for the given photolysis pulse and chosen photodissociation objective.

Such an identification of structural components of these superpositions responsible for selective flux maximization can provide critical insight into the mechanistic basis for photodynamic control of reactions and is the subject of following subsections. The basic thurst of the detailed discussion to follow is an attempt to search for simplifying features so that the onus for selective control of chemical reactions does not lie entirely on the laser fields which thereby may come out to be complicated[15] but the task of selective control is split into different parts[16,17] which could be comparatively easier to realize in ordinary laboratory conditions.

The methodology of the Rayleigh-Ritz variational maximization of flux and the TDWP analysis is already available in detail elsewhere[16,38,41] and only a skeletal outline is offered in the following subsections.

4.1 Method

For molecules possessing a dipole moment $\vec{\mu}$, the effect of the radiation field $\vec{\varepsilon}(t)$ may be obtained by solving the time dependent Schrödinger equation,

$$i\hbar\frac{\partial}{\partial t}\psi = \hat{H}(t)\psi, \qquad \dots (10)$$

where

$$\hat{H}(t) = \hat{H}_0 - \vec{\mu}.\vec{\varepsilon}(t)$$

with H_0 being the field free Hamiltonian. The solution ψ at some time T can be expressed as

$$\psi(T) = \hat{U}(T,0)\psi(0), \qquad \dots (11)$$

where $\hat{U}(T,0)$ is the (not necessarily unitary) propagator and ψ_0 is the wavefunction for the initial state of the molecule to which the photodissociation pulse $\vec{\varepsilon}(t)$ is applied. As defined in eq. (3), the photolysis yield in a given channel under the influence of the chosen field form $\vec{\varepsilon}(t)$ is given by

$$\int^{T} dt\langle\hat{j}\rangle_t = \langle\psi(0)|\hat{F}|\psi(0)\rangle, \qquad \dots (12)$$

where,

$$\hat{F} = \int dt\hat{U}^{\dagger}(t,0)\hat{j}\hat{U}(t,0), \qquad \dots (13)$$

is the time integrated flux operator defined earlier and it is seen from this equation that the product yield may be controlled by both altering the field dependent part $\hat{F}$ or the field free initial state $\psi(0)$. Earlier control schemes[8-11,15,42-44] have attempted control over photodissociation entirely through field manipulation for a fixed $\psi(0)$. In the FOIST scheme, control over product yield is sought through preparation of them initial wavefunction $\psi(0)$ as a coherent superposition of vibrational eigenstates of the ground electronic state for the chosen photolysis pulse[16,17] (for the short femtosecond pulses to be considered here, rotational motion is ignored). Of course, the field itself may also be altered which will change the nature of the optimal $\psi(0)$.

By expanding $\psi(0)$ in a basis of $(M+1)$ field free vibrational eigenfunctions,

$$\psi(0) = \sum_{m=0}^{M} c_m\phi_m, \qquad \dots (14)$$

flux maximization is reduced to the familiar Rayleigh-Ritz variational optimization[16] of $\{c_m\}$ through diagonalization of a $(M+1 \times M+1)$ matrix **F** whose elements are

$$F_{kl} = \langle\phi_k|\hat{F}|\phi_l\rangle \approx \Delta t\sum_{n=0}^{N_t}\langle\psi_k(n\Delta t)|\hat{j}|\psi_l(n\Delta t)\rangle, \qquad \dots (15)$$

with Δt as the step size for the numerical time propagation and $N_t\Delta t = T$.

The largest eigenvalue f_{max} of **F** is the maximum product yield (flux) and the corresponding eigenvector $\{c_m^{ax}\}$ is the set of coefficients which define the optimal initial wavefunction

$$\psi^{\max}(0) = \sum_{m=0}^{M} c_m^{\max}\phi_m, \qquad \dots (16)$$

constituting the superposition that will provide the maximum achievable product yield f_{max} out of the particular channel specified by $\hat{F}$ for the chosen field $\vec{\varepsilon}(t)$. As in other variational calculations, the larger the basis set size, "better" the results. However, due to the difficulties in the simultaneous overtone excitation of many vibrational levels, the basis set expansion in eq. (14) is restricted to only the first few vibrational eigenstates (only the ground plus the first two excited vibrational levels in our case) and so the size of the **F** matrix is small (3×3) and therefore computationally trivial to diagonalize. The solution proceeds by propagating the full TDSE including all electronic states $M+1$ times from $t=0$ to $t=T$ for each initial condition $\psi(0)=\phi_m$, $m=0,1,\dots\dots,M$ in the basis set expansion (eq. (14)). During the propagation, the matrix elements F_{kl} are accumulated according to eq. (15) to construct the time integrated flux matrix **F** which is diagonalized to obtain $f_{\max}$ and $\psi_{\max}(0)$. The total time T is chosen to ensure near total dissociation of the molecule.

In the Time Dependent Wave Packet analysis (TDWP)[38] the Schrödinger equation

$$H_{ex}\chi_\ell(t) = i\hbar\frac{\partial\chi_\ell(t)}{\partial t} \qquad \dots (17)$$

is solved with $\chi_\ell = \mu_{0\ell}\phi(0)$ as the initial wavefunction on the $\ell-th$ excited state and $\mu_{0\ell}$ is the transition dipole moment between the ground (0) and the $\ell-th$ excited state. The field free vibrational ground state $\phi(0)$ in our case is the optimal linear combination $\psi^{\max}(0)$. The time-evolution of the promoted wavefunction $\chi_l(0)$ is governed by,

$$\chi_l(t) = \exp(-iH_{ex}t/\hbar)\chi_\ell(0) \qquad \ldots (18)$$

and the overlap $\langle \chi_\ell(0)|\chi_\ell(t)$ of the time evolving wavefunction $\chi_\ell(t)$ with the initial $\chi_\ell(0)$ is called the autocorrelation function.

To ensure correct branching ratio[41], the autocorrelation function is evaluated after a sufficiently large time interval τ such that the norm of the wavefunction on different curves has stabilized and the system population is completely out of the curve crossing region. The Fourier transform of the autocorrelation function yields frequency dependent partial absorption cross-section

$$\sigma(\omega) = C\omega \int_{-\infty}^{+\infty} e^{-i(\omega+E_0)t} \langle \chi_\ell(\tau) \,|\, \chi_\ell(\tau+t)\rangle dt \ldots (19)$$

where C is a constant[38], ω is the frequency of the incident radiation and E_0 is the energy corresponding to the initial state. The branching ratio is given by the ratio of the sum of partial photoabsorption cross-sections for the two channels.

We should however mention that the fields employed to obtain $\psi_1^{\max}$ and $\psi_2^{\max}$ for both IBr and HI are quite intense and since the TDWP formulation is perturbative, the branching ratios obtained using TDWP, in general, may not match those using full solutions from the TDSE. It has however been shown[16] that for HI, the branching ratios obtained as a function of field frequency using TDSE, with v=0, v=1 and v=2 as initial states and the same field amplitude (0.01 a.u.) are very similar to that obtained by Kalyanaraman and Sathyamurthy[34] using Heller's TDWP technique.

These branching ratios peak at different frequencies[16] for v=0, v=1 and v=2 and in keeping with the reflection principle, v=1 and v=2 branching ratios have multiple maxima. An effective map of branching ratios as a function of field amplitude and frequency using TDSE can therefore be very demanding. Also, since the optimal linear combinations $\psi_1^{\max}$ and $\psi_2^{\max}$ combining v=0, v=1 and v=2 are field specific, such an exercise is not meaningful in the present context specifically since branching ratio is only one of the ingredients in the unfolding of the mechanistic picture to be probed here. The TDWP can provide the branching ratios for a broad frequency range from a single calculation and is our method of choice for investigating the role of FOIST in selective control of photodissociation.

The split-operator fast Fourier transform with Pauli matrix propagation[45-47] algorithm was utilized to integrate the time dependent Schrödinger equation in both the FOIST and the TDWP schemes. The FOIST scheme requires a full solution of the time dependent Schrödinger equation including all the electronic states. In the TDWP calculation, the optimal wavepacket $\psi^{\max}(0)$ resulting from the FOIST scheme is propagated only on the excited electronic states to obtain the absorption spectrum and branching ratio resulting from the use of $\psi^{\max}(0)$ as the initial condition.

The results to be presented here are from modelling of the molecules as rotationless oscillators. For the ultrashort , pulses employed in these calculations, the neglect of rotational effects may be taken to be permissible, since a recent *ab-intio* investigation of the photofragmentation of HCl[48] has shown negligible influence of molecular rotation on the branching ratio. In any case, treatment of rotational effects will increase the computational complexities by at least an order of magnitude[49] and we have therefore found it judicious to neglect rotational motion in this initial application. Photodissociation of IBr[15,17,50-55] and HI[16,26,31-34,56-58] have been studied extensively and are our representative systems of choice. In the following section we analyze some representative $\psi^{\max}(0)$ for IBr and HI to investigate the mechanistic underpinning of photodynamic control of product selectivity and yield.

4.2 Applications of FOIST

The Rayleigh-Ritz variational procedure outlined in the previous section provides the optimal linear combination of initial vibrational eigenstates (within the chosen manifold of $M+1$ vibrational eigenstates) that selectively maximizes flux out of the desired channel for the photolysis pulse of choice. Such a linear combination leads to an altered spatial profile for the initial wavefunction *vis-a-vis* those offered by the eigenfunctions for the individual vibrational eigenstates. This alteration in the spatial profile has to be at the core of the mechanism for FOIST based flux maximization and since changes in flux are due to the flow of probability density, one can understand the structural features responsible for selective flux maximization by comparing the probability density plots of the optimal superpositions with those from individual pure vibrational eigenstates and by using these field optimized linear combinations as initial states in the TDWP calculation of the absorption cross-sections and branching ratios.

The analysis to be presented here is for the photolysis of both IBr and HI molecules employing a multicolour cw field of the form $\varepsilon(t) = A\sum_{p=0}^{2}\cos(\omega - \omega_{p,0})t$ where A is the amplitude, ω the photodissociation frequency and $\omega_{p,0} = (E_p - E_0)/\hbar$ is the Bohr frequency for transition between the p_{th} and the ground (0_{th}) vibrational energy levels. The vibrational eigenvalues E_p and corresponding eigenfunctions ϕ_p of the electronic ground state for both these systems are computed using the Fourier grid Hamiltonian (FGH) method[59]. A total of three (M=2 in eqs. (14) and (16)) initial vibrational eigenstates ϕ_0 (v=0), ϕ_1 (v=1) and ϕ_2 (v=2) are considered for the superposition to derive the optimal initial state for the desired photodissociation objective. The optimal linear combination maximizing flux out of the lower channel (I+Br for IBr and H+I for HI to be labelled as 1) is denoted by $\psi_1^{\max}$ and $\psi_2^{\max}$ represents the combination which maximizes flux out of the upper channel (labelled 2) with I+Br*/ H+I* as the dissociation products.

The mechanistic underpinnings of the FOIST based selective control of IBr and HI photodissociation are further probed by the use of $\psi_1^{\max}$ and $\psi_2^{\max}$ in the TDWP calculation of branching ratios $\Gamma(\mathrm{Br}^*/\mathrm{Br})$ and $\Gamma(\mathrm{I}^*/\mathrm{I})$. For the sake of brevity, in further discussions, instead of writing $\chi_l = \mu_{0l}\psi_1^{\max}$ and $\chi_l = \mu_{0l}\psi_2^{\max}$ repeatedly to signify the transport of the optimal wavepackets $\psi_1^{\max}$ and $\psi_2^{\max}$ to the excited curves in the TDWP analysis, we will assume this to be the case when $\psi_1^{\max}$ and $\psi_2^{\max}$ are mentioned as the initial conditions. The figures labelled with $\psi_1^{\max}$ and $\psi_2^{\max}$ will therefore have this same connotation that TDWP calculations have been done with $\chi_l = \mu_{0l}\psi_1^{\max}$ and $\chi_l = \mu_{0l}\psi_2^{\max}$ as the initial condition.

In the following subsections, we first analyse the simpler IBr photodissociation modeled by only three potential energy curves, two optical and one non-adiabatic coupling is analysed first. Results from the controlled photodissociation of the HI molecule modeled by five potential energy curves with three nonadiabatic and four optical couplings is taken up in the next subsection.

4.2.1 IBr

The potential energy curves as seen in Fig. 9a, the non-adiabatic coupling, transition dipole moments and other systemic parameters are same as those used in our previous work[15,17,51]. The excited states $B(^3\Pi_0^+)$ and $Y(O^+)$ are non-adiabatically coupled and their potential energy curves cross at R=6.08 a.u. The ground $X(^1\Sigma_0^+)$ state (0) is optically coupled to both the $Y(O^+)$ (1) and the $B(^3\Pi_0^+)$ (2) states with the transition dipole moment $\mu_{01} = 0.25\mu_{02}$. Our FOIST scheme for selective flux maximization out of the I+Br/I+Br* channels has been studied for a range of field amplitudes (0.01-0.1 a.u.) and frequency (ω) values (0.081-0.093 a.u. or 17770-20410 cm^{-1}/563-490 nm)[17]. All these frequencies lie well above the crossing point and permit dissociation out of both the channels.

The probability density plots for the first three vibrational states ϕ_0, ϕ_1 of the IBr molecule are plotted in Fig. 9b and the probability density profile from the optimal superpositions $\psi_1^{\max}$ and $\psi_2^{\max}$ which maximize flux out of I+Br and I+Br* channels respectively for a field frequency ω = 0.087 a.u. (19094 cm^{-1}/524 nm) and amplitude A=0.03 a.u. are displayed in Fig. 9c. This amplitude is the lowest for which almost 100% dissociation[17] occurs using a pulse length of 480 fs (20,000 a.u.), followed by further propagation without the field for another 387 fs (16,000 a.u.). The probability density for the ground vibrational level ϕ_0 peaks at 4.66 a.u., that for $\psi_1^{\max}$ at 4.8 a.u. and for $\psi_2^{\max}$ at 4.58 a.u. The optimal wavefunction $\psi_1^{\max}$ seems to maximize flux out of

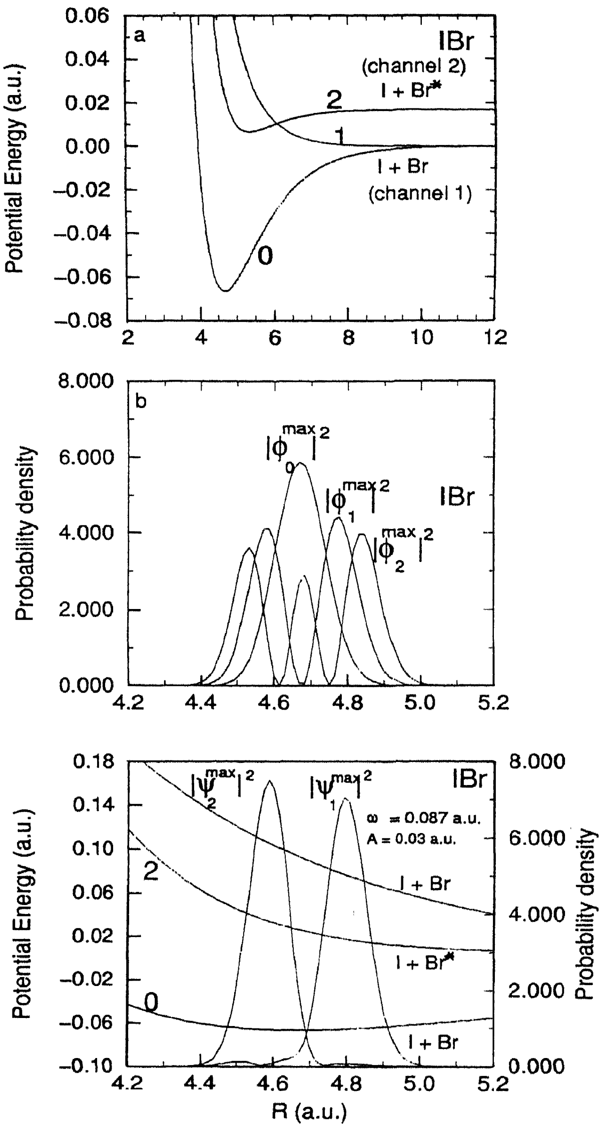

Fig. 9 (a) Potential energy curves of IBr. (b) Probabilitydensity plots for the *IBr* vibrational eigenstates ψ_0, ϕ_1 and ϕ_2 of ground electronic curve, (c) Probability density plots for $\psi_1^{\max}$ and $\psi_2^{\max}$ for flux maximization through I+Br and I+Br* channels respectively.

channel 2 (I+Br*) by localizing the probability density to the left of ϕ_0 that given by the wavefunction and $\psi_1^{\max}$ maximizes flux out of channel 1 (I+Br) by localizing probability density to the right of the ϕ_0 probability density peak. Though the results presented here are for a single representative frequency, this trend of $\psi_2^{\max}$ peaking to the left of ϕ_0 and $\psi_1^{\max}$ to its right persists throughout the frequency range specified earlier. The probability density profiles for $\psi_1^{\max}$ and $\psi_2^{\max}$ are mutually exclusive and much more compact as compared to those from ϕ_0, ϕ_1 or ϕ_2. Furthermore, the probability density profiles from pure eigenstates ϕ_0, ϕ_1 and ϕ_2 subsume the spatial attributes of both $\psi_1^{\max}$ and $\psi_2^{\max}$ which explains why selective photodissociation cannot ensue from the use of only one of these molecular eigenstates as the initial state.

This need for a suitable mixing of vibrational states for selective control of photodissociation is also seen in the optimal control theory based calculations on IBr[15] where the additional frequency components of the optimal field separated from each other by IBr ground state vibrational spacings (Fig. 8), large expectation value for the internuclear distance on the electronic ground state corresponding to vibrational stretch for highly excited vibrational levels of IBr (Fig. 7) and extremely intense fields required to achieve this (Fig. 4) in the very beginning of the control procedure point to the same central role of initial mixing of vibrational states in achieving selective control. In our FOIST scheme, $\psi_1^{\max}$ and $\psi_2^{\max}$ represent the premixing of vibrational states required for selective control with an additional advantage that the photolysis pulse may be chosen beforehand for practical convenience.

In the FOIST based selective control, it is the $\psi_1^{\max}$ or the $\psi_2^{\max}$ which are transported to the excited electronic states. In the case of IBr the $B(^3\Pi_0^+)$ state (2) is coupled four times more strongly with the ground state $\mu_{01} = 0.25\mu_{02}$ as compared to the $Y(O^+)$ state (1). Also, the $Y(O^+)$ state is far off resonance within the frequency band considered by us and the amplitude transferred to the $B(^3\Pi_0^+)$ level will therefore be much larger and dominate the photodissociation outcome. The broad mechanistic details may therefore be inferred from arguments employing the dynamics ensuing from the evolution of the wavepacket on the $B(^3\Pi_0^+)$ curve alone. We may therefore infer from the structural features of $|\psi_2^{\max}|^2$ portrayed in Fig. 1c that for any given frequency, transitions from the initial state represented by $\psi_2^{\max}$ will occur to the energetically higher or steeper, more repulsive region of the excited $B(^3\Pi_0^+)$ potential energy curve. The excited molecule described by $\psi_2^{\max}$ will therefore traverse the $B(^3\Pi_0^+)-Y(O^+)$ crossing with greater velocity and exit out of the excited I + Br* channel compared to where the molecule is represented by $\psi_1^{\max}$ which transfers it to a relatively smoother region of the $B(^3\Pi_0^+)$ state potential energy curve thereby facilitating a slower adiabatic exit out of the lower I + Br channel.

This interpretation of the control mechanism utilizing $\psi_1^{\max}$ and $\psi_2^{\max}$ as the initial states is consistent with the analysis of the frequency dependence of *IBr* photodissociation as a function of the molecular radial velocity using the Landau - Zener theory presented by De Vries *et al.* where increase in photodissociation yield out of the *I* + *Br** channel with increase in frequency is well correlated with an increase in radial velocity at the crossing point[60]. From Fig. 1c, it is obvious that $|\psi_2^{\max}|^2$ and $|\psi_1^{\max}|^2$ are localized in a mutually exclusive manner and that the optimization leads to a significant altering of the spatial profiles to excite the molecule to the region most suited for directing flux out of the desired channel.

These optimal linear combinations being field specific, a comprehensive analysis will require that the optimizations be carried out and the structural features of the optimal initial state be analysed for sufficiently large number of field parameters. Such an attempt will be extremely demanding (specially for IBr) and the proposed central role of the FOIST generated altered spatial profile of the initial state to be subjected to the photolysis pulse is best checked by the application of the TDWP method[38] which permits the calculation of absorption cross-section and branching ratios at all frequencies from a single calculation. The TDWP calculations for the curve crossing problems however require that the branching ratios be calculated from Fourier transform of autocorrelation function $\langle \chi_\ell \mid \chi_\ell(\tau+t)\rangle$ after a time τ such that the norm of the wavefunctions have stabilized for all excited states and are completely out of the curve crossing region[41].

To ensure that this indeed is the case, in Figs 10a and 10b we have plotted the norm $\langle \chi_\ell(t) \mid \chi_\ell(t)\rangle$ from TDWP analysis using both $\psi_1^{\max}$ and $\psi_2^{\max}$ as the initial conditions. Figs. 2a and 2b present the evolution of these norms on both the excited states 1 ($Y(O^+)$) and 2 ($B(^3\Pi_0^+)$)respectively and it is seen that the norms have indeed stabilized at the end of 170 fs by which time the position expectation values $\langle \chi_\ell(r,t)|r|\chi_\ell(r,t)\rangle / \langle \chi_\ell(t) \mid \chi_\ell(t)\rangle$, with both ψ_1^{max} (Fig. 10c) and $\psi_2^{\max}$ (Fig. 10d) as initial condition are well past the crossing point. Further examination of Fig. 10c and 10d reveals that the position expectation value on curve 1 increases gradually till the amplitude on curve 2 reaches the crossing point with a portion crossing over to the lower r values of curve 1. This crossed over amplitude at lower *r* value decreases the average position expectation value on curve 1. A comparison of $\langle r\rangle_t$ from Figs. 10c and 10d shows that as surmised earlier, approach to the crossing point is indeed much faster when the molecule is represented by $\psi_2^{\max}$.

The norm on the excited curves are well past the crossing point and have completely stabilized by 170 fs. The wavefunction on each curve at the end of 170 fs were therefore stored and used to calculate the total auto-correlation functions $\sum_\ell \langle \chi_\ell(\tau) \mid \chi_\ell(\tau+t)\rangle$ which are plotted in Figs. 11a and 11b with $\psi_1^{\max}$ and $\psi_2^{\max}$ as the initial states respectively.

As can be seen from Fig. 11a, with $\psi_1^{\max}$ as the initial condition, the auto-correlation function decreases to zero at around 18 fs and with $\psi_2^{\max}$ as the initial condition, the fall to zero is approximately twice as rapid (10 fs). This is as we would expect from the time evolution of $\langle r\rangle_t$ in Figs. 10c and 10d discussed earlier where the molecule when described by $\psi_2^{\max}$ is placed on the steeper part of the excited curve and rolls down more rapidly and therefore should lose the correlation with $\chi_i(0)$ much faster in comparison with when it is represented by $\psi_1^{\max}$. This loss of correlation in case of $\psi_2^{\max}$ is much more complete as compared to that for $\psi_1^{\max}$ since the longer time

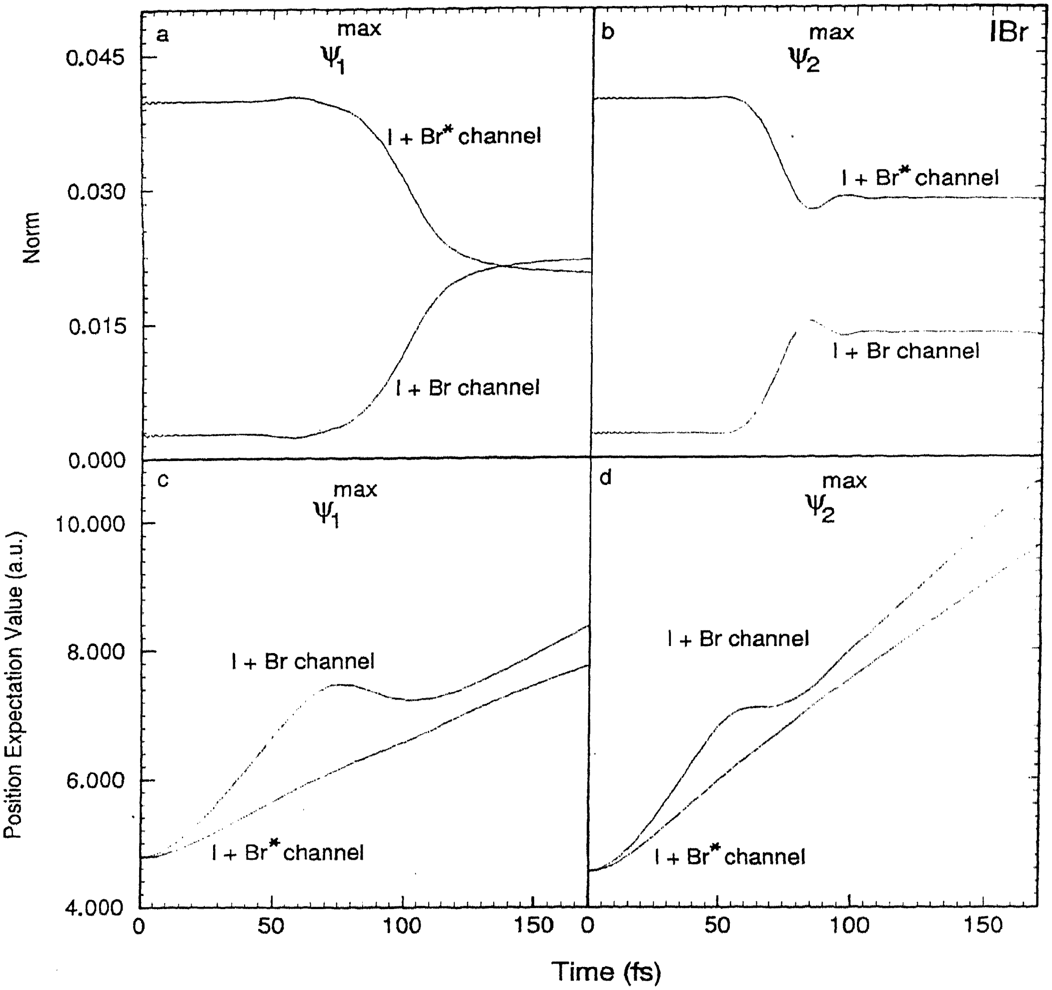

Fig. 10 Norm evolution on different potential energy curves of IBr with (a) $\psi_1^{\max}$ and (b) $\psi_2^{\max}$ as the initial condition ; position expectation values $\langle r \rangle_t$ on different curves of IBr with (c) $\psi_1^{\max}$ and (d) $\psi_2^{\max}$ as the initial condition.

autocorrelation function with $\psi_2^{\max}$ as the initial state is approximately two orders of magnitude smaller compared to that with $\psi_1^{\max}$ as the initial condition.

The absorption cross-section obtained using $\psi_2^{\max}$ as the initial condition is smooth with only a negligible interference pattern around 600 nm. The absorption spectrum from $\psi_1^{\max}$ as the initial condition contains a series of sharp peaks characteristic of predissociation dynamics[52] in the higher wavelength region due to a slower approach to the $B(^3\Pi_0^+)-Y(O^+)$ crossing. The longer wavelength region is dominated by pre-dissociation in the vicinity of the energy values around the $B(^3\Pi_0^+)-Y(O^+)$ crossing leading to the complicated interference pattern seen in the $\psi_1^{\max}$ absorption profile.

In contrast, the smoothness of the absorption spectrum from $\psi_2^{\max}$ as the initial condition stems from the initial placement of the $\psi_2^{\max}$ wavepacket on the steeper part of the excited curve which facilitates faster diabatic exit with little time for interference. The absorption spectrum from ϕ_0 as the initial condition has also been plotted and

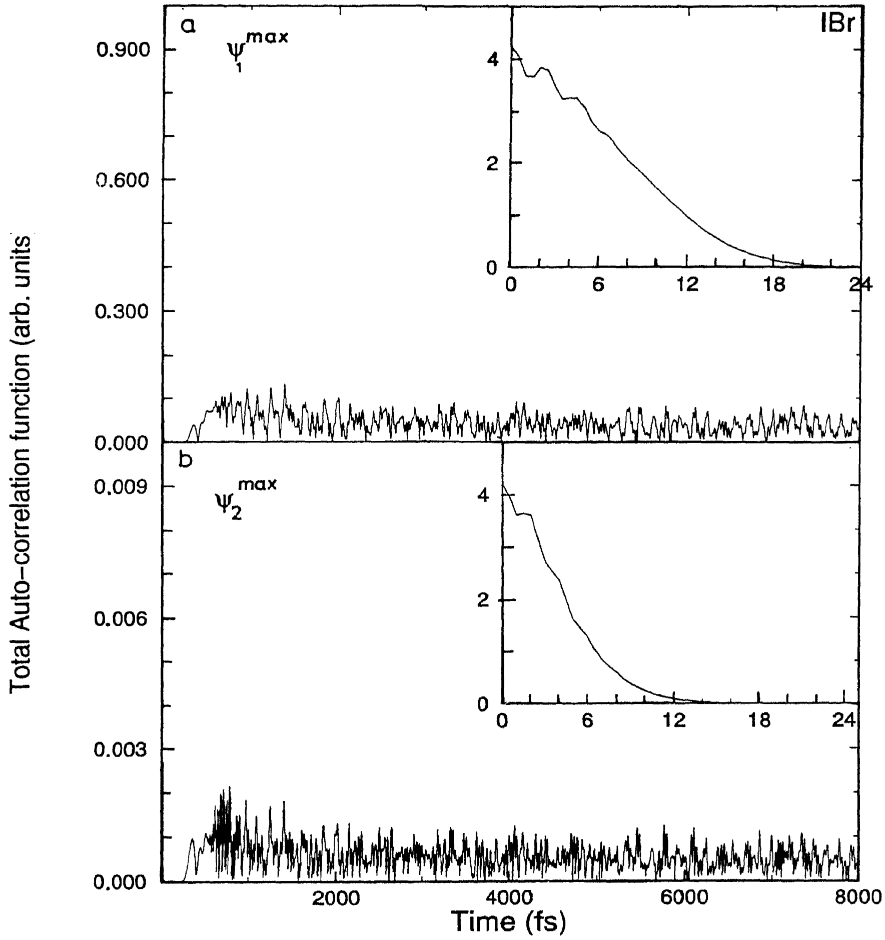

Fig. 11 Total autocorrelation functions for IBr with (a) $\psi_1^{\max}$ and (b) $\psi_2^{\max}$ as the initial condition.

compares well with other calculated[51,52] and experimental[54,55] absorption spectra for IBr. The absorption spectra peak at the wavelengths corresponding to the vertical Franck-Condon transition energies with $\psi_1^{\max}$, $\psi_2^{\max}$ and ϕ_0 as the initial states.

The branching ratios $\Gamma(Br^*/Br)$ with ϕ_0, $\psi_1^{\max}$ and $\psi_2^{\max}$ as the initial conditions are plotted in Fig. 13. At all energy values, $\Gamma(Br^*/Br)$ is much larger in magnitude with $\psi_2^{\max}$ as the initial condition compared to that with ϕ_0 or $\psi_1^{\max}$ as the initial condition and $\Gamma(Br^*/Br)$ is uniformly smaller with $\psi_1^{\max}$ as the initial condition as compared to $\psi_2^{\max}$ or ϕ_0 as the initial condition. This does seem to suggest that preparation of the initial state for a suitable photolysis pulse using the FOIST scheme can provide selective control through constructing appropriate linear combination of vibrational states. The field optimized superposition modifies the probability density profile to enable Franck-Condon transitions to appropriate region of the excited electronic state potential energy curves to enable a faster diabatic ($\psi_2^{\max}$) or slower adiabatic ($\psi_1^{\max}$) exit to maximize flux out of the I+Br*/I+Br channel respectively.

HI

The potential energy curves (Fig. 14a) and nonadiabatic/optical coupling elements used for

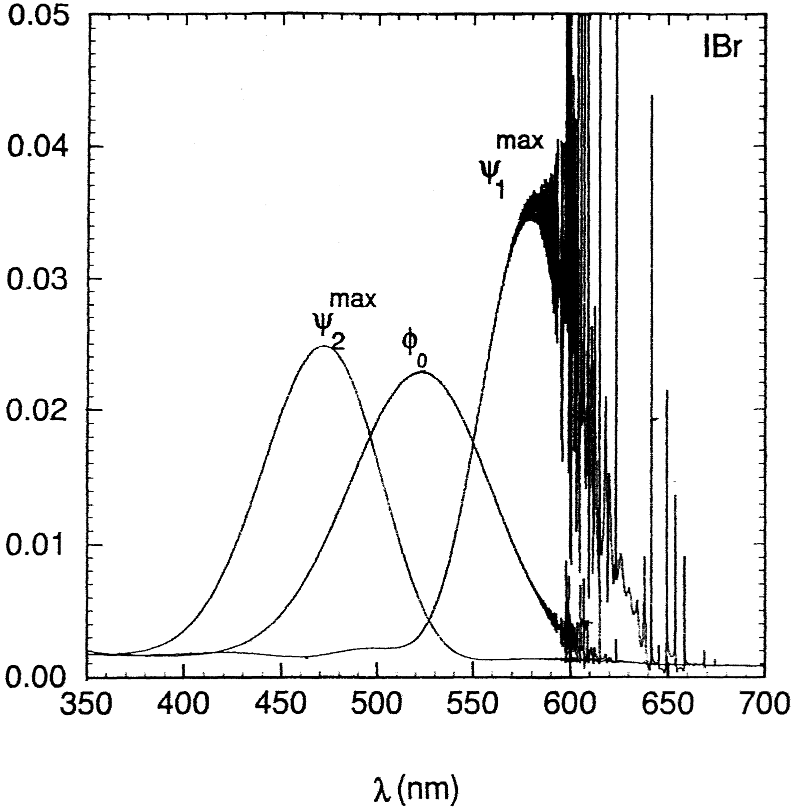

. 12 Total absorption spectrum for IBr with (a) ψ_1^{max} and (b) ψ_2^{max} as the initial condition.

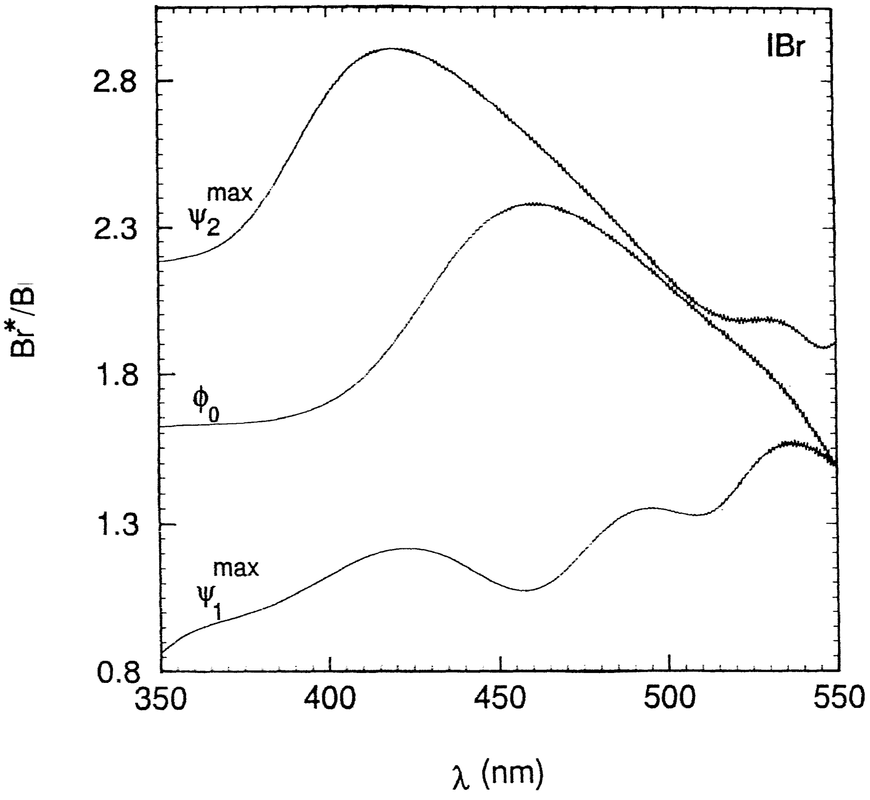

Fig. 13 Branching ratio $\Gamma(Br^*/Br)$ with with ϕ_0, ψ_1^{max} and ψ_2^{max} as the initial condition.

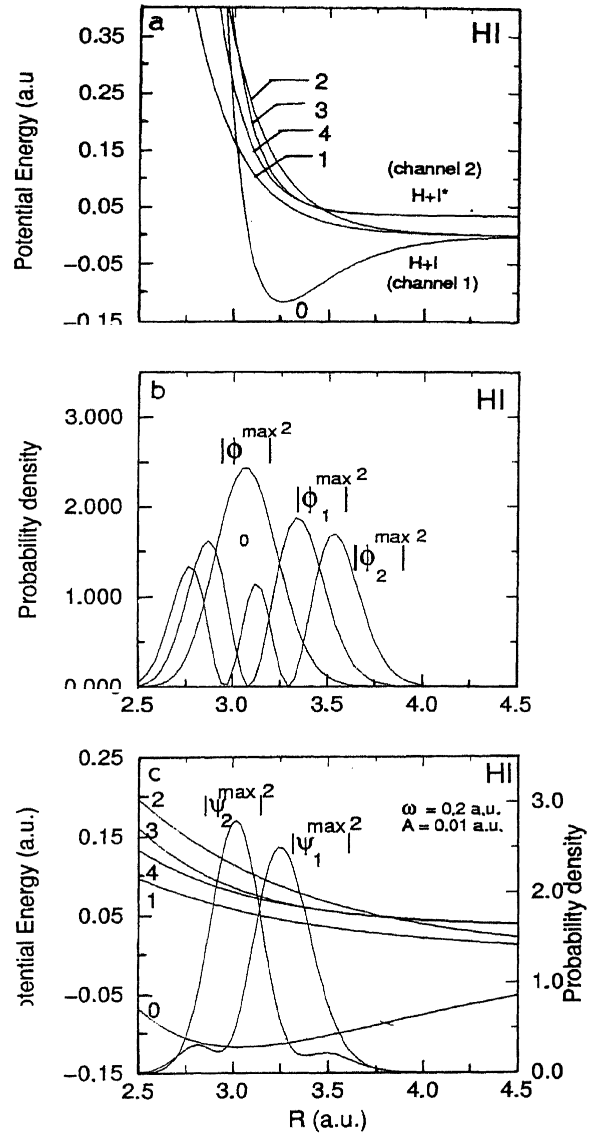

Fig. 14 (a) Potential energy curves of HI. (b) Probability density plots for the HI vibrational eigenstates ψ_0, ϕ_1 and ϕ_2 of ground electronic curve, (c) Probability density plots for ψ_1^{max} and ψ_2^{max} for flux maximization through H + I and H+I* channels respectively.

our investigation of the HI photodissociation here are same as those utilized earlier[16,33,34]. Probability density profiles from ϕ_0, ϕ_1 and ϕ_2 eigenfunctions included in the optimization manifold are plotted in Fig. 14b. The $^1\Sigma_0$ ground state (labelled 0) is optically coupled to all the four excited states $^3\Pi_1$, $^1\Pi_1$, $^3\Pi_0$ and $^3\Sigma_1$ (labelled 1,2,3, and 4 respectively). Furthermore, the states $^3\Pi_1(1)$–$^1\Pi_1(2)$ $^3\Pi_1(1)$–$^1\Sigma_1(4)$ and $^1\Pi_1(2)$–$^3\Sigma_1(4)$ are non-adiabatically coupled with each other, while the $^3\Pi_0^+$ state (3) has no nonadiabatic coupling with any other state. The outermost crossing between states 2 and 4 which will control the final flux redistribution occurs at $R=3.83$ a.u. The altered spatial profiles for ψ_1^{max} and ψ_2^{max} from our investigations spanning the frequency range of 0.16-0.26 a.u. (or 36000-56000 cm^{-1}/ 285-175 nm) are similar and we offer a representative probability density plot of $|\psi_1^{max}|^2$ and $|\psi_2^{max}|^2$ for $\omega = 0.20$ a.u. (44000 cm^{-1}/228 nm) and $A=0.01$ a.u. in Fig. 14c where ψ_1^{max} and ψ_2^{max} once again represent the field optimized initial states which maximize flux out of the lower H + I and the higher H+I* channels respectively. The probability density of the ground vibrational level peaks at 3.08 a.u., that for the $|\psi_1^{max}|^2$ maximizing flux out of channel 1 (H+I/states 0, 1 and 2) peaks at 3.29a.u. and that for $|\psi_2^{max}|^2$ maximizing flux out of channel 2 (H+I/states 3 and 4) at 3.01 a.u., i.e, just like in the case of IBr discussed earlier ψ_2^{max} is peaked once again to the left and ψ_1^{max} to the right of the ϕ_0 peak.

In Figs. 15a and 15b, we present a plot of the variation in the individual norm $\langle \chi_i(t) | \chi_i(t) \rangle$ on each excited state and also the total norm in the H+I/H+I* channels resulting from the use of ψ_1^{max} and ψ_2^{max} as initial states in the TDWP calculation. As seen in Fig. 15a, with ψ_1^{max} as the initial state, there is a net transfer of amplitude from H+I* channels (states 1 and 2) to H+I channel (state 4). The $^3\Pi_0^+(3)$ has no nonadiabatic coupling to any other state and therefore experiences no change in the norm transferred to it. There is a steady depletion from both states 1 and 4 into 2 initially, but within 5 fs the norm on all these repulsive curves for this extremely light $\mu \approx m_H$ system is well past the outermost crossing point (Fig. 15c) and unlike in the case of the heavy and slow moving IBr, the norms stabilize much more quickly and the system covers an average distance of 12.5 a.u. within 25 fs.

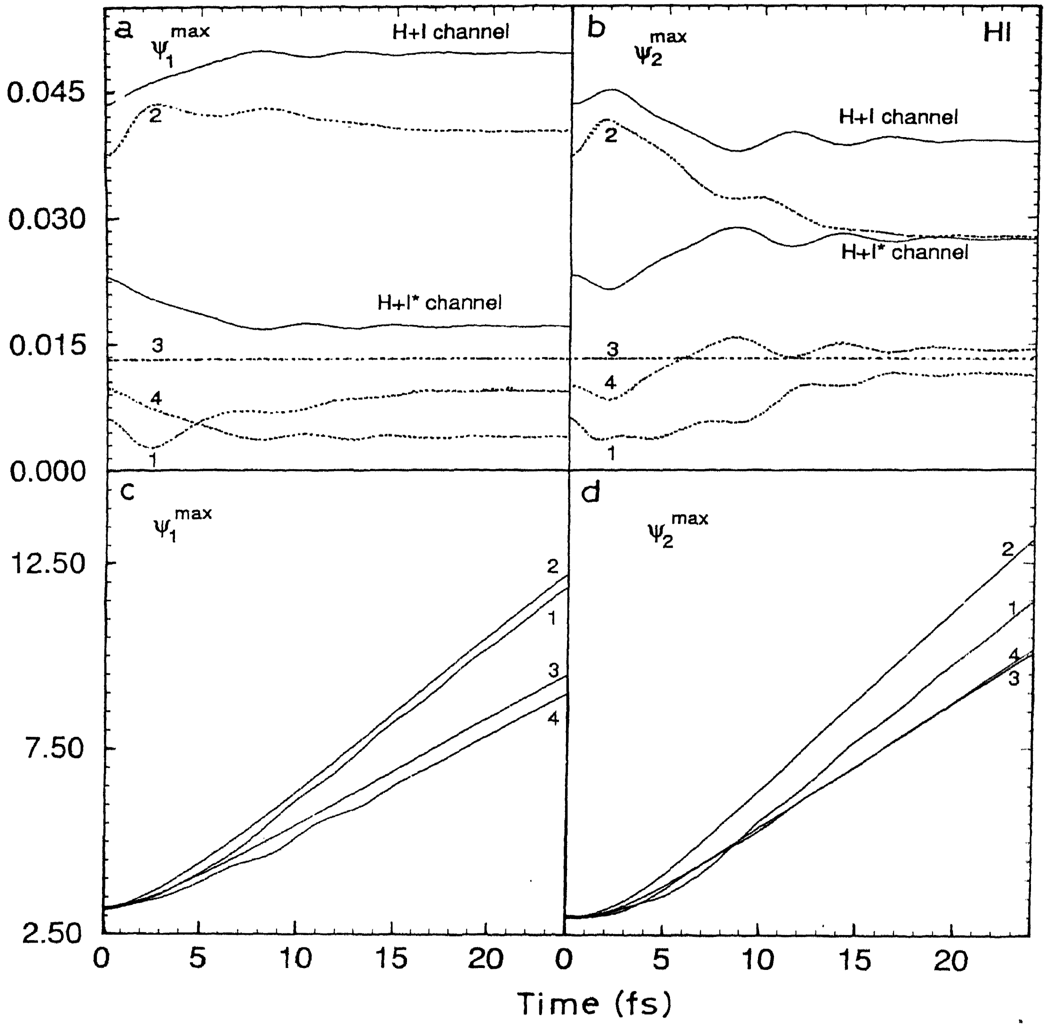

Fig. 15 Norm evolution on different potential energy curves of HI with (a) $\psi_1^{\max}$ and (b) $\psi_2^{\max}$ as the initial condition; position expectation values $\langle r \rangle_t$ on different curves of HI with (c) $\psi_1^{\max}$ and (d) $\psi_2^{\max}$ as the initial condition.

Results from the TDWP analysis with $\psi_2^{\max}$ as the initial condition are plotted in Fig. 15b where a fast depletion from state 2 into both state 4 (H + I*) and state 1 (H + I) is clearly seen. The build up in H + I* channel is therefore entirely due to depletion from the more repulsive ${}^1\Pi_1$ state and selectivity will be assisted by tuning the laser to the frequency corresponding to Franck - Condon transitions to ${}^1\Pi_1$ state. The molecule when described by $\psi_2^{\max}$ has to travel greater distance but still does traverse the outermost crossing between the states 2 and 4 faster than when described by $\psi_1^{\max}$, however, due to the low reduced mass of *HI* and consequently very fast motion as also considerable overlap between the spatial profiles of $\psi_1^{\max}$ and $\psi_2^{\max}$ for *HI*, the net change in the $\langle r \rangle_t$ at 25 fs is only marginally higher with $\psi_2^{\max}$ as the initial state.

At around 25 fs, the norms are well stabilized and as seen from the position expectation value plots of Figs. 15c and 15d the wavefunction is indeed well past the outermost crossing. The total auto-correlation functions $\sum_\ell \langle \chi_\ell(\tau) \mid \chi_\ell(\tau + t) \rangle$

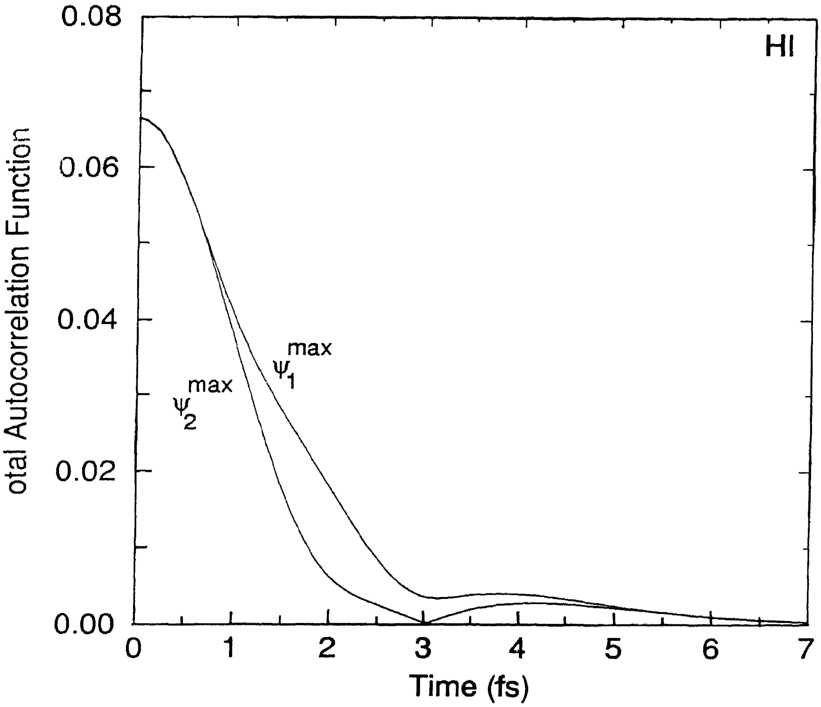

Fig. 16 Total autocorrelation functions for HI with (a) ψ_1^{m} and (b) ψ_2^{max} as the initial condition.

with both ψ_1^{max} and ψ_2^{max} as the initial condition have therefore been calculated with $\tau = 25$ fs and are displayed in Fig. 16.

In the case of HI, since all the four excited curves are repulsive, the possibility for recurrences is negligibly small and, the autocorrelation plots in Fig. 16 fall to zero much faster due to a quick dephasing of the wavepacket in the co-ordinate space. Fig. 17 contains the total absorption cross-sections obtained from the full Fourier transform of the autocorrelation function where the absorption spectrum with ϕ_0 as the initial states is once again in excellent agreement with experimental absorption profile for HI[33], and Fig. 18 portrays the branching ratio $\Gamma(I^*/I)$ with ϕ_0, ψ_1^{max} and ψ_2^{max} as the initial conditions. The magnitude of $\Gamma(I^*/I)$ over a large frequency range is indeed much less with ψ_1^{max} as the initial condition compared to that from ϕ_0 or ψ_2^{max} as the initial conditions and the ratio $\Gamma(I^*/I)$ with ψ_2^{max} as the initial condition is much larger than that obtained with ϕ_0 or ψ_1^{max} as the initial conditions. Hence the linear combination of vibrational eigenfunctions leading to ψ_1^{max} favours the formation of H + I products whereas the linear combination ψ_2^{max} favours H + I* formation as expected from the analysis presented earlier for IBr.

The use of FOIST, even for this much more complicated system leads to requisite alterations in the spatial profiles so that they peak at the internuclear distances required to facilitate Franck-Condon transitions to appropriate portion of the excited state potential curves enhancing photodissociation out of the desired channel.

Our investigation of the selective control of IBr and HI photodissociation using the optimal superpositions selected by the Rayleigh-Ritz variational procedure for maximization of flux out of the desired channel for the chosen field reveals that the selective maximization is effected through localization of the probability density at internuclear distances which enable Franck-Condon transitions to appropriate region of the excited states. Transfer of the wavefunction to the more steep, repulsive part of the excited potential

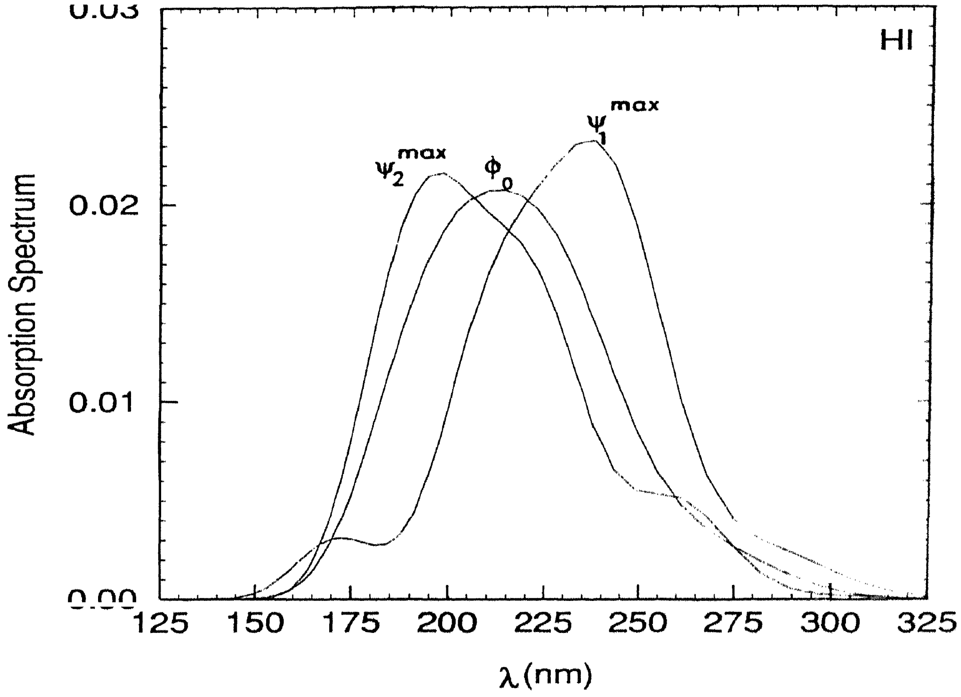

Fig. 17 Total absorption spectrum for HI with (a) ψ_1^{max} and (b) ψ_2^{max} as the initial condition.

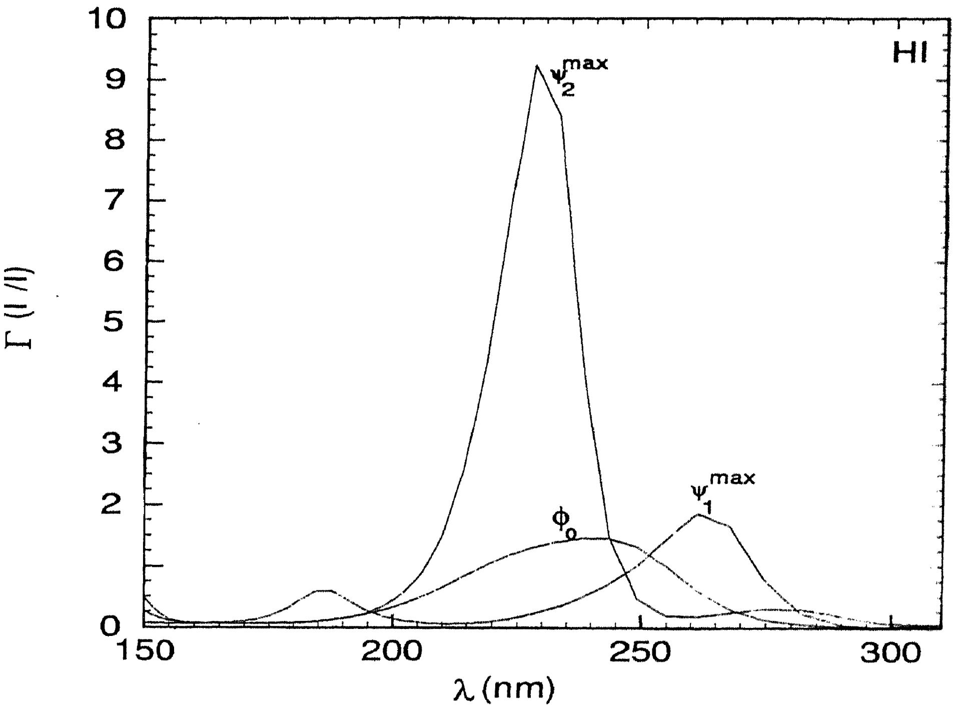

Fig. 18 Branching ratio Γ(I*/I) with with ϕ_0 ψ_1^{max} and ψ_2^{max} as the initial condition.

energy curves favours high velocity diabatic exit into the higher channel. Localization away from the repulsive wall favours slow adiabatic exit into the lower channel. Uniformity in the results obtained for the two fairly disparate systems investigated here seems to confirm the utility of the FOIST approach advocated here. The nascent mechanistic notions linking selectivity to appropriate modification of the initial state have been further examined by an analysis of the evolution of norm and position expectation values, autocorrelation functions, resulting absorption spectrum and branching ratios and this central role for modified spatial profile in selective control provides a new possibility for experimental exploration.

The experimental realization of the optimal initial states is however a completely uncharted area at this time. In an earlier paper[16] we have presented the formulae to obtain field parameters required to achieve these field optimized initial states and the optimal control[61] approach may also be easily and profitably employed to attain this FOIST comprising of only three vibrational levels.

We however believe that while the theoretical tools are useful, the central result from our investigation is that instead of putting the entire onus of selective control on a theoretically designed laser pulse which may not be easy to realize in practise, the approach where different vibrational population mixes are experimentally obtained and subjected to readily attainable photolysis pulses leading to an empirical experimental correlation between selectivity attained for diverse photolysis pulses and initial vibrational population mix used, represents a more promising and desirable alternative. Our results, we hope will spur such experimental tests and a concerted partnership between field and initial state shaping is required to better realize the chemical dream[4,12] of using lasers as molecular scissors and tweezers to control chemical reactions. It is our hope that the approach advocated here will merit experimental attention where instead of attempting selective control by using an active field manipulating a passive molecule in the ground vibrational state, experiments will be planned to use a variety of population mixes as the initial state.

The mechanistic notions rooted in our intense field optimal control and FOIST results are corroborated by the perturbative TDWP analysis and thereby become accessible to easy experimental checks without requiring ultrashort high intensity lasers. Should a pattern of the kind where altered spatial probability density profiles of the type studied here are experimentally confirmed to lead to selective control, generation of these profiles can be reduced to finding a suitable linear combination of known vibrational eigenfunctions without requiring any time dependent quantum mechanical calculations whatsoever. In an extremely optimistic scenario, since the profile of the standard simple harmonic oscillator eigenfunctions is well known, a lot can be done by mere inspection as well. Also, we have utilized three vibrational states, but there could be frequency ranges where only two vibrational states play a dominant role and further simplification may be obtained by examining flux as a function of initial vibrational states for an even easier shaping of the optimal linear combination.

In conclusion, the Rayleigh-Ritz variational maximization of flux by generating an optimal spatial profile for the initial wavefunction offers a new and flexible alternative for laser assisted selective control of chemical reactions. It is our hope that the FOIST based approach analyzed here will attract requisite experimentation and will assist in keeping the dream of controlling chemical reactions by modifying the underlying quantal dynamics, alive, and attractive for further pursuit.

Furthermore, in the results presented from the application of FOIST to IBr photodissociation, the IBr dynamics has been investigated using a three state model. There is a more comprehensive six state model[62] utilized by Levy *et al.* for more accurate reproduction of Raman Excitation Profiles (REPs). It is therefore useful to ensure that the three state IBr model utilized in our work is adequate and dependable. Authentication of the three state model used herein through a detailed analysis of IBr photodissociation using Raman Excitation Profiles (REP) is presented in the following section.

5 Detailed Investigation of Photodissociation using Raman Excitation Profiles: An Application to IBr

Resonance Raman spectroscopy has emerged as a powerful and sensitive probe for deciphering the detailed dynamics of chemical reactions[63]. Resonance Raman intensities observed at different excitation wavelengths, termed as Raman excitation profiles (REPs) have been shown to be particularly sensitive to minor variations in the underlying potential energy curves and coupling elements controlling the photodynamics of a system[51,52,64,65].

IBr has served as a prototype for detailed theoretical investigation and possible selective control of photodissociation processes[15-20,62-65]. The investigations however have employed different sets of potential energy curves and non-adiabatic/optical coupling matrix elements, with the six state model of Levy *et al.*[62] being the most comprehensive. The three state model employed for optimal control[15] and for FOIST based selective contro[116,18-20] of IBr photodissociation products has however captured the essential photodynamical features quite adequately. An even simpler three state model with only one optically coupled excited state and a constant nonadiabatic coupling matrix element between the two excited states has been employed by Guo[52], who calculated both photoabsorption spectrum and REP for IBr utilizing a spatial grid consisting of only 512 grid points.

Due to the large reduced mass of IBr and importance of much slower predissociation in its photodynamics, the wavepacket on the excited state can be highly delocalized and most calculations routinely employ 1024 spatial grid points. The use of six state model for treating IBr photodissociation, therefore, is computationally demanding and it is desirable to investigate if the more economic three state model is adequate to reproduce the essential features of IBr photodynamics. Since REPs are sensitive to even minor systemic details, their calculation using both the three and the six state models and a comparative analysis of the results can provide a very sensitive probe of the IB*r* photodissociation and may be utilized for investigating the adequacy of the three / six state IBr models[51].

The Time-Dependent Wave Packet (TDWP) calculation of the IBr REPs have been carried out earlier by Guo[52]. His calculations, however, utilized many approximations mentioned earlier. Furthermore, the three state model of Guo gives REPs that are structureless in the direct dissociation ($\lambda < 548$ nm, the $Br^* + I$ dissociation limit) region, while the first order perturbation theoretic calculations of Levy *et al.*[62] yield structures that have been utilized to deduce that the REPs retain the memory of the final vibrational state.

It is therefore useful to calculate the IBr REPs accurately using both the three and the six state models to investigate the competing dynamic effects from different states and to ascertain if the more accurate TDWP calculations undertaken here using the same states and couplings as those employed by Levy *et al.*[62] can reproduce the structure seen in the REP in the direct dissociation regime ($\lambda < 548$ nm). These calculations should also provide a rigorous assessment of the comparative adequacy of the more economic three state model for IBr photodissociation, so that, if the three state model is found to be sufficiently accurate, it may be employed routinely to provide substantial computational economy without sacrificing the essential features of the photodynamics. In view of the strong interference effects seen in the continuum Raman REPs[62,63,66-68] and close proximity of the additional curves in the six state model such an investigation for IBr assumes added significance.

5.1 The TDWP method for Raman Excitation Profile

In the time-dependent wave packet method, the Schrödinger equation is solved with $|\phi^{\ell}(0)\rangle = \mu_{0\ell}|\psi_0\rangle$, where ψ_0 is the initial ground state wavefunction and $\mu_{0\ell}$, the transition dipole moment between the ground and the $\ell - th$ excited state. The time evolution of the promoted state wavefunction is described by

$$| \phi_l(t) >= \exp(-iH_{ex}t / \hbar \,| \phi_l(0) > \quad \ldots (20)$$

where H_{ex} is the excited state Hamiltonian[38,67,68] The overlap of the time evolving wavefunction $\phi_{\ell}(t)$ with the initial promoted state wave function $\phi_{\ell}(0)$ is the autocorrelation function $C_{00}^{\ell}(t) = \langle \phi_{\ell}(0) | \phi_{\ell}(t) \rangle$ and is a measure of how fast the promoted state leaves the Franck-Condon region[67,69,70] . The total autocorrelation function is the sum of the individual autocorrelation functions for different channels and is given by,

$$C_{00}(t) = \sum C_{00}^{\ell}(t) \quad \ldots (21)$$

Fourier transform of the individual autocorrelation functions yields the partial absorption cross sections[38]

$$\sigma_A^\ell(\omega) \propto \omega \int^{+\infty} C_{00}^\ell(t) e^{i(\omega+\omega_0)t} dt \qquad (22)$$

where ω is the frequency of the incident laser and $\hbar\omega_0$ is the energy of the initial ground state ψ_0. Total absorption cross section is a sum of the partial absorption cross sections:

$$\sigma_A(\omega) = \sum_\ell \sigma_A^\ell(\omega) \qquad \ldots\ (23)$$

The overlap of the final vibrational wavefunction (on the ground electronic state) with the time evolving promoted state wavefunction (on the excited state) $C_{f0}^\ell(t) = \langle \phi_f(0) \mid \phi^\ell(t) \rangle$ is termed the cross-correlation or Raman correlation function[38,67-74] and for Raman intensity analysis, the Raman amplitude $\alpha_{f0}(\omega)$ for each channel is obtained from the corresponding Raman correlation function:

$$\tau_{f0}^\ell(\omega) \propto (i/\hbar) \int^{+\infty} C_{f0}^\ell(t) e^{i(\omega+\omega_0)t} dt \qquad (24)$$

and the Raman excitation profile from the Raman amplitude:

$$I_{f0}^\ell(\omega) = \omega\omega_s^3 \left|\alpha_{f0}^\ell(\omega)\right|^2, \qquad \ldots\ (25)$$

with ω_s being the frequency of the scattered radiation. The total observable Raman intensity $I_{f0}(\omega)$ is computed from the total Raman amplitude, which is a sum of the partial Raman amplitudes:

$$I_{f0}^\ell(\omega) = \omega\omega_s^3 \left|\alpha_{f0}(\omega)\right|^2 = \omega\omega_s^3 \left|\alpha_{f0}^\ell(\omega)\right|^2 \qquad \ldots\ (26)$$

Interference among the Raman amplitudes $\alpha_{f0}^\ell(\omega)$ corresponding to different channels results in structures in the total Raman intensity profile.

Vibrational eigenfunctions ψ_i and the corresponding eigenvalues for IBr in its ground electronic state have been calculated using the Fourier grid Hamiltonian method[45]. The split-operator fast Fourier transform (SOFFT) algorithm[46-47] was utilized to integrate the time-dependent Schrödinger Equation. A total spatial grid of 14 a_0 (2-16 a_0) was used in IBr bond length and it was divided into 1024 equally spaced grid points. A linear ramp (optical potential) with a maximum height of 0.01 Hartree was set up near the edge of the grid ranging from 14.85 a_0 to 16.0 a_0. The wavefunction was propagated on the excited states for a total of 8192 fs (T) in time steps of 0.5 fs each providing a resolution ($\sim 2\pi/T$) of 5.1×10^{-4} eV.

5.2 Results from Application to IBr

Potential energy curves used for IBr [0: $X^1\Sigma_{0^+}$, 1: $A(^3\Pi_1)$, 2: $B(^3\Pi_{0^+})$, 3: $Y\ (O^+)$, 4: $Y'(O^+)$ and 5: $B'(^3\Pi_{0^+})$] are plotted in Fig. 19a and the systemic parameters are those tabulated in ref. [62]. The three state model is a truncation, where only the ground state $X^1\Sigma_{0^+}$ and the second and the third excited states $B(^3\Pi_{0^+})$ and $Y(O^+)$ respectively are retained. To ensure a proper comparison between the three and the six state models, same systemic parameters for both the sets have been used, i.e. the three state model is a subset of the six state model. The nonadiabatic and dipole coupling matrix elements used by Guo are different, yet the IBr REPs reported in his work[52] are comparable to the three state results presented here.

The autocorrelation function and cross correlation function for the fundamental Stokes line from the three and six state models and the corresponding absorption spectra are plotted in Figs. 19b, 19c and 19d, respectively. The value of $C_{00}^t(t)$ at $t=0$ from the two models represents the sum $|\mu_{02}|^2 + |\mu_{03}|^2$ and $\sum_{\ell=1}^{5} |\mu_{0\ell}|^2$, respectively.

The $C_{00}^t(t)$ from both the models have essentially the same form and decay time. This similarity between results from the two models persists in the case of the cross-correlation function (Fig. 19c) and also the computed absorption spectra (Fig. 19d). The latter follow closely the experimental absorption spectrum[62]. The absorption spectra from the two models differ in the predissociative regime, where, as expected, the presence of the lower lying excited state $A(^3\Pi_1)$ in the six state model leads to the longer wavelength structure missing in the three state model.

The REPs obtained from both the models are structureless in the direct dissociation region (λ =400-540 nm) and are reproduced only for the fundamental in the insets of Fig. 20a. These are however similar to each other, decrease

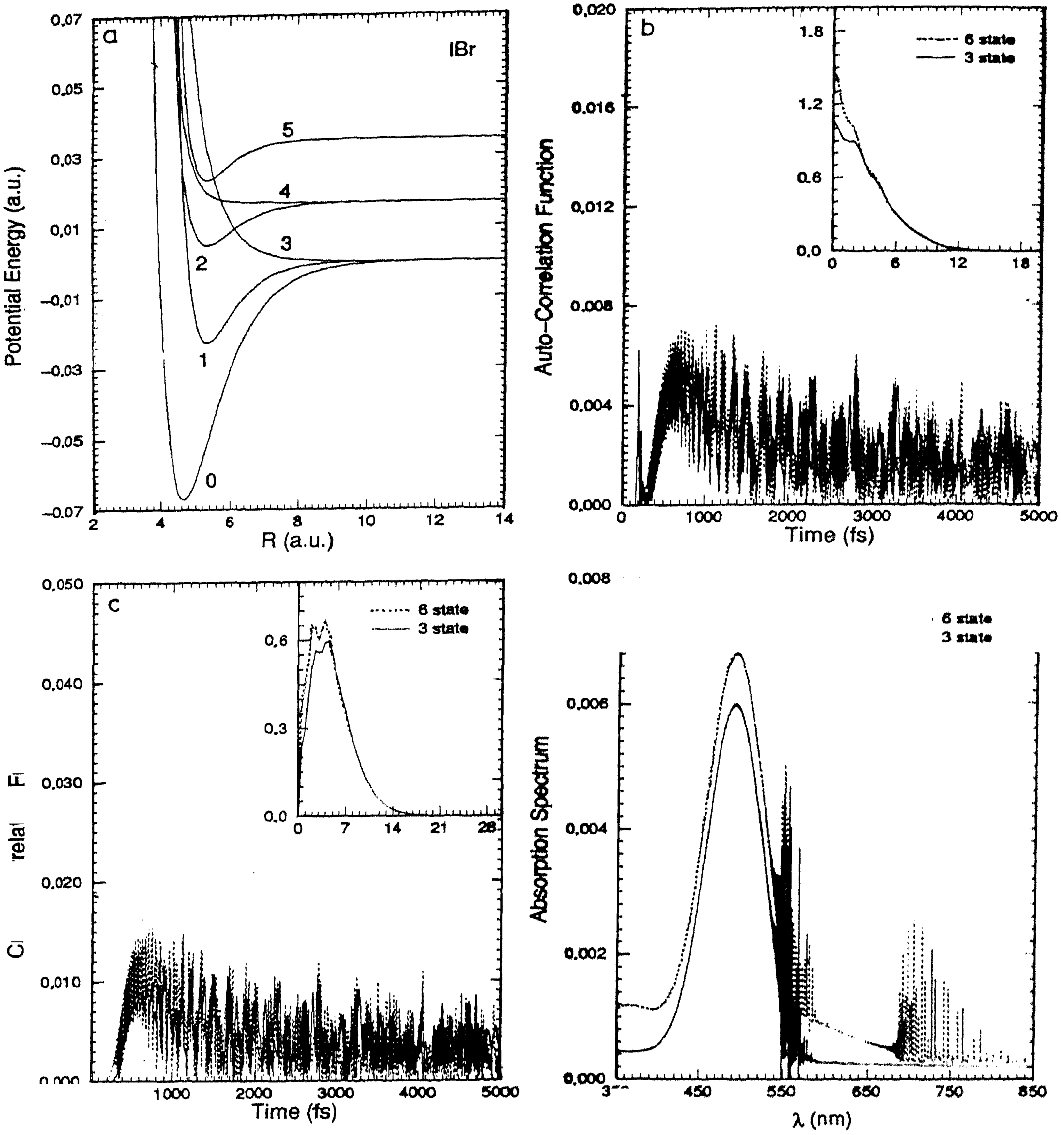

Fig. 19 (a) IBr Potential energy curves. (b) Total autocorrelation function (c) crosscorrelation function (d) Absorption spectrum from 3 and 6 state models.

progressively for higher overtones and do not mirror the topology of the final vibrational state wavefunctions. The REPs in the range λ =540-590 nm for the overtones are shown in Figs 20b-20d. Results from the two models differ from each other. Those from the six state model with a larger number of channels for the leakage of the initial amplitude are smaller in magnitude in comparison to that from the three state model. This assertion is buttressed by Figs. 21a and 21b, wherein we have plotted the evolution of probability density for each excited state as a function of time. It is clear from Figs. 21a and 21b that the depletion of norm is larger in the six state model due to the availability of extra pathways offered by the additional states. The six state model yields some additional long wavelength peaks due to the presence of the lower lying $A(^3\Pi_1)$ state. The decrease in intensity of the REP peaks from the six state model is similar to that seen for REPs calculated by including

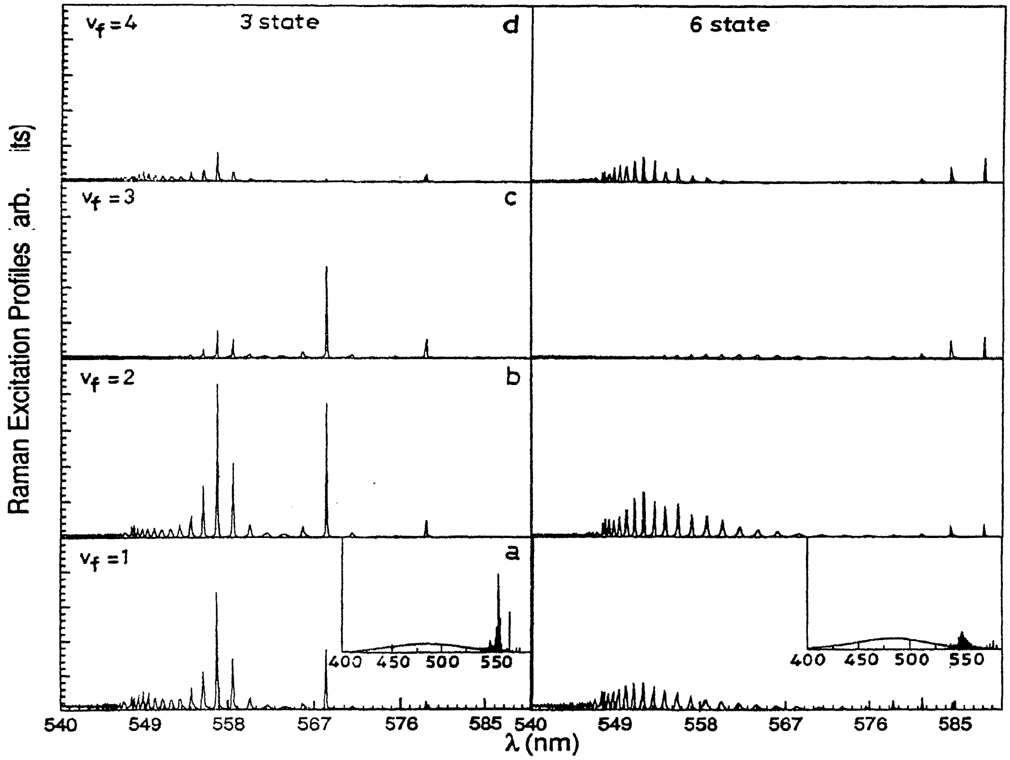

Fig. 20 (a–d) : Raman excitation profile for the fundamental and overtones for IBr from both the three and the six state models.

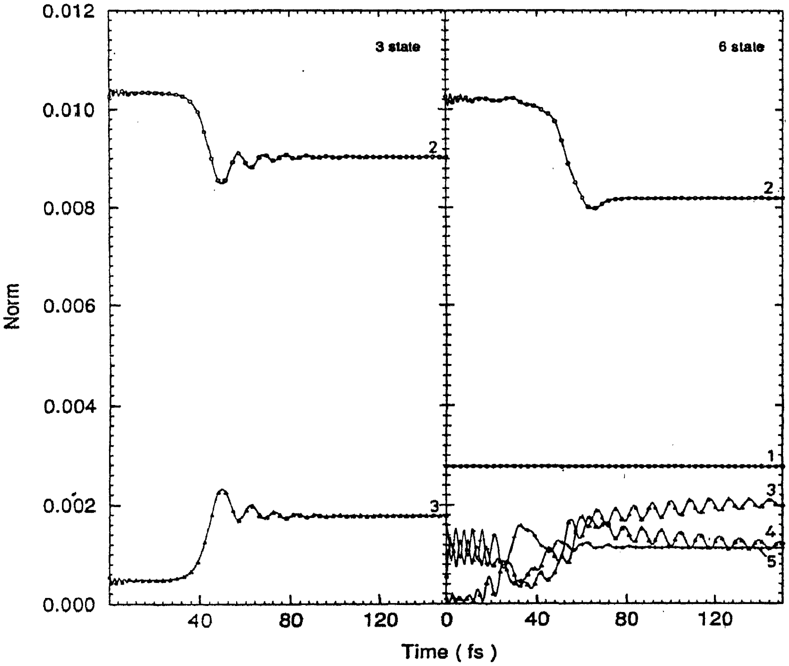

Fig. 21 Norm of the wavefunction as a function of time on different excited states in the three and the six state models.

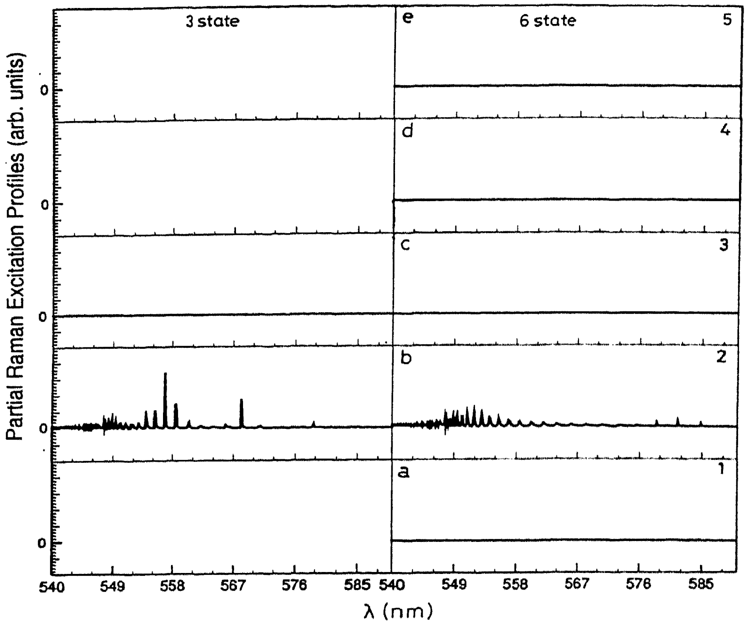

Fig. 22 Partial contributions from individual excited states to the fundamental REP.

nonadiabatic coupling between the $B(^3\Pi_{0^+})$ and $Y(O^+)$ states in Guo's work[52] in which the presence of nonadiabatic coupling diminished the intensity pattern when compared to the REPs calculated without including the nonadiabatic coupling.

The partial REPs from each excited state in both the models are plotted in Fig 21 and 22. They are completely determined by the optically brightest $B(^3\Pi_{0^+})$ state in both the models. The other states seem only to be additional outlets for funnelling amplitude away from the brightest state thereby decreasing the intensity of the REP peaks common to both models. The dominant role of the $B(^3\Pi_{0^+})$ state is further confirmed by the partial absorption crossection profiles plotted in Fig. 23.

The results presented here suggest that the more economic three state model is quite adequate for eliciting the essential features of the IBr photodynamics. The effect of introducing additional states is minimal and easily understood. The unraveling of contributions from individual states to the fundamental Stokes REP $I_{10}(\omega)$ in this work and also in that of Guo's calculations, wherein only the $B(^3\Pi_{0^+})$ state was taken to be optically bright indicate that the photodynamics is largely determined by the attributes of the brightest state and that simpler models involving the correct electronic states could be employed advantageously in all photodynamic investigations.

Finally, the basic premise that Raman excitation profiles may be used for model authentication and for obtaining detailed insight into the dynamics of photodissociation seems to be a valid proposition in the light of the results presented here.

6 Summary

The detailed insights available from investigation of photodissociation of diatomic and small polyatomic molecules have motivated the use of this knowledge to selectively control the outcome of photodissociation reactions. The Pump and Dump, the Coherent Control and the Optimal Control schemes emphasize the design of appropriate laser pulses for the given objective and their weaknesses and strength have been assessed earlier. The Pump and Dump scheme demands a simple and compact distribution of wavepacket amplitude on the excited potential energy surface over the product exit channel on the ground state potential energy surface. This remains unattainable as the evolving wavepacket on the excited potential

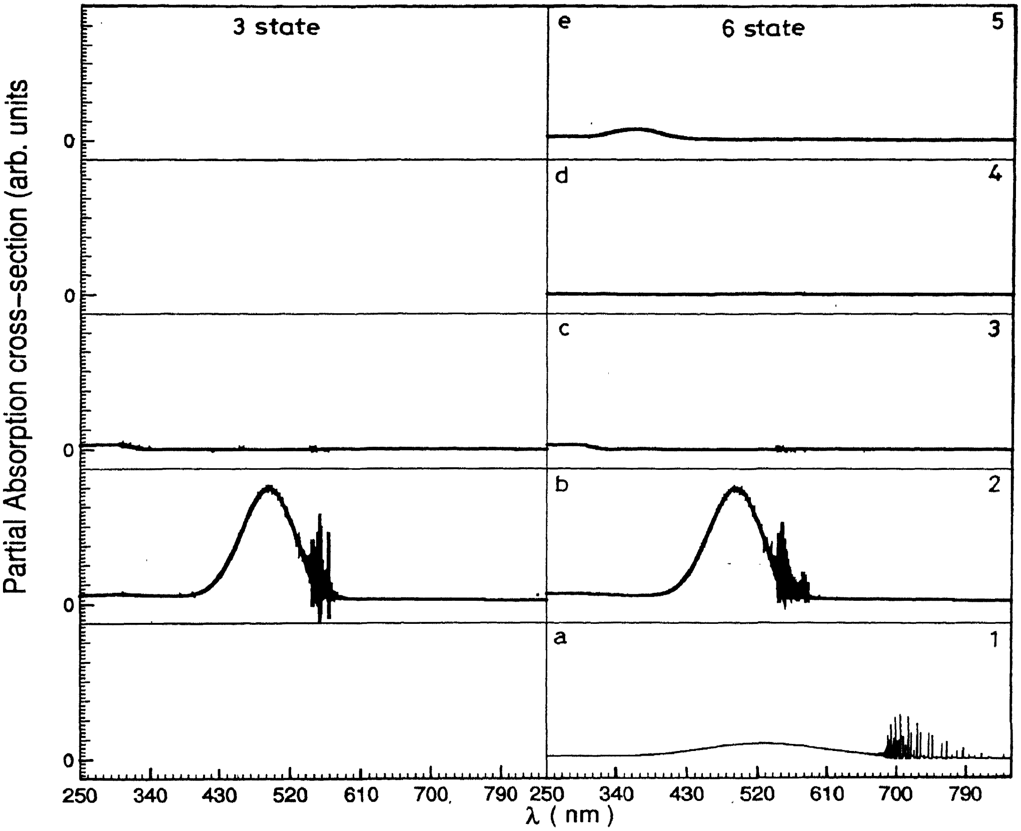

Fig. 23 Partial contributions $\sigma_A^{\ell}(\lambda)$ from individual excited states to the absorption spectrum $\sigma_A(\lambda)$, as obtained from the three and the six state models. The $B(^3\Pi_{0^+})$ state makes the dominant contribution.

energy surface generates a very complicated amplitude distribution over the product exit channel and an efficient transfer of amplitude to the exit channel by a simple dump pulse may be unattainable. A possible alternative is to determine the amplitude distribution in the excited PES in advance corresponding to the desired amplitude distribution over the product exit channel. However, the amplitude distribution obtained from such calculations is not easily created by Franck-Condon transitions. Nevertheless, the Pump and Dump calculations resulted in the seminal idea of using a temporal and spectrally shaped field continuously back and forth between the ground and the excited state surfaces which finally lead to the method of optimal pulse shaping for selective control of products in a reaction.

The coherent control theory formulated by Brumer and Shapiro has provided a variety of alternative control scenarios only one of which has been presented here. The effectiveness of the 1 photon-3 photon pathway interference based coherent control has been demonstrated experimentally and its intuitive simplicity is most appealing. As shown by Gross and Rabitz[75] coherent control is a perturbation theoretic approximate of the Optimal Control in the weak field regime. Although, product selectivity can be ensured, substantive yield requires high intensity lasers and the general validity of the coherent control formulation becomes questionable.

The optimal control theory approach is completely general and is applicable to fields of high intensity thereby ensuring substantial yield. The computational procedure behind the scheme is however extremely demanding. It requires the forward and the backward solution of TDSE and also a similar equation for the Lagrangian constraint function coupled to an iterative optimization of the objective functional[76] where these demanding tasks needs to be performed many many times (55 times for IBr) for each objective. At the end of this demanding procedure, the optimal field obtained is very often of a shape and intensity which cannot be reproduced in the laboratory.

It therefore becomes most desirable to search for alternatives which are as general in their applicability and yet can deliver similar selectivity and yield using laser attributes which can be easily obtained in ordinary chemical laboratories. We hope that the results presented here portray FOIST as an alternative that fulfills these demands. Results from the selective control of IBr and HI photodissociation using the optimal superpositions selected by the Rayleigh-Ritz variational procedure for maximization of flux out of the desired channel for the chosen field confirms the utility of the FOIST approach advocated here. The results demonstrate excellent selectivity with mutually exclusive range of field parameters for maximizing the products from competing channels and at the same time ensure almost total dissociation[16,17]. A detailed analysis of these results seems to link selective maximization to localization of the probability density at internuclear distances which enable Franck-Condon transitions to appropriate region of the excited potential energy curves. Transfer of the wavefunction to the more steep, repulsive part of the excited potential energy curves favours high velocity diabatic exit into the higher channel. Localization away from the repulsive wall favours slow adiabatic exit into the lower channel. These new mechanistic notions advocating selectivity due to appropriate modification of the initial state have been further examined by an analysis of the resulting absorption spectrum and branching ratios using the TDWP analysis and this central role for modified spatial profile in selective control verifies the same centrality to initial state modification envisaged in our earlier discussion of the IBr results from the application of the optimal control theory.

The experimental realization of the optimal initial states however deserve more detailed attention. Formulae to obtain field parameters required to achieve these field optimized initial states have been presented elsewhere[16] and the optimal control approach[12,43,61] may also be easily and profitably employed to attain this FOIST comprising of only three vibrational levels. The Parametric Equations of Motion (PEM) for time dependent Schrödinger equation also provide an economic map of vibrational population as a function of field parameters[76] and PEM too may be harnessed for this task. While the theoretical tools mentioned here may be easily utilized for this objective and perhaps even better theoretical techniques can be designed to achieve this FOIST, We believe that simple interpretation of the optimal coefficients as being indicative of population ratios is perhaps easier to check experimentally and should be the preferred choice for further exploration. Our results, we hope will spur such experimental tests and instead of a passive molecule being manipulated by an active field, a concerted partnership between field and initial state shaping advocated here will assist in expediting the use of lasers as molecular scissors and tweezers to control chemical reactions. At this stage of development, however, what would serve the purpose better is an experimental test of the ideas presented here and hopefully the detailed demonstration of its promise will stimulate expeditious experimental investigations.

The use of REPs in detailed investigation of photodynamics is another promising extension presented here. The validity of various sets of potential energy curves and functional forms of non-adiabatic coupling/optical coupling used and the details of the dynamics of IBr photodissociation are probed effectively by calculating the Raman Excitation Profiles. The results presented confirm that the economic three state model is quite adequate and the REPs provide very detailed insights into the dynamics of IBr photodissociation. The individual contributions of the different curves for the fundamental Stokes line reveals that the dynamics of IBr photodissociation is largely determined by the $B(^3\Pi_{0^+})$ state. The structurelessness of the REPs below 540nm indicates that the REPs are influenced by the long time features where the correlation is lost due to the difference between the initial and the final probability density patterns. Finally the results confirm that Raman Excitation Profiles provide an exciting new tool for comprehensive probe of photodissociation models.

In conclusion, we see that the photodissociation of small molecules displays a richness of quantum effects replete with details which have fueled the dream of using lasers with appropriately designed attributes to cleave bonds selectively. In this review we have tried to present an overview of some of the more promising approaches to this fascinating and critical chemical goal of providing only the desired products without any trace of unwanted fragments which could be toxic and/or difficult to extricate. The experimental results adduced here are bound to provide further fillip to the dream of using lasers as molecular scissors. While none of the approaches reviewed here can promise universal applicability, it is our hope that the examples with emphasis on use of easily available lasers will motivate new experiments and the dream of using lasers to control chemical reaction will move further towards realization.

7 Acknowledgements

One of the authors, Dr Vandana K acknowledges support from the CSIR, India (SRF 2-14/94(II)/EUII). The author (MKM) is pleased to acknowledge financial support from the Board of Research in Nuclear Sciences (BRNS 37/19/97-R & D-II) of the Department of Atomic Energy, India.

References

1 J G Calvert and J N Pitts *Photochemistry* Wiley New York (1966), NY Turro *Modern Molecular Photochemistry* Benjamin MenloPark (1978), A Ben-Shaul, Y Haas, K L Kompa and R D Levine *Lasers and Chemical Change* Springer-Heidelberg (1981), R P Wayne *Principles and applications of Photochemistry* Oxford University Press Oxford (1988)
2 R Schinke, *Photodissociation Dynamics : Spectroscopy and Fragmentation of Small Polyatomic Molecules*, Cambridge University Press (1993)
3 R J Gordon and S A Rice *Ann Rev Phys Chem* **48** (1997) 601
4 F F Crim *Annu Rev Phys Chem* **44** (1993) 397
5 R N Zare *Science* **279** (1998) 1875
6 D J Tannor and S A Rice *J Chem Phys* **83** (1985) 5013
7 D J Tannor and S A Rice *Adv Chem Phys* **70** (1988) 441
8 P Brumer and M Shapiro *Chem Phys Lett*, **126** (1986) 126
9 P Brumer and M Shapiro *Acc Chem Res* **22** (1989) 407
10 P Brumer and M Shapiro *Ann Rev Phys Chem* **43** (1992) 257
11 P Brumer and M Shapiro *In Molecules in Laser Fields* (Ed A D Bandrauk) NewYork Dekker (1994) 287
12 W A Warren, H A Rabitz and M Dahleh *Science* **259** (1993) 1581
13 H Rabitz and S Shi *In Advances in Molecular Vibrations and Collision Dynamics* (Ed. J Bowman) Jai Greenwich C T (1991) 187
14 H Rabitz *In Atomic and Molecular Processes with Short Intense Laser Pulses* (Ed. A Bandrauk) Plenum New York (1988) 389
15 P Gross, D B Bairagi, M K Mishra and H A Rabitz *Chem Phys Lett* **223** (1994) 263
16 P Gross, A K Gupta, D B Bairagi and M K Mishra *J Chem Phys* **104** (1996) 7045
17 D B Bairagi, P Gross and M K Mishra *J Phys Chem A* **101** (1997) 759
18 Vandana K, D B Bairagi, P Gross and M K Mishra *Pramana J Phys* **50** (1998) 521
19 Vandana K and M K Mishra *J Chem Phys* **110** (1998) 5140
20 Vandana K and M K Mishra *Advances in Quant Chem* **35** (1999) xxx (in press)
21 F F Crim *Science* **249** (1990) 1387
22 N Bloemberben and A H Zewail *J Phys Chem* **88** (1984) 5459
23 M Gruebele and A H Zewail *Phys Today* **43** (1990) 24
24 A H Zewail and R B Bernstein *Chem & Engg News* **66** (1988) 24
25 E Charron, A Guitsi-Suzor and F H Mies *Phys Rev Lett* **71** (1993) 692
26 S M Park, S P Lu, Y Xie and R J Gordon *J Chem Phys* **94** (1991) 8622
27 X Wang, R Bersohn, K Takahashi, M Kawasaki and HL Kim *J Chem Phys* **105** (1993) 2992
28 T Baumert and G Gerber *Isr J of Chem* **34** (1994) 103
29 C Chen, Y Y Yin and D S Elliot *Phys Rev Lett* **64** (1990) 507
30 N Chakrabarti, V Balasubramaniam, N Sathyamurthy and J W Gadzuk *Chem Phys Lett* **242** (1995) 490
31 S I Chu *J Chem Phys* **94** (1991) 7901
32 J Wang and S I Chu *Chem Phys* **227** (1994) 663
33 I Levy and M Shapiro *J Chem Phys* **89** (1988) 2900
34 C Kalyanaraman and N Sathyamurthy *Chem Phys Lett* **209** (1993) 52
35 Y Cohen, I Bar and S Rosenwaks *J Chem Phys* **102** (1995) 3612
36 B Amstrup and NE Henriksen *J Chem Phys* **97** (1992) 8285
37 H Gresonde, S Hennig and H Gabriel *J Chem Phys* **101** (1994) 9558
38 E J Heller *Acc Chem Res* **14** (1981) 368
39 K C Kulander and E J Heller *J Chem Phys* **69** (1978) 2439
40 S Y Lee and E J Heller *J Chem Phys* **71** (1979) 4777
41 S Das and D J Tannor *J Chem Phys* **91** (1989) 2324
42 D J Tannor, R Kosloff and S A Rice *J Chem Phys* **85** (1986) 5805
43 S H Shi and H Rabitz *J Chem Phys* **92** (1990) 2927
44 S Shi and H Rabitz *Comput Phys Commun* **63** (1991) 71
45 M D Feit, J A Fleck and A Steiger *J Comput Phys* **48** (1982) 412
46 R Kosloff *J Phys Chem* **92** (1998) 2087
47 P Gross, D Neuhauser and H Rabitz *J Chem Phys* **96** (1992) 2834
48 M Alexander, B Pouilly and T Duhoo *J Chem Phys* **99** (1993) 1752
49 M Kaluza, J T Muckerman, P Gross and H Rabitz *J Chem Phys* **44** (1994) 4211

50 C K Chan, P Brumer and M Shapiro *J Chem Phys* **94** (1991) 2688

51 Vandana K, N Chakrabarti, N Sathyamurthy and M K Mishra *Chem Phys Letts* **288** (1998) 545

52 H Guo *J Chem Phys* **99** (1993) 1685

53 MS Child *Mol Phys* **32** (1976) 1495

54 H Bony, M Shapiro and A Yogev *Chem Phys Letts* **107** (1984) 603

55 I Levy, M Shapiro and A Yogev *J Chem Phys* **96** (1992) 1858

56 L Zhu, V Kleiman, X Li, S P Lu, K Trentelman and R J Gordon *Science* **270** (1995) 77

57 X Wang, R Bersohn, K Takahashi, M Kawasaki and H L Kim *J Chem Phys* **105** (1993) 2992

58 T Baumert and G Gerber *Isr J Chem* **34** (1994) 103

59 C C Marston and G G Balint-Kurti *J Chem Phys* **91** (1989) 3571

60 M S Devries, N J A van Veen and A E DeVries *Chem Phys Letts* **56** (1978) 15

61 S Shi, A Woody and H A Rabitz *J Chem Phys* **88** (1988) 6870

62 I Levy, M Shapiro and A Yogev *J Chem Phys* **96** (1992) 1858

63 A B Myers *Laser Techniques in Chemistry* (Ed. A B Myers and T R Rizzo) John Wiley and Sons Inc New York **23** (1995) 325

64 B Hartke *Chem phys Letters* **160** (1989) 538

65 B Hartke *J Raman Spectry* **22** (1991) 131

66 I Levy, M Shapiro and P Brumer *J Chem Phys* **93** (1990) 2493

67 N Chakrabarti, C Kalyanaraman and N Sathyamurthy *Chem Phys Letts* **267** (1997) 31

68 D Imre, J L Kinsey, A Sinha and J Krenos *J Phys Chem* **88** (1984) 3956

69 E J Heller, R L Sundberg and D J Tannor *J Phys Chem* **86** (1982) 1822

70 P Baierl, W Kiefer, P F Williams and D L Rousseau *Chem Phys Letts* **50** (1977) 57

71 M Jacon, O Atabek and C Leforestier *J Chem Phys* **91** (1989) 1585

72 A B Myers *J Opt Soc Am* **7** (1990) 1665

73 A B Myers, R A Mathies, D J Tannor and E J Heller *J Chem Phys* **77** (1982) 3857

74 B R Johnson and J L Kinsey *J Chem Phys* **99** (1993) 7267

75 D L Rousseau and P F Williams *J Chem Phys* **64** (1976) 3519

76 P Gross and H Rabitz, *J Chem Phys* **105** (1996) 1299

77 A K Gupta, P Gross. D B Bairagi and M K Mishra *Chem Phys Letts* **257** (1996) 658

DYNAMICS OF (He,H_2^+) COLLISIONS

B MAITI AND N SATHYAMURTHY*

Department of Chemistry, Indian Institute of Technology, Kanpur 208 016 (India)

Being one of the simplest three atoms-three electrons systems, (He,H_2^+) collisions have been studied extensively over the years, experimentally as well as theoretically. It was the first ion-molecule system for which vibrational enhancement was demonstrated experimentally and the existence of reactive scattering resonances was pointed out by quantum mechanical calculations. Efforts to identify these resonances experimentally have not been successful so far. The system continues to draw the attention of experimentalists and theorists because of the richness of its dynamics and noticeable discrepancies between theory and experiment on some aspects of its dynamics. We have tried to review the literature on the dynamics of (He,H_2^+) collisions at moderate energies, highlighting our own contributions to its understanding, in this paper.

Key Words: **Quasiclassical Trajectory Calculations; Reactive Scattering; Transition State Resonances; Quantal Calculations**

1 Introduction

The (He,H_2^+) system represents one of the simplest polyatomic systems that one could think of. It contains three nuclei and three electrons. It is isoelectronic with H_3 and at the same time, serves as a prototype ion-molecule system. Even at moderate energies, collisions between He and H_2^+ in their ground electronic states can result in various dynamical outcomes:

$$He(^1S_0)+H_2^+(^2\Sigma_g^+)\rightarrow He(^1S_0)+H_2^+(^2\Sigma_g^+) \quad \ldots (R1)$$

$$\rightarrow HeH^+(^1\Sigma^+)+H(^2S_{1/2}) \quad \ldots (R2)$$

$$\rightarrow He(^1S_0) + H(^2S_{1/2}) + H^+(^1S_0) \quad \ldots (R3)$$

$$\rightarrow He^+(^2S_{1/2})+H_2(^1\Sigma_g^+) \quad \ldots (R4)$$

While channel (R1) is nonreactive, with no electron excitation, (R2) is reactive, representing the exchange reaction, (R3) is dissociative and (R4) represents charge transfer. The energetics for the different channels is summarized in the form of an adiabatic state correlation diagram[1] in Fig. 1.

To the best of our knowledge, it is the first ionic system for which vibrational enhancement of reaction cross section was demonstrated experimentally[2], by photoionizing H_2 into specific vibrational (v) states and letting it collide with He at different relative translational energies. The potential energy surface (PES) for the ground electronic state dynamics was computed *ab initio*, to chemical accuracy (± 1 kcal.mol^{-1}), two decades ago[3]. Dynamics of (He,H_2^+) collisions has been studied theoretically, using classical mechanics and also quantum mechanics—time—dependent as well as time-independent. Its classical dynamics has been shown to be partly irregular and the quantum dynamics rich in reactive scattering resonances (RSRs). Although the existence of RSRs in (He,H_2^+) collisions was pointed out as early as 1972[4], they have eluded experimental verification till this date. While much of the experimental results (effect of reagent vibration and relative translation on the reaction cross section for exchange and collision-induced dissociation processes, for example) could be accounted for theoretically (see below), some discrepancies between experiment and theory remain. In this review we summarize the experimental findings in the 0-10 eV energy range till date and then review the theoretical studies.

2 Experiment

Early experiments of Koch and Friedman[5] on the system, involving electron impact ionization of H_2

---

*Honorary Professor, Jawaharlal Nehru Centre for Advanced Scientific Research, Jakkur P.O., Bangalore-560 064.

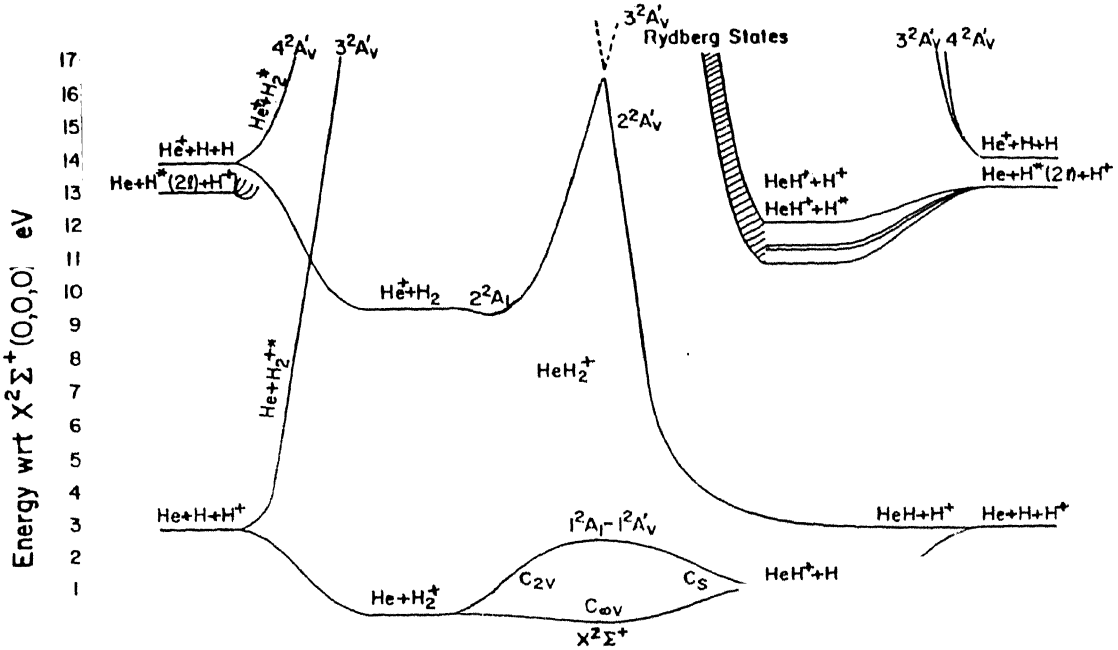

Fig. 1 Adiabatic state correlation diagram for HeH_2^+ system[1].

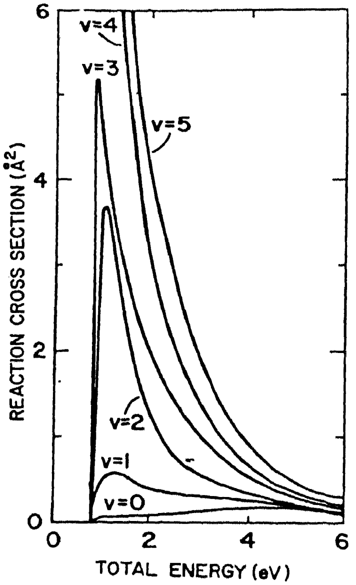

Fig. 2 Reaction cross section as a function of total energy E for reaction (R2) from different vibrational states of H_2^{+}[6].

in a mixture of H_2 and He showed that the resulting H_2^+ reacted with He to yield HeH^+.

$He+H_2^+ \rightarrow HeH^+ + H$ ... (R2)

It also became clear that the reaction utilised the vibrational energy of H_2^+ much more effectively than the relative translational energy (E_{trans}) of the reactants and that there was a translational threshold. The reaction cross section for

$He^+ + H_2 \rightarrow HeH^+ + H$ ... (R5)

in comparison, was very small despite reaction (R5) being highly exothermic (~ 8 eV).

Using photoionization as a means of vibrational state selection, Chupka and Russell[2] showed that the excitation function, that is, the reaction cross section (σ^R) as a function of E_{trans}, increased from zero at threshold to a maximum and then declined with increase in E_{trans}, for the low vibrational states (v = 0-3). For higher vibrational states (v = 4 and 5) $\sigma^R(E_{trans})$ was a decaying function, as shown in Fig. 2. There was a clear cut vibrational enhancement of the reaction at low and moderate E_{trans} ($\leq$ 5 eV) and at higher E_{trans}, $\sigma^R(E_{trans})$ criss-crossed for some v states. It was also clear from the work of Chupka and coworkers that the dynamical threshold (E_{th}^{dy}) coincided with the energetic threshold (E_{th}^{e}) for collision-induced dissociation (CID) process

$He+H_2^+ \rightarrow He+H+H^+$ ... (R3)

and an increase in $\sigma^D(E_{trans})$ occurred in the same energy range in which $\sigma^R(E_{trans})$ declined.

Vibrational enhancement of the CID process was also established by these workers.

Schneider *et al.*[7] studied the dynamics of reaction (R2) by using a beam of H_2^+ produced from H_2 by electron impact, and thermal energy He atoms. Although H_2^+ was not vibrationally selected, they could study the product angular and energy distributions for E_{trans} in the range 0.84-3.36 eV. It was clear that the product molecules were predominantly forward scattered with respect to the incoming He. Collisions of He with H_2^+ (v = 0, 1) at E_{trans} = 3.58 eV[8] yielded product angular distribution that is asymmetric (more scattering of HeH^+ in the forward direction than in the backward). The relative translational energy of the products peaked at an energy higher than that predicted by the spectator stripping mechanism. Havemann *et al.*[9] found that the CID process at E_{trans} = 3.03 and 5.04 eV was vibrationally enhanced and the resulting H^+ was predominantly backward scattered.

van Pijkeren *et al.*[10] used the photoelectron-secondary-ion-coincidence (PESICO) method to study reaction (R2) at thermal energies for v = 0-8 and established the dramatic vibrational enhancement of the reaction cross section when $3 \leq v \leq 8$. Results of Chupka *et al.*[2] for v = 0-4 eV were further confirmed by Baer *et al.*[11] using the threshold-electron-secondary-ion-coincidence (TESICO) technique.

Turner *et al.*[12] photoionized a beam of H_2 using wavelength selected UV photons, accelerated the resulting H_2^+ ions in selected vibrational states, allowed them to interact with a beam of He gas and extracted the resulting product HeH^+ ions, mass analyzed them and counted them to determine σ^R for v = 0-4 over a range of E_{trans}: 0-10 eV. It became clear that their results were comparable to those of Chupka *et al.*[2] in terms of the overall effect of v and E_{trans} on σ^R, but were consistently smaller and differed by a factor of two for low v at low E_{trans}.

Turner *et al.*[12] had also reported the vibrational state-selected σ^R values for the isotopic analog of reaction (R2)

$$He+HD^+ \rightarrow HeH^+ + D \quad \ldots \text{(R6a)}$$

$$\rightarrow HeD^+ + H \quad \ldots \text{(R6b)}$$

and the isotopic branching ratio Γ^R = $\sigma^R(HeH^+)/\sigma^R(HeD^+)$ for the two isotopically distinct channels. They showed that $\sigma^R(HeH^+)$ decayed more sharply with E_{trans} than $\sigma^R(HeD^+)$. For E_{trans} = 1-2 eV, both the channels showed vibrational enhancement, which became less marked around 4 eV. At 8 eV the HeD^+ channel was actually showing a slight vibrational inhibition. The preference of HeH^+ formation over HeD^+ was reflected in the branching ratio $\Gamma^R = 1.79$ for $HD^+(v=4)$ at E_{trans} = 1 eV.

In a subsequent experimental study using the threshold-photoelectron/photoion coincidence (TPEPICO) technique, Govers and Guyon[13] reported σ^R values for the exchange reaction (R2) and also σ^D for the CID process (R3) at E_{trans} = 3.1 ± 0.7 eV for v = 0-6 of H_2^+. They showed that the branching ratio, $\Gamma^D = \sigma^D/\sigma^R$ remained approximately constant at 0.3 for v = 0-3, rising subsequently through 1.6 for v = 4-6.

Gislason and Guyon[14] made an interesting observation. When He and H_2^+ approach each other, the positive charge that is equally shared initially by the two H atoms begins to migrate towards H that is closer to He. This results in weakening of the H_2^+ bond and may eventually lead to HeH^+ and H formation. However, during this process, one electron may hop from one H nucleus to the other and result in HeH and H^+. The former being unstable would dissociate to He and H. This would mean CID has taken place through electronically excited state of (He,H_2^+). By a clever analysis of H^+ velocity distribution in the laboratory, the authors concluded that CID in (He,H_2^+) collisions proceeds through excited electronic state for v = 0 and 1 of H_2^+.

Achtenhagen *et al.*[15] measured the σ^R values for v = 0, 1 and j = 1, 3 of H_2^+ using (3 + 1) resonantly enhanced multiphoton ionization (REMPI) technique over a range of E_{trans}.

Pollard *et al.*[16] measured the differential reaction cross section ($d\sigma^R/d\theta$) for reaction (R2) for v = 0-2, j = 1 of H_2^+ at the centre-of-mass scattering angle (relative to the incident He) $\theta = 0^0$ and 180^0 as a function of E_{trans}. Although their results reiterated the earlier findings of vibrational enhancement in the system, they did not reveal any structure in the plot of ($d\sigma^R/d\theta$) versus E_{trans}, implying that the reactive scattering resonances, if any, in the system are narrower than the energy resolution of 0.15 eV used in the study.

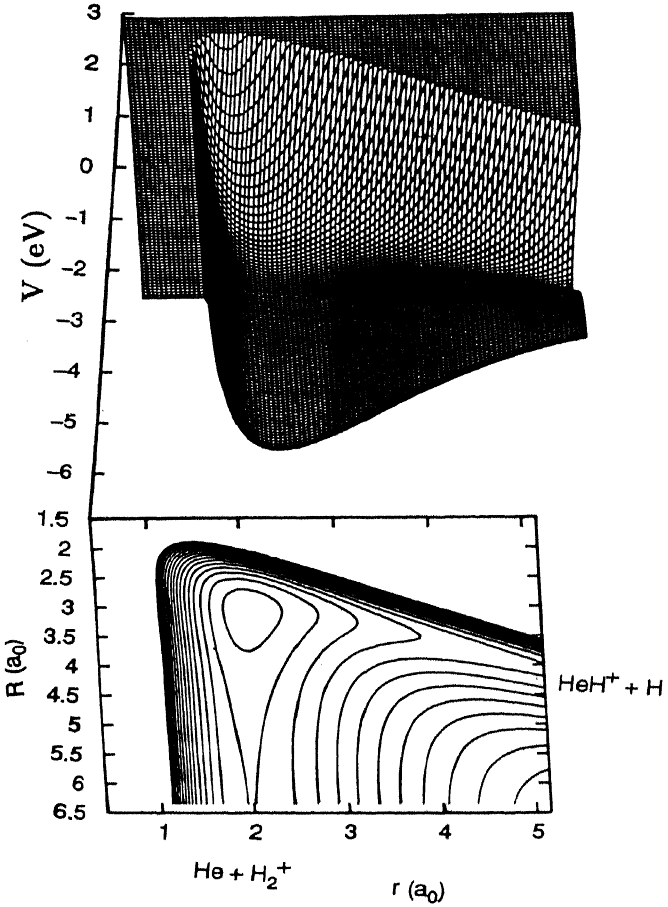

Fig. 3 Three dimensional perspective diagram and contour plot of the McLaughlin-Thompson-Joseph-Sathyamurthy (MTJS) PES for HeH_2^+ system in jacobi coordinates (R,r) for collinear geometry. R refers to the centre-of-mass separation between He and H_2^+, while r the H-H bond distance.

3 Potential Energy Surface

Edmiston *et al.*[17] computed the potential energy surface for collinear $HeHH^+$ and also $HHeH^+$ for a limited range of geometries using pseudonatural orbitals as a basis for the superposition of configurations. They established the existence of a potential energy minimum of ~ 5 kcal/mol depth for $R_{HHe} = R_{HH} = 2.0\ a_0$ and showed that the barrier for the symmetric $HHeH^+$ formation was ~ 25 kcal/mol. Brown and Hayes[18] used the LCAO-MO-SCF method using a constrained Gaussian basis set to reiterate the findings of Edmiston *et al.* In addition, they showed that the barrier for reaction (R2) occurred rather "late" and that the collinear approach was the most preferred. The potential energy (PE) values reported by Brown and Hayes for the collinear approach of He and H_2^+ to form $HeH^+ + H$ were represented by an analytic function within the diatomics-in-molecules (DIM) framework by Kuntz[19]. Kuntz and Whitton[20] extended the surface to three dimensions. Sathyamurthy *et al.*[21] splinefitted the *ab initio* surface[18] for the collinear geometry and pointed out that the dynamics of (He,H_2^+) collisions is very sensitive to the details of the potential energy surface. Hopper[22] published a multi-configuration-self-consistent-field (MCSCF) surface for a limited range of geometries. McLaughlin and Thompson[3] computed the potential energy values of chemical accuracy for 596 different nuclear arrangements of HeH_2^+ by including most of the configuration interaction. Joseph and Sathyamurthy[23] reported an analytic function with 26 parameters, fitted to the *ab initio* surface[3] with a root-means-square (rms) deviation of 0.07 eV. The resulting PES is shown in the form of a three dimensional perspective diagram and potential energy contours in Jacobi coordinates for collinear HeH_2^+ in Fig. 3. This has come to be known as the McLaughlin-Thompson-Joseph-Sathyamurthy (MTJS) surface in the literature. More recently, Aguado and Paniagua[24] have reported a slightly improved analytic fit to the *ab initio* surface using 37 linear and 2 nonlinear parameters with an rms deviation of 0.003 eV and a maximum deviation of 0.011 eV. Špirko and Kraemer[25] and Meuwly and Hutson[26] have recently reported improved *ab initio* PESs in the potential well region.

Some of the potential energy surfaces that are close to the ground state surface have been computed and the nonadiabatic coupling elements determined by different workers[1,3,27-30]. Of particular interest is the $He^+ + H_2$ channel. Aguado *et al.*[31] have provided an accurate fit of the two lowest excited-state potential energy surfaces published by McLaughlin and Thompson[3]. Hopper has reported potential energy values for a limited range of geometries for some of the low lying Rydberg states also[32]

4 Theory

4.1 Phase Space Theory

In the absence of accurate *ab initio* PESs, one can obtain an estimate of σ^R and its dependence on E_{trans}, vibrational energy (E_{vib}) and rotational energy (E_{rot}) if spectroscopic parameters such as bond length (r_e), bond dissociation energy (D_e), fundamental vibrational frequency (ω_e) and rotational constant (B_e) are known for the reactant and product molecules using phase space theory[33]. This theory assumes that, on forming the intermediate (from the reactants), the probability of outcome in each (reactant/product) channel is directly proportional to the number of states available in that channel. The available energy and angular momentum, of course decide the number of available states. An account of phase space theory and its application to HeH_2^+ and its isotopomers can be found elsewhere[34-37].

An examination of the energetics of reaction (R2) along with the available vib-rotational states for reactants and products reveals that the reaction has a threshold (E_{th}) of 0.955 eV. Although the number of available reactant as well as the product states increase with energy above E_{th}, the proportion of reactant states starts decreasing. Therefore, one expects an increase in σ^R with E_{trans} and also with E_{vib} and E_{rot} of the reactants, in qualitative accord with experiment. However, with substantial increase in E_{trans}, there would be a substantial increase in the magnitude and the role of the orbital angular momentum and hence the centrifugal barrier. It became clear from the studies mentioned above that the vibrational enhancement observed experimentally is much more than what is predicted by the phase space theory, emphasizing the need for a dynamical treatment.

Implications of the potential well for the dissociative dynamics of HeH_2^+ have been examined by Song and Chesnavich[38]. Cumulative reaction probabilities for reaction (R2) at zero total angular momentum have been computed and compared with the variational transition state theoretic calculations for the system[39].

In the case of (He,HD^+) collisions, the number of available product states are different for channels (R6a) and (R6b). As a result, $\Gamma^R \neq 1$. As a matter of fact, HeD^+ formation would be preferred over HeH^+ and Γ^R is expected to be less than unity, in qualitative accord with experiment[40]. Quantitative agreement between experiment and theory would require a detailed dynamical investigation.

4.2 Quantum Mechanical Studies

Kouri and Baer[4] computed the vibrational state-selected reaction probability (P_v^R) for v = 0-5 of reaction (R2) in collinear geometries, for total energy E = 0.93-1.4 eV using the DIM surface and found that there were a number of oscillations in $P_v^R(E)$ plots, which suggested the existence of a large number of dynamical resonances in the system. Interestingly, their results did not show vibrational enhancement that was evident in the experimental results. Another interesting aspect of their results was that P_v^R values for v = 0 and 2 were strongly coupled to each other in that they were mirror images of each other, for $E \leq 1.28$ eV (threshold for product (HeH^+) vibrational state v' = 1). A similar mirror image relation was found between P_1^R and P_3^R. Adams[41] obtained identical results using an alternative (integral equation) approach for E = 0.95-1.19 eV, v = 0-4. Using a time-dependent quantum mechanical (TDQM) approach, Stroud *et al.*[42] pointed out that the lack of vibrational enhancement noticed by Kouri and Baer and Adams for the collinear reaction (R2) was due to the DIM fit to the *ab initio* surface and that the dynamics on a splinefitted *ab initio* surface yielded vibrational enhancement, in qualitative accord with experiment.

Chapman and Hayes[43] pointed out that the vibrational inelastic transition probability ($P_{0\to1}$) for (He,H_2^+) collisions in the energy range 0.4-0.65 eV (well below the reaction threshold) also showed several oscillations. They characterized one of the oscillations to be a shape (open) resonance and the others as Feshbach (compound) resonances.

The importance of three dimensional (3D) collisions for reaction (R2) was emphasized by Tang *et al.*[44], who showed that a distorted-wave-Born approximate calculation using a generalized DIM fit of the Brown-Hayes surface could reproduce qualitatively the vibrational enhancement.

A quantum reactive infinite order sudden approximate treatment[11,45] of 3D (He,H_2^+) collisions on the MTJS surface for v = 0-7 over the energy range 1.3-1.8 eV reproduced the observed vibrational enhancement for reaction (R2) and it also suggested that the collisions are direct and some of them follow the spectator-stripping mechanism.

Joseph and Sathyamurthy[46] reported the P_v^R values for collinear reaction (R2) obtained using an R matrix approach[47] and the MTJS PES for v = 0-4 over a range of 0 955 ≤ E ≤ 1.44 eV. These results also showed a large number of oscillations, when P_v^R was plotted as a function of E and these oscillations were subsequently[48] characterised as Feshbach resonances arising from the bound states supported by the vibrational adiabatic potential in hyperspherical coordinates[49] as illustrated in Fig. 4. By examining cuts of the PES in hyperspherical coordinates, Sathyamurthy *et al.*[48] argued that the oscillations might be observed experimentally in energy resolved differential cross section data for backward scattering as they would be dominated by zero impact parameter, collinear collisions. Interestingly, $P_v^R(E)$ values for the collinear geometry did not show any vibrational enhancement.

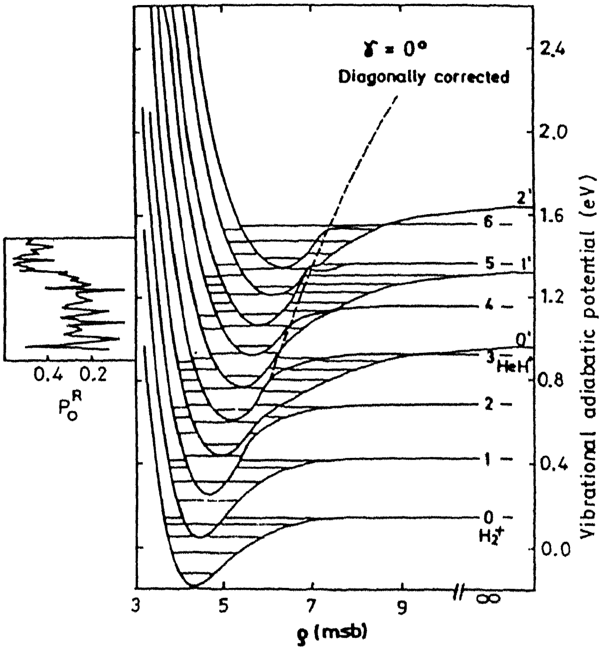

Fig. 4 The diagonally corrected vibrational adiabatic potentials for collinear HeH_2^+, for different v and v' states of H_2^+ and HeH^+, respectively. The dashed line shows the ridge on the PES, separating the reactants and the products. The horizontal lines indicate the various bound states. Included on the left-hand side is a plot of $P_0^R(E)$ with the coincident energy axis.

More recent time-independent quantum mechanical (TIQM) calculations by Sakimoto and Onda[50] and TDQM calculations by Balakrishnan and Sathyamurthy[51] (using the MTJS surface) revealed additional oscillations in the $P_v^R(E)$ values for reaction (R2) in the collinear geometry for energies up to the three body dissociation limit (2.78 eV), and for different initial vibrational states of H_2^+. Mahapatra and Sathyamurthy[52] analyzed some of the resonances in terms of their eigenvalues, eigenfunctions and lifetimes by analyzing the transition state spectrum (TSS), obtained by Fourier transforming the time autocorrelation function for the unimolecular decay of the collinear HeH_2^+ complex. The correspondence of some of the resonances with the classical resonant periodic orbits has also been established[52-54].

The role of kinematic factors in collinear (He,H_2^+) collisions has been investigated by

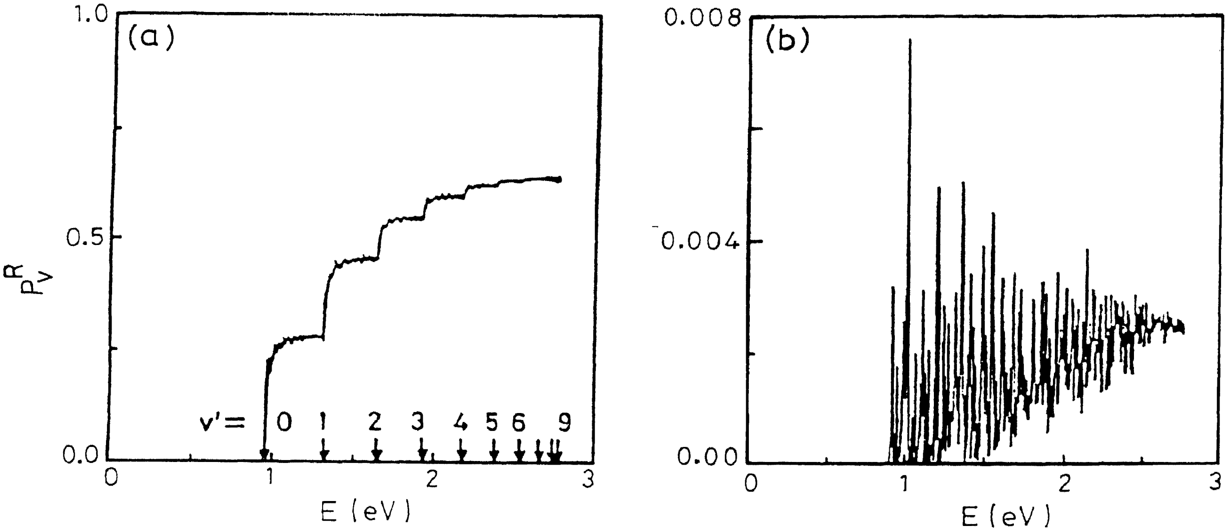

Fig. 5 State-selected reaction probabilities for the collinear reaction (a) He + HD$^+$(v = 0) → HeH$^+$ + D and (b) He + DH$^+$(v = 0) → HeD$^+$ + H. The threshold energies of different v' channels are marked in the lower abscissa of panel (a) to illustrate the occurrence of sharp variations in the P_0^R near each channel threshold.

Sakimoto[55,56] by considering various mass combinations. He considered ^{3}He as well as ^{4}He and also varied the mass of H to that of Mu, D and T at either end of H$_2^+$, for v = 0-2, $1 \leq E \leq 6$ eV and found that the magnitude and E-dependence of P_v^R was sensitive to the choice of mass combination for the reactant species. While he could not arrive at any conclusion about the dynamics because of a large number of oscillations in $P_v^R(E)$ below the dissociation threshold, he could correlate the magnitude of dissociation probability to the skew angle[57]. Mahapatra and Sathyamurthy[58] used the time-dependent quantum mechanical wave packet approach to investigate resonances in collinear (He,HD$^+$) and (He,DH$^+$) collisions. While the $P_v^R(E)$ values for HeDH$^+$ showed a characteristic staircase-like structure that could be related to threshold resonances, $P_v^R(E)$ values for HeDH$^+$ were found to be highly oscillating, in keeping with the densely packed transition state spectrum as illustrated in Fig. 5.

TIQM calculations for reaction (R2) in three dimensions, for total angular momentum J = 0 showed vibrational enhancement of the reaction[59-61]. In addition, they showed a large number of reactive scattering resonances. The TIQM results of Zhang *et al.*[59] on the DIM PES differed from those of Kress *et al.*[60] and Lepetit and Launay[61] on the MTJS PES, the differences arising from the differences in the two PESs. The results of Kress *et al.*[60] obtained by the adiabatically adjusting principal axis hyperspherical method for 3D J = 0 collisions revealed a high degree of similarity to those of Lepetit and Launay[61] obtained by the hyperspherical method, in terms of the oscillations in the vib-rotational (v,j) state-selected reaction probability, P_{vj}^R as a function of E. But they differed from each other in terms of the position of the resonances. Furthermore, many additional resonances were reported by Lepetit and Launay[61]. 3D TIQM calculations as well as the reduced dimensionality bending corrected rotating linear model studies by Kress *et al.*[60] indicated that many of the 3D resonances were very long lived (up to 7.7 ps), and that the significant forward-backward symmetry in the observed angular distribution of the products must originate from those long lived resonances.

Preliminary calculations by Balakrishnan and Sathyamurthy[62] for reaction (R2) in three dimensions using the TDQM approach in hyperspherical coordinates also confirmed the vibrational enhancement. In addition, they revealed a lot of structure in the probability density ($|\Psi|^2$) plots in configuration space indicating the existence of resonances in three dimensional collisions. Recently, Mahapatra and Sathyamurthy[64] have computed the energy resolved

$P_v^R(E)$ for $v = 0\text{-}3$, $j = 0\text{-}3$, $J = 0$ of reaction (R2) using the time-dependent wave packet method. While reiterating the large number of narrow resonances and the vibrational enhancement obtained by the earlier workers for the system, they also showed that rotational excitation has only a marginal influence on the reaction probability. Kalyanaraman *et al.*[64] have extended the study to an examination of isotopic branching in 3D (He,HD$^+$) collisions and found that the narrow resonances persist for both the HeH$^+$ and HeD$^+$ channels. They also showed that the branching ratio obtained from quantum calculations are closer to the classical results than to the experimental results, suggesting that the latter may require reexamination.

4.3 *Quasiclassical Trajectory Studies*

Sathyamurthy *et al.*[21] showed that quasiclassical trajectory (QCT) calculations for reaction (R2) in collinear geometry could not reproduce the oscillations in $P_v^R(E)$ results obtained by the quantal calculations on the DIM surface. Nevertheless, they were able to show that the lack of vibrational enhancement reported by Kouri and Baer[4] was not only due to the collinear model but also due to the use of the DIM surface and that QCT calculations using the splinefitted *ab initio* PES for the collinear reaction could reproduce qualitatively the vibrational enhancement obtained experimentally. They also[65] established that the dynamics of (He,H$_2^+$) collisions was sensitive to small differences in the PES, particularly in the inner repulsive wall region. In yet another study, Sathyamurthy[66] showed that the potential well for the system played only a marginal role in influencing the dynamics. The inadequacy of the collinear model for reaction (R2) was reiterated[67] by showing that vibrational enhancement could be obtained on a less accurate (Hartree-Fock) surface, but not on the more accurate MTJS surface that included electron correlation, although both studies involved a collinear arrangement.

Schneider *et al.*[7] and Pacák *et al.*[8] showed that 3D QCT calculations using the DIM surface could reproduce nearly quantitatively the product energy and angular distributions obtained from electron impact ionization experiments for reaction (R2) over a range of E_{trans} (0.5-4.0 eV). The same research group[68] investigated in detail the effect of v on σ^R and σ^D for $E = 0.5\text{-}5.0$ eV and confirmed the declining excitation function $\sigma^R(E)$ for the exchange reaction, while $\sigma^D(E)$ increased. By comparing their 3D QCT computed σ^D results with those from experiments, Havemann *et al.*[9] concluded that the collision-induced dissociation (CID) was electronically adiabatic. Studies by Zuhrt *et al.*[69] showed that while low rotational excitation of H$_2^+$ had negligible effect on σ^R, high rotational excitation had a similar influence as vibrational excitation of the same magnitude on σ^R.

From a detailed dynamical investigation, Joseph and Sathyamurthy[23] showed that the vibrational enhancement and the initial steep increase, followed by a steep decline in $\sigma^R(E)$ for $v = 1\text{-}3$ obtained from experiments[2] were nearly quantitatively reproduced by 3D QCT calculations using the MTJS PES. Their studies also reproduced the product energy and angular distributions reported from the electron impact ionization studies by Pacák *et al.*[8]. The experimentally observed threshold behaviour and the vibrational enhancement of CID and the E_{trans} dependence of σ^D for $v = 0$ and 3 were also reproduced nearly quantitatively by 3D QCT calculations[70,71]. The competition between exchange and dissociation processes as reflected in the branching ratio and its dependence on v were also predicted satisfactorily by the 3D QCT calculations, thus lending credence to the accuracy of the PES and the reliability of the QCT approach. The limitations of collinear calculations were reiterated by Dove *et al.*[72]. As energy resolved differential cross section data for $v = 0\text{-}2$, $E_{trans} = 0.3\text{-}1.9$ eV became available from experiments using H$_2^+$ produced from resonantly enhanced four-photon ionization and accelerated impulsively and colliding with a beam of He[16], Kumar *et al.*[73] showed that the same could be largely accounted for by 3D QCT calculations using the MTJS PES. A few quantitative discrepancies remained.

Standard QCT calculations[74] assign quantum mechanically allowed vibrational energies to reactant molecules and assign product vibrational states (v') using a histogram procedure. As a result, in a QCT calculation for reaction (R2), product HeH$^+$ with v' falling within the range -0.5 to 0.5 would be taken to be in $v' = 0$ state. This means that the trajectories leading to $v' < 0$ would also be

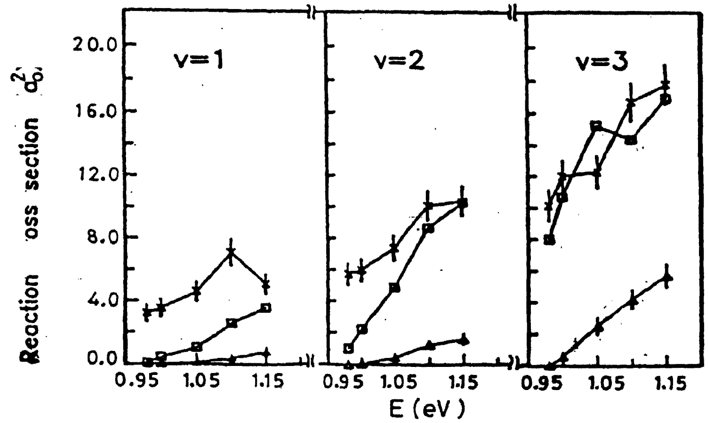

Fig. 6 Comparison of zero-point corrected (Δ) and uncorrected (×) integral cross section values as a function of E for $v = 1\text{-}3, j = 0$ with those from a 3D TIQM calculation[61] (□) for reaction (R2).

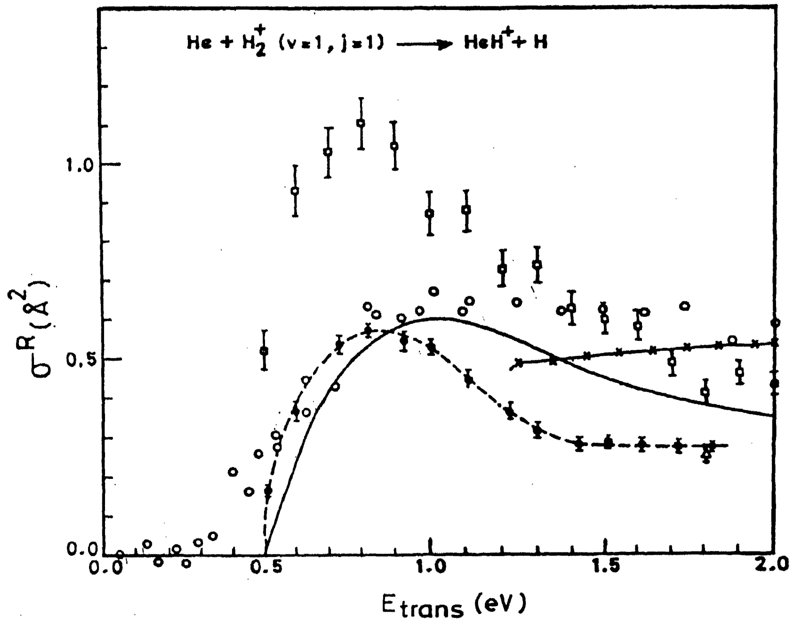

Fig. 7 Comparison of zero-point uncorrected σ^R values obtained from 3D QCT calculations for reaction (R2) using the MTJS (□) surface and new analytic fit (•) published by Aguado and Paniagua[24], with the experimental results: (—) Chupka and coworkers[2], (×) Turner *et al.*[12], (o) Achtenhagen *et al.*[15]. Results of Achtenhagen *et al.* are for a ($v = 0,1$; $j = 1,3$) mixture. The error bars are of 68% confidence level.

counted as reactive, although we know that quantum mechanically this is not possible. Some authors suggest that such "leaky" trajectories not be counted and some suggest that they be counted. The former procedure, referred to as zero-point correction, sometimes results in excellent agreement between experiment and theory and sometimes it does not, as discussed in detail elsewhere[75]. In the case of three dimensional (He,H_2^+) collisions, zero-point correction tends to underestimate σ^R. If such a correction is not made, σ^R gets overestimated for low v states, as illustrated in Fig. 6.

Recent investigations[76] of QCT dynamics of (He,H_2^+) collisions using the new analytic fit of *ab initio* PES published by Aguado and Paniagua[24] revealed that the resulting collinear reaction probabilities and differential and integral cross sections are indistinguishable from those computed using the MTJS surface, for different v states of H_2^+ over a range of E_{trans}. But for the reaction from the $v = 1$ state of H_2^+, there were some noticeable differences between them, as illustrated in Fig. 7.

3D QCT calculations using the MTJS surface for (He,HD$^+$) collisions[77] were able to predict correctly the qualitative dependence of σ^R on v(HD$^+$) and E_{trans} for HeH$^+$ and HeD$^+$ formation. But when the computed isotopic branching ratio values were compared with the available experimental results[12], there were some discrepencies. For example, Γ^R obtained from QCT calculations was only half of what was reported from experiments for HD$^+$($v = 4$) at $E_{trans} = 1.0$ eV, at which $\Gamma_{expt}{}^R$ is perhaps the most reliable as the σ^R values are the largest at that energy for both the channels. Although $\Gamma_{expt}{}^R$ exhibited a minimum as a function of E_{trans} around 2-4 eV as predicted by theory for different vibrational states of HD$^+$, it increased as a function of v at 1 eV, in contrast to the nearly constant value of $\Gamma_{QCT}{}^R$. It was not clear at that time whether the discrepancy was partly due to noninclusion of nonzero J states in the calculations. Subsequently, it was shown that rotation has very little influence on Γ^R (in the QCT calculation)[73]. Following the analysis of Gislason and Guyon[14], Sizun and Gislason[78-80] used the surface-hopping-trajectory method to demonstrate the role of the first excited electronic state in influencing the dynamics of (He,H$_2^+$) and (He,HD$^+$) collisions.

4.4 Chaos, Fractals and Quantal Resonances

Detailed examination of individual trajectories for collinear (He,H$_2^+$) collisions revealed that some of them are highly sensitive to the choice of initial conditions, a characteristic that is described as classical chaos[81]. For collinear atom-diatom collisions, for a specific choice of (v, E_{trans}), the only variable that remains to be specified is the initial vibrational phase ϕ_i. A plot of the final vibrational action (n_f) of the reactant/product molecule as a function of ϕ_i reveals a large number of oscillations on either side of the banded region, for energies below E_{th}. On finecombing the ϕ_i dependence, these oscillations reveal a self-similar pattern lying underneath, with a fractal dimension of 1.38-1.68 over a wide range of E_{trans}[82]. For energies above the reaction threshold, the fractal zones were shown to occur between reactive and nonreactive bands and were thought to be related to the known quantal reactive scattering resonances.

By a detailed analysis of the phase portrait of collinear nonreactive (He,H$_2^+$) collisions plotted in terms of Poincare surface of section, it was shown[83] that there exists an intermolecular bottleneck, which could be identified with the zero-order separatrix. It was also shown that the regular trajectories never crossed the intermolecular bottleneck but the irregular trajectories did.

Pechukas and Pollak[84] had argued that in the switchover region between two bands, there would

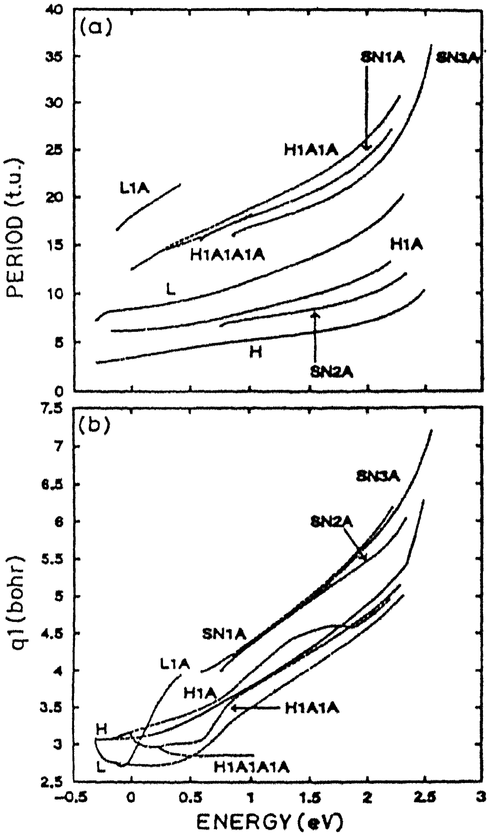

Fig. 8 Continuation /bifurcation diagram for collinear HeH$_2^+$. (a) The variation of the period of the POs in different families with total energy. (b) The initial value of the approach coordinate q_1 versus total energy for different families of POs. The solid lines represent stable POs and the dashed lines unstable POs.

be trapped trajectories, which would live forever. This led to the identification of resonating periodic orbits (POs) and their relation to reactive scattering resonances[85]. Marston[53] had characterized some of the POs for collinear HeH_2^+ as belonging to R, M or W types, from a topological point of view. He computed the semiclassical eigenfunctions corresponding to these POs and showed that their time evolution and the resulting power spectra could account for some of the resonances. Recently we have identified[54] the principal families of POs and examined their (in)stabilities for collinear HeH_2^+ and its isotopic variants $HeHD^+$ and $HeDH^+$ on the MTJS PES. Continuation/bifurcation diagrams of these POs over a range of energies revealed a number of bifurcations and the period doubling route to classical chaos, as shown in Fig. 8. The existence of a number of POs at any given energy suggested that there could be constructive and destructive interference between their contributions to the eigenfunction at that energy, resulting in quantum mechanical resonances for these systems.

5 Summary and Conclusions

It becomes clear from the above discussion that seemingly simple collisions between the smallest rare gas atom (He) and the simplest (one electron) diatomic species (H_2^+) are actually rich in their dynamics. While the experimentally observed v and E_{trans} dependence of differential and integral cross sections for reaction (R2) could be accounted for qualitatively by QCT and quantum mechanical calculations using the available *ab initio* PES, quantitative agreement between experiment and theory in some respects is still lacking. The role of reagent rotation in influencing the dynamics of reactions (R2) is yet to be established experimentally. The reactive scattering resonances that raised the curiosity about the dynamics of the system remain as elusive as ever for experimental verification. It is not even clear whether the RSRs for the system would survive "*l*-averaging" or not. While the competition between the exchange and dissociation channels is largely understood, the predicted isotopic branching ratio values for the exchange reaction are not in agreement with some of the state-selected results available from experiments, suggesting the need for additional experimental investigation. Gislason and Guyon have pointed out the importance of the lowest lying excited electronic state of the system to its dissociation dynamics. The influence of the charge transfer channel on the exchange and dissociation dynamics remains to be investigated.

6 Acknowledgement

This study was supported in part by a grant from the Department of Science and Technology, New Delhi.

References

1 D G Hopper *J Chem Phys* **73** (1980) 3289

2 W A Chupka, M E Russell and K Refaey *J Chem Phys* **48** (1968) 1518; W A Chupka and M E Russell *J Chem Phys* **49** (1968) 5426; W A Chupka, J Berkowitz and M E Russell *Sixth Inter.Conf Physics Electr Atom Collis* MIT Cambridge (1969) 71; W A Chupka *Ion-Molecule Reactions* (Ed. by J L Franklin) Plenum New York **1** (1972) 72

3 D R McLaughlin and D L Thompson *J Chem Phys* **70** (1979) 2748

4 D J Kouri and M Baer *Chem Phys Lett* **24** (1974) 37

5 H von Koch and L Friedman *J Chem Phys* **38** (1963) 1115

6 R D Levine and R B Bernstein *Molecular Reaction Dynamics* Oxford University New York (1974) 6

7 F Schneider, U Havemann, L Zálicke, V Pacák, K Birkinshaw and Z Herman *Chem Phys Lett* **37** (1976) 323

8 V Pacák, U Havemann, Z Herman, F Schneider and L Zülick *Chem Phys Lett* **49** (1977) 273

9 U Havemanná, V Pacák, Z Herman, F Schneider, Ch Zührt and L Zülicke *Chem Phys* **28** (1978) 147

10 D van Pijkeren, J van Eck, A Niehaus *Chem Phys Lett* **96** (1983) 20; D van Pijkeren, E Boltjes, J van Eck and A Niehaus *Chem Phys* **91** (1984) 293

11 M Baer, S Suzuki, K Tanaka, I Koyano, H Nakamura, Z Herman and D J Kouri *Phys Rev* **A 34** (1986) 1748; Z Herman and I Koyano *J Chem Soc Faraday Trans* 2 **83** (1987) 127

12 T Turner, O Dutuit and Y T Lee *J Chem Phys* **81** (1984) 3475

13 T R Govers and P-M Guyon *Chem Phys* **113** (1987) 425

14 E A Gislason and P-M Guyon *J Chem Phys* **86** (1987) 677

15 M Achtenhagen, M Schweizer and D Gerlich (private commun)

16 J E Pollard, J A Syage, L K Johnson and R B Cohen *J Chem Phys* **94** (1991) 8615; J E Pollard, L K Johnson and R B Cohen *ibid* **95** (1991) 4894

17 C Edmiston, J Doolittle, K Murphy, K C Tang and W Willson *J Chem Phys* **52** (1970) 3419

18 P J Brown and E F Hayes *J Chem Phys* **55** (1971) 922

19 P J Kuntz *Chem Phys Lett* **16** (1972) 581

20 P J Kuntz and W N Whitton *Chem Phys Lett* **34** (1975)

340; W N Whitton and P J Kuntz *J Chem Phys* **64** (1976) 3624

21 N Sathyamurthy, R Rangarajan and L M Raff *J Chem Phys* **64** (1976) 4606

22 D G Hopper *Int J Quant Chem Symp* **12** (1978) 305

23 T Joseph and N Sathyamurthy *J Chem Phys* **80** (1984) 5332; **86** (1987) 704

24 A Aguado and M Paniagua *J Chem Phys* **96** (1992) 1265

25 V Špirko and W P Kraemer *J Mol Spectrosc* **172** (1995) 265

26 M Meuwly and J M Hutson *J Chem Phys* **110** (1999) 3427

27 R K Preston, D L Thompson and D R McLaughlin *J Chem Phys* **68** (1978) 13

28 F Schneider and L Zülicke *Chem Phys Lett* **67** (1979) 491

29 C Kubach, C Courbin-Gaussorgues and V Sidis *Chem Phys Lett* **119** (1985) 523

30 R J Furlan, G Bent and A Russek *J Chem Phys* **93** (1990) 6676

31 A Aguado C Suárez and M Paniagua *J Chem Phys* **98** (1993) 308

32 D G Hopper *J Chem Phys* **73** (1980) 4528

33 J C Light *J Chem Phys* **40** (1964) 3221

34 J C Light and J Lin *J Chem Phys* **43** (1965) 3209

35 J C Light *Disc Faraday Soc* **44** (1967) 14

36 D G Truhlar *J Chem Phys* **56** (1972) 1481

37 A F Wagner and D G Truhlar *J Chem Phys* **57** (1972) 4063

38 K Song and W J Chesnavich *J Chem Phys* **91** (1989) 4664

39 S J Klippenstein and J D Kress *J Chem Phys* **96** (1992) 8164

40 F S Klein and L Friedman *J Chem Phys* **41** (1964) 1789

41 J T Adams *Chem Phys Lett* **33** (1975) 275

42 C Stroud, N Sathyamurthy, R Rangarajan and L M Raff *Chem Phys Lett* **48** (1977) 350

43 F M Chapman Jr and E F Hayes *J Chem Phys* **62** (1975) 4400; **65** (1976) 1032

44 K T Tang, Y Y Yung, B H Choi and T R Poe: *Electronic and Atomic Collisions (*Ed. N Oda and K Takayanagi) North-Holland XI ICPEAC (1979) 894

45 H Nakamura, A Ohsaki and M Baer *J Phys Chem* **90** (1986) 6176; M Baer and H Nakamura *J Phys Chem* **91** (1987) 5503

46 T Joseph and N Sathyamurthy *J Indian Chem Soc* **62** (1985) 874

47 J C Light and R B Walker *J Chem Phys* **65** (1976) 1598; **65** (1976) 4272; R B Walker, J C Light and A Altenberger-Siczek *J Chem Phys* **64** (1976) 1166; E B Stechel, R B Walker and J C Light *J Chem Phys* **69** (1978) 3518

48 N Sathyamurthy, M Baer and T Joseph *Chem Phys* **114** (1987) 73

49 J Manz *Comments At Mol Phys* **17** (1985) 91

50 K Sakimoto and K Onda *Chem Phys Lett* **226** (1994) 227

51 N Balakrishnan and N Sathyamurthy *Comput Phys Commun* **63** (1991) 209; *Chem Phys Lett* **201** (1993) 294; **240** (1995) 119

52 S Mahapatra and N Sathyamurthy *J Chem Phys* **102** (1995) 6057

53 C C Marston *J Chem Phys* **103** (1995) 8456

54 P Bhatia, B Maiti, N Sathyamurthy, S Stamatiadis and S C Farantos *Phys Chem Chem Phys* **1** (1999) 1105

55 K Sakimoto *Chem Phys Lett* **248** (1996) 414

56 K Sakimoto *J Chem Soc Faraday Trans* **93** (1997) 791

57 S Glasstone, K J Laidler and H Eyring *The Theory of Rate Processes* McGraw Hill New York 1941 p 101

58 S Mahapatra and N Sathyamurthy *J Chem Phys* **105** (1996) 10934; S Mahapatra, N Sathyamurthy and R Ramaswamy *Pramana-J Phys* **48** (1997) 411

59 J Z H Zhang, D L Yeager and W H Miller *Chem Phys Lett* **173** (1990) 489

60 J D Kress, R B Walker and E F Hayes *J Chem Phys* **93** (1990) 8085

61 B Lepetit and J M Launay *J Chem Phys* **95** (1991) 5159

62 N Balakrishnan and N Sathyamurthy *Proc Indian Acad Sci (Chem Sci)* **106** (1994) 531

63 S Mahapatra and N Sathyamurthy *J Chem Phys* **107** (1997) 6621

64 C Kalyanaraman, D C Clary and N Sathyamurthy *J chem Phy* **111** (1999) 10910

65 N Sathyamurthy, J W Duff, C Stroud and L M Raff *J Phys Chem* **67** (1977) 3563

66 N Sathyamurthy *Chem Phys Lett* **59** (1978) 95

67 N Sathyamurthy *Chem Phys* **62** (1981) 1

68 F Schneider, U Havemann, L Zülicke and Z Herman *Chem Phys Lett* **48** (1977) 439

69 Ch Zuhrt, F Schneider, U Havemann, L Zülicke and Z Herman *Chem Phys* **38** (1979) 205

70 J E Dove, M E Mandy, N Sathyamurthy and T Joseph *Chem Phys Lett* **127** (1986) 1

71 S Kumar and N Sathyamurthy *Chem Phys* **137** (1989) 25

72 J E Dove, M E Mandy, V Mohan and N Sathyamurthy *J Chem Phys* **92** (1990) 7373

73 S Kumar, N Sathyamuthy and K C Bhalla *J Chem Phys* **98** (1993) 4680

74 L M Raff and D L Thompson *Theory of Chemical Reaction Dynamics* (Ed. M Baer) CRC Press Boca Raton Fl; **III** Ch (1) (1985)

75 S Kumar, N Sathyamurthy and R Ramaswamy *J Chem Phys* **103** (1995) 6021

76 S Kumar, H Kapoor and N Sathyamurthy *Chem Phys Lett* **289** (1998) 361

77 K C Bhalla and N Sathyamurthy *Chem Phys Lett* **160** (1989) 437

78 M Sizun, G Parlant and E A Gislason *J Chem Phys* **88** (1988) 4294

79 M Sizun and E A Gislason *J Chem Phys* **91** (1989) 4603

80 K Dong, E A Gislason and M Sizun *Chem Phys* **179** (1994) 143

81 G L Baker and J P Gollub *Chaotic Dynamics* Cambridge University Cambridge (1990)

82 V Balasubramanian, B K Mishra, A Bahel, S Kumar and N Sathyamurthy *J Chem Phys* **95** (1991) 4160

83 A Rahaman and N Sathyamurthy *J Phys Chem* **98** (1994) 12481

84 P Pechukas and E Pollak *J Chem Phys* **67** (1977) 5976

85 E Pollak *Theory of Chemical Reaction Dynamics* (Ed. M Baer) CRC Press Boca Raton Fl; **III** (2) (1985)

FREE ELECTRON LASER PHOTOCHEMISTRY : CURRENT DEVELOPMENTS AND FUTURE PROSPECTS

SISIR K SARKAR
Laser & Plasma Technology Division, Bhabha Atomic Research Centre
Mumbai-400 085, India

Wide range tunability, high spectral brightness and high efficiency are the most appealing features of Free Electron Laser (FEL) due to the characteristic nature of the interaction between a beam of relativistic electrons and a magnetic wiggler. FELs have been built around the world covering the electromagnetic spectrum from millimeter waves to vacuum ultraviolet. The last two decades have seen the science and technology of FELs progress rapidly to the point where several user facilities exist all over the world today. Here we present the state of the art of FEL equipment and a review of its applications in photochemistry along with issues related to the size, complexity, availability and performance capability of this new tool. A variety of applications have been made possible by the attractive features of FELs in the fields of infrared multiple photon chemistry, laser isotope separation, vibrational spectroscopy in gas and adsorbate phase and chemical dynamics. In the coming century, we hope that FELs will be widely introduced to high technology industries, as compact and economical devices become available.

Key Words : Free Electron Laser; Infrared Multiple Photon Chemistry; Laser Isotope Separation; Chemical Dynamics; Laser Chemical Processing

1 Introduction

Chemical changes can be best understood on a fundamental level or turned to practical purposes with the knowledge and control of acquisition, storage and disposal of specific amounts of energy involved during the transformations. Photochemistry, a truly interdisciplinary field, can fruitfully be used to effect such changes in atomic and molecular systems and such explicit control of energy changes is becoming feasible with the advent of lasers by virtue of their inherent properties of monochromaticity and high intensity.

Since the introduction of the laser some forty years ago the sequence of new discoveries and further developments in laser technology has continued unabatedly. Wavelength coverage from the VUV to the far IR is now possible and the spectral purity, coherence, pulse performance and repetition rates of the most type of lasers have been improved. A systematic comparison of the advantages of lasers with conventional photochemical lamps indicate that lasers are superior by virtue of their higher intensity, better monchromaticity, higher quantum fluence per frequency interval, better beam divergence or beam collimation, polarization characteristics and short/ultrashort pulses. Especially, the combination of several of these features in a single laser source makes it highly attractive. The laser chemist now has a reliable, truly ideal light source for spectroscopic, dynamic and analytical studies. However, as far as laser requirements are concerned, photochemistry often requires moderate spectral resolution as compared to spectroscopic applications but better time resolution and higher power and energies to effectively induce molecular transformations to a substantial degree. The present status of such laser technology for industrial chemistry still needs considerable development in this regard.

In recent years a completely novel concept of a tunable laser has been developed which does not use atoms or molecules as an active medium but rather "free" electrons. When a beam of electrons

e-mail : mipslptd@magnum. barc.emet.in
Fax : 91-22-550 5151, 551 9613

with velocities near the speed of light moves through a static, periodically alternating magnetic field (a "wiggler"), light is emitted in the direction of electron beam propagation. The wavelength of the light is determined by the period of the wiggler field and the energy of the electrons. This provides a "gain medium", which when placed between the mirrors of a conventional laser, can emit coherent laser light. Such a device is called a Free Electron Laser (FEL) and was first realized by Madey and coworkers[1].

FELs are presently being developed as tools for a wide range of applications in science and technology. In principle, they can cover the frequency range from microwaves to the X-ray region with desirable performance parameters such as broad spectral tunability, high efficiency, high power and high repetition rates. Such performance would open up the way to many novel applications in chemistry such as vibrational relaxation, multiphoton excitation/dissociation, nonlinear processes in the infrared region, fast chemical dynamics, infrared study of adsorbed molecules and light catalyzed chemical reactions.

In the present article we will focus our attention on various photochemical processes using FELs. However, this is not intended to be comprehensive on either FEL or laser photochemistry, but is meant to provide a range of applications of FEL to photochemical problems. However, excellent texts and reviews are available on both FEL[2-8] and laser photochemistry[9-14]. Broadly, the purpose of this review is threefold : Firstly, to assist chemists, who plan on utilizing FELs for their research, to orient themselves in the bewildering array of information contained in many articles, often written by physicists or engineers for a highly specialized readership. Secondly, to show to the fast-growing community of chemists who, one way or the other, are "laser consumers", what has been achieved in related chemical disciplines using FELs. In this connection, it is gratifying to note the wide-ranging impact chemistry has made in the development of lasers and various laser based techniques. Thirdly, we address ourselves to non-chemists who sometimes are led into practicing chemistry, for example in the field of isotope separation. We hope they too will benefit from this expose, thus furthering the fruitful interdisciplinary efforts that have brought the laser field to prominence.

The organization of the review is as follows : The following section treats fundamentals of FEL, while sections 3 and 4 summarize existing devices and their properties. They are included here mainly for the sake of completeness and can be skipped by laser practitioners. In the last section, we describe various applications of FEL in the areas of photophysics and chemistry, IR spectroscopy, chemical dynamics and future industrial processing. The subject matter reflects to a certain extent the personal interest of the author. However, we believe that we have presented a balanced view of the subject, as it emerges from the current literature.

2 Basic Principle

Conceptually, free-electron lasers are simple, consisting of an electron beam in a magnetic field. Because of this simplicity, the theoretical treatment of free-electron lasers has often, especially in the begining, preceded the experimental development of these devices. This is a significant deviation from the mode of development of conventional lasers and is quite fortunate in view of the cost of building and operating high-energy electron accelerators for free-electron laser experiments.

The configuration of the electron beam and wiggler magnets in a free-electron laser is shown in Fig 1(a). The magnets are arranged with their poles alternating so that the magnetic field reverses every few centimeters. The overall length of the wiggler is typically a few meters, which corresponds to about 100 periods. The electron beam is injected into the end of the wiggler and travels down its length. Due to Lorentz force, as the electrons proceed down the wiggler they are deflected alternately left and right by the magnetic field and follow a wiggly path. For an electron oscillating around a point at rest, the angular distribution of such a dipole radiation is : $I(\theta) = I_0 \sin^2 \theta$ as shown in Fig 1(b). In contrast, for a relativistic electron with a velocity $v = \beta c$, where c is the velocity of light, it is sharply peaked in the forward direction within a cone of solid angle θ which is given as $(1-\beta^2)^{1/2}$. Therefore the divergence of such radiation emitted from electrons of energy E = 100 MeV is only about 2 mrad. The wavelength λ_L of the emitted light can be worked out by examining radiation from a single electron travelling down the wiggler with a velocity $v = \beta c$.

As shown in Fig 1 (c), the electron executes N_W

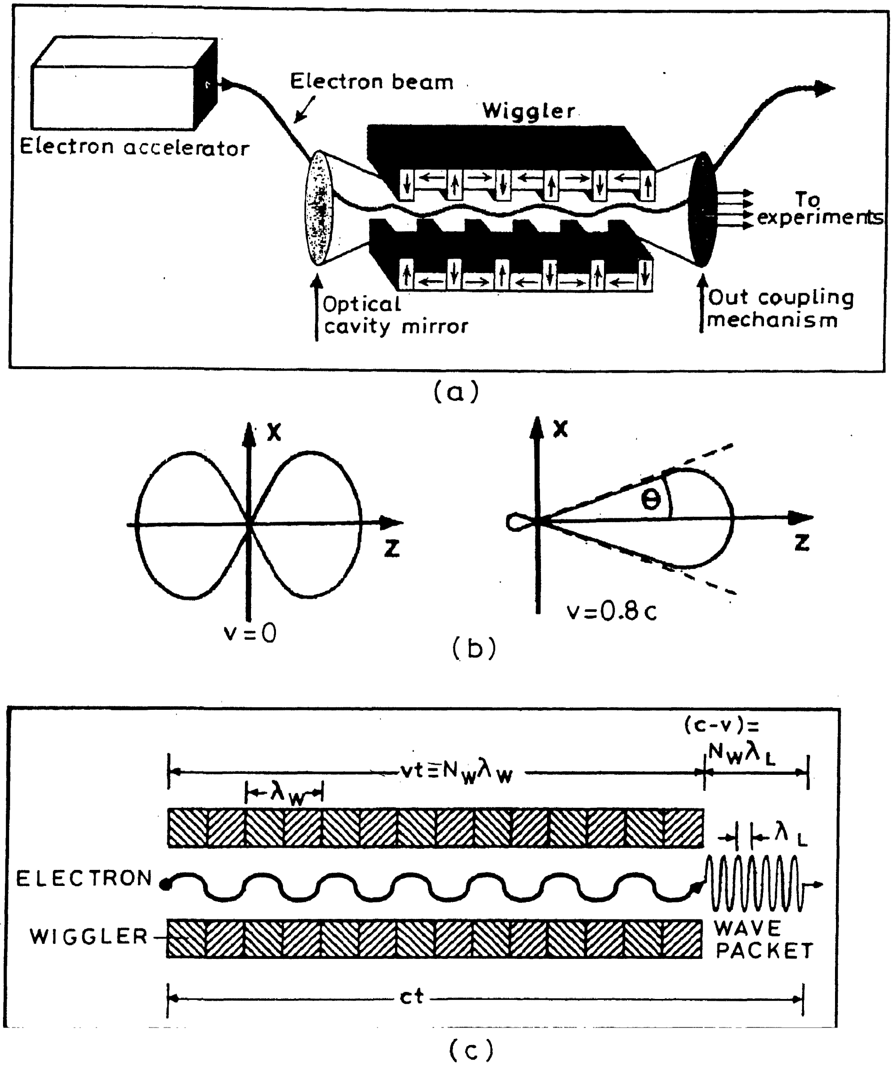

Fig. 1 (a) Schematic diagram of a Free Electron Laser, (b) Radiation of a dipole at rest (v = 0) and a moving dipole with v = 0 8 c, and (c) Correlation of the electron motion and the emitted wave packet

wiggles as it passes through the wiggler in a time $t = N_W\lambda_W / v$, where λ_W is the length of one period of the wiggler i.e. , the distance over which the magnetic field undergoes one complete alternation and returns to its original value. By the time the electron has reached the end of the wiggler, the front of the wave packet, which was emitted by the electron at the entrance of the wiggler, has moved a distance ct. But the back of the wave packet is just at the end of the wiggler, so the total length of the wave packet is (c-v)t. Since the wave packet, like the wiggler contains N_W oscillations, the laser wavelength λ_L is given by the expression:

$$\lambda_L = (c-v)t / N_W = \lambda_W (1-\beta)/\beta \quad \ldots (1)$$

Assuming that for relativistic electron $\beta \approx 1$ and its energy γ expressed in units of rest energy (mc^2 / e=511 MeV) can be written as $\gamma = (1 - \beta^2)^{-1/2}$, the laser wavelength becomes

$$\lambda_L = \lambda_W / 2\gamma \quad \ldots (2)$$

In this treatment, the effect of the wiggle motions on the velocity of the electron through the wiggler has not been considered. For moderate to strong magnetic fields, the wiggles can significantly increase the path length of the electron trajectory through the wiggler. And this slows down the electrons through the wiggler thereby increasing the wavelength of the light. By properly accounting for this effect, the laser wavelength is obtained as:

$$\lambda_L = [\lambda_W/2\gamma^2][1+\{eB_W\lambda_W/2\pi mc\}^2] \quad \ldots(3)$$

where B_W is the rms average magnetic field. Typically the magnetic field is made as large as possible to maximize the wiggle motion and the electron radiation, subject to the constraint that the wavelength does not become too long. This means that the magnetic field term in eq (3), $\{eB_W\lambda_W / 2\pi mc\}$ is generally of the order of unity. Using currently available permanent magnet material, the average magnetic field strength is typically of the order of 0.5 T for a wiggler period of 2 cm. Therefore for 100 MeV electron, one can obtain a very useful wavelength λ_L 500 nm in the green region of the electromagnetic spectrum. The linewidth of such radiation is of the order of $1/N_W$, so that the radiation has a line-width of about 1 percent with the state-of-art wigglers having typically 100 periods.

The radiation discussed above is analogous to the spontaneous emission in conventional lasers and can be used to initiate stimulated emission in the FEL. It is also the incoherent radiation which is called wiggler or undulator radiation in synchrotron radiation sources. Because the electrons passing through the wiggler are randomly positioned in the electron beam, the waves they emit have random phases with respect to one another. When the field amplitude of the radiation emitted by a single electron is Ej, the total intensity radiation by N independent electrons becomes

$$I_{tot} = |\Sigma E_j \exp(i\varphi)|^2 \quad \ldots(4)$$

where the phases φ_j of the different contributions are randomly distributed. If it could be achieved somehow that all electrons emit with the same phase, the total intensity for the case of equal amplitudes Ej $= E_o$ becomes

$$I_{\text{coherent (tot)}} = |\Sigma E_j \exp(i\varphi)|^2 \,\alpha\, |NE_o|^2 \,\alpha\, N^2 I_{el} \quad \ldots(5)$$

when I_{el} α ^{2} the intensity emitted by a single electron coherent emission with equal phases therefore yields N times the intensity of the incoherent emission with random phases.

Since the number of electrons is very large, typically of the order of 10^8 in the length of the wave packet from a single electron [Fig. 1 (c)], the coherent emission is much more powerful than the incoherent emission. In fact, the intensity of coherent emission is proportional to the square of the electron-beam current.

In order to understand how this can be achieved we consider first laser beam with the correct wavelength λ_m which passes along the axis of the wiggler. Electron those move at the critical velocity v_c, being $v_c = c\lambda_w / (\lambda_w + m\lambda_m)$, are in phase with the laser wave and can be stimulated to emit a photon which amplifies the laser wave (stimulated Compton scattering). The electron loses the emitted radiation energy and becomes slower. All electrons that are a little bit faster than v_c can lose energy by adding radiation to the laser wave without coming out of phase as long as they are not slower than v_c. On the other hand, electrons which are slower than v_c can absorb photons which makes them faster until they reach the velocity v_c. This means that faster electrons contribute to the amplification of the incident laser wave whereas the slower electrons attenuate it. This stimulated emission of the faster electrons and the absorption of photons by the slower electrons leads to a velocity bunching of the electrons towards the critical velocity v_c and enhances the coherent superposition of their contributions to the radiation field. The energy pumped by the electrons into the radiation field comes from their kinetic energy and has to be replaced by acceleration in RF cavities, if the same electrons are to be used in storage rings for multiple traversions through the wiggler.

Therefore, such a device is referred to as an free-electron amplifier with external source acting as a master oscillator. Clearly, the wavelength of the output beam is the same as that of the master oscillator, and the electron energy and magnetic field must be adjusted to satisfy eq. (3). If the master oscillator is a conventional laser, then the wavelength is restricted to the specific values achievable with that laser.

This free electron radiation amplifier can be converted into a laser oscillator by providing reflecting mirrors for optical feedback as shown in Fig.1(a). Such FELs are now in operation at several places in the world (cf Section 3). Their advantages are their tunability over a large spectral range from millimeter waves into the VUV region by changing the electron energy. Their potential high output power represents a further plus point for FELs. We will discuss in detail in section 4 about these unique properties which make FELs so attractive.

3 Operating FELs

The broad wavelength range provided by the various operating FELs shown in Fig 2 (adapted from ref. [3]) depends not only to a broad range of electron energy but to a variety of accelerator technologies as well. Since almost all wigglers have a period of the order of a few centimeters long, the wavelength of a free-electron laser is largely determined by the electron energy. Since a given type of accelerator is more useful over a

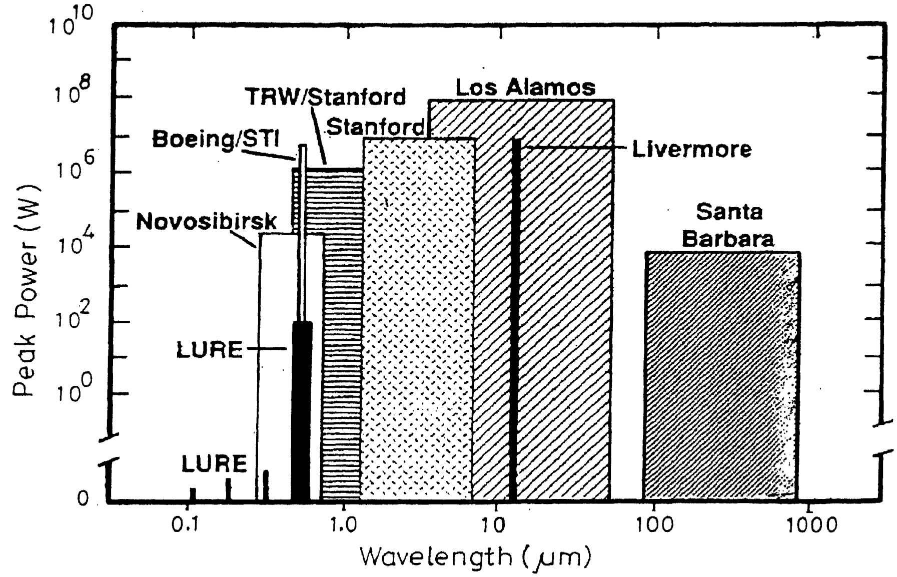

Fig. 2 Several FEL devices with their operating wavelength and peak power (adopted from ref. [3])

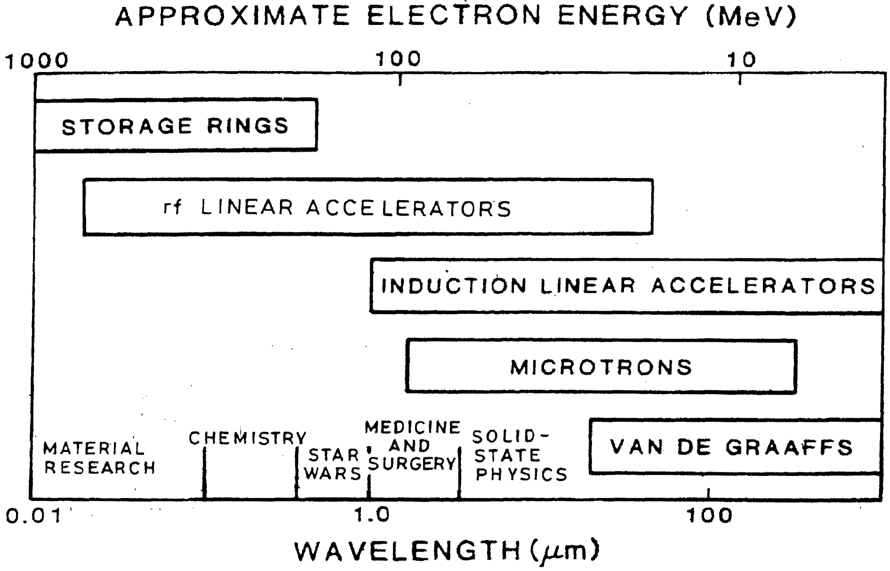

Fig. 3 Correlation between accelerator technology and FEL wavelength. Also shown are the spectral regions of interest for a number of applications

Table I

Operating FELs

FEL	λ (μm)	σ_z	E (MeV)	I (A)	N_w	λ_w (cm)	K (rms)	Acc Typ
UCSB (mm FEL)	340	25 μs	6	2	42	7.1	0.7	EA, O
Florida (CREOL)	355	8 μs	1.3	0.13	185	0.8	0.1	EA, O
Stanford(FIRFEL)	80-200	15 ps	4	8	50	1	0.7	RF, O
Himeji(LEENA)	65-75	10 ps	5.4	10	50	1.6	0.5	RF, O
UCSB(FIRFEL)	60	25 μs	6	2	150	2	0.1	EA, O
Osaka(ILE/ILT)	47	3 ps	8	50	50	2	0.5	RF, O
Tokyo(UT-FEL)	43	10 ps	13	20	40	4	0.7	RF, O
Nieuwegein FELIX I	5-35	5 ps	25	50	38	6.5	1.2	RF, O
FELIX II	20-100	5 ps	45	50	38	6.5	1.8	RF, O
Osaka (ISIR)	40	30 ps	17	50	32	6	1	RF, O
Bruyerest(ELSA)	20	30 ps	18	100	30	3	0.8	RF, O
Stanford (FIREFLY)	15-65	1-5 ps	15-32	14	25	6	1	RF, O
Frascati(LISA)	15	7 ps	25	5	50	4.4	1	RF, O
Grumman (CIRFEL)	12-21	5 ps	9-14	100	73	1.4	0.2	RF, O
Beijing(IHEP)	10	4 ps	30	14	50	3	1	RF, O
Orsay(CLIO)	3-53	0.1-3 ps	21-50	80	38	5	1.4	RF, O
LANL (RAFEL)	16	15 ps	17.4	300	200	2	0.9	RF, O
Osaka(FELI 1)	5.5	10 ps	33.2	42	58	3.4	1	RF, O
Darmstadt (IR-FEL)	5	2 ps	40	2.7	80	3.2	1	RF, O
Stanford (SCAFEL)	3-13	0.7-12 ps	22-45	10	72	3.1	0.8	RF, O
Vanderbilt(FELI)	2-9.8	0.7 ps	43	50	52	2.3	1	RF, O
Duke (MarkIII)	3	3 ps	44	20	47	2.3	1	RF, O
Osaka(FELI 2)	1.88	10 ps	68	42	78	3.8	1	RF, O
BNL(ATF)	0.5	6 ps	50	100	70	0.88	0.4	RF, O
Tsukuba(NIJI-IV)	0.35	160 ps	300	5	2x42	7.2	2	SR, O
Orsay (Super-ACO)	0.35	26 ps	800	0.1	2x10	13	4	SR, O
DUKE(OK-4)	0.34	2.5 ps	500	30	2x33	10	2.4	SR, O
Okazaki(UVSOR)	0.24	6 ps	500	5	2x8	11	2	SR, O

Note : λ = operating wavelength in μm; E = electron beam energy; I = peak current provided by the accelerator; N_w number of wiggler periods; λ_w = wiggler wavelength in cm; K = wiggler parameter; σ_z = electron pulse length divided by speed of light c; EA is electrostatic accelerator, RF is rf linac accelerator, SR is storage ring ; O stands for oscillator and A for amplifier

certain energy range, it is possible to correlate each type of accelerator with a useful wavelength range of the FEL. This correlation is shown in Fig. 3 where the spectral regions of interest to a number of applications are also indicated[3]. Interestingly, the operating regions for the various types of accelerator technology are not well defined and as the technology improves, the boundaries keep on expanding. It may be emphasised that the relation between energy and wavelength is not exact, since the wiggler period and magnetic field are somewhat variable.

However, the electron energy is not the only factor, which determines the useful wavelength range for each type of accelerator. Both induction linacs and RF linacs can be operated at electron energies sufficient to achieve much shorter wavelengths than indicated in Fig. 3. For short wavelength operation, it is necessary to focus the electron beam more carefully inside the laser beam and this requires a better electron-beam quality. The measure of the electron-beam quality called the emittance, is normally measured by the product of the radius and divergence of the electron beam. If the emittance is very much larger than the wavelength, then the electron beam cannot be focused inside the laser beam. The emittance is determined largely by the electron source; called the electron gun or injector, and the injector is different for each accelerator technology. Thus, the short-wavelength limit of each technology is set mainly by the injector technology.

Table I gives a fairly updated account of the operating FELs around the world at the present time[15]. For the conventional wiggler, the peak optical power can be estimated by the fraction of electron beam peak power that spans the wiggler spectral band width, $1/4\,N$ or $P \approx EI / 4eN$. For the FEL using storage ring, the optical power causing saturation is substantially less than this estimate and depends on ring properties. For the high-gain FEL amplifier, the optical power at saturation can be substantially more. The average FEL power is determined by the duty cycle and is generally many orders of magnitude lower than the peak power. In the FEL oscillator, the optical mode that best couples to the electron beam in a wiggler of length $L = N\lambda w$ has Rayleigh length $z_o \approx L / \sqrt{12}$ and has a mode waist radius of $w_o \approx \sqrt{N\gamma\lambda} / \pi$. The FEL optical mode typically has more than 90% of the power in the fundamental mode described by these parameters.

In the future, free-electron lasers are expected to operate at much higher power and shorter wavelengths. Power level will depend in part on the development of higher-current accelerators, but even more importantly on the development of optics with higher damage threshold. Damage to optical coatings has already been observed in FEL experiments at several laboratories, because the optical beam is narrowly confined in the optical resonator and becomes quite intense. However, new optical resonator configurations using grazing-incidence mirrors are being developed and with improved coatings and higher laser gain it should be possible in the future to achieve power levels exceeding those of any other lasers.

Shorter-wavelength lasers, operating in VUV and beyond, will depend not only on the development of improved injectors, as mentioned above, but also on the development of better

As the electron moves down the wiggler of an FEL, it loses energy to the growing electromagnetic wave and consequently, no longer satisfies the resonance condition. As a result, the FEL stops working, that is , "reaches saturation". This can be avoided if the wiggler field B, is varied to match the changing resonance condition. With this so-called "tapering", the FEL continues to operate even when the wiggler is very long. A broader spectrum may be emitted by such a tapered wiggler Edighoffer *et al.* [16], for example, measured a time-averaged spectral bandwidth of 1.3% for 1.57 μm emission from a 1% tapered wiggler with 4 ps current pulses. This bandwidth corresponds to 83 cm^{-1} which is much larger than the 4 cm^{-1} pulse transform limit. Hopefully, further time-resolved spectral measurements with tapered-wiggler oscillators will clarify this issue.

(c) Temporal Structure

The FEL pulsed output has essentially the same temporal structure as the electron pulses supplied by the accelerator. For RF linacs, the current is supplied in picosecond-duration micropulses spaced about every 1-100 ns (10^7-10^9 pps) and within a continuous train (macropulse), typically 10 μs to 10 ms long. These macropulses are periodic (to allow recharging of the primary power supply for the microwave klystrons) with repetition rates between 1 and 100 pps. A typical macro and micropulse structure is shown in Fig. 4. By use of cw klystrons, the macropulse can become infinite

Table II

Proposed FELs

FEL	λ (μm)	σ_z	E (MeV)	I (A)	N_w	λ_0 (cm)	K (rms)	Acc Typ
Harima (SUBARU)	0.2-10	26 ps	1500	50	33-65	16.32	8	SR, O
BNL(DUVFEL)	0.075	6 ps	310	300	682	2.2	1.5	RF, A
Frascati(COSA)	0.08	10ps	215	200	400	1.416	1	RF, O
DESY(TTF1)	0.042	0.8 ps	390	500	490	273	0.9	RF, A
DUKE(VUV)	0.05-1	10μs	1000	350	2x33	10	2	SR, O
DESY(TTF2)	0.006	0.17ps	1000	2500	981	2.73	0.9	RF, A
SLAC(LCLS)	0.00015	0.08ps	14350	3393	3312	3	3.7	RF, A
DESY(TESLA)	0.0001	0.08ps	35000	5000	1200	5	4.2	RF, A

Table III[1]

Useful Properties of Free-Electron Lasers

(a)	Wavelengths accessiblity	Millimeter to XUV
	Wavelength tunability	Continuous
(b)	Spectral bandwidth	Pulse-transform limited
(c)	Pulse width duration	1 ps to 1 ns (accelerator dependent)
(d)	Spatial output	Diffraction-limited
(e)	Emission	Polarized
(f)	Optical damage to gain medium	Nil
(g)	Power:	>10 MW peak, >1 kW average
(h)	Efficiency	High >20% wall plug
(i)	Maintenance	Infrequent and low-cost

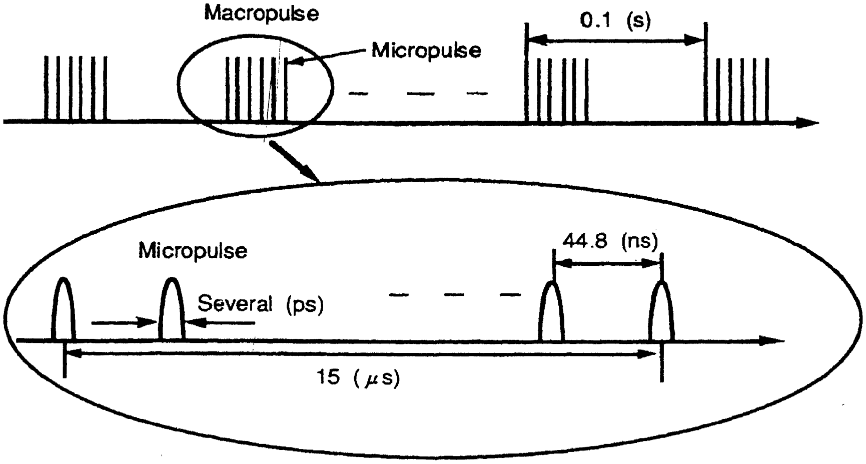

Fig. 4 Schematic illustration of FEL double pulse structure. Such pulses were used in our investigation on laser separation of C-13 isotopes

in duration. Near-cw operation is normal for electron storage rings which produce current pulses 10 ps to 1 ns long every 100 ns or so for storage times from about ten minutes to one hour.

(d) Spatial Beam Quality

Due to the narrow diameter of the electron beam within the wiggler, it is possible to obtain essentially diffraction-limited spatial output with minimal intracavity aperturing. Near-Gaussian output beams have been produced from the Stanford and Los Alamos FELs.

(e) Polarization

The polarization of the laser light is determined by the wiggler structure. Permanent magnet wigglers are usually planar devices, whereas superconducting and other wire-wound magnets driven by electric current generally have a helical field. Therefore, the laser output from the first kind of wiggler is linearly polarized while in the second case, the output is circularly polarized.

(f) Optical Damage

The absence of a material gain medium in an FEL cavity precludes laser damage and contamination of the cavity optics. However, cavity optics (windows and mirrors) can degrade in the presence of neutrons and x-rays generated by electron collisions in the accelerator beam line. Also, harmonic emission at sub-multiples of the primary laser wavelength can be powerful enough to induce transient or permanent absorption via photo-dissociation, colour centers and other processes in dielectric optics. Proper choice of optical materials and radiation shielding can minimize these effects. As in the case with any high-power laser, laser damage to the cavity optics is an issue that may be avoided by optimized materials and cavity optics design.

(g) Power Output

The FEL is potentially capable of giving both high-peak and high-average power output. As a natural result of picosecond pulse structure, peak powers at multimegawatt levels are possible. The magnitude of the average optical power depends primarily on the ability of the accelerator to supply continuous, high-current pulses, the extraction efficiency of the wiggler and the damage resistance and distortion limits of the cavity optics. The average powers called for by industrial laser-chemical processes range from 1 to 100 kW. Such powers greatly exceed those produced in the FEL demonstrated to date, but a good start toward attaining high-average power capability has been made in the Los Alamos FEL with output of 1 kW average power in a 70 μs macropulse at 1 Hz.

FELs can be scaled to high power because of the availability of high-power accelerators. For example, the large electron accelerator at the Stanford Linear Accelerator Center (SLAC) has a 200-kW electron beam operating round the clock. However, parallel efforts are also needed in the area of developing high quality electron beams along with high power.

(h) Efficiency

Normally in all lasers, most of the input energy is converted into waste heat and this must be removed by cooling the laser medium. In the case of high power gas lasers, this is done by flowing the hot laser gas out of the laser at very high speed. In the free-electron laser, the waste heat remains in the relativistic electron beam, which moves about a million times faster than a high-speed flowing gas. Therefore, the electron beam exits the laser in a few billionths of a second, carrying the waste heat with it. Moreover, recent experiments at Los Alamos have shown that the spent electron beam from the laser can be decelerated to recover as much as 70 percent of the leftover energy, thereby increasing the overall efficiency. Such an efficiency enhancement scheme[17] is shown in Fig. 5. Therefore, FEL's have the potential for very high overall efficiency, perhaps as high as 20% wall plug. Klystrons with high efficiencies (70% cw and 50% pulsed) are commercially available, tapered wigglers can efficiently (10%) extract energy from the electrons and almost all of the unused energy in the electron beam can be recovered and recycled.

(i) Maintenance

The primary expenditure to maintain an FEL is the cost of replacing the microwave klystrons (about $ 100,000 each) required to run the accelerator, which have a life time of about five to ten thousand hours. Operating at a 50% duty factor, each klystron will, therefore, have an average life of 1-2 years. The power level of a particular FEL will dictate the number of klystrons required in the system.

5 Applications

Applications of the FEL in chemistry are envisioned for both scientific research and industrial production. The status and prospects for scientific use were evaluated by the Solid State Sciences Committee of the National Research Council quite sometime back[18]. The committee concluded that chemistry and surface chemistry would be areas that would particularly benefit from FEL advances. Infrared FEL's are at this time the most developed reliable systems that offer clear advantages over available benchtop lasers. The most important spectral region for chemical

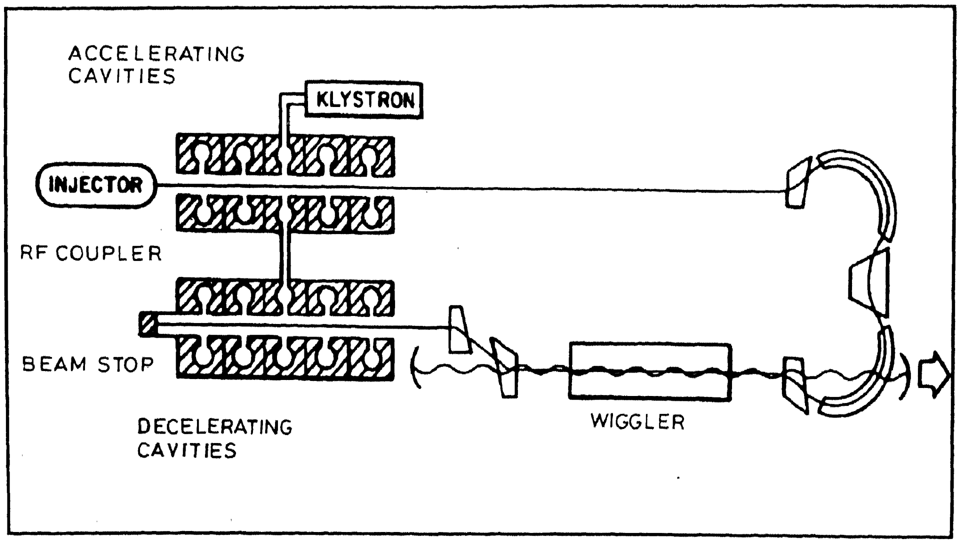

Fig. 5 Efficiency enhancement scheme for a FEL. Most of the energy of the electrons leaving the magnetic wiggler may be recovered in a separate decelerating and can be fed back into the primary accelerator to accelerate new electrons

applications is the vibrational IR region (3-30 μm), although many interesting applications involve the near IR (1-3 μm) as well.

Radiation from an IR FEL can be used to manipulate molecular vibrations and chemical reactions in both the condensed and the gas phase. The IR pulses will make possible new studies on intramolecular vibrational energy transfer by means of IR multiple photon excitation and dissociation (IRMPE & IRMPD), a technique thus far limited to the molecular species that can be excited by CO_2 lasers. With broadly tunable IR FELs, the technique can be extended to practically all molecular species. Such new studies will provide valuable information on, for example, the combustion phenomena. High average power of IR FELs would ultimately allow materials to be synthesized from a wide range of elements across the periodic table. The pump-probe type experiments involving IR FEL and a second light source (which can be another FEL, a conventional laser or a synchrotron light source), will allow quantitative studies of many surface phenomena, such as time-dependent redistribution of surface molecules, diffusion, desorption and so on.

In the following, we will discuss in detail the applications of FEL in IRMPE & IRMPD and isotope separation processes. We will also examine infrared spectroscopy and dynamics of some interesting systems in condensed / gas phase and on surface as well. Finally, we will look into the various aspects of industrial application of FEL which have been advocated for this promising laser source.

5.1 Infrared Multiple Photon Chemistry

Probably none of the phenomena in laser photochemistry discovered in the recent past is as exciting as IRMPE and IRMPD. Recognition of this method as a means by which selective photochemistry may be realised, has whetted the appetite of photochemists who are excited by its possible applications in dissociation, isomerisation, control of chemical equilibria, synthesis of complex molecules and finally in bond selective chemistry[9-14].

With vigorous activity in IRMPE and IRMPD, the phenomenon is now well established as a general one. In more than hundred molecules - from 3 to 62 atomics - unimolecular dissociation, isomerization, inverse electronic relaxation, electron detachment processes etc have been triggered in this way. A compilation of some representative systems are presented in Table IV.

The nature and characteristics of the photophysical and photochemical processes induced by multiphoton excitation (MPE) of collisionless, isolated molecules triggered hectic experimental and theoretical activities Current understanding of the mechanism of MPE of a molecular level structure is still incomplete and relevant data accumulate quite slowly. The elucidation of the mechanism of energy acquisition by MPE is crucial for its better understanding. The following qualitative picture has emerged out of the numerous experimental and theoretical studies in this subject.

The molecular energy levels are separated into three regions as shown in Fig. 6. In the lowest energy range (region I), the density of molecular states is very low and laser field interacts with isolated discrete molecular states. Several possible mechanisms to overcome the anharmonic detuning at several successive transitions of the excited vibrational mode have been considered viz. (a) power broadening (b) rotational anharmonicity

Table IV

Some representative molecules which have been studied by IRMPE and IRMPD

Triatomics	OCS, O_3
4-atomics	BCl_3, H_2CO, HDCO, D_2CO, $CSCl_2$, COF_2, HN_3
5-atomics	CDF_3, CTF_3, CF_3X (X = Cl, Br, I), OsO_4, SiF_4, CrO_2Cl_2, CH_2= CO
6-atomics	CH_3OH, CH_3NC, CH_2=CH_2, CH_2=CF_2, N_2F_4, CH_2=CHCl, SF_5^+
7-atomics	SF_6, UF_6, CH_3NH_2, CH_3NO_2, CH_2=CHCN, SF_5Cl, MoF_6, SeF_6
8-atomics	CH_3-CF_3, $CClF_2$-CH_3, C_2F_6, CH_3COOH, C_2F_5H, C_2F_5D, C_2F_5T
9-atomics	C_2H_5CN, C_2H_5NC, C_2H_5OH, CH_3OCH_3, SF_5NF_2, $C_3F_6^+$
10-atomics	$C_2H_5NH_2$, CF_3COCF_3, Cyclo-C_4F_6
11/12 atomics	C_3F_7I, n-C_3H_7OH, S_2F_{10}, Cyclo-C_4F_8, $CH_3COCOCH_3$
> 12 atomics	$CH_3COOC_2H_5$, $U(OCH_3)_6$, $C_6H_5CN^+$, $UO_2(hfacac)_2$ THF, $[UO_2(hfacac)_2]_2$ (hfacac = hexafluoroacetylacetone)

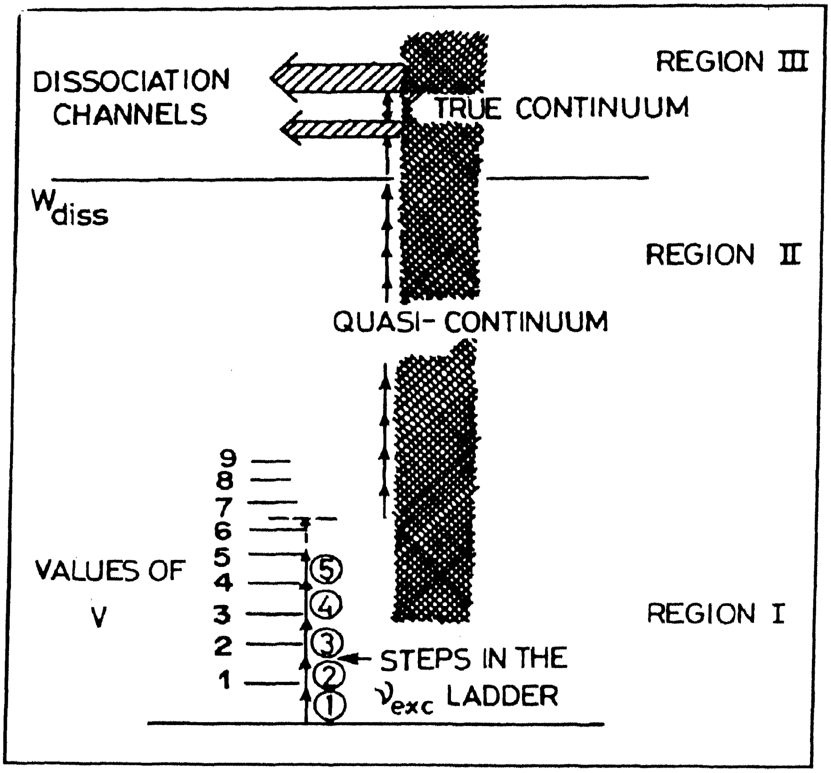

Fig. 6 Schematic model for infrared multiple photon excitation (IRMPE) and dissociation (IRMPD)

compensation (c) multiphoton transitions and (d) leakage effect. Once the molecule has absorbed a few quanta, the density of molecular states become very large and time evolution can no longer be described in terms of a few isolated molecular states. This region is denoted as quasi-continuum (region II) and its exact theoretical treatment is the subject of current debate. A proper description of the molecular time evolution in this range requires a quantitative understanding of the mechanism of intramolecular energy transfer and of line broadening of highly excited polyatomics of which very little is known at present. However, the recent developments in high resolution spectroscopy, coherent transients and overtone spectroscopy are currently yielding novel information in these areas. Finally, when the molecule acquires enough amount of internal energy, it enters a true continuum (region III) where in addition to all the complications of region II, dissociation or predissociation or isomerisation channels open up.

It should nevertheless be emphasised that there is no sharp boundary between regions I and II, which have been labelled for convenience only. The present theory has by no means been proved conclusively and the ideas are believed to be those most widely accepted amongst workers in the field at present. It is believed that the absorption mechanism is such that the molecule finds a near resonant pathway for absorption of about 4-5 photons through the discrete states. There upon the molecule can be considered to be in the quasicontinuum where restrictions for absorption are less severe and the energy leaks from the driven mode to the other modes, building up until dissociation takes place. Details and further developments of these processes can not be brought out here for limitation of space. Interested readers are referred to various reviews on this subject. However, we will present an account of various laser isotope separation schemes amongst which the most viable method is provided by irradiation of gas samples with high intensity IR laser causing IRMPD. The principle of state-selective, chemically irreversible MPD has been applied to a host of molecules and the separation of isotopes[9-11, 19-20] present major challenges in today's laser research in chemistry. A brief survey of the great amount of work currently in progress will be made concentrating mainly on those aspects studied in our laboratory.

5.1.2 Laser Isotope Separation

The main thrust is aimed at developing workable isotope separation method for uranium-235, the fissile isotope of uranium which is needed to fuel light water moderated reactors. Conventional gas diffusion separation methods consume ten million times as much energy as is theoretically necessary (i e entropy of mixing 1 Kg of $^{235}UF_6$ with 139 Kg of $^{238}UF_6$, of about 6 1 × 10^4 J). In addition, there is also a promising market for isotopes of lighter elements such as D, ^6Li, ^{10}B, ^{13}C, ^{15}N, ^{17}O, ^{18}O, ^{34}S etc. some in connection with energy production (D. Li, B) and others as non-radioactive tracers in analytical, medical and environmental studies In comparison with various existing methods of isotope separation laser process promises to yield higher enrichment per stage, consume less power and savings in capital investment.

All laser enrichment strategies have three requirements in common. Firstly, the isotopic absorption features with a well-resoled spectroscopic isotope shift. In the visible or ultraviolet portion of the spectrum of gaseous atoms or molecules, the dense array of electronic transitions display small isotope shifts (due to different nuclear mass, size, shape and spin) which range from $1:10^5$ to $1:10^8$ of transition energy. In the infrared spectral region the vibrational transitions of molecules are directly related to the reduced mass of constituent atoms and the relative isotope shift is typically of the order of 1:100 to 1:1000. Secondly, the laser employed must be monochromatic (to the limit of the spectral line width of the absorber) and preferably, tunable so as to allow selective excitation of the desired isotope without having to rely on fortuitous coincidences between laser emission lines and isotopic absorption features. Thirdly, there must be an efficient extraction step of the desired isotope, which may be magnetic, electrical, optical, thermal or chemical that acts preferentially on the excited species before relaxation, collisional energy transfer or charge transfer can occur. This turns out to be the most stringent condition for practical implementation of laser enrichment of isotopes. Several schemes, as shown in Fig 7, have been explored on a laboratory scale, viz , (1) single photon (2) two photon and (3) multiple photon processes.

The classical photochemical process (Fig. 7a) is based on a one-step ultraviolet / visible excitation of an electronic state of a molecule. Single step excitation of an electronic state of molecule has serious disadvantage, particularly for polyatomics of having broad structureless electronic absorption bands at room temperature. The scheme cannot be used for isotopically selective excitation. Only for a few simple molecules the absorption line is narrow enough for isotope selection. However, excitation of electronic state does give a high quantum yield for the photochemical reaction.

On the other hand, single step excitation of molecular vibrational state features rather high excitation selectivity for both simple and complex molecules. The main disadvantage of this method is that the fast relaxation of vibrational excitation to heat leads to a low quantum yield of the subsequent photochemical processes. But two step excitation (Fig 7b) of a molecular electronic state through an intermediate vibrational state by joint action of IR and UV radiation removes the above disadvantages. Thus this kind of two frequency (IR + UV) excitation combines sufficiently high selectivity with high quantum yield for photochemistry. The infrared multiple photon process (Fig 7c) differs fundamentally from all other methods in that infrared photons alone are responsible for both exciting selectively and subsequently dissociating the molecule. The manifold of vibrational energy states of one or more modes of the molecule in the ground electronic state acts as a selective infrared pathway through which the absorption of photons excites the molecule to a level at which dissociation occurs.

5.1.3 Laser Arsenal . FEL Versus Conventional lasers

The high power requirement for IRMPD allows only a few IR lasers to be attractive and some of them are the CO_2, CO, chemical lasers such as HF / DF, optically pumped molecular lasers such as NH_3, CF_4 and para-H_2 Raman laser The useful characteristics of FEL have already been presented in section 4. One can have a quick comparison of

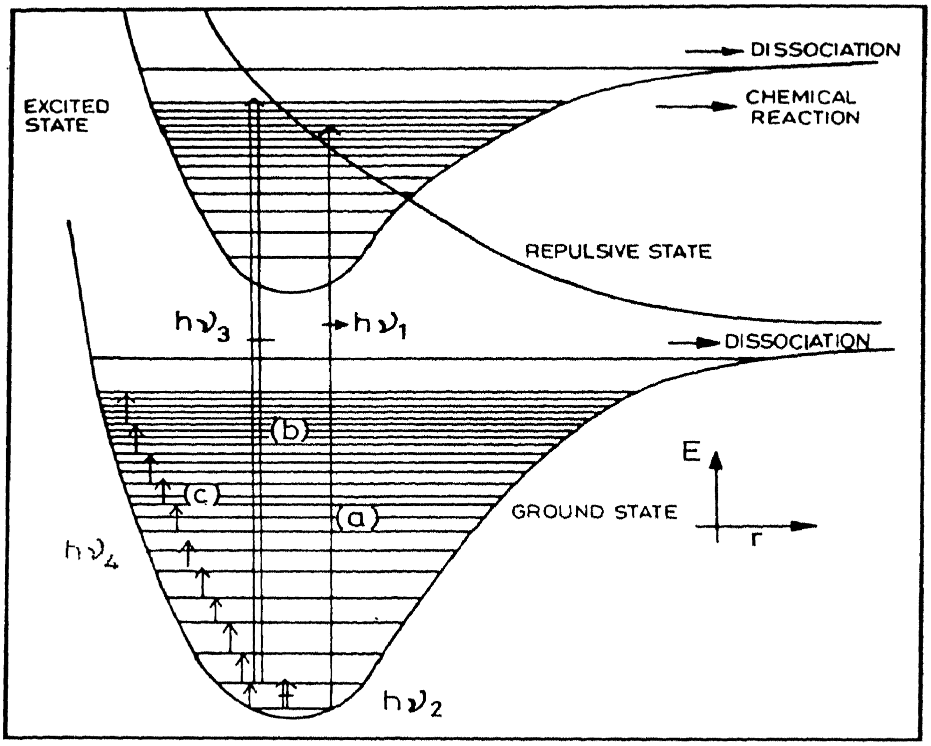

Fig. 7 Various types of selective excitation : (a) single step electronic excitation (ν_1). (b) two step electronic excitation through intermediate vibrational state ($\nu_2 + \nu_3$) and (c) multiple photon excitation in the ground electronic state (ν_4)

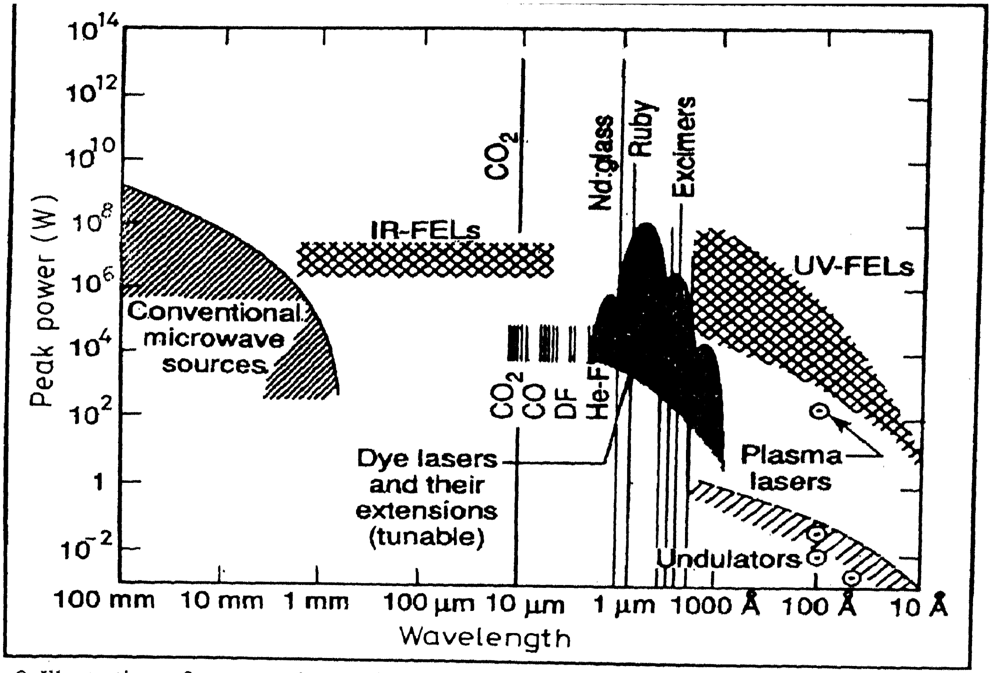

Fig. 8 Illustration of comparative peak power of some conventional light sources and FELs at various wavelengths

the power and wavelengths of some conventional light sources and FELs as shown in Fig 8. Therefore, to have an ovreall assessment, we will briefly review the characteristics of a few main conventional lasers. The CO_2 laser[21] is the main work-horse laser and by far the greatest number of studies have been carried out using this laser. This is mainly due to its suitability in terms of energy, power, efficiency and convenience of operation. Many different versions of this laser are available commercially, both cw and pulsed. Continuous powers of over 10kW and pulsed outputs of many megawatts are currently available. Normal cw operation occurs near 10.6 μm but with a grating in the cavity the laser can be tuned to obtain about hundred discrete vibration-rotation transitions between 886 and 1096 cm^{-1}. The cw laser can also be pulsed and Q-switched to provide short high power pulses, typically 10 kW in pulses of 300 ns wide for a 2 m cavity. A significant advance in IR laser chemistry was made by the introduction of the transversely excited atmospheric pressure (TEA) laser. By operating the active medium at atmospheric pressure, vacuum problems are eliminated and the output power per unit volume is increased. To achieve uniform excitation at atmospheric pressure it is necessary to preionise the gas to initiate a uniform glow discharge between the main electrodes. A typical pulse from a TEA laser varies from about 70 to 300 ns in width and powers of several megawatts are readily available. When shorter pulse widths are required active mode locking techniques are employed Single pulse can then be selected from the train by use of a suitable switching element. Typically, pulses of 1 to 10 ns duration with an energy in the mJ range are obtained which can be energy upgraded by further amplification in a separate TEA amplifier. Greater tunability in TEA CO_2 laser is achieved by operating the laser at high pressures, when pressure broadening effects result in continuous absorption over the whole vibration-rotation band. High pressure electrical excitation of CO_2 and other simple molecules has been demonstrated using various discharge techniques. Electron beam sustained CO_2 lasers at pressures ≥ 15 atm have been operated with efficiencies of about 3% and cavity energy densities of 60 J / lit. This technique clearly offers the potential of tunable, very high-power single-pulse energies and is well suited for industrial applications.

Chemical lasers[22] such as the HF-DF laser, operating between 2.8 and 4.0 μm, can produce large output powers and fluences. However, their use in laser chemistry have been limited partly because of the involvement of handling and disposal of corrosive gases and partly to the lack of flexibility compared with the CO_2 laser. A large number of chemical lasers have now been studied giving output at large number of laser lines in the mid IR region. With some commercial TEA CO_2 lasers, it is possible to change the optics and electrical discharge parameters and operate the laser with a different gas mixture, generating a number of different laser frequencies. The CO laser (5.1 to 5.6 μm) is generally operated cw, but at low powers than the CO_2 laser.

Interest in other pulsed tunable sources has been increased for a number of spectroscopic, dynamic and analytical studies. There are essentially four techniques to generate coherent, broadly and continuously tunable IR radiation of high power[23]: down conversion of dye laser radiation by difference frequency generation (DFG) in non-linear crystals, down conversion via stimulated electronic Raman scattering (SERS) in atomic metal vapours, stimulated Stokes Raman shifting (SSRS) and optical parametric oscillators (OPO). The performance data of the OPO, DFG and SSRS techniques provide 10 mJ, 10 ns pulses in the region of 700 to 10000 nm with bandwidth of 0.15-0.3 cm^{-1}. A particularly efficient device for generating tunable IR radiation in the important C-H stretching region is OPO which consists of a cylindrical $LiNbO_3$ crystal rod that is mounted in a cavity with an etalon, a grating and an output coupling mirror. On pumping the crystal longitudinally by 1064 nm fundamental beam of a Nd:YAG laser, parametric conversion of the pump radiation takes place to a pair of tunable output waves of lower frequency resulting in the generation of two tunable beams (the signal and the idler) which are collinear with the fixed frequency pump beam. This device provides tunability between 7000 and 2800 cm^{-1}. The alternative DFG scheme also utilises a non-linear $LiNbO_3$ crystal but requires Nd:YAG pumped dye laser operating on several dyes in the 640 to 850 nm region to achieve similar tunability. Commercial IR wavelength extension devices of this type give typical pulse energies of 0.5 mJ at 3.7 μm and 5mJ at around 1.5 μm. The cw tunable IR lasers are best represented by semi-conductor diode lasers (SDL) These lasers have been extensively used for high resolution spectroscopy of transient species involved in laser chemistry experiments[24-26]. They are capable of line widths less than 100 MHz and are tunable in spectral regions where nearly all molecular species, radicals or ions give rise to characteristic absorption.

5.1.4 Isotope Selective IRMPD

Isotopically selective MPD have been performed on several isotopes, from light ones (H, D, T) to heavy ones (Os, U) contained in very different molecules. Many of these became the basis of laser isotope separation methods developing in numerous laboratories of several countries Table V represents some of our activities in this area[27-37]

We present now detailed studies on separation of carbon isotopes which is currently under development in our laboratory. Natural carbon consists of two stable isotopes, viz C-13 (1.11%) and C-12 (98.99%) These isotopes are widely used in various branches of science and technology Carbon-13 is an important isotope as a tracer in areas ranging through chemistry, life sciences, medicine, environmental sciences and biochemical synthesis. Although the current production of 90% C-13 is about 10 kg per annum, an optimistic projection of hundred fold increase in the market demand is anticipated in view of rapid development of routine medical applications such as breath tests and whole body NMR. Diamonds made from C-13 depleted carbon (0.1%) has interesting physical properties like higher thermal conductivity and higher laser damage threshold Other applications of C-12 are solvents for NMR spectroscopy and monoisotopic fullerene for mass spectrometry.

The current method of C-13 separation by low-temperature distillation of carbon monoxide has inherent drawbacks such as low separation factor, high energy consumption and huge distillation

Table V

Isotope Selective Laser Photochemistry at B A R C

Isotopes	System Pressure (Torr)	Laser line	Typical results Fluence (J/cm^2)	Selectivity
Sulphur 34 / 32	SF_6 1.0	10 P(20) CO_2 laser	2.0	10
Carbon 13 / 12	CF_3Cl 15.0	9 P(18) CO_2 laser	3.0	80
	CF_2HCl 100.0	9 P(20) CO_2 laser	4.0	60
Stage 1	CF_3Br/Cl_2(1:4) 50.0	9 P(32) CO_2 laser	4.5	65
Stage 2	CF_3Cl/Br_2 (1:6) 20.0	9 P(8) CO_2 laser	1.7	200
Deuterium D / H	CHF_3/Ar (1:2) 75.0	10 R(10) CO_2 laser	30.0	> 40
Tritium T / H	CHF_3/Ar (1:2.5) 28.0 (0.2 ppm CTF_3)	9 R(8)-9 R(14) CO_2 laser	65.0	38
T / D	$CDCl_3$/Ar (1:5) 12.0	828 cm^{-1} NH_3 laser	21.0	5000.0

tower leading to a high production cost. In view of the growing demand for carbon isotopes and the shortcomings of the current technology for scaling up, we are actively engaged in developing laser photochemical methods.

IR laser chemistry of carbon compounds has been studied extensively. A large number of halogenated molecules, mostly methanes, have been subjected to isotope selective IRMPD Among these, CF_3X (X = I, Br, Cl) and CF_2HX (X =Br, Cl) are most promising. Although enrichment ≥ 90% C-13 has been achieved in a modified scheme of IRMPD of CF_3X system in presence of suitable scavenger in a two-stage process[30], here we will discuss the investigation on CF_2HX systems.

Under selective excitation CF_2HX system undergoes IRMPD with clean and simple chemistry to yield isotopically enriched product C_2F_4:

$$^{13}CF_2HX \xrightarrow{nh\nu} {}^{13}CF_2 + HX$$

$$^{13}CF_2 +^{13} CF_2 \quad \overset{M}{} \quad {}^{13}CF_2{}^{13}CF_2 \qquad \ldots (7)$$

5.1.4.1 Results With CO_2 laser

Excitation and dissociation selectivities are so good for this system that MPD of CF_2HCl is possible even at fairly moderate pressure (~133 mbar) at room temperature yielding C_2F_4 with 50% ^{13}C. However, the end product C_2F_4 poses difficulty in closing the chemical cycle for further enrichment in the second stage. In the above schemes, the residual reactant gets enriched in C-12 and thus large quantities of C-13 depleted material can be produced in the same apparatus. Therefore, significant quantities of carbon bearing material can be rapidly subjected to a complete isotope separation. As a spin-off, such system lends itself to enrichment of carbon-14 as well and problems related to calibration can be obviated in radiocarbon dating systems. It would be of interest to note that all the end products from various schemes can readily be converted into CO_2 which is an important basic building block for C-13 labelled compounds.

We have carefully evaluated IRMPD of CF_3Br / Cl_2, $^{13}CF_3$ Cl / Br_2 mixture and of neat CF_2HCl and arrived at the optimum experimental conditions to maximise the dissociation yield and enrichment factor. We have also carried out comparative evaluation of these systems in terms of quantity of product per pulse, its C-13 content and energy expenditure in keV per separated C atom. Both the schemes have been found to be energy competitive[29] when compared with the conventional cryogenic process. From the data generated we have demonstrated production of laboratory scale quantities of C-13 material enriched to various levels from 50% to ≥ 90% and also used them in high resolution spectroscopic studies[31] of such labelled compounds.

5.1.4.2 Results with FEL

Although we can select any of rotational lines of 9 and 10 μm vibrational bands of CO_2 laser, the so-called line-tunability is limited to the wavelength region from 9 to 11 μm. On the other hand, FEL having perfect continuous tunability enables us to examine IRMPD for a variety of molecules in vicinity of their active IR absorption. However, the inherent line width, usually a few percents of a photon energy, is expected to lower the isotopic selectivity to a certain extent.

As has been indicated earlier, the pulse energy and pulse duration of an FEL depend on features of electron beams generated by an accelerator or those stored in a storage ring. A typical pulse of our FEL with the use of a linear accelerator has a double pulse structure. Though the energy of a micropulse may be too small to achieve IRMPD, the macropulse is considered to be intense enough to cause IRMPD, if the beam is focussed into a small area[38]

We have used the FEL of Free Electron Laser Research Institute, Inc. (FELI) located at Kansai Science City in Japan In the present investigation we attempted to induce IRMPD of CF_2HBr and CF_2HCl using the FEL[39,40]. We have observed the definite occurrence of IRMPD as well as appreciable 13-C selectivity, which are then compared to those obtained with a CO_2 TEA laser.

FELI has five facilities numbered from 1 to 5. Facility 1 is open to the study of IRMPD. Briefly, the 30 MeV S-band linac is used for the acceleration of electrons. The kinetic energy of electrons is transformed into laser radiation via a 2-in Halbach type wiggler equipped with an optical laser cavity. The cavity is consisted of two concave gold-coated mirrors, one of which has a small aperture in the center for output coupling. The total

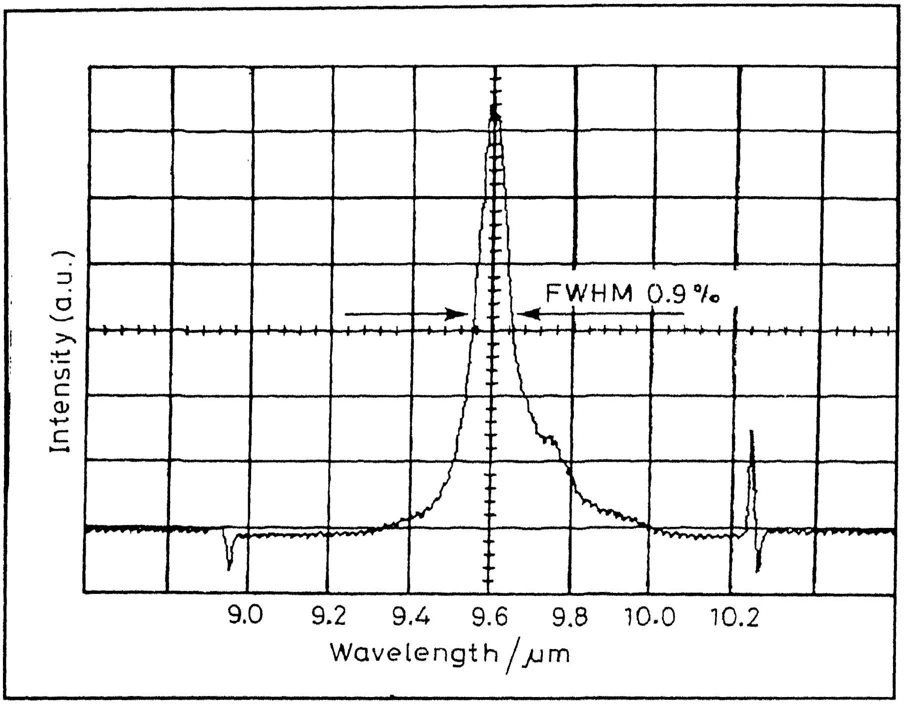

Fig. 9 Typical spectrum of FEL pulse at 9 6 μm used in C-13 selective experiments

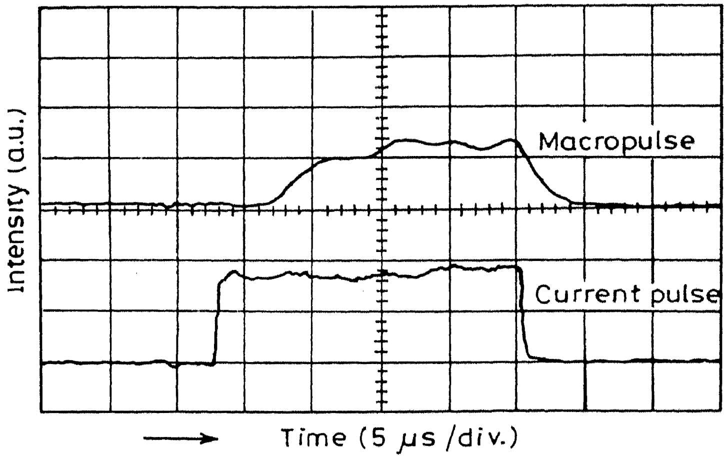

Fig. 10 Correlation of electron beam current pulse (lower trace) and resulting FEL macropulse (upper trace) at 9 6 μm

cavity length is 6.72 m and the periodical length of the wiggler is 3.4 cm. The continuous tunability in the region from 5 to 20 μm has been verified in wavelength measurements. However, the FEL has an unavoidable wavelength spread originating from the distribution of an electron speed. Fig. 9 shows the spectrum of the laser radiation at 9.6 μm, the FWHM is 0.09 μm, i.e., 0.9% of the photon energy. The beam size on the optical table in user's laboratory was as large as 35 mm in diameter and the beam divergency was 0 8 m rad. Fig. 10 shows an electron current macropulse generated by the linac and a 9.6 μm FEL macropulse measured with an HgCdTe detector. Both growth and decay are slow in the FEL macropulse with a relatively flat top measuring about 17 μs. As described earlier, the macropulse consists of a train of micropulses, the duration of which is a few picoseconds (cf Fig. 4). Since in the present case, the interval between two consecutive micropulses is 44.8 ns, one macropulse contains about 380 micropulses Since electron current and FEL intensity of Fig. 10 have been measured with the slow response detectors such as a button monitor, one can not observe fine structure due to micropulses in the figure. The repetition rate of a macropulse is 10 Hz and the laser power was in the range of 20-40 mW

The main part of an optical cell was a cylindrical tube made of stainless steel fitted with NaCl or BaF_2 windows. The cell length was 50 mm and the inner diameter of the tube was 24 mm. The volume of the cell including a side arm and a metal valve was about 24.6 cm^3. The laser beam was focused into an optical cell by means of an infrared lens with a focal length 50 mm in the present experiment. Infrared absorption spectra have been measured before and after laser irradiation using a FTIR spectrophotometer. Amounts of C_2F_4 and 13-C atomic fractions in C_2F_4 were determined for irradiated samples using a gas chromatograph-mass spectrometer equipped with a GS-Q capillary column (30 m length × 0.32 mm inner diameter). The temperature of the oven was changed from the room temperature to 120°C according to a specified program. We have carried out a few IRMPD experiments using a TEA-CO_2 laser and the results were compared to those obtained with FEL.

The infrared absorption spectrum for CF_2HBr has been measured in a wide range from 600 to 5000 cm^{-1}. Observed and predicted peaks have been assigned to nine fundamental vibration modes, their overtones, and their combinations. Since the FWHM of 9 cm^{-1} in FEL is about two fifths of the carbon isotope shift, there is a possibility to observe isotope selective IRMPD in the present experiment. Fig. 11 shows yields of C_2F_4 and 13~C atomic fractions in C_2F_4 as a function of FEL wavelength. The yield of C_2F_4 increases with decreasing wavelength, while the atomic fraction of 13-C in C_2F_4 increases from 1.3 % to 6 %.

The spatial distribution of the relative fluence or relative local light intensity of FEL across the beam was measured using a pin hole with a diameter of 50 μm. Fig. 12 shows the transverse energy profile of the laser beam at a focal point. The observed distribution appears to fit the Gaussian function with a full width of 180 μm at $I = I_{peak} / e^2$, where I_{peak} is the intensity at a peak. Since the output of the laser is 40 mW at a repetition rate of 10 Hz, one macropulse contains an energy of 4 mJ. The fluences of one micro- and one macropulse are estimated to be 0.04 and 16 J cm^{-2} respectively,

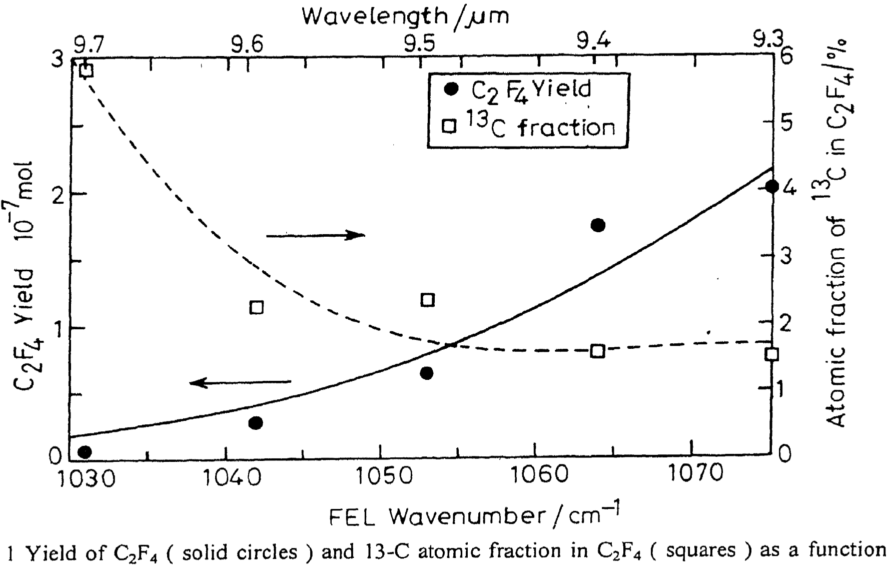

Fig. 11 Yield of C_2F_4 (solid circles) and 13-C atomic fraction in C_2F_4 (squares) as a function of irradiation wavelength of FEL. 5 Torr of CF_2HBr was irradiated with 36,000 FEL macropulses of energy 4 mJ

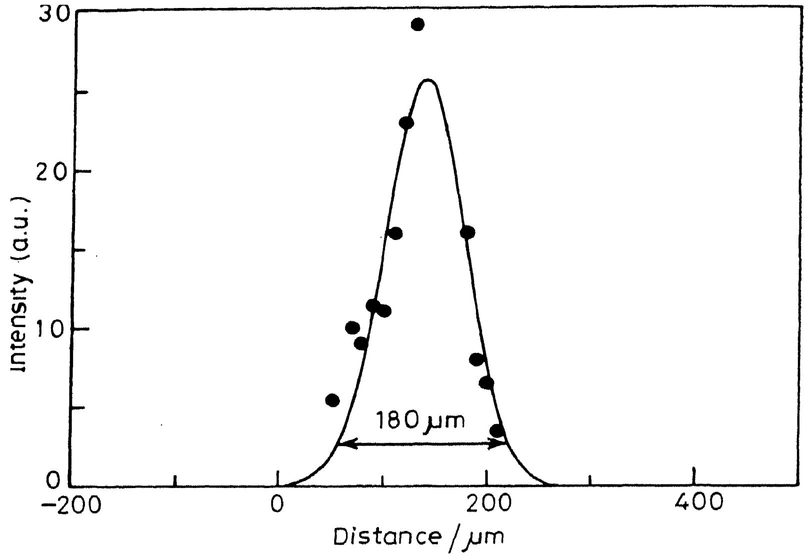

Fig. 12 Spatial beam profile of FEL pulse at a focal point obtained by focussing with 50 mm focal length lens. Relative intensities have been measured using a pin-hole with a diameter of 50 μm. The beam size of 180 μm refers to the 1/ e^2 point of the intensity

from a beam cross section of π (90 μm)^2. We tentatively assume that the length of the photolysis volume along the beam is 2 × 180 μm × (focal length / beam diameter) = 500 μm and therefore the photolysis volume is π (90 μm)^2 × 500 μm = 1.3 $\times 10^{-5}$ cm^3. The fluence is regarded as being constant and homogeneous inside the volume. The fluence of 16 J cm^{-2} at 9.3μm coressponds to 7.4 $\times 10^{20}$ photon cm^{-2}. If the average cross section of multiple photon absorption is less than the cross section of usual absorption by one order of magnitude, i e , 2 $\times 10^{-19}$ cm^2 , each CF_2HBr molecule in the fluence region of 16 J cm^{-2} can absorb 150 laser photons during a macropulse. Since 12-CF_2HBr molecules, the percentage of which is 98.9%, resonate with laser photons at 9.3 μm, highly excited molecules are surrounded with other excited molecules. As a result subsequent collisions do not cause effective deactivation. On the assumption that all molecules in the photolysis volume decompose during a macropulse, the irradiation of 5 Torr CF_2HBr for one hour would cause IRMPD of 120 n mol of CF_2HBr and therefore yield 60 nmol C_2F_4. In the experiment, however, we obtained about 200 nmol C_2F_4, as shown in Fig. 11. This three-fold increase in yield suggests that many fresh molecules which flow into the photolysis volume during the macropulse (17 μs) also decompose. In other words, the yield is affected by inflow and outflow of CF_2HBr molecules inside the photolysis volume. The estimation of gas diffusion distance supports such additional decomposition of fresh molecules.

Since the CO_2 laser action corresponds to the induced emission between two vibrational levels, the width of the laser line is considerably narrower than the spread in FEL. The line usually has a width of 0 03 cm^{-1}, which is much smaller than 13-C isotope shift by a factor of 10^{-3}). Therefore one can expect better enrichment of 13-C compared to FEL irradiation. We attempted to compare selectivities in the IRMPD by the CO_2 laser to those obtained with FEL. The results are shown in Fig. 13 where 13-C atomic fraction in C_2F_4 is found to be as high as about 40 %, and much better than 6 % in FEL. Therefore, the isotope selectivity in FEL photolysis is much less than that in CO_2 laser case. The FEL laser pulse having the wavelength spread comparable to 13-C isotope shift apparently diminishes the isotope selectivity in the multiple photon excitation. In addition, the fluence employed in FEL is considerably higher than that in CO_2 laser. Normally, the isotope selectivity in IRMPD markedly decreases with increasing fluence. Therefore, the high fluence in FEL also contributes in lowering the process selectivity.

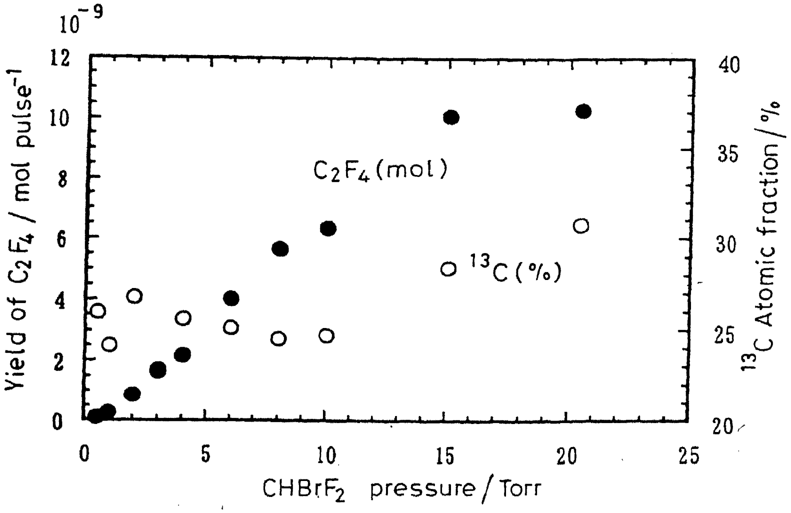

Fig. 13 Pressure dependence of C_2F_4 yield (solid circles) and 13-C selectivity (open circles) in IRMPD of CF_2HBr with 9P(22) line of TEA CO_2 laser at a fluence level of 4 J cm^{-2}

However, the volume illuminated with FEL pulses is so small that most of the molecules are likely to diffuse out before the total fluence reaches 16 J cm^{-2}. Therefore, the effective fluence, although unknown, may probably be lower than 16 J cm^{-2}. In the FEL irradiation of natural CF_2HBr with pulses at 9·7μm, 13- CF_2HBr molecules (1·1 %) are selectively excited, while 12- CF_2HBr molecules (98.9%) remain unexcited. However, collisional energy transfer produces moderately excited I2- CF_2HBr in the quasi-continuum region. Such moderately excited 12- CF_2HBr molecules are expected to contribute to IRMPD through their subsequent optical excitation and lowering the selectivity.

We have also investigated the FEL photochemistry of CF_2HCl and observed the formation of C_2F_4 in the irradiation of 5 Torr CF_2HCl at 9.3 μm. The yield was about a half of that in CF_2HBr case. However, it did not decompose at all in with FEL radiation at 9.6 and 9.7 μm. We failed to observe any meaningful isotope selectivity in IRMPD of this system even at 9.5 μm.

From the above studies, it is quite clear that FEL is an effective tool for investigation of wavelength effects in IRMPD. If isotope shifts are large enough compared to the wavelength spread in FEL, one will be able to observe isotope selective IRMPD, as demonstrated in the present study. A conventional laser, if available at the desired wavelength, can give a better selectivity in IRMPD. From this view point, FEL may not be economic for practical laser isotope separation. However, the observation of wavelength effects on IRMPD using an FEL provides most valuable information of selection of a working molecule and irradiation wavelength suitable for practical separation procedure. Such information can be utilized to promote development of high-power lasers necessary for practical isotope separation.

Several other isotopes have also been separated using FEL radiation[41]. The experiments todate have been carried out in the gas phase at pressures upto 10 Torr, at wavelengths in the vicinity of CH, CO and NO vibrational bands at 2950, 1760 and 1580 cm^{-1}. Significant isotope enrichments of 13-C, 15-N and 18-O have been accomplished in these experiments using Mark III FEL of Duke University, USA The following systems were studied:

I. C_2H_5Cl, $CHClF_2$: with (C-H) excitation at 3 μm; $C_2H_5Cl \rightarrow C_2H_4 + HCl$ ... 8)

$CHClF_2 \rightarrow :CF_2 + HCl$ ... (9)

II. HCOOH : with (C-H) excitation at 3 μm and (C=O) excitation at 5.5 μm

$HCOOH \rightarrow CO + H_2O$ ... (10)

Isotope selective MPD : 13-C / 12-C; 18-O / 16-O

III. CH_3NO_2 : with (C-H) excitation at 3 μm
and (N=O) excitation at 6.2 μm
Isotope selective MPD : 15-N / 14-N

The interesting aspect of spectral dependence of MPD yield and MPD action spectra and excitation of different vibrations in the same molecule could be studied using the versatile FEL pulses. Normally, the action spectrum is shifted towards the long wavelength region relative to ground state spectrum (known as "red shift"). This "red shift" has been interpreted as arising from the anharmonicity of the pumped mode. High fluence absorption involves excitation up several rungs of the anharmonic ladder with the resonant frequency quickly becoming mismatched. A somewhat lower frequency that matches an intermediate transition, rather than v = 1← 0 (low fluence absorption spectrum), is optimum because it averages the mismatch over many levels. For example, a 70 cm^{-1} "red shift" was observed for the MPD of CF_2HCl molecules irradiated in the region of the C-H stretch vibrational band. While for the C_2H_5Cl molecule excited in the vicinity of the C-H vibrational band, the red shift was very small. Such large shifts are characteristic for the MPD of molecules containing one C-H bond, the vibration of which is weakly anharmonically coupled with the other normal vibrations of the molecule.

A large red shift of 70 cm^{-1} was also observed for the MPD of formic acid molecules irradiated in C-H stretch vibration (3 μm), while C=O vibration (6 μm) excitation leads to a small red shift of about 10 cm^{-1}. The fluence requirement to affect similar yield is one order of magnitude higher in case of C-H excitation. These differences could be attributed to the smaller absorption cross section and significant anharmonicity of the C-H stretch vibrational band.

Nitrogen isotope selective IRMPD has been performed by irradiation of naturally abundant (0.4 % 15-N) nitromethane molecules. The molecules were excited in the region of the N=O stretch vibrational band. This band has strong absorption and also displays about 30 cm^{-1} isotope shift. The MPD yield was 2 to 6% when 0.25 to 6 Torr nitromethane was irradiated for about 10 to 30 minutes. Two decomposition channels are likely to be operative under the irradiation condition:

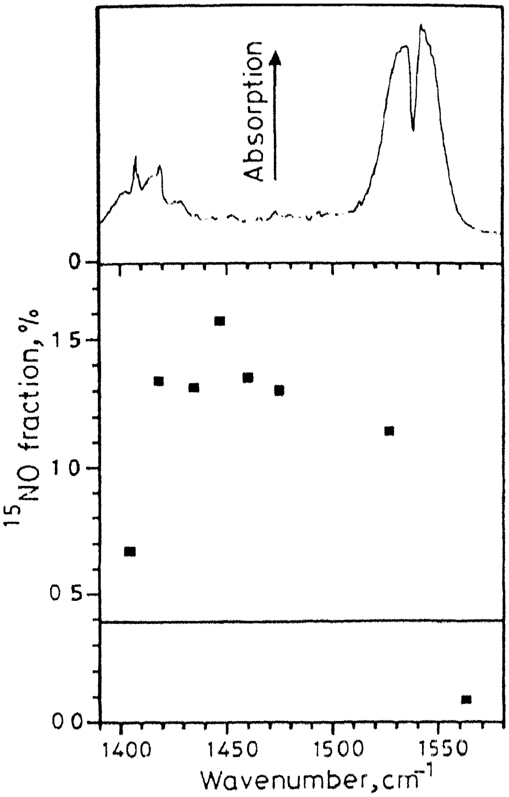

Fig. 14 Enrichment in 15-N isotope achieved (lower square points) in irradiation of 1 Torr nitromethane as a function of FEL wavelength. The solid line represents natural abundance of 15-N isotope. Also shown is the IR absorption specrum of Nitromethane (upper trace)

dissociation : $CH_3NO_2 \rightarrow CH_3 + NO_2$ ...(11)

and isomerization : $CH_3NO_2 \rightarrow CH_3ONO$ ...(12)

followed by dissociation of vibrationally excited product

$CH_3ONO^* \rightarrow CH_3O + NO$ ...(13)

The main products were identified to be CH_3ONO and NO indicating that the isomerization with subsequent dissociation is the most probable route. Istope selectivity was determined from the mass spectral measurements on isotopic composition of NO. Fig. 14 shows the variation of 15-NO fraction as a function of FEL wavelength along with the IR absorption band of nitromethane in the same spectral region. A four-fold increase or decrease in the 15-N content can be obtained depending on the FEL frequency.

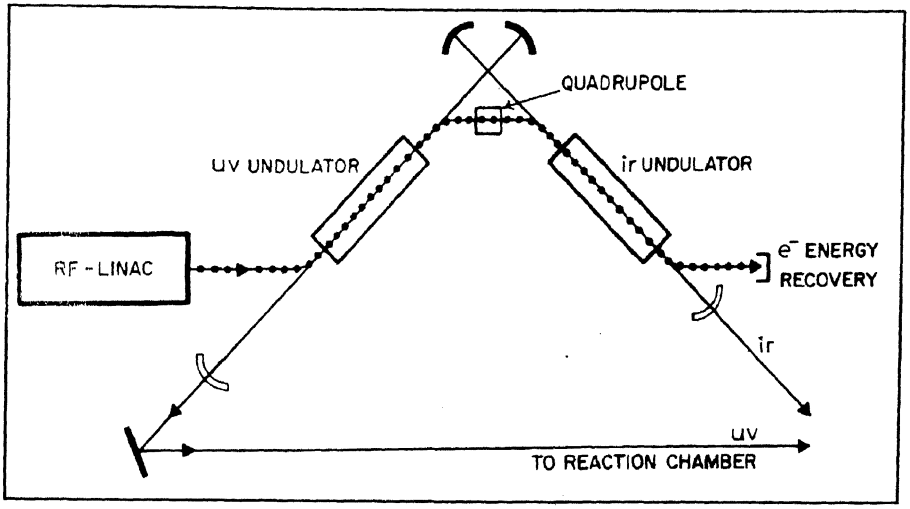

Fig. 15 Two colour (IR + UV) FEL irradiation scheme for molecular laser isotope separation (adopted from [7]). Such scheme can also be useful in multiple frequency IR irradiation to enhance the process yield and selectivity

It can be mentioned here that the above investigations were carried out mostly with a high-power single frequency laser. Application of two (or multiple) frequency fields essentially widens the scope of IRMPD. Two-frequency irradiation, for example, allows using rather low power tunable lasers at the first step which will provide the required high spectral selectivity of excitation. At the second step it is possible to use more powerful lasers which can be tuned to the red shifted excited state spectrum for efficient dissociation. Such multiple frequency in IRMPD has been utilized for highly efficient selective processes for several isotopes[33,34,42]. Apart from this, as has been mentioned in sec. 5.1.2, certain system requires two different colour photons in IR + UV scheme of LIS[9]. In such situations, FEL offers yet another advantage as shown in Fig. 15. The two colour photons can be delivered in required time synchronization by supplying electrons from the same accelerator to two appropriately designed wigglers in sequence. Since the accelerator represents most of the capital and operating costs of the FEL system, the second colour photons are very inexpensive. Thus the net production cost per mole of the product can be substantially reduced.

5.2 FEL Spectroscopy and Dynamics

5.2.1 IR spectroscopy

Traditionally, molecular vibrational spectroscopy is studied by analyzing the amount of light absorbed as a function of IR frequency after passing through either a solid, liquid or gas phase sample. A serious limitation of this approach is its inherent low sensitivity and its lack of selectivity. In a mixture of compounds or in an impure sample, it is not quite obvious which constituent is responsible for the observed absorption. In the UV and visible regions, well established techniques exist such as Resonance Enhanced MultiPhoton Ionization (REMPI) and Laser Induced Fluorescence (LIF) which combine a high sensitivity with species selectivity. Some multiphoton ionization and fluorescence studies where one photon is in the IR do exist. In addition, it has been shown that by combining the technique of stimulated Raman spectroscopy with resonant laser ionization, the sensitivity can considerably be improved. To obtain information similar to that obtained in direct absorption spectroscopy, a widely tunable IR excitation source as well as a detection method is needed.

In two complimentary experiments mass selective gas phase IR spectroscopy was demonstrated using pulsed high power FEL radiation from "Free Electron Laser for Infrared experiments" (FELIX) in Nieuwegein, The Netherlands[43]. In the first experiment, para amino benzoic acid (PABA) is first excited by FEL and then ionised by a VUV excimer laser operating on

F_2 at 158 nm[44]. PABA is an elegant system where the ionisation potential is about 1000 cm^{-1} above the F_2 laser photon energy, thereby enabling selective ionization of IR excited levels. In the second experiment, gas phase C_{60} molecules are resonantly excited by FELIX to very high internal energies by absorption of several hundred IR photons per molecule where it undergoes auto-ionization without the need for VUV photon[45]. In both experiments, scanning the IR laser and recording the mass-selected ion yield as a function of IR frequency, results in an "action spectrum" that closely resembles the gas phase absorption of the sample. In both experiments, the density of neutral molecules is very low and spectra can be recorded with sensitivities that are many orders of magnitude higher than in conventional absorption spectroscopy.

The FELIX produces pulsed IR radiation that is continuously tunable over 100 - 2000 cm^{-1} range with a bandwidth that can be varied from 0.5 to 5% of the central frequency. The output consists of macropulse of about 5μs duration containing typically 50 mJ of energy. Each macropulse consists of a train of micropulses which are about 1 ns apart. In the present experiments, the micropulses have a FWHM of approximately 10 optical cycles i.e. , a pulse duration of 300 fs at 10μm. The experimental apparatus consists of a turbo-pumped vacuum chamber containing a TOF mass spectrometer (Fig. 16). In the IR / VUV double resonance experiment, extremely small amount (1×10^7 Torr) of PABA was irradiated with parallel but counter propagating FEL pulses and 1 μs delayed excimer laser beam (0.1 - 1 mJ) in the extraction region of the linear TOF setup. While in the IR - REMPI experiment, an effusive molecular beam of C_{60} (number density of about 10^{10} molecules cm^{-3}) from a quartz oven (T=875 K) was irradiated with a focussed FEL beam. The beam waist varied from about 60 to 200 μm in scanning the FELIX from 6 to 20 μm, yielding maximum power densities of 1×10^{12} to 3×10^{10} W cm^{-2} per micropulse respectively. The gas phase absorption spectrum of PABA taken at 444 K matched very well with the double resonance spectrum in terms

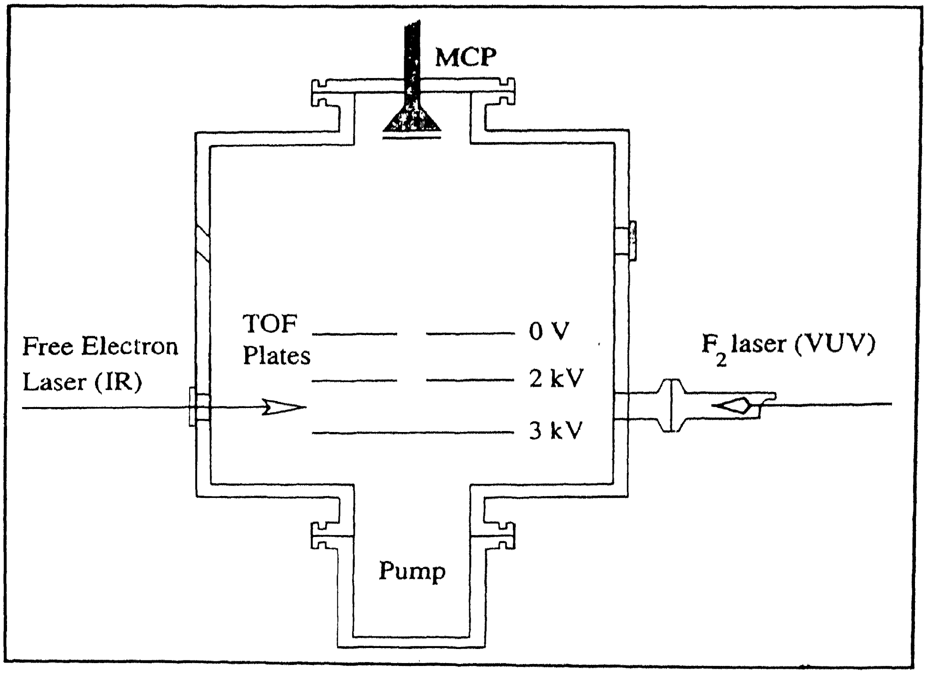

Fig. 16 Schematic of the TOF apparatus used for IR spectroscopy. Molecules are ionized between the lower two TOF plates In the case of IR / VUV double resonance experiments on PABA, unfocussed IR and VUV laser beams are used while focussed IR laser beam only is used in IR REMPI experiments on fullerene

of number of peaks, peak width and relative intensity except with a small average shift in peak position to lower frequency of about 11 cm^{-1}.

Fig. 17 shows the TOF mass spectrum (C_{60}^+ and C_{58}^+) obtained when C_{60} being ionized wth the focussed FELIX beam at 19.2 μm. The small amount of C_{58}^+ recorded is rather surprising, since, in MPI studies of C_{60} with UV and visible laser, large amounts of fragmentation are reported[46]. In fact even more surprising is the observation of C_{60}^+, since for C_{60} to thermally ionize, an internal energy of 35 - 40 eV is required, which means 600 photons to be absorbed at 19.2 μm The C_{60}^+ ion yield was measured as a function of FELIX frequency and the resulting spectrum is shown in Fig. 18 along with the IR absorption spectrum of a thin film of solid for C_{60} sample. The observed four peaks correspond to the four well known IR allowed F_{1u} fundamental modes of icosahedral C_{60}[47]. The two spectra show a clear matching in their line positions as well as in their relative intensities. The observation that so many IR photons are absorbed by the molecule can be explained on the basis of Intramolecular. Vibrational energy Redistribution (IVR)[10]. For a large molecule like this, IVR is expected to be occurring on a sub-nanosecond time scale. Therefore, the molecule can absorb one photon from the micropulse and by the time next pulse arrives after 1 ns, the energy of the previous pulse is completely randomised in the molecule. With 174 internal degrees of freedom and an average vibrational frequency of 950 cm^{-1}, on average less than two quanta are needed to be deposited in each vibrational mode of C_{60} to reach the necessary energy of 35 - 40 eV. Hence, by sequential absorption of IR photons, accompanied by thermalization via IVR, the C_{60} molecule can be resonantly heated upto energies at which ionization becomes efficient.

These elegant excitation and ionization schemes demonstrated that IR spectra of gas phase molecule could be obtained by this highly sensitive and species selective technique and such procedure can comfortably be adopted for many more systems.

5.2.2 Photodynamic Processes

The excellent properties of FEL can be exploited to induce some biological level interaction between photons and living tissues. The average power of the FEL is sufficient for most of thermal coagulation therapy and photodynamic therapy (PDT) which is a light activated chemotherapy for cancer and other indications[48,49]. In advanced

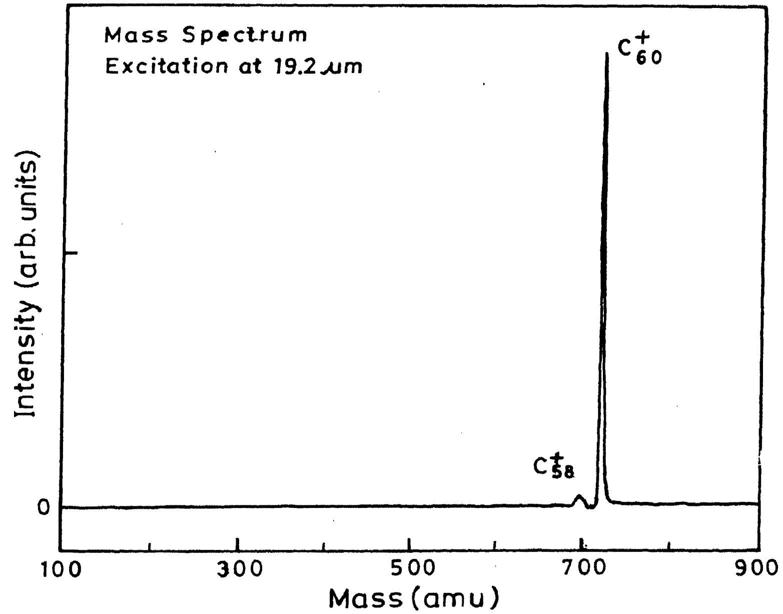

Fig. 17 TOF spectrum, recorded with FELIX on the C_{60} resonance at 19.2 µm, following resonant absorption of about 600 photons. The only fragment observed is due to C_2 loss

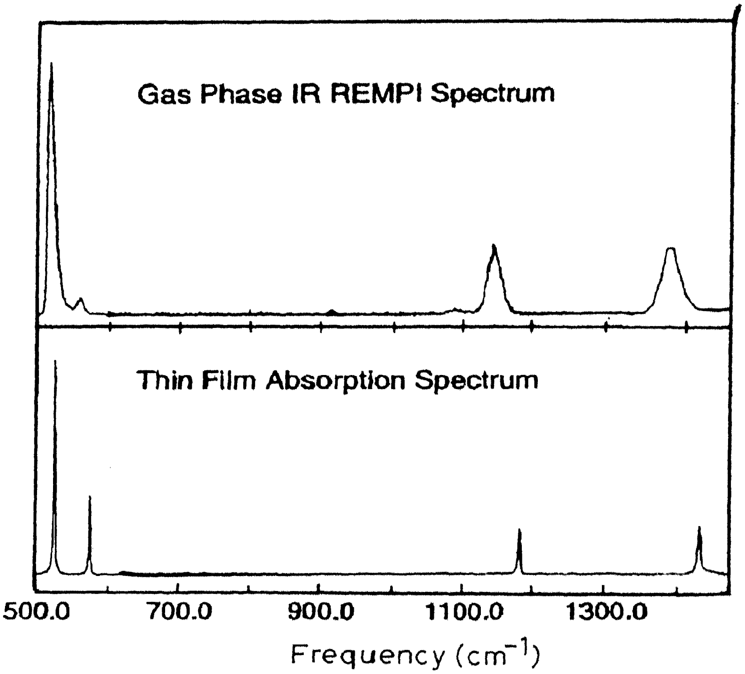

Fig. 18 IR REMPI spectrum of gas phase C_{60} effusing from an oven at 875 K (upper trace) and IR absorption spectrum of a thin film of solid C_{60} at room temperature (lower trace). Four IR allowed absorption features can be seen in both the spectra

atherom atherosclerosis, a large amount of lipids, particularly choleserol esters, accumulates on the arterial wall In more advanced cases, the lipids also accumulate in the interstitial spaces. Therefore, the PDT is being applied as a less invasive method for effective removal of cholesteryl ester from atheroma using mono-L-aspartyl chlorin e6 (Npe6) as a photoresponsive material and a diode laser at 664 nm as an excitation source[50]. Recently an IRFEL was employed tuned to 5.75μm corresponding to the stretching vibrations of ester bonds to remove by direct dissociation of cholesteryl oleate (hereafter designated as {CO}). Very interesting results were obtained for wavelength sensitive removal process and such photodynamic processes are of great importance for biomedical applications[51].

The model compound cholesteryl oleate ($C_{45}H_{78}O_2$) in which the cholesterol ($C_{27}H_{46}O$) and oleate ($C_{18}H_{34}O_2$) are connected to each other through ester bonds (R-COO-R') was investigated to understand the photodynamical process for actual atheroma. The chemical changes in the oleate as a function of exposure time were examined by Raman spectroscopy and FTIR micro-spectroscopy upon FEL irradiation. Samples of {CO} were prepared as a film on BaF_2 substrate for FEL exposure, FTIR and Raman spectra measurements. The sample was irradiated at 5.79 μm with focussed beam (about 500 μm radius) of 3 mW FEL for various exposure times of 10, 60 and 300 sec. The time evolution of the process is shown in Fig. 19. It was found that not only the ester bond decomposed but also it transformed into aldehyde (RCHO), carboxylic acid (RCOOH), carboxylate (RCOO-) or ketone (RCOR') which can be seen from the FTIR spectrum. The mechanistic aspect of the process is schematically shown in Fig. 20. The R-C-O-R' bonds, which are parts of ester bonds (RCOOR') and connect between oleate (R) and cholesterol (R') molecules, respectively dissociate into (a) carboxylate : $RCOO^- + -R'$ and (b) RCO- + -OR' as shown in routes (a) and (b). The dissociated ($RCOO^-$ + -R') bonds are oxidized to carboxylic acid (RCOOH) with ketone (RCOR) as shown in step (c), and the dissociated (RCO- + -OR') bonds are hydrogenated and /or oxidized to both aldehyde (RCHO) with ketone (RCOR) and carboxylate ($RCOO^-$) with ketone (RCOR) as shown in steps (d) and (e). The origin of oxidation

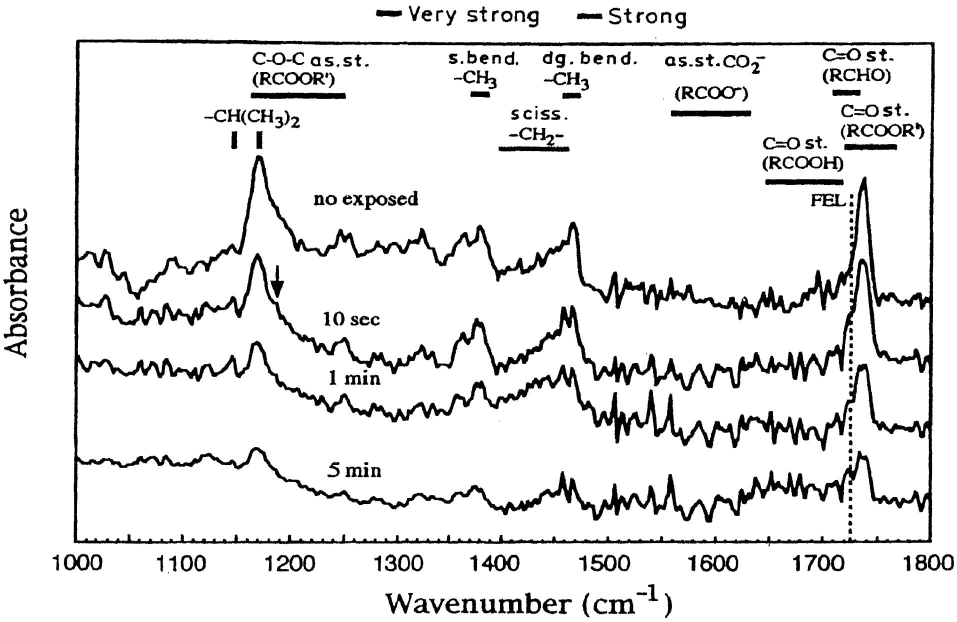

Fig. 19 Time evolution of photodynamic process of irradiation of cholesteryl oleate with a focussed 5.79 μm FEL beam

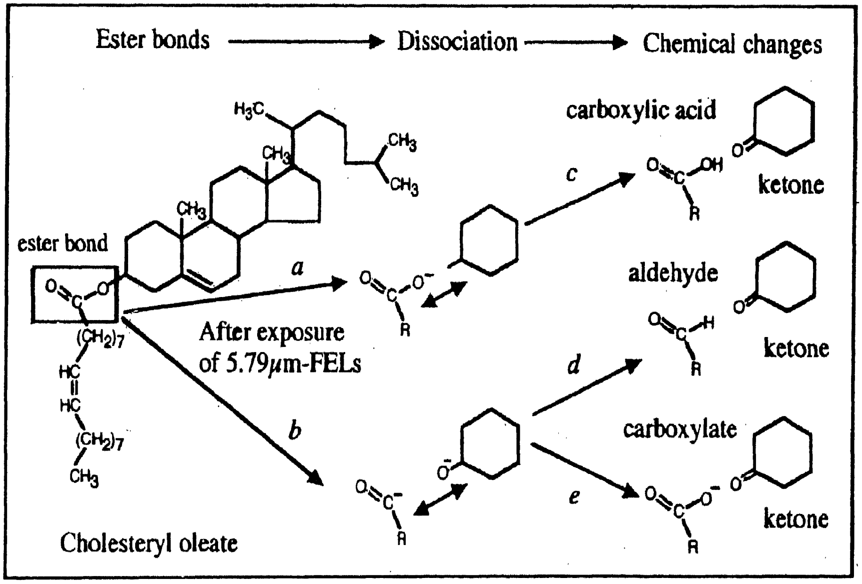

Fig. 20 Mechanistic illustration of photodynamic process in irradiation of cholesteryl oleate, {CO}

of the ester bonds has not yet been understood. It has been speculated that active oxygen or radical hydrogen can be generated through some photochemical reactions induced by strong excitation of the FEL. One of them could be IR photochemical dissociation of water due to excitation of bending vibrations of H-O-H (1640 cm^{-1}) by the 5.79 μm FEL.

The thermal effect of FEL radiation was considered by estimating the maximum temperature of {CO} during various exposure times T$_{max}$ obtained were 27-30°C for 10s, 58-60°C for 60s and 380-400°C for 300s. When these values were compared with melting and boiling point of {CO} of 149 and 360°C, one can expect ablation or evaporation of the films, although only melting of the films were observed. This shows that the actual temperature is lower than the estimated one due to the thermal conduction.

5.2.3 Photon Echo Experiments

Vibrational excitations and vibrational energy transfer within a molecule or among adjacent molecules play important role in all chemical processes in condensed phases and in the gas phase. Broadly there are four important categories, namely, (1) vibrational relaxation (2) vibrational cooling (3) vibrational dephasing and (4) the relationship between vibrational relaxation and chemical reaction dynamics. Vibrational relaxation involves loss of excess energy to the surrounding bath in condensed phases and by collisions in the gas phase from an initially prepared excited state, which can be characterized by T_1. Large molecules have many different vibrational levels, thus excitation of a high frequency vibration usually results in a series of relaxation steps, known as cascade, before all the initial excess energy is dissipated in a process called vibrational cooling. Understanding such cooling requires a knowledge of the rate of energy loss from the initial state and the rate parameters for all intermediate states. Vibrational dephasing involves the loss of phase coherence of the excited state which occurs via the interaction of the initial state and a bath consisting of other, isoenergetic states in isolated molecules. In condensed phases, dephasing occurs via T_1 processes or via pure dephasing caused by stochastic interactions with the bath. Coherence loss may be investigated by a variety of optical coherence measurements including free-induction decay or photon echo.

The echo method originally developed as the spin echo in NMR was extended to optical frequencies for probing the electronic excited state dynamics in many condensed matter systems[52]. The vibrational echo (VE) experiments permit the use of optical coherence methods to study the dynamics of the mechanical degrees of freedom of condensed phase system from low (<3K) to high (>300K) temperatures. The VE measures the homogeneous vibrational linewidth even if the absorption line is heavily inhomogeneously broadened. When combined with pump-probe (transient absorption) experiments, the homogeneous pure dephasing (energy level fluctuations) is obtained. Conducting these experiments as a function of temperature provides information on dynamics and inter molecular interactions. Further, VE probe dynamics on the ground state potential surface only. Therefore, the excitation of the mode causes a minimal perturbation of the solvent. Recently VE has been applied to wide variety of systems like liquids, glasses and proteins[53].

Using VE experiments to measure the homogeneous dephasing time (T_2) and IR pump-probe experiments to measure the vibrational lifetime (T_1), the homogeneous pure dephasing time (T_2^*) can be obtained. Pure dephasing arises from the energy level fluctuations caused by the ultrafast intra and inter molecular perturbations. Thus by using non-linear vibrational experiments in the time domain, it is possible to determine the homogeneous spectrum and all dynamical contributions to it. VE experiments generally yield decay curves of the form : $I(\tau) = I_0 \exp(-4\tau / T_2)$ where T_2 is the homogeneous dephasing time The homogeneous linewidth (Γ) is composed of both pure dephasing (T_2^*) and vibrational lifetime (T_1) components:

$$\Gamma = 1 / \pi T_2 = 1 / \pi T_2^* + 1 / 2\pi T_1 \qquad \ldots(14)$$

Here we will discuss VE studies on HITCI, an ionic cyanine dye, doped poly methyl methacrylate (PMMA)[54]. A block diagram of the VE apparatus is shown in Fig. 21. The beam from the SCA / FEL (superconducting accelerator pumped FEL at Stanford University) is converted to its second harmonic at the experimental wavelength of 0.776 μm, at the red edge of the S_0 - S_1 absorption band of HITCI, in a 20 mm thick $LiIO_3$ crystal (the conversion efficiency was 25%). The intensity fluctuation of 10% gets doubled on frequency doubling. However, this could be reduced to about ± 1% over a time period of hours by providing an error signal to an acusto-optic modulator (AOM) to stabilize the intensity. A second AOM was used to select single micropulse (repetition rate 11.8 MHz) with a rise time of 20 *n*s. The dependence of the echo decay on pulse repetition rate was carefully studied to avoid any thermal heating. A He-Ne laser was made collinear with the FEL output after the second AOM using a dichroic

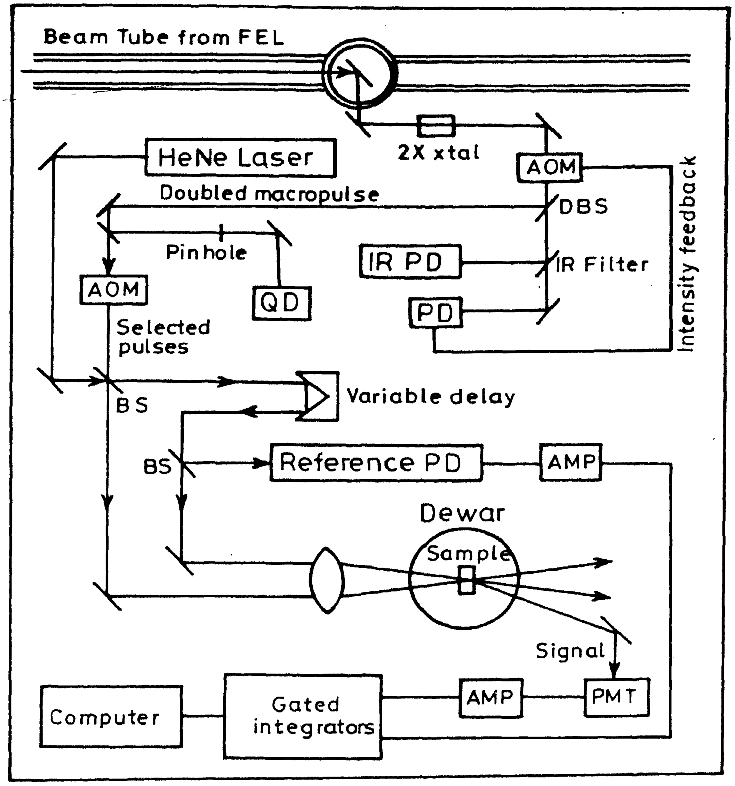

Fig. 21 Block diagram of experimental apparatus for vibrational echo studies using the second harmonic radiation from the SCA / FEL. One acusto-optic modulator (AOM) is used to stabilize the intensity to 1% while a second AOM selects a single micropulse out of the macropulse. The quad detector QD is used to reproducibly realign the FEL beam, PD is photo-diode, BS is beam splitter, PMT is photomultiplier tube and AMP refers to operational amplifier

beam splitter. This helped in aligning the major part of the apparatus in the absence of the FEL beam. The remainder of the setup produces a fixed and a variable delay pulse, which are focussed on the sample (1 cm diameter and 1 mm long) in a variable temperature He cryostat. The two pulses are crossed in the sample at a small angle and focussed to about 100 μm. Because of wave-vector matching conditions, the photon echo signal pulse propagates in a unique direction so that it can be isolated by a spatial filter. Finally the echo detection is accomplished by a photomultiplier, a gated intregator and a computer.

An experimentally determined echo decay curve at 1.5 K is shown in Fig 22. The fast decay near $\tau =$ 0 arises from the broad phonon side band, whereas the experimental decay with time constant 284 ps reflects the optical dephasing of the zero-phonon line of interest. Temperature dependent decays obtained at several temperatures between 1.5 and 10K revealed that in the intermediate temperature regime, optical dephasing was caused by thermal excitation of 20 cm^{-1} mode of the polymer matrix. This observation was found to be similar in studies with ionic xanthine dye, Rhodamine B (RB). Considering the differences in structure of HITCI and RB, it was inferred that this mode is intrinsic to the PMMA polymer itself, rather than arising as a consequence of impurity perturbations.

This elegant VE technique can be applied to biological systems to extract many interesting informations, for example, by examining the ultrafast dynamics of myoglobin and myoglobin mutants[55]. The dynamics of the CO ligand bound at the active site of the protein myoglobin are evaluated and compared with that in myoglobin mutants. The results provide insights into protein dynamics and how protein structural fluctuations

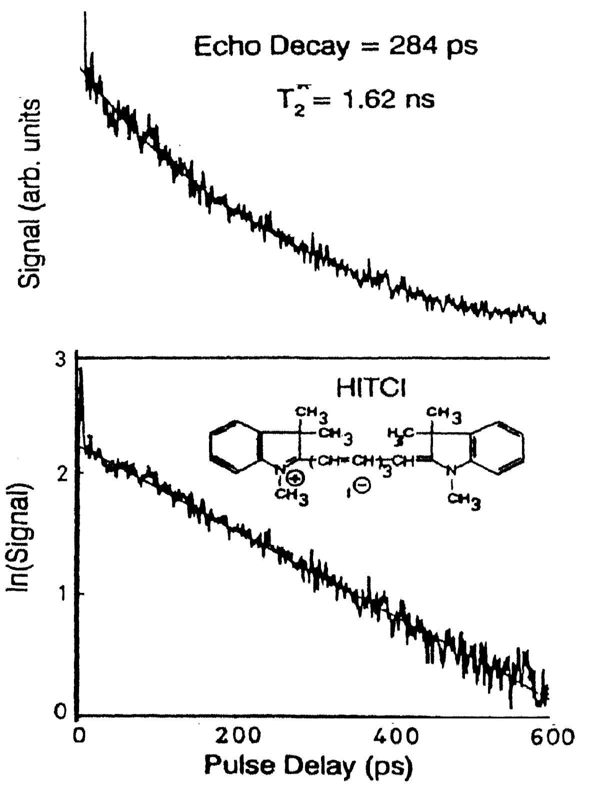

Fig. 22 Picosecond vibrational echo decay curve for HITCI dye embedded in an amorphous polymeric glass at 1.5 K. The decay is exponential and the decay constant of 284 ps yields a value for the pure dephasing time of 1.6 ns

are communicated to a ligand bound at the active site.

Myoglobin, a small 153 amino acid protein has the primary biological function of the reversible binding and transport of oxygen in muscle tissues. Myoglobin's ability to bind oxygen and other biologically relevant ligands, such as CO or NO, is due to a non-peptide prosthetic group, heme, which is covalently bound at the proximal histidine of the globin. The interior of the protein consists almost entirely of non-polar amino acids while the exterior part of the protein contains both polar and non-polar residues. The only internal polar amino acids are two histidines, the proximal one is covalently bonded to the Fe forming the fifth coordination site of the heme. The sixth coordinate site of the heme is the active site of the protein where the ligand binds. The distal histidine is physically near the sixth coordination site but not directly bonded to it. When bound to Mb, the CO vibrational frequency is substantially red shifted from the gas phase frequency and separated into several distinct bands, labeled A_0, A_1 and A_3 in order of decreasing carbonyl frequency. These three bands, which appear around 1969, 1945 and 1930 cm^{-1} , reflect distinct conformational substrates.

VE and lifetime measurements have been made on CO bound to the active site of native Mb and two myoglobin mutants, H64V and H93G(N-Melm). The temperature dependence studies show that the pure dephasing of H64V is 21 ± 3% slower than native Mb while it is same in case with H93G(N-Melm). A model was proposed[56] to explain this behaviour where it states that protein molecules produce fluctuating electric fields which are responsible for the pure dephasing of CO. Replacing the polar distal histidine with the non-polar valine removes one source of the fluctuating electric fields, thus reducing the coupling between the protein fluctuations and the measured pure dephasing. The fact that emerges is that the heme acts as an antenna that receives and then communicates protein fluctuations to the vibration of the CO ligand bound at the active site. VE data obtained on H93G(N-Melm) in which the covalent linkage between heme-CO and the protein is broken, show temperature dependence of vibrational pure dephasing is identical to native Mb. These studies demonstrate that local mechanical motions of the proximal histidine which directly couple the Fe are not responsible for vibrational pure dephasing of CO bound at the active site of myoglobin.

The photon echo experiments demand stringent requirement for the optical source[54]. In the small flip angle limit, an echo signal depends on the cube of the intensity and therefore, in experiment utilizing second harmonic frequency, the actual signal is dependent on sixth power of the FEL intensity. Furthermore, the stability of the doubled light depends not only on the amplitude stability of the FEL, but also on the pointing stability, the frequency stability and the pulse duration stability. These experiments provide excellent examples of the state of the art FEL investigations whereas similarly complex experiments are difficult even with conventional laser.

5.2.4 Adsorbate vibrational spectroscopy

The use of IR FEL allows adsorbate vibrational spectroscopy by IR-visible sum-frequency generation (SFG) beyond the frequency range accessible by benchtop IR lasers. Application of this technique is hindered by the narrow tunability range of benchtop picosecond IR lasers those, at present, do not produce optical pulses at wavelengths exceeding about 4 μm for the commercially available systems and about 10 μm for a very few laboratory-made sources. SFG relies on the second-order non-linear surface polarizability and depends directly on the overlapping IR and visible laser pulse energy and inversely with the pulse duration and irradiated area. Therefore, SFG is favoured at short pulse duration. Picosecond pulse is indeed the good compromise between high SFG yield and loss of spectral resolution due to the Fourier transform of short pulse. SFG is resonantly enhanced when the IR laser is tuned in resonance with an adsorbate vibration that is both IR and Raman active.

The feasibility of this technique is demonstrated by recording the SFG vibrational spectrum near 5μm of the CO adsorbate on a Pt surface resulting either from direct CO adsorption from an electrolyte saturated with CO or from electrochemical decomposition of methanol on Pt / $HClO_4$[57]. This system is of particular interest to the prospect of fuel cell development.

The apparatus consists of a synchronized and frequency doubled mode locked YAG laser with the CLIO-FEL, which is tunable from 2 to 17.5 μm. During SFG spectroscopy , the green (532 nm, 200 ps, 100mW) and IR FEL beam are focussed on the sample with an angle of about 55° and 65° to the surface normal. The SFG beam is spectrally filtered through a monochromator from the green light before detection by a photomultiplier. The Pt electrode cleanliness and CO adlayer formation is controlled by voltammogram measurements[58].

The SFG spectrum of CO/Pt interface following the adsorption of CO from the CO saturated electrolyte showed a sharp resonance at about 2030 cm^{-1} which corresponds to linearly bound CO. Fitting the spectra with the established SFG model, indicated the presence of an additional weak and broad peak centered around 1950 cm^{-1} which probably due to doubly-bounded CO. However, the SFG spectrum of CO from the methanol dissociative adsorption on the Pt electrode showed clearly two resonances at 2053 and 1977 cm^{-1} with a damping value of 22 and 136 cm^{-1} respectively. Comparing with literature data, it appears that linearly and doubly-bounded species coexist in the system. Actually, the vibration strength of the SFG resonance at 1977 cm^{-1} is found to be three times higher than at 2053 cm^{-1} resonance in contrast to the previous studies where the multibounded species was barely detectable.

5.3 Future Industrial Applications

The attractive features associated with FEL do not come without disadvantages. The single, most important disadvantage of FEL is their high cost. Electron accelerators are expensive, costing more than a million dollars even for a small one, so free-electron lasers don't lend themselves to small devices. On the other hand, in very large sizes the unit cost of laser power becomes quite competitive and it is hoped that, some day, FELs of 100 kW and larger at unit costs of less than $500 per watt will be available. Meanwhile, applications will be limited to those specialized areas which can bear the high cost.

One of the most promising opportunity for FEL is micro-fabrication of semiconductor circuits. In the conventional process, the circuit is imaged from a mask onto the surface of a silicon chip covered with a thin layer of SiO_2 and a layer of photoresist. When the photoresist is exposed to light it is either hardened or softened by the photochemical effect of the light and can be selectively removed by a chemical bath. Subsequently, the SiO_2 can be etched from the exposed areas, where the photoresist has been removed, to form the image of the microcircuit on the silicon chip. Presently, shorter wavelengths are being exploited to extend this technology to circuit features with dimensions smaller than one micrometer, and synchrotron radiation sources are being built for this purpose. In the future, however, these processes are likely to be replaced by new technologies which are just now emerging. For example, it is possible to use a scanning laser to print the pattern on the photoresist by direct writing, the way a laser prints the image in a computer laser printer. With sufficient laser intensity, the resist can be removed directly by the laser without the need for chemically developing the image[59]. In fact, with sufficiently high laser intensity, the SiO_2 layer can be removed directly by the laser. It is even possible to use an ultraviolet laser to initiate chemical reactions in a gas or liquid over the surface of the silicon chip to deposit the microcircuit on the chip[60]. By tuning the laser wavelength and / or varying the composition of the gas or liquid, it should be possible to construct various features of the microcircuit FELs in terms of high intensity and tunability at very short wavelengths are potential tools for this type of application.

The power and wavelength tunability of free-electron lasers make them intrinsically well suited to large-scale chemical processing. The issue is generally one of the cost of a laser photochemical process compared with the conventional process[61-63]. Laser photons are generally expensive ingredients. Capital and operating costs of lasers are relatively high in comparison to the cost of chemicals.

Figure 23 (a) relates the cost of laser photons to the selling price of chemicals and other substances to consider the economics of laser photochemistry

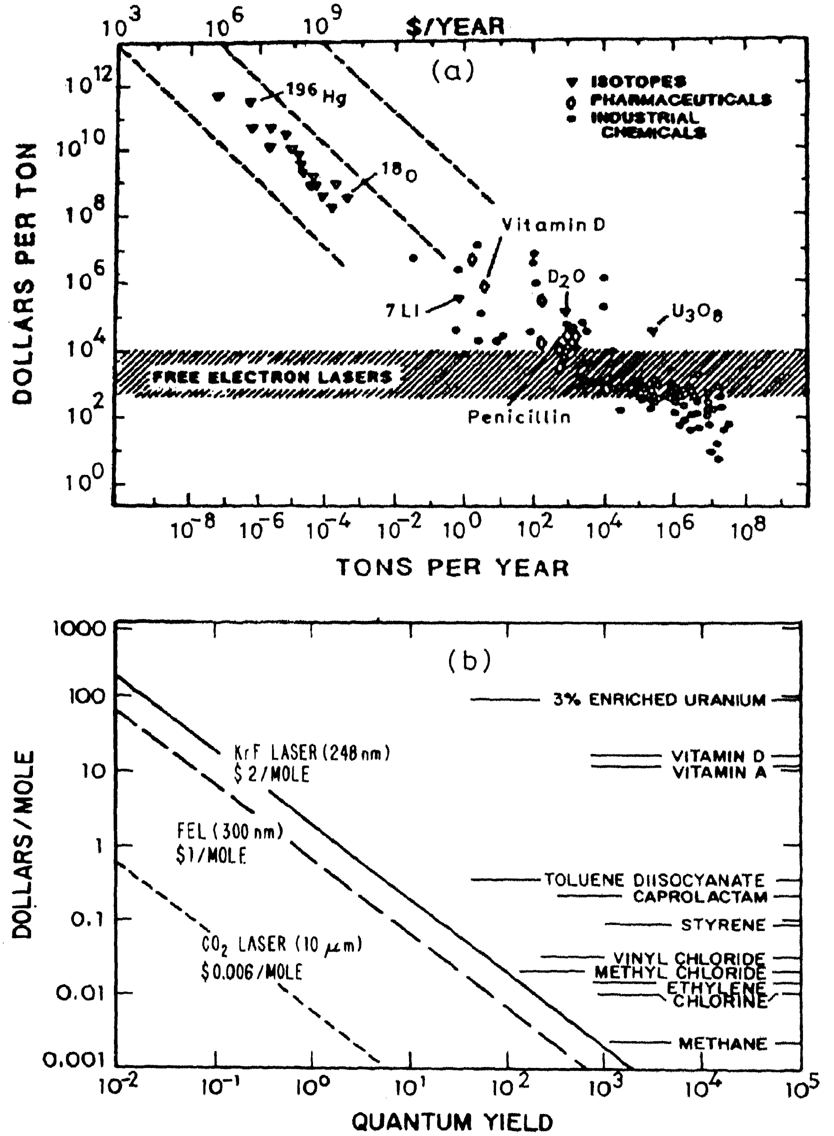

Fig. 23 Economics of laser photochemistry : (a) price-volume correlation for several classes of substances. The cost per ton of FEL laser photons (6.02 x 10^{27} photons) is indicated by the hatched horizontal bar, (b) price per mole of selected products is plotted against quantum yield. Costs of various laser photons are also shown (adapted from ref.[7])

where the annual sales volumes are also shown. FEL photon cost can be estimated by assuming that each photon (300 nm) generates a product with molecular weight 100 and the FEL device has a capital cost of between \$40 to 400 / W. This when amortized over 5 years (1 6 × 10^8 s), correspond to \$2 5 × 10^{-7} / J to 2 5 x 10^{-6} / J for the laser photons, ignoring the electricity and operating costs. The diagonal lines in the figure indicate the price - volume correlation and several conclusions can be drawn from the figure : (1) most bulk chemicals are too inexpensive to be produced using laser if short wavelengths are required (2) most isotopes, precious metals and pharmaceuticals are sufficiently expensive to make potential laser photochemistry viable and (3) if a yield multiplier (e.g., each photon has a quantum yield of 10 - 100) could be obtained, even some bulk chemical syntheses using laser might be economically attractive. Conclusion (2) should also be modified to consider realistic businesss : the present annual sales (P X V) are too small in the upper left hand corner of the figure to provide a business incentive Of course, the price -volume correlation suggests that new markets (and hence larger sales volumes) for these substances would emerge if their prices lowered.

Fig. 23 (b) shows similar information about the economics of laser photochemistry in terms of quantum yield[64]. The photon costs for three types of lasers are also projected on to the figure. It is clear from both the presentations that a wide variety of specialty chemicals and isotopes are, at least in principle economically accessible to photochemical production with FELs. However, to address the interesting chemicals in the lower right-hand corner of the chart such as styrene, vinyl chloride, phenol and ethylene, the process must be highly leveraged. This is especially true when it is recognized that for large-scale chemical processes the cost of the raw materials are typically 60 - 80% of the cost of the final product[61].

Two important processes have been identified in which such a large quantum yield is possible. In the first process, a laser is used to purify chemical compounds by removing a few impurity molecules from a large number of desired molecules. A good example is the purification of silane (SiH_4)[65]. High-purity silane is the starting material for the production of certain types of semiconductors and optical materials. Experiments with an excimer laser at 193 nm have demonstrated that this method produces extremely pure product material with high quantum yield.

A second class of photochemical processes having high quantum yield is that of laser-initiated chain reactions. In this case, a single photon is used to initiate a chain reaction which may yield thousands of molecules of product before the chain is broken. A good example of such a process is offered by the synthesis of vinyl chloride[66], which is the starting material for the production of polyvinyl chloride (PVC). In experiments with ultraviolet lasers the quantum yield has been observed to be as high as 20,000.

Nuclear engineering is another promising field for application of FELs[67]. The attractive features for this application are high power, widely tunable spectral range and quasi-cw operation. These features are of advantage for obtaining enriched fuel, reprocessing of spent nuclear fuel, synthesizing new strategic materials etc. The process of isotope separation and producing enriched uranium fuel have already been discussed. The reprocessing of spent nuclear fuel requires separation of the elements U and Pu from the noble metals Ru, Rh, Pd, other elements including Sr, Cs and long lived elements Am, Cm, Np etc. The quantity of Pu obtained is about 10 kg per one ton of PWR fuel producing power of 34000 MW per day. Handling of such highly radioactive stream by non-contact, remotely controlled lasers is extremely desirable. If a 3 eV photon (~400 nm) is utilized in reducing this Pu with a quantum efficiency of 0.5, then 1.5 × 10^{26} photons, would be required which corresponds to one day of operation of a laser with average power of 300 W. Considering this aspect, it is quite promising to employ a FEL for this application.

Nuclear reactor technology requires developing new materials with low neutron absorption cross-section. It is required not only to improve the neutron economy, but also to suppress the activation and disintegration of materials due to α-particle decay. The interesting materials with small neutron absorption cross sections are : 90-Zr, 50-Ti, 53-Cr, 56,57,58- Fe and 96,97-Mo. On the other hand, the isotopes 157-Gd and 155-Gd, which are added as a burnable poison in light water reactor fuel, have unusally large absorption cross sections for thermal neutrons. Depending on the isotope shift of the elements, any one of the two approaches namely. Atomic Vapour Laser Isotope Separation (AVLIS) or Molecular Laser Isotope Separation (MLIS) could be employed. Overall, it appears that versatile high power, tunable FELs from the UV to IR could be very useful for these processes.

Deviating from our main discussion, at the end, it can be mentioned that FELs are leading candidates for demanding and challenging opportunities in military applications. The ability of lasers to transport energy over long distances in almost no time makes them attractive for strategic defense against missiles. Using lasers, the missiles can be attacked when they are most vulnerable, in their boost phase. To do this, the laser may be sited on the ground, with mirrors in orbit to redirect the beam over the horizon to the target or the laser itself may be sited in orbit. Tremendous amounts of laser power, estimated to be as high as 10 GW will be required to defend against a large number of simultaneously launched missiles which could be delivered by the FELs operating at high power and short wavelength.

5 Conclusions

It is now almost 25 years since John Madey showed the world a new way to make light from electrons. Since then the physics of FELs has been extensively investigated. Although no one would claim that everything is understood, certainly a deep and broad knowledge base is available so that operating machines can be built.

A key milestone marking progress is that FELs have moved from the era of being built to study laser action to a time when user oriented lab facilities have been built in several locations worldwide; making it possible for scientists in other fields to use FEL photons for inquiry. Economic realities suggest that FEL applications be generally limited to cases where the FEL, provides a significant performance advantage over conventional laser systems. FEL users expect that the cost in time and money of travel to an FEL facility should be rewarded by data that cannot be obtained in the laboratory at home. Further, the FEL community has been effective enough in communicating the potential for further progress still as to convince the broader scientific community that the FEL really is the appropriate next step in user light sources to develop further, the so-called "Fourth Generation Light Source" of Birgeneau report[68].

Therefore, from this brief but extensive account of FEL photochemistry, it is apparent that significant advances in our fundamental knowledge of photon-molecule interaction and also in the technology of lasers have been made. The application of this new knowledge and technology to more general areas in chemical processing like selective chemical synthesis, purification, dynamics has a great future. It has been predicted that in the coming century, FELs will be widely introduced to high technology industries if compact and economical devices become available. Using beams with very high brightness, as much as five orders of magnitude beyond those in use today, it is possible to construct compact Cherenkov and Thompson FELs at wavelengths ranging from far infrared to the UV[69]. Opportunities in this field of study are enormous and lots of exciting questions are at hand and if they can be answered, selective chemistry with FELs might revolutionize the world of science.

6 Acknowledgements

The author is thankful to Prof S Arai for introducing him to the fascinating field of FEL photochemistry during his stay at Kyoto Institute of Technology, Japan. He also thanks his many colleagues in the FEL community upon whose work this article is written and apologize to those whose work could not be discussed. In addition, the author would like to put on record his special thanks to Dr J P Mittal, Dr D D Bhawalkar and Dr S K Sikka for their constant encouragements and Bhabha Atomic Research Centre for continuing support for the research activities.

References

(a) J M J Madey *J Appl Phys* **42** (1971) 1906
(b) L R Elias, W M Fairbank, J M J Madey, H A Schwettman and T I Smith *Phys Rev Lett* **36** (1976) 717
(c) D A G Deacon, L R Elias, J M J Madey, G J Ramian, H A Schwettman and T I Smith *Phys Rev Lett* **38** (1977) 892
T C Marshall *Free Electron Lasers* MacMillan New York (1985)

3 C A Brau *Free Electron Lasers* Academic Press New York (1990)
4 H P Freund and T M Antonsen Jr *Principles on Free Electron Laser Theory and Related Topics* World Scientific Singapore (1993)
5 *Free Electron Lasers and its Application in Asia* (Eds T Tomimasu, E Nishimura, T M Isuya and K Awazu Ionics Publishing Co Tokyo (1997)
6 K J Kim and A Sessler *Science* **250** (1990) 88
7 B E Newnam *SPIE* **461** (1984) 90
8 G P Gallerano *Nucl Instr & Meth Phy Res* **A 340** (1994) 11
9 V S Letokhov *Non-linear Laser Chemistry* Springer Berlin (1983)
10 V B Bagratashvili, V S Letokhov, A A Makarov and E A Ryabov *Multiple Photon Infrared Laser Photophysics ana Photochemistry*, Harwood Academic New York (1985)
11 D W Lupo and M Quack, *Chem* **87** (1987) 181
12 M Quack *Infrared Phys* **29** (1989) 441; M Quack *Infrared Phys* **36** (1995) 365
13 S K Sarkar, A K Nayak, V Parthasarathy, K V S Rama Rao and J P Mittal *Infrared Phys* **33** (1992) 493
14 S K Sarkar and J P Mittal *Lasers in Materials Science* (Ed.)R P Agarwala Trans Tech Publication Switzerland (1999) pp 46
15 W B Colson *Nucl Instr and Meth in Phy Res* **A 407** (1998) 26
16 J A Edighoffer, G K Neil, C E Hess, T I Smith, S W Fornaca and H A Schwettman *Phys Rev Lett* **52** (1984) 344
17 C A Brau *Laser Focus* **17** (1981) 48
18 C K N Patel *National Research Council Report* National Academy Press, Washington DC (1982)
19 C D Cantrell, S M Fraund and J L Lyman *Laser induced chemical reactions and isotope separation*, in Laser Handbook Vol 3 (Ed M L Stitch) North Holland Publishing Company (1979)
20 C B Moore and V S Letokhov *Chemical and Biochemical Application of Lasers* Vol 3 Ed C B Moore (Academic Press) New York (1977)
21 W W Duley *CO_2 Lasers, Effects and Applications* Academic Press New York, (1976)
22 M C Lin, M E Umstead and N Djeu *Ann Rev Phys Chem* **34** (1983) 557
23 D S Bethune and A C Luntz *Appl Phys* **B 40** (1986) 107
24 E Hirota and K Kawasushi *Ann Rev Phys Chem* **36** (1985) 53
25 J F Hershberger, S A Hewitt, S K Sarkar, G W Flynn and R E Weston Jr *J Chem Phys* **91** (1989) 4636
26 S K Sarkar, J P Mittal and G W Flynn *Proc Ind Acad Sci (Chem Sci)* **106** (1994) 1307
27 S K Sarkar, J P Mittal, K V S Rama Rao, A K Nath and U K Chatterjee *Ind J Phys* **54B** (1980) 311
28 S K Sarkar, V Parthasarathy, A Pandey, K V S Rama Rao and J P Mittal *Chem Phys Lett* **78** (1981) 479
29 V Parthasarathy, S K Sarkar, N V Iyer, K V S Rama Rao and J P Mittal *Appl Phys* **B56** (1993) 321
30 A Batra, S K Sarkar and V Parthasarathy *J Photochem Photobiol A : Chem* **83** (1994) 193
31 A Batra, R D'Cunha, M N Deo, V Parthasarathy and S K Sarkar *Spectrochim Acta* **51A** (1995) 71
32 V Parthasarathy, S K Sarkar, K V S Rama Rao and J P Mittal *Appl Phys* **B 39** (1986) 187
33 A K Nayak, R S Karve, S K Sarkar, K V S Rama Rao and J P Mittal *Appl Phys* **B49** (1989) 139
34 R S Karve, A K Nayak, S K Sarkar, K V S Rama Rao and J P Mittal *Appl Phys* **B49** (1989) 571
35 A K Nayak, S K Sarkar, D J Biswas, K V S Rama Rao and J P Mittal *Appl Phys* **B53** (1991) 246
36 V Parthasarathy, S Sethi, L M Gantayet, P Nilaya, D J Biswas, N V Iyer, K A Rao and S K Sarkar *J Photochem Photobiol A : Chem* **110** (1997) 11
37 V Parthasarathy, S Nad, K A Rao and S K Sarkar *J Photochem Photobiol A:Chem* **115** (1998) 1
38 B E Newnam, J W Early, J L Lyman *Nucl Instr and Meth in Phy Res* **A 341** (1994) 142
39 S Kuribayashi, T Tomimasu, S Kawaniski and S Arai *Appl Phys* **B 65** (1997) 393
40 S Arai, K Ikawa, Y Matsumoto, Y Iizuka, K Sugita, S K Sarkar and S Kuribayashi *Nucl Instr and Meth in Phys Res* **B 144** (1998) 193
41 A K Petrov, E N Chesnokov, S R Gorelik, Yu N Molin, K D Straub, E B Szarmes, J M J Madey *Nucl Instr and Meth in Phys Res* **B 144** (1998) 203
42 A V Evseev, V S Letokhov, A A Puretzky *Appl Phys* **B 36** (1986) 93
43 G von Helden, I Holleman, M Putter and G Meijer *Nucl Instr and Meth in Phys Res* **B 144** (1998) 211
44 M Putter, G von Helden and G Meijer *Chem Phys Lett* **258** (1996) 118
45 G von Helden, J Holleman, G M H Knippels, A F G Vander Meer and G Meijer *Phys Rev Lett* **79** (1997) 5234
46 P Wurz and K R Lykke *J Phys Chem* **96** (1992) 10129
47 D S Bethune, G Meijer, W C Tang, H J Rosen, W G Golden, H Seki, C A Brown and M S deVries *Chem Phys Lett* **179** (1991) 181
48 K Awazu, S L Jacques, *Proc of 12th International Symp On Analytical Biosciences* (1997) 92
49 J Bedwell, A J MacRobert, D Phillips and S G Bown *Br J Cancer* **65** (1993) 818
50 J Hayashi, T Saito and K Aizawa *Lasers Surg Med* **21** (1997) 287
51 Y Fukami, Y Maeda and K Awazu *Nucl Instr and Meth in Phys Res* **B 144** (1998) 229
52 D D Dlott *Nucl Instr and Meth in Phys Res* **A 318** (1992) 26
53 K D Rector, J R Engholm, J R Hill, D J Myers, R Hu, S G Boxer, D D Dlott and M D Fayer *J Phys Chem* **B102** (1998) 331
54 D D Dlott and M D Fayer *IEEE J Quantum Electron* **27** (1991) 2697
55 K D Rector and M D Fayer *Nucl Instr and Meth in Phys Res* **B144** (1998) 218
56 C W Rella, K D Rector, A S Kwok, J R Hill, H A Schwettman, D D Dlott and M D Fayer *J Phys Chem* **100** (1996) 15620
57 A Peremans, A Tadjeddine, P Guyot-Sionnest, R Prazeres, F Glotin, D Jaroszynski, J M Berset and J M Ortega *Nucl Instr and Meth in Phys Res* **A 341** (1994) 146
58 M I S Lopez, B Beden, F Hahn, J M Leger and C Lamy *J Electroanal Chem* **313** (1991) 323
59 R Srinavasan *Science* **234** (1986) 559
60 D J Erlich *Nucl Instr and Meth* **A 239** (1985) 397
61 R B Hall *Laser Focus* **18** (1982) 57

62 *Laser Induced Chemistry* JASON Report SRI International Stanford **JSR 78-11** (1979)

63 S H Bauer *SPIE* **458** (1984) 2

64 K V Reddy *SPIE* **458** (1984) 53

65 A Hartford Jr J H Clark in *Chemical and Biochemical Application of lasers* 5 (Ed C B Moore), Academic Press New York (1980) 217

66 J Wolfrum, M Kneba and P N Clough *US Patent* 4, 417, **964** (1983)

67 C Yamanaka *Nucl Instr and Meth in Phys Res* **A 318** (1992) 1

68 R Birgeneau Synchrotron Research Report *Science* **278** (1997) 25

69 C A Brau *Nucl Instr and Meth in Phy Res* **A 407** (1998) 1

LASER GAS-PHASE PHOTOLYSIS OF ORGANOSILICON COMPOUNDS: APPROACH TO FORMATION OF HYDROGENATED Si/C, Si/C/F, Si/C/O AND Si/O PHASES

JOSEF POLA
Institute of Chemical Process Fundamentals, Academy of Sciences of the Czech Republic, 165 02 Prague, (Czech Republic)

A review on studies of laser photolysis of single organosilicon compounds for chemical vapour deposition silicon-containing phases conducted in the Laser Chemistry Group of the Institute of Chemical Process Fundamentals in Prague is presented. The IR and UV laser photolysis of acyclic and cyclic organosilanes, fluoromethylsilanes, alkoxysilanes and disiloxanes is shown to yield films of polycarbosilanes, polytrimethylsiloxyhydrocarbons and of hydrogenated SiC, Si/C/F, Si/C/O and Si/O materials. The chemistry occurring in the gas phase is discussed in conjunction with properties of the deposited materials and the technique is demonstrated to represent an easy and efficient way of chemical vapour deposition of the Si-based phases onto low-temperature substrates.

Key Words: **IR Laser; UV Laser Photolysis; Organosilicon Compounds; Chemical Vapour Deposition; Si-Based Phases**

1 Introduction

Various silicon-based films and powders containing Si-C, Si-O and Si-N bonds are of considerable importance, because they find many applications in microelectronics, photo-electronics and high-temperature ceramics. For their production a number of chemical vapour deposition techniques in which plasma, heat or laser radiation interact with mixtures of silane and another reactant gas (NH_3, CH_4, etc.) were used. The IR laser technique has been introduced for this purpose in 1980[1]. An alternative way is the application of the energy sources to specially designed organosilicon precursors in which some bonds between silicon and the other atom are already created. Of different methods, the photochemical and laser-induced processes possess special charm due to enabling the chemical vapour deposition of materials at substrates kept at relatively low temperatures.

We have been involved in applying IR and UV laser radiation to many organosilicon precursors and investigated both gas-phase chemistry and properties of the deposited materials for several years. The UV laser photolysis (UVLP) was carried out by an ArF laser, while the IR laser photolysis was conducted by *cw* or TEA CO_2 lasers. IR laser heating and subsequent decomposition of the precursor molecule was achieved *via* direct absorption (infrared multiphoton decomposition, (IRMPD)[2]) or *via* energy transfer from the IR-laser radiation absorbing photosensitizer (laser photosensitized decomposition, LPD[3]). Both methods make possible two unique features. First, heterogeneously catalysed steps normally occurring on hot vessel walls of conventional pyrolyzers are utterly avoided and non-volatile products deposited on cold vessel walls of laser reactor cannot be further pyrolyzed by high temperatures of a small-volume hot zone produced by laser beam in the gas phase. Second, high concentrations of excited molecules or reactive intermediates effectively generated in the hot zone favour recombination (polymerization) of these species and not reactions which are of the first order in them.

Laser-induced IRMPD, LPD or UVLP were usually accomplished with several tenths up to several kPa of organosilicon compound in a standard 100 ml reactor. The deposition of solid materials on substrates accommodated in the reactor from the decomposition/ photolysis of micromolar quantities of organosilicon compound can be achieved within several seconds of laser irradiation.

The present paper reviews our over ten years lasting work on IR and UV laser irradiation of representatives of silacycles, monoorganylsilanes, diorganylsilanes, alkoxysilanes and disiloxanes. It shows the gas-phase chemistry involved in the laser-induced decomposition/photolysis of these compounds as well as properties of solid products deposited from the gas phase.

2 Laser Photolysis of Silacycles

Laser-induced decomposition of Si-substituted silacyclobutanes, 1,3-disilacyclobutane, 3-silacyclopentene, silaspiroalkanes and silacyclohexane affords reactive silenes and silylenes both of which take part in polymerization to polycarbosilanes or polymerization/ dehydrogenation to silicon carbide. These two major routes appear to be of different importance in the ArF and CO_2 laser-induced processes; thus the dehydrogenation reactions are significant in the IR laser-induced photolysis of silacyclobutanes but are very minor steps in the ArF laser photolysis of these compounds.

Polycarbosilanes represent important class of organosilicon polymers and have many applications. They can be also used as precursors to silicon carbide. The LPD, IRMPD and UVLP of silacycles can thus be utilized as an efficient technique for production of both types of materials.

2.1 Silacyclobutanes

The 4-membered silacyclobutanes are known to be thermally or photolytically decomposed into transient silenes which undergo mostly cyclodimerization[4] (Scheme 1).

Conversely to the parent silacyclobutane $H_2\overline{SiCH_2CH_2CH_2}$, its derivatives without Si-H bonds are not good absorbers of CO_2 laser radiation and must be decomposed in the presence of photosensitizer. All these compounds have, however, a good absorption at 193 nm and their UV photolysis can be efficiently induced by ArF laser.

2.1.1 LPD of Si-substituted Silacyclobutanes

LPD of silacyclobutanes $R_1R_2\overline{SiCH_2CH_2CH_2}$ into transient silenes $R_1R_2Si{=}CH_2$ is induced through collisions between silacyclobutane and photosensitizer (energy rich but chemically inert) sulfur hexafluoride. Its progress is affected by silacyclobutanes structure and this is why LPD of structurally different silacyclobutanes will be discussed separately for several groups of these compounds.

2.1.1a LPD of Silacyclobutanes with H or Unsaturated Substituent at Silicon

The LPD of silacyclobutanes $R_1R_2\overline{SiCH_2CH_2CH_2}$ (R_1, R_2 = H, CH_3, $H_2C{=}CH$, $HC\equiv C$)[5] affords gaseious products – ethene and propene- and solid transparent material depositing

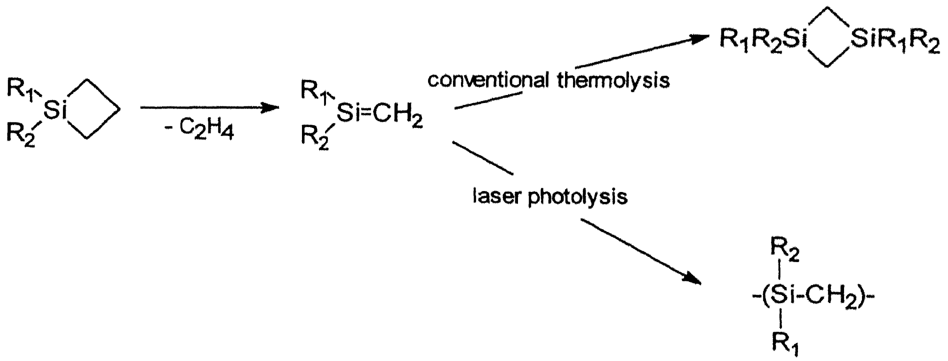

Scheme 1

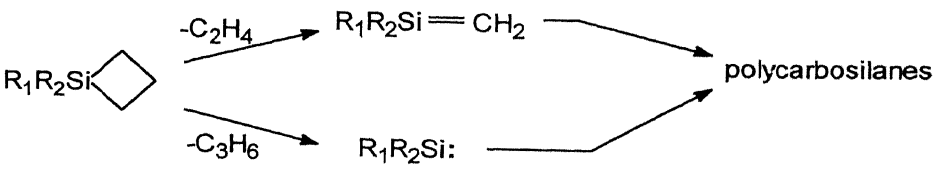

Scheme 2

from the gas phase to reactor surface. The gaseous products indicate that apart from (2+2) cycloreversion into ethene and silene (a major route), cleavage into silylene and propene (minor route) takes place (Scheme 2).

The intermediacy of transient 2-methyl-2-silabuta-1,3-diene (silaisoprene) in LPD of 1-methyl-1-vinyl-1-silacyclobutane was confirmed by trapping reactions with hexafluoroacetone and tetrafluoroethene, and that of 1,1-diethynylsilene in LPD of 1,1-diethynyl-1-silacyclobutane was proved by scavenging this species with methanol (Scheme 3).

The gas-phase polymerization of silicon-containing transients leads to the formation of transparent coatings on the reactor surface. The coatings are insoluble in organic solvents, suggesting that they have a cross-linked structure. Scanning electron microscopy (Fig. 1) reveals network morphology and FTIR spectroscopy shows a pattern of absorption bands lacking that of C=CH or C≡CH vibrational modes (Fig. 2). The decompositions of silacyclobutanes with unsaturated R_1 and R_2 substituents, i.e. those of 1-methyl-1-vinyl-1-silacyclobutane and bis(1-ethynyl)-1-silacyclobutane can thus be inferred to yield completely saturated polycarbosilanes in which not only the Si=C but also C=C and C≡C bonds are completely lost. It is thus evident that the efficient and complete polymerization of transient silaisoprene produced from the former and of the most (ever observed) unsaturated diethynylsilene produced from the latter parent must be achieved by sequence of steps shown in Scheme 4.

Corresponding multiply unsaturated carbon analogues of silenes are rather stable and do not efficiently polymerize even at high temperatures. This difference in reactivity in polymerization can be only explained by a "catalytic effect" of the Si=C bond.

2.1.1b LPD of 1,1-Dichloro-1-Silacyclobutane

Laser heating of SF_6 - 1,1-dichloro-1-silacyclobutane mixtures results[6] in the formation of ethene, methyltrichlorosilane and traces of methane, a less volatile 1,1,3,3-tetrachloro-1,3-disilacyclobutane and non-volatile polymeric material being deposited concurrently. These products were rationalized in Scheme 5 involving cleavage of ethene from, and dehydrochlorination of 1,1-dichloro-1-silacyclobutane as initial steps.

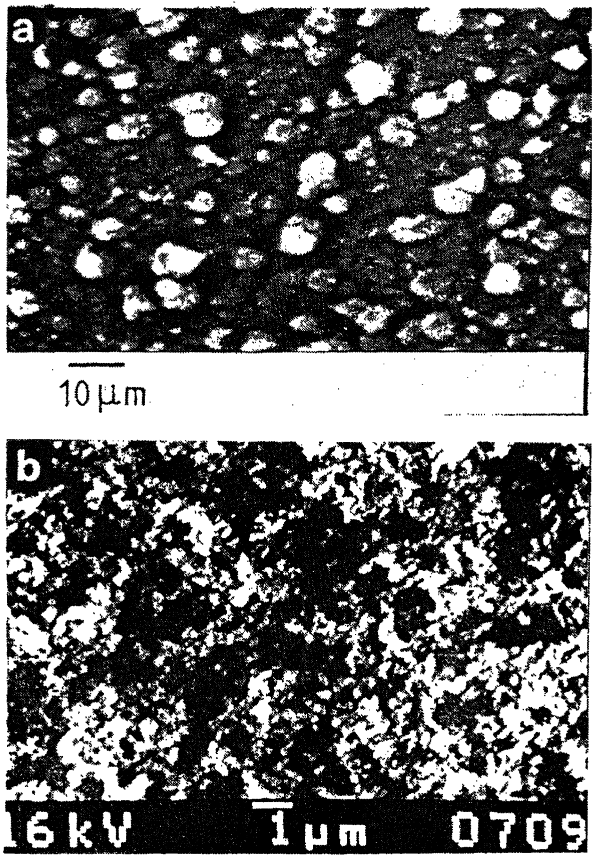

Fig. 1 SEM of the deposit from LPD of (a) 1-methyl-1-vinyl-1-silacyclobutane and of (b) 1, 1-diethynyl-1-silacyclobutane

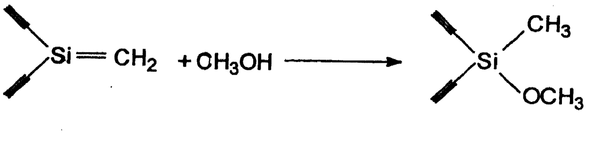

Scheme 3

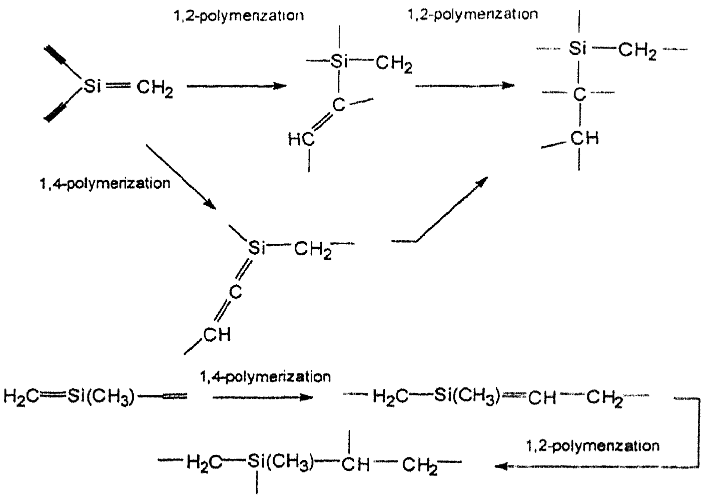

Scheme 4

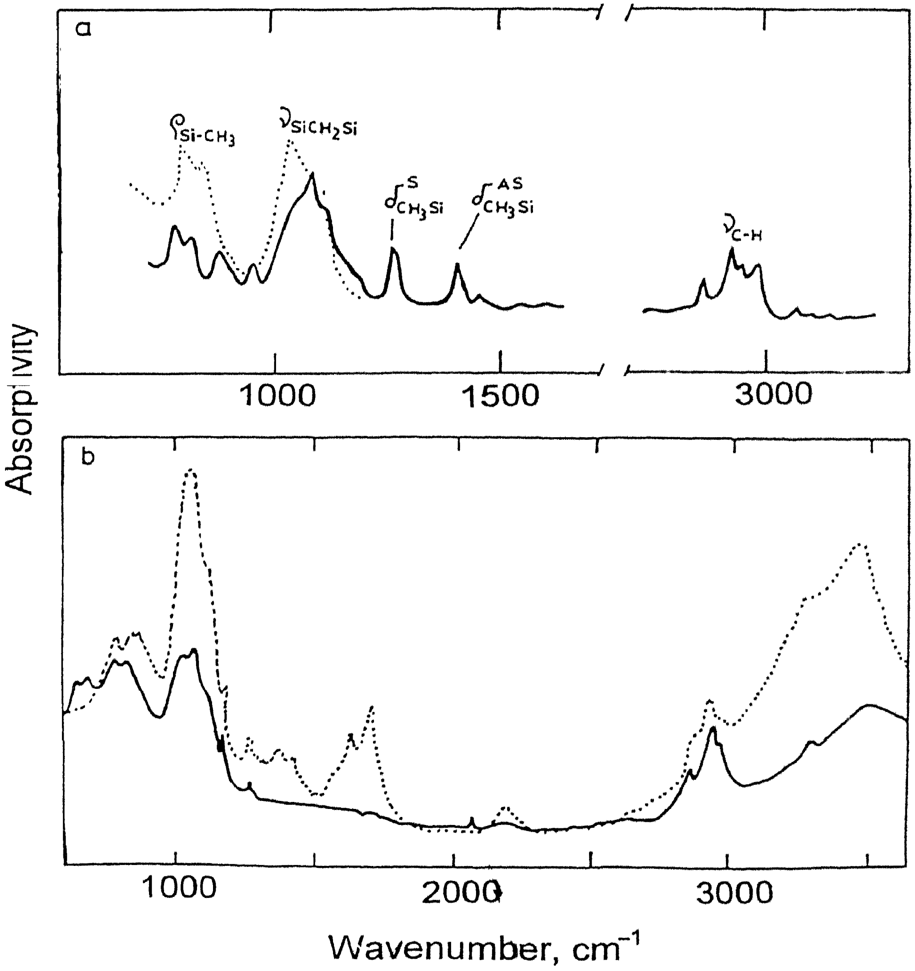

Fig. 2 FTR spectrum of the deposit from LPD of (a) 1-methyl-1-vinyl-1-silacyclobutane and of (b) 1, 1-diethynyl-1-silacyclobutane (Dotted curve relates to the deposit exposed to air).

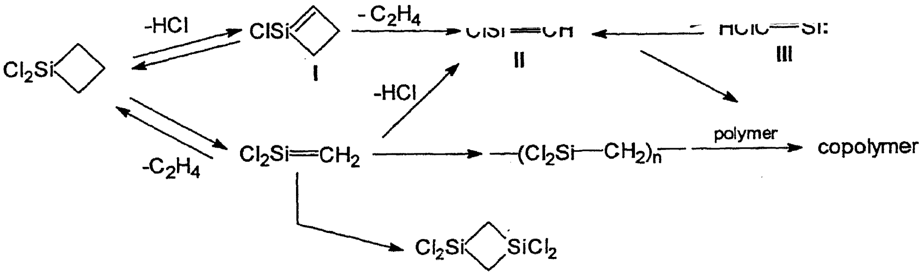

Scheme 5

$$\mathrm{ClSi{\equiv}CH} \xrightarrow{\mathrm{DCl}} \mathrm{Cl_2Si{=}CH_2} \xrightarrow{\mathrm{DCl}} \mathrm{Cl_3Si{-}CHD_2}$$

Scheme 6

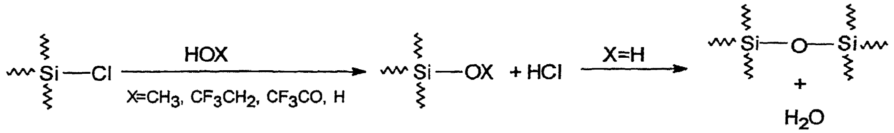

Scheme 7

The formation of elusive species I, II and III is difficult to prove unequivocally. Nevertheless, LPD carried out in the presence of DCl yielded $D_2HCSiCl_3$ and has given the indirect evidence on dichlorosilene and species II and/or III (Scheme 6).

Deposited polymeric material was judged as composed mostly of -(Cl_2SiCH_2)-units, and arise mainly *via* polymerization of dichlorosilene, because of two reasons: first, 2+2 cycloreversion of 1,1-dichloro-1-silacyclobutane is favoured over dehydrochlorination, and second, chlorosilyne can disappear upon the addition of HCl and be changed into dichlorosilene. The deposited material rapidly reacts with vapours of alcohols and water and evolves hydrogen chloride. The IR spectrum of the modified deposits (Fig.3) proved the occurrence of the gas-solid esterification of the Si-Cl moieties of the chlorosubstituted polymer. The exposure of the chlorinated deposit to water vapour results in the production of a siloxane-type deposit, which implies that the Si-OH bonds which must have been primarily formed upon the gas-solid phase hydrolysis, and whose presence has been revealed by an absorption band at 3400 cm^{-1} are not so far separated as to prevent their condensation. This gas-solid chemistry is depicted in Scheme 7.

Scanning electron micrograph of the deposit modified with methanol and trifluoroethanol vapour (Fig. 4) reveals a continuous structure and EDX-SEM analysis of the deposit after exposure to air shows the presence of Si, O, but also Cl, which indicates that some proportion of the Si-Cl bonds

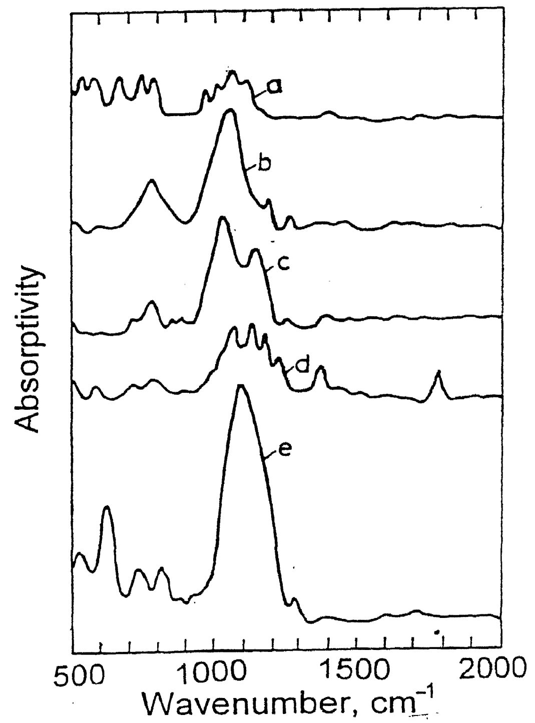

Fig. 3 FTIR spectrum of the deposit from LPD of (a), 1,1-dichloro-1-silacyclobutane and of (b) that obtained by subsequent treatment with gaseous methanol (c) 1,1,1-trifluoroethanol, (d) trifluoroacetic acid and (e) water

remains unhydrolyzed even upon long contact of the film with atmosphere. The materials are thus examples of reactive polycarbosilane polymers that can be modified by subsequent chemical treatment.

2.1.2. IRMPD and LPD of Sila- and 1,3-Disilacyclobutane

Silacyclobutane and 1,3-disilacyclobutane are promising precursors for silicon carbide and their IR laser photolysis is a convenient way for chemical vapour deposition of Si/C/H phases and/or silicon carbide[7].

The IRMPD of silacyclobutane leads to the formation of gaseous ethene (as a major product), propene, methane, methylsilane and n-propylsilane, and also to the deposition of a solid white material. With higher energy density (focused radiation), the decomposition rate is enhanced, the gaseous products contain ethyne and the deposit shows a grey colour. The LPD of silacyclobutane in the presence of SF_6 and excess of argon resembles the IRMPD in products. The determined absolute amounts of gaseous products in both decompositions were rationalized in terms of reactions in Scheme 8 where extrusion of silene $H_2Si{=}CH_2$ is a dominating pathway. This transient was proved by a time-resolved study of the TEA CO_2 laser induced IRMPD of silacyclobutane in the Bhabha Atomic Research Centre in Trombay as a major species having optical absorption spectrum with $\lambda_{max} \approx 260$ nm[8].

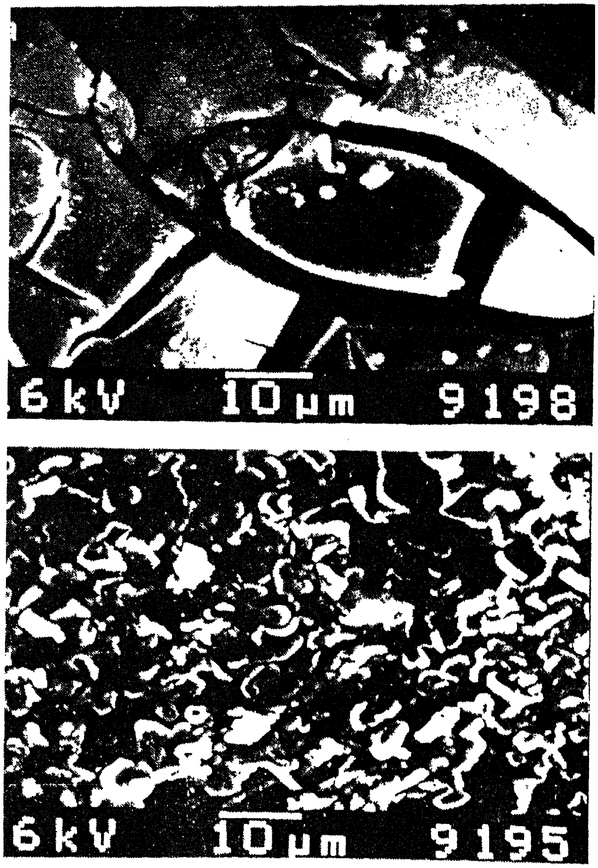

Fig. 4 SEM of the deposit from LPD of (a), 1,1-dichloro-1-silacyclobutane obtained by subseuqnet treatment with gaseious 1,1,1-trifluoroethanol and (b) methanol .

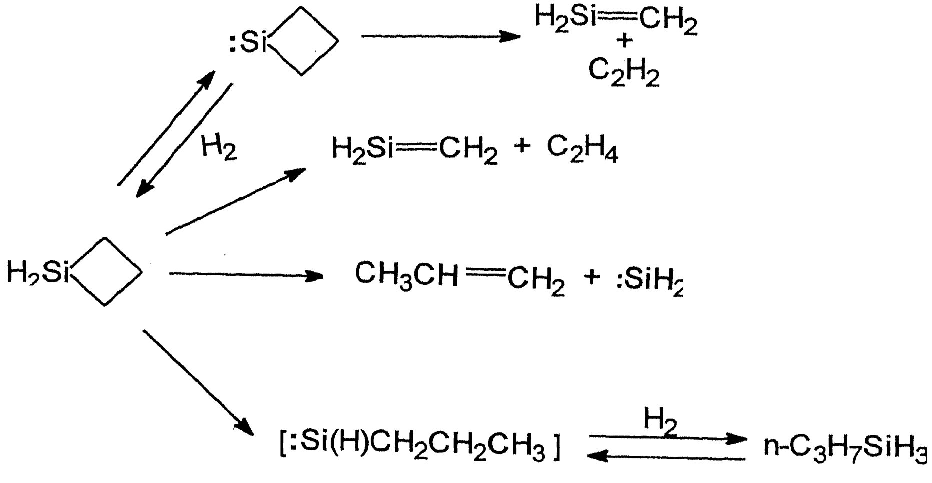

Scheme 8

This mechanism has been further refined in recent studies of LPD of 1,1-dideutero-1-silacyclobutane[9]. The identified volatile and solid products and the hydrogen and deuterium content in them are in accord with 1,2-H(D)-shift in intermediate silene and also with radical reactions.

The IRMPD of 1,3-disilacyclobutane results in the formation of minute amounts of gaseous methane, ethene, ethyne, propene, methylsilane and dimethylsilane, and a high-yield deposition of a solid material. Of these hydrocarbons, methane is an important product and the total yield of methylsilane and dimethylsilane corresponds to ca. 10 % of the decomposed 1,3-disilacyclobutane. The LPD of 1,3-disilacyclobutane leads to the same products in similar distribution. As identified by the time resolved study[8], the major pathway of the IRMPD is formation of silene, i.e. the reaction 1,3-disilacyclobutane → 2 $H_2Si{=}CH_2$. Minor methylsilane and dimethylsilane were accounted for to arise from a sequence of reactions consisting of homolytic cleavage and H rearrangements and further steps as depicted in Scheme 9.

Analysis of solid deposits from both silacyclobutane and 1,3-disilacyclobutane helped to more understand reaction steps in the gas phase. FTIR spectra of the deposits are in line with almost equal content of H(Si) and H(C) atoms, and show that content of H in them is significantly lower than in poly(silene) -(SiH_2CH_2)-. They also reveal that the deposits obtained by the IRMPD with nonfocused radiation or in the LPD possess two very strong bands of almost equal absorptivity associated with ν(Si-C) and ν(Si-H), and that the deposits from the IRMPD with focused radiation have only one very strong band in the ν(Si-C) region. XPS analysis supports these findings. Thus, the core level binding energies of the silicon and carbon and the shape of the Si(2p) and C(1s) spectral bands reveal the occurrence of chemically inequivalent forms, one being an organosilicon polymer and the other one a silicon carbide. The band belonging to silicon carbide is more intense for the deposits obtained with focused radiation. Typical examples of XPS analysis are given in Fig. 5. These analyses allow impli-

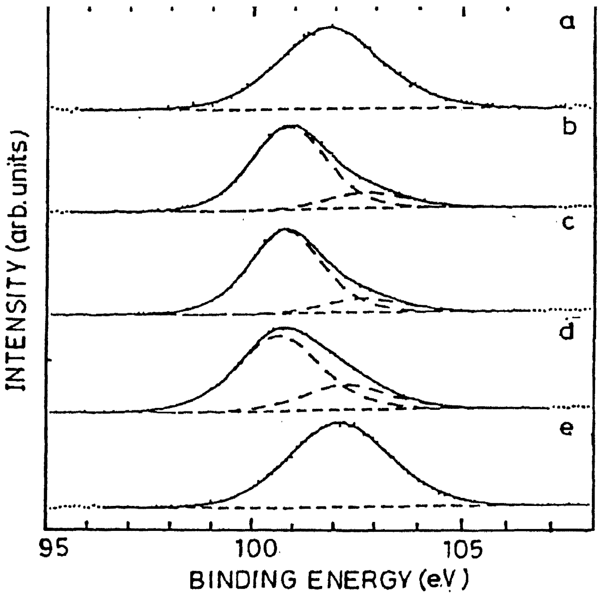

Fig. 5 The Si (2p) core-level spectra of the deposits from 1, 3-disilacyclobutane: (a) IRMPD unfocused radiation, (b), (c), (d) IRMPD focused radiation, (e) LPD. (The lower binding energy component relates to SiC and the higher one to polycarbosilane)

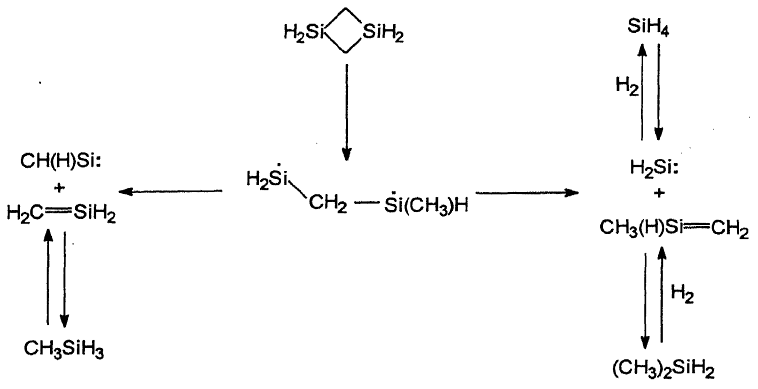

Scheme 9

cations that dehydrogenation of silene, which precedes the polymerization of $SiCH_n$ (n<4) and apparently of HSi≡CH and SiC species, is an important route (Scheme 10).

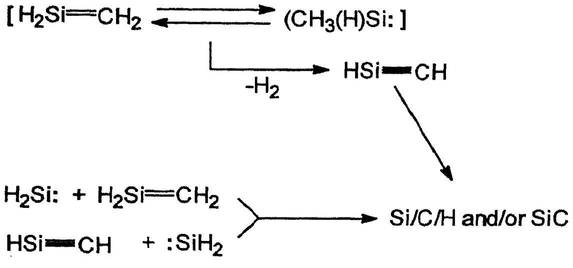

Scheme 10

SEM images of the deposits show fluffy structures, which do not differ whether they were obtained using focused and nonfocused radiation (Fig. 6).

Both LPD and IRMPD of silacyclobutane and 1,3-disilacyclobutane are clean reactions producing silene (and isomeric methylsilylene), the $H_2Si{=}CH_2$ transient being identified by the time resolved UV[8] (in BARC) and millimeter wave[10] (in CNRS) spectrum. These transients very efficiently polymerize, or dehydrogenate/polymerize, to yield copious amounts of Si/C/H and Si/C particles. The techniques are thus promising for low-temperature chemical vapour deposition of silicon carbide.

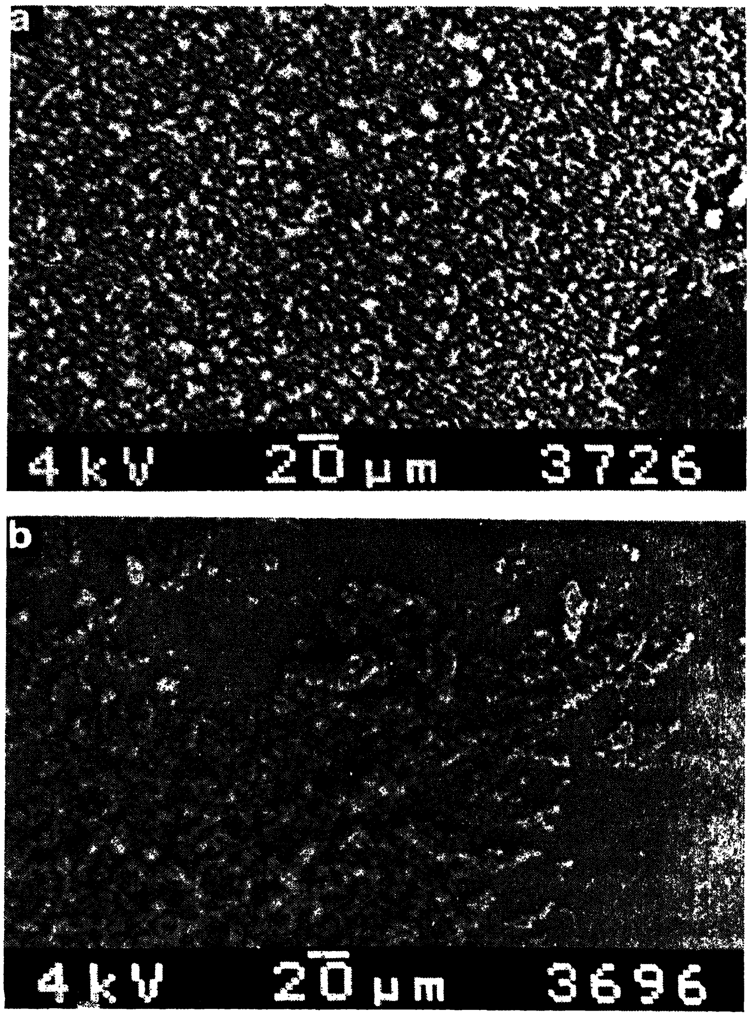

Fig. 6 SEM of the deposits from (a) IRMPD of silacyclo-butane and (b) 1, 3-disilacyclobutane

2.1.3 UVLP of Sila-, 1-Methylsila- and 1,3-Disilacyclobutane

UVLP of sila-, 1-methylsila- and 1,3-disilacyclobutanes does not involve dehydrogenation steps observed in the IRMPD or LPD of these compounds[11]. ArF laser photolysis of 1-methyl-1-silacyclobutane yields ethene (a major product), ethyne and methane, and that of silacyclobutane results in the formation of ethene (a major product) along with minor amounts of ethyne and silane. This is consistent with the extrusion of ethene as a major photolytic pathway. The only gaseous products observed in the photolysis of 1,3-disilacyclobutane are methane and silane which are produced in yields only below 10 %. In all the photolyses, solid deposits were produced concomittantly. The FTIR spectrum of the solid material from 1-methyl-1-silacyclobutane resembles that of poly(silapropene) and the spectra of the deposits from sila- and 1,3-disilacyclobutane are almost identical to that of poly(silaethene). These solid products thus could be accounted for by polymerization of transient silenes $CH_3(H)Si=CH_2$ and $H_2Si=CH_2$. The evidence for the intermediacy of these silenes in the ArF laser-induced decomposition of sila-, 1-methylsila- and 1,3-disilacyclobutane was supplied by the time resolved UV[12] and millimeter wave[10] spectral studies. The polymeric films are composed of agglomerates, which are bonded together (Fig. 7) and were accounted for by dominant gas-phase polymerization of transient silene or 2-silapropene (Scheme 11).

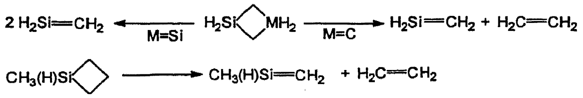

Scheme 11

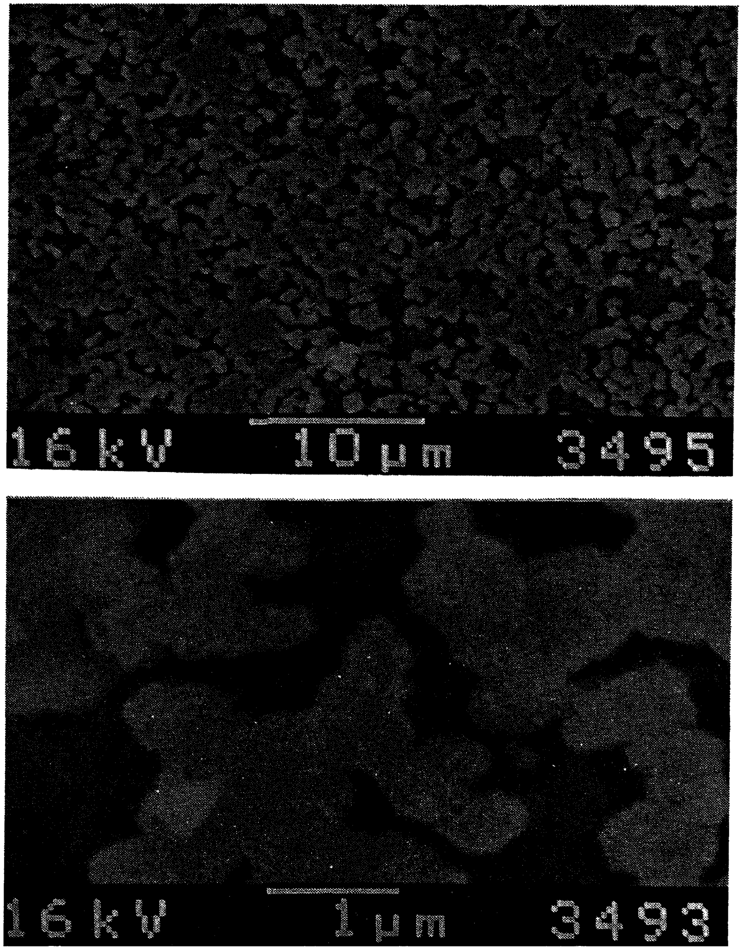

Fig. 7 SEM of the deposit from UVLP of 1,3-disilacyclobutane

The continuous structure of agglomerates is consistent with spontaneous polymerization of reactive particles taking place also after their deposition onto the substrate surface. The SEM pattern thus indicates that silenes generated in the gas phase undergo polymerization into depositing agglomerates that retain some degree of polymerization reactivity and can incorporate transient silenes or silylenes, or combine with other agglomerates. Due to the absence of dehydrogenation steps, these solids differ from the films deposited from the same precursors by irradiation with CO_2 lasers.

2.2 *Silaspiroalkanes*

The cw CO_2 laser induced LPD of 4-silaspiro[3.4]octane[13] is an efficient method for the gas phase deposition of organosilicon polymer produced from 1-methylene-1-silacyclopentane generated upon the elimination of ethene from the parent molecule (Scheme 12).

The same type of decomposition of 4-silaspiro[3.3]heptane is dominated[14] by transient formation and polymerization of 2-silaallene. The first experimental indirect evidence for this intermediate has been obtained by scavenging it with alcohols to afford dialkoxy(dimethyl)silanes (Scheme 13).

Both reactions afford polycarbosilane materials which are insoluble in common organic solvents and have obviously a cross-linked structure; the films possess very good adhesion to NaCl and metal surfaces. The FTIR spectral pattern of the white material from 4-silaspiro[3.4]octane shows the ring vibration of silacyclopentane rings and SEM reveals agglomerates bonded together (Fig. 8). The FTIR spectral pattern of the white material from 4-silaspiro[3.3]heptane does not possess absorption bands typical for the silacyclobutane ring. The deposit has SiC_2 stoichiometry, which is compatible with the major route of the LPD being the polymerization of SiC_2 transients, and consists of nanostructured particles forming dendrimer-type network (Fig. 9).

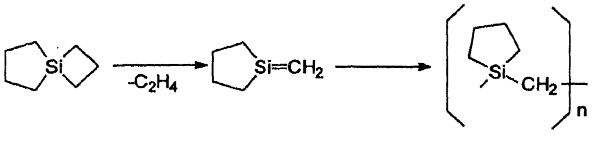

Scheme 12

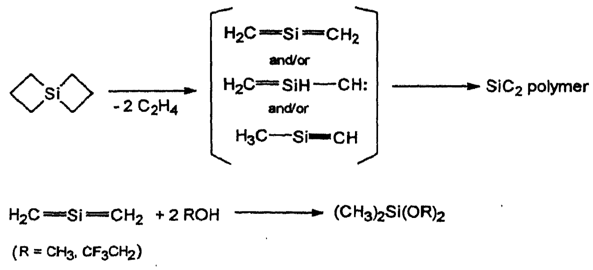

Scheme 13

The LPD of 4-silaspiro[3.3]heptane leading to polymerization of 2-silaallene provides a new example of the very efficient polymerization of Si=C bond-containing transients in the gas phase, this polymerization occurring much more readily than that of allene.

2.3 *Silacyclohexane*

The cw CO_2 LPD of silacyclohexane yields a variety of volatile hydrocarbons - ethene (major product), methane, propene, buta-1,3-diene, penta-1,4-diene- and minor amounts of methylsilane, dimethylsilane, trimethylsilane and silacyclo-butane, and leads to the deposition of solid films of polycarbosilane[15]. The ratio $[(CH_3)_nSiH_{4-n}$ (n=1-3) + silacyclobutane]/decomposed silacyclohexane ranging at different decomposition progress between 0.02 - 0.10 indicates that the silicon of the parent is mostly incorporated in the solid deposit. The multitude of the products is in line with a complex reaction scheme. The low yield of ethene disproved that cleavage of silacyclohexane into two ethene molecules is a major route; this pathway results in the observed silacyclobutane, which can undergo decomposition as described in the section 2.1.2. Other plausible routes are isomerization of silacyclohexane into silenes and alkenylsilanes. The former can undergo a 1,2-H shift to silylenes, and the latter can take part in the retroene reaction. The ability of both silenes and silylenes to polymerize explains the insufficiency of silicon in the volatile products. Other possible routes leading to the silicon unsaturates are the Si-C and C-C homolyses of silacyclohexane to alkyl, alkenyl and organosilicon carbon- and silicon-centered radicals. Studies on LPD of 1,1-dideutero-1-silacyclohexane revealed the occurrence of products with Si-H and C-D bonds and formation of solid materials containing a significant degree of Si-H bonding (Scheme 14).

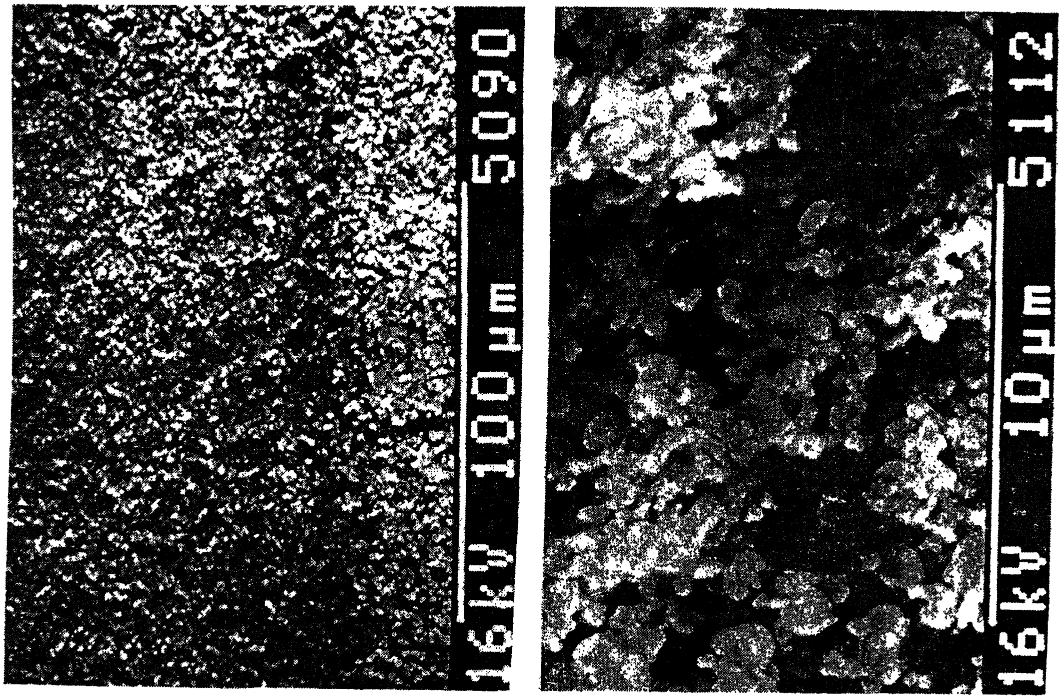

Fig. 8 SEM of the deposit from LPD of 4-silaspiro [3.4]octane

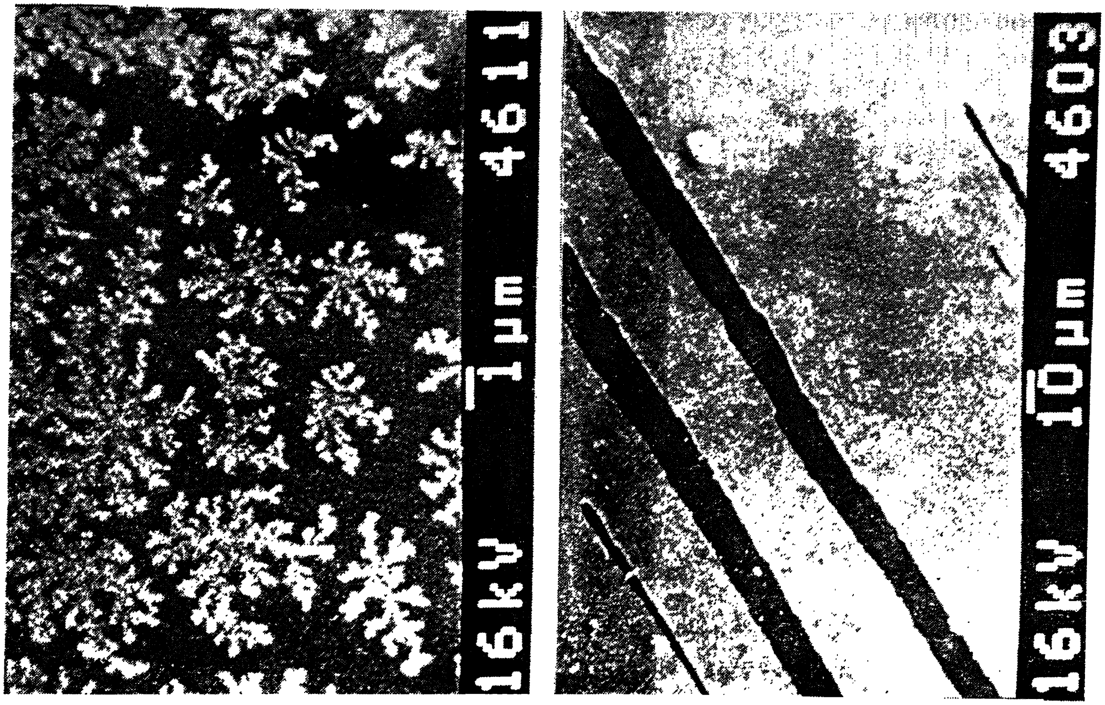

Fig. 9 SEM of the deposit from LPD of 4-silaspiro[3.3]heptane

These products were rationalized in terms of abstraction of deuterium from the Si-D bond of the parent or in terms of the known 1,2-H shift in the silylmethyl radical (H-$(R_2)Si\text{-}CH_2^{\bullet} \rightarrow {}^{\bullet}Si(R_2)\text{-}CH_3$) and similar 1,n-shifts of D in silylalkyl radicals. The high efficiency of the deposit formation thus reflects the availability of many pathways contributing to the production of macromolecules. Agglomerates with areas in the range 1-10 μm^2 show discontinuous structure, which implies that the majority of the polymerization (agglomerization) takes place in the gas phase.

2.4 Silacyclopent-3-ene

Thermal or photolytic decomposition of silacyclopent-3-enes is known to be the reversible process occurring *via* transient 2-vinyl-1-silirane and affording products of rearrangement and silylene extrusion (Scheme 15). The extent of these paths depends on the substituents at the silicon.

The UVLP of gaseous 3-silacyclopentene[16] results in the formation of volatile hydrocarbons, silane (traces) and 1-silyl-1-silacyclopent-3-ene, and in deposition of a white solid material. The film is opaque to the 193 nm radiation and detrimental to the photolytic progress: thus only 30% decomposition can be achieved by a prolonged irradiation. The hydrocarbon products distribution (in relative mole %) - buta-1,3-diene (60-90), buta-1,2-diene (< 5), ethane (8-22), ethene (5-8) ethyne (1-4), propane and methane (both <1) - varies at different photolysis stages (Fig. 10). The main product being buta-1,3-diene reveals that the major decomposition channel of 3-silacyclopentene is extrusion of silylene. The observation of 1-silyl-1-silacyclopent-3-ene and silane confirms this view, since these are the products of silylene reaction with 3-silacyclopent-3-ene and H_2, respectively. The availability of hydrogen in the system can be explained by 1,1-H_2 elimination, the path common

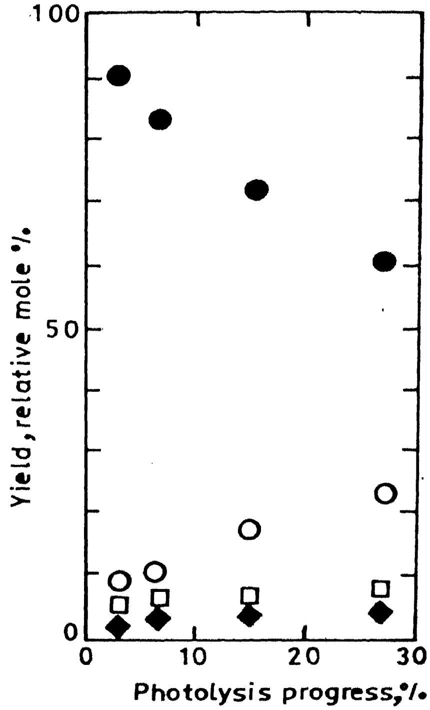

Fig. 10 Gaseous product yield (in relative mole percent) at different stages of UVLP of 3-silacyclopentene. (• C_4H_6, ○ C_2H_6, □ C_2H_4, ◆C_2H_2, × $CH_3CH{=}C{=}CH_2$)

silacyclohexane-d_2 → ethene, propene, buta-1,3-diene, penta-1,4-diene (all -$d_{0\text{-}2}$), methylsilane-$d_{0\text{-}3}$, silacyclobutane-$d_{0\text{-}2}$ and silacyclohexane-$d_{0\text{-}2}$

Scheme 14

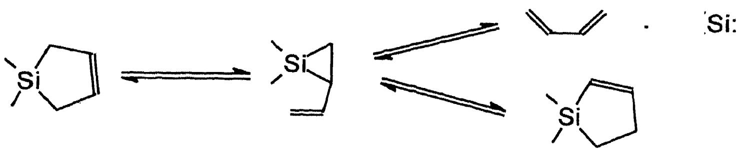

Scheme 15

for decomposition of organylsilanes. The C_1-C_3 hydrocarbons and buta-1,2-diene slightly increase in amounts in the course of the photolysis while amounts of buta-1,3-diene diminish. The former hydrocarbons are identical to the products of UV photolysis of buta-1,3-diene which takes place *via* (i) isomerization into buta-1,2-diene and subsequent cleavage into CH_3 and C_3H_3 radical, (ii) decomposition into C_2H_4 and C_2H_2 couple, (iii) decomposition into vinylacetylene and H_2 and (iv) polymerization. They thus confirm that 1,3-butadiene does not survive under photolytic conditions and that its photolysis is a concurrent process. The products observed in the silacyclopent-3-ene photolysis can thus be rationalised in terms of Scheme 16.

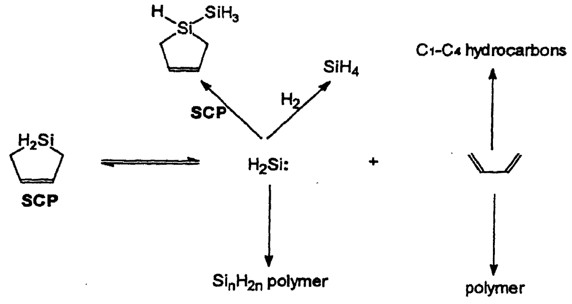

Scheme 16

IR spectrum of the deposit consists of bands at ν/cm^{-1}: 855m (ν_{Si-C}), 950m (δ_{Si-H}), 1070m ($\nu_{Si-C-Si}$ and/or ν_{Si-O}), 2130-2150s (ν_{Si-H}) and 2920w (ν_{C-H}) and is in accord with a polymer possessing H_2Si groups in a Si/C/H skeleton. SEM analysis reveals that the deposits have structure of tightly bonded agglomerates of ca. 1 μm size and TEM analysis proves that these agglomerates can be described as a net of ca. 20 nm sized dots (Fig. 11). The films are not soluble in common organic solvents (ben-

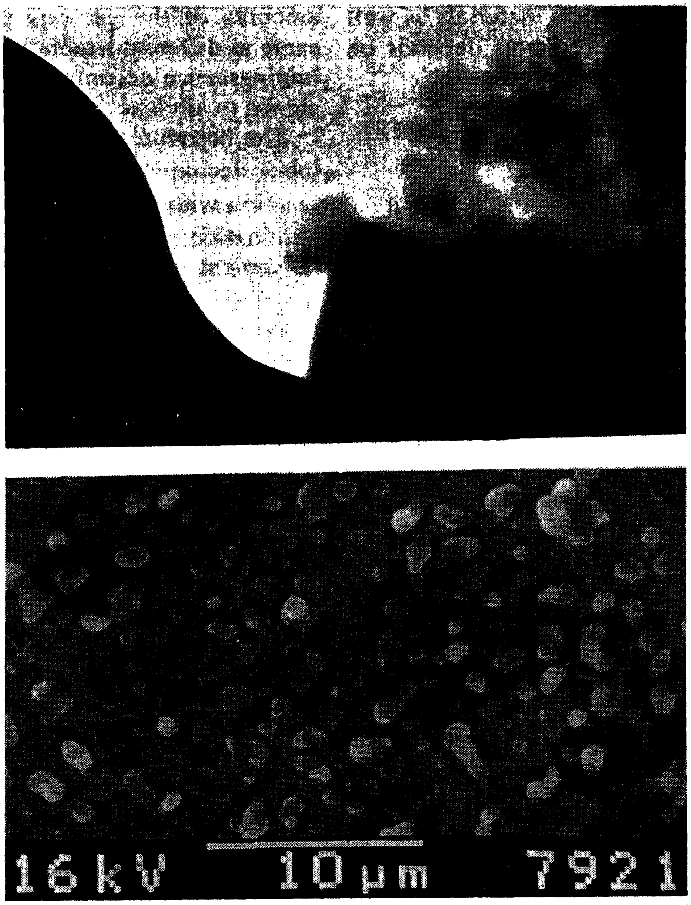

Fig. 11 SEM and TEM (magnification 100,000 x) of the deposit from UVLP of 3-silacyclopentene

zene, dichloromethane, tetrahydrofuran), which indicates a high degree of cross-linking. They exert excellent adhesion strength to glass and metals.

3 Laser Photolysis of other Silahydrocarbons

In this section, infrared (TEA - CO_2) laser irradiation of $RSiH_3$ with R= $H_2C{=}CH$, $ClHC{=}CH$ and $H_2C{=}CHCH_2$, of $(H_2C{=}CH)_nSiH_{4-n}$, with n =2,4 and of $H_3SiCH_2CH_2SiH_3$, and also ultra-violet photolysis of some of these compounds will be discussed. The gas-phase chemistry and properties of the deposited materials will be dealt with separately.

3.1 IRMPD of other Silahydrocarbons

Irradiation of the monoorganylsilanes $RSiH_3$ (R= $H_2C{=}CH$, $ClHC{=}CH$ and $H_2C{=}CHCH_2$), $(H_2C{=}CH)_2SiH_2$ and $H_3SiCH_2CH_2SiH_3$ by a TEA CO_2 laser into $\delta(H_3Si)$ mode using fluences below 1 J.cm^{-2} results in the formation of multitude of gaseous products and the deposition of solid coatings. The composition of the solid materials as well as the nature of the gaseous products depends on the structure of the organosilicon precursor.

3.1.1. Gas-Phase Chemistry

2-Chloroethenylsilane

Irradiation of $ClHC{=}CH{-}SiH_3$ (1.3 kPa)[17] leads to the formation of H_2, ethyne, hydrogen chloride, ethene, silane, ethenylsilane, ethynylsilane, chloroethene and ethynyldisilane which are consistent with two decomposition pathways, namely 1,2-dehydrochlorination and 1,1-hydrocarbon elimination, and with the known four-process decomposition of the intermediary ethynylsilane of which 1,1-H_2 elimination is dominating. These important steps are shown in Scheme 17.

$$H_3SiCH{=}CHCl \rightarrow HCl + H_3SiC{\equiv}CH$$
$$H_3SiCH{=}CHCl \rightarrow H_2C{=}CHCl + H_2Si{:}$$
$$H_3SiCH{=}CHCl \rightarrow HC{\equiv}C(H)Si{:} + H_2$$

Scheme 17

Ethyne being by far the major product and the amounts of chloroethene and ethene being very small along ~ 10 - 70 % decomposition progress imply that the 1,1-chloroethene elimination is not important compared to dehydrochlorination and that the major decomposition mode of the intermediary ethynylsilane is $H_3SiC{\equiv}CH \rightarrow HC{\equiv}CH + H_2Si{:}$. Small amounts of gaseous silane, ethenylsilane and ethynylsilane, but copious quantities of a solid Si/C/H deposit indicate that the major sink reactions for transient silylenes are silylene recombinations, additions and dehydrogenation of the adducts, all leading to Si/C/H material with no unsaturated C=C bonds.

Ethynylsilane

A single pulse irradiation of $HC{\equiv}CSiH_3$ results in an explosive reaction which is accompanied with a yellow luminescence[18]. The threshold of this explosive decomposition depends on ethynylsilane pressure and the irradiation fluence (Fig. 12); a nonexplosive decomposition could not be induced below the threshold with as many as hundred pulses. The products are ethyne (major product), ethene, methane (traces), silane and noncondensable dihydrogen together with a dark soot-like fog which slowly descends to form solid film. Relative amounts of the gaseous products are almost the same at different irradiation conditions. The strong luminescence accompanying IRMPD has been assigned to silylene[19].

The literature data show that the thermal (shock tube) decomposition of $HC{\equiv}CSiH_3$ is a complex reaction with major dissociation route being 1,1-H_2 elimination and with some contribution from rearrangement pathways yielding C_2H_2 + $H_2Si{:}$,

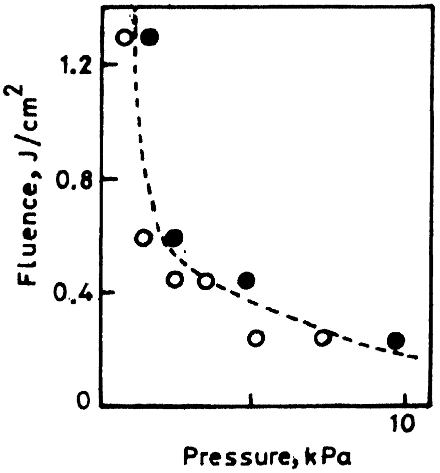

Fig. 12 Laser fluence vs. pressure dependence of the explosion limit for IRMPD of ethynylsilane. (Filled and empty circles relate to explosive reaction and no reaction, respectively.)

$H_2C{=}CH(H)Si{:}$, or C_2H_4 + Si. The products of the IRMPD ($C_2H_2 >> C_2H_4 \approx SiH_4$) are in keeping with the major role of the route $HC{\equiv}C\text{-}SiH_3 \rightarrow C_2H_2 + H_2Si{:}$. The main species forming the solid deposit must be $HC{\equiv}C\text{-}(H)Si{:}$, $H_2Si{:}$ and $H_2C{=}CH(H)Si{:}$ unsaturates which take part in polymerization/dehydrogenation to produce the observed silicon carbide.

2-Propenylsilane

Irradiation of $H_2C{=}CHCH_2SiH_3$ leads to the formation of a number of gaseous products (hydrogen, ethene, methylsilane, propene, C_3H_4 hydrocarbons, methane, silane, ethyne) and a deposition of a grey solid[18]. The distribution of volatile products (in molar %) does not significantly change within the 20-80 % decomposition progress: CH_4 (1.5-5.2), SiH_4 (3.4-10), C_2H_4 (38-48), C_2H_2 (11-18), CH_3SiH_3 (1-5.5), C_3H_6 (17-25), C_3H_4 (2-7). The observed products imply the occurrence of the earlier recognized decomposition modes of $RSiH_3$ organosilanes - 1,1-H_2, 1,2-H_2, alkane and alkene elimination- and a route occurring *via* a four-centre activated complex. The presumed transient silylenes $H_2Si{:}$ and $H_2C{=}CHCH_2(H)Si{:}$ can in principle, undergo insertion into Si-H bonds or addition on double bonds to yield higher ~~molecular prod~~ucts; however, the absence of such products indicates that these compounds undergo consecutive decomposition or polymerization/dehydrogenation.

The presence of very large amount of ethene is in line with a rearrangement of 2-propenylsilane into silacyclobutane (Scheme 18) which involves a closure at Si and 1,3-H shift, and would be followed by reactions affording ethene and silene (major products) and propene and silylene (minor products)[7]. This rearrangement and subsequent intermediacy of silene, methylsilylene and silylene would also explain observed formation of methylsilane and silane. The prevalence of silene and dehydrogenation of this transient (due to its likely absorption of the laser radiation), as well as polymerization/dehydrogenation of other transient unsaturates are plausible steps of the IRMPD of silacyclobutane[7].

1,4-Disilabutane

Irradiation of $H_3SiCH_2CH_2SiH_3$ leads to the formation of hydrogen, ethene, ethyne, methane, silane, vinylsilane, ethylsilane and 1,2,5-trisilapentane, is accompanied by a strong luminescence and affords a solid deposit whose formation is most effective within the first 40 pulses[20]. The products distribution is strongly dependent on the decomposition progress. The volatile products are formed by less than 20 % of the decomposed 1,4-disilabutane, which shows that the parent is mostly utilised for the formation of the solid deposit. The products are compatible with a number of initial reactions as 1,1-H_2, 1,2-H_2, alkane (ethylsilane), alkene (vinylsilane) and 1,4-H_2 elimination prototypes. Low amounts of $RSiH_3$ ($R{=}C_2H_5$ and C_2H_3) products are consistent with decomposition routes of these compounds into C_2H_4, $C_2H_5(H)Si{:}$, $H_2Si{:}$ and $CH_3CH{=}CH_2$, and H_2Si and C_2H_4, respectively. The depletion of ethene in the course of IRMPD indicates that ethene is removed by reactions with silylenes. The intermediacy of the simplest $H_2Si{:}$ silylene is revealed by the presence of 1,2,5-trisilapentane (insertion of $H_2Si{:}$ into 1,4-disilabutane) and by that of silane (reaction of $H_2Si{:}$ with H_2). The accumulation of silane at higher IRMPD progress gives evidence of dihydrogen produced by H_2-eliminations.

Divinylsilane

IRMPD of divinylsilane results[21] in the formation of dihydrogen, ethene, ethyne, propene, propadiene, vinylsilane, buta-1,3-diene, but-1-ene-3-yne, buta-1,3-diyne and benzene. These products are in line with the initial 1,1-H_2 ($(H_2C{=}CH)_2SiH_2 \rightarrow (H_2C{=}CH)_2Si{:} + H_2$), 1,2-$H_2$- and ethene elimination as well as with the silylene chain sequence similar to that earlier observed in the shock-tube

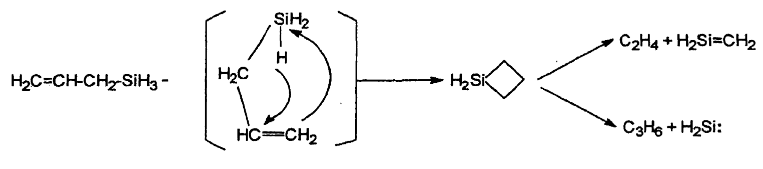

Scheme 18

decomposition of vinylsilane ($(H_2C{=}CH)_2Si: \rightarrow (H_2C{=}CH)HSi: + C_2H_2$ and $(H_2C{=}CH)HSi: \rightarrow H_2Si: + C_2H_2$) which affords ethyne. Significant formation of ethene (the C_2H_4/C_2H_2 ratio gradually diminishing from 0.8 to 0.5 along 10-50 % decomposition progress) is in accord with the occurrence of the alkene elimination pathway ($(H_2C{=}CH)_2SiH_2 \rightarrow (H_2C{=}CH)HSi: + C_2H_4$). Very low yields of the C_4 hydrocarbons indicated that the role of homolytic Si-C cleavage into $H_2C{=}CH$ radical is not important. This is in accordance with the observation of very small yields of buta-1,3-diene and with the known fact that combination of small radicals is preferred over their disproportionation.

Tetravinylsilane

IRMPD of tetravinylsilane in flow and batch reactors results[22] in the formation of gaseous ethyne, ethene, buta-1,3-diene and a solid a-SiC:H deposit. Ethyne was a major product and its amounts for up to 60 % of tetravinylsilane decomposition were 2-4 times higher than those of ethene. Molar amounts of butadiene and propene were about 20 - 30 and 10^2 times lower, respectively, than that of ethyne. These hydrocarbons are consistent with the homolytic fission of the Si-C bond of the parent and with reactions of the $H_2C{=}CH^{\cdot}$ radical. Recombination of this radical gives butadiene, its abstraction of hydrogen from the parent gives ethene and the $(H_2C{=}CH)_3Si\text{-}CH{=}CH^{\cdot}$ radical, and its disproportionation gives ethene and ethyne. Ethyne can be also formed by molecular elimination from the parent and/or $(H_2C{=}CH)_nSiH_{4-n}$ ($n = 1\text{-}3$) intermediates, or by cleavage of $(H_2C{=}CH)_nSi\text{-}CH{=}CH^{\cdot}$ radicals to afford $(H_2C{=}CH)_nSi^{\cdot}$ radicals. The observed preponderance of ethyne over ethene is in line with these routes.

3.1.2. Properties of Solid Deposits

FTIR Spectra

The solid films obtained from ethynylsilane, 2-propenylsilane (Fig. 13), 2-chloroethenylsilane and 1,4-disilabutane show IR absorption at ~800, 2110-2140 and 2900-2960 cm^{-1}. The first (vs) and the latter two (vw) bands constitute the typical pattern of a-SiC:H and reveal characteristic absorptions of ν(Si-C), ν(Si-H) and ν(C-H) modes in saturated moieties. Upon exposure to air these films develop a new absorption band at ca. 1050 cm^{-1} which is assignable to the ν(Si-O) mode. The films deposited from ethynylsilane and divinylsilane are dominated by a (vs) absorption band at ca. 800 cm^{-1}; whilst the absorptions at ca. 2130 and 2850-2930 cm^{-1} are almost negligent. This pattern is compatible with the occurrence of silicon carbide.

XPS Analysis

XPS spectra show that the composition of super-

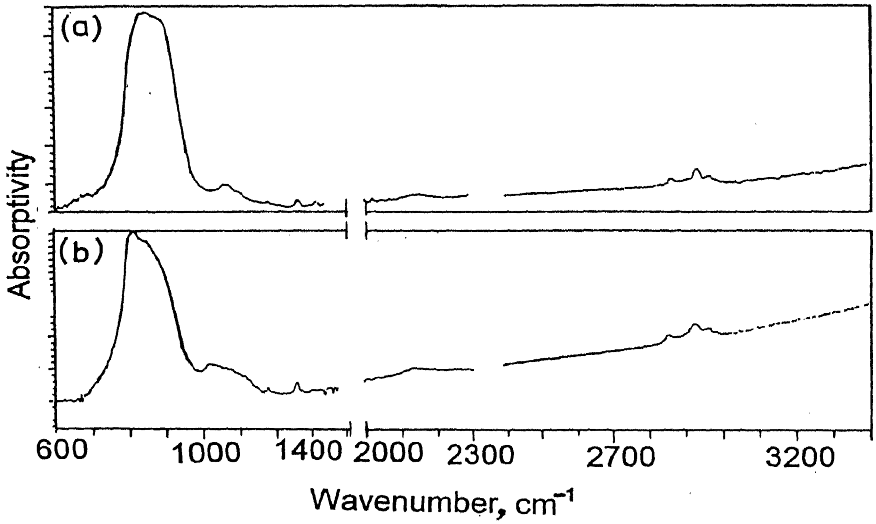

Fig. 13 FTIR spectrum of the desposits from (a) IRMPD of ethynylsilane and (b) 2-propenylsilane.

Table I

The Si (2p) and C (1s) core level binding energies (B.E.) of the photoemission lines, their assignment, the overall surface stoichiometry and the SiC content in the deposits from IRMPD of organosilanes.

Organosilane	B.E. Si (2p) eV	Assignment	B.E. C (1s) eV	Assignment	Stoichiometry	SiC content
$ClHC=CHSiH_3$	100.8 102.5	Si carbide polycarbosilane	283.0 287.0	carbide polycarbosilane	$Si_{1.0}C_{1.1}O_{1.0}$	60
$H_2C=CHCH_2SiH_3$	100.6 102.0	Si carbide polycarbosilane	283.6 284.8	carbide polycarbosilane	$Si_{1.0}C_{1.4}O_{0.4}$	50
$HC\equiv CSiH_3$	101.0	Si carbide	283.7 284.8	carbide polycarbosilane	$Si_{1.0}C_{1.5}O_{0.2}$	~90
$H_3SiCH_2CH_2SiH_3$	99.6 100.8 102.1 103.2	Si Si carbide polycarbosilane Si oxide	283.1 284.4	carbide polycarbosilane	$Si_{1.0}C_{0.6}O_x$	34
$(H_2C=CH)_2SiH_2$	100.5 102.1	Si carbide polycarbosilane	283.4 284.8	carbide polycarbosilane	$Si_{1.0}C_{1.9}O_{0.7}$	57

ficial layers of the deposits obtained from the individual organosilanes differ (Table I). The deposits from monoorganylsilanes $RSiH_3$ are composed of silicon carbide and saturated polycarbosilane, while that from 1,4-disilabutane contains these two constituents together with elemental silicon and silicon oxide. The oxygen incorporation is apparently associated with a residual reactivity of superficial layers to air and can be explained by reaction of O_2 with Si=C bonds of the topmost layers.

Scanning Electron Microscopy

SEM images of the deposits show that the deposits have particulate structure and consist of agglomerates (Fig. 14). There are some differences in morphology; the agglomerates formed from ethynylsilane form a web (Fig. 14 b), while those obtained from the other organosilanes (as from 2-chloroethenylsilane, Fig. 14 a) show small particles not bonded together.

3.2 UVLP of other Silahydrocarbons

ArF laser photolysis of monoorganylsilanes $RSiH_3$ ($R=H_2C=CH$, $HC\equiv C$, $ClHC=CH$ and $H_2C=CHCH_2$, each 1 kPa) is achieved due to good absorption of the laser radiation at 193 nm in these compounds[23]. The photolysis with many pulses affords H_2 and volatile products (C_2H_2, CH_4, C_2H_4, HCl, SiH_4) together with a white solid material. With ethynylsilane (3.6 and more kPa) the violent single-pulse explosive decomposition is observed which yields black soot-like fog.

3.2.1 Gas-Phase Chemistry

The major dissociation route in conventional thermolysis of ethenyl- and ethynylsilane is 1,1-H_2 elimination accompanied by 1,2-H_2 and hydrocarbon elimination; our observation of an uncondensible hydrogen is in line with elimination of hydrogen. The hydrocarbon elimination from ethenylsilane should yield ethene, that from ethynylsilane when occurring *via* silirane should give $C_2H_2 + H_2Si$, and when occurring *via* silirene C_2H_4 + Si products. The presence of ethyne, and no detection of ethene in the UVLP of ethenyl- and ethynylsilane implies the occurrence of steps $CH_2=CHSiH_3 \rightarrow CH_2=CHSiH: \rightarrow C_2H_2 + H_2Si:$, and $HC\equiv CSiH_3 \rightarrow C_2H_2 + H_2Si:$, while the absence of elemental Si in the deposits rules out step $HC\equiv CSiH: \rightarrow C_2H_2 + Si$.

The same assumptions apply to the UVLP of 2-chloroethenylsilane. This parent undergoes dehydrochlorination and the reactions judged for ethynylsilane. β-Haloalkenylsilanes, contrary to facile elimination of β-haloalkylsilanes into alkenes, are known not to undergo similar reaction into alkynes. The observed dehydrochlorination of 2-chloroethenylsilane and no production of chlorosilane is in accord with this view. The formation of ethyne in the photolysis of 2-propenylsilane indicates cleavage of the C-C bond and shows that this channel contributes to an apparently major 1,1-H_2 elimination route. Silane, observed as a minor product in the photolysis of ethenyl- and 2-

propenylsilane, indicates formation of silylene and its reaction with H_2.

3.2.2. Properties of Solid Deposits

FTIR Spectra

FTIR spectra of the deposits (Table II) show typical pattern of a-SiC:H films and reveal characteristic absorption of saturated moieties containing Si-C, Si-H and C-H bonds. Thin layers from ethenylsilane show a dominant absorptions of Si-H bonds. The ν(C-H) absorptivity being lower than that of the ν(Si-H) by a factor of ~ 5 is in line with roughly equal concentration of H(C) and H(Si) atoms.

The material photodeposited from 2-propenylsilane possesses significant contributions from Si-C, Si-H and C-H bonds as reflected by absorptions at ν(Si-C), ν(Si-H) and ν(C-H). The ν(C-H) absorptivity is lower than that of | | (Si-H) by less than a factor ~ 5, which implies more H atoms bonded to carbon than to silicon. Considering the partial cleavage of the C-C bond (and the escape of C_2H_2 into the gas phase), this preference of H(C) atoms proves the importance of the 1,1-H_2 elimination.

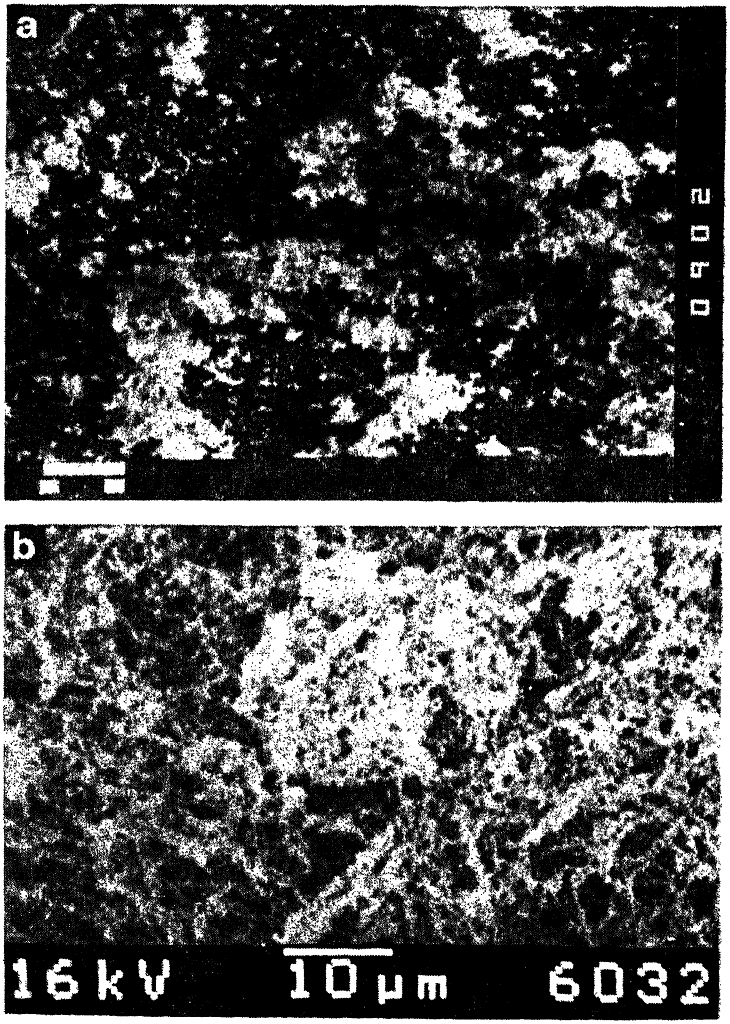

Fig. 14 SEM of the deposit from (a) IRMPD of ethynylsilane and (b) 2-chloroethenylsilane (Magnification 10,000 x).

Table II

FTIR spectra of the deposits from UVLP of monoorganylsilanes[a]

vibrational mode	Wavenumber/cm^{-1} (absorptivity) of the deposit from			
	H_2C=$CHSiH_3$	H_2C=$CHCH_2SiH_3$	ClHC=$CHSiH_3$	HC≡$CSiH_3$
ν(Si-C)	801 (0.54)	803 (1.72)	801 (3.04)	-
δ(Si-H)	926 (1.0)	-	919 (0.47)	928 (1.60)
δ(C-H)	1061 (0.28)	-	1028 (0.70)	-
ν(Si-H)	2145 (1.0)	2122 (1.0)	2138 (1.0)	2131 (1.0)
ν(C-H)	2891 (0.21)	2917 (0.35)	2880 (0.01)	2923 (0.20)

[a] Absorptivity normalized to that of the ν(Si-H) band.

The IR spectrum of the material from the photolysis of 2-chloroethenylsilane is dominated by a strong absorption at ν(Si-C) and shows a very low ν(C-H)/ν(Si-H) absorptivity ratio (~ 10^{-2}). This indicates the predominance of hydrogen atoms bonded at silicon. The prevalence of H(Si) over H(C) atoms in the deposit is consistent with an efficient expulsion of ethyne, this reaction being more facile than in the photolysis of 2-chloroethenylsilane.

The nature of thin layers from the photolysis of ethynylsilane is strongly affected by the pressure at which the photolysis is carried out. The white deposit obtained at 1 kPa shows strong absorptions at δ(Si-H), ν(Si-H) and ν(C-H) with only a very small absorption at ν(Si-C). Dissimilarly, the black deposit formed during the explosive photolysis reveals solely a strong absorption at ν(Si-C). The absorptivity ν(C-H)/ν(Si-H) ratio of the white material being 0.2 is similar to that of the deposit from ethenylsilane and is in keeping with an equal number of hydrogen atoms bonded to Si and C. The low absorptivity at ν(Si-C) suggests that the white material does not contain a lot of Si-C bonds and is composed of $-(SiH_n)_x-(CH_m)_y$ moieties.

Similarly to the deposits from the IRMPD of $RSiH_3$ compounds, the IR spectra of all the deposits do not show any absorption of multiple bonds between C atoms and all the ν(C-H) bands belong to the region of saturated C-H bonds (< 3000 cm^{-1}). This indicates that all the unsaturated bonds containing intermediates got lost in a process of very efficient polymerization.

IR spectra of the deposits after their exposure to air reveal that the films incorporate oxygen: while the ν(Si-C) band remains almost unaltered, a new very strong ν(Si-O) absorption band at 1060 cm^{-1} and a broad diffuse weak ν(Si)OH band around 3600 cm^{-1} develop while the ν(Si-H) band diminishes.

XPS Analysis

XPS analysis of the superficial layers of the deposits exposed to air confirms that the films are composed of silicon, carbon and oxygen. The observed values of Si (2p) core level binding energies as well as the differences between the energies of the O (1s) and Si (2p) electrons are consistent with the presence of an oxygen-containing organosilicon polymer. The reactivity of the superficial layers of the UVLP-produced films towards oxygen can be also accounted for by a fast addition of molecular oxygen to residual Si=C and/or Si=Si bonds.

Scanning Electron Microscopy

SEM images of the deposits reveal that the deposits have particulate structure and consist of agglomerates the size of which is typically less than 1 μm. This is illustrated for the deposit from 2-chloroethenylsilane in Fig. 15.

In conclusion, the analyses show that both UV and IR laser radiation absorbed in a number of organosilanes affords Si-containing materials. Their composition can be described by contributions of elemental silicon, SiC and polycarbosilanes (IRMPD of $H_3SiCH_2CH_2SiH_3$), of SiC and polycarbosilanes (IRMPD of $RSiH_3$ with R = ClHC=CH, H_2C=$CHCH_2$ and HC≡C and of $(H_2C=CH)_2SiH_2$), and by polymeric carbosilane (UVLP of $RSiH_3$ with R = H_2C=CH, ClHC=CH, H_2C=$CHCH_2$ and HC≡C).

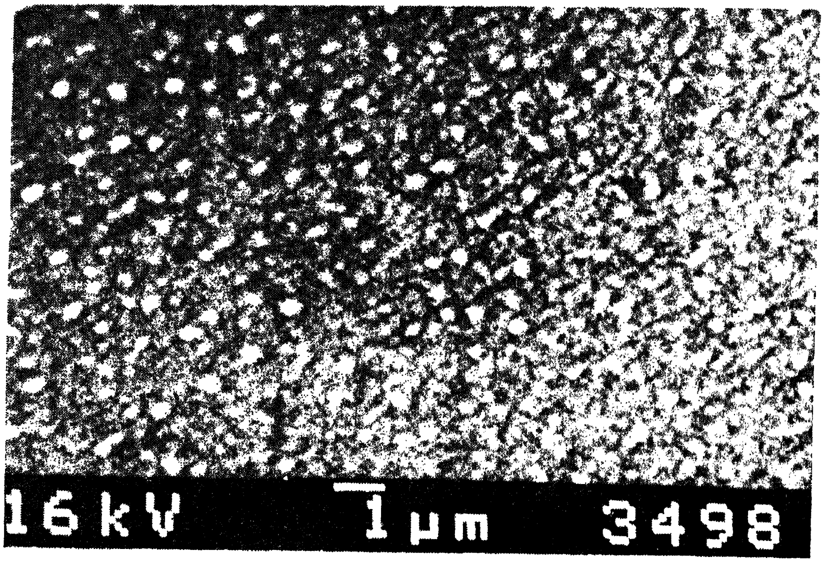

Fig. 15 SEM of the deposit from UVLP of 2-chloroethenylsilane.

4 Laser Photolysis of Fluoromethylsilanes

((Polyfluoro)methyl)silanes $H_{3-n}CF_nSiH_3$, constituted of fluorocarbon and silane moieties may have a tendency to decompose in significant heterogeneous steps, which happen with fluorocarbons, silane and methylsilanes. These heterogeneous processes can be efficiently avoided in IRMPD.

4.1 Gas-Phase Chemistry

The IRMPD of the fluoromethylsilanes H_2CFSiH_3, HCF_2SiH_3, F_3CSiH_3 and $(F_3C)_2SiH_2$ induced at pressures 0.1-6.7 kPa is an explosive reaction requiring just a 1 pulse of the CO_2 laser radiation for its initiation[24]. The irradiation with a single pulse results in the explosive decomposition when the pressure exceeds a certain limit, which depends on the laser fluence and the wavelength. The explosion limit pressure with each compound increases as the laser fluence decreases. This is demonstrated for fluoromethylsilane in Fig. 16. Below this threshold some noticeable chemical changes can be detected only after irradiation with

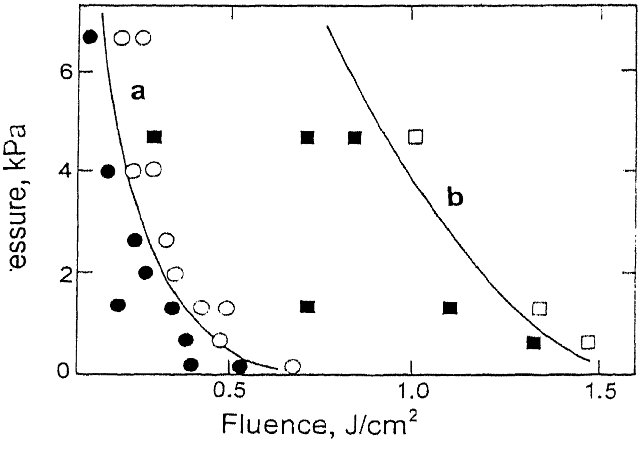

Fig. 16 The pressure/laser-fluence diagram of the explosion limit for IRMPD of F_3CSiH_3 with irradiation at (a) 916.6 cm^{-1} and (b) 1082.3 cm^{-1}. (Empty and full symbols relate to explosive reaction and no reaction, respectively.)

as many as 10^3 pulses. Above the threshold, an extensive chemiluminescence is observed and the parent compounds are completely or almost completely depleted. Gaseous silicon-containing products (SiF_4 and $SiHF_3$) were the same with all IRMPD's studied, while carbon-containing products (gaseous or solid) differed.

Fluoromethylsilane

Irradiation of H_2CFSiH_3 results in the formation of methane (a major product) and $HSiF_3$, C_2H_2 and SiF_4 together with a solid material. More than 80% of the silicon of the parent was exploited in the formation of the deposit, only small quantities of SiF_4 and $HSiF_3$ being formed.

(Difluoromethyl)silane

The explosive IRMPD leads to the same products as with fluoromethylsilane, more C_2H_2 instead of CH_4 being formed together with ethynyltrifluorosilane. At lower pressures (< 3 kPa), no obvious solid products were visible and the interior of the reactor remained clean after 10 or more explosive reactions. The determined amounts of gaseous products - CH_4, C_2H_2, $HSiF_3$ and SiF_4 - showed that carbon and fluorine of the parent were almost completely exploited for the formation of the gaseous compounds, while hydrogen and silicon were not. At higher pressures (5.3 kPa), the explosive reaction is accompanied by the formation of a black smog, which deposits only reluctantly onto the reactor walls.

(Trifluoromethyl)silane

Irradiation of (trifluoromethyl)silane yields significant amounts of C_2H_2, SiF_4 and $HSiF_3$ along with traces of C_2F_4 and cyclo-C_3F_6. A solid black product is also formed. The material balance revealed that Si, C, H and F originating from the parent are contained in the gaseous products only in fractional amounts and that their deficiency corresponds to 40-70 (Si), 20-65 (C), 67-85 (H), and 27-65 % (F). These deficiencies increase with the increasing pressure of (trifluoromethyl)silane.

Bis (trifluoromethyl)silane

Irradiation of $(F_3C)_2SiH_2$ results in the formation of SiF_4 and minor amounts of $HSiF_3$ and C_2F_4 accompanied by traces of C_2H_2, copious black material being deposited concomittantly. The material balance for the gas-phase compounds showed that silicon and fluorine of the parent are exploited for the formation of both gaseous and solid products, while carbon is almost completely utilized for the formation of solid deposits.

Decomposition Mechanism

The gaseous decomposition products indicated an almost complete migration of fluorine from carbon to silicon, the thermodynamically stable fluorosilanes $HSiF_3$ and SiF_4 being formed. Carbon is recovered in the gas phase as CH_4 and the high-temperature species C_2H_2. The fraction of the two latter decreases with the increasing fluorine content in the parent molecule, (trifluoromethyl)silane and bis(trifluoromethyl)silane forming no CH_4 at all (Fig. 17). Only traces of C_2H_2 were observed with bis(trifluoromethyl)silane, C_2F_4 formed by dimerization of CF_2 being obtained instead. The plausible mechanism for the IRMPDs are a dyotropic rearrangement and a sequence of carbene elimination and insertion reactions (Scheme 19).

These reactions are followed by further steps differing in their extent with particular fluoromethylsilanes. Methane was inferred to arise from precursors with CH_3Si group, while ethyne and fluoro-

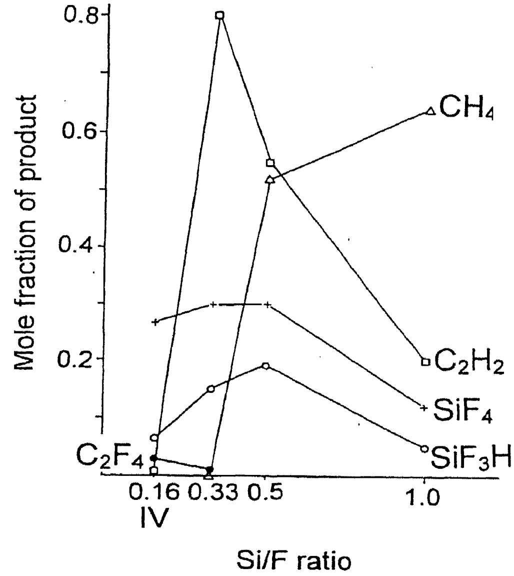

Fig. 17 Mole fraction of gaseous products formed by single-pulse IRMPD of fluoromethylsilanes I-IV interpolated to ca. 1 kPa. (I, II, III and IV relate, in the given order, to FH_2CSiH_3, F_2HCSiH_3, F_3CSiH_3 and $(F_3C)_2SiH_2$.)

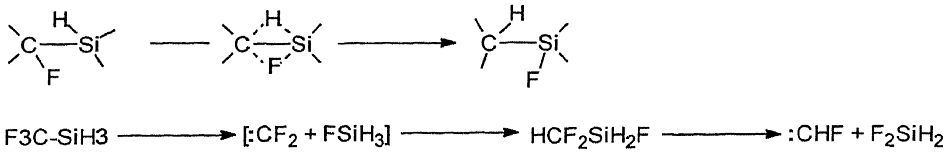

Scheme 19

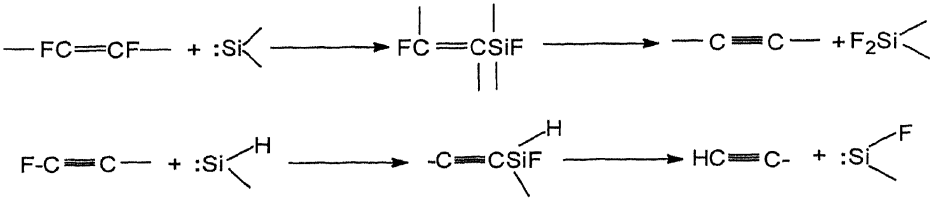

Scheme 20

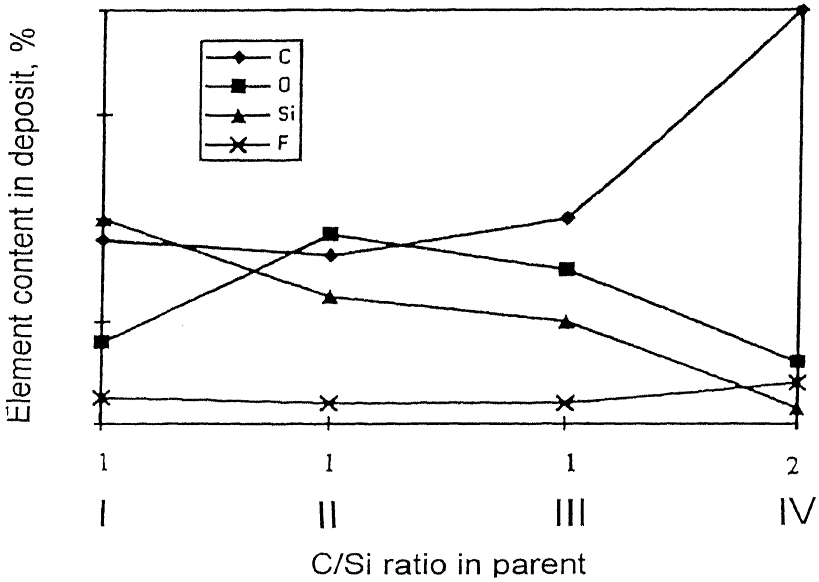

Fig. 18 Composition of the deposits obtained from IRMPD of fluoromethylsilanes I-IV.

silanes were accounted for by a sequence of reactions of intermediary fluorovinylsilanes and ethynylsilanes (Scheme 20).

The explosive IRMPD of fluoromethylsilanes can be induced with significantly less energy fluences compared to laser driven reactions in mixtures of silane with fluorohydrocarbons or fluoro- and carbonyl- groups containing compounds[25]. This is consistent with the collisional energy pooling process during the IRMPD, which contrasts with the energy transfer from vibrationally excited, activated molecule to a cold (nonabsorbing) collisional partner in bimolecular laser-induced reactions.

4.2 Properties of Solid Deposits

Properties of the deposits reflected by ESCA, IR, Raman and SEM data differ depending on the structure of the precursor[26]. The ESCA data on the topmost layers are given in Fig. 18.

The IR and Raman spectrum of the deposit from (fluoromethyl)silane have features of those of silicon carbide and of amorphous carbon. ESCA analysis is consistent with the concentration of carbon and silicon about seven times higher than that of fluorine. Both carbon and silicon are present in chemically inequivalent forms.

The deposit from (difluoromethyl)silane obtainable at lower pressures consists of hydrogenated amorphous silicon, while that produced at higher pressures is rich in Si-C but poor in Si-H and C-H bonds.

The IR spectrum of the deposit from (trifluoromethyl)silane reveals the presence of SiF_6^{2-} and also that of Si-C and C-H bonds. It contains twice as much carbon as silicon and also low concentration of fluorine.

The deposit from bis(trifluoromethyl)silane is composed mostly of carbon; the Raman spectrum confirms the structure of graphite. The IR spectrum reveals the presence of C-H but not Si-H bonds, while ESCA analysis showed the preponderance of carbon and some content of silicon and fluorine.

The deposits are extremely sensitive to atmosphere and incorporate oxygen. The main reaction producing the deposit is polymerization of unsaturated alkenyl- and alkynylsilanes, while the formation of graphite and amorphous carbon takes place *via* silicon-free or silicon-containing unsaturates and their dehydrofluorination and dehydrofluorosilylation (Scheme 21).

The deposited layers show different morphology (Fig. 19): that of (fluoromethyl)silane is a compact

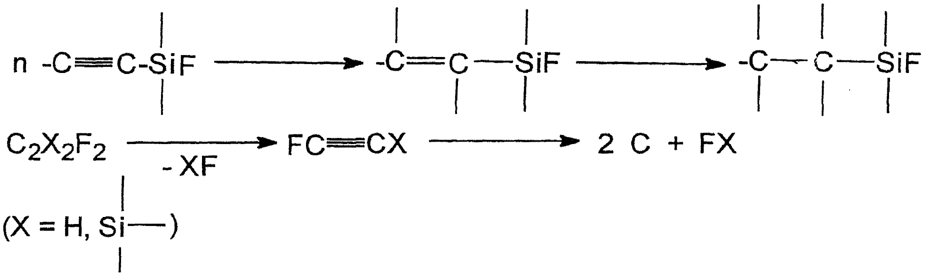

Scheme 21

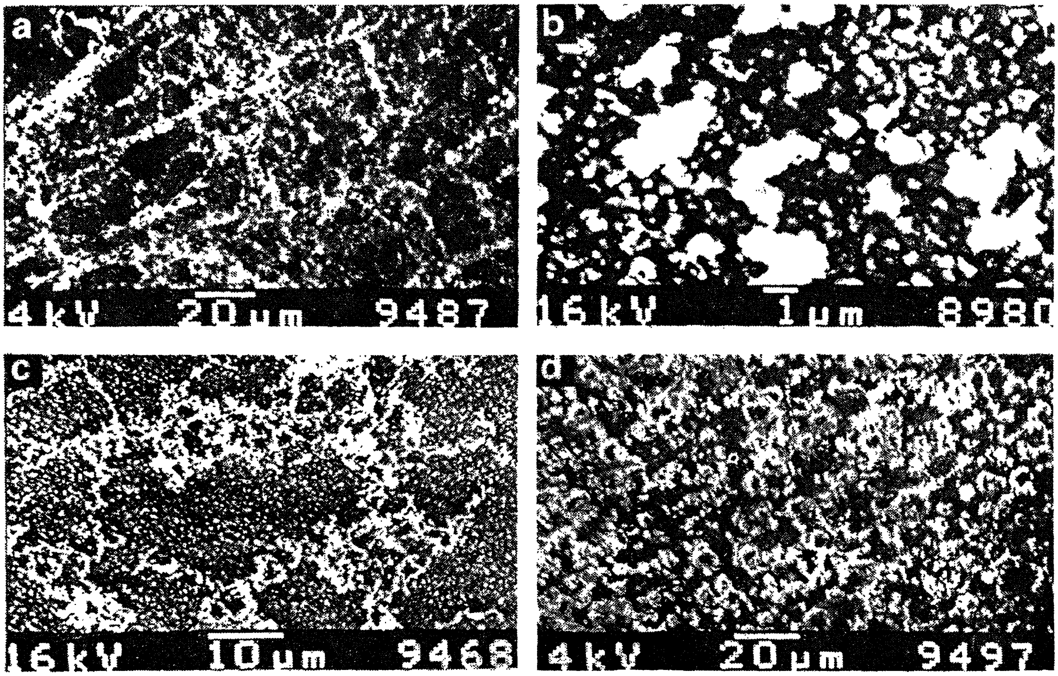

Fig. 19 SEM images of the deposits form (a) IRMPD of FH_2CSiH_3 (b) F_2HCSiH_3 (c) F_3CSiH_3 and (d) $(F_3C)_2SiH_2$.

material overlaid with a light woven structure, that of (difluoromethyl)silane is composed of agglomerates whose size ranges from less than 1 μm at the low pressure and to more than 10 μm in the high pressure experiments, that from (trifluoromethyl)silane is a compact black material (apparently carbon) covered with white particles of organosilicon polymer, and that from bis-(trifluoromethyl)silane is a light network texture (on Al) or a light, bulkier, island structure (on NaCl).

The deposited layers do not adhere strongly to metal surfaces, but their adhesion can be dramatically increased upon a long (several months) exposure to atmosphere. This was indicated by Nd:YAG laser spallation experiments. The spallation of the deposit from (trifluoro-methyl)silane results in a disappearance of the white layer of agglomerates, and is, as confirmed by ESCA analysis, related to a removal of silicon.

These results suggest that the IRMPD of fluoromethylsilanes can be used as a simple and efficient method for the gas-phase deposition of layers of reactive agglomerates of poly-carbosilanes, and that these reactive particles can be deliberately modified afterwards by chemical reactions.

5 Laser Photolysis of Alkoxysilanes and Disiloxanes

IRMPD and UVLP of selected unsaturated alkoxysilanes -$(HC\equiv CCH_2O)Si(CH_3)_3$ and $H_2C{=}CHOSi(CH_3)_3$- has been studied with the aim to achieve gas-phase polymerization at the unsaturated substituent, while those of selected disiloxanes-($H_3SiOSiH_3$ and $(CH_3)_2HSiOSiH(CH_3)_2$ has been examined to prepare Si/O or Si/C/O materials.

5.1 Gas-Phase Polymerization/Photolysis of Alkoxysilanes

Lasers are finding increasing use in inducing polymerization, but their role is mostly confined to the liquid phase. Laser-induced polymerization in the gas phase is initiated through excitation of gaseous molecules producing chemically reactive species which intermolecularly react to yield agglomerates. The method is documented in the literature by only few examples such as UV laser photopolymerization of methyl acrylate, acrolein and carbon disulphide[27] and IR laser-induced thermal polymerization of azetidine, pyridine thiophene and some organosilicon or organogermanium compounds[28].

Trimethyl (propinyloxy)silane

UV photolytically induced gas-phase polymerization of organic compounds possessing C≡C bonds has been known for long and regarded as a nuisance rather than a useful feature. With intense radiation from lasers, this reaction can, however, serve for chemical vapour deposition of polymeric coatings. Although the oligomers and polymers of acetylenic compounds R-C≡CH (R = alkyl, alkoxy, CN and other substituents) can be obtained by using catalysts in the liquid phase or plasma in the gas phase, their properties are affected by small amounts of catalyst inadvertently embedded in the polymer or by specific steps occurring in the ionized gas.

UV laser-initiated gas-phase photolysis of trimethyl(2-propynyloxy)silane affords[29] a white smog. Minor volatile products are ethyne, hexamethyldisiloxane and a $Si_2C_5H_{14}O$ compound. They are produced in very low, ca. < 6 % yields; hence more than 90 % of the photolysed parent is consumed for the formation of the polymer.

FTIR spectrum of the deposit consists of bands at ν/cm^{-1}: 800w, 837w ($\nu_{Si\text{-}C}$ and δ_{CH3Si}), 1060vs ($\nu_{Si\text{-}O}$), 1178w, 1257w, 1381w (both δ_{CH3Si}), 1620m ($\nu_{C=C}$), 1730w , 2838vw, 2916w and 2956w (all $\nu_{H\text{-}C\text{-}}$), and it is in accord with a partly unsaturated polyhydrocarbon with Si-O bonds. No absorption due to $\nu_{H\text{-}C\equiv}$ stretch behind 3000 cm^{-1} but a significant absorption due to $\nu_{H\text{-}C}$- reveals that H atoms are very mostly bonded to saturated fractions of the polymer framework. The deposit is insoluble in organic solvents (tetrahydrofuran, dichloromethane, acetone, toluene), which is compatible with a higly crosslinked structure. SEM pattern of the deposited white smog (Fig. 20) reveals agglomerates which are bonded together. This indicates that the deposited particles retain some degree of polymerization reactivity. The partly unsaturated structure is confirmed by UV spectrum of the deposit which shows absorption peaking at 190 nm, having a shoulder at ~260 nm and tailing to 500 nm.

These data thus prove an efficient polymerization on the triple bond, which results in the formation of $—\{[(CH_3)_3SiOCH_2]C{=}CH\}_x—\{[(CH_3)_3SiOCH_2]C\text{-}CH\}_y$. agglomerates. The known reactivity of

$(CH_3)_3Si\text{-}O$ moiety towards hydrolysis makes these agglomerates promising precursors to macromolecules possessing OH bonds which can find use as permeation barrier coatings, pH responsive films andsensing materials.

LPD of trimethyl (propinyloxy)silane affords a multitude of unsaturated hydrocarbons and a polydimethylsiloxane phase[30]. This process of chemical vapour deposition in which all the silicon of the parent is completely utilized in the formation of the solid phase is thus very different from the UVLP of trimethyl (propinyloxy)silane.

Trimethyl (vinyloxy)silane

UV laser induced gas-phase photolysis of trimethyl (vinyloxy)silane $(CH_3)_3SiOCH=CH_2$ cannot be used to achieve photolytically induced polymerization at the double bond, since an efficient cleavage of all but the Si-O bonds of this molecule take place and results in the deposition of solid polysiloxane films[31]. The ArF laser irradiation results in the parent depletion and the formation of volatile hydrocarbons (in mole/mole of decomposed trimethyl (vinyloxy)silane x 100)- methane (25-27), ethene (19-21), ethane (13-17), propene (7-9) and buta-1,3-diene (2-3), propane (<1), and traces (< 0.5) of trimethylsilane and tetramethylsilane. The formation of these products is accompanied by deposition of thin transparent films on the inside of the entire reactor. The relative amounts of the gaseous products are virtually independent of the photolysis progress and are in line with combination, dis-proportionaltion, cross-disproportionation and H-abstraction reactions of $H_2C=CH^{\bullet}$ and $CH_3^{\bullet}$ radicals produced upon cleavages of the $CH_3\text{-}Si$ and $O\text{-}CH_2$ bond of trimethyl (vinyloxy)silane. Another plausible route is subsequent decay (β-cleavage,) of the radical (I) yielding very reactive dimethylsilanone which is known to polymerize. These plausible steps are shown in Scheme 22.

$(CH_3)_3SiOCH=CH_2 \longrightarrow$

$CH_3^{\bullet} + {}^{\bullet}Si(CH_3)_2OCH=CH_2$ **(I)**

$\longrightarrow H_2C=CH^{\bullet} + {}^{\bullet}Si(CH_3)_3$

$2\,R^{\bullet} \longrightarrow CH_3\text{-}CH_3,\ CH_3\text{-}CH=CH_2,\ H_2C=CH\text{-}CH=CH_2$

$2\,H_2C=CH^{\bullet} \longrightarrow H_2C=CH_2 + HC\equiv CH$

$CH_3^{\bullet} + H_2C=CH^{\bullet} \longrightarrow CH_4 + HC\equiv CH$

$R^{\bullet} + (CH_3)_3SiOCH=CH_2 \rightarrow RH\ (R = CH_3, C_2H_3) + {}^{\bullet}H_2C(CH_3)_2SiOCH=CH_2$

${}^{\bullet}Si(CH_3)_2OCH=CH_2 \text{—}\beta\text{-cleavage}\rightarrow H_2C=CH^{\bullet} + (CH_3)_2Si=O$

$n\,(CH_3)_2Si=O \longrightarrow /(CH_3)_2SiO/_n$

Scheme 22

Insignificant amounts of trimethylsilane and tetramethylsilane were explained by very minor cleavage of the Si-O bond and by consecutive H-

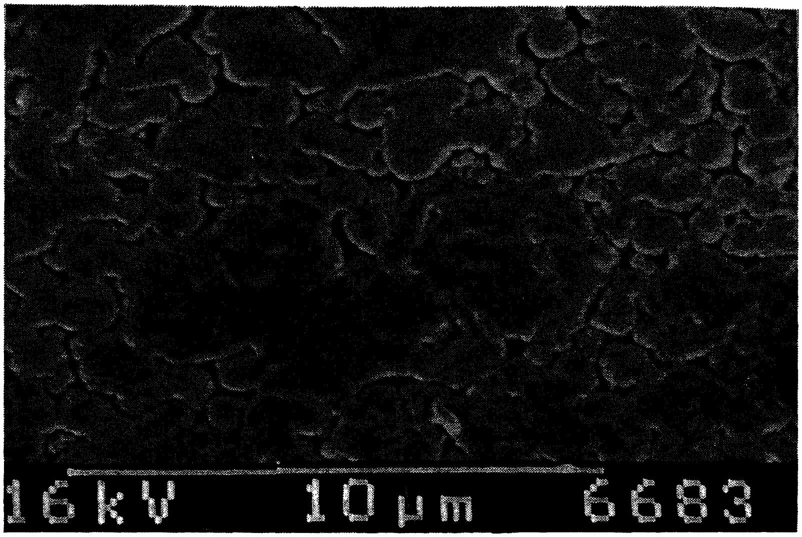

Fig. 20 SEM of the deposit from UVLP of trimethyl (propinyloxy)silane

abstraction by $(CH_3)_3Si^{\cdot}$ radical, and by recombination of $CH_3^{\cdot}$and $(CH_3)_3Si^{\cdot}$radicals, respectively. The detected final products indicate that trimethyl(vinyloxy)silane depletes by a blend of monomolecular decomposition and consecutive H-abstraction reactions of the parent with radicals producing unstable unsaturated which can be expected to split methyl radical and yield silene II ($.H_2C(CH_3)_2SiOCH{=}CH_2 \rightarrow CH_3.+ H_2C{=}Si(CH_3)OCH{=}CH_2$(II). The assumed steps thus produce very reactive products which can undergo a multitude of reactions as further cleavage and polymerizations. The complex reaction scheme and the occurrence of thermal radical chain reactions is supported by the estimated number of parent molecules depleated with one 193 nm photon. Within less than 5 % photolysis progress, this value ranges between 4-5.

The films deposited onto the substrates accommodated in the reactor show IR absorption spectrum [wavenumber/cm^{-1}, (normalised absorptivity)] - 806 (0.35), 845 (0.42), 1040 (1.00), 1260 (0.41), 2853 (0.10), 2926 (0.23) and 2962 (0.14) - which is the same regardless of the substrate positioning and which can be assigned, in the given order, to ν(Si-C), $\rho(CH_3Si)$, ν(SiO), $\delta(CH_3Si)$ and ν(C-H) vibrations. The absence of absorption bands belonging to C=C bonds (above 3000 cm^{-1}) indicates that the deposits can be described as a completely saturated polysiloxane. UV spectrum of these possess a maximum at ca. 204 nm, while the parent itself shows, due to a blend of contributions of both chromophore $H_2C{=}CH$ and Si-O-C groups, a bathochromic shift (maximum at 212 nm). The films deposited onto the reactor bottom which is outside the laser beam possess stoichiometry $Si^{\alpha}_{0.1}Si^{\beta}_{1.0}C_{4.5}O_{1.0}$, while those deposited onto the substrates affixed several mm behind the entrance quartz window and facing the laser beam show stoichiometry $Si^{\beta}_{1.0}C_{3.3}O_{1.0}$. The Si^{α} relates to elemental silicon and Si^{β} to silicon in organosiloxane polymer, respectively. The organosiloxane silicon highly prevails in the former and is the only form of silicon in the latter.

Silicon oxycarbides are of increasing interest in various fields of applied research and find use in ceramic sensors for oxygen detection in high temperature corrosive conditions and in photodetectors and solar cells. Different kinds of these Si/C/O and Si/C/H/O materials are known: black glasses were prepared by pyrolysis of polysiloxane gels, nanosized particles were synthesized by pyrolytic laser-aerosol interaction, and solid films were plasma-or IR laser-chemical-vapour-deposited by pyrolysis of gaseous organosilicon monomers. The presented results confirm that the UVLP of trimethyl (vinyloxy)silane adds to the list of the above techniques.

Laser Photolysis of Silane or Silacycle with Common Monomers

LPD of 1,1-dimethylsilacyclobutane[32] or IRMPD of silane[33] in the presence of some common monomers as vinyl acetate, allyl methyl ether, acrolein, methyl vinyl ether, methyl acrylate and methyl methacrylate affords both a number of volatile compounds and viscous or solid organosilicon products which are formed *via* addition of organosilicon transients to the double bond of the monomers. These photolyses can, in fact, be also used as the method of producing Si/C/H/O materials.

5.2 Photolysis of Disiloxanes

There has not been much interest in the thermal gas-phase behaviour of siloxanes despite broad-range application of these compounds. Disiloxanes are potential sources of silicon oxycarbides which are important in various fields of applied research and find use in ceramic sensors and solar cells. The Si/C/O films are known to be formed as an interface phase between SiC and SiO_2. The $Si_xO_yC_z$:H films were produced by plasma-enhanced chemical vapour deposition of siloxanes. There has, as yet, been little interest in the laser-induced gas phase decomposition of siloxanes for production of hydrogenated Si/C/O phases. Although some of the siloxanes were studied to reveal their modes of decomposition, no attention has been paid to solid materials produced. It is well established that (i) polydimethylsiloxanes thermally degrade in conventional (hot wall) pyrolytic reactors *via* cleavage of the thermodynamically stable Si-O bond, and that (ii) IR laser induced thermolysis of hexamethyl-disiloxane[34] occurring strictly in the gas phase (with no contribution from cold reactor surface) is controlled by cleavage of the relatively weak Si-C bond. These findings can only be explained by an enhancement of the Si-O cleavage *via* heterogeneous steps on hot reactor surface. Here we show IRMPD of two different disiloxanes, namely of

1,1,3,3-tetramethyldisiloxane and disiloxane and reveal that these compounds are excellent precursors for chemical vapour deposition of Si/C/O and Si/O films.

IRMPD of 1,1,3,3-tetramethyldisiloxane

The TEA CO_2 laser irradiation into the strong δ(SiH) absorption band of 1,1,3,3-tetramethyldisiloxane yields methane, ethane, ethene, ethyne, dimethylsilane and trimethylsilane together with solid films being concomittantly deposited onto the substrate surface. The stoichiometry of the topmost layers determined from the XPS data was $Si_{1.00}C_{1.06}O_{0.90}$ and the binding energy of Si 2p electrons of the deposit was consistent with that of organosilicon polymers. The spectrum of Si 2p electrons revealed two different chemical states of Si assignable to C-Si-C and C-Si-O bonding. The ratio of absorptivities A[ν(C-H): A[ν(Si-H)] ranged between 0.9-1.2, which is higher than that for the parent compound and shows that the deposits possess lower content of H (Si) relative to H (C). The deposited films are composed of agglomerates larger than 10 μm which are bonded together. The observed gaseous products and the stoichiometry of the deposited films are consistent with the cleavage of both Si-C and Si-O bonds. The cleavage of the Si-C bond is the channel producing a methyl radical which can abstract H (Si) from the parent to form methane, and recombine to ethane. Ethyne and ethene apparently arise from hot ethane molecules. The thermal split of the strong Si-O bond in of 1,1,3,3-tetramethyldisiloxane is surprising, since this cleavage of peralkylsiloxanes is prohibited under catalyst-free conditions. The observation of both Si-C and Si-O bond cleavages in the IRMPD of 1,1,3,3-tetramethyldisiloxane is thus indicative of a feasible split of the Si-O bond in disiloxanes possessing Si-H bonds and suggests that the ease of the Si-O bond cleavage is enhanced by H-substitution at the silicon.

LPD of disiloxane

The absorption of the cw CO_2 laser radiation in the δ(H_3Si) mode of $H_3SiOSiH_3$ and ν(S-F) mode of SF_6 results in decomposition of disiloxane, the formation of gaseous silane and hydrogen and deposition of a solid material manifesting itself as thin transparent films or thicker yellowish layers[35]. The yield of silane is within the 30-70 % decomposition range ~ 0.75-0.90 mole/mole of disiloxane decomposed. This value being lower than 1 can be rationalised in terms of a minor silane decomposition into H_2 and a solid Si/H or Si^o material.

Photoelectron spectroscopy of the films reveals that the O/Si ratio in all the deposits is close to 1. The IR spectra of the deposited films show very strong and broad band due to ν(Si-O-Si) mode at ~1086 cm^{-1} and several minor bands assignable to vibrations of H_nSi (O) moiety at 803, 870, 980, 2183 and 2250 cm^{-1}. The bands observed at 2183 and 2250 cm^{-1} can be unambiguously assigned to the H_2Si (O) structural unit; the lack of bands at ca. 2100 and 2000 cm^{-1} is indicative of an absence of $(SiH_2)_n$ and $(SiH)_n$ structures in which the Si-H bond is isolated from oxygen by at least two silicon atoms.

The observed volatile products can in principle, be formed by three different mechanisms. These are (a) bimolecular formation of a four-centre intermediate depicted for the primary reaction stage by Scheme 23, (b) monomolecular cleavage *via* a four-centre transition state (Scheme 24), and (c) a radical chain process similar to that reported

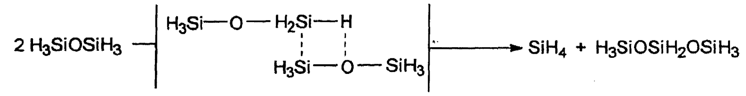

Scheme 23

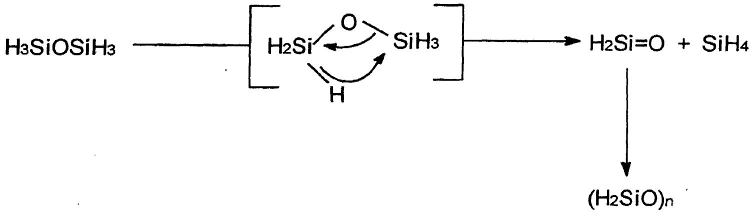

Scheme 24

for decomposition of dimethyl ether (Scheme 25).

$H_3SiOSiH_3 \longrightarrow H_3Si^{\cdot} + {}^{\cdot}OSiH_3$
$H_3Si^{\cdot} + H_3SiOSiH_3 \longrightarrow SiH_4 + {}^{\cdot}SiH_2OSiH_3$
${}^{\cdot}SiH_2OSiH_3 \longrightarrow H_2SiO + SiH_3$
$n\ H_2SiO \longrightarrow (H_2SiO)_n$

Scheme 25

Neither scavenging experiments, nor experiments with isotopomeric precursors helped decide: silanone trapping with alkoxysilanes was unsuccessful, and the irradiation of $H_3SiOSiH_3$ - $D_3SiOSiD_3$-SF_6 mixtures afforded all the H_nSiD_{4-n} isotopomers. The latter fact cannot, however, be taken as an evidence of the radical chains, since the SiH_4 and SiD_4 once produced by the molecular elimination could undergo H/D scrambling.

Irradiations of disiloxane and c-hexene (chemical thermometer) in the presence of SF_6 –the procedure for non-interfering systems - allowed to estimate the Arrhenius parameters of the decomposition of disiloxane as log A = 13.1 ± 0.8 s^{-1} and E_a = 234 ± 8 $kJ.mol^{-1}$ (Fig. 21) which are in keeping with the suggested four-centre cyclic transition state of the unimolecular decomposition depicted in Scheme 24. Provided that the activation energy of the overall dimethyl ether decomposition corresponds to essentially the C-O bond energy (approximately 300 kJ. $mole^{-1}$), the operation of the analogous radical-chains in the disiloxane decomposition would lead to the much higher activation energy reflecting the dissociation energy of the Si-O bond (ca. 500 kJ. $mole^{-1}$). The transient occurrence of silanone $H_2Si{=}O$ is supported by a very minor formation of trisiloxane, cyclotrisiloxane, tetrasiloxane and cyclo-tetrasiloxane all of which were identified by GC/MS technique. These products can be only rationalized in terms of $H_2Si{=}O$ insertion into disiloxane, or of $H_2Si{=}O$ cyclotrimerization and cyclotetramerization.

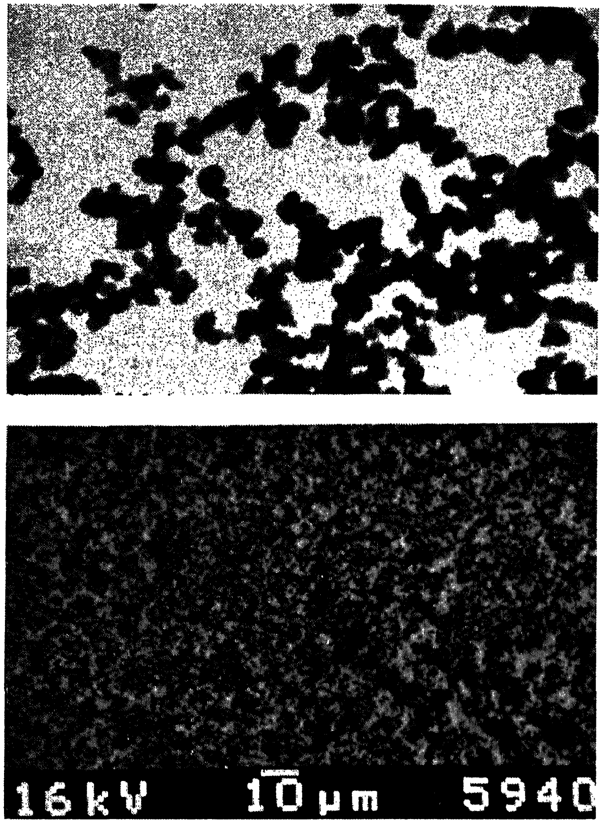

Fig. 22 SEM and TEM (magnification 30,000 x) of the deposit from LPD of disiloxane

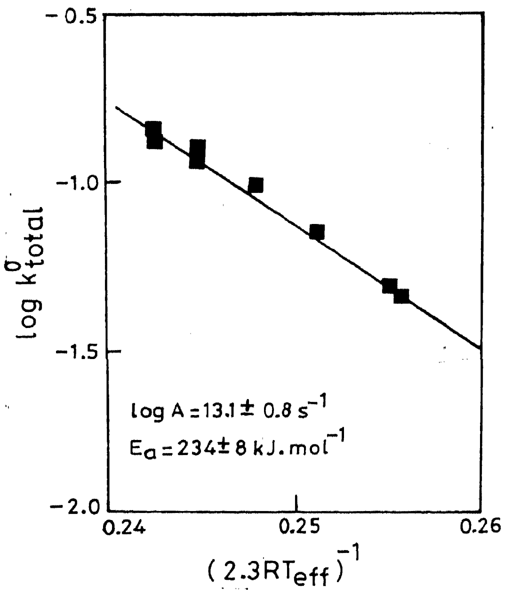

Fig. 21 The Arrhenius log k^0_{total} vs T_{eff}^{-1} plot for cw CO_2 LPD of disiloxane using c-hexene as marker

The deposited films consist of agglomerates which have continuous structure (Fig. 22). Transmission electron microscopy analysis confirms this fact and shows particles of ca. 100 nm size which are bonded together (Fig. 22). Also these features are consistent with residual reactivity of depositing agglomerates which increase their size not only in the gas phase but also after their deposition on the reactor surface.

We conclude that the continuous-wave CO_2 laser induced gas-phase decomposition of $H_3SiOSiH_3$, dominated by elimination and polymerization of transient silanone $H_2Si{=}O$ and yielding silane and hydrogen as side-products, represents a convenient process for chemical vapour deposition of poly(hydridosiloxane) films which are promising materials for microelectronics. The procedure represents a convenient alternative to formation Si/O phases achieved through gas-phase oxidation of hazardous silane.

6 Acknowledgement

The author is thankful to the Grant Agency of the Academy of Sciences of the Czech Republic (Grant No. A4072806) for support.

References

1 J S Haggerty and W R Cannon in *Laser Induced Chemical Processes* (Ed J I Steinfeld) Plenum Press New York (1981)

2 (a) V S Letokhov *Nonlinear Laser Chemistry* Springer Berlin (1983)
(b) W C Danen J C Jang in *Laser-induced Chemical Processes* (Ed J I Steinfeld Plenum New York (1981)
(c) (Ed C D Cantrell) *Multiple-photon Excitation and Dissociation of Polyatomic Molecules* Springer Berlin (1986)

3 (a) W M Shaub and S H Bauer *Int J Chem Kinet* 7 (1975) 509
(b) D K Russell *Chem Soc Rev* **19** (1990) 407
(c) J Pola *Spectrochim Acta* Part A **46** (1990) 607

4 G Raabe and J Michl *Chemistry of Organic Silicon Compounds* (EdsD Patai and Z Rappoport) Wiley New York 198

5 (a) J Pola V Chvalovský E A Volnina and L E Gusel'nikov *J Organometal Chem* **341** (1988) C13
(b) J Pola E A Volnina and L E Gusel'nikov *J Organometal Chem* **391** (1990) 275
(c) D Čukanová and J Pola *J Organometal Chem* **453** (1993) 17

6 M Jakoubková R Fajgar J Tláskal and J Pola *J Organometal Chem* **466** (1994) 29

7 Z Bastl H Bürger R Fajgar D Pokorná J Pola M Senzlober J Šubrt and M Urbanová *Appl Organometal Chem* **10** (1996) 83

8 S Dhanya A Kumar R K Vatsa R D Saini J P Mittal and J Pola *J Chem Soc Faraday Trans* **92** (1996) 179

9 L Khachatryan E A Volnina R Fajgar and J Pola *J Organometal Chem* **566** (1998) 263

10 (a) S Bailleux M Bogey J Breidung H Bürger R Fajgar Y Liu J Pola M Senzlober and W Thiel *Angew Chem Int Ed Engl* **35** (1996) 2513
(b) S Bailleux M Bogey J Demaison H Burger M Senzlober J Breidung W Thiel R Fajgar and J Pola *J Chem Phys* **106** (1997) 10016

11 J Pola Z Bastl J Šubrt and R Taylor *J Mater Chem* 5 (1995) 1345

12 R K Vatsa A Kumar P D Naik H P Upadhyaya U B Pavanaja R D Saini J P Mittal and J Pola *Chem Phys Lett* **255** (1996) 129

13 M Sedláčková J Pola E A Volnina and L E Gusel'nikov *J Anal Appl Pyrol* **14** (1989) 345

14 M Urbanová E A Volnina L E Gusel'nikov Z Bastl J Pola *J Organometal Chem* **509** (1996) 73

15 M Urbanová and J Pola *J Anal Appl Pyrol* **24** (1993) 325

16 J Pola A Ouchi M Urbanová Y Koga Z Bastl and J Šubrt *J Organometal Chem* **575** (1999) 246

17 M Santos L Díaz Z Bastl V Hulínský M Urbanová J Vítek and J Pola *J Mater Chem* 6 (1996) 975

18 J Pola J Vítek Z Bastl M Urbanová J Šubrt and R Taylor *J Mater Chem* 7 (1997) 1415

19 M Santos L Díaz J A Torresano and J Pola *J Photochem Photobiol A: Chem* **104** (1997) 19

20 E A Volnina J Kupčík Z Bastl J Šubrt L E Gusel'nikov and J Pola *J Mater Chem* 7 (1997) 637

21 V Dřínek Z Bastl J Šubrt and J Pola *Appl Organometal Chem* **12** (1998) 427

22 V Dřínek Z Bastl J Šubrt R Taylor and J Pola *J Anal Appl Pyrol* **35** (1995) 199

23 J Pola Z Bastl J Šubrt J R Abeysinghe and R Taylor *J Mater Chem* 6 (1996) 155

24 (a) J Pola Z Bastl J Tláskal H Beckers H Bürger and P Moritz *Organometallics* **12** (1993) 171
(b) J Pola H Beckers and H Bürger *Chem Phys Lett* **178** (1991) 192
(c) C L Siguenza L Díaz P F González-Díaz H Bürger H Beckers and J Pola *Spectrochim Acta* 50A **1207** (1994)

25 (a) J Pola and S Simeonov J Chem Soc Perkin 2 (1991) 101
(b) L Díaz M Santos C L Siguenza S A Simeonov P F González-Díaz J A Garcia Dominguez R Fajgar Z Bastl J Tláskal J Pola *J Chem Soc Faraday Trans* **89** (1993) 3907
(c) J Pola Z Papoušková Z Bastl and J Tláskal *Appl Phys* **B 56** (1993) 313
(d) J Pola Z Bastl and J Tláskal *Infrared Phys* **30** (1990) 355
(e) S Simeonov and J Pola *Spectrochim Acta* 46A (1990) 443

26 J Pola Z Bastl J Tláskal H Beckers H Bürger P Moritz P Weiss and M Sigrist *Appl Organometal Chem* 7 (1993) 381

27 (a) H Morita and T Sadakiyo *J Photochem Photobiol A* : Chem **87** (1995) 163
(b) H Morita and M Shimizu *J Phys Chem* **99** (1995) 7621
(c) A Matsuzaki Y Hamada H Morita and T Matsuzaki *Chem Phys Lett* **190** (1992) 337

28 (a) J Pola A Lyčka L E Gusel'nikov and V V Volkova *J Chem Soc Chem Commun* (1992) 20
(b) M Urbanová J Vítek Z Bastl K Ubik and J Pola *J Mater Chem* 5 (1995) 849
(c) M Jakoubková Z Bastl R Fajgar and J Pola *Appl Surf Sci* **86** (1995) 530

(d) J Pola *J Anal Appl Pyrol* **30** (1994) 73

29 J Pola and H Morita *Tetrahedron Lett* **38** (1997) 7809

30 M Urbanová H Morita V Dřínek Z Bastl J Šubrt and J Pola *J Anal Appl Pyrol* **44** (1998) 219

31 A Ouchi Y Koga Z Bastl and J Pola *Appl Organometal Chem* **13** (1999) 643

32 J Pola D Čukanová M Minárik A Lyčka and J Tláskal *J Organometal Chem* **426** (1992) 23

33 (a) R Alexandrescu J Morjan C Grigoriu I N Mihailescu Z Bastl J Tláskal R Mayer and J Pola *Appl Phys* A **46** (1988) 768

(b) Z Papoušková J Pola Z Bastl and J Tláskal *J Macromol Sci : Chem* A **27** (1990) 1015

34 (a) W F Manders and J M Bellama *J Polym Sci Polym Chem* **23** (1985) 351

(b) J Pola R Alexandrescu J Morjan and D Sorescu *J Anal Appl Pyrol* **18** (1990) 71

35 J Pola M Urbanová V Dřínek J Šubrt and H Beckers *Appl Organometal Chem* **13** (1999) 655.

RESONANCE RAMAN INTENSITY ANALYSIS APPLIED TO PHOTODISSOCIATION REACTIONS OF POLYATOMIC MOLECULES

DAVID LEE PHILLIPS*

Department of Chemistry, University of Hong Kong, Pokfulam Road, Hong Kong

We present several applications of resonance Raman intensity analysis to the investigation of direct photodissociation reactions in polyatomic haloalkane molecules. Our studies show that direct C-I bond cleavage in polyatomic iodoalkanes and other haloalkanes have multidimensional reaction coordinates that appear to be qualitatively consistent with impulsive "semi-rigid"radical descriptions of the photodissociation dynamics. We also find that the initial photodissociation dynamics show interesting correlation with trends observed in the results of energy partitioning to the reaction products as determined by time-of-flight photofragment spectroscopy experiments. Comparison of gas and solution phase short-time photodissociation dynamics shows that they are generally very similar in the Franck-Condon region of the reaction but can be significantly different in the case where symmetry breaking occurs such as in the diiodomethane molecular system. We have examined several examples of bond selective electronic excitation in dihalomethane and dihaloethane molecules and have found that the short-time photodissociation dynamics show some correlation with the degree of interaction between the two carbon-halogen chromophores and we discuss the implications for bond selective photochemistry and energy partitioning.

Key Words: Raman Spectroscopy; Photodissociation; Chemical Dynamics; Iodoalkanes; Haloalkanes

Introduction

This review article will focus on using resonance Raman intensity analysis to examine the Franck-Condon region of molecular electronic excited states associated with direct photodissociation reactions. This article is not intended to be comprehensive on either resonance Raman intensity analysis or direct photodissociation reactions, but is meant to provide a range of examples of the applications of resonance Raman intensity analysis to direct photodissociation reactions. There are several excellent reviews on the general aspects of resonance Raman intensity analysis and the reader is referred to these for more details and a broader understanding of this topic.[1-8] Examples of molecular systems studied by the author in the laboratory over the past six years have been stated in this article alongwith a number of other selected applications. For the purpose of this review article, a focus on haloalkane molecular systems have been given since they were extensively studied as examples and prototypes for understanding direct photodissociation reactions.

Haloalkanes and in particular the A-band photodissociation reactions of iodoalkanes have been intensely studied as model molecular systems for better understanding direct photodissociation reactions. The A-band absorption spectra of gas and solution phase iodoalkanes are smooth and featureless. They are composed of three transitions ($^3Q_0$, $^1Q_1$, and $^3Q_1$) of which the $^3Q_0$ transition accounts for most of the oscillator strength and correlates with production of I* photofragments.[9-11] Ground electronic state iodine atoms (I) may be produced in significant amounts due to an electronic non-adiabatic curve-crossing of the $^3Q_0$ state by the $^1Q_1$ state.[12-19] Photofragment anisotropy measurements from molecular beam experiments have demonstrated that the direct C-I bond breaking process occurs much faster than the rotational period of the parent molecule.[19-26]

Iodomethane has been by far the most intensively examined A-band photodissociation reaction for iodoalkane molecules. Magnetic

*E-mail: Phillips@HKUCC.HKU.HK. Fax: 852-2857-1586

circular dichroism (MCD) measurements have shown that the $^3Q_0$ transition located near the center of the A-band absorption has approximately 70-80% of the total oscillator strength with the $^3Q_1$ and $^1Q_1$ near the red and blue edges of the absorption having the rest of the oscillator stength.[10] High resolution time-of-flight photofragment spectroscopy experiments displayed noticeable internal energy in the umbrella mode vibration of the methyl radical photofragment.[20,21] Several different techniques such as multiphoton ionization (MPI), coherent anti-Stokes Raman scattering (CARS), diode laser absorption, and others have been used to measure the vibrational and rotational state distributions of the methyl radical photofragments produced from the A-band photodissociation reaction.[27-32] The iodomethane A-band photodissociation reaction time has been directly measured using femtosecond time-resolved pump-probe experiments.[33,34] Different potential energy surfaces and theoretical models with differing degrees of complexity have been used to simulate the A-band photodissociation reaction of iodoalkanes.[35-44] Much of the experimental data available for iodomethane has been simulated using fully quantum mechanical calculations with fairly accurate *ab initio* potential energy surfaces.[43,44] Thus, the major aspects of the A-band photodissociation reaction of iodomethane have been elucidated.

The A-band photodissociation reactions of larger iodoalkanes as well as dihaloalkanes have not been nearly as intensively investigated as has iodomethane. Inspection of larger haloalkanes allow one to examine how the molecular structure and substituents change the photodissociation dynamics, energy partitioning to the photofragments and the probability of $^3Q_0$ to $^1Q_1$ curve crossing. Time-of-flight translational spectroscopy experiments carried out for several larger iodoalkanes have shown that as the alkyl group becomes more massive and/or more branched in structure then the amount of internal excitation of the alkyl radical photofragment increases.[19-26,45-53] A variety of experimental determinations of the I*/I ratio as a function of the structure and mass of the parent iodoalkane demonstrated that more I photofragment is produced as the iodoalkane molecule becomes more massive or more branched in structure.[12-19,54-61] These results imply that the $^3Q_0$ to $^1Q_1$ curve crossing probability has a degree of dependence on the amount of internal energy imparted to the alkyl photofragment: less of the available energy of the photodissociation reaction is imparted into translational of the two photofragments as more of the available energy is partitioned to internal excitation of the alkyl photofragment and this leads to an increase in the curve crossing probability.

The energy partitioning associated with A-band iodoalkane photodissociation reactions have been interpreted in terms of two simple models for the photodissociation dynamics of direct bond breaking reactions.[20,23-25] One model called the "rigid radical" model assumes that the alkyl radical maintains the same structure during the photodissociation and this results in only internal excitation of the rotational degree of freedom for the alkyl radical. The other model called the "soft radical" model assumes that the α-carbon atom is very loosely linked to the rest of the alkyl radical which results in the α-carbon atom being shoved into the rest of the radical during the C-I bond breaking and this gives rise to internal excitation of both vibrational and rotational degrees of freedom. Both the "rigid radical" and "soft radical" models of the photodissociation dynamics do not realistically describe the α-carbon atom bonding to the rest of the radical during the photodissociation reaction. In the "rigid radical" model the α-carbon atom is too strongly bonded to the rest of the radical in order to maintain a rigid alkyl radical structure during the photodissociation. However, in the "soft radical" model the α-carbon atom is too weakly bonded to the rest of the alkyl radical during the photodissociation reaction. The energy disposal observed for most iodoalkane molecular systems examined so far are somewhere between the results predicted by the "rigid radical" and "soft radical" models although most experimental results are closer to the values of the "soft radical" model.[20,23-25] More accurate and realistic models for direct photodissociation dynamics need to be developed to better describe the energy partitioning. In order to do this, it would be very helpful to examine the initial photodissociation dynamics at the vibrational-mode specific level. Resonance Raman spectroscopy can be used to investigate the initial or short-time photodissociation dynamics at the vibrational-mode specific level and provide an additional experimental constraint on newly developed models of direct photodissociation reactions. In this review article results of several resonance Raman intensity analysis investigations done for selected haloalkane molecular systems have been presented. These resonance Raman studies examine how the initial or short-time photodissociation dynamics are influenced by substituents and molecular structure.

Experimental

A brief description of the experimental apparatus and methods to obtain resonance Raman spectra of photodissociating molecules[62-73] is now presented. Spectroscopic grade solvent (usually cyclohexane, methanol or acetonitrile) and the haloalkane under investigation were used to prepare samples for the solution phase resonance Raman experiments. Concentrations for the samples could vary from 0.05 to 0.3 M depending on the strength of the A-band absorption. The harmonics of a nanosecond Nd:YAG laser and their hydrogen Raman shifted laser lines provided the excitation wavelengths for the resonance Raman experiments. Typically, the excitation laser used 50 to 100 μj loosely focused to a 1 mm diameter on the flowing liquid stream of sample. A backscattering geometry was used to collect the Raman scattered light from the excited portion of the flowing liquid sample. Reflective optics (an ellipsoidal mirror with f/1.4 and a flat mirror) were used to collect the Raman light and image it through a depolariser and the entrance slits of a 0.5 metre spectrograph. The 1200 groove/mm grating of the spectrograph dispersed the Raman scattered light onto a liquid nitrogen cooled CCD detector mounted on the exit port of the spectrograph. The signal of the CCD was acquired from 60 to 600 s before being read out from the CCD detector to an interfaced PC computer. The summation of ten to thirty of these readouts gave the resonance Raman spectrum.

The gas phase resonance Raman experiments used the same excitation source, collection optics, and detection equipment as the solution phase experiments. The gas phase sample handing apparatus was composed of a heated reservoir of liquid and vapour haloalkane connected to a heated pipette. Dry nitrogen was flowed through this sample reservoir to take away some of the haloalkane vapour with it out through the pipette nozzle. The excitation laser beam was loosely focused near the exit of the pipette nozzle. An approximate 90 degree geometry was used for collection of the Raman scattered light using the reflective optics. So as to avoid interference from photoproduct bands, the excitation laser power was kept fairly low (typically < 100 μj over a 2 mm beam diameter). The excitation laser light was not noticeably attenuated by the vapour haloalkane sample in the gas phase experiments and the sample reabsorption of the resonance Raman scattering was minimal for the gas phase resonance Raman spectra.

The wavenumber Raman shifts of the resonance Raman spectra were calibrated by the known vibrational frequencies of the solvent for the solution phase spectra and the mercury emission lines as well as gas phase nitrogen and oxygen Raman bands for the gas phase spectra. The reabsorption of the Raman scattered light by the sample in the solution phase experiments was minimized by the backscattering geometry employed in the experiments. Any remaining sample reabsorption of the resonance Raman scattering in the solution phase spectra was corrected for by the methods described in ref. [74]. An appropriately scaled solvent spectrum was subtracted from the reabsorption corrected solution phase resonance Raman spectrum in order to eliminate the solvent Raman bands. The channel to channel variation of the entire detection apparatus was corrected for using a spectrum obtained of a calibrated intensity standard deuterium lamp and/or a calibrated intensity standard tungsten lamp. Portions of the corrected resonance Raman spectra were fitted to a base line plus a sum of Lorentzians to obtain the integrated areas of the Raman bands. Absolute Raman cross sections were determined using spectrophotometrically measured sample concentrations and previously measured absolute Raman cross sections for solvent bands[75,76] as an internal standard. For the experimental details associated with any particular molecular system, the reader is referred to the original publications.

Theory and Calculations

The theory and calculations used to simulate the experimental resonance Raman and absorption cross sections associated with the A-band photodissociation reactions of haloalkanes[62-73] are now described. We have used a relatively simple model and time-dependent wavepacket calculations in order to extract the major features of the A-band haloalkane short-time photodissociation dynamics. The models and calculations that we use are not intended to be a complete description of the resonance Raman and absorption spectra, but are meant to provide a modest beginning to better understand the vibrational mode-specific dynamics of the initial bond cleavage process in A-band haloalkanes. The simulation results will also provide a useful reference to which more sophisticated computational results can be compared to assess the relative importance of effects like the possible Duschinsky rotation of normal coordinates, nonadiabatic curve crossings, possible coordinate dependence of the transition dipole moment, and others.

We generally use the following formula to simulate the A-band absorption spectra of haloalkanes:

$$\sigma_A(E_L) = (4\pi e^2 E_L M^2 / 3n\hbar^2 c) \sum_i P_i \operatorname{Re} [\int_0^\infty \langle i|i(t)\rangle \exp[i(E_L+\varepsilon_i)t/\hbar]\exp[-g(t)]\, dt] \quad \ldots (1)$$

The resonance Raman cross sections were computed from the following expression:

$$\sigma_{R,}(E_L, \omega_s) = \sum_i \sum_f P_i\, \sigma_{R,i\to f}(E_L)\, \delta(E_L + \varepsilon_i - E_S - \varepsilon_f)$$

with

$$\sigma_{R,i\to f}(E_L) = (8\pi e^4 E_S^3 E_L M^4 / 9\hbar^6 c^4) \left| \int_0^\infty \langle f|i(t)\rangle \exp[i(E_L+\varepsilon_i)t/\hbar] \exp[-g(t)]\, dt \right|^2 \quad \ldots (2)$$

where E_L is the incident photon energy, E_S is the scattered photon energy, M is the transition length evaluated at the equilibrium geometry, n is the solvent index of refraction, P_i is the initial Boltzmann population of the ground-state energy level $|i\rangle$ which has energy ε_i, f is the final state for the resonance Raman process, and ε_f is the energy of the ground state energy level $|f\rangle$. $\delta(E_L + \varepsilon_i - E_S - \varepsilon_f)$ is a delta function to sum cross sections with the same frequency and $|i(t)\rangle = e^{-iHt/\hbar}|i\rangle$ is $|i(t)\rangle$ propagated on the excited state surface for a time t where H is the excited state vibrational Hamiltonian. The $exp[-g(t)]$ term in eqs. (1) and (2) is a damping function which is usually expected for the directly photodissociating A-band haloalkanes to be mostly direct photodissociation population decay with some solvent dephasing for the solution phase reactions. Addition over a ground state Boltzmann distribution of vibrational energy levels (298 K temperature distribution) was usually used to compute the absorption and resonance Raman cross sections.

The ground and excited state potential energy surfaces were approximated by harmonic oscillators displaced by Δ in dimensionless normal coordinates. We assumed the Condon approximation (e.g. no coordinate dependence of the transition length). The resonance Raman intensities of the first several overtones and combination bands are determined mainly by the slope of the excited state surface in the Franck-Condon region when no vibrational recurrences take place as is the case for a direct photodissociation reaction. The gas and solution phase A-band absorption spectra of haloalkanes are typically structureless and this suggests that the total electronic dephasing is mostly due to direct photodissociation prior to the first vibrational recurrence time. The wavepacket propagation in the calculations was usually cut off after 30 or 40 fs in order not to allow any significant recurrences of the wavepacket to the Franck-Condon region. The $\langle f|i(t)\rangle$ overlaps decay and reach a negligible value after 20 to 30 fs for the resonance Raman bands observed in our experimental spectra for the haloalkanes we have examined so far. Thus, the cut-off at 30 to 40 fs only prevents the wavepacket to return to the Franck-Condon region and helps to better model the direct photodissociation reactions of A-band haloalkanes. For the solution phase studies, the effects of solvent dephasing collisions on the absorption and resonance Raman cross sections were modeled by an exponential decay (where the $exp[-g(t)]$ term in equations (1) and (2) was replaced by $\exp[-t\Gamma/\hbar]$). The bound harmonic oscillator model for the excited state used for our simulations of the A-band haloalkanes only provides us a convenient method to mimic the portion of the excited state that determines the resonance Raman intensities and absorption spectrum and does not imply the excited state is bound.

The potential parameters in equations (1) and (2) are typically given in terms of dimensionless normal coordinates. So as to easily visualize the short-time photodissociation dynamics in terms of bond length and bond angle changes, we converted the normal coordinate motions into internal coordinate motions. The center of the wavepacket motion undergoing separable harmonic dynamics in terms of dimensionless normal coordinates at time t after photoexcitation to the excited state can be expressed by

$$q_\alpha(t) = \Delta_\alpha (1-\cos\omega_\alpha t) \qquad (3)$$

The time, t, is in units of fs and the vibrational frequency, ω_α, is in units of fs^{-1}. We fix $q_\alpha = 0$ for each mode α at the ground electronic state equilibrium geometry. At different times t the internal coordinate displacements are obtained from the dimensionless normal mode displacements ($q_\alpha(t)$) using the following formula:

$$s_i(t) = (h/2\pi c)^{1/2}\, \Sigma_\alpha A_{\alpha i}\, \varpi_\alpha^{-1/2}\, q_\alpha(t) \qquad \ldots (4)$$

S_i are the displacements of the internal coordinates (bond stretches, bends, torsions, and wags as defined by Wilson, Decius, and Cross) from their ground electronic state equilibrium values. $A_{\alpha i}$ is the normal-mode coefficient ($\partial s_i/\partial Q_\alpha$) with Q_α = the ordinary dimensioned normal coordinate. ω_α is the vibrational frequency in units of cm^{-1}. For each of the haloalkane molecular systems that has been investigated, normal coordinate calculations have been done using a modified version of the Snyder and Schachtschneider FG program[77] and used either a previously reported force field to which small modifications were incorporated to better fit the experimental vibrational frequencies or a force field that has been derived. The results of these normal coordinate calculations were then used to compute the normal mode vectors for the haloalkane under investigation. For more detailed descriptions of the models and calculations used for any particular haloalkane, the reader is referred to the original publications associated with that particular haloalkane molecular system.

Results and Discussion

A. Iodomethane

There have been many resonance Raman and/or emission studies done for the A-band iodomethane direct photodissociation reaction. Brus and Bondybey[78] first examined the emission produced by iodomethane in low temperature matrices following A-band absorption photoexcitation and they observed many C-I stretch higher overtones. Kinsey and coworkers carried out the first resonance Raman experiments on the A-band photodissociation reaction of iodomethane in the gas phase.[79-81] Their initial resonance Raman experiments[79] published in 1984 showed a long overtone progression in the nominal C-I stretch mode ($n\nu_3$) with a small combination band progression of the methyl umbrella mode plus the C-I stretch overtones ($\nu_2+n\nu_3$). These spectra were consistent with a qualitative model of the photodissociation in which the C-I bond lengthens during the photodissociation and the CH_3I tetrahedral angles relax toward a planar CH_3 photofragment. The observed slow increase in the combination band progression of the methyl unmbrella mode plus the C-I stretch overtones ($\nu_2+n\nu_3$) relative to the C-I stretch overtones ($n\nu_3$) with an increase in n reflects the progressive preference for planar CH_3 geometries as the C-I bond becomes longer on the $^3Q_0$ potential energy surface. Kinsey and coworkers later carried out higher resolution studies on both CH_3I and CD_3I.[80] They also obtained detailed excitation profiles and depolarization ratio experiments for gas phase iodomethane.[81] Kinsey and coworkers found that the depolarization ratios of all of the Raman bands examined were close to one third which is the value expected for a parallel transition to one or more excited states.[81] They also found that the Raman excitation profiles for overtones and combination bands had simple smooth contours and could be fit well using the short-time theory of Raman scattering for motion on a single repulsive potential energy surface.[81] However, the C-I stretch fundamental Raman excitation profile had a bimodal shape and could be fit reasonably well using a model where the C-I stretch fundamental was perturbed by off resonant interference from a higher energy state or states with parallel transition character.[81] The next section discusses this type of resonant-preresonant interference in the Raman excitation profiles of fundamental bands.

Several other groups have also examined various aspects of the A-band iodomethane photodissociation reaction. Butler and coworkers[82] measured depolarization ratios of gas phase iodomethane for the C-I stretch overtones ($n\nu_3$) up to n=12. They found that while the fundamental and lower overtones had depolarization ratios close to one third, the higher overtone depolarization ratios progressively increased noticeably.[82] This behaviour was ascribed to effects of the amount of wavepacket sampling of the $^3Q_0$-$^1Q_1$ conical intersection.[82] However, a later study by Ziegler *et* *al.*[83] using higher resolution and a different depolarization ratio measurement method found Raman depolarization ratios that disagree a bit with previous results by Butler and coworkers[82] as well as Kinsey and coworkers.[81] Ziegler and coworkers[83] did not find as strong a change in depolarization ratio with vibrational quantum number as did Butler and coworkers.[82] Ziegler and coworkers used the ratio of oscillator strengths of the $^3Q_0$ and $^1Q_1$ transitions found by the MCD measurements of Gedanken and Rowe and showed that their Raman depolarization ratios and rotational contours can be modeled reasonably well using interference due to two processes: parallel absorption followed by parallel emission ($^3Q_0$) and perpendicular absorption followed by perpendicular emission ($^1Q_1$).[83] This is somewhat different from the conclusions of Butler and coworkers[82] and Kinsey and coworkers.[81] Further work is needed to completely resolve the issue of how sensitive the iodomethane Raman depolarization ratios are to nonadiabatic interactions and/or how much direct excitation of the $^1Q_1$ transition contributes to the resonance Raman intensities.

Myers *et al.*[84-86] examined the solution phase resonance Raman spectra of iodomethane in several different solvents. The solution phase spectra were very similar to those in the gas phase and also exhibited most of their intensity in the C-I stretch overtone progression. Detailed comparison of the iodomethane spectrum in hexane solution with previous gas phase spectra showed the spectra were almost the same up to n= 9 of the C-I stretch overtone progression and very similar to one another up to n=16 (though the solution Raman band positions shifted slightly to lower frequency due to solvent-solute attractive interactions). The solution phase Raman band positions may shift slightly relative to the gas phase values due to the balance of attractive versus repulsive solvent-solute forces on the ground state potential energy surface. The solution phase resonance Raman relative intensities may change somewhat in the Franck-Condon region due to solvent effects on the excited state. However, the solution phase resonance Raman spectra of iodomethane are very similar to the corresponding gas phase spectra and indicate that the short-time photodissociation dynamics near the Franck-Condon geometries are very similar to one another.

Many theoretical models and potential energy surfaces have been developed and applied to the A-band photodissociation of iodomethane over the years.[35-44] These models and potential energy surfaces have become increasingly sophisticated and better able to model the experimental data available. Fully quantum mechanical simulations using fairly accurate *ab initio* potential energy surfaces were used to fit much of the available experimental data for iodomethane[43,44] and it appears the major features of the A-band photodissociation have been elucidated. However, there are still some aspects of the A-band photodissociation of iodomethane that need to be better understood such as the role of the $^1Q_1$ transition in the A-band absorption and resonance Raman spectra and nonadiabatic effects on the resonance Raman depolarization ratios. For a more complete discussion of the A-band photodissociation reaction of iodomethane and the interplay between theory and experiment in better understanding this reaction, the reader is referred to the excellent recent review article by Kinsey and coworkers.[6]

B. Higher Iodoalkanes: Effects of Mass and Branching of the Alkane Chain

Fig. 1 shows the absorption spectra of iodoethane, 2-iodopropane, and 2-methyl-2-iodopropane in cyclohexane solution. The excitation frequencies for the resonance Raman experiments are shown in nm above each absorption spectrum. All of the iodoalkanes have very similar A-band absorption spectra with a maximum near 260 nm and modest intensity.[87-90] The iodoalkanes also have a much larger B-band absorption ~196 nm due to transitions to a bound Rydberg state which predissociates to the lower purely repulsive electronic states.

Figs. 2-4 give an overview of the A-band and B-band resonance Raman spectra obtained for iodoethane, 2-iodopropane, and 2-methyl-2-iodopropane for the excitation wavelengths indicated in Fig. 1.[89] Fig. 5 presents an expanded view of the 258 nm A-band resonance Raman spectrum of iodoethane in cyclohexane solution. The spectra in Figs. 2-5 have been corrected for sample reabsorption of the Raman light, sensitivity corrected for the wavelength dependence of the detection system, and solvent subtracted. The subtraction of the very strong C-H bands of the

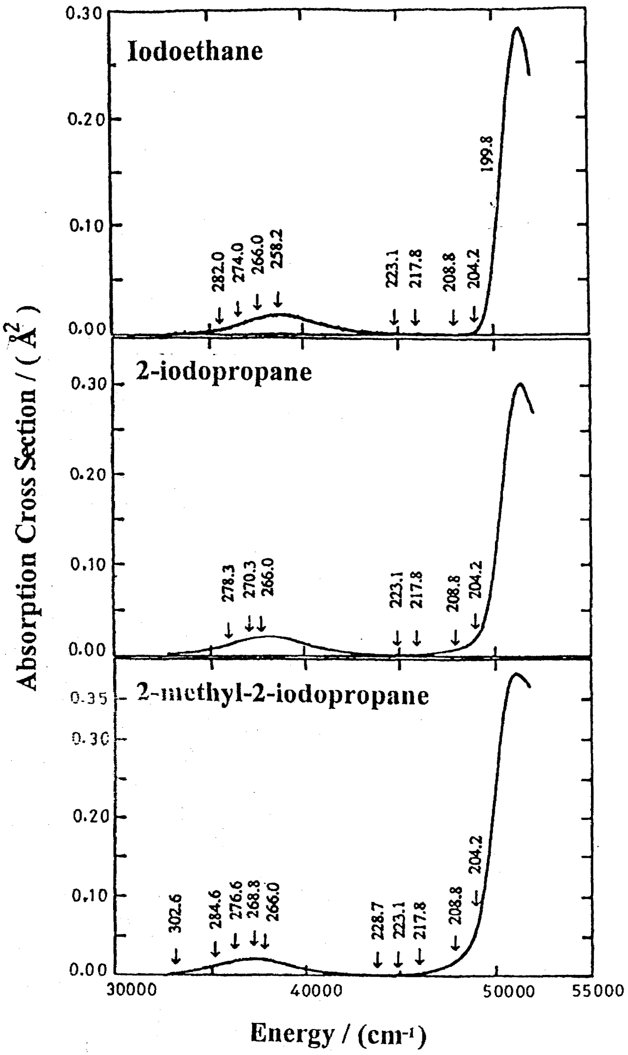

g. 1 Absorption spectra of iodoethane, 2-iodopropane, and 2-methyl-2-iodopropane in cyclohexane solution. The resonance Raman excitation frequencies are shown above each absorption spectrum. The A-band absorption is the weak band around 30,000 cm^{-1} to 45,000 cm^{-1}.

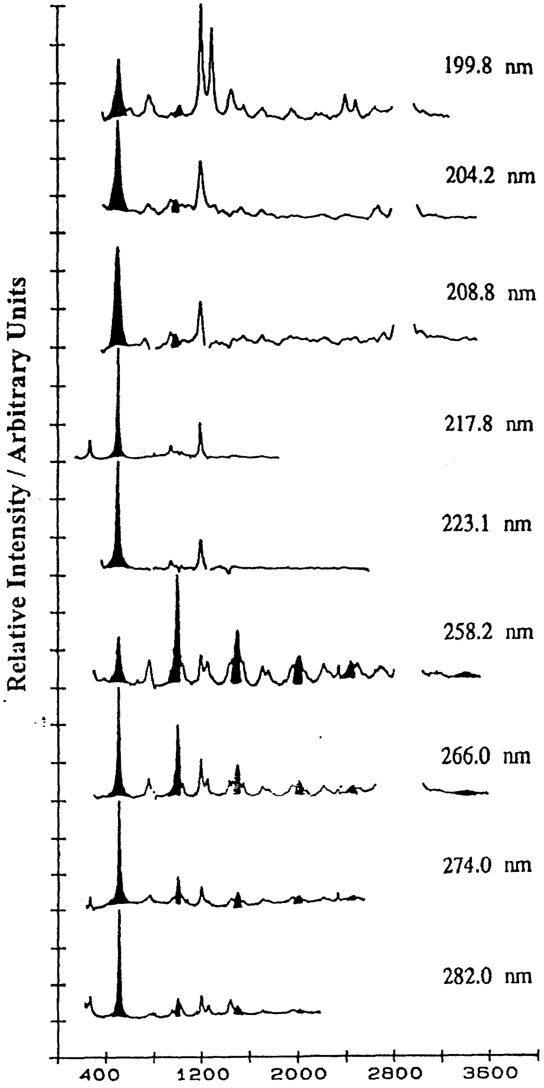

Fig. 2 Overview of the iodoethane resonance Raman spectra. The spectra are intensity corrected and solvent subtracted. The shaded bands in the spectra are the nominal C-I stretch progression. The CH stretch region is not shown because of a very big solvent subtraction artifact.

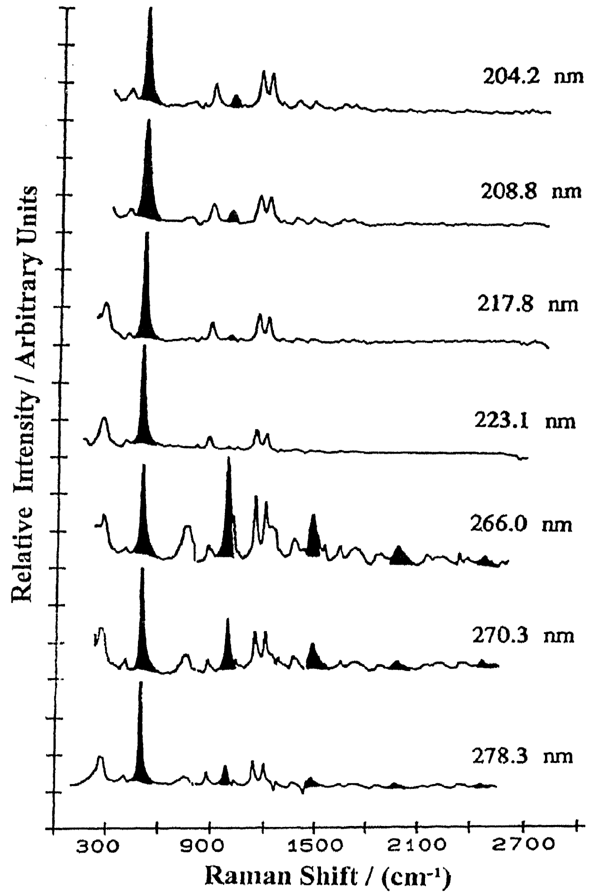

Fig. 3 Overview of the 2-iodopropane resonance Raman spectra. The spectra are intensity corrected and solvent subtracted. The shaded bands in the spectra are the nominal C-I stretch progression. The CH stretch region is not shown because of a very big solvent subtraction artifact.

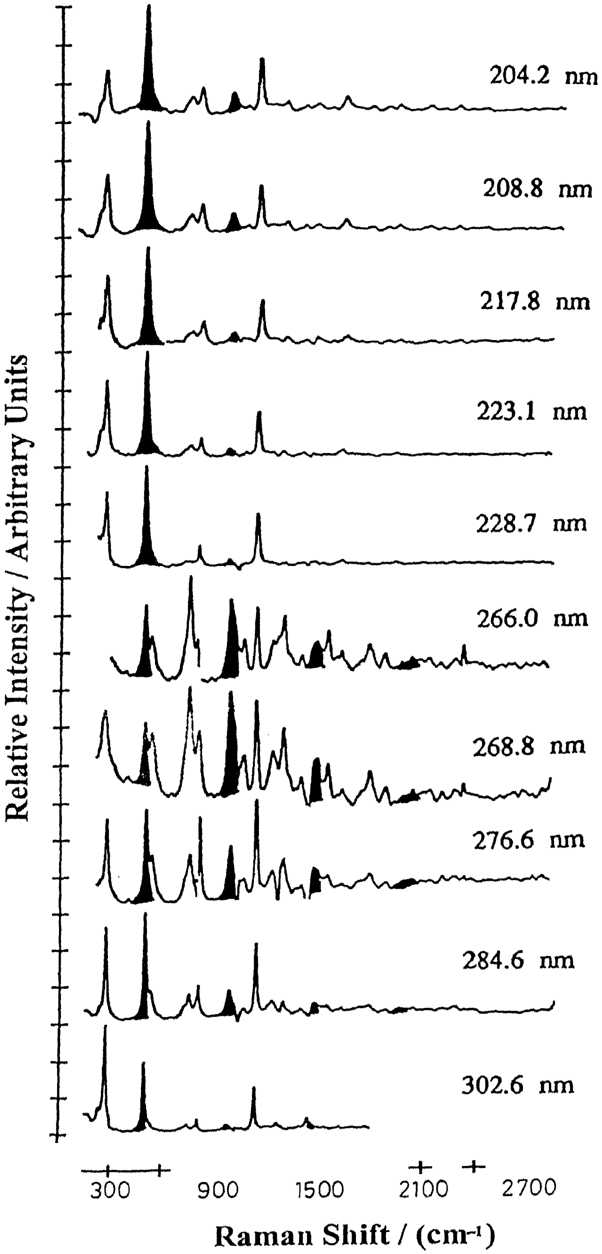

Fig. 4 Overview of the 2-methyl-2-iodopropane resonance Raman spectra. The spectra are intensity corrected and solvent subtracted. The shaded bands in the spectra are the nominal C-I stretch progression. The CH stretch region is not shown because of a very big solvent subtraction artifact.

solvent leaves the 2800-3100 cm^{-1} with large artifacts and this region is omitted from the spectra. The nominal C-I stretch fundamental and overtone bands have been shaded in Figs. 2-5.

The A-band resonance Raman spectra of iodoethane Figs. (2 and 5) have most of their intensity in the nominal C-I stretch overtone progression ($n\nu_{10}$).[89] The rest of the noticeable intensity appears in combination bands of the CCI bend, the CH_3 rock, the CH_2 wag, and the CH_3 antisymmetric stretch plus the nominal C-I stretch (ν_{11} + $n\nu_{10}$, ν_8 + $n\nu_{10}$, ν_7 +$n\nu_{10}$, and ν_4 +$n\nu_{10}$ respectively). The A-band resonance Raman spectra of 2-iodopropane (Fig. 3) also have most of their intensity in the nominal C-I stretch progression ($n\nu_8$). The rest of the significant intensity appears in combination bands of the CCI bend, the C-C stretch, CH_3 rock, and the HCC methine bend plus the nominal C-I stretch (ν_{10} +

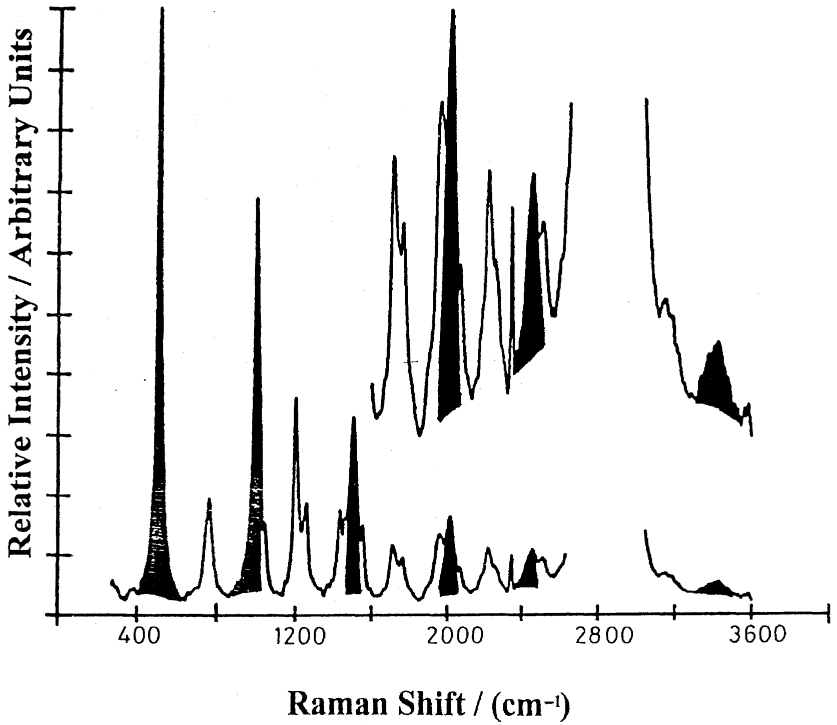

Fig. 5 Expanded view of the 258.2 nm iodoethane resonance Raman spectrum. The spectrum is intensity corrected and solvent subtracted. The shaded bands in the spectra are the nominal C-I stretch progression. The CH stretch region is not shown because of a very big solvent subtraction artifact.

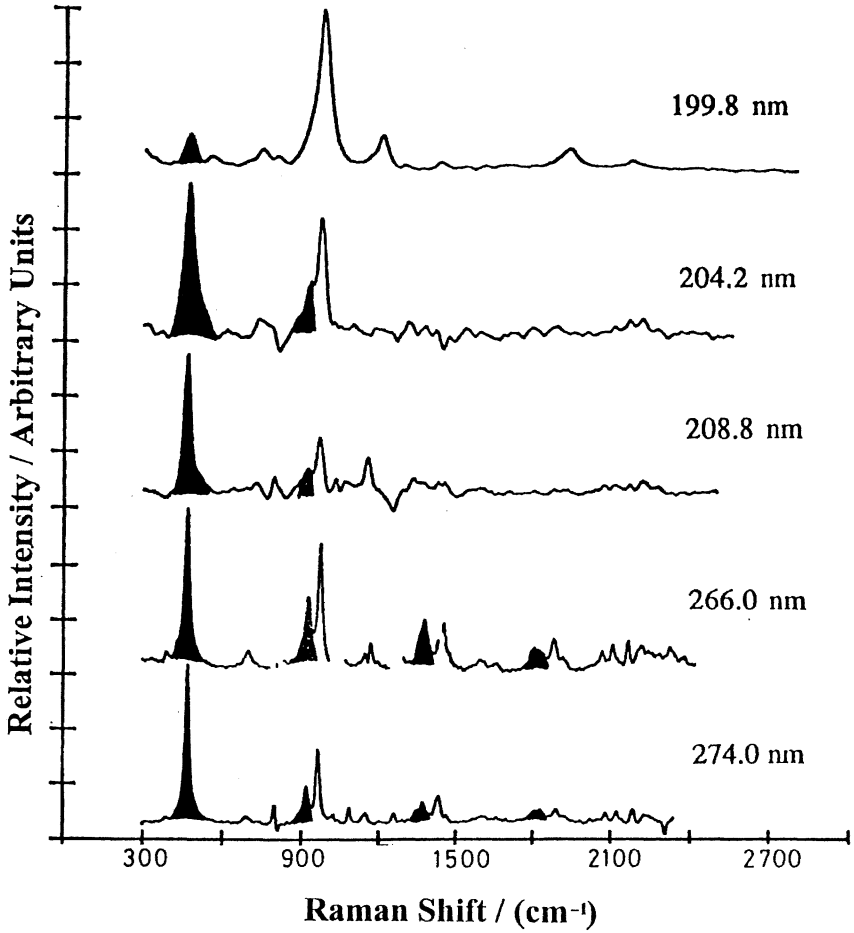

Fig. 6 Resonance Raman spectra of fully deuterated iodoethane in cyclohexane solution. The spectra have been intensity corrected and solvent subtracted. Small portions of of the 266.0 nm spectrum are not shown due to large solvent subtraction artifacts. The shaded bands in the spectra are the nominal C-I stretch progression.

$n\nu_8$, $\nu_7 + n\nu_8$, $\nu_5 + n\nu_8$, and $\nu_4 + n\nu_8$ respectively). The A-band resonance Raman spectra of 2-methyl-2-iodopropane have most of their intensity in the nominal C-I stretch progression ($n\nu_7$) and the combination band progression of the nominal CCI bend plus the C-I stretch ($\nu_8 + n\nu_7$). The remaining noticeable intensity appears in the combination bands of the C-C stretch and methyl rock plus the C-I stretch ($\nu_6 + n\nu_7$ and $\nu_5 + n\nu_7$ respectively). The resonance Raman spectra of iodoethane, 2-iodopropane, and 2-methyl-2-iodopropane display several common features and trends: the nominal C-I stretch progression has the largest amount of intensity in all the spectra, the second largest progression is the nominal CCI bend fundamental plus C-I stretch progression in all the spectra, and the intensity of the combination band progressions become larger as the molecule increases in size and/or becomes more branched relative to the C-I stretch overtone progression. In order to extract the A-band short-time photodissociation dynamics from the resonance Raman spectral intensities, there is a need to make a quantitative analysis using the normal mode descriptions for the Franck-Condon active modes.

Fig. 6 gives the resonance Raman spectra for the fully deuterated iodoethane isotopic derivative at five excitation wavelengths over the A-band and B-band region. The C-D stretch bands in the A-band region show no discernible intensity in combination bands or overtones and appear to arise mainly from presonance enhancement from the B-band or other higher energy states. This suggests that the C-H (D) stretches do not participate in the short-term photodissociation dynamics very much. The deuterated iodoethane resonance Raman spectra of Fig. 6 are noticeably different from the protonated spectra in Figs. 2 and 5. It is noted that the resonance Raman intensities in isotopically substituted molecules can be very useful in choosing among the many possible sign combinations of the excited-state displacement parameters.[2,5,8,89]

Table I

Measured nominal C-I stretch fundamental absolute resonance Raman cross sections at different wavelengths.

Absolute resonance Raman cross section (Å^2/molecule)			
Wave-length (nm)	Iodoethane	2-Iodopropane	2-Methyl-2-Iodopropane
199.8	3.9×10^{-8}		
204.2	5.6×10^{-9}	1.4×10^{-8}	7.4×10^{-8}
208.8	3.0×10^{-9}	6.6×10^{-9}	3.3×10^{-8}
217.8	1.7×10^{-9}	3.6×10^{-9}	9.0×10^{-9}
223.1	8.7×10^{-10}	2.3×10^{-9}	3.8×10^{-9}
228.7			2.2×10^{-9}
258.2	5.0×10^{-11}		
266.0	2.0×10^{-10}	1.4×10^{-10}	8.3×10^{-11}
268.8			8.7×10^{-11}
270.3		1.9×10^{-10}	
274.0	2.4×10^{-10}		
276.6			1.3×10^{-10}
278.3		2.8×10^{-10}	
282.0	2.2×10^{-10}		
284.6			2.1×10^{-10}
302.6			1.7×10^{-10}

The depolarization ratios were measured for all three iodoalkanes with 266 nm excitation and the values for the C-I stretch fundamental obtained were 0.37, 0.39, and 0.34 (all ± 0.03) for iodoethane, 2-iodopropane and 2-methyl-2-iodopropane respectively.[89] These values are close to one third and suggest that most of the preresonant enhancement of the C-I stretch fundamental contributes to the same component of the Raman tensor as does the principal resonant contribution. The observed depolarization ratios of the first few overtones (~0.39) provides further support for this conclusion. The absolute resonance Raman cross sections for the nominal C-I stretch fundamental were measured for all of the Raman spectra shown in Figs. 2-6 and these values are listed in Table I. Inspection of Table I shows that the absolute cross sections preresonant to the B-band in the 200 to 230 nm region are much larger than those in the A-band region. Fig. 7 displays an A-term fit to the C-I stretch absolute Raman cross section preresonant to the B-band and an extrapolation of this fit into the A-band region. Fig. 7 clearly shows that the preresonant Raman contribution is of similar magnitude as the resonant contribution in the A-band and this is true for most of the iodoalkanes studied to date (including iodomethane). This gives rise to significant preresonant-resonant interference in the Raman excitation profile of the C-I stretch fundamental band in the A-band resonance Raman spectra. Since the preresonant contributions for combination bands and overtones decrease much faster than those for fundamentals as one goes farther from band responsible for the preresonant contribution, the preresonant-resonant interference

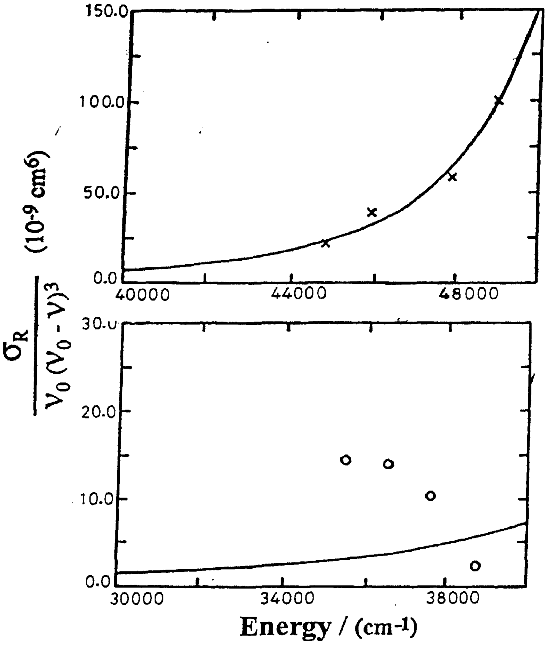

Fig. 7 The experimental absolute resonance Raman cross sections of the ν_{10} fundamental of iodoethane with excitation preresonant to the B-band absorption are shown by x in the top panel. The same measurements taken with A-band resonant wavelengths are given as o in the bottom panel. An Albrecht A-term fit is extrapolated into the A-band absorption region as presented in the bottom panel. The extrapolated preresonant contribution to the C-I stretch fundamental is not negligible compared with the experimental determinations of the C-I stretch fundamental cross sections in the A-band region.

is negligible for the overtones and combination bands of the A-band resonance Raman spectra. One can extract the short-time photodissociation dynamics from the A-band resonance Raman spectra by just modeling the overtones and combination band intensities. In order to simulate the fundamental Raman cross sections, one can use the A-term fits to the preresonant Raman cross sections to extrapolate into the A-band region and estimate the size of the preresonant contribution to the Raman tensor and calculate the fundamental cross sections. The equations and method of the fundamental calculations for the A-band iodoalkane resonance Raman intensities are given in detail in refs. [66] and [89]. The fundamental Raman bands of the A-band resonance Raman spectra of haloalkanes are susceptible to preresonant-resonant interference effects and care should be used in interpretation of their Raman intensities.[66,81,86,89]

The iodoethane, 2-iodopropane, and 2-methyl-2-iodopropane A-band absorption spectra and resonant absolute Raman cross sections were simulated using time-dependent wavepacket calculations as described in ref. [89] (for the overtones and combination bands these calculations are very similar to the description given in the Theory and Calculations section of this review article). The parameters for the best fit simulations are given in ref. [89] (also see ref. [69] for parameters for deuterated 2-iodopropane and 2-methyl-2-iodopropane). The spectra with excitation wavelengths nearer the A-band

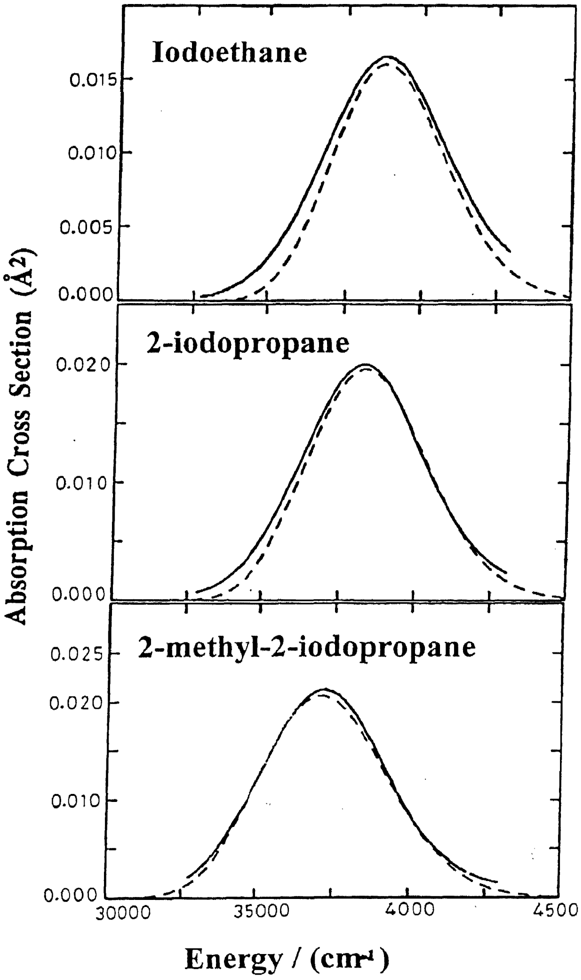

Fig. 8 Comparison of the A-band experimental (solid lines) and calculated (dashed line) absorption spectra. The dashed curves are calculated using the best fit parameters and model given in reference [89].

maximum were given greater weight in determining the best fit simulation parameters since the dominant $^3Q_0$ transition makes its largest contribution near the center of the absorption band. Fig. 8 presents a comparison of the calculated and experimental A-band absorption spectra for iodoethane, 2-iodopropane, and 2-methyl-2-iodopropane. There is reasonable agreement between the calculated and experimental absorption spectra in Fig. 8 taking into account we

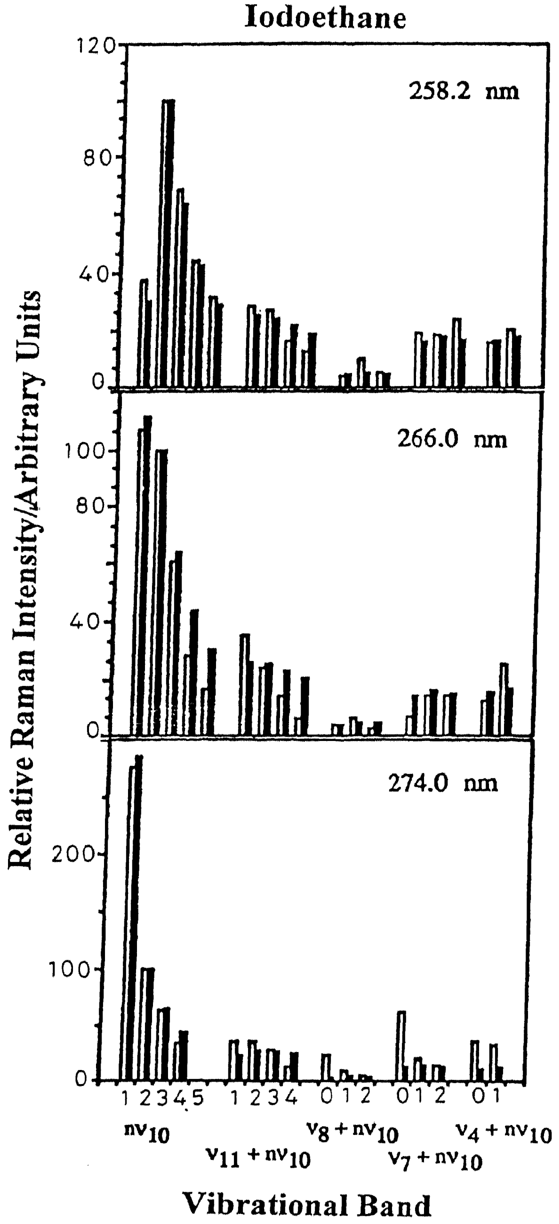

Fig. 9 Comparison of the experimental (open bars) and calculated (solid bars) relative Raman intensities for three A-band excitation wavelengths for iodoethane. The best fit parameters and model given in reference [89] were used for the calculations.

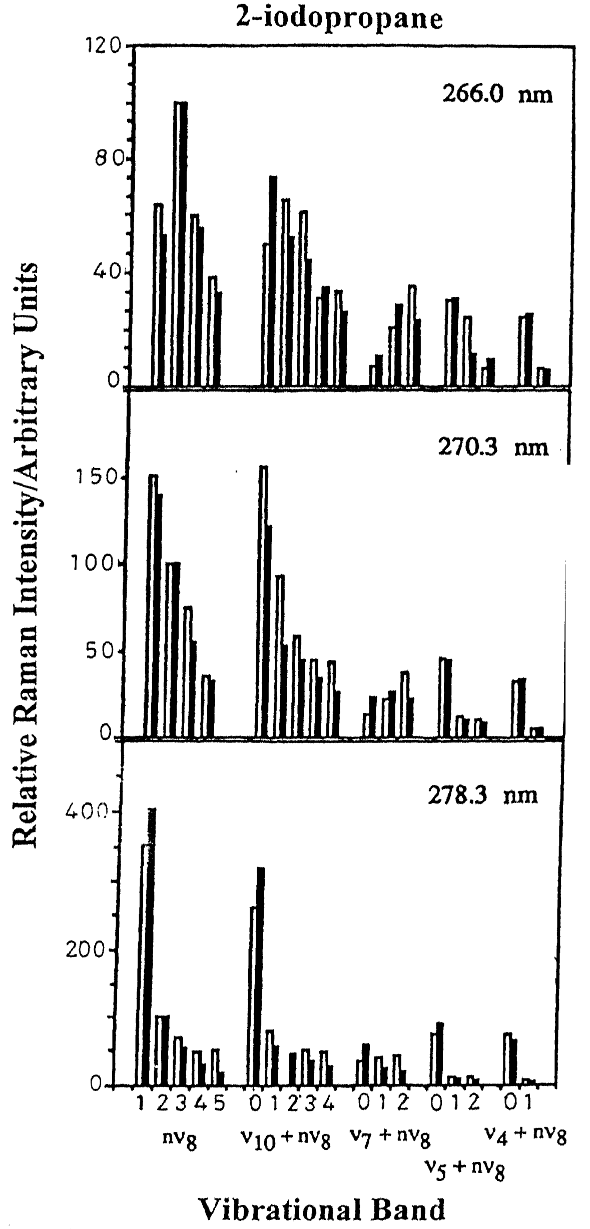

Fig. 10 Comparison of the experimental (open bars) and calculated (solid bars) relative Raman intensities for three A-band excitation wavelengths for 2-iodopropane. The best fit parameters and model given in reference [89] were used for the calculations.

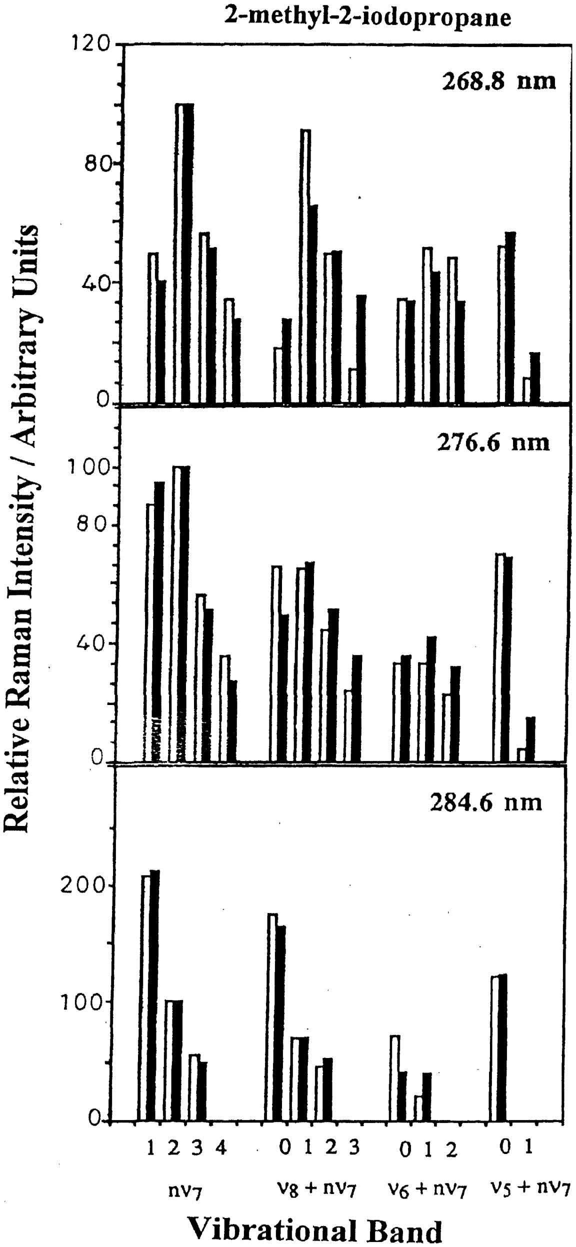

Fig. 11 Comparison of the experimental (open bars) and calculated (solid bars) relative Raman intensities for three A-band excitation wavelengths for 2-methyl-2-iodopropane. The best fit parameters and model given in reference [89] were used for the calculations.

are neglecting the small contributions of the $^{3}Q_{1}$ and $^{1}Q_{1}$ to the red and blue edges of the A-band absorption. Figs. 9-11 display comparisons of the calculated and experimental A-band resonance Raman intensities for iodoethane, 2-iodopropane, and 2-methyl-2-iodopropane in cyclohexane solution. There is generally good agreement between the experimental and calculated Raman intensities and provides confidence that the simulation parameters can be used to extract the major features of the short-time photodissociation dynamics.

Fig. 12 presents the experimental ratio of the fundamental to the first overtone ($\nu_{10}/2\nu_{10}$) for the nominal C-I stretch for iodoethane compared to the same ratio obtained from simulations including the preresonant contributions from higher energy excited states and simulations which do not include preresonant contributions. Good agreement between the experimental values and the simulations occurs when one includes the preresonant contribution. Fig. 12 illustrates the importance of preresonant-resonant interferene in simulating the observed fundamental intensities in iodoalkanes.[66,81,85,89]

Using the results of normal coordinate calculations for iodoethane, 2-iodopropane, and 2-methyl-2iodopropane (described in reference and its supplementary material) and eqs. (3) and (4) we can obtain the possible range of internal coordinate displacements associated with the short-time photodissociation dynamics. Because the simulation parameters of refs. [89] and [69] only give the absolute magnitude of each normal mode displacement, 2^{n} different choices for the n Franck-Condon active normal modes are consistent with the simulation results.[2,5,8,89] We can eliminate half of these possible sign combinations by making use our chemical knowledge about direct photodissociation reactions: direct cleavage of the C-I bond should lengthen the C-I bond. We can further reduce the number of possible sign combinations by using the redundancy present in the resonance Raman intensities of isotopic derivatives. Since the electronic structure is invariant with isotopic substitution, the isotopic derivatives should all have the same photodissociation dynamics but they usually have different resonance Raman intensities. Each possible choice of sign for each isotopic derivative will give a different excited state geometry and the geometry that has the least variance across a set of isotopic derivatives is chosen as the most possible short-time photodissociation dynamics. The reader is referred to an excellent review article by Myers[5] for further discussion of the problem of choosing

Table II

Most Probable Internal Coordinate Displacements at t=10 fs After Photoexcitation for Iodoethane, 2-Iodopropane, and 2-Methyl-2-Iodopropane.

Compound	Coordinate	Range of Displacements at 10 fs
Iodoethane[a]	$r_{C\text{-}I}$	+0.13 to +0.15 Å
	r_{BC}	−0.06 to −0.05 Å
	$\angle BCI$	−6° to −3°
	$\angle HCI$	−7° to −3°
	$\angle BCH_6$	+6° to +9°
	$\angle H_6CH_7$	−6° to +5°
	$\angle CBH_2$	−1° to +5°
	$\angle CBH_3$	−1° to −3°
	$\angle H_2BH_3$	−4° to +5°
	$\angle H_2BH_4$	−8° to +8°
2-Iodopropane[b]	$r_{C\text{-}I}$	+0.09 to +0.12 Å, [c]
	r_{BC}	+0.02 to +0.05 Å, [c]
	$\angle BCI$	−2.7° to −4.2°, [c]
	$\angle BCB$	−2° to +5°
	$\angle H_7CI$	−3° to +5°
	$\angle BCH_7$	−1° to +6°
	$\angle CBH_2$	−10° to +4°
	$\angle CBH_3$	−10° to +5°
	$\angle CBH_4$	−1° to +8°
	$\angle H_2BH_3$	−3.6° to +1.3°, [c]
	$\angle H_2BH_4$	−1° to −2°, [c]
	$\angle H_3BH_4$	−2° to +2°, [c]
2-Methyl-2-Iodopropane[d]	$r_{C\text{-}I}$	+0.03 to +0.12 Å, [c]
	r_{BC}	+0.03 to +0.05 Å, [c]
	$\angle BCI$	−2° to −4.7°, [c]
	$\angle BCB$	+1° to +6°
	$\angle CBH_4$	−4° to +7°
	$\angle H_4BH_5$	−3.5° to +1°, [c]
	$\angle H_4BH_6$,	−1.6° to −0.9°, [c]
	$\angle H_5BH_6$	

[a] Values from ref. [89] and comparison of fully protonated and deuterated iodoethane data.

[b] Values from ref. [89].

[c] Values have been narrowed by using comparison with a deuterated isotopic derivative set data (see ref. [69]).

[d] Values from ref. [89].

[e] Values from reference have been narrowed by using comparison with a deuterated isotopic derivative set of data (see ref. [69]).

the sign of the normal mode displacements. In ref. [89] we made comparisons of fully protonated and deuterated derivatives of iodoethane to help eliminate most of the possible sign combinations of the normal mode displacement parameters. Further comparisons to deuterated derivatives of 2-iodopropane and 2-methyl-2-iodoproane were done to help narrow the possible number of sign combinations (see ref. [69]). Table II lists the most probable A-band short time photodissociation dynamics at 10 fs derived from resonance Raman intensity analysis of iodoethane, 2-iodopropane, and 2-methyl-2-iodopropane by author's group.

Inspection of Table II shows that the C-I bond cleavage short-time dynamics are multidimensional in nature with significant motion along other parts of the molecule other than the C-I bond alone. The C-I bond lengthens faster in iodoethane than in the larger iodoalkanes (+0.13 to +0.15 Å for iodoethane, +0.09 to +0.12 Å for 2-iodopropane and +0.03 to +0.12 Å for 2-methyl-2-iodopropane) and these results display a good correlation with the amount of internal energy found in the radical photoproducts and the widths of their internal energy distributions measured in previous time-of-flight photofragment spectroscopy experiments (for example, the internal excitation of the alkyl radical increases from 28% to 38% for iodoethane[19,20,24,52] to 43% to 67% in 2-iodopropane[19,20,25]). Both the short-time and long time dynamics suggest that less of the absorption photon energy goes into cleaving the C-I bond with more energy partitioned to changing the structure of the rest of the molecule in 2-iodopropane than in iodoethane. Our results in Table II also suggest that the larger amount of energy partitioned to the alkyl group as the alkyl group becomes more massive and/or branched starts in the Franck-Condon region of the photodissociation reaction. This implies that the $^3Q_0$ to $^1Q_1$ curve crossing probability is affected by this Franck-Condon region energy partitioning in addition to mass effects. The C-C bond(s) shorten in iodoethane but lengthen in 2-iodoproane and 2-methyl-2-iodopropane. The parent iodoalkanes have C-C bond lengths of 1.54 Å in their ground electronic states and the corresponding alkyl radicals have C-C bond lengths ~1.49 Å in their ground electronic states as determined in several *ab initio* investigations.[91-93] The initial short-time dynamics of C-I bond cleavage in iodoethane brings the ethyl group C-C bond length closer toward the value found for the ground state ethyl radical. However, the initial photodissociation motion is in the opposite direction for 2-iodopropane and 2-methyl-2-iodopropane. This would suggest that there will be less C-C vibrational excitation of the nascent ethyl radical

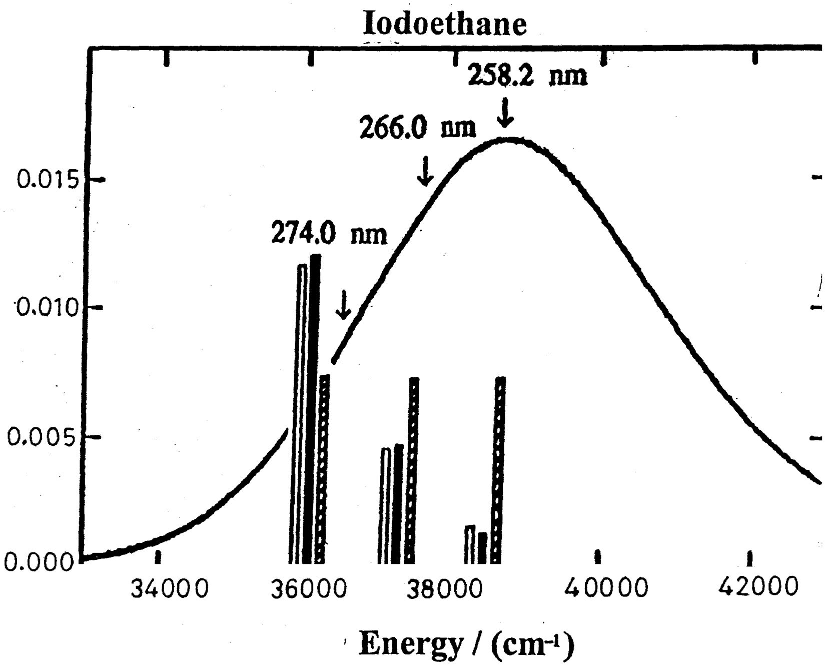

Experimental ratio of the nominal C-I stretch fundamental to its first overtone ($\nu_{10}/2\nu_{10}$) for iodoethane in cyclohexane solution (open bars) compared to the same ratio calculated including the nonresonant A-term contributions (solid bars) and the ratio calculated without the nonresonant contribution (striped bars). The A-band absorption spectrum for iodoethane is shown for reference.

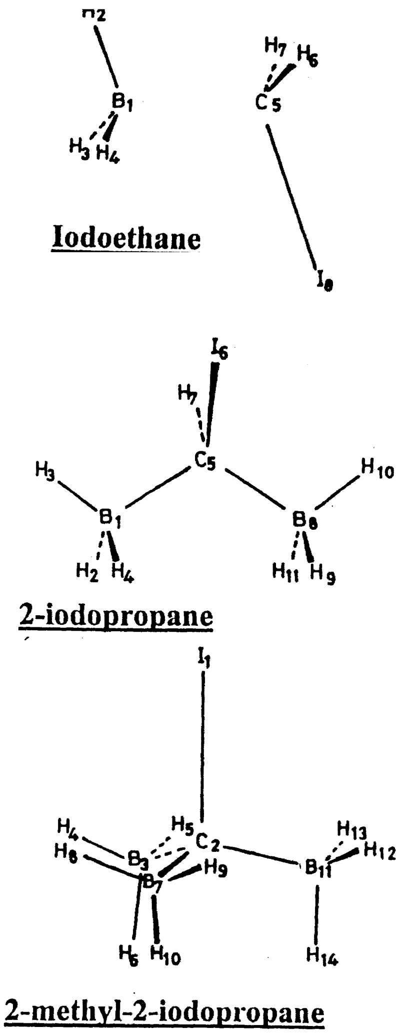

Fig. 13 Simple diagrams of the geometries of iodoethane (top), 2-iodopropane (middle), and 2-methyl-2-iodopropane (bottom). The CH bond length is 1.09 Å, the CC bond length is 1.54 Å, the CI bond length is 2.135 Å, and the angles are 109.5 degrees (e.g. a tetrahedral geometry about the carbon atoms). C represents the α-carbon atoms, B represents the β-carbon atoms, H are hydrogen atoms, and I are iodine atoms.

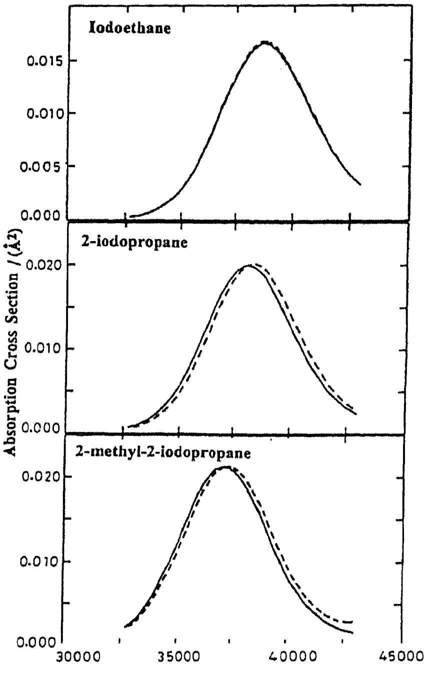

Fig. 14 Absorption spectra of iodoethane, 2-iodopropane, and 2-methyl-2-iodopropane in the gas phase (dashed line) and in cyclohexane solution (solid line). The iodoethane spectra are almost identical while the solution phase spectra of 2-iodopropane and 2-methyl-2-iodopropane are red-shifted by a small amount relative to their respective gas phase spectra.

photoproduct compared to the isopropyl and tert-butyl radicals to the degree that the short-time photodissociation dynamics can be extrapolated outside the Franck-Condon region. Our work strongly suggests that it would be very interesting to directly measure the vibrational product state distributions for the ethyl, isopropyl, and tert-butyl radicals formed from the A-band photodissociation of the corresponding parent iodoalkanes. Such studies would help generate an increased understanding of how the initial photodissociation dynamics influence the product-state energy partitioning. Several of these types of investigations have been reported for the A-band photodissociation of iodomethane to determine the vibrational-rotational state distributions of the methyl radical and applications of these types of experiments to higher iodoalkanes would likely be very rewarding.

Examination of the A-band short-time photodissociation dynamics given in Table II shows that in general there is a flattening about the α-carbon atom of the alkyl group and that the C-I bond cleavage takes place on a time-scale similar to the vibrational motions of the rest of the molecule. The results obtained by the author on resonance Raman intensity indicate that the Franck-Condon region photodissociation dynamics are somewhere between the simplistic "soft

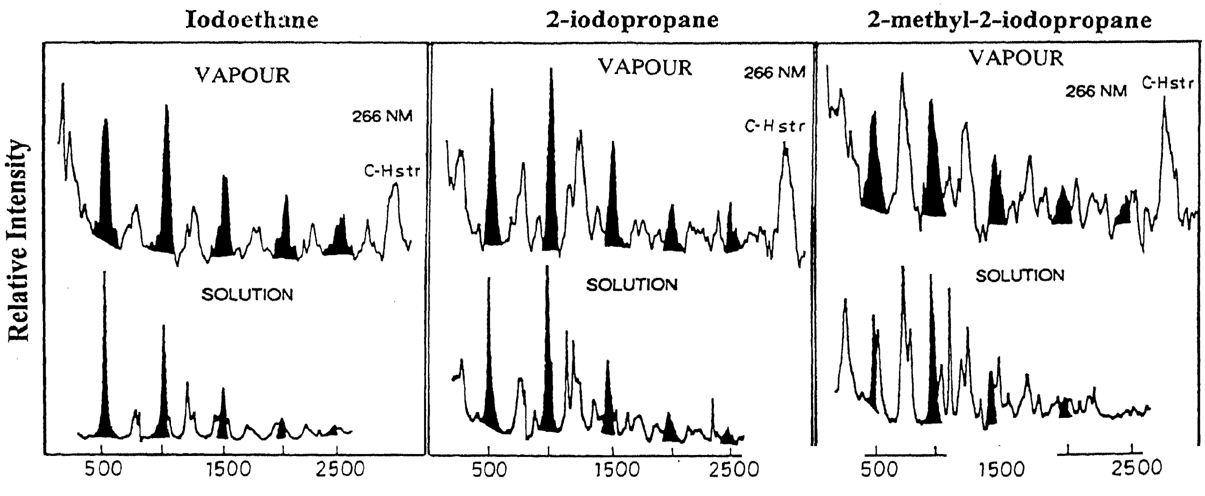

Fig. 15 Resonance Raman spectra of iodoethane, 2-iodopropane, and 2-methyl-2-iodopropane in the gas phase and in cyclohexane solution. The excitation wavelengths are all 266.0 nm except for the 2-methyl-2-iodoproane spectrum which is 268.8 nm. The gas phase spectra have instrumental resolution of 40-60 cm^{-1} while the solution phase spectra have a resolution of 8-10 cm^{-1}.

radical" and "rigid radical" descriptions of the photodissociation dynamics and that a "semi-rigid" radical model of the photodissociation dynamics would be a more appropriate description. "Semi-rigid" radical descriptions of the photodissociation dynamics could better account for the molecular bond strengths and the changes in the molecular bonds during the photodissociation process.

Comparison of the gas and solution phase iodoalkane A-band absorption and resonance Raman spectra are very similar to one another as illustrated in Figs. 14 and 15 respectively. Fig. 16 compares the gas and solution phase resonance Raman intensities for the 266 nm spectra of iodoethane, 2-iodopropane, and 2-methyl-2iodopropane shown in Fig. 15. The relative Raman intensities for the gas and solution phase spectra of the higher iodoalkanes are very similar to one another and this implies there is little solvation effect on the short-time photodissociation dynamics. This is similar to the situation in iodomethane and is not unexpected since the intramolecular forces along the reaction coordinate are much larger than solvent-solute forces in the Franc-Condon region of the A-band photodissociation. Solvation effects should become increasingly more noticeable outside the Franck-Condon region where the intramolecular forces of the photodissociation become more comparable in size to the solvent-solute forces.

C. Solvation Effects on the A-Band Photodissociation of Diiodomethane

Fig. 17 displays the ultraviolet absorption spectra of diiodomethane in the gas phase, in methanol solution, and in cyclohexane solution. The strong coupling between the two C-I chromophores causes the absorption spectra to significantly red shift relative to single chromophore iodoalkane absorption spectra as well as cause different separation and intensity in the individual transitions.[62,65,94,95] The lowest transition ~32,000 cm^{-1} forms only ground state iodine atoms while the second and higher transitions gives both ground and excited electronic states of iodine atoms.[65,94,95] The present investigation has been focused on the lowest energy transition ~32,000 cm^{-1} associated the A-state. Resonance Raman spectra (shown in Figs. 18 and 19) were obtained for diiodomethane in the gas phase (355 nm), in methanol solution (342 nm and 355 nm), and in

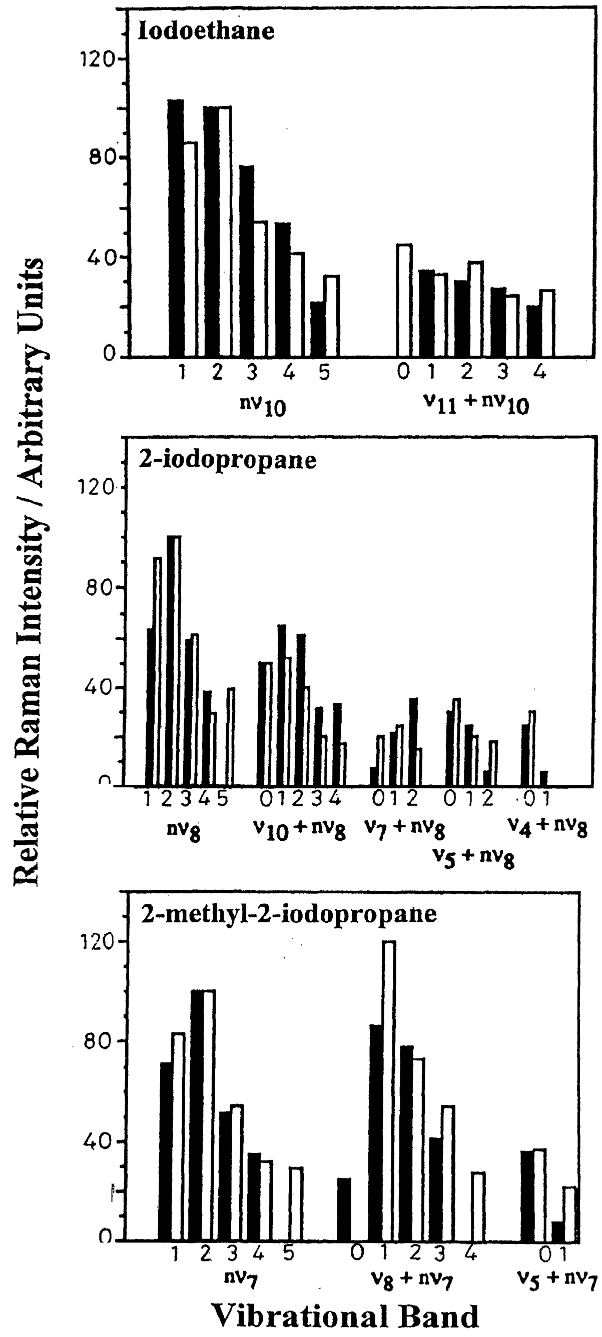

Fig. 16 Comparison of the relative Raman intensities of iodoethane, 2-iodopropane, and 2-methyl-2-iodopropane in the gas phase (open bars) and in cyclohexane solution (solid bars). Intensities of nearly degenerate bands resolved only in the solution phase have been combined as described in reference [90]. Estimated uncertainties are about ±15% for the gas phase and ±10% for cyclohexane solution.

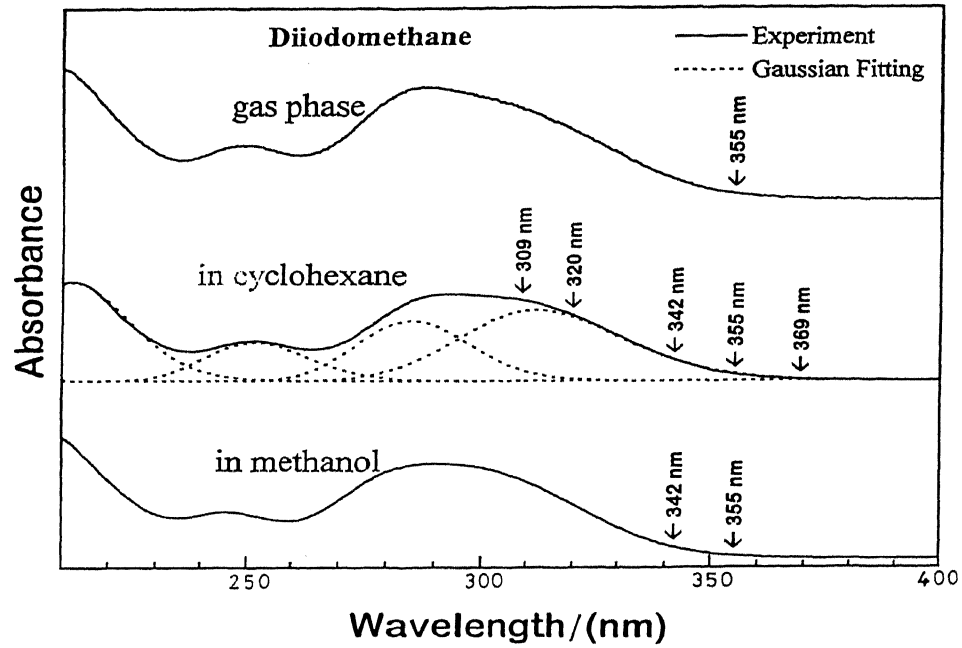

Fig. 17 Diiodomethane absorption spectra in the gas phase, in cyclohexane solution and in methanol solution. The resonance Raman excitation wavelengths are indicated by the arrows and numbers (in nm) above each spectrum. The dashed lines represent a best fit Gaussian deconvolution of the absorption spectrum.

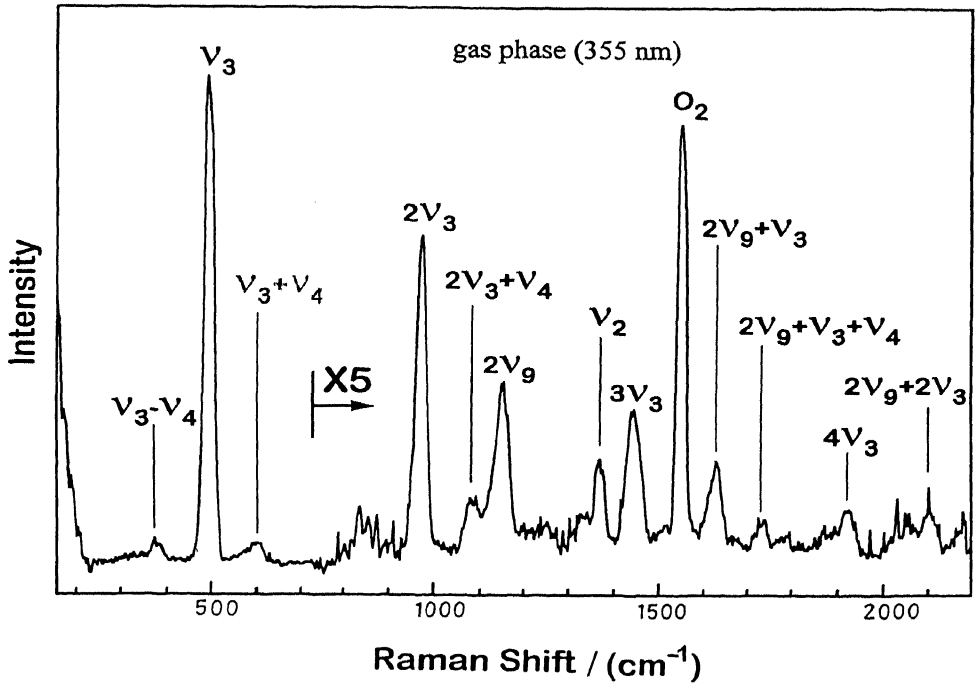

Fig. 18 Gas phase diiodomethane 355 nm resonance Raman spectrum. The spectrum has been intensity corrected .and the assignments of the larger Raman bands are given.

Table III

(A.) Parameters for calculation of resonance Raman intensities and absorption spectrum of vapour phase diodomethane and diiodomethane in methanol solution. (B.) Most probable internal coordinate displacements of diiodomethane at t= 15 fs assuming the C-I bond becomes longer.

(A.) Vapour Phase Diiodomethane	Transition length, M=0.197 Å, E_0 = 25,700 cm^{-1}		
Vibrational Mode	Ground state Vibrational Frequency (cm-1)	Excited state Vibrational Frequency (cm-1)	$\lvert\Delta\rvert$
ν_4 (I-C-I bend)	134 cm^{-1}	134 cm^{-1}	5.6
ν_3 (I-C-I symmetric stretch)	499 cm^{-1}	499 cm^{-1}	4.0
ν_9 (I-C-I anti-symmetric stretch)	581 cm^{-1}	-770 cm^{-1}	0.00
ν_2 (CH_2 scissor)	1379 cm^{-1}	1379 cm^{-1}	0.56

Diiodomethane in Methanol Solution	Transition length, M=0.256 Å,	E_0 = 25,800 cm^{-1}	
Vibrational Mode	Ground state Vibrational Frequency (cm^{-1})	Excited state Vibrational Frequency (cm^{-1})	$\lvert\Delta\rvert$
ν_4 (I-C-I bend)	141 cm^{-1}	180 cm^{-1}	5.9
ν_3 (I-C-I symmetric stretch)	501 cm^{-1}	501 cm^{-1}	2.4
ν_9 (I-C-I anti-symmetric stretch)	585 cm^{-1}	780 cm^{-1}	1.3
ν_5 (CH_2 twist)	1032 cm^{-1}	1032 cm^{-1}	0.24
ν_2 (CH_2 scissor)	1375 cm^{-1}	1375 cm^{-1}	0.24

(B.) Short-Time Photodissociation Dynamics at t=15 fs After Photoexcitation

	Gas Phase	Solution Phase (in methanol solvent)	
Internal Coordinate	[a]15 fs	[b]15 fs with Δ_9=+1.3	[c]15 fs with Δ_9=-1.3
C-H bonds	-0.008 Å (-0.009 Å)	-0.004 Å (-0.006 Å)	-0.004 Å (-0.006 Å)
C-I bond, atoms 1 and 4	+0.146 Å (+0.142 Å)	+0.169 Å (+0.162 Å)	+0.010 Å (+0.004 Å)
C-I bond, atoms 1 and 5	+0.146 Å (+0.142 Å)	+0.010 Å (+0.004 Å)	+0.169 Å (+0.162 Å)
H-C-H angle, atoms 2, 1, and 3	-2.4° (-2.5°)	-1.5° (-1.4°)	-1.5° (-1.4°)
H-C-I angle, atoms 2, 1, and 4	+2.8° (+3.2°)	-0.4° (+0.1°)	+3.5° (+4.0°)
H-C-I angle, atoms 3, 1, and 5	+2.8° (+3.2°)	+3.5° (+4.0°)	-0.4° (+0.1°)
H-C-I angle, atoms 2, 1, and 5	+2.9° (+3.3°)	+3.5° (+4.0°)	-0.2° (+0.3°)
H-C-I angle, atoms 3, 1, and 4	+2.9° (+3.3°)	-0.2° (+0.3°)	+3.5° (+4.0°)
I-C-I angle, atoms 4, 1, and 5	-8.9° (-11°)	-4.9° (-7.0°)	-4.9° (-7.0°)

[a] Values without parentheses are for the sign combination of Δ_3=-4.0 and Δ_4=+5.6, while values within parentheses are for the sign combination of Δ_3=-4.0 and Δ_4=-5.6.

[b] Values without parentheses are for the sign combination of Δ_3=-2.4, Δ_4=+5.9, and Δ_9=+1.3 while values within parentheses are for the sign combination of Δ_3=-2.4 and Δ_4=-5.9, and Δ_9=+1.3.

[c] Values without parentheses are for the sign combination of Δ_3=-4.0, Δ_4=+5.9, and Δ_9=-1.3 while values within parentheses are for the sign combination of Δ_3=-4.0 and Δ_4=+5.9, and Δ_9=-1.3.

cyclohexane solution (369 nm, 355 nm, and 342 nm).[62,65] The resonance Raman spectra have most of their intensity in the fundamentals, overtones, and combination bands associated with the nominal I-C-I symmetric stretch, I-C-I bend, and I-C-I anti-symmetric stretch vibrational modes. The A-state absorption spectra and resonance Raman intensities were simulated using time-dependent wavepacket

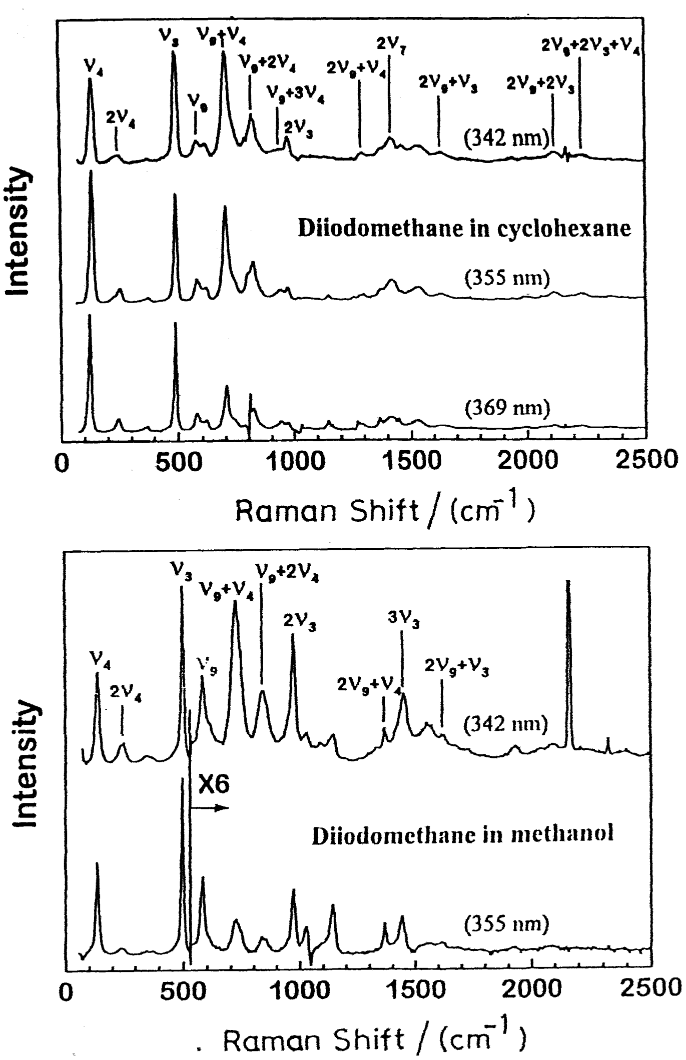

9 Resonance Raman spectra of solution phase diiodomethane in cyclohexane and methanol solvents. The spectra have been intensity corrected and solvent subtracted. The asterisks mark portions of the spectra with solvent subtraction artifacts. The assignments of the larger Raman bands are also shown.

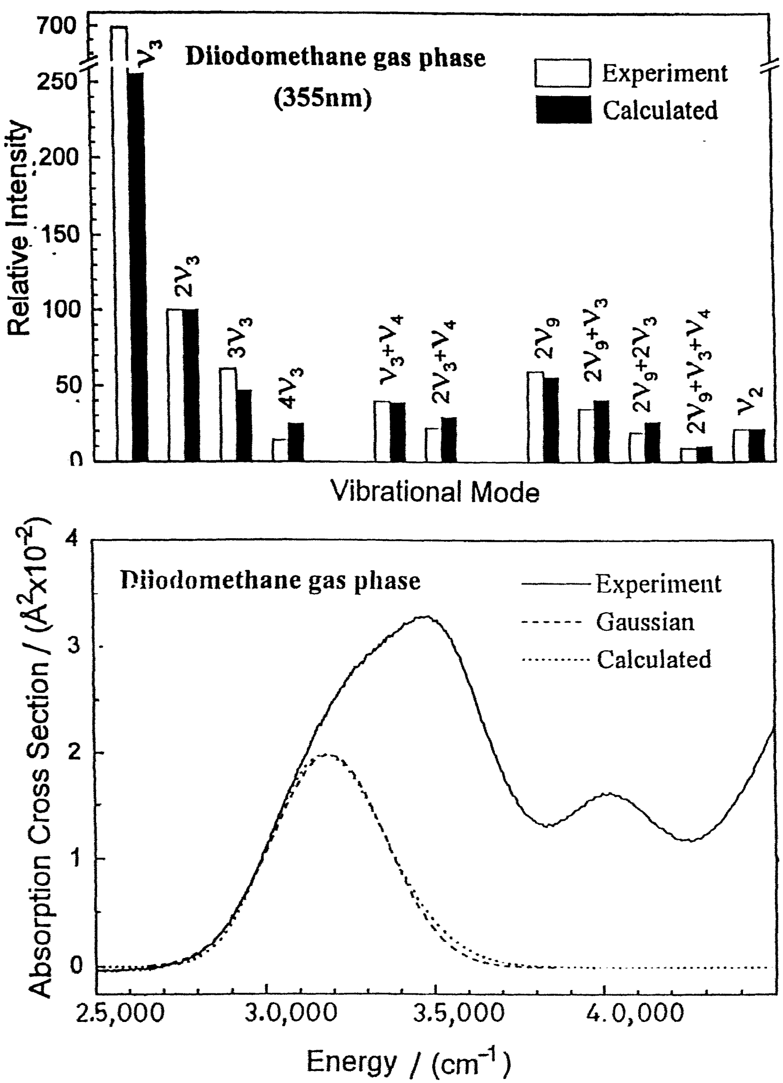

Fig. 20 Comparison of experimental (open bars) and calculated (solid bars) resonance Raman intensities for the gas phase diiodomethane 355 nm resonance Raman spectrum. Comparison of the experimental (solid line), Gaussian band of the A-state deconvolution (dashed line), and calculated (dotted line) absorption spectra. The calculations made use of the parameters and simple model given in reference [65].

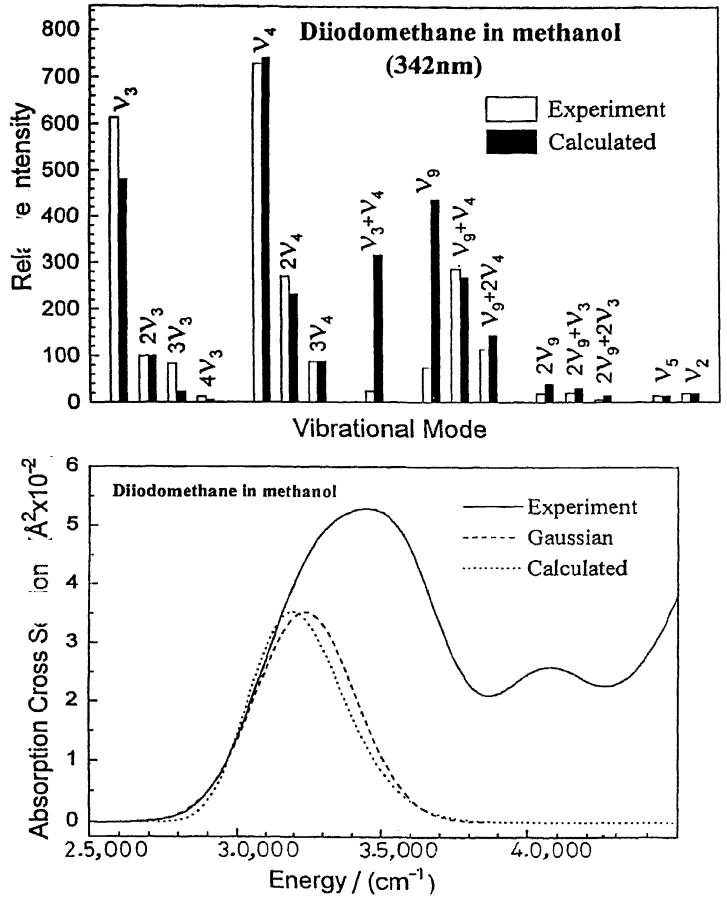

Fig. 21 Comparison of experimental (open bars) and calculated (solid bars) resonance Raman intensities for the solution phase diiodomethane in methanol solvent 342 nm resonance Raman spectrum. Comparison of the experimental (solid line), Gaussian band of the A-state deconvolution (dashed line), and calculated (dotted line) absorption spectra. The calculations made use of the parameters and simple model given in reference [65].

calculations and a simple model similar to that described in the Theory and Calculations section (also described in detail in ref. [65]). Comparisons of the experimental and the best fit calculated absorption spectra and the resonance Raman intensities are shown in Fig. 20 for the gas phase and Fig. 21 for the methanol solution. Considering the simple model we used in the simulations, we obtain reasonable agreement between the calculated and experimental data. The best fit simulation parameters are listed in Table III. The normal mode coefficients from normal coordinate calculations (described in ref. [65] and its supplementary material) were used in conjunction with eqs. (3) and (4) to convert the motion of the wavepacket on the excited state from

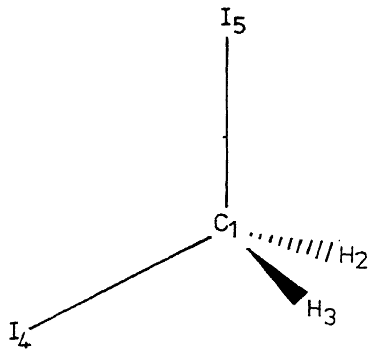

Fig. 22 Geometry of diiodomethane with each atom labeled with a number 1 through 5. All C-H bond lengths are 1.093 Å, the C-I bond lengths are 2.1195 Å, and all bond angles are 109.45°.

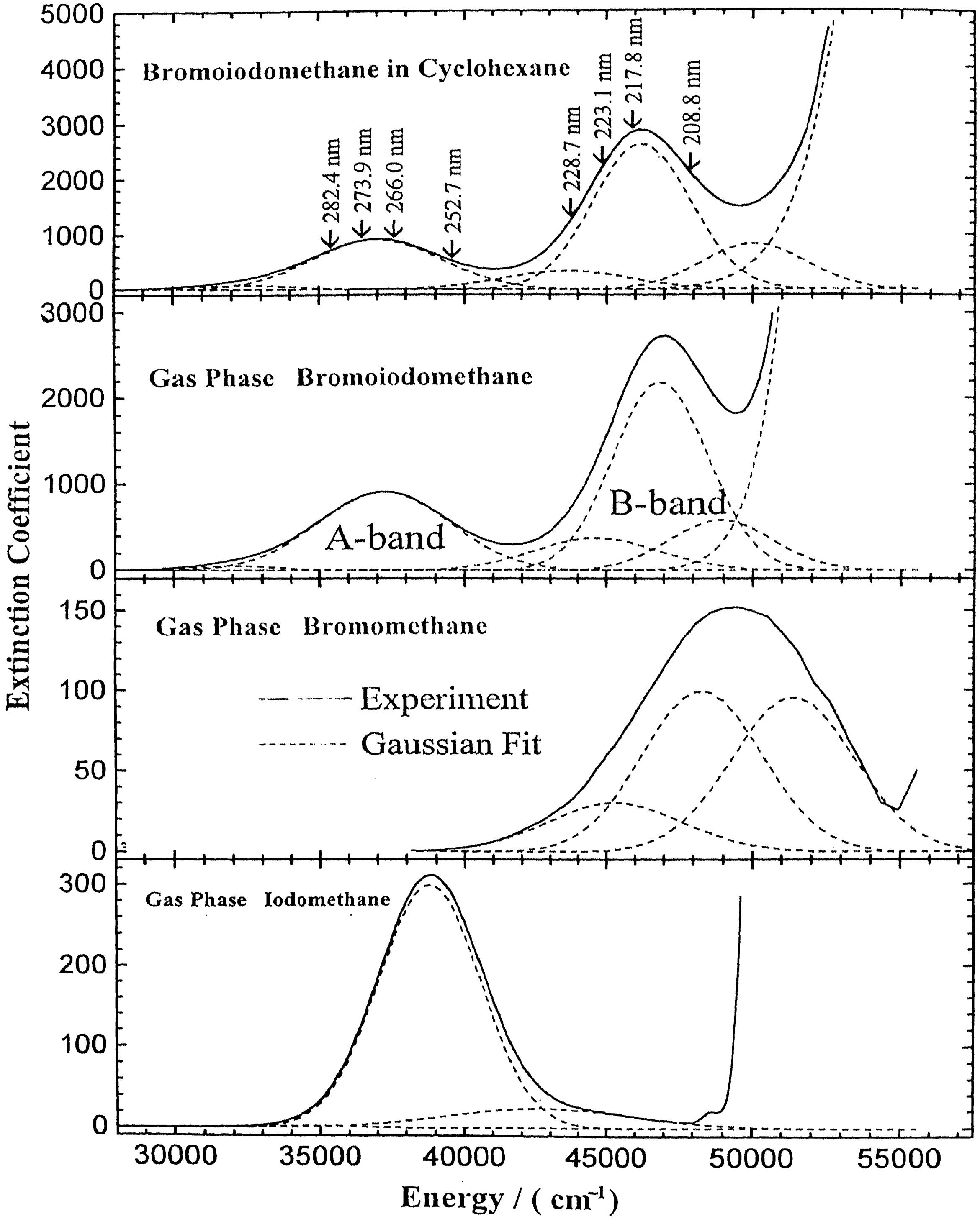

Fig. 23 Absorption spectra of bromoiodomethane in cyclohexane solution and in the gas phase. Absorption spectra for gas phase bromomethane and iodomethane are also displayed. Gaussian curve fits to the absorption spectra are given by dashed lines. The resonance Raman excitation frequencies for the bromoiodomethane in cyclohexane solution experiments are shown above its absorption spectrum.

dimensionless normal coordinates into internal coordinates of the molecule. It is assumed that the C-I bond becomes longer in the excited state because the A-state photodissociates in a direct manner. Table III presents the short time photodissociation dynamics obtained for t=15 fs after photoexcitation for diiodomethane in the gas phase and in methanol solution and the simple diagram of the diiodomethane molecule in Fig. 22 can be used to better visualize the dynamics

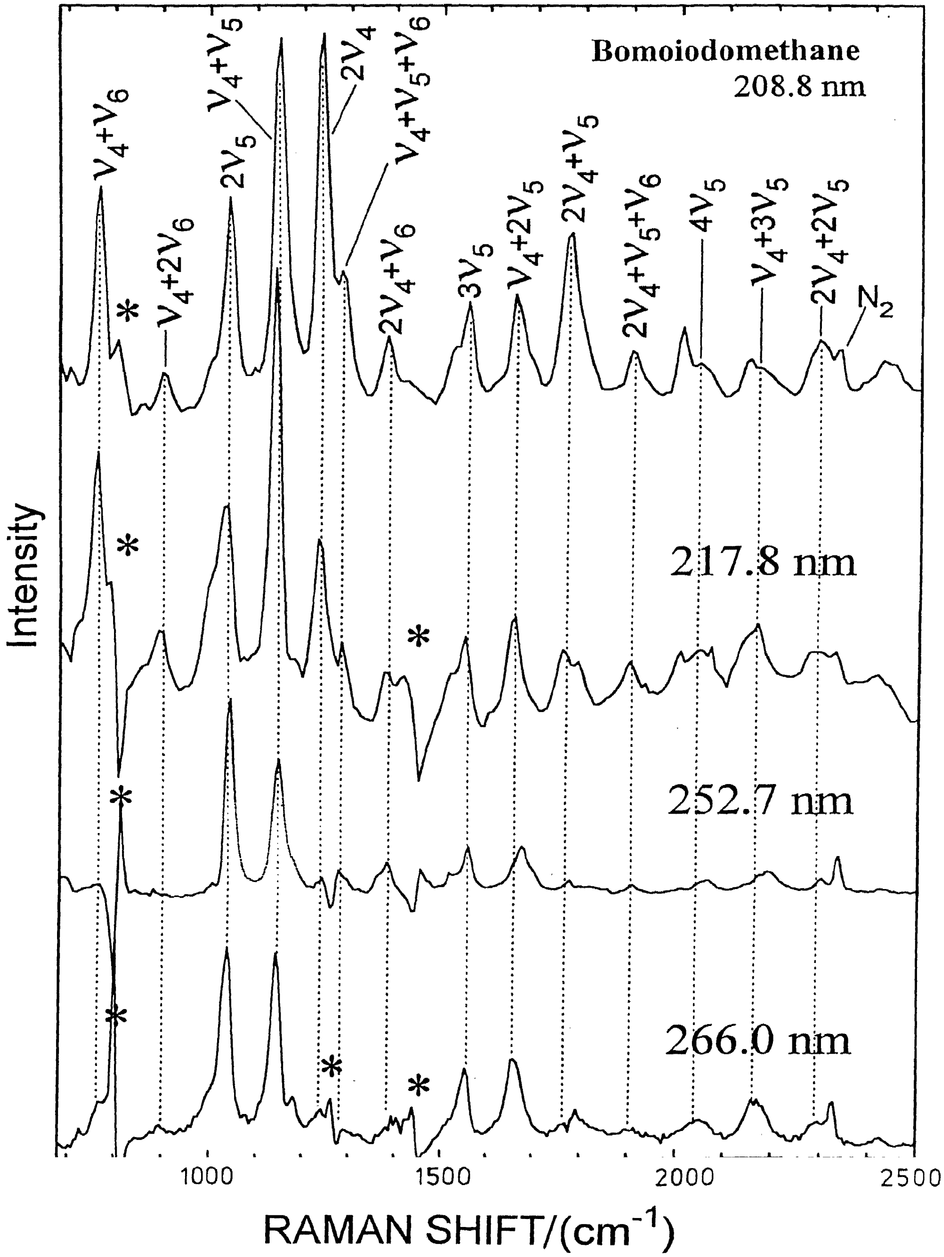

Fig. 24 Enlarged views of the B-band 208.8 and 217.8 nm resonance Raman spectra and the A-band 252.7 and 266.0 nm resonance Raman spectra. The spectra have been intensity corrected and solvent subtracted (asterisks indicate regions with solvent subtraction artifacts). The tentative assignments of some of the larger Raman bands are shown above the spectra.

presented in Table III. Inspection of Table III shows that the two C-I bonds lengthen by the same amount, the I-C-I becomes smaller, the H-C-I becomes larger, and the H-C-H angle becomes smaller in the A-state gas phase short-time photodissociation dynamics. The two C-I bonds appear equivalent in the Franck-Condon region of the gas phase photodissociation and this indicates that the molecule decides which of the two bonds are broken after the wavepacket has left the Franck-Condon region of the surface. The lack of intensity in the I-C-I anti-symmetric stretch fundamental and odd overtones or combination bands of the fundamental with other modes in the gas phase resonance Raman spectrum (see Fig. 18) is due to this symmetry of the two C-I bonds in the gas phase Franck-Condon region of the dissociation. Comparison of the gas and solution phase resonance Raman spectra indicates that there is a large solvent-induced symmetry breaking. This gives rise to significant intensity in the I-C-I anti-symmetric stretch fundamental and odd overtones or combination bands of the fundamental with other modes in the solution phase resonance

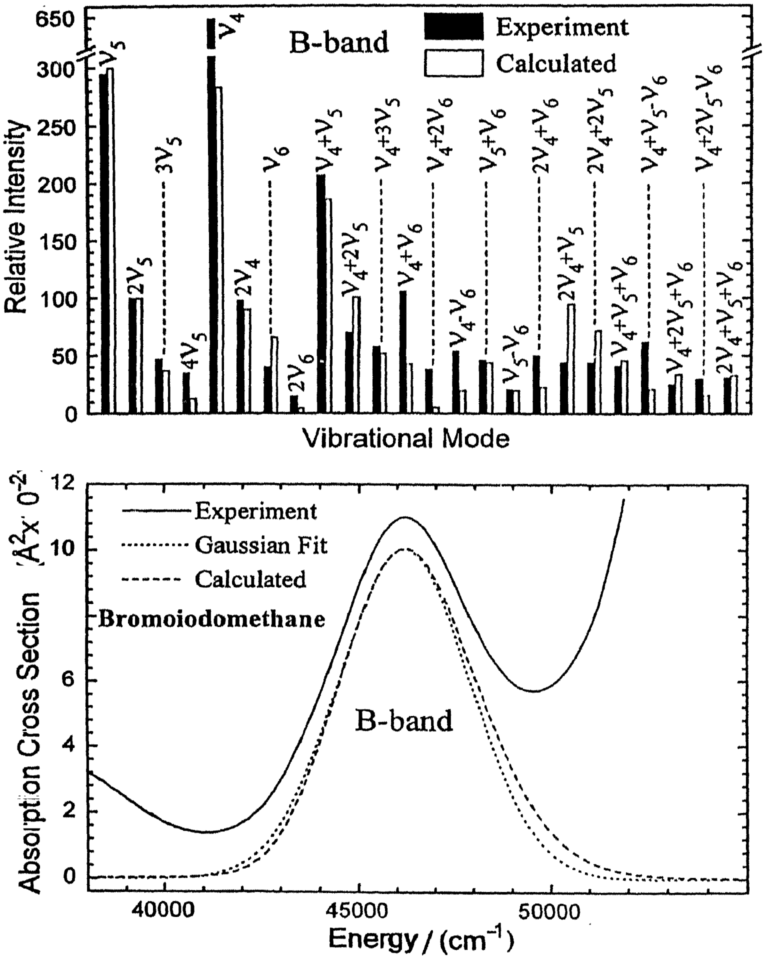

Fig. 25 Comparison of experimental (solid bars) and calculated (open bars) resonance Raman intensities for the solution phase bromoiodomethane in cyclohexane solvent 217.8 nm resonance Raman spectrum. Comparison of the experimental (solid line), Gaussian band of the A-state deconvolution (dotted line), and calculated (dashed line) B-band absorption spectra for bromoiodomethane in cyclohexane solution. The calculations made use of the parameters and simple model given in reference [67].

Raman spectra that are not observed in the gas phase. Table III shows that the short-time photodissociation dynamics of the A-state of diiodomethane in the solution phase have the two C-I bonds become larger by differing degrees, the I-C-I angles becomes smaller, the H-C-H angle becomes smaller and the H-C-I angles differ becomes larger. For the Franck-Condon region photodissociation dynamics, the two C-I bonds are not the same and this implies that the molecule chooses soon after photoexcitation which C-I bond undergoes cleavage. One of the reasons that the effects of solvation is very noticeable for the direct photodissociation of the A-state of diiodomethane compared to C-I bond cleavage in other iodoalkanes with only one C-I bond is that the symmetry of the two C-I bonds in diiodomethane is very sensitive to perturbation so only a small amount of solvent-solute interaction can noticeably break the symmetry of the two C-I bonds.

D. Bond Selective Electronic Excitation in Bromoiodomethane

Bromoiodomethane is an important prototype molecule for bond selective photochemistry and provides a dramatic illustration of selective bond

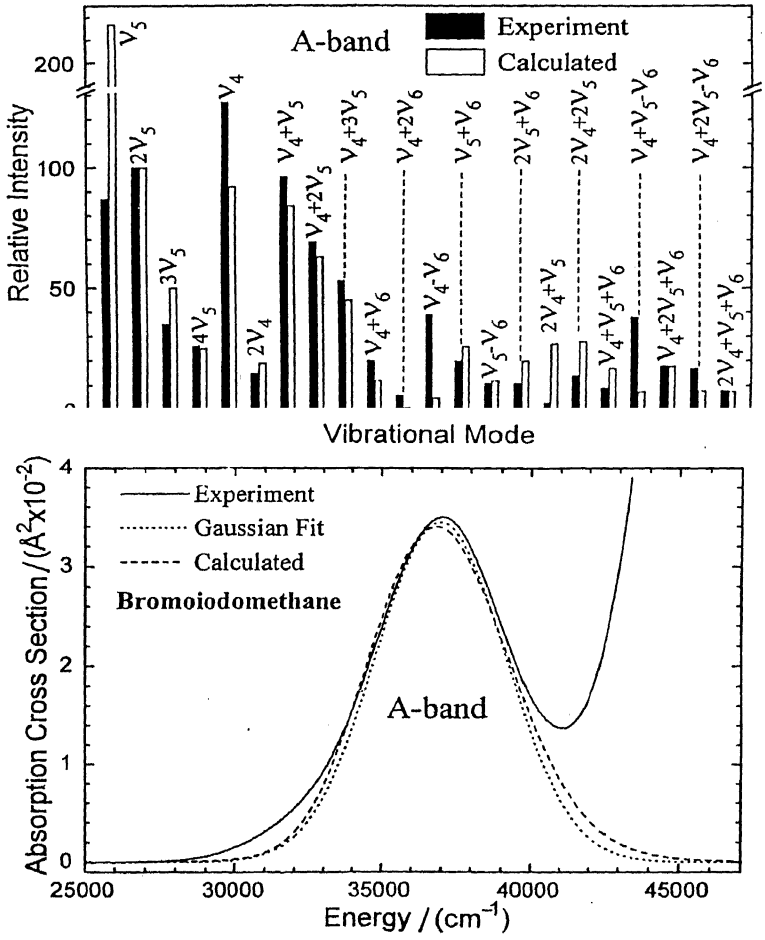

Fig. 26 Comparison of experimental (solid bars) and calculated (open bars) resonance Raman intensities for the solution phase bromoiodomethane in cyclohexane solvent 266.0 nm resonance Raman spectrum. Comparison of the experimental (solid line), Gaussian band of the A-state deconvolution (dotted line), and calculated (dashed line) A-band absorption spectra for bromoiodomethane in cyclohexane solution. The calculations made use of the parameters and simple model given in reference [67].

cleavage by using electronic excitation of two different bonds (the C-Br and the C-I bonds).[96-98] Resonance Raman spectra were obtained including absolute Raman cross section measurements at excitation within the A-band (associated with the C-I bond) and the B-band (associated with the C-Br bond) absorptions in order to better understand the initial photodissociation dynamics associated with the bond selective electronic excitation and photochemistry. Fig. 23 shows the absorption spectra of gas and solution phase bromoiodomethane as well as bromomethane and iodomethane for comparison. Fig. 24 displays the resonance Raman spectra obtained with A-band (252.7 nm and 266.0 nm) and B-band (208.8 nm and 217.8 nm) excitation. The resonance Raman have almost all of their intensity in three Franck-Condon active vibrational modes: the nominal C-I stretch, C-Br stretch, and I-C-Br bend modes. Although the A-band and B-band have the same Franck-Condon active modes their intensity patterns are significantly different from one another and therefore their initial photodissociation dynamics are different from each other. We simulated the resonance Raman and absorption cross sections using a simple model and time dependent wavepacket calculations. Figs. 25 and 26 display comparisons of the experimental and calculated absorption spectra and resonance Raman intensities for the A-band and B-band of bromoiodomethane respectively.[67] The parameters for the best fit calculations are given in Table IV. There is reasonable agreement between the experimental and calculated absorption spectra and resonance Raman intensities shown in Figs. 25 and 26. We have obtained the short-time photodissociation dynamics in terms of internal coordinate motions associated with the A-band and B-band photodissociation reactions (we used the results of normal mode calculations in conjunction with the best fit normal mode displacements and eqs. (3) and (4)). Table IV presents the A-band and B-band short-time photodissociation dynamics at t=15 fs after photoexcitation and the diagram of bromoiodomethane shown in Fig. 27 can be used to better visualize these dynamics. Inspection of Table IV shows that the A-band initial photodissociation dynamics have the C-I bond becoming much longer, the I-C-Br angle becomes smaller, the C-Br bond becomes smaller, the H-C-I angles become smaller, the H-C-Br angles become larger, and the H-C-H angle becomes slightly smaller. The B-band short-time photodissociation dynamics show that the C-Br bond becomes much longer, the C-I bond becomes a little longer, the I-C-Br angle becomes smaller, the H-C-I angles become larger and the H-C-H angle becomes a little smaller. The short-time photodissociation

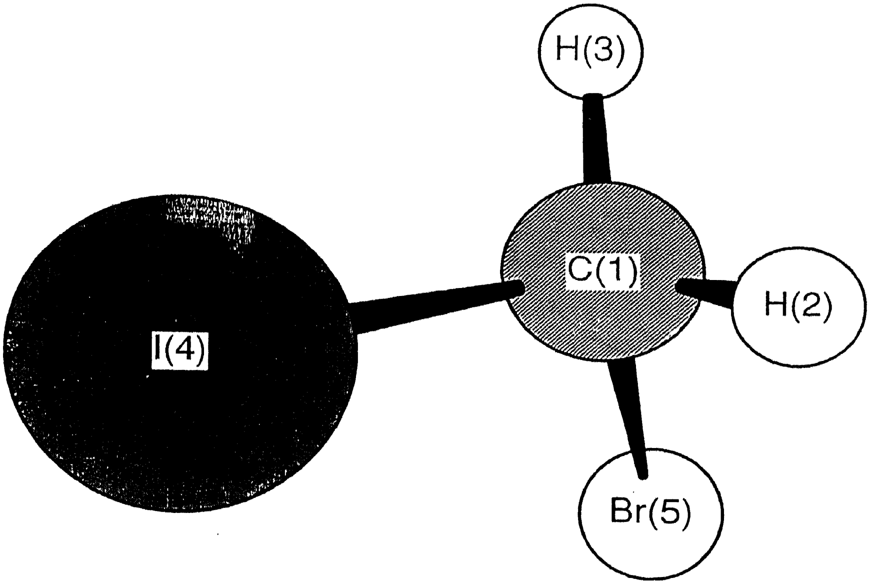

Fig. 27 Geometry of bromoiodomethane with each atom numbered 1 through 5.

Table IV

(A.) Parameters for calculation of resonance Raman intensities and absorption spectra of A-band and B-band bromoiodomethane. (B.) Most probable internal coordinate displacements of bromoiodomethane in cyclohexane solution at t = 15 fs assuming the C-I bond lengthens in the A-band and the C-Br bond lengthens in the B-band.

(A.) Simulation Parameters

A-Band Parameters

Vibrational Mode	Ground State Vibrational Frequency (cm^{-1})	Excited State Vibrational Frequency (cm^{-1})	$\lvert\Delta\rvert$
ν_4	621 cm^{-1}	621 cm^{-1}	2.65
ν_5	521 cm^{-1}	521 cm^{-1}	4.8
ν_6	151 cm^{-1}	151 cm^{-1}	4.5
Transition Length, M=0.287 Å,	E_0 = 27,200 cm^{-1},	HWHM of damping function, Γ = 50 cm^{-1}	

B-Band Parameters

Vibrational Mode	Ground State Vibrational Frequency (cm-1)	Excited State Vibrational Frequency (cm-1)	$\lvert\Delta\rvert$
ν_4	621 cm^{-1}	621 cm^{-1}	2.5
ν_5	521 cm^{-1}	521 cm^{-1}	3.0
ν_6	151 cm^{-1}	151 cm^{-1}	3.6
Transition Length, M=0.38 Å	E_0 = 41,100 cm^{-1}	HWHM of damping function, Γ = 50 cm^{-1}	

(B.) Short-Time Photodissociation Dynamics at t=15fs

		[a]Range of Displacements at t = 15 fs	
A-Band		Δ_4=-2.65	Δ_4=−2.65
Internal Coordinate	Δ_5=+4.8, Δ_6=+4.5	Δ_5=+4.8, Δ_6=−4.5	
C-H bonds	<0.01	<0.01	
C-I bond, atoms 1 and 4	+0.38	+0.37	
C-Br bond, atoms 1 and 5	−0.10	−0.10	
H-C-H angle, atoms 2, 1, and 3	−1.6	−1.4	
H-C-I angle, atoms 2, 1, and 4	−1.0	−0.4	
H-C-Br angle, atoms 2, 1, and 5	+6.5	+6.9	
H-C-I angle, atoms 3, 1, and 4	−1.0	−0.4	
H-C-Br angle, atoms 3, 1, and 5	+6.5	+6.9	
I-C-Br angle, atoms 4, 1, and 5	−9.9	−12	

B-Band

		[a]Range of Displacements at t = 15 fs	
		Δ_4=+2.5	Δ_4=+2.5
Internal Coordinate	Δ_5=+3.0, Δ_6=+3.6	Δ_5=+3.0, Δ_6=−3.6	
C-H bonds	−0.01	−0.01	
C-I bond, atoms 1 and 4	+0.02	+0.01	
C-Br bond, atoms 1 and 5	+0.26	+0.26	
H-C-H angle, atoms 2, 1, and 3	−0.7	−0.5	
H-C-I angle, atoms 2, 1, and 4	+7.6	+8.1	
H-C-Br angle, atoms 2, 1, and 5	−2.7	−2.5	
H-C-I angle, atoms 3, 1, and 4	+7.6	+8.1	
H-C-Br angle, atoms 3, 1, and 5	−2.7	−2.5	
I-C-Br angle, atoms 4, 1, and 5	−8.8	−11	

[a] Values are for the two most probable sign combinations of the normal mode displacements (see ref. [67]).

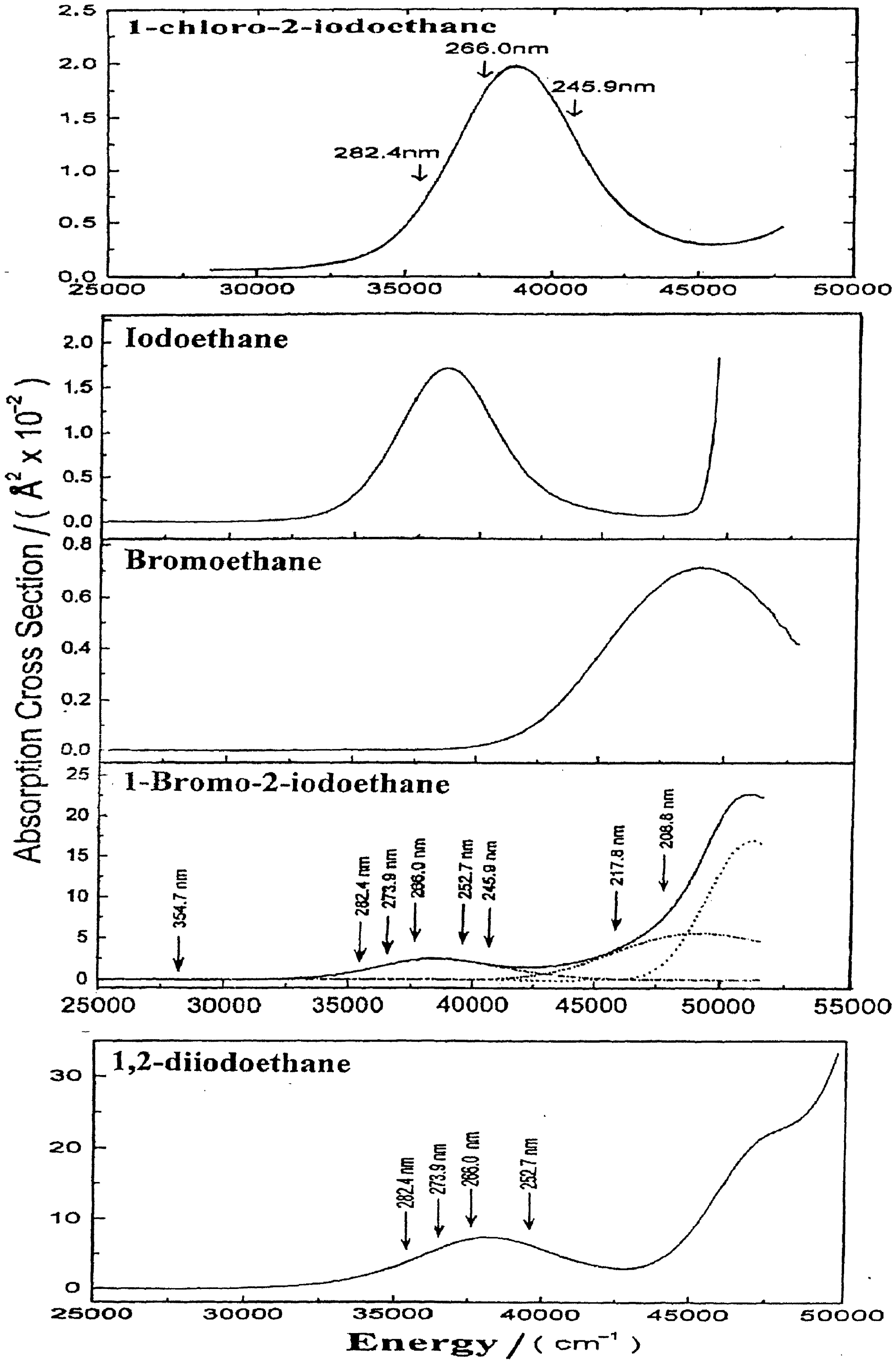

Fig. 28 Absorption spectra of 1-chloro-2-iodoethane, iodoethane, bromoethane, 1-bromo-2-iodoethane, and 1,2-diiodoethane in cyclohexane solution. The excitation frequencies for the resonance Raman spectra are shown above the 1-chloro-2-iodoethane, 1-bromo-2-iodoethane, and 1,2-diiodoethane spectra

dynamics of both the A-band and B-band are consistent with an impulsive "semi-rigid" radical description of the photodissociation with the CH_2Br radical group moving towards a more planar structure in the A-band and the CH_2I radical group moving towards a more planar structure in the B-band. We have done a gaussian deconvolution of the A-band and B-band absorption spectra of bromoiodomethane in order to estimate the relative contributions of the different $n \rightarrow \sigma^*$ transitions to the absorption bands. The comparison of this gaussian deconvolution for bromoiodomethane with the deconvolutions for the corresponding single chromophore molecules (e.g. bromomethane and iodomethane) indicates that the $^3Q_0$ transition receives significantly more enhancement of its oscillator strength than the $^1Q_1$ and $^3Q_1$ transitions as one goes from the single chromophore molecule to the two chromophore bromoiodomethane molecule. In addition, the B-band transitions have their oscillator strengths enhanced to a noticeably greater extent than the A-band transitions in bromoiodomethane. The patterns in the gaussian deconvolutions of the absorption spectra, the experimental resonance Raman intensities and the deduced short-time photodissociation dynamics of bromoiodomethane all suggest a noticeable amount of coupling between the C-I and C-Br chromophores. The reader is referred to ref. [67] for more details on this prototypical molecule for bond selective electronic excitation and photochemistry as well as a hypothesis for the B-band photodissociation reactions that is consistent with our results and those of previous molecular beam experiments.[96-98]

E. Substituent Effects and Influence of a Second Carbon-Halogen Chromophore in 1-Halo-2-Iodoethanes

We have investigated the A-band photodissociation dynamics of three dihaloethanes (1-chloro-2-iodoethane, 1-bromo-2-iodoethane, and 1,2-diiodoethane) in order to examine substituent effects on the photodissociation dynamics and how the presence of an additional carbon-halogen

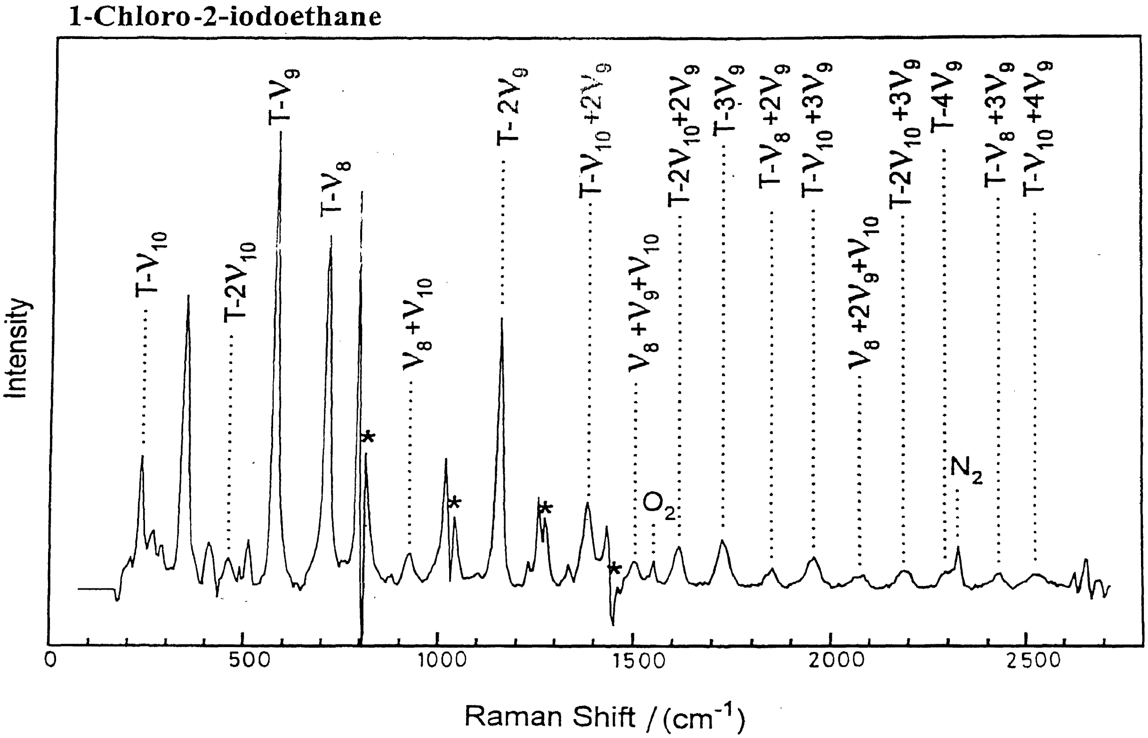

Fig. 29 Enlarged view of the 266.0 resonance Raman spectrum of 1-chloro-2-iodoethane in cyclohexane solution. The spectrum has been intensity corrected and solvent subtracted. Regions with solvent subtraction artifacts have been marked by asterisks. The more intense Raman bands have their tentative assignments displayed.

1-Bromo-2-iodoethane

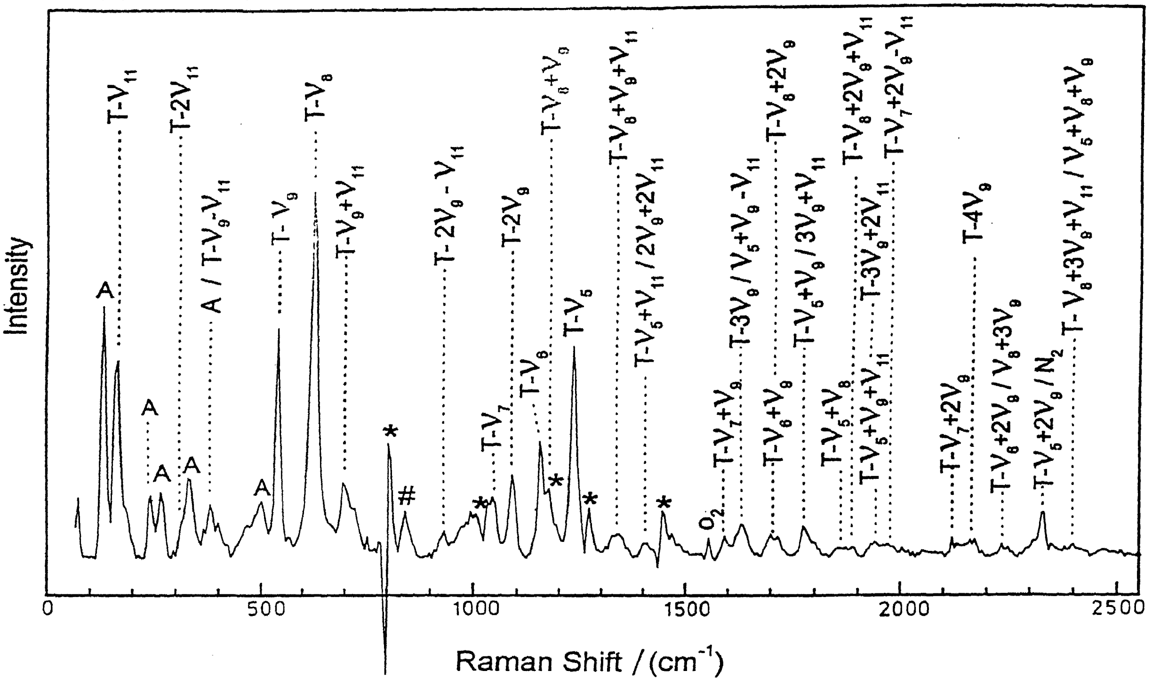

Fig. 30 Enlarged view of the 266.0 resonance Raman spectrum of 1-bromo-2-iodoethane in cyclohexane solution. The spectrum has been intensity corrected and solvent subtracted. Regions with solvent subtraction artifacts have been marked by asterisks. The more intense Raman bands have their tentative assignments displayed. The symbol A represents Raman bands due to an apparent transient species (see ref. [73]).

1,2-Diiodoethane

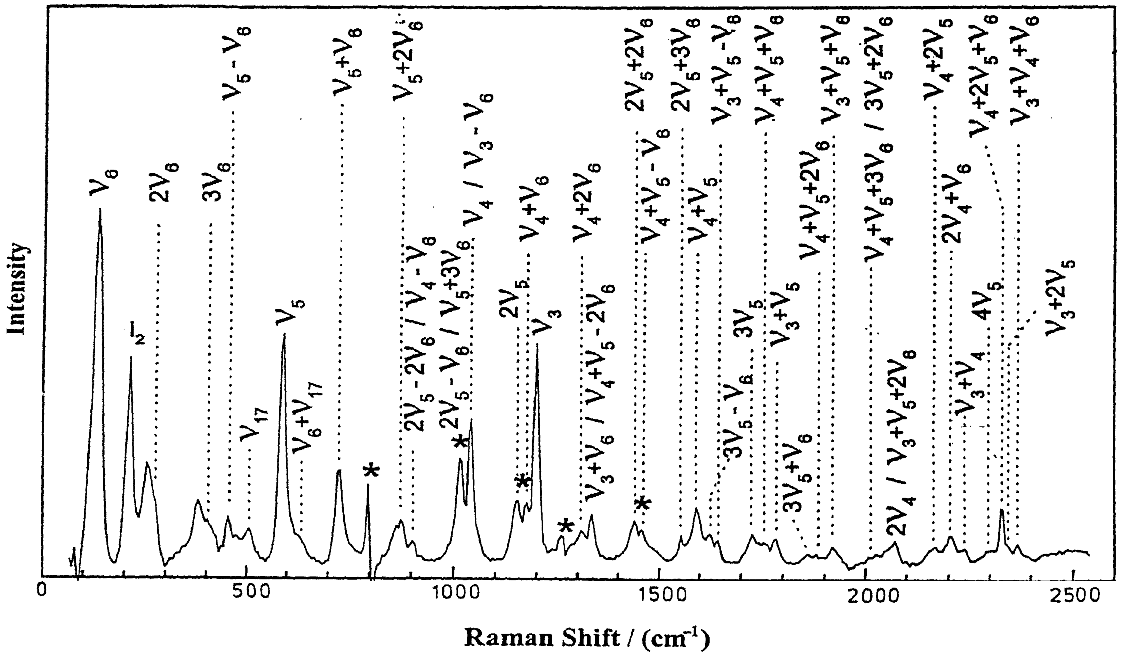

Fig. 31 Enlarged view of the 266.0 resonance Raman spectrum of 1,2-diiodoethane in cyclohexane solution. The spectrum has been intensity corrected and solvent subtracted. Regions with solvent subtraction artifacts have been marked by asterisks. The more intense Raman bands have their tentative assignments displayed.

Table V

Most probable A-band internal coordinate displacements of trans-1-bromo-2-iodoethane at t=10 fs assuming the C-I bond becomes longer and the CCI angle becomes smaller. Comparison to previous results for iodoethane, trans-1-chloroethane and trans-1,2-diiodoethane.

Trans-1-bromo-2-iodoethane (Ref. 73)			
Set A (the C-Br bond becomes longer)		Set B (the C-Br becomes shorter)	
Coordinate	Range of Displacements at t=10 fs	Coordinate	Range of Displacements at t=10 fs
r_{CI}	+0.115 to +0.196 Å	r_{CI}	+0.115 to +0.196 Å
r_{CBr}	+0.013 to +0.094 Å	r_{CBr}	−0.102 to −0.021 Å
r_{BC}	−0.145 to +0.047 Å	r_{BC}	−0.115 to +0.077 Å
r_{CH}	< ±0.006 Å	r_{CH}	< ±0.006 Å
$\angle BCI$	−11.3° to −3.3°	$\angle BCI$	−7.6° to +0.5°
$\angle HCB$	−10° to +11.6°	$\angle HCB$	−11° to +10.6°
$\angle ICH$	−8.1° to +13.6°	$\angle ICH$	−8.8° to +12.9°
$\angle CBBr$	−11.9° to −3.4°	$\angle CBBr$	−8.2° to +0.2°
$\angle CBH_{7\text{ or }8}$	−11.2° to +16°	$\angle CBH_{7\text{ or }8}$	−11.3° to +14.8°
$\angle HCH$	−1.2° to +1.9°	$\angle HCH$	−1.6° to +1.9°
$\angle HBH$	−1.9° to +2.5°	$\angle HBH$	−1.8° to +2.6°
$\angle HBBr$	−13.2° to +14.2°	$\angle HBBr$	−13.8° to +13.6°

1-Chloro-2-Iodoethane (from Ref. 70)		**Iodoethane (from Ref. 89)**	
Coordinate	Range of Displacements at t=10 fs	Coordinate	Range of Displacements at t=10 fs
r_{CI}	+0.09 to +0.18 Å	r_{CI}	+0.13 to +0.15 Å
r_{CCl}	−0.01 to −0.18 Å		
r_{BC}	−0.024 to +0.012 Å	r_{BC}	−0.06 to −0.05 Å
r_{CH}	< ±0.004 Å	r_{CH}	< ±0.004 Å
$\angle BCI$	−7.8° to +2.5°	$\angle BCI$	−6° to −3°
$\angle HCB$	−0.8° to +0.8°	$\angle HCB$	+6° to +9°
$\angle ICH$	−0.4° to +2.5°	$\angle ICH$	−7° to −3°
$\angle CBCl$	−8.8° to +3.2°	$\angle CBH_8$	−1° to +5°
$\angle CBH_{7\text{ or }8}$	−0.7° to +2°	$\angle CBH_{7\text{ or }6}$	−3° to −1°
$\angle HCH$	−0.6° to +1°	$\angle HCH$	−6° to +5°
$\angle HBH$	−0.2° to +1.1°	$\angle H_7BH_6$	−8° to +8°
$\angle HBCl$	−0.8° to +1.4°	$\angle H_8BH_{7\text{ or }6}$	−4° to +5°

1,2-Diiodoethane (from Ref. 72)	
Coordinate	Range of Displacements at t=10 fs
first r_{CI}	+0.068 to +0.116 Å
second r_{CI}	+0.033 to +0.068 Å
r_{CC}	−0.138 to +0.071 Å
r_{CH}	< ±0.005 Å
$\angle CCI$	−8.7° to −1.8°
$\angle HCC$	−6.8° to +7.6°
$\angle ICH$	−4.6° to +7.8°
$\angle HCH$	0.0° to +2.5°

chromophore on the β-carbon atom position affects the C-I bond cleavage.[70,72,73] We have obtained a number of resonance Raman spectra at excitation wavelengths within the A-band absorptions of 1-chloro-2-iodoethane, 1-bromo-2-iodoethane and 1,2-diiodoethane in cyclohexane solutions. The absorption spectra of 1-chloro-2-iodoethane, 1-bromo-2-iodoethane and 1,2-diiodoethane in cyclohexane solution are shown in Fig. 28 and the excitation wavelengths (in nm) are indicated above each absorption spectrum. Figs. 29-31 display representative A-band resonance Raman spectra for

1-chloro-2-iodoethane, 1-bromo-2-iodoethane and 1,2-diiodoethane. The fundamentals, overtones and combinations bands of the nominal CCCl bend (ν_{10}), C-I stretch (ν_9) and C-Cl stretch (ν_8) modes account for most of the resonance Raman intensity in the A-band spectra of 1-chloro-2-iodoethane. The A-band resonance Raman spectra of 1-bromo-2-iodoethane have most of their intensity in the trans conformer fundamentals, overtones, combination bands of six Franck-Condon active

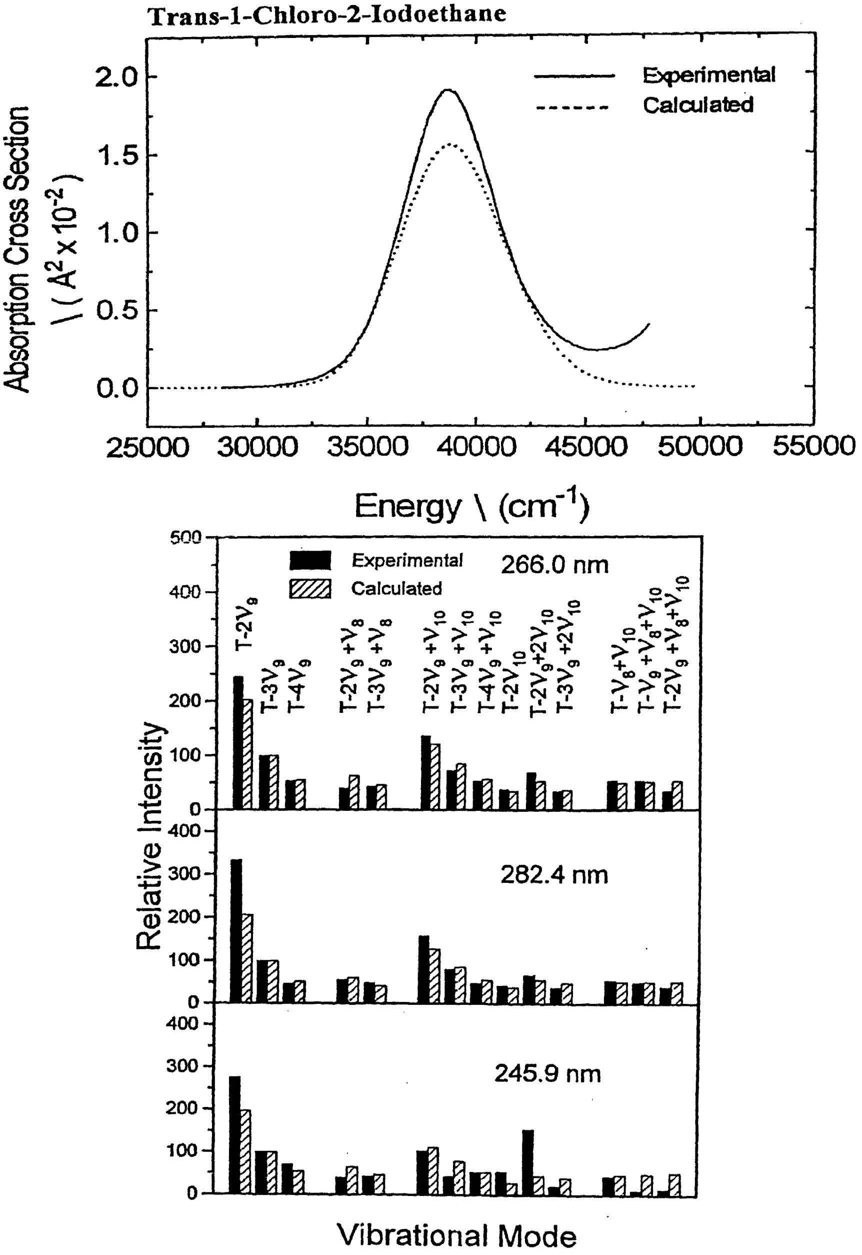

Fig. 32 Comparison of experimental (solid bars) and calculated (striped bars) resonance Raman intensities for the solution phase 1-chloro-2-iodoethane in cyclohexane solvent 266.0 nm, 282.4 nm, and 245.9 nm resonance Raman spectra. Comparison of the experimental (solid line) and calculated (dotted line) absorption spectra. The calculations made use of the parameters and simple model given in reference [70].

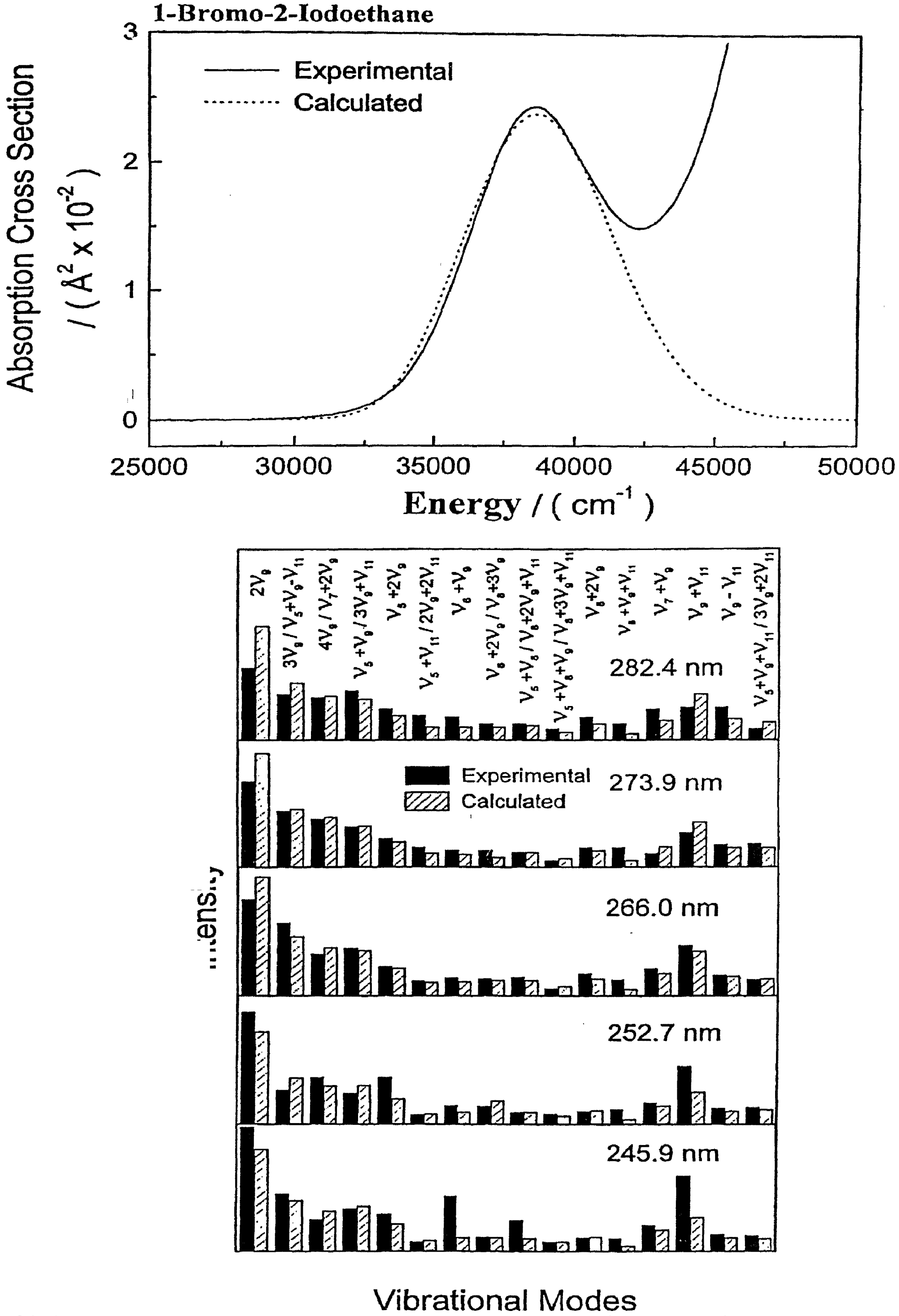

Fig. 33 Comparison of experimental (solid bars) and calculated (striped bars) resonance Raman intensities for the solution phase 1-bromo-2-iodoethane in cyclohexane solvent 282.4 nm, 273.9 nm, 266.0 nm, 252.7 nm and 245.9 nm resonance Raman spectra. Comparison of the experimental (solid line) and calculated (dotted line) absorption spectra. The calculations made use of the parameters and simple model given in reference [73].

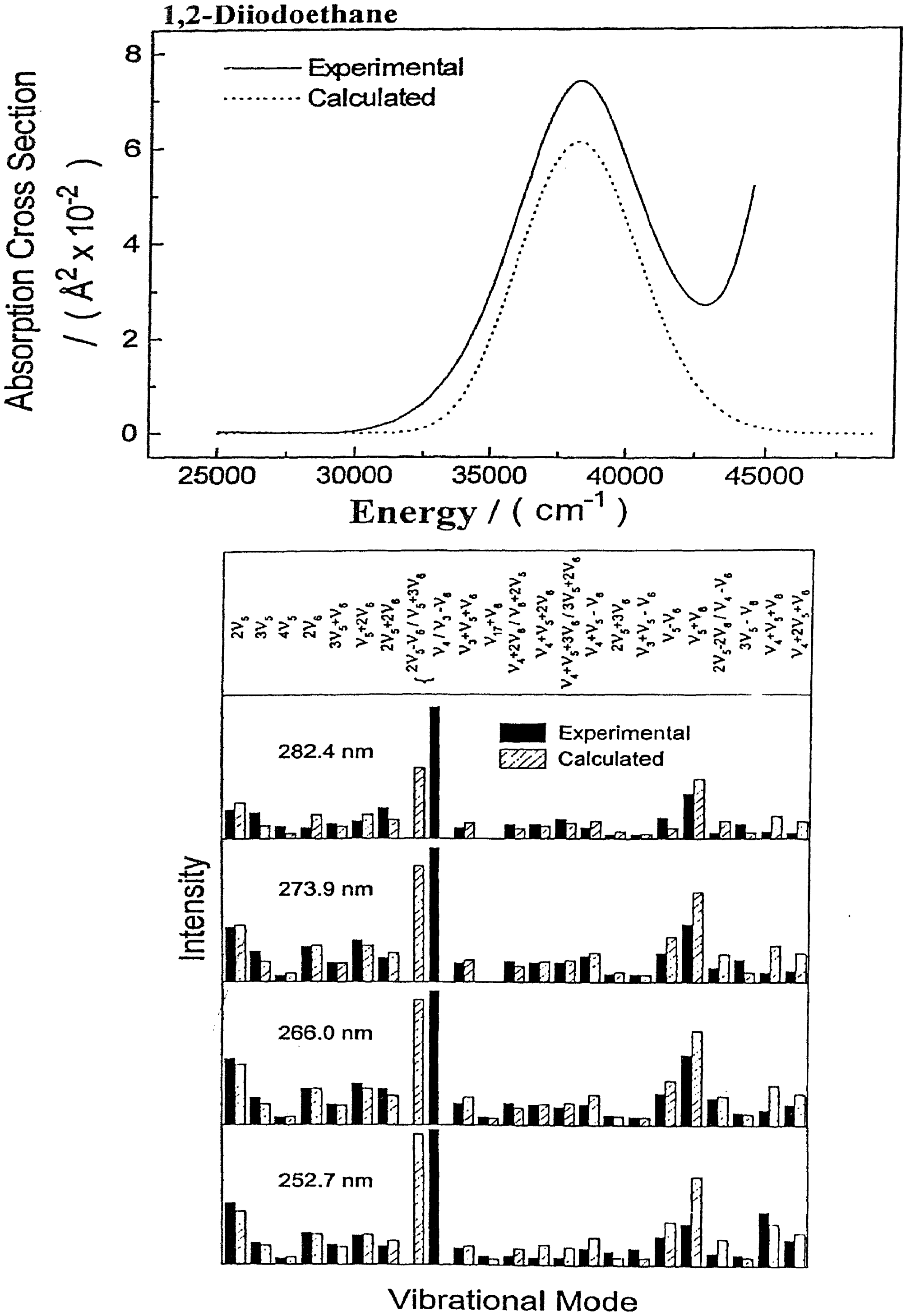

Fig 34 Comparison of experimental (solid bars) and calculated (striped bars) resonance Raman intensities for the solution phase 1,2-diiodoethane in cyclohexane solvent 282.4 nm, 273.9 nm, 266.0 nm, and 252.7 nm resonance Raman spectra. Comparison of the experimental (solid line) and calculated (dotted line) absorption spectra. The calculations made use of the parameters and simple model given in reference [72].

modes: the nominal CCI bend (ν_{11}), C-I stretch (ν_9), C-Br stretch (ν_8), C-C stretch (ν_7), CH_2 wag with the I atom attached to the CH_2 group (ν_6) and the CH_2 wag with the Br atom attached to the CH_2 group (ν_5) vibrational modes. The A-band resonance Raman spectra of diiodoethane have most of their intensity from the trans conformer fundamentals, overtones, and combination bands of five Franck-Condon active vibrational modes: the nominal CCI bend (ν_6), C-I stretch (ν_5 and ν_{17}), C-C stretch (ν_4), and CH_2 wag (ν_3) modes.

The A-band resonance Raman intensities and absorption spectra for the three 1-halo-iodoethanes were simulated using time-dependent wavepacket calculations as described in the Theory and Calculations section (and in the original publications of refs [70], [72] and [73]). Figs. 32-34 present comparisons of the experimental and calculated absorption spectra and resonance Raman intensities for 1-chloro-2-iodoethane, 1-bromo-2-iodoethane, and 1,2-diiodoethane respectively. The best fit parameters for the simulations are given in refs. [70], [72] and [73]. The experimental and calculated absorption spectra show reasonable agreement considering we are only simulating the largest $^3Q_0$ transition that accounts for most of the oscillator strength (70-90%). There is also reasonable agreement between the experimental and calculated resonance Raman intensities. The results of the best fit simulation were used in conjunction with the results of normal coordinate descriptions in order to find the short-time photodissociation dynamics in terms of easy to visualize internal coordinate changes. Table V lists the short-time photodissociation dynamics at time 10 fs after photoexcitation obtained from the

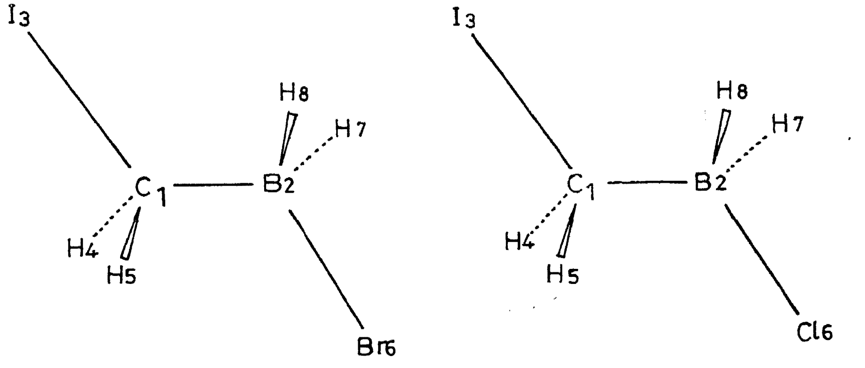

Trans-1-Bromo-2-Iodoethane **Trans-1-Chloro-2-Iodoethane**

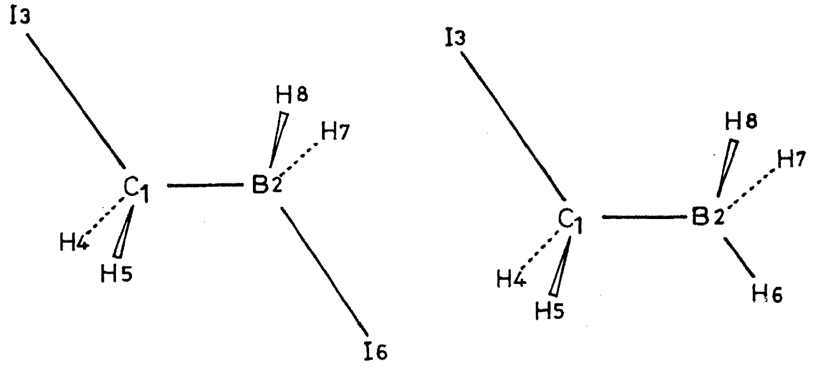

Trans-1,2-Diiodoethane **Iodoethane**

Fig. 35 Simplified geometries of the ground electronic states of trans-1-chloro-2-iodoethane, 1-bromo-2-iodoethane, and 1,2-diiodoethane which can be used to better visualize the short-time photodissociation dynamics presented in Table V.

resonance Raman intensity analysis studies done for 1-chloro-2-iodoethane, 1-bromo-2-iodoethane, and 1,2-diiodoethane. Previous results for the A-band iodoethane photodissociation are also shown in Table V for comparative purposes. Fig. 35 which displays simple diagrams of the iodoethane, 1-chloro-2-iodoethane, 1-bromo-2-iodoethane, and 1,2-diiodoethane can be used to help better visualize the short-time dynamics.

The ground state of the ethyl radical is close to a nearly planar structure and inspection of Table V shows that the initial photodissociation dynamics for the A-band of iodoethane brings the ethyl radical group closer to a planar structure and about the α-carbon atom. This suggests that there is probably little vibrational excitation of the ethyl radical photofragment in so far as the short-time dynamics translate into internal excitation of the alkyl fragment. *Ab initio* investigations indicate that the C-C bond length for iodoethane in its ground state is 1.54 Å and the C-C bond length in the ground state of the ethyl-radical is 1.49 Å.[91-93] The initial photodissociation dynamics in Table V for the C-C bond length (-0.05 to –0.06 Å) brings the bond length close to that of the ground state of the ethyl radical and this also suggests that there is likely little vibrational excitation in the C-C mode of the ethyl fragment. The initial dynamics of the A-band photodissociation of iodoethane is consistent with the experimental observation that the ethyl radical photoproduct gets relatively little internal excitation (32-39% of the available energy) compared to more massive and/or branched iodoalkanes. Examination of Table V indicates that the A-band initial photodissociation dynamics of 1-chloro-2-iodoethane are significantly different from iodoethane. Both the C-I (+0.09 to +0.18 Å) and the C-Cl (-0.01 to –0.18) bond lengths at 10 fs have large displacements or range of displacements while the C-C bond length does not change much (-0.024 to +0.012 Å). The range of C-I bond displacements for 1-chloro-2-iodoethane is more similar to that of 2-iodopropane or 2-methyl-2-iodopropane which have greater internal excitation of the alkyl radical fragments than iodoethane. The initial A-band photodissociation dynamics for 1-chloro-2-iodoethane do not go toward a more planar structure about the α-carbon nearly as much as iodoethane does and this suggests that there is more internal excitation of the chloroethyl radical then the ethyl radical photoproduct (assuming the chloroethyl and ethyl radicals have a similar ground state structure-which is very likely) in so far as the Franck-Condon region dynamics determines the internal excitation of the alkyl photofragments. This is consistent with TOF photofragment spectroscopy experiments which show show a greater degree of internal excitation of the chloroethyl radical (42% to 54% of the available energy)[19,20,24,52] from 1-chloro-2-iodoethane photodissociation than the ethyl radical (32%-39% of the available energy)[99] from iodoethane photodissociation.

Comparison of the short-time photodissociation dynamics presented in Table V reveals some interesting trends. As the molecule becomes more massive, the C-I bond length changes generally proceed from a long and narrow range (such as +0.13 to +0.15 Å at 10 fs for iodoethane) to shorter and broader range (such as +0.068 to +0.116 Å and +0.033 to +0.068 Å at 10 fs for the two C-I bonds of 1,2-diiodoethane). There is also a similar trend in the C-C bond lengths (-0.05 to –0.06 Å at 10 fs for iodoethane to –0.138 to +0.071 Å at 10 fs for 1,2-diiodoethane). These trends in the C-I and C-C bond lengths for the A-band short-time photodissociation dynamics suggest that the haloethyl radical receives more internal excitation as it becomes more massive in as much as the short-time dynamics determines the photodissociation energy partitioning. This is similar to trends in the C-I bond lengths for the A-band short-time dynamics of iodoalkanes as the alkyl group becomes more massive and/or branched. The trends in the C-I and C-C bond lengths for iodoethane, 1-chloro-2iodoethane, 1-bromo-2-iodoethane, and 1,2-diiodoethane also exhibit a good correlation with time-of-flight molecular beam experimental results that indicate the available energy that goes into internal excitation of the (halo)alkyl radical product is 32%-39% for ethyl radicals from iodoethane[19,20,24,52], 42%-54% for chloroethyl radicals from 1-chloro-2-iodoethane[99], and 53%-58% for bromoethyl radicals from 1-bromo-2-iodoethane.[100]

There is one intriguing puzzle in the trends shown in Table V: The C-I bond lengths do not change much in going from 1-chloro-2-iodoethane, but the C-C bond length changes are substantially greater in 1-bromo-2-iodoethane than for 1-chloro-2-iodoethane. Why are the C-C bond length changes so similar for 1-bromo-2-iodoethane and 1,2-diiodoethane and very different from 1-chloro-2-iodoethane? To help answer this, it is useful to examine the absorption spectral trends for the (halo)iodoethanes. The absorption coefficients for iodoethane and 1-chloro-2-iodoethane are very similar and indicate that the transitions are mainly due to the C-I bond alone. However, the absorption coefficients for 1-bromo-2-iodoethane and 1,2-diiodoethane are substantially larger and this increase in oscillator strength for the A-band absorptions cannot be simply accounted for by simple addition of the iodoethane and bromoethane absorptions for 1-bromo-2-iodoethane or two iodoethane absorptions for 1,2-diiodoethane. The observed additional increase in the A-band absorption oscillator strength for 1-bromo-2-iodoethane and 1,2-diiodoethane presumably results from significant interaction between the two carbon halogen chromophores (we note that the trans conformer accounts for most of the population in both of these molecules). Thus excitation within the A-band absorption of 1-bromo-2-iodoethane and 1,2-diiodoethane would most likely excite both the carbon halogen chromophores to some extent and this would cause the two carbon atoms of the 1,2-dihaloethanes to experience noticeable forces from both halogen atoms. Whether these forces oppose or do not oppose one another, these forces would cause additional strain on the carbon-carbon bond to give larger and broader displacements in the haloethyl group during the photodissociation. This is consistent with the initial photodissociation dynamics observed in Table V and the significantly larger C-C displacements found for the short-time photodissociation dynamics of 1-bromo-2-iodoethane and 1,2-diiodoethane is most likely due to some simultaneous photoexcitation of the carbon-halogen bonds.

Our resonance Raman studies of the dihaloethanes show that substitution of a hydrogen atom to the β-carbon of iodoethane by a more massive halogen atom leads to substantial substituent effects on the A-band short-time photodissociation dynamics. All of the dihaloethanes examined so far have multidimensional dynamics with the C-I bond cleavage occurring on a similar time scale as vibrational motion in the rest of the molecule. The initial photodissociation dynamics of the dihaloethanes are somewhere between the simple impulsive "rigid radical" and "soft radical" models of photodissociation dynamics and more similar to an impulsive "semi-rigid radical" model of the photodissociation dynamics. The dihaloethanes investigated (1-chlro-2-iodoethane, 1-bromo-2-iodoethane, and 1,2-diiodoethane) display noticeable bond length changes in the secondary carbon-halogen bond during the initial A-band photodissociation reaction arising from kinematics and/or simultaneous excitation of both C-X chromophores.

Conclusion

The resonance Raman intensity analysis studies presented here for the direct photodissociation reactions associated with excitation within the A-band absorption of polyatomic iodoalkanes and dihaloalkanes molecules show the multidimensional nature of the initial photodissociation coordinate. There is not nearly as much experimental or theoretical work done for the higher iodoalkanes and dihaloalkanes as has been done for iodomethane (the smallest iodoalkane) and this highlights the need for more experimental and theoretical work to enable a better and deeper understanding of direct polyatomic photodissociation reactions. Experiments such as magnetic circular dichroism (MCD), multiphoton ionization (MPI), femtosecond time-resolved pump-probe experiments, infrared emission and others which have been invaluable in better understanding the details of the A-band iodomethane photodissociation reaction are needed for many of the larger haloalkane and dihaloalkane molecular systems. These types of experiments and relevant theoretical investigations should enable a much higher level of understanding of the direct A-band photodissociation reactions as well as the interaction of the two C-X chromophores in dihaloalkane molecules.

Acknowledgements

The author would like to thank Professor James J Valentini and Professor Anne B Myers for many useful discussions and their encouragement. The author would also like to thank his former Ph.D. student, Dr. Wai Ming Kwok, who carried out much of the work on dihalomethanes and his current Ph.D. student, Mr. Xuming Zheng who did much of the work on the dihaloethanes. Further, the author would also like to acknowledge his current M.Phil. student Miss Yung Fong Cheng who helped in the 1,2-diiodoethane work and Mr. King Hung Leung and Mr. Mong Yin Lau who helped to prepare the figures. Financial support from several RGC grants from the UGC of Hong Kong and CRCG grants from the University of Hong Kong are acknowledged.

References

1 E J Heller, R L Sundberg and D J Tannor *J Phys Chem* **86** (1982) 1822
2 A B Myers and R A Mathies *Biological Applications of Raman Spectroscopy* Wiley New York (1987) 1
3 R J H Clark and T J Dines *Agnew Chem Int Ed Engl* **98** (1986) 131
4 J I Zink and K S K Shin *Adv Photochem* **16** (1991) 119
5 A B Myers, *Laser Techniques in Chemistry*; Wiley: New York (1995) 325
6 B R Johnson, C Kittrell, P B Kelly and J L Kinsey *J Phys Chem* **100** (1996) 7743
7 A B Myers *Chem Rev* **96** (1996) 911
8 A B Myers, *Acc Chem Res* **30** (1997) 519
9 K Kinmura and S Nagakura *Spectrochim Acta* **17** (1961) 166
10 A Gedanken and M D Rowe *Chem Phys Lett* **34** (1975) 39
11 A Gedanken *Chem Phys Lett* **137** (1987) 462
12 T Donohue and J Wiesenfeld *Chem Phys Lett* **33** (1975) 176
13 T Donohue and J Wiesenfeld *J Chem Phys* **63** (1975) 3130
14 W H Pence, S L Baughchum and S L Leone *J Phys Chem* **85** (1981) 3844
15 P Brewer, P Das, G Ondrey and R Bersohn *J Chem Phys* **79** (1983) 720
16 W P Hess, S J Kohler, H K Haugen and S R Leone *J Chem Phys* **84** (1986) 2143
17 R Ogorzalek-Loo, G E Hall, H-P Haerri and P L Houston *J Phys Chem* **92** (1987) 5
18 F G Godwin, P A Gorry, P M Hughes, D Raybone, T M Watkinson and J C Whitehead *Chem Phys Lett* **135** (1987) 163
19 Q Zhu, J R Cao, Y Wen, J Zhang, Y Huang, W Fang, and X Wu *Chem Phys Lett* **144** (1988) 486
20 S J Riley and K R Wilson *Faraday Discuss Chem Soc* **53** (1972) 132
21 R K Sparks, K Shobatake, L R Carlson and Y T Lee *J Chem Phys* **75** (1981) 3838
22 G N A Van Veen, T Baller, A E Devries and N J A Van Veen *Chem Phys* **87** (1984) 405
23 M D Barry and P A Gorry *Mol Phys* **52** (1984) 461
24 C Paterson, F G Godwin and P A Gorry *Mol Phys* **60** (1987) 729
25 F G Godwin, C Paterson and P A Gorry *Mol Phys* **61** (1987) 827
26 J F Black and I Powis *Chem Phys* **125** (1988) 375
27 I Powis and J F Black *J Phys Chem* **93** (1989) 2461
28 R Ogorzalek-Loo, H-P Haerri, G E Hall and P L Houston *J Chem Phys* **90** (1989) 4222
29 D W Chandler, M H M Janssen, S Stolte, R N Strickland, J W Thoman, Jr and D H Parker *J Phys Chem* **94** (1990) 4839
30 N E Triggs, M Zahedi, J W Nibler, P A Debarber and J J Valentini *J Chem Phys* **96** (1992) 2756
31 G E Hall, T J Sears and J M Frye *J Chem Phys* **89** (1988) 580
32 J W G Mastenbroek, C A Taatjes, K Nauta, M H M Janssen and S Stolte *J Phys Chem* **99** (1995) 4360
33 J L Knee, L R Khundar and A H Zewail *J Chem Phys* **83** (1985) 1996
34 L R Khundar and A H Zewail *Chem Phys Lett* **142** (1987) 426
35 M Shapiro and R Bersohn *J Chem Phys* **72** (1980) 3810
36 S K Gray and M S Child *Mol Phys* **51** (1984) 189
37 M Shapiro *J Phys Chem* **90** (1986) 3644
38 M Tadjeddine, J P Flament and C Teichteil *Chem Phys* **118** (1987) 45
39 H Guo and G C Schatz *J Chem Phys* **93** (1990) 393
40 Y Amatatsu, K Morokuma and S Yabushita *J Chem Phys* **94** (1991) 4858
41 H Guo and G C Schatz *J Chem Phys* **95** (1991) 3091
42 H Guo *J Chem Phys* **96** (1992) 2731
43 A D Hammerich, U Manthe, R Kosloff, H-D Meyer and L S Cederbaum *J Chem Phys* **101** (1994) 5623
44 Y Amatatsu, S Yabushita and K Morokuma *J Chem Phys* **104** (1996) 9783
45 M K Dzvonik, S Yang and R Bersohn *J Chem Phys* **61** (1974) 4408
46 M Kawasaki, S J Lee and R Bersohn *J Chem Phys* **63** (1975) 809
47 P M Kroger, P C Demou and S J Riley *J Chem Phys* **65** (1976) 1823
48 T K Minton, P Felder, R J Brudzynski and Y T Lee *J Chem Phys* **81** (1984) 1759
49 D Krajnovitch, L J Butler and Y T Lee *J Chem Phys* **81** (1984) 3031
50 G N A Van Veen, T Baller, A E DeVries and M Shapiro *Chem Phys* **93** (1985) 277
51 Q-X Xu, K-H Jung and R B Bernstein *J Chem Phys* **89** (1988) 2099
52 W K Kang, K W Jung, D C Kim, K-H Jung and H S Kim *Chem Phys* **196** (1995) 363
53 W K Kang, K W Jung, D-C Kim and K-H Jung *J Chem Phys* **104** (1995) 5815
54 R J Donovan, F G M Hathorn and D Husain *Trans Faraday Soc* **64** (1968) 3192
55 T F Hunter, S Lunt and K S Kristjansson *J Chem Soc Faraday Trans II* **79** (1983) 303
56 E Gerck *J Chem Phys* **79** (1983) 311
57 S Uma and P K Das *Can J Chem* **72** (1994) 865
58 D H Fairbrother, K A Briggman, E Wietz and P C Stair *J Chem Phys* **101** (1994) 3787
59 P L Ross and M V Johnston *J Phys Chem* **99** (1995) 4078
60 S Uma and P K Das *Chem Phys Lett* **241** (1995) 335
61 S Uma and P K Das *J Chem Phys* **104** (1996) 4470

62 W M Kwok and DL Phillips *Chem Phys Lett* **235** (1995) 260
63 D L Phillips and W M Kwok *Chem Phys Lett* **241** (1995) 267
64 S Q Man, W M Kwok and D L Phillips *J Phys Chem* **99** (1995) 15705
65 W M Kwok and D L Phillips *J Chem Phys* **104** (1996) 2529
66 W M Kwok and D L Phillips *J Chem Phys* **104** (1996) 9816
67 S-Q Man, W M Kwok, A E Johnson and D L Phillips *J Chem Phys* **105** (1996) 5842
68 W M Kwok, P K Ng, G Z He and D L Phillips *Mol Phys* **90** (1997) 127
69 D L Phillips and A B Myers *J Raman Spectrosc* **28** (1997) 839
70 X Zheng and D L Phillips *Chem Phys Lett* **286** (1998) 79
71 X Zheng and D L Phillips *J Chem Phys* **108** (1998) 5772
72 X Zheng and D L Phillips *Chem Phys Lett* **292** (1998) 295
73 X Zheng and D L Phillips *J Chem Phys* **110** (1999) 1638
74 A B Myers, B Li and X Ci *J Chem Phys* **89** (1988) 1876
75 M O Trulson and R A Mathies *J Chem Phys* **84** (1986) 2068
76 B Li and A B Myers *J Phys Chem* **94** (1990) 4051
77 B U Curry, PhD dissertation (1983) University of California, Berkeley
78 L E Brus and V E Bondybey, *J Chem Phys* **65** (1976) 71
79 D G Imre, J L Kinsey, A Sinha and J Krenos *J Phys Chem* **88** (1984) 3956
80 M O Hale, G E Galica, S G Glogover and J L Kinsey *J Phys Chem* **90** (1986) 4997
81 G E Galica, B R Johnson, J L Kinsey and M O Hale *J Phys Chem* **95** (1991) 7994
82 K Q Lao, M D Person, P Xayaroboun and L J Butler *J Chem Phys* **92** (1990) 823
83 P G Wang and L D Ziegler *J Phys Chem* **97** (1993) 3139
84 F Markel and A B Myers *Chem Phys Lett* **167** (1990) 175
85 A B Myers and F Markel *Chem Phys* **149** (1990) 21
86 F Markel and A B Myers *J Chem Phys* **98** (1993) 21
87 D L Phillips, B A Lawrence and J J Valentini *J Phys Chem* **95** (1991) 7570
88 D L Phillips, B A Lawrence and J J Valentini *J Phys Chem* **95** (1991) 9085
89 D L Phillips and A B Myers *J Chem Phys* **95** (1991) 226
90 D L Phillips, J J Valentini and A B Myers *J Phys Chem* **96** (1992) 2039
91 J Pacansky and J Schrader *J Chem Phys* **78** (1983) 1033
92 B H Lengsfield, P E M Siegbahn and J Liu *J Chem Phys* **81** (1984) 710
93 J Pacansky, W Koch, M D Miller *J Am Chem Soc* **113** (1991) 317
94 J Zhang and D G Imre *J Chem Phys* **89** (1988) 309
95 F Duschek, M Schmitt, P Vogt, A Materny and W Kiefer *J Raman Spectrosc* **28** (1997) 445
96 S J Lee and R Bersohn *J Phys Chem* **86** (1982) 728
97 L J Butler, E J Hintsa and Y T Lee *J Chem Phys* **84** (1986) 410
98 L J Butler, E J Hintsa, S F Shane and Y T Lee *J Chem Phys* **86** (1987) 2051
99 T K Minton, G M Nathanson and Y T Lee *J Chem Phys* **86** (1984) 1991
100 G M Nathanson, T K Minton, S F Shane and Y T Lee *J Chem Phys* **90** (1990) 6157

ULTRAFAST ELECTRON TRANSFER DYNAMICS IN SENSITIZED TiO_2 NANOPARTICLES

HIRENDRA N GHOSH, JOHN B ASBURY, AND TIANQUAN LIAN*

Department of Chemistry, Emory University, Atlanta, GA 30322, (USA)

We have studied electron transfer dynamics between TiO_2 nanoparticles and molecular adsorbates using femtosecond mid-infrared spectroscopy. We have demonstrated that dynamics of the injected electrons in TiO_2 could be directly monitored through their mid-IR absorption and those of the adsorbates could be measured by their vibrational spectral change. $Ru(dcbpy)_2(NCS)_2$ (dcbpy=2,2′-bypyridine-4,4′-dicarboxylate) sensitized TiO_2 nanocrystalline films were studied as a model system for ultrafast electron injection from the excited state of the sensitizer to nanoparticles. Optical excitation of the MLCT band at 400 nm promotes an electron from a filled Ru d orbital to the π^* orbital of the dcbpy ligand. The subsequent electron injection to TiO_2 was found to occur with a time constant of *ca* 50 fs by directly measuring the transient IR absorption signal of the injected electrons in TiO_2. These injection dynamics are as fast as, if not fast than, the electronic or vibrational relaxation within the excited states. Back electron transfer from nanoparticles to the adsorbates was studied in interfacial charge transfer complexes formed by $Fe(II)(CN)_6^{4-}$ and TiO_2 colloidal nanoparticles. Optical excitation at 400 nm directly promotes an electron from $Fe(II)(CN)_6^{4-}$ to TiO_2 as indicated by the measured instrument-response-function limited appearance time of transient IR signal. The back electron transfer time from TiO_2 to $Fe(III)(CN)_6^{3-}$ was measured by the bleach recovery of CN stretching mode. A highly non-single-exponential recombination process was observed and was tentatively attributed to different recombination rates for injected electrons trapped at different sites in TiO_2. The measured decay of the IR absorption of electrons can be attributed to back electron transfer and electron trapping. Since the back electron transfer kinetics can be measured independently, the trapping dynamics can be determined. Electron trapping dynamics in a bulk crystal and nanocrystalline thin films were found to be similar in the first nanosecond, showing a >> 1 ns decay time. Trapping dynamics are much faster in the colloidal nanoparticles, indicating a much higher trap state density.

Key Words: Ultrafast Electron Transfer Dynamics; Nanoparticles; Femtosecond Spectroscopy; Solid-Liquid Interface; Relaxation Dynamics; Molecular Adsorbates

1 Introduction

Electron transfer (ET) between molecular adsorbates and semiconductor nanoparticles has been a subject of intense research interests[1-3]. The understanding of this fundamental process is essential for the application of semiconductor nanoparticle materials in photography[4], solar energy conversion[5], waste degradation[6], and nano-scale devices[7]. For example, photoelectrochemical solar cells based on dye sensitized nanocrystalline TiO_2 thin films[8] have received much attention in recent years because of their potential applications as a cost effective alternative to silicon based cells[1-3,9,10]. Gratzel's group reported that solar cells based on $Ru(dcbpy)_2(NCS)_2$ [dcbpy=(4,4′-Dicarboxy-2,2'-Bipyridine)] (or Ru N3) sensitized nanocrystalline TiO_2 thin films could achieve a solar to electric power conversion efficiency of about 10%[8,11]. The high conversion efficiency can be attributed to high solar energy harvesting by the sensitizer and high photon to current conversion efficiency. A schematic of various processes in dye sensitized semiconductor nanomaterials is shown in Fig. 1. A high photon to current conversion efficiency requires a fast electron injection rate from the sensitizer to the semiconductor and a much slower back electron transfer rate to the sensitizer[9].

Unlike in homogeneous solutions[12-14], electron

---

*To whom correspondence should be addressed. tlian@emory.edu

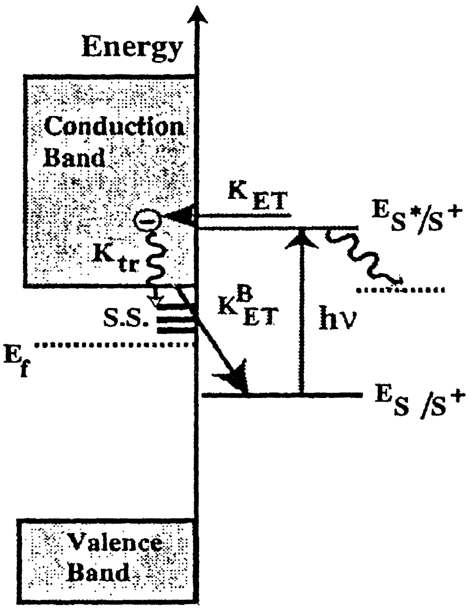

Fig. 1 A schematic of interfacial electron transfer

transfer dynamics in the solid-liquid interface[15-18] are still poorly understood[1,2,19]. The interfacial nature of these processes has hindered the theoretical and experimental studies in the past. In the solid, electrons can be delocalized in the continuous electronic levels that form the conduction band, or they can be localized on the surface or in trap states. The exact nature of the states that couple to the adsorbates is still unclear. Experimentally, the study of bulk surface often demands sophisticated surface science methods in UHV chambers[20]. Studies of adsorbates on semiconductor or metal surfaces by these techniques have gained great insights into small molecule/solid interaction. Ultrafast time resolved techniques have also been applied to study dynamical processes on well-defined surfaces[20-25]. Although they may be over simplified models for the solid-liquid interface, the detailed knowledge of these systems is crucial for understanding electron transfer process in the bulk solid/liquid interface. Most of the previous understanding of interfacial charge transfer is derived indirectly from steady-state photocurrent measurements in electrochemical cells[1,19,26-28]. Unfortunately, obtaining ET rates from steady state photocurrent is often quite complicated because the latter depends on many other interface and bulk properties in addition to the interfacial ET rates[1,19]. Time-resolved photoluminescence measurements have also been used successfully to obtain electron transfer dynamics in the solid-liquid interface of strongly luminescence semiconductor electrodes[29-31]. Efforts in developing *in situ*, direct and interface specific spectroscopic techniques for studying interfacial ET have resulted in some elegant yet complicated techniques, such as sum frequency (SFG) and second harmonic (SHG) generation[32-34], and surface restricted grating techniques[35].

In recent years, there has been a rapid development in the synthesis and characterization of nanometer size metal and semiconductor particles. In addition to their fascinating properties resulting from quantum size confinement, the large surface area and small size of these materials also enable the study of their properties by time-resolved absorption techniques. The surface chemistry of these materials can be readily studied without sophisticated surface science techniques and in more realistic environments. Although it is still unclear whether the knowledge of the nanoparticle/liquid interface can be applicable to the bulk/liquid interface, the understanding of nanoparticle/liquid interface is important in its own right. The operation of most devices based on this new class of materials is directly related to the charge transfer dynamics in and out the nanoparticles and carrier relaxation/combination dynamics within the nanoparticles. For this reason, photophysics of and carrier relaxation and recombination dynamics in metal and semiconductor nanoparticles have been actively studied in recent years[36-41]. Interested readers can refer to review articles[36,38,39] for more details on that subject. In this article, we will focus on ultrafast interfacial charge transfer between semiconductor nanoparticles and molecular adsorbates. In recent years there have been many studies of electron transfer dynamics in dye sensitized semiconductor nanoparticles and thin films using time-resolved laser spectroscopy[35,42-56]. By measuring the excited state dynamics of the sensitizer through transient absorption[46-48,55] or fluorescence decay[49,56], the electron injection rates from various adsorbed dye molecules into various semiconductor nanoparticles have been determined[35,46-49,55,56], ranging from subpicoseconds[43,48-50], to 10's of picoseconds[57], and even nanoseconds[58]. Back ET times were often measured by monitoring the bleach recovery of the ground state absorption. Although much insight into interfacial ET has been gained through these studies, transient absorption studies in the visible and near IR region are often hindered by spectral overlap of absorptions in various electronic states, such as the excited, oxidized, and ground states, as well as stimulated emission. Fluorescence quenching studies can sometimes be complicated by non-ET related quenching pathways, such as energy transfer among sensitizer molecules[45,51], and the dynamic fluorescence Stokes shift[56]. Because of these complexities, a systematic study of the dependence of interfacial ET rates on various adsorbate/nanoparticle properties has not been achieved.

In order to systematically study ET dynamics in the solid-liquid interface, new *in situ* techniques that are capable of assigning the ET process unambiguously and that complement the existing visible/near-IR transient absorption and fluorescence quenching techniques are needed. Femtosecond mid-IR spectroscopy[59] provides such an approach for these interfacial problems because it can directly study the dynamics of electrons in the semiconductor in addition to the dynamics of the adsorbates. As demonstrated in bulk[60,61] and quantum well[62] semiconductor materials, valence band holes and conduction band electrons in semiconductors have strong absorptions in the infrared region. These absorptions consist of Free Carrier Absorption[63], which is often broad and increases with wavelength, Intra-Band Transitions[63] between different valleys (or subbands) within the conduction or the valence bands, as well as absorptions of trap states. Since these IR absorptions of electrons are direct evidence for the arrival of electrons inside semiconductors, they provide an unambiguous spectroscopic probe for studying interfacial electron transfer between semiconductors and adsorbates. Furthermore, unlike fluorescence quenching, femtosecond mid-IR spectroscopy is a general technique. It can be used for any adsorbate/nanoparticle system, allowing a systematic study of the dependence of ET rates on the properties of the adsorbates, semiconductors and the solvent environments. It should be pointed out that injected electrons in semiconductors could also absorb in the near IR region. Near-IR probed of electron injection dynamics have been reported[43,44]. However, in the near IR region, it may be difficult to avoid the spectral overlap with the electronic transitions of large dye molecules[64], which is not a problem in the mid-IR region. Injected electrons can also be probed in the far IR and microwave region. Direct measurement of microwave absorption of injected electrons in dye sensitized nanocrystalline thin films has been demonstrated in the nanosecond time scale[58]. Ultrafast THz spectroscopy[65-67] should provide another convenient probe for ultrafast electron injection dynamics.

Recently, transient mid-IR spectroscopy was used to study electron transfer in sensitized nanoparticles by Heilweil's group in NIST[42,68] and us[42,64,69-71]. This technique can directly probe the mid-IR absorption of electrons inside semiconductors without the complication of broad electronic transitions of the adsorbates. We have applied this approach to TiO_2 nanoparticles sensitized with $Ru(dcbpy)_2(SCN)_2$ and related compounds[64,70,72], coumarin 343[69] and related organic dyes and even smaller ions such as $Fe(II)(CN)_6^{4-71}$ and SCN^{-73}. The ability to study small adsorbates allows for more detailed and quantitative study of interfacial ET dynamics. In this paper, we will give an overview of our recent studies of interfacial electron transfer between TiO_2 nanoparticles and molecular adsorbates. This paper is not intended as a comprehensive review on interfacial electron transfer on TiO_2 nanoparticles, although relevant comparisons with closely related works are made. The paper is organized as follows.

In Section 2, the experimental technique used for this study is described. The results and discussions are presented in Section 3. We will start out with the assignment of the transient mid-IR absorption in TiO_2. Electron transfer dynamics in Ru N3 sensitized TiO_2 nano-films will be discussed with emphasis on electron injection dynamics. The electron transfer dynamics in $TiO_2/Fe(CN)6$ complex will be analyzed as a model for back electron transfer from TiO_2 to $Fe(III)(CN)_6^{3-}$. A discussion of the electron relaxation dynamics in bulk crystal, nano-films and nanoparticles will also be presented.

2 Experimental Section

Femtosecond Tunable Spectrometer

The femtosecond tunable visible and infrared spectrometer used for this study is based on a regeneratively amplified femtosecond Ti:Sapphire laser system from Clark-MXR (1KHz repetition rate at 800 nm, 100 fs, 900 μJ/pulse), and nonlinear frequency mixing techniques as shown in Fig. 2. The 800 nm output pulse from the regenerative amplifier is split into two parts to generate pump and probe pulses. One part, with 300 μJ/pulse, is frequency doubled and tripled in BBO crystals to generate pump pulses at 800, 400 or 267 nm.

IR Probe

In the IR probe experiments, the remaining 600 μJ of the 800 nm pulse is used to pump a Clark IR Optical Parametric Amplifier to generate two tunable near IR pulses from 1.1 to 2.5 μm. These signal and idler pulses are combined in a $AgGaS_2$ crystal to generate mid-IR pulses from 3 to 10 μm by difference frequency generation. The mid-IR pulses have a typical intensity fluctuation of 1 to 3%. The probe IR pulses are divided into a signal and reference beam. While the signal beam measures the absorption of the sample, the reference beam is used to normalize the laser intensity fluctuations. These probe beams are vertically displaced and dispersed in a monochromater, from which a 2 to 3 cm^{-1} slice of the total spectrum (approximately 200 cm^{-1}) is measured by a pair of Mercury Cadmium Telluride (MCT) detectors. To minimize low frequency laser fluctuations, the main noise source, every other pump pulse is blocked with a synchronized chopper (New Focus model 3500) at 500 Hz, and the absorbance change is calculated with two adjacent probe pulses (pump blocked and pump unblocked). About 4% of the chopped pump beam is split by a beam splitter and detected in a photodiode (Thorlab, PDA 50) to monitor the intensity of the pump beam and phase of the chopper (pump blocked *vs.* unblocked). The output from the MCT detectors and the photodiode are integrated in three separate gated boxcar integrators (Stanford Research Systems SR 250), digitized in a 12 bit A/D converter (National Instrument AT-MIO-64E-3), and recorded by a Pentium PC for each laser pulse. The typical noise in the measured absorbance change is about 0.4 to 0.8% for every pair of laser pulses. Transient absorption spectra are recorded by scanning the monochromater at fixed delay times, and the kinetics traces at fixed wavelengths are recorded by scanning the delay time. The zero delay time and instrument response for a 400 nm pump/ mid-IR probe experiment are determined in a thin silicon wafer or thin film of TiO_2 nanoparticles, in which absorption of 400 nm photons lead to the instantaneous generation of charge carriers that absorb strongly in the mid-IR region[63]. The typical

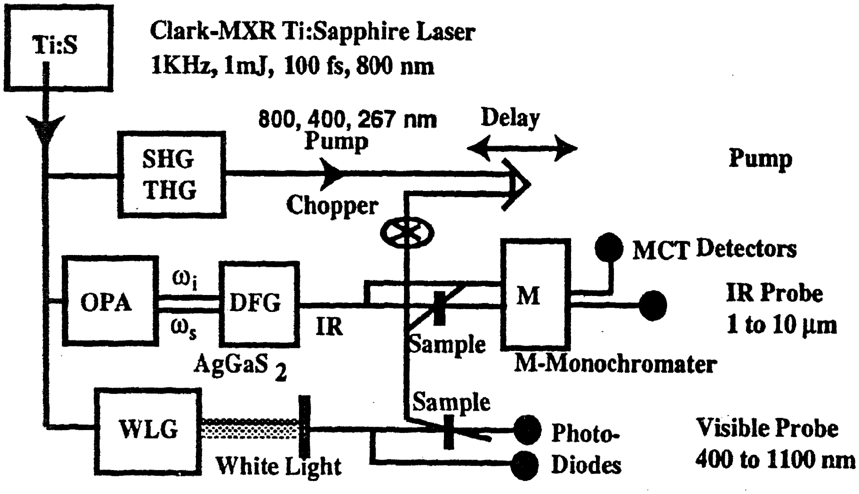

Fig. 2 A schematic of the tunable femtosecond spectrometer

instrument response, which is determined in every experiment, can be well presented by a Gaussian function with FWHM ranging from 150 to 320 femtosecond.

Visible Probe

To generate visible probe pulses, about 6 μJ of the 800 nm beam is focused onto a 2 mm thick sapphire window. The intensity of the 800 nm beam can be adjusted by iris size and ND filters to obtain a stable white light continuum in the 430 nm to over 1000 nm region. A variable interference filter (from Optical Coating Laboratory Inc.) selects approximately 10 nm slices of the white light to provide tunable probe pulses. The probe pulses are split into the signal and reference beams, which are detected by two matched photodiodes with variable gain (PDA50 from Thorlabs Inc.). The noise level of the white light is about 0.4% with occasional spikes due to fluctuations in the oscillator output. We have noticed that most laser noise is low frequency noise and can be eliminated by comparing the adjacent probe laser pulses (pump blocked vs. unblocked) similar to the IR setup. The typical noise in the measured absorbance change is about 0.1 to 0.2%. Additional laser intensity normalization with the signal and reference beams is often found to be unnecessary.

Materials

Synthesis of TiO_2 Nanoparticles

Nanometer sized TiO_2 was prepared by controlled hydrolysis of titanium(IV) tetraisopropoxide[74]. 100 ml solution of $Ti[OCH(CH_3)_2]_4$ (Aldrich, 97%) dissolved in isopropyl alcohol (5:95) was added dropwise (1ml/min) to 900 ml of doubly distilled water (2°C) at *p*H 1.5 (adjusted with HNO_3). The solution was continuously stirred for 10-12 hours until a transparent colloid was formed. Both titanium(IV) tetraisopropoxide and isopropyl alcohol were purified by distillation. The colloidal solution was concentrated at 35-40°C with a rotary evaporator and then dried with a nitrogen stream to yield a white powder. The estimated size of the particles is ca. 5 nm.

Preparation of $Fe(II)(CN)_6^{4-}$ Sensitized TiO_2 Nanoparticles

TiO_2 nanoparticle powder was dissolved in D_2O solution to obtain colloidal solution of 10g/L concentration. The colloid was protected by 10g/L polyvinyl alcohol (PVA) and kept at *p*H 2 by adding 10^{-2} M of $HClO_4$. The colloidal solution was then mixed with $K_4Fe(CN)_6$ (25 mM), and kept in the dark and in N_2 atmosphere. After stirring for >10 hours, a deep orange coloured solution was formed and remained stable for a few days. The visible absorption is attributed to a charge transfer complex formed between $Fe(CN)_6^{-4}$ and TiO_2 nanoparticles. The optical density of the solution in a 100 μm thick cell was about 0.3 at 400 nm. The unsensitized TiO_2 colloidal solution sample used in the experiment had no noticeable absorption at 400 nm. D_2O was used instead of H_2O to improve the transmission in the 1900 to 2200 cm^{-1} region.

Film Sample Preparations

Concentrated TiO_2 nanoparticle colloids were first prepared as previously described, using Degussa P25 TiO_2 (about 70% anatase and 30% rutile) as the starting material[11]. Thin films were prepared using these colloids according to a published procedure[64]. The films were prepared on c-cut polished sapphire substrates and fired at 450°C for 45 minutes in air. TiO_2 films were 5 μm thick with good transparency. The Al_2O_3 films were ~15 μm thick and showed greater scattering than the TiO_2 films. Immersion and storage of the TiO_2 and Al_2O_3 films in a room temperature ethanol solution containing 200 μM Ru N3 and 20 mM chenodeoxycholic acid resulted in adsorption of the Ru N3 to the porous film surface. The resulting dye-sensitized films showed an absorbance of ~1.0 at 400 nm and 550 nm. The absorbance at 400 nm for a typical naked film used in the experiment was about 0.3 OD with contributions from both absorption and scattering of the nanocrystalline films. High purity Ru N3 was purchased from Solaronix (Lausanne, Switzerland).

3 Mid-IR Absorption of Electrons in TiO_2

The mid-IR absorption of free carriers in many different semiconductor materials has been reported[63]. Reduced rutile TiO_2 crystals were also found to have significant absorption in the mid-IR region due to excess electrons in the conduction band[75]. There has not been any careful characterization of mid-IR absorption of electrons in TiO_2 nanoparticles. Since electrons can be generated through excitation of the bandgap transitions in unsensitized nanomaterials or injection from dye-sensitizers, their IR absorption spectra can be characterized by transient IR spectroscopy. We have observed mid-IR absorption signals of electrons in or trapped below the TiO_2 conduction band generated by both approaches.

For the rutile type TiO_2 crystals, whose bandgap is around 3.02 eV (or 413 nm)[75], optical excitation at 400 nm leads to the generation of electrons in the conduction band and holes in the valence band. The absorption of these carriers was characterized by measuring the transient IR signal in the mid-IR region before the recombination of electrons and holes. Shown by the connected open circles in Fig. 3 is the transient IR signal in the 5 μm (2000 cm^{-1}) region for a rutile TiO_2 crystal at 3 ps after 400 nm excitation. This signal is very broad and is present in the mid-IR region from 1700 to 2400 cm^{-1}, although the detailed structure is yet to be carefully characterized. The typical mid IR absorption spectra of electrons in many semiconductor materials are broad consisting of Free Carrier Absorption, Intraband Transitions, and trap states[63]. While the observed IR signal shown in Fig. 3 is consistent with the broad IR absorption of electrons, the assignment of the relative contributions of different transitions to the observed signal is not possible due to the very small spectral region studied so far. The rise time of the signal in the bulk TiO_2 crystal is instrument response time limited[69], as shown in Fig. 5, consistent with a direct generation of electrons and holes by the excitation pulse. The decay of the signal within the first nanosecond is characterized by a pulse width limited decay, shown in Fig. 5, and a subsequent slow decay of the amplitude with a time constant >> 1 ns as shown in Fig. 14. Also shown in Fig. 3 (the connected full circles) is the transient IR signal in the nanocrystalline thin film at 3ps after 400 nm excitation. Again similar broad IR features are observed for electrons and holes. Here direct excitation into trap states near the band edge may be responsible for the absorption at 400 nm.

Similar broad transient mid-IR absorption for injected electrons can also be observed in sensitized nanoparticles. Shown in Fig. 4 are transient IR spectra of coumarin 343 (C-343) sensitized TiO_2 nanoparticle colloidal solution after 400 nm excitation. C-343 sensitized TiO_2 nanoparticles have been shown to undergo efficient electron injection from the C-343 excited state to TiO_2 conduction band upon photo-excitation of the dye[49,76]. Using fluorescence up-conversion technique, forward electron injection time of 180± 50 fs was inferred from the fluorescence decay time of C-343 in a colloidal solution of sensitized TiO_2 nanoparticles in H_2O (with 5% acetone)[49]

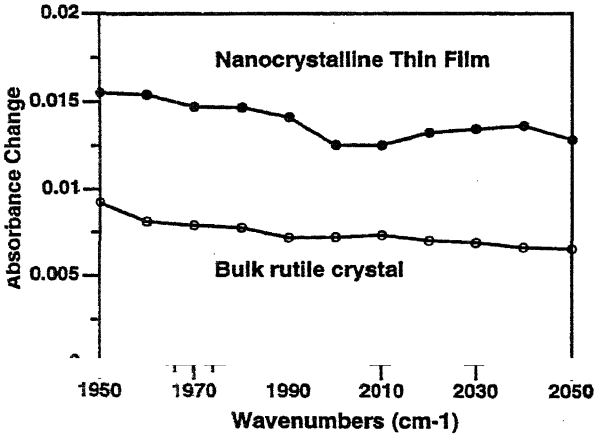

Fig. 3 Transient mid IR absorption in a bulk rutile TiO_2 crystal (open circles) and nanocrystalline TiO_2 thin film at 3 ps after 400 nm excitation

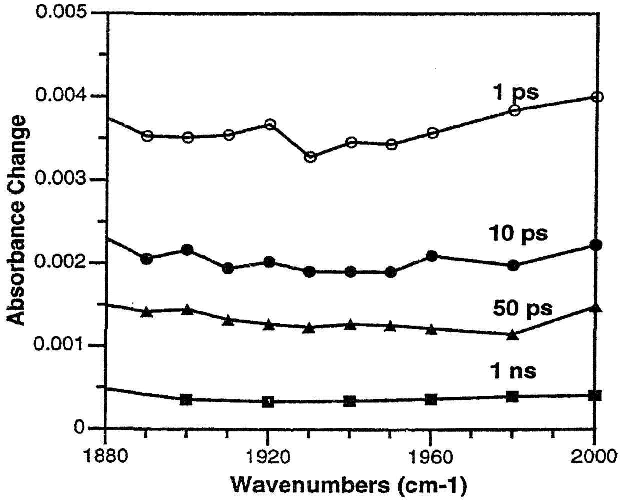

Fig. 4 Transient mid IR absorption C343 sensitized colloidal TiO_2 nanoparticles at 1, 10, 50 and 1000 ps after 400 nm excitation. The absorption is assigned to injected electrons in TiO_2.

While the broad absorption feature shown in Fig. 4 is a typical signature of electrons in semiconductor, this assignment is further confirmed by the lack of similar signals in blank samples of C-343 molecule in ethanol, D_2O solvent, and unsensitized TiO_2 nanoparticles in D_2O[69].

Since the mid-IR absorption is a direct probe of injected electrons, the rise time of the signal should correspond to the electron injection time. The kinetics trace for C-343 sensitized TiO_2 nanoparticles at 2000 cm^{-1} is shown by the full circles in Fig. 5. We have subtracted a small solvent background absorption signal at around t=0[69]. The rise time of the observed signal can be well fit by convolution of a single exponential rise and the instrument response function, represented by a Gaussian function with 160 fs FWHM. The solid line in Fig. 5 is a fit to the kinetics at 2000 cm^{-1} with a rise time constant of 135 fs. The best fit to the kinetics at 1900, 1950, and 2000 cm^{-1} yields time constants ranging from 100 to 150 fs. We therefore report an average rise time of 125 ± 25 fs. The risetime of the transient IR signal represents the formation time of electrons in TiO_2 through injection from the excited state of C-343. Our result is in agreement with other reported ultrafast injection times of 180±50 fs[49].

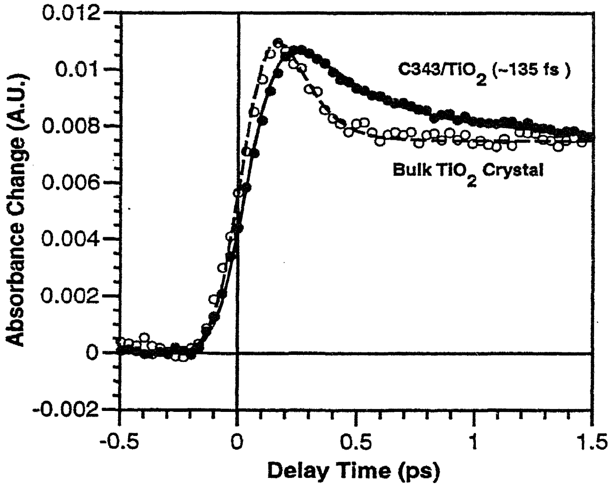

Fig. 5 Transient kinetics in C343 sensitized TiO_2 nanoparticles (full circles) probed at 2000 cm^{-1} after 400 nm excitation. The measured 135 fs rise time is attributed to the electron injection time from the excited state of c343 to TiO_2. Also shown is the kinetics trace in a bulk rutile crystal (open circles) at 1960 cm^{-1} after 400 nm excitation. Here the direct band gap excitation leads to instantaneous generation of electrons and holes.

This study demonstrated that injected electrons have strong mid-IR absorption that can be used to follow the injection kinetics. We have used this spectral signature to study electron transfer process between molecular adsorbates and semiconductor nanoparticles. It should be noted here that there is more information contained in the IR absorption signal that can be further obtained. Although the mid IR absorption spectra shown in Figs. 3 and 4 are very similar in the 5 μm region for these three different TiO_2 materials, the exact shape in a wider region has yet to be determined. The spectral dependence in a wider range should reveal the nature of the electrons, because trapped and free electrons may have very different spectral dependence. In addition, the time dependence of the IR spectra should contain information about electron relaxation (cooling and trapping) within the nanoparticles and back transfer to the adsorbates.

4 Ru N3 Dye Sensitized TiO_2 Thin Film : Ultrafast Electron Injection Dynamics

Since the report by Gratzel's group that solar cells based on $Ru(dcbpy)_2(NCS)_2$ [dcbpy=(4,4′-Dicarboxy-2,2′-Bipyridine)] (or Ru N3) sensitized nanocrystalline TiO_2 thin films can achieve a solar to electric power conversion efficiency of about 10%[8,11], electron injection and recombination properties of Ru dye sensitized semiconductors have been studied by many groups[42,43,48,51,58,64,68,70,77-86]. The exact nature and time scale of the electron injection step for Ru N3 has been a subject of a recent debate[43,48]. To unambiguously resolve the electron injection step, we have recently studied the Ru N3 sensitized TiO_2 thin film with femtosecond mid IR spectroscopy. We also investigated the photophysics of the sensitizer to compare the excited state relaxation and electron injection dynamics.

Photophysics of Ru N3 in Ethanol and on Al_2O_3

In order to understand the detailed electron injection dynamics of the Ru N3 sensitized TiO2 films, the excited state dynamics of the sensitizer molecules themselves, without the complication of electron injection, need to be understood. We have studied the photophysics of Ru N3 1) in ethanol solution; and 2) adsorbed on Al_2O_3 film after 400 nm excitation. The band gap for Al_2O_3 is about 8 eV[87], and its conduction band is not accessible by the MLCT excited state of the sensitizer[84]. Thus this system should serve as a good model for the photophysics of the adsorbate.

Shown in Fig. 6 are transient IR spectra in the CN stretching mode region of Ru N3 in ethanol (connected full circles) and adsorbed in Al_2O_3 film (connected open circles) at 5 ps after 400 nm excitation. The excitation leads to bleach of the ground state absorption at 2115 cm^{-1}, while creating a new band at 2040 cm^{-1}. The bleach at 2115 cm^{-1} is identical to the peak of the CN stretching mode of freshly prepared Ru N3 in ethanol. The transient spectra in these two samples are almost identical except for the small shoulder at 2140 cm^{-1} and its corresponding excited absorption at 2075cm^{-1} that is present only in the ethanol solution[72].

In a previous study on $Ru(bpy)_3^{+2}$, it was found that the long-lived ^{3}MLCT state in this Ru complex was formed on the subpicosecond time scale[88]. We thus expect that the Ru N3 may also relax from the initially excited ^{1}MLCT state to its lowest-lying excited state, ^{3}MLCT, in the subpicosecond time scale. The observed new absorption peak at 5 ps is assigned to that of the ^{3}MLCT state. The formation and decay time of the excited ^{3}MLCT state, can be obtained from the kinetics measured at the peak positions for the ground and excited state. Shown in Fig. 7 are transient kinetics measured at the peaks of the transient spectra (2040 cm^{-1}) for a) Ru N3 in ethanol and b) RuN3 adsorbed on an Al_2O_3 thin film. The full circles in these figures are the experimental data and the solid lines are fits obtained by convolution of a single exponential rise function with the instrument response function.

For Ru N3 in ethanol solution, the rise time of the signal appears to be instrument response time limited. A fit with a 75 fs single exponential rise time (solid curve) is shown for comparison. Within the signal to noise ratio of the data, a satisfactory fit can be obtained for a single exponential rise time constant of <75 fs, which is considered as the upper limit of the rise time. For the Ru N3 adsorbed on Al_2O_3 film, because of the poor data quality and small number of data points on the rising edge of the data, the rise time of the signal

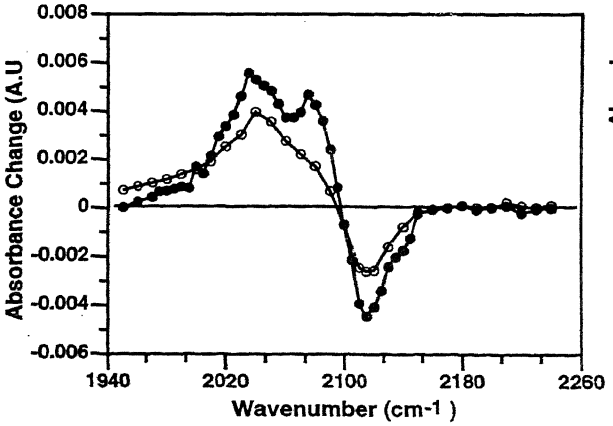

Fig. 6 Transient IR spectra of $Ru(dcbpy)_2(NCS)_2$ in ethanol (full circles) and adsorbed on nanocrystalline Al_2O_3 thin film (open circles) at 5 ps after 400 nm excitation.

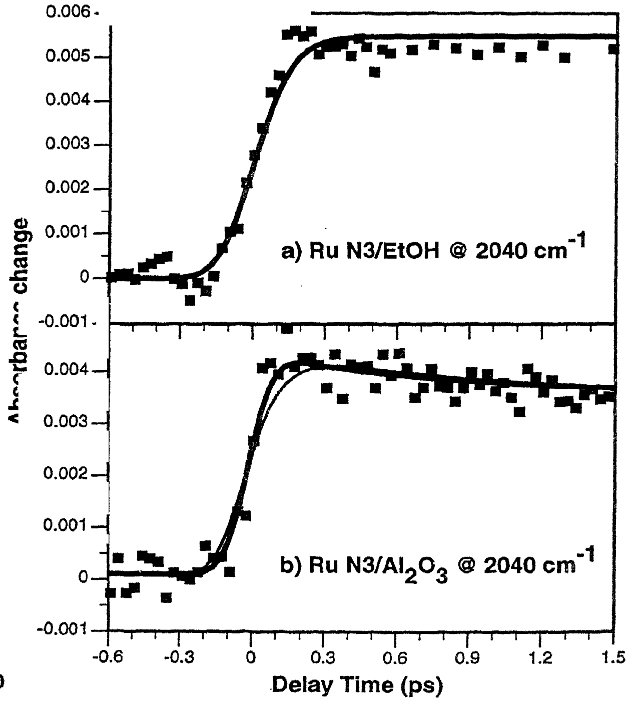

Fig. 7 Comparison of excited state formation kinetics probed at 2040 cm^{-1} for $Ru(dcbpy)_2(NCS)_2$ (a) in ethanol solution and (b) adsorbed in nanocrystalline Al_2O_3 thin film after 400 nm excitation. The solid lines represent fits to the data.

can not be accurately determined. Shown by the thick and thin solid lines are fits with single exponential rise time of 1 fs (to represent no rise time) and 100 fs. Within the signal to noise, satisfactory fits to the data can be obtained with a single exponential rise time of <100 fs. This result suggests that upon 400 nm excitation of ^{1}MLCT state, the molecules relax to their lowest lying triplet ^{3}MLCT state in less than 100 fs, consistent with the previous observation of an ultrafast formation time[88].

It should be pointed out that the above assignment of the ^{3}MLCT state formation time is based on the assumption that the CN stretching mode in the ^{3}MLCT state is different from that in the ^{1}MLCT state. To the best of our knowledge, we are not aware of any published results on the possible shift of CN stretching frequency in similar compounds. However, if the CN stretch frequencies are similar in the ^{1}MLCT and ^{3}MLCT states, the measured <100 fs rise time does not indicate the ^{3}MLCT state formation time.

The excited state decay kinetics at longer time scale for the Ru N3 on Al_2O_3 and Ru N3 in solution are shown in Fig. 8a (2115 cm^{-1}) and Fig. 8b (2040 cm^{-1}). The best fits to the data at 2115 cm^{-1} (the solid lines) for both samples are similar and show a > 1 ns recovery time, indicating negligible recovery of ground state molecules on the 1 ns time scale. The decay of the transient absorption at 2040 cm^{-1} is quite different for these two samples. For Ru N3 in solution, there is no noticeable decay, consistent with previous observation of a 59 ns lifetime of the ^{3}MLCT state[11]. For Ru N3 on Al_2O_3 the excited state absorption peak decays by about 50% by 1 ns. The decay kinetics can be fit by a bi-exponential decay function plus a long-lived component with the following time constants and initial amplitudes (in parenthesis): 3.5 ps (21%), 130 ps (26%) and >> 1 ns (53%), as shown in Fig. 8b. Since no ground state bleach recovery was observed, the decay of the excited state must produce a new species that is different from the ground state and lowest lying ^{3}MLCT state.

In this experiment, we are probing the IR absorption of the lowest lying excited state, not the fluorescence. Therefore, energy transfer between sensitizers would not cause any decay of the observed signal. One possibility of this new species corresponds to the injection of an electron from the dcbpy π^* orbital to the substrate. Although electron injection into the conduction band of Al_2O_3 is not possible in this large band gap material, a pathway involving electron transfer to surface states is possible. This pathway was invoked in a previous experiment of cresyl violet sensitized Al_2O_3[89], in which the fluorescence lifetime of the adsorbed dye at low coverage was found to be shorter compared to those in solution..

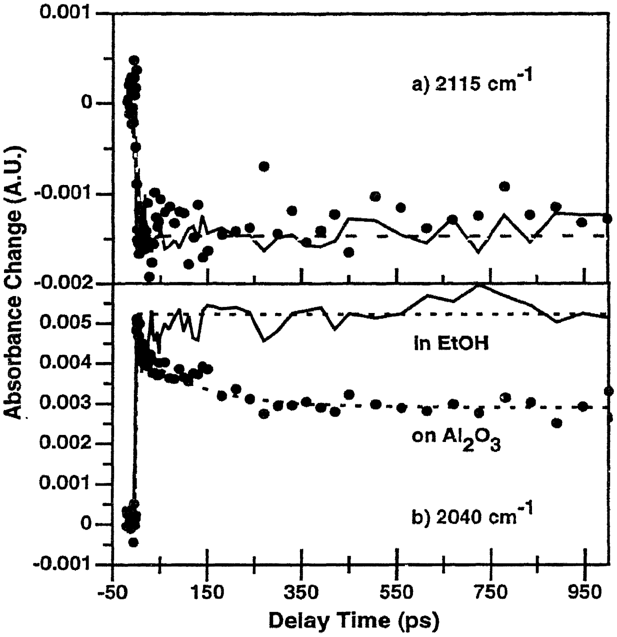

Fig. 8 Comparison of (a) excited state decay kinetics probed at 2040 cm^{-1} and (b) ground state recovery kinetics probed 2115 cm^{-1} for $Ru(dcbpy)_2(NCS)_2$ in ethanol solution (thin solid line) and adsorbed in nanocrystalline Al_2O_3 thin film (full circles) after 400 nm excitation. The dash lines are best fits to the data.

Electron Injection from Ru N3 to TiO_2

In order to unambiguously identify the injection step in Ru N3 dye sensitized TiO_2, we compare the transient IR absorption signal in the N3 sensitized TiO_2 films with naked TiO_2 films and Ru N3 sensitized Al_2O_3 thin films. Shown in Fig. 9 is one of such comparison of transient IR signals measured at 2040 cm^{-1} with 1.1 μJ of 400 nm excitation. It should be pointed out that the data shown in Figs. 6, 7, and 8 for Ru N3 sensitized Al_2O_3 were collected with about 7 times higher

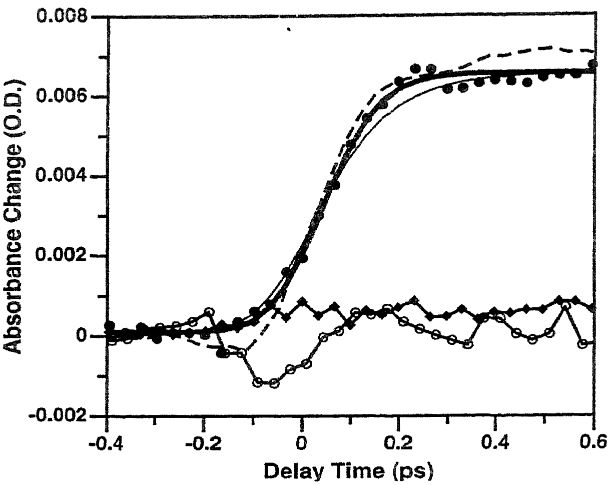

Fig. 9 Comparison of transient mid IR signal probed at 2040 cm^{-1} for Ru N3 sensitized TiO_2 (full circles), Ru N3 sensitized Al_2O_3 (open circles) and naked TiO_2 (full diamonds) thin films. The dash line shows an instrument response measure in a thin silicon wafer. The signal in Ru N3 sensitized TiO_2 thin films is assigned to injected electrons (see text). The best fit (thick solid line) to the data yields a 50 fs rise time, i.e. electron injection time. Also shown by the thin solid line is a fit with a 100 fs rise time.

pump power. At the reduced pump power of 1.1μJ, the amplitude of the signal due to Ru N3 vibrational spectral change can be estimated to be < 0.5 mOD, consistent with the negligible transient IR signal for Ru N3 sensitized Al_2O_3 indicated by the open circles in Fig. 9. The signal in the naked TiO_2 film is about 0.6 mOD, attributed to direct excitation of electrons near the conduction band edge and holes in the valence band[90]. Since both Ru N3 sensitized Al_2O_3 and naked TiO_2 films have negligible transient IR signals after 400 nm excitation, the observed 6 mOD absorption signal in the Ru N3 sensitized TiO_2 film can be attributed to electrons injected into TiO_2 from the sensitizer excited state.

Furthermore, the observed signal is very broad, present in all the mid IR wavelength probed so far, ranging from 1700 to 2400 cm^{-1}. This type of broad mid IR absorption signal can be attributed to injected electrons as discussed in earlier section.

Since the observed IR absorption for Ru N3 sensitized TiO_2 thin film shown in Fig. 9 is due to injected electrons, its rise time is the electron injection time from the sensitizer to TiO_2. The rise time of the data can be well fit by a single exponential rise function convoluted with the instrument response function. The best fit to the data at 2040 cm^{-1} yielded a 50 ± 25 fs rise as shown by the solid line. The error bar reflects a 50% increase of the χ^2 of the fit. The light line in Fig. 9 shows a similar curve with a 100 fs rise time, which can not give a satisfactory fit to the data. A similar rise time has been observed at probe wavelength in the 2000 to 2200 cm^{-1} region. We therefore report an average rise time of 50 ± 25 fs. In addition to this fast injection component, there appears to be a much smaller and slower rise component with time constant of 1.7 ± 0.5 ps[72]. We found that this second component was very sensitive to the sample condition. Its amplitude appeared to be bigger, ca. 16%, in freshly prepared samples and became smaller, ca. 5%, when the samples aged, although no noticeable difference could be observed from the static UV/Vis and FTIR spectra of the films. The exact origin of the second component is so far unknown. More experiments that carefully correlate sample preparation and transient kinetics will be carried out to resolve this issue. Our result clearly demonstrates that >84% of the electrons are injected in about 50 fs after the excitation of Ru N3 molecules at 400 nm.

It should be pointed out that the instrument response functions used in the deconvolution were determined in a thin silicon wafer, in which 400 nm excitation leads to instantaneous generation of electrons and holes. The Ru N3 sensitized TiO_2 films are highly porous consisting of interconnected nanoparticles of ca. 20 nm average diameter. Although negligible scattering of the probe IR beam is expected, some scattering of the 400 nm pump beam may be possible. This scattering process, if not negligible, may lengthen the effective instrument response function in these porous films compared to those measured in a silicon wafer. We have recently compared the instrument response function (IRF) determined from the rise time of the transient IR signal in a thin silicon wafer and unsensitized TiO_2 thin films, which were prepared under the same condition as those films used for the Ru N3 sensitized samples. It was found that observed IRF for the porous films was about 20 fs longer than that in the silicon wafer. Since the amount of scattering in the Ru N3 sensitized film may be smaller due to its stronger absorption, the amount of correction for the IRF can be estimated to be < 20 fs, although the exact amount needed is unknown. A lengthened instrument response function due to scattering would require an even faster rise time to fit the data. Without a more accurate way of measuring the instrument response function in the porous film and because of the limited time resolution, we cannot exclude the possibility that the electron injection time is even faster than 50 ± 25 fs.

Comparison with Previous Works

Ultrafast electron injection dynamics in Ru N3 sensitized TiO_2 films have been studied by other groups[43,48]. Tachibana *et al.*[48], reported an almost equal amplitude biphasic injection process with time constants of <150 fs and 1.2 ps. Here the electron injection process was identified by measuring the apparent[91,92] transient spectrum in the 500 to 900 nm region of the oxidized form of N3 dye. The 1.2 ps rise component was directly measured at the peak of the oxidized dye absorption at 750 nm. The <150 fs injection component was inferred from the observation that the transient spectrum at 150 fs, the earliest time measured, was already half of the magnitude of the total spectral change at later time. The fast component appears to be consistent with our measured 50 fs injection time. However, the intensity of the second component with 50% of the total amplitude was much bigger than our 1.7± 0.5 ps (<16%) component. The origin for the discrepancy is so far unclear.

A more recent study of the same system in a UHV chamber[43] reported a different transient absorption in the visible and near IR region. The reason for the different transient spectra in UHV and solution is still a subject of further debate[91,92]. In this study a near IR absorption at 1100 nm was observed and assigned to injected electrons. Based on the rise time of the near IR signal, a <25 fs injection time was obtained. Our measured electron injection time is in agreement with the <25 fs injection time they reported[43]. However, it was found that similar near IR absorptions at 1500 nm could be observed under atmospheric conditions for Ru N3 on TiO_2, N3 in solution and N3 on ZrO_2 after excitation of the MLCT band[64]. The amplitudes of the latter two signals are about 70% of that for Ru N3 sensitized TiO_2 film under the same pump energy. This result indicates that under atmospheric conditions there may be significant absorption from the sensitizer excited state in the near IR region. More recently, Heimer and Heilweil also used mid-IR femtosecond IR spectroscopy to study the electron injection dynamics of Ru N3 and related Ru dye [Ru(5,5'-COCH2Ch3)2-2,2'-bippyridine)$(NCS)_2$] sensitized TiO_2 film. The Electron injection times in both films were found to be <350 fs[68]. It appears that all four measurements suggest that the electron injection from the MLCT state of Ru N3 sensitizer to TiO_2 can be on the 100 fs or faster time scale.

Identity of the Injecting State: Comparison with $Fe(dcbpy)_2(CN)_2$

The observed 50 fs injection time from Ru N3 to TiO_2 is on the same time scale of or faster than the intramolecular vibrational energy relaxation as well as intersystem crossing time of adsorbate molecules. The time scale of vibrational energy redistribution for large molecules in solution was often found to be on the order of 10s to 100s of femtosecond[93,94], although the exact time scale for Ru N3 molecules has yet to be determined. Electronic relaxation from the initially prepared Frank-Condon state to the long lived ^{3}MLCT state for $Ru(bpy)_3^{2+}$ in solution was found to occur on the 100 fs time scale[88]. Our measurement of the formation time of the CN stretch mode in the ^{3}MLCT excited state also yields a rise time of < 75 fs for Ru N3 in ethanol and adsorbed on Al_2O_3. If we assume a noticeable shift of CN stretching frequency from ^{1}MLCT state to the ^{3}MLCT state, the measured time suggests that the formation time of ^{3}MLCT state in Ru N3 is also occurring in the < 75 fs time scale. While it is possible that electron injection may occur in the same time scale or even prior to vibrational energy redistribution and intersystem crossing, as suggested in a recent paper[43], our data do not provide unambiguous evidence for the identity of the injecting state. Ongoing pump-wavelength dependent experiments may provide more insight into these important issues.

If electron injection can occur prior to excited state relaxation, one can also expect to observe electron injection in $Fe(dcbpy)_2(CN)_2$ sensitized nanocrystalline TiO_2 films. In this system, the lowest lying excited state is the ligand field state, in which the excited electron populates the metal based d orbitals. Because of the poor orbital overlap between the d orbitals with the TiO_2 conduction band and unfavourable driving force, electron injection from the ligand field state to TiO_2 is expected to be unlikely[95] or much slower compared to injection from dcbpy π^* orbitals. In a recent study of solar cells based on $Fe(dcbpy)_2(CN)_2$ sensitized nanocrystalline TiO_2 film electrodes[95], photo-current was recorded when the cell was illuminated in the MLCT charge transfer band at wavelengths shorter than 500 nm. This result is interpreted as ultrafast electron injection from the excited MLCT state to TiO_2 prior to intersystem crossing from ^{1}MLCT state to lower lying ligand field states[95]. We have also conducted a preliminary investigation of the electron injection dynamics in $Fe(dcbpy)_2(CN)_2$ sensitized nanocrystalline TiO_2 thin films. Shown in Fig. 10 are transient IR signals in the $Fe(dcbpy)_2(CN)_2$ sensitized nanocrystalline TiO_2 thin film. Again, a broad IR absorption of injected electron was observed. The electron injection time appears to be faster than 100fs. However the amplitude of the transient signal in sensitized film relative to unsensitized film appears to be smaller compared to that of Ru N3 sensitized films, indicating a smaller injection efficiency for the $Fe(dcbpy)_2(SCN)_2$ sensitized film. This result is consistent with the reported smaller photon to current conversion efficiency in $Fe(dcbpy)_2(SCN)_2$ sensitized films[95]. Although much more work is needed to carefully compare these two different films, this study suggests that electron injection occurs on the same time scale of excited state electronic relaxation.

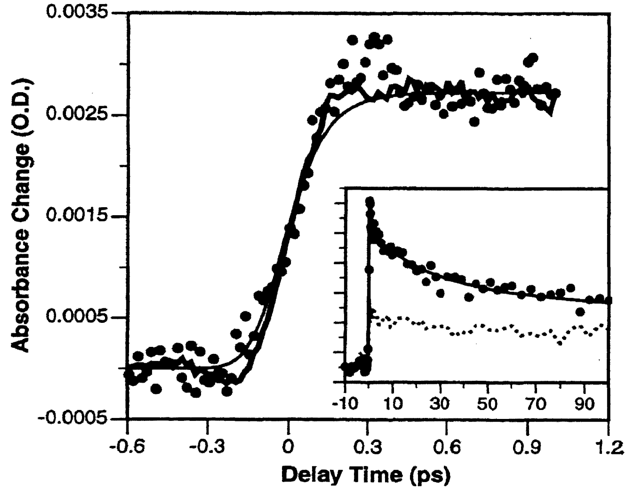

Fig. 10 Transient kinetics for $Fe(dcbpy)_2(CN)_2$ sensitized TiO_2 thin films probed at 2000 cm^{-1} after 400 nm excitation. The full circles are the data points, the thick solid line is the instrument response measured in a silicon wafer, and the thin solid line is a fit with 100 fs rise time. Shown in the inset is a comparison of mid IR absorption signal in sensitized (full circles) and unsensitized (dot line) TiO_2 thin films.

Related Ultrafast Electron Injection Dynamics

Many research groups have reported ultrafast electron injection from various sensitizers to TiO_2 in recent years. Using the fluorescence up-conversion technique, a forward electron injection time of 180± 50 fs was inferred from the fluorescence decay time of C-343 in a colloidal solution of sensitized TiO_2 nanoparticles in H_2O (with 5% acetone)[49]. More recent unpublished result from Castner *et al.* on C343 sensitizer TiO_2 nanoparticle colloidal solution suggested that the injection rate may be around 20 fs. These authors also reported a ca. 330 fs injection time in C343 sensitized ZnO nanoparticle colloids[56]. We have also measured the electron injection dynamics in C343 sensitized TiO_2 nanoparticles using transient IR absorption spectroscopy and reported a 125±25 fs electron injection time[69]. Electron injection dynamics in other dye sensitized TiO_2 nanoparticles have also been reported. Cherepy *et al.* measured a <100 fs electron injection time from anthocyanin dye sensitized TiO_2 nanoparticles. Martini *et al.*[46,97] have investigated electron injection dynamics in a series of anthracene dye sensitized TiO_2 nanoparticles. For 9-anthracene sensitized anatase TiO_2 nanoparticles, a < 200 fs electron injection time was observed, while for an amorphous form of TiO_2, a 1.5 ps electron injection time was measured. Burfeindt et al. have studied modified-perylene sensitized TiO_2 thin films in ultrahigh vacuum chamber. A 190 fs electron injection time was first reported[54] and a more recent measurement with improved time resolution yielded a 75 fs electron injection time[98]. Ultrafast electron injection on Oxazine sensitized bulk SnS_2 crystal surface has also been studied by the fluorescence quenching technique. A 40 ± 20 fs electron injection time was inferred[50].

Mechanism of Ultrafast Electron Injection Process

Our measurement of Ru N3 sensitized TiO_2 thin film and C343 sensitized TiO_2 nanoparticle colloid as well as many similar measurements by other groups all reported ultrafast electron injection times on the 100 fs or faster time scale. In these dye sensitized systems, the sensitizer molecules attach strongly to the semiconductor. The exact reason for the ultrafast injection of electrons from the sensitizer to TiO_2 is so far unclear. In the case of Ru N3 dye sensitized TiO_2 films, a direct charge transfer transition from Ru to TiO_2 is not likely because of the lack of direct spectral overlap between Ru and TiO_2 orbitals. This notion is supported by the observation of only a small red shift of the Ru N3 absorption spectrum when adsorbed on TiO_2[19]. One possibility for the observed fast injection is a strong coupling of the dcbpy π^* orbital with TiO_2, leading to an adiabatic electron transfer from dcbpy to TiO_2. In this case, the optical transition corresponds to excitation from a Ru d orbital to a mixed state of dcbpy π^* and Ti 3d orbital. The electron transfer process would correspond to the motion of the initial wavepacket, which is prepared in the dcbpy side because of Frank-Condon overlap, to the TiO_2 side along the adiabatic surface. However, it is still unclear whether strong coupling is necessary for fast interfacial electron transfer processes from adsorbate to semiconductors, which have large density of states. According to Fermi's Golden rule, a large accepting state density in TiO_2 would also give rise to ultrafast injection time even when the coupling between dcbpy π^* orbital and TiO_2 is weak or intermediate. The extent of electronic coupling and origin of the ultrafast injection dynamics will be investigated in future experiments by systematically varying the coupling strength and density of accepting states.

5 Back ET from TiO_2 to $Fe(III)(CN)_6^{3-}$

While fast electron injection from sensitizer to semiconductor is essential for a high photon to current conversion efficiency, a slow recombination rate is also required. The back electron transfer in Ru N3 sensitized TiO_2 films has been determined to occur in the microsecond to millisecond time scale. The combined ultrafast electron injection and slow recombination is responsible for the almost 100% conversion efficiency for this sensitizer. In this section, we will focus on the back electron transfer dynamics from the semiconductor nanoparticles to the adsorbate. To achieve a more quantitative understanding of this process, we chose to study simple adsorbates, such as $Fe(II)(CN)_6^{4-}$ and SCN^-, that form charge transfer complexes with TiO_2 nanoparticles. In these complexes, a charge transfer transition can be directly excited with optical excitation, so the electronic coupling matrix elements of relevant potential energy surfaces and the Frank Condon active vibrational modes involved in the ET process can be determined experimentally[53,99-102]. These systems may serve as a good model system for quantitative analysis of interfacial ET. This type of treatment, which is common for intramolecular ET in homogeneous solutions[100-102], is rare for interfacial ET processes studied so far[53].

TiO_2 nanoparticles and $Fe(II)(CN)_6^{4-}$ molecules form charge transfer complexes under low *p*H[52,53,103-105] indicated by the formation of a new absorption band at 430 nm. Excitation of the charge transfer band leads to injection of electrons into TiO_2 and the formation of $Fe(III)(CN)_6^{3-}$[52,53]. The measured photon to current quantum efficiency was only 37% at 430 nm on a nanocrystalline anatase TiO_2 electrode[105], suggesting a substantial amount of back transfer of injected electrons from TiO_2 to ferric cyanide. Back ET to $Fe(III)(CN)_6^{3-}$ and related mono-substituted derivatives[52,105] has been well characterized on the sub-microsecond time scale. The detailed mechanisms of the back ET transfer dynamics in the sub-nanosecond regime have not been studied. In an effort to quantitatively understand interfacial ET dynamics, we have recently studied photoinduced electron transfer (ET) in $Fe(II)(CN)_6^{4-}$ sensitized TiO_2 nanoparticles in colloidal D_2O solution using sub-picosecond laser spectroscopy in the visible and in the mid infrared region. Non-single-exponential recombination kinetics were observed and the origin of this behaviour was investigated by modelling of the dependence of back ET rates on the spatial and energetic distribution of the trap states.

Structure of Fe(II)(CN)$_6^{4-}$ /TiO$_2$ Charge Transfer Complexes

Resonant Raman spectra of adsorbed Fe(II)(CN)$_6^{4-}$ on TiO$_2$ nanoparticles in colloidal solution at pH 1 to 3 show three peaks at 2058, 2072, and 2118 cm^{-1}[53]. These peaks were assigned to the trans(terminal), cis (radial) and bridging CN stretching modes of a singly CN bridged structure with C$_{4v}$ symmetry[53]. Here, trans and cis are relative to the bridging CN. The IR spectrum of adsorbed Fe(II)(CN)$_6^{4-}$ on TiO$_2$ nanoparticles in D$_2$O solution has three CN stretching peaks at 2053, 2068 and 2093 cm^{-1}[71]. Under C$_{4v}$ symmetry, CN stretching modes that are Raman allowed are also IR active[106], although the relative intensities of these modes are very different in the two spectra[107]. We therefore assigned the observed peaks in the IR spectra of the adsorbed Fe(II)(CN)$_6^{4-}$ in colloidal solution, at 2053, 2068 and 2093 cm^{-1}, to the terminal, cis and bridging CN stretching modes. The IR spectrum indicates that under our experimental conditions, the adsorbed Fe(II)(CN)$_6^{4-}$ on TiO$_2$ nanoparticles in the colloid and in the film has a singly CN bridged structure. It should be pointed out that adsorption of Fe(II)(CN)$_6^{4-}$ on metal electrodes can occur through singly, doubly or triply bridged structures depending on the pH of the solution and the size of the cations[106,108].

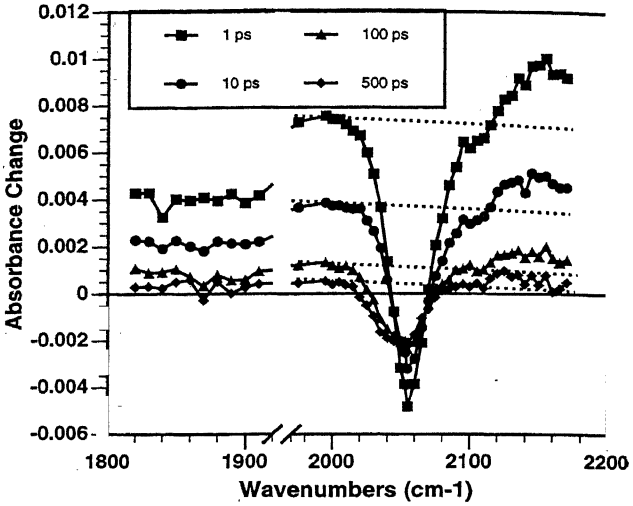

Fig. 11 Transient IR difference spectra of Fe(II)(CN)$_6^{4-}$ /TiO$_2$ in D$_2$O at 1, 10, 100 and 500 ps after 400 nm excitation. The spectrum at each delay time consists of a broad positive feature in the 2000 to 2150 cm^{-1} region (the dash line), a bleach of parent CN stretching modes at 2053 cm^{-1}, and a new positive peak centered around 2160 cm^{-1}. These features are assigned to injected electrons, depletion of Fe(II)(CN)$_6^{4-}$, and formation of Fe(III)(CN)$_6^{3-}$ respectively. The broad absorption feature of injected electrons can also be seen in the 1800-1900 cm^{-1} region.

Assignment of Transient IR Spectra

Shown in Fig. 11 are transient IR spectra of Fe(CN)$_6^{4-}$ sensitized TiO$_2$ colloid at 1, 10, 100 and 500 ps after 400 nm excitation. The spectrum at each delay time consists of a broad positive feature in the whole spectral region (the dashed lines), a bleach of parent CN stretching modes centered at *ca.* 2055 cm^{-1} and a new positive peak centered around 2160 cm^{-1}. These observed signals were shown to result from the excitation of the charge transfer complex, since blank experiments in unsensitized TiO$_2$/D$_2$O solution and Fe(II)(CN)$_6^{4-}$ solution yielded negligible signals. As demonstrated previously[52,105], excitation at the charge transfer band centered at 430 nm promotes electrons from Fe(II)(CN)$_6^{4-}$ to TiO$_2$. 400 nm excitation should also lead to electron injection to TiO$_2$, depletion of Fe(II)(CN)$_6^{4-}$ and formation of Fe(III)(CN)$_6^{3-}$. The depletion of Fe(II)(CN)$_6^{4-}$ is clearly shown by the observed bleach, relative to the dashed lines, in the 2030 to 2110 cm^{-1} region with a peak centered at about 2055 cm^{-1}. Free Fe(III)(CN)$_6^{3-}$ molecules in solution have a CN stretching band at 2115 cm^{-1} [103] and we have recently recorded a FTIR spectrum of adsorbed Fe(III)(CN)$_6^{3-}$ on TiO$_2$, which has a main CN stretching band at 2153 cm^{-1}. We therefore assigned the absorption feature in the 2120 to 2180 cm^{-1} region with a center frequency at about 2160 cm^{-1} to the adsorbed Fe(III)(CN)$_6^{3-}$ created as a result of electron injection. The broad positive feature, indicated by the dashed line in Fig. 11, is assigned to the IR absorption of injected electrons inside TiO$_2$ nanoparticles[63], as discussed in section 3. This feature is more clearly shown in the 1800 to 1900 cm^{-1} region, where there is no overlap with adsorbate CN stretching bands.

Direct Electron Injection

To quantify the time evolution of the observed spectral features, kinetics at different wavelengths in the 1800 to 2150 cm^{-1} region were measured.

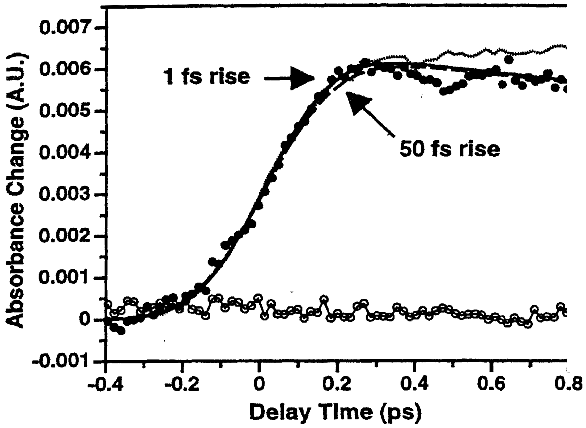

Fig. 12 Kinetics of the transient IR signal at 1850 cm^{-1} for Fe(CN)$_6^{4-}$ /TiO$_2$ colloidal solutions after 400 nm excitation (the full circles). The dotted line is the instrument response function measured in a nanocrystalline TiO$_2$ thin film. The solid lines is a fit of the data by convolution of the instrument response function with a 1 fs single exponential rise and the dashed line is a similar fit with a 50 fs rise time. The connected open circled are transient IR signals of unsensitized TiO$_2$ in D$_2$O under the same pump power.

Shown in Fig. 12 are kinetics measured at 1850 cm^{-1}. The dotted line is the instrument response measured in a naked TiO$_2$ thin film under the same pump power, which can be well represented by a Gaussian function with 320 fs FWHM. At 1850 (Fig. 12) and 1800 cm^{-1} (data not shown), the rise time of the signal appears to be instrument response time limited. Fits with single exponential rise functions yield satisfactory fits with time constants between 0 and 25 fs. A fit with time constant of 50 fs, shown by the dash line in Fig. 4, yields a noticeably worse fit to the data. Within the signal to noise of the data, no rise time is needed to fit the appearance of the IR signal. This instrument response time limited electron injection time is consistent with the charge transfer nature of the optical transition, which directly promotes an electron from a donor orbital in Fe(II)(CN)$_6^{4-}$ to an acceptor orbitals in TiO$_2$.

Back Electron Transfer Dynamics

The excitation of the direct electron transfer transition promotes an electron from the adsorbate molecules to the nanoparticle. The injected electron can relax within the nanoparticles and recombine with the adsorbate molecules. The bleach recovery in the CN stretch band is directly related the back electron transfer from the nanoparticle to the adsorbate and can be monitored independently.

The kinetics at 2053 cm^{-1} contain two contributions: the decay of the broad electron signal and the recovery of the CN stretching band. The kinetics for the CN stretch recovery alone can be obtained by subtracting the broad absorption signal indicated by the dash line in Fig. 11. Since the exact wavelength dependence of the amplitude of the signal is not known, the average of the kinetics at 2000 and 2115 cm^{-1} is used to describe the decay of the background at 2053 cm^{-1}. This approach assumes that the electron absorption signal depends linearly on wavenumbers in this narrow spectral region, which is a pretty good approximation because the electron absorption feature is very broad. Shown in Fig. 13 are the subtracted kinetics for the colloidal solution. The bleach recovery in the colloidal solution can be fit by a multi-exponential recovery with time constants of 3 ps (35%), 40 ps (30%) and > 1 ns (35%). To confirm the validity of the subtraction approach, the bleach recovery of the charge transfer band centered at 430 nm was also measured[71]. Similar multi-exponential recovery

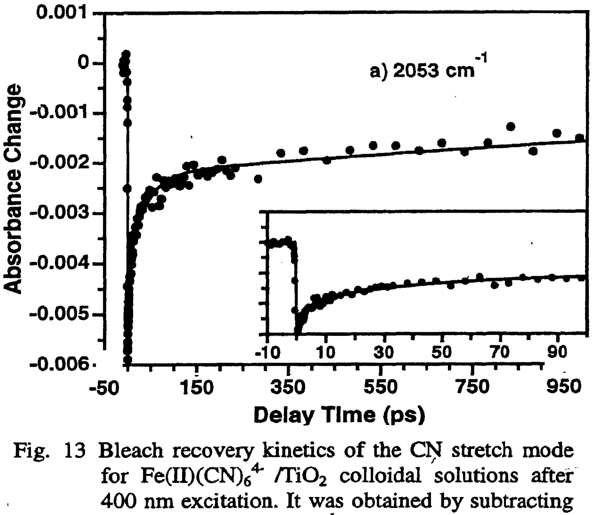

Fig. 13 Bleach recovery kinetics of the CN stretch mode for Fe(II)(CN)$_6^{4-}$ /TiO$_2$ colloidal solutions after 400 nm excitation. It was obtained by subtracting the kinetics at 2053 cm^{-1} by the averaged kinetics of 2000 and 2115 cm^{-1}. The bleach recovery is attributed to back electron transfer from TiO$_2$ to Fe(III)(CN)$_6^{3-}$. The solid line is the best three-exponential fit to the data. Displayed in the insert are the same kinetics in a shorter time scale.

kinetics were observed. The similarity between these two different measurements further confirms that the observed kinetics shown in Fig. 13 indeed describe the back ET dynamics.

The recovery of the CN bleach signal indicates the reformation of $Fe(II)(CN)_6^{4-}$ in its ground vibrational state. The observed recovery time constants can be directly related to back ET time, except for in the < 10s of picosecond time scale, in which vibration relaxation of hot $Fe(II)(CN)_6^{4-}$ formed after back ET may also contribute to the measured time. Ultrafast back ET is expected to produce vibrationally hot donor molecules as shown recently in intramolecular charge transfer complexes[107,109,110]. Unfortunately, the quality of the data is not adequate to allow more detailed analysis of vibrational relaxation dynamics. These dynamics, which contain information about back ET active vibrational modes, is of great interest to current ET research[107,109,110] and will be carefully examined in the future.

Back ET of $Fe(II)(CN)_6^{4-}$ sensitized TiO_2 in solution has been studied previously in the nanosecond to microsecond[52,105] time scale. In an earlier experiment with 20 ns time resolution[105], back ET was measured by monitoring the bleach recovery at 480 nm after 530 nm excitation. Back ET was found to be complete in 10 μs, with a half-life of 3 μs. More recently, in a similar measurement with 2 ns resolution[52], back ET time was found to be well represented by two components. The fast component, with about 50 % of the total amplitude, occurred with a time constant of 270 ns, and the slow non-exponential component appeared to be similar to that observed in the earlier measurement[105]. Combining all the results together, the back ET process is highly non-exponential, containing at least five different time constants, ranging from 3 ps to 3 μs. It is interesting to note that about 70% of the recombination occurs within 1 ns.

Origin of Non-Single-Exponential Back Electron Transfer Kinetics

The origin of the highly non-single-exponential nature of the back ET process has not been fully examined. Non-single-exponential recombination kinetics from TiO_2 to adsorbates have also been observed in $Ru(dcbpy)_2(SCN)_2$ sensitized TiO_2 thin film electrodes[48,111]. The back ET time was found to fall in the nanosecond to millisecond time scale and depend on bias-voltage of the electrode. There are at least three different reasons that can attribute to the nonexponential nanoparticle-to-adsorbate back electron transfer. First, there may be a large inhomogeneous distribution of adsorption sites. This leads to a distribution of donor-acceptor electronic coupling matrix elements, and therefore a distribution of the ET rates[12]. While an inhomogeneous distribution of adsorbing sites is possible, it is unlikely to be the only cause for the observed nonexponential ET process. If it is the dominating factor, then the observed back ET time, spanning 6 decades, suggests that the value for the square of the coupling matrix elements would need to vary by six order of magnitudes for different adsorbing sites. Secondly, unlike intramolecular ET, the injected electrons in the semiconductor nanoparticles can be localized at different parts of the nanoparticles. These different sites are located at varying distances away from the adsorbate molecule, ranging from a few to 50 A, the average diameter of the particles. This inhomogeneous distribution is further broadened by the inhomogeneous distribution of the particle sizes existing in the sample. If the trapped electrons recombine with the adsorbates through tunneling, the electronic coupling matrix element between the trap site and adsorption site is distance dependent, and the back ET reaction from these sites is expected to be non-single-exponential. For shallow trap sites, the trapped electrons may recombine with the adsorbate through diffusion encounter. In this case, the distribution in distance would lead to a distribution in the required diffusion time. Finally, in addition to the spatial distribution, these trap sites may also have very different energies, leading to a distribution of driving force and therefore the back ET rates[12]. The existence of trapping states with different energies has been observed in previous studies of TiO_2 thin film electrodes[90,112]. Similar trapping states can be expected for TiO_2 nanoparticles. The observed IR decay kinetics of electrons in TiO_2, as shown in Fig. 14 and discussed below, show electron trapping dynamics occurring in the picosecond to subnanosecond time scale in addition to back ET. Existence of relaxation processes that compete with electron transfer makes this an interesting and challenging system for study.

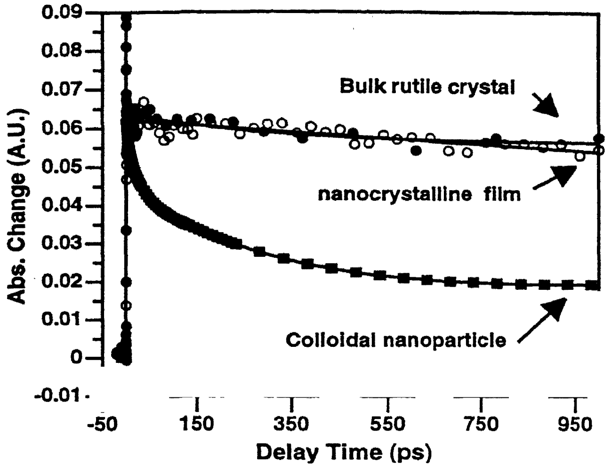

Fig. 14 Comparisons of decay kinetics probed in the mid IR region for electrons in three different TiO_2 materials: $Fe(II)(CN)_6^{4-}$ sensitized colloidal nanoparticles (connected filled squares), Ru N3 sensitized nanocrystalline thin films, and a bulk rutile crystal.

It appears that back ET from TiO_2 to $Fe(III)(CN)_6^{3-}$ involves electrons trapped in many different trapping sites, giving rise to highly non-exponential back ET dynamics. We also found recently that there was very little difference in the back electron transfer rate from TiO_2 to $Fe(III)(CN)_6^{3-}$ for particle sizes of about 3 and 11 nm[113]. This result indicates that the injected electrons are trapped at sites that are close to the adsorbates and are not homogeneously distributed over the entire particle. We are currently using the Marcus electron transfer rate theory and models of trapping site and energy distribution to model the nonexponential behaviour and the particle size independence of the back ET kinetics. The details of modelling will be communicated in future publications[113].

6 Relaxation Dynamics of Injected Electrons

The mid-IR absorbance of the injected electrons is proportional to the density of the injected electrons and their absorption cross section. The time dependence of the electron population reflects the electron transfer kinetics and the temporal evolution of the absorption cross section can be related to the electron relaxation processes within TiO_2. The observed decay of IR absorption signal contains the relaxation dynamics of electrons in TiO_2 in addition to the electron transfer dynamics discussed earlier. Shown in the Fig. 14 is a comparison of the electron relaxation dynamics in bulk rutile TiO_2 crystal, Ru N3 sensitized TiO_2 thin films and $Fe(CN)_6$ sensitized nanoparticles in solution.

For the bulk rutile crystal, the electrons and holes are generated through direct excitation of the bandgap transition. The decay of the signal within the first nanosecond is characterized by a pulse width limited decay (Fig. 5), and a subsequent slow decay of the amplitude with a time constant >> 1 ns. The fast decay can be attributed to fast cooling or recombination dynamics of the electrons. Subpicosecond electron cooling dynamics have been observed in many bulk semiconductor materials[114]. The slow subsequent decay suggest little carrier recombination or trapping dynamics in the ns time scale. For Ru N3 sensitized TiO_2 thin films, back ET time has been observed to occur in the μs to ms time scale. So there is no decay of population of the injected electrons in the < 1ns time scale. The observed decay of the IR signal can be attributed to the electron relaxation in the thin films only. The decay kinetics in different films vary slightly depending on film preparation.

For $Fe(II)(CN)_6^{4-}$ sensitized TiO_2 nanoparticles, at a probe wavelength that is far away from the CN bleach, such as 2000 cm^{-1}, the decay of the signal can be attributed to back electron transfer and electron trapping. If we assume a time dependent average cross section $\sigma(t)$ for the injected electrons as a result of trapping, the time-dependent mid IR absorption signal, $A(t)$, can be described by:

$$A(t) = \overline{\sigma}(t) * N_e(t)$$

where $N_e(t)$ is the population of injected electrons. The electron population is proportional to the amplitude of the CN bleach and can be determined independently as shown in Fig. 13. The average cross section of electrons can be obtained by dividing the observed absorbance change at 2000 cm^{-1} by the bleach recovery kinetics. The average cross section calculated according to this procedure is shown by connected squares in Fig. 14. It contains multi-exponential decay functions: 7 ps (8%), 35 ps (22%), 300 ps (40%), and >> 1ns (30%). This curve then represents the electron relaxation dynamics in TiO_2 colloidal nanoparticles.

It is interesting to note that the trapping dynamics in the sensitized film and in a bulk TiO_2 crystal are similar[69,70], but they are much slower than those in colloidal nanoparticles[69-71]. Qualitatively, these decay kinetics can be attributed to relaxation of electrons from shallow trap to deep trap states. The trend in the electron relaxation rates is consistent with the trend of the density of trap states in these different crystalline TiO_2 materials. In principle, given the trap state density distribution and relaxation pathway, one can model quantitatively the electron relaxation kinetics. Unfortunately, the trap state density distribution is not well characterized and a detailed modelling of the decay kinetics has yet to be carried out.

7 Summary and Future Works

Electron transfer dynamics between semiconductor nanoparticles and molecular adsorbates have been studied using femtosecond mid-IR spectroscopy. With this technique, both the adsorbate vibrational spectral change and the mid IR absorption of injected electrons can be directly monitored. The direct observation of injected electrons allows for the unambiguous assignment of the electron transfer process.

The mid-IR absorption signal of electrons in or trapped below the conduction band were observed in the 5 μm region for bulk rutile TiO_2 crystal, nanocrystalline TiO_2 thin films, and colloidal nanoparticles. There appears to be very little spectral dependence in the 1950 to 2050 cm^{-1} region. The exact contribution of free carrier absorption, intraband transition and trapped electron absorption to the mid-IR absorption signal has yet to be determined. Ongoing measurements in a wider spectral region should allow a more detailed assignment of the observed signal. The time evolution of the absorption spectra will also provide insight into the relaxation dynamics of electrons in these materials. The trapping dynamics of electrons in nanocrystalline thin films and in a bulk single crystal are similar, showing very little decay on the < 1ns time scale. The trapping dynamics are much faster in colloidal nanoparticles, consistent with the trend of trap state densities in these materials.

Electron injection dynamics from adsorbate to TiO_2 were studied in Ru N3 dye sensitized nanocrystalline TiO_2 thin films. After the excitation of the ^{1}MLCT band of Ru N3 dye at 400 nm, electrons were excited from the Ru d orbital to the dcbpy π^* orbital. The subsequent electron injection time to TiO_2 was measured to be ca. 50 fs. The excited state dynamics of the Ru N3 dye in ethanol and adsorbed on Al_2O_3, a wide gap semiconductor, were also studied. The excited state relaxation from the initially excited singlet to the long-lived triplet MLCT state was found to occur on the < 100 fs time scale. This result indicates that electron injection from Ru N3 to TiO_2 may occur on a time scale that is the same as or faster than that for excited state relaxation.

Back electron transfer dynamics from TiO_2 to adsorbate were studied in $Fe(II)(CN)_6^{4-}$ sensitized TiO_2 colloidal solution. $Fe(II)(CN)_6^{4-}$ and TiO_2 forms a charge transfer complex, in which the excitation of the charge transfer band leads to direct promotion of an electron from $Fe(II)(CN)_6^{4-}$ to TiO_2. The appearance of the IR absorption signal for the injected electrons after 400 nm excitation was found to be instrument response time limited, consistent with the charge transfer nature of the optical transition. The injected electrons recombines with the adsorbate through a non-single-exponential process. A multi-exponential fit of the data yielded time constants ranging from 3ps to > 1 ns according to our measurement on the < 1ns time scale. Even longer recombination time constants of 270 ns[52] to 3 μs[105] were observed in previous studies in the nanosecond to microsecond time scale. The detailed origin of this nonexpoential process is being examined in our laboratory. Qualitatively, non-exponential recombination can be attributed to injected electrons in different trap sites. A quantitative model with spatial and energetic distribution of trapped electrons will be used to account for the non-single-exponential back ET dynamics.

Our study has shown that femtosecond mid IR spectroscopy can be used to study interfacial electron transfer between nanoparticles and molecular adsorbates. With this technique and complementary techniques in the visible region, we can now start to systematically examine the dependence of interfacial ET rates on the properties of the adsorbates, nanoparticles, and interfacial environment. Quantitative comparison with interfacial electron transfer theory may now be possible since simple interfacial charge transfer complexes, such as $Fe(II)(CN)_6^{4-}/TiO_2$, can be studied and various parameters can be systematically changed. We are also extending this technique to study charge transfer dynamics in other nano-materials such as polymer/nanoparticle composites and nanoparticle arrays.

8 Acknowledgements

The authors would like to thank other collaborators of this project, R J Ellingson, S Ferrere and A J Nozik in NREL for their contribution in the Ru N3/TiO_2 study[64,70,72]. This work is supported in part by The Petroleum Research Fund, administered by the ACS, the Emory University Research Committee, and the National Science Foundation CAREER award under grant No. 9733796, and the Division of Chemical Sciences of the US Department of Energy.

References

1 R J D Miller, G L McLendon, A J Nozik, W Schmickler and F Willig *Surface Electron Transfer Processes* VCH Publishers Inc (1995)

2 A J Nozik and R Memming *J Phys Chem* **100** (1996) 13061

3 P V Kamat *Prog Reac Kinet* **19** (1994) 277

4 K I Jacobson and R E Jacobson *Imaging Systems* John Wiley & Sons New York (1976)

5 A Kay and M Gratzel *Solar Energy Materials and Solar Cells* **44** (1996) 99

6 N Serpone *Research On Chemical Intermediates* **20** (1994) 953

7 V L Colvin, M C Schlamp and A P Alivisatos *Nature* **370** (1994) 354

8 B Oregan and M Gratzel *Nature* **353** (1991) 737

9 A Hagfeldt and M Gratzel *Chem Rev* **95** (1995) 49

10 P V Kamat and D Meisel *Semiconductor Nanoclusters - Physical, Chemical and Catalytic Aspects* Elsevier Amsterdam **103** (1997)

11 M K Nazeeruddin, A Kay, I Rodicio, R Humphrybaker, E Muller, P Liska, N Vlachopoulos and M Gratzel *J.Chem Soc* **115** (1993) 6382

12 R A Marcus and N Sutin *Biochem Biophys Acta* **811** (1985) 265

13 M D Newton and N Sutin *Ann Rev Phys Chem* **35** (1984) 437

14 P F Barbara, T J Meyer and M A Ratner *J Phys Chem* **100** (1996) 13148

15 R A Marcus *J Chem Phys* **43** (1965) 679

16 H Z Gerischer *Phys Chem Frankfurt* **26** (1960) 223

17 H Z Gerischer *Phys Chem Frankfurt* **27** (1961) 48

18 V G Levich and R R Dogonadze *Dokl Akad Nauk SSSR* **124** (1959) 123

19 N S Lewis *Ann Rev Phys Chem* **42** (1991) 543

20 *Laser Spectroscopy and Photochemistry on Metal Surface Part I & II* (Eds. H -L Dai and W Ho) World Scientific Publishing Co Singapore 5 (1995)

21 W Ho *Surf Sci* **300** (1994) 996

22 J P Culver, M Li, R M Hochstrasser and A G Yodh *Chem Phys* **205** (1996) 159

23 J P Culver, M Li, R M Hochstrasser and A G Yodh *Surf Sci* **368** (1996) 9

24 C M Wong, J D McNeill, K J Gaffney, N H Ge, A D Miller, S H Liu and C B Harris *Phys Chem* **B103** (1999) 282

25 C B Harris, N H Ge, R L Lingle, J D McNeill and C M Wong *Ann Rev Phys Chem* **48** (1997) 711

26 R Memming *Topics Curr Chem* **169** (1994) 105

27 J F Smalley, S W Feldberg, C E D Chidsey, M R Linford, M D Newton and Y P Liu *J Phys Chem* **99** (1995) 13141

28 S B Sachs, S P Dudek, R P Hsung, L R Sita, J F Smalley, M D Newton, S W Feldberg and C E D Chidsey *J Am Chem Soc* **119** (1997) 10563

29 Y Rosenwaks, B R Thacker, R K Ahrenkiel and A J Nozik *J Phys Chem* **96** (1992) 10096

30 Y Rosenwaks, B R Thacker, A J Nozik, R J Ellingson, K C Burr and C L Tang *J Phys Chem* **98** (1994) 2739

31 G N Ryba, C N Kenyon and N S Lewis *J Phys Chem* **97** (1993) 13814

32 K B Eisenthal *Chem Rev* **96** (1996) 1343

33 Y R Shen *Solid St Commun* **102** (1997) 221

34 G L Richmond *Anal Chem* **69** (1997) A536

35 J M Lanzafame, S Palese, D Wang, R J D Miller and A A Muenter *J Phys Chem* **98** (1994) 11020

36 A P Alivisatos *J Phys Chem* **100** (1996) 13226

37 D J Norris and M G Bawendi *Phys Rev B-Cond Matter* **53** (1996) 16338

38 B A Smith, D M Waters, A E Faulharber, M A Kreger, T W Roberti and J Z Zhang *J Sol-Gel Sci Tech* **9** (1997) 1

39 J Z Zhang *Acc Chem Res* **30** (1997) 423

40 V F Kamalov, R Little, S L Logunov and M El-Sayed *J Phys Chem* **100** (1996) 6381

41 J H Hodak, I Martini and G V Hartland *J Phys Chem* **B102** (1998) 6958

42 T Heimer and E J Heilweil *J Phys Chem* **B101** (1997) 10990

43 T Hannappel, B Burfeindt, W Storck and F Willig *J Phys Chem* **B101** (1997) 6799

44 A J Nozik, R J Ellingson, A Meieer, S Kocha, B B Smith and M Hanna *Proc Twenty-first DOE Solar Photochem Res Conf* (1997) 9

45 I Martini, G V Hartland and P V Kamat *J Phys Chem* **B101** (1997) 4826

46 I Martini, J H Hodak, G V Hartland and P V Kamat *J Chem Phys* **107** (1997) 8064

47 N J Cherepy, G P Smestad, M Gratzel and J Z Zhang *J Phys Chem* **101** (1997) 9342

48 Y Tachibana, J E Moser, M Gratzel, D R Klug and J R Durrant *J Phys Chem* **100** (1996) 20056

49 J M Rehm, G L McLendon, Y Nagasawa, K Yoshihara, J Moser and M Gratzel *J Phys Chem* **100** (1996) 9577

50 J M Lanzafame, R J D Miller, A Muenter and B Parkinson *J Phys Chem* **96** (1992) 2820

51 R Eichberger and F Willig *Chem Phys* **141** (1990) 159

52 H Lu, J N Prieskorn and J T Hupp *J Am Chem Soc* **115** (1993) 4927

53 R L Blackbourn, C S Johnson and J T Hupp *J Am Chem Soc* **113** (1991) 1060

54 B Burfeindt, T Hannapel, W Storck and F Willig *J Phys Chem* **100** (1996) 16463

55 D Liu, R W Fessenden, G L Hug and P V Kamat *J Phys Chem* **B101** (1997) 2583

56 K Murakoshi, S Yanagida, M Capel and J E W Castner *Interfacial Electron Transfer Dynamics of Photosensitized Zinc Oxide Nanoclusters ACS Symposium Series* (1997) 679

57 D Liu, P V Kamat, K G Thomas, K J Thomas, S Das and M V George *J Chem Phys* **106** (1997) 6404

58 R W Fessenden and P V Kamat *J Phys Chem* **99** (1995) 12902

59 J C Owrutsky, D Raftery and R M Hochstrasser *Ann Rev Phys Chem* **45** (1994) 519

60 M A Cavicchia and R R Alfano *Phys Rev B-Cond Matt* **51** (1995) 9629

61 M Woemer, T Elsaesser and W Kaiser *Phys Rev* **B45** (1992) 8378

62 K Faist, F Capasso, D L Sivco, C Sirtori, A L Hutchinson and A Y Cho *Science* **264** (1994) 553

63 J I Pankove *Optical Processes in Semiconductors* Dover New York (1975)

64 R J Ellingson, J B Asbury, S Ferrere, H N Ghosh, T Lian and A J Nozik *J Phys Chem* **B102** (1998) 6455

65 R McElroy and K Wynne *Phys Rev Lett* **79** (1997) 3078

66 D S Venables and C A Schmuttenmaer *J Chem Phys* **108** (1998) 4935

67 G Haran, W D Sun, K Wynne and R M Hochstrasser *Chem Phys Lett* **274** (1997) 365

68 T Heimer and E J Heilweil Measuring Ultrafast Sensitizer-TiO_2 Electron Dynamics with Mid-Infrared Spectroscopy *Ultrafast Phenomena* **XI** (1998)

69 H N Ghosh, J B Asbury and T Lian *J Phys Chem* **B102** (1998) 6482

70 J B Asbury, H N Ghosh, R J Ellingson, S Ferrere, A J Nozik and T Lian Femtosecond IR Study of Ru Dye Sensitized Nanocrystalline TiO_2 Thin Films: Ultrafast Electron Injection and Relaxation Dynamics *Ultrafast Phenomena* **XI** (1998)

71 H N Ghosh, J B Asbury, Y Weng and T Lian *J Phys Chem* **B102** (1998) (in press)

72 J B Asbury, R J Ellingson, H N Ghosh, S Ferrere, A J Nozik and T Lian *J Phys Chem* **B103** (1999) (in press)

73 H N Ghosh, J B Asbury and T Lian (unpublished results)

74 D Bahnemann, A Henglein, J Lilie and L Spanhel *J Phys Chem* **88** (1984) 709

75 R G Breckenridge and W R Hosler *Phys Rev* **91** (1953) 793

76 Enea, J Moser and M Gratzel *Electroanal Chem* **259** (1989) 59

77 S A Haque, Y Tachibana, D R Klug and J R Durrant *J Phys Chem* **B102** (1998) 1745

78 S G Yan and J T Hupp *J Phys Chem* **B101** (1997) 1493

79 S G Yan and J T Hupp *J Phys Chem* **100** (1996) 17

80 A Zaban, S Ferrere and B A Gregg *J Phys Chem* **B102** (1998) 452

81 A Zaban, S Ferrere, J Sprague and B A Gregg *J Phys Chem* **B101** (1997) 55

82 K Vinodgopal, X Hua, R L Dahlgren, A G Lappin, L K Patterson and P V Kamat *J Phys Chem* **99** (1995) 10883

83 R Argazzi, C A Bignozzi, T A Heimer, F N Castellano and G J Meyer *J Phys Chem* **B101** (1997) 2591

84 T A Heimer and G J Meyer *J Luminescence* **70** (1996) 468

85 T A Heimer, S T Darcangelis, F Farzad, J M Stipkala and G J Meyer *J Inorg Chem* **35** (1996) 5319

86 W E Ford and M A J Rodgers *J Phys Chem* **98** (1994) 3822

87 V E Henrich and P A Cox *The Surface of Metal Oxides* Cambridge University Press (1994)

88 N H Damrauer, G Cerullo, A Yeh, T R Boussie, C V Shank and J K McCusker *Science* **275** (1997) 54

89 R Kietzmann, F Willig, H Weller, R Vogel, D N Nath, R Eichberger and P Liska and J Lehnert *Molecul Cryst Liqui Cryst* **194** (1991) 169

90 G Rothenberger, D Fitzmaurice and M Gratzel *J Phys Chem* **96** (1992) 5983

91 T Hannappel, C Zimmermann, B Meissner, B Burfeindt, W Storck and F Willig. *J Phys Chem* **B102** (1998) 3651

92 J E Moser, D Noukakis, U Bach, Y Tachibana, D Klug, J R Durrant, R Humphry-Baker and M Gratzel *J Phys Chem* **B102** (1998) 3649

93 A Mokhtari, A Chebira and J Chesnoy *J Opt Sci Am* **B7** (1990) 1551

94 F Laermer and T Elsaesser *J Opt Soc Am* **B7** (1990) 1604

95 S Ferrere and B A Gregg *J Am Chem Soc* **120** (1998) 843

97 I Martini, J H Hodak and G V Hartland *J Phys Chem* **B102** (1998) 607

98 B Burfeindt, S Ramakrishna, C Zimmermann, B Meissner, T Hannappel, W Storck and F Willig *Ultrafasrt Phenomena* **XI** (1998)

99 N S Hush *Electrochimica Acta* **13** (1968) 1005

100 A B Myers *Chem Phys* **180** (1994) 215

101 J T Hupp, Y H Dong, R L Blackbourn and H Lu *J Phys Chem* **97** (1993) 3278

102 W Klaas and R M Hochstrasser *Advan Chem Phys* (1997) (In press)

103 J Desilvestro, S Pons, E Vrachnou and M Gratzel *J Electroanal Chem* **246** (1988) 411

104 E M G Vrachnou and A J McEvoy *J Electroanal Chem* **258** (1989) 193

105 E Vrachnou, N Vlachopoulos and M Gratzel *J Chem Soc Chem Commun* (1987) 868

106 C Korzeniewski, M W Severson, P P Schmidt, S Pons and M Fleischmann *J Phys Chem* **91** (1987) 5568

107 C Wang and G C Walker *J Am Chem Soc* (1998) (Submitted)

108 C M Pharr and P R Griffiths *Anal Chem* **69** (1997) 4665
109 S K Doom, R B Dyer, P O Stoutland and W H Woodruff *J Am Chem Soc* **115** (1993) 6398
110 K G Spears, X N Wen and R H Zhang *J Phys Chem* **100** (1996) 10206
111 S A Haque, Y Tachibana, D R Klug and J R Durrant *J Phys Chem* **B102** (1998)
112 A Kay, R Humphrybaker and M Gratzel *J Phys Chem* **98** (1994) 952
113 Y Weng, H Ghosh, J B Asbury, Y Wang and T Lian (mss in preparation)
114 J Shah *Ultrafast Spectroscopy of Semiconductors and Semiconductor Nanostructures* Springerverlag **115** (1996)

PHOTOPHYSICAL PROCESSES IN ORGANIZED ASSEMBLIES

KANKAN BHATTACHARYYA*

Physical Chemistry Department, Indian Association for the Cultivation of Science, Jadavpur, Calcutta-700 032 (India)

Dynamics of different photophysical processes are markedly affected in organized media. Confinement of the probe in a small volume seriously hinders the free motion of the probes. The local properties such as, polarity, viscosity and *p*H in an organized media are very different from those in an ordinary liquid. The extreme sensitivity of the dynamics of the photophysical processes have been utilized to infer the microscopic properties of the organized media.

Key Words: Photophysical Processes; Photoisomerisation; Nanoenvironment; Micelles; Lipid Vesicles; Solvation Dynamics; Organized Assemblies

1 Introduction

Self-organized molecular assemblies play a major role in many natural and biological processes. The spontaneous formation of these assemblies particularly in aqueous medium is a result of the interplay between the very strong water-water interactions and the weak interaction among the organic molecules. In an organized assembly, the active chemical species remains confined in a small region, a few nm in size. Such confinement in a small volume imposes severe restrictions on the free motion of the probe and the confined solvent molecules. The 'local' properties e.g. polarity, viscosity and *p*H in such a nanoenvironment are often vastly different from those in a bulk medium. Chemical reactivity and dynamics in such a confined environment are vastly different from those in any homogeneous fluid medium due to the proximity and the favourable disposition of the confined reactants and the markedly altered local properties. Chemistry in organized media mimic the extremely efficient chemical processes occurring in the biological systems.[1-5] This provides the main impetus to study organized assemblies. Photophysical processes in organized assemblies are interesting particularly for two reasons. In the present review, we will discuss how rate of some of the photophysical processes change quite dramatically in organized assemblies and how this remarkable sensitivity can be utilized to probe the organized assemblies.

There are several types of organized molecular assemblies. Some of them are molecular aggregates formed in polar liquids (e.g. micelles in water) or nonpolar liquids (e.g. reverse micelles or micro-emulsions in hydrocarbons). Further examples include several cage like hosts soluble in many liquids (cyclodextrins or calixarenes), microporous solids (e.g. zeolites), and semirigid materials (e.g. polymers, hydrogels etc.) which can encapsulate suitably sized guest molecules.

The organization of the present review is as follows. In Section 2, we will give a general overview of several photophysical processes which are used as a probe for the organized assemblies. In Section 3, we will describe the architecture of some organized assemblies. Finally, in Section 4 we will discuss the recent results on the dynamics of various photophysical processes in these assemblies.

Photophysical processes in organized assemblies have been discussed in many recent reviews. In the volume edited by Ramamurthy, several authors summarized the progress in this area up to 1991.[1] Several authors have discussed the effect of cyclodextrins on many photophysical processes.[2] The hydrophobic effect, which causes binding of organic probes with cyclodextrins and other hosts in aqueous medium has been reviewed thoroughly.[3]

---

*e-mail: pckb@mahendra.iacs.res.in fax: 91-33-473-2805

Many organized assemblies involve an interface between two drastically different media. Chemical and physical processes at various interfaces have been recently studied using a number of new experimental and theoretical techniques.[4-5]

2 Photophysical Processes

In this Section, we will discuss the salient features of several photophysical processes. Due to our interest in the dynamics of the photophysical processes we will emphasize the factors which govern the dynamics of these processes.

Solvent Relaxation

Solvent relaxation refers to the reorientation of polar solvent molecules about a dipole instantaneously created in a polar solvent. For this purpose, one uses a solute which is non-polar or weakly polar in the ground state and is highly polar in the electronically excited state. A dipole can be created instantaneously by exciting such a probe with an ultrashort picosecond or femtosecond light pulse. When the probe solute is in the ground state, the polar solvent molecules remain randomly oriented around the non-polar or weakly polar probe solute molecule. Immediately after excitation by an ultrashort pulse, the polar solvent molecules remain randomly oriented around the dipole created as the solvent relaxation is very much slower than the excitation process. Subsequently, the solvent molecules gradually reorient around the newly created electron or dipole. This process of reorientation of the solvent dipoles around an electron or a dipole is referred to as the solvation dynamics. The system eventually reaches the fully solvated state. The solvation time, τ_s, is defined as the time taken for the solvent molecules in going from the randomly oriented configuration to the fully solvated state. As the solute dipole, in the excited state, is gradually stabilized through solvation, the incompletely solvated species decays rapidly giving rise to a fast decay at the blue end of the emission spectrum. The solvated species however, grows with time, and this growth is manifested at the red end of the emission spectrum. This results in the gradual decrease in the emission energy i.e. red shift of the emission spectra with increase in time. This phenomenon is known as the time dependent Stokes shift (TDSS).[6-7] The wavelength dependent temporal decays of emission and TDSS are regarded as the evidences of solvation dynamics. The TDSS technique is the most popular method of studying solvation dynamics. The solvation dynamics is followed by the decay of the solvent response function, $C(t)$, which is defined as,

$$C(t) = \frac{\nu(t) - \nu(\infty)}{\nu(0) - \nu(\infty)}$$

where $\nu(0)$, $\nu(t)$ and $\nu(\infty)$ are the emission frequencies at time zero, t and infinity respectively. The solvation time, τ_s, is the time constant of the decay of the response function $C(t)$, so that $C(t)=\exp(-t/\tau_s)$. If the decay of $C(t)$ is multiexponential, e.g. $a_1\exp(-t/\tau_1)+a_1\exp(-t/\tau_2)$, one considers the average solvation time $<\tau_s> = a_1\tau_1 + a_1\tau_2$. The solvation time is also known as the longitudinal relaxation time of the solvent. According to the simple continuum theory, the solvation time is related to the dielectric relaxation time, τ_D, as,[8-9]

$$\tau_s = (\varepsilon_\infty/\varepsilon_0)\ \tau_D$$

where ε_∞ and ε_0 are respectively the dielectric constants at high frequency and that at zero (static) frequency. For most polar liquids, $(\varepsilon_\infty/\varepsilon_0) < 1$. As a result the solvation time, τ_s is shorter than the dielectric relaxation time. It is obvious that solvation dynamics studies provide valuable information on the mobility of confined solvent molecules in an organized assembly. Since water is by far the most important solvent for the biological systems, in the next section, we will briefly discuss some recent results on solvation dynamics and dielectric relaxation in pure water.

Solvation Dynamics and Dielectric Relaxation in Water

For water, $\varepsilon_\infty \approx 5$, $\varepsilon_0 \approx 80$ and the dielectric relaxation time $(\tau_D)^{12}$ is 10 ps. Thus, according to the simple continuum theory, the solvation time of water should be $\approx (5/80) \times 10$ or 0.6 ps. The first experimental study on the solvation dynamics of the water molecules around a dye molecule, coumarin 343, was performed by Barbara *et al.*[9] They reported solvation times of 0.16 ps and 1.2 ps with relative contributions of 1:2. Later using a set up with a better time resolution, Fleming *et al.*[9] detected an initial ultrafast Gaussian component ($a_g e^{-\frac{1}{2}\omega_g^2 t^2}$) with a frequency ω_g=38.5 ps^{-1} and a slower biexponential decay with time constants of 126 fs and 880 fs, respectively. They assigned the ultrafast gaussian component to the intramolecular vibration and librational motions of the water molecules and the slower component, to their diffusive, reorientational motion. Using molecular hydrodynamic theory, Bagchi *et al.* discussed the role of different vibrational modes on the solvation dynamics in water and showed that the initial ultrafast part is controlled by the intramolecular vibration and the librational modes of water.[10] This model predicts a deuterium isotope effect at long time. Schwartz and Rossky later calculated a similar 20% isotope effect.[10]

While the properties of the water molecules in bulk have been studied quite thoroughly for a very long time, much less is known about the behaviour of water molecules in confined environments. There is considerable recent interest on the structure and dynamics of water molecules at various interfaces. Recent molecular dynamics simulations indicate that the dielectric constant of water decreases by as much as a factor of 16, when the water molecules are confined in a volume of dimension 27 Å.[13]

The dynamics of the so called "biological water" molecules, in the immediate vicinity of a protein, has been studied using various techniques. While the dielectric relaxation time of ordinary water molecules is 10 ps,[12] both the dielectric[14-16] and NMR relaxation studies,[17] indicate that near the protein surface the relaxation dynamics is bimodal with two components in the 10 ns and 10 ps time scale, respectively. The 10 ns relaxation time can not be due the motion of the peptide chains which occurs in the 100 ns time scale. From the study of NMR relaxation times of ^{17}O at the protein surface, Halle *et al.*[17] suggested a dynamic exchange between the slowly rotating internal and the fast external water molecules. To explain the bimodal dielectric relaxation in aqueous protein solutions, Nandi and Bagchi proposed a similar dynamic exchange between the "bound" and the free water molecules.[18] The "bound" water molecules are those which are attached to the biomolecule by strong hydrogen bonds. Their rotation is coupled with that of the biomolecule. The water molecules, beyond the solvation shell of the proteins, behave as free water molecules. The free water molecules rotate freely and contribute to the dielectric relaxation process, whereas the rotation of the doubly hydrogen-bonded "bound" water molecules is coupled with that of the biomolecule and hence, is much slower.

Using conjugate peak refinement method, Fischer *et al.*[19] calculated the reaction path of the motion of the biological water molecules. They also compared the computed transition state and activation energy to those in ice. Their calculation shows that the motion of the water molecules, buried in the proteins, involves exchange of two water hydrogen atoms and involves two successive rotations around orthogonal axes.

In a later section, we will show that the substantially slower dielectric relaxation times of water in organized assemblies, markedly slow down the solvation dynamics, in some cases by 4 orders of magnitude, compared to bulk water.

Photoisomerisation

In the ground state of a molecule *cis-trans* isomerisation i.e. rotation about an olefinic double bond is not allowed because it involves a very large barrier, roughly equal to the π-bond energy. However, the π-bond order becomes zero in the $\pi\pi^*$ excited state and thus, rotation about double bond and hence, *cis-trans* isomerisation is possible in the $\pi\pi^*$ excited state. The interconversion of different rotational and geometric isomers via the excited state is known as photoisomerisation. In the excited state, the system moves freely along the torsional coordinate. When it reaches the perpendicular geometry, it undergoes rapid transition from the excited electronic state to the nearly isoenergetic ground state. Once the system is at the peak of the barrier between the *cis* and the *trans* isomer in the ground state, it can go to either of them with equal probability, resulting in photoisomerisation.[20] The photoisomerisation plays an important role in many chemical and biological processes, which include the vision process. The vision process involves such a *cis-trans* photoisomerisation about the C_{11}-C_{12} double bond of a retinyl polyene attached to the opsin part of a 7-helix membrane protein, rhodopsin.[21-22]

The dynamics of the photoisomerisation process depends on the friction offered by the medium to the motion of the system along the torsional coordinate. In Kramers' seminal work,[23] the isomerisation process is viewed as a one dimensional barrier crossing and the rate constant k_{iso} is given by,

$k_{\text{iso}} = \{[\zeta/2\omega_b I]^2 + 1\}^{1/2} - [\zeta/2\omega_b I]$,

where ζ, denotes the friction, ω_b, the barrier frequency and I is the moment of inertia. If the friction is purely hydrodyamic in nature,

$\zeta = 4\pi\eta dr^2$,

where η, is the bulk viscosity, d and r, are molecular dimensions associated with the isomerising groups. At very high viscosity, the Kramers' relation reduces to a simple relation where k_{iso} becomes inversely proportional to the viscosity of the medium. This is known as the Smoluchowski limit. The failure and success of the Kramers' theory has been the subject of intense debate. The failure of Kramers' theory is often ascribed to three factors. Firstly, the friction is often described incorrectly by the hydrodynamic model. There are several improved models, e.g. the time dependent friction model where the friction is assumed to be different at different parts of the potential barrier.[24] Secondly, for many probes (e.g. stilbene, diphenylbutadiene etc.) the isomerisation process is not strictly one dimensional. Thirdly, the microviscosity around a probe molecule may not be same as the bulk viscosity.[25-26] Several authors tried orientational relaxation time as an empirical parameter for microviscosity and found good correlation between the rate of isomerisation and that of orientational relaxation.[25]

According to the Kramers' expression the viscosity dependence of the isomerisation process is rather complicated. However, the relation becomes very simple at very high viscosity (i.e. Smoluchowski limit). Since many organized assemblies possess very high microviscosity it is reasonable to assume that the Smoluchowski limit is valid for them. We will demonstrate that assuming the Smoluchowski limit, the microviscosities of some organized assemblies can be estimated quite accurately.

For some probes, the activation barrier for the isomerisation process and hence, the isomerisation dynamics depends on the polarity of the media. For *trans*-stilbene, Hicks *et al.*[27] observed that the slope of the isoviscous plots of $\ln(k_{\text{iso}})$ against $1/T$ decreases with increase in the viscosity. Since for alcohols, higher viscosity is associated with lower polarity, Hicks *et al.*[27] proposed that the barrier for the isomerisation process, decreases at higher viscosity and hence, at lower polarity. However, for the cyanine dye DODCI, slopes of the isoviscous plots of $\ln(k_{\text{iso}})$ against $1/T$ in alcoholic solvents do not vary much with increase in viscosity.[28] This indicates that the photoisomerisation of DODCI is more or less unaffected by the polarity of the medium.[32] Waldeck *et al.*[20] showed that a barrier for the isomerisation process can be extracted only for solvents like nitriles where the solvent relaxation is much faster than the excited state isomerisation process. In slower solvents like alcohols, the slow and incomplete solvation obscures observation of a well-defined barrier for the isomerization process.

Excited State Proton Transfer

Acid-base properties of many molecules in the excited state differ considerably from those in the ground state.[27] For instance, aromatic amines are weakly basic in the ground state. But, many of them become acidic in the excited state and readily donate a proton to a proton-acceptor to produce the anion in the excited state. Such a molecule which behaves as an acid in the excited state, is called a photoacid and similarly photobases are those which display basic properties in the excited state. In many cases, excited state proton transfer (ESPT) results in dual emission bands. One of these emission bands arises from the neutral excited state and bears mirror image relation with the absorption spectrum. The other emission band is due to the excited deprotonated (anion) or protonated species and exhibits large Stokes shift. In an intermolecular proton transfer process, the proton is transferred from one molecule to another. In this case, the basic issues are whether the acid-base equilibrium is attained within the excited state lifetime of the photoacid or the photobase. If the acid-base equilibrium is attained in the excited state, excited state pk_a and pk_b are determined by steady state or time resolved emission spectroscopy. Ireland and Wyatt summarized the excited state pk_a and pk_b of many organic molecules.[29]

There have been several attempts to determine the exact number of solvent molecules, needed to solvate and stabilize the ejected proton.[30-36] It has been demonstrated that for proton transfer from 1-naphthol to protic solvents in ultracold solvent clusters in supersonic jet, 3 ammonia and 2 piperidine molecules are needed to solvate the ejected proton while for water clusters no proton transfer is observed in jets even for clusters containing 21 water molecules.[30] For liquid solutions, Robinson *et al.* suggested that 4±1 water molecules are needed to solvate a proton to form a cluster $H^+(H_2O)_{4\pm1}$.[31] In an organized assembly the local pH is often very different from the bulk pH. Again, in an organized medium adequate number of water molecule (4±1) are often unavailable to solvate the ejected proton. As a result, the proton transfer processes in the organized assemblies differ considerably from those in the ordinary solutions.

ESPT is the main nonradiative pathway in the excited state of many biological probes. One of the most prominent among them is the popular DNA probe ethidium bromide (EB).[37-39] On addition of DNA, EB readily intercalates in the double helix of DNA in aqueous solutions.[37-38] The intercalation causes nearly 11 fold increase in the emission intensity and lifetime of EB. The fluorescence enhancement of EB on intercalation, is not due to high local viscosity as the emission quantum yield and lifetime of EB are very similar in methanol and glycerol, whose viscosity differ by a factor of 2000.[39] Emission intensity of EB is low in highly polar, protic solvents, such as alcohol and water, compared to polar, aprotic solvents, e.g., acetone or pyridine. It is proposed that water quenches emission of EB by abstracting the amino proton.[39] If this conjecture is correct, the emission intensity of EB should depend on the hydrogen bond acceptor (HBA) basicity of the solvent, β, instead of the polarity. The HBA basicity, β, introduced by Kamlet *et al.* and other polarity scales of various solvents are elaborately discussed in the literature.[40] Polarity of acetone (dielectric constant, $\varepsilon = 20.7$ and $E_T(30) = 42$) is less than that of another polar, aprotic solvent, acetonitrile ($\varepsilon = 37.5$ and $E_T(30) = 46$).[40] However, the HBA basicity, β, of acetone (0.48) is greater than that of acetonitrile (0.31) and thus, acetone is a better proton acceptor than acetonitrile. Pal *et al.*[41] observed that in the more polar but weaker proton acceptor, acetonitrile, the fluorescence intensity and lifetime of EB are 1.25±0.1 times those in acetone. This conclusively establishes that the high is HBA basicity of the solvent, the high is the nonradiative rates of EB, and hence, the low is the emission intensity. Thus the nonradiative rates of EB are controlled by the HBA basicity of the solvent rather than the solvent polarity. This lends further support to the contention that ESPT is the main nonradiative pathway for EB.

Twisted Intramolecular Charge Transfer

If an electron donor and an acceptor is joined by a flexible single bond, electronic excitation results initially a "nonpolar" excited state. Subsequently an intramolecular electron transfer occurs from the donor to the acceptor and simultaneously the donor and the acceptor undergo a twist about the flexible bond joining them. This process is known as twisted intramolecular charge transfer (TICT) and the resulting highly polar state is known as a TICT state. The TICT process often results in dual emission from the "nonpolar" and the TICT state.[42-43] This phenomenon was first proposed to explain the dual emission of *p*-dimethylamino benzonitrile (DMABN). Subsequently, this phenomenon is observed in many other systems. The relative energies of the TICT and LE state change markedly with solvent polarity. In a nonpolar solvent, the LE state remains lower in energy compared to the TICT state and hence, a single emission band due to the LE state is observed. In a polar solvent, the more polar TICT state becomes stabler than the LE state. This is manifested in the dual emission from the LE and TICT state. The solvent dependence of the TICT process has been investigated using several theoretical models.[43-45] Soblewski *et al.*[45] used CIS, CASSCF and CASPT2 methods to calculate the reaction path for the TICT process in DMABN and its analogues. Unlike earlier calculations which considered a single internal coordinate, Soblewski *et al.* took into account more than one internal coordinates.[45] Their calculation support the TICT hypothesis for DMABN. For DMABE, for which dual emission is not observed in a polar solvent like acetonitrile, they proposed strong quenching via the weakly fluorescent rehybridised-ICT state. The effect of polar solvents on the spectra of molecules undergoing TICT in supersonic jet has been studied by many groups. Most recently, Ishida *et al.*[46] studied the dynamics of the intramolecular charge transfer process in ultracold clusters of 9,9'-bianthryl with water in supersonic jet using picosecond time resolved spectroscopy. They observed that the LE state is converted to the unrelaxed CT state in a time scale of <20 ps. Following this, the unrelaxed CT state relaxes in 50 ps time scale to a new equilibrated state. The dynamics of the TICT process can be followed by the decay of the nonpolar emission and the rise in the TICT emission. The dynamics of the TICT process depends strongly on the polarity of the medium. It has been proposed that the energy barrier for the TICT process for dimethylaminobenzonitrile (DMABN) decreases linearly with the polarity parameter $E_T(30)$[47] of the medium as

$E_B = E_B^0 - A\ [E_T(30)\text{-}30]$,

where E_B^0, is the barrier in a hydrocarbon medium of $E_T(30)=30$. The polarity dependent barrier model is subsequently extended to many other TICT probes.[43,48] In many cases, the TICT state is non-emissive and for them the TICT process is simply a nonradiative decay process in the "nonpolar" excited state of these molecules. The nonradiative rate is obtained from the emission quantum yield (ϕ_f) and lifetime (τ_f), as $k_{nr}=(1-\phi_f)/\tau_f$. The TICT rate is very much sensitive to the polarity of the medium. For instance, in the case of TNS, ϕ_f changes 300 times from 0.3 in dioxane ($E_T(30)=36$) to 0.001 in water ($E_T(30)=63$) and τ_f changes over 100 times from 8 ns in dioxane to 0.06 ns in water. Thus the rate constant of TICT is a very sensitive indicator of the microscopic polarity of an organized media and has been used quite extensively for this purpose.[43]

3 Organized Media

In this Section, we will discuss the architecture of a few organized media. Since structures of these organized media have already been discussed in a number of reviews we will present only a brief overview instead of giving a comprehensive summary.

Micelles

Amphiphilic surfactant molecules form spherical or nearly spherical aggregates called micelles, above a certain critical concentration, known as the critical micellar concentration (cmc) and above a critical temperature, called "Kraft temperature".[49] The size of the micellar aggregates is usually 1-10 nm and the aggregation number, i.e. the number of surfactant molecules per micelle, ranges from 20 to 200. The core of a micelle is essentially "dry" and consists of the hydrocarbon chains with the polar and charged head groups projecting outward into the bulk water. The core is surrounded by a polar shell, which is called the Stern layer for an ionic micelle and palisade layer for a neutral micelle. The Stern (palisade) layer comprises of the ionic or polar head groups, bound counter ions and water molecules. Between the Stern layer and the bulk water there is a diffuse layer, termed the Guoy-Chapman (GC) layer which contains the free counter ions and water molecules.

Detailed information on the structure of the micelles has recently been obtained through small angle X-ray and neutron scattering studies.[50] According to these studies, the thickness of the Stern layer is 6-9 Å for cationic cetyl trimethyl ammonium bromide (CTAB) micelles and anionic sodium dodecyl sulfate (SDS) micelles, whereas the palisade layer is about 20 Å thick for neutral triton X-100 (TX-100) micelles. Radius of the dry, hydrophobic core of TX-100 is 25-27 Å, and thus the overall radius of TX-100 micelle is about 51 Å. The overall radius of CTAB and SDS micelles are about 50 Å and 30 Å, respectively.

Telgmann and Kaatze studied the structure and dynamics of micelles using ultrasonic absorption in the 100 KHz to 2 GHz frequency range.[51] They detected several relaxation times in the long (µs), intermediate (10 ns) and fast (0.1-0.3 ns) time scale. The longest relaxation time has been attributed to the exchange of monomer between the bulk and the micelles while the fastest to the rotation of the alkyl chains of the surfactants in the core of the micelle. The intermediate relaxation time has not been assigned to any particular motion. We will discuss later that the intermediate relaxation times in the 10 ns time scale may well be due to the solvent relaxation in the Stern layer.

Reverse Micelles and Microemulsions

The reverse micelles refer to the aggregates of surfactants formed in non-polar solvents, in which the polar head groups of the surfactants point inward while the hydrocarbon chains project outward into the nonpolar solvent.[52-58] Their cmc depends on the non-polar solvent used. The cmc of aerosol-OT (sodium dioctyl sulfosuccinate, AOT), in a hydrocarbon solvent is about 0.1 mM.[52] The AOT reverse micelle is fairly monodisperse with aggregation number around 20 and is spherical with a hydrodynamic radius of 1.5 nm.

The most important property of the reverse micelles is their ability to encapsulate fairly large amount of water to form what is known as a "microemulsion". Up to 50 water molecules, per molecule of the surfactant, can be incorporated inside the AOT reverse micelles. Such a surfactant-coated nanometer-sized water droplet, dispersed in a nonpolar liquid, is called a "water pool". The radius (r_w) of the water pool varies linearly with the water to surfactant mole ratio, w_0. In *n*-heptane, r_w (in Å) $\approx 2w_0$.[53] The structural information on the microemulsions i.e. radius of the micellar aggregates and that of the water pool has been obtained using dynamic light scattering,[57] transient grating, ultrasound velocity measurements,[55] FT-IR,[56] dielectric relaxation[58] etc. Several non-ionic or neutral surfactant, (e.g. triton X-100, etc) have recently been reported to form reverse micelles in pure and mixed hydrocarbon solvents.[59] Finally, apart from water, confinement of other polar solvents such as, acetonitrile, alcohol and formamide, have been reported in such microemulsions.[60]

The water molecules confined in the water pool of the microemulsions differ in a number of ways from ordinary water. In a microemulsion, the first 2-4 water molecules are very tightly held by the surfactant and all the water molecules except the 6 most tightly held ones freeze at –50°C. The FT-IR[56] and the compressibility studies[55] indicate that the first three water molecules "lubricate" the dry surfactants. During this process the compressibility of the AOT microemulsion increases steeply. The next three water molecules solvate the counterion (Na^+ for Na-AOT) and starts the self-organization process. At this stage, the head groups of AOT become linked by hydrogen bonds through the water molecules and the compressibility gradually decreases. For w_o>6, the water pool swells in size but the compressibility reaches a plateau. Around w_o=13, the first solvation shell of AOT becomes complete and up to this point, the water structure remain severely perturbed inside the water pool. But even in the very large water pools, the compressibility of the microemulsions remains at least two times higher than that of ordinary water.[55] Behaviour of the microemulsions containing neutral surfactants are similar except that they exhibit only a monotonic increase of compressibility reaching a plateau and does not show the decrease of compressibility observed for the ionic surfactants arising from the solvation of the counter ions. In the water pool, there may be three kinds of water molecules, the "bound" ones near the polar head group of the surfactant and hence, held strongly, the "free" ones near the central region of the water pool and the "trapped" ones between the surfactants. Using FT-IR spectroscopy, Jain *et al.*[56] determined the relative amounts of the three kinds of water molecules. Obviously, the "free" water molecules expected to be faster than "bound" ones. In the solvation dynamics experiments to be are discussed later, it will be seen that even the "free" water molecules, in the water pools, are significantly slower than ordinary water molecules.

Dielectric relaxation studies have revealed a component of 7 ns in the microemulsions which suggest significant retardation of the motion of the confined water molecules in the water pool.[58]

Lipid Vesicles

Vesicles are basically a water pool entirely enclosed by a membrane which is basically a bilayer of the lipid molecules which are dispersed in aqueous medium.[61-69] For an unilamellar vesicle there is only one such bilayer while a multilamellar vesicle (radius ~1000 nm) consists of several concentric bilayers. Unilamellar vesicles can be produced by breaking the multilamellar vesicles by sonication. In such a system there are two kinds of water molecules present, those in the bulk and those entrapped within the water pool of the vesicles. The entrapped water pool of a small unilamellar DMPC vesicle is much bigger (radius ≈250 nm) than those of the water pool of the reverse micelles (radius < 10 nm). In recent years, several groups studied chain dynamics of lipids using SANS, ESR of spin-labelled lipids and fluorescence of pyrene-labelled lipids.[61] Recent molecular dynamics (MD) simulations,[63] crystal structure[64] and other studies indicate that above transition temperature (≈23°C) each DMPC molecule is hydrogen bonded to about 4.5 water molecules which form an inner hydration shell of the polar head group of the lipids and about 70% of the DMPC molecules remain connected by the water bridges.

The vesicles undergo phase transition at a well-defined temperature. Above the phase transition temperature, the viscosity of the lipid bilayer remains quite low and the permeability of the bilayer wall remains high so that small molecules easily pass through the bilayer to enter the inner water pool. Below the transition temperature, viscosity of the lipid bilayer becomes high and also the permeability across the bilayer membrane decreases significantly. The change in the viscosity of the lipid bilayers with temperature is usually monitored by optical anistropy studies. The transport of small organic molecules across the lipid bilayer above transition temperature is most elegantly demonstrated in a recent surface second harmonic (SSH) generation study by Srivastava and Eisenthal.[69] The SSH signal is obtained as long as the molecule stays in an inhomogeneous region i.e. at the lipid bilayer. Above the transition temperature of the lipids, the SSH signal decays in a time scale of 100 seconds which denote the residency time of the probe in the bilayer or the time taken by the probe to diffuse through the bilayer membrane from bulk water to the inner water pool. For lipids below the transition temperature no such time dependence of the SSH signal is observed which indicates that at a temperature below the transition temperature the bilayer membrane does not allow transport of molecules to the inner water pool.

Polymers and Hydrogels

Water soluble polymers and the microporous synthetic polymer hydrogels, have generated considerable recent interest because of their versatile applications and compatibility with biological systems.[70-80] The hydrogels are inherently insoluble in water but can entrap considerable amount of water within their polymer networks.[76-77] They have versatile applications as biomaterials (e.g. contact lenses), chromatographic packings, in devices for controlled-release of drugs, and as electrophoresis gels. The polyacrylamide (PAA) hydrogel is obtained by polymerising acrylamide in the presence of N,N′-methylene bisacrylamide as a crosslinker.[78] The pore size in such a gel can be varied by varying the concentration of the monomer (acrylamide).[76] Among the various types of hydrogels PAA is most suitable for photophysical studies as it is optically transparent over a wide range of concentrations of the monomer and the cross-linker. On absorption of water such a hydrogel swells in size. The swelling and other properties of this interesting semirigid material has recently been studied using light scattering,[74] NMR and calorimetry.[79] The bulk viscosity of any hydrogel is very high. However, since the hydrogels contain large pores even very large biological macromolecules like DNA pass through such hydrogels during gel electrophoresis. Several groups attempted to immobilise small probe molecules (e.g. nile red)[80] within the hydrogels. Using far field fluorescence microscopy Moerner *et al.* demonstrated that in PAA hydrogel while most nile red molecules move freely, motion of a minute fraction (~2%) of them becomes severely restricted so that the Brownian motion of *individual* nile red molecules may be recorded.[80]

Zeolites

Zeolites are open structures of silica in which some of the silicon atoms in the tetrahedral sites are replaced by aluminium ions.[81-83] Counterions like Na^+, K^+ maintain the electroneutrality and reside freely inside certain locations in the zeolite cages. Zeolites can be represented by the empirical formula $M_{2/n}Al_2O_3 . xSiO_2 . yH_2O$, where M is an alkali metal or an alkaline earth metal cation of valence n, $x>2$ and y varies from 0 to 10. Depending on the Si/Al ratio and the cations, zeolites can have various rigid and well defined structures which can be classified into cage and channel types. For the ZSM-5 zeolite, there are two intersecting channel systems. One system consists of straight channels with a free cross-section of 5.4×5.6 Å^2 and the other consists of sinusoidal channels with free diameter of 5.1×5.5 Å^2. Faujasite zeolites are made up of a nearly spherical supercage of diameter 13 Å, surrounded by sodalite cages.

The structure and dynamics of zeolites have been studied by molecular dynamics (MD) simulation, Monte Carlo simulation, density functional theory and stochastic models.[83,89] These studies indicate that the spatial locations are similar for different cations. The mobile cations are responsible for the electrical conductivity of dehydrated zeolites. The mechanism of electrical conduction in a zeolite has been the subject of several studies. Conduction of dehydrated potassium zeolite L has been found to involve a thermally activated process. Dielectric properties of the zeolites depend on the degree of hydration. The zeolites can act as a host for a large number of guest molecules. Neutron diffraction study suggests that in zeolite Y, cyclohexane stays in the 12-ring window site. This is in agreement with the MD simulations. Similar results are obtained for benzene in zeolites.[88] NMR line width and simulation studies indicate that in the faujasite zeolites the guest aromatic molecules hop from one cage to another in the nanosecond time scale.[89]

The photophysics and photochemistry of organic molecules change remarkably on encapsulation in zeolite.[81] The marked changes caused by the zeolites result partly from their rigid structure which imposes considerable restriction on molecular motion within a zeolite. Secondly, the presence of cations in close proximity with organic guest molecules exert significant influences because of the strong local electric field produced by the cations and also the enhanced singlet-triplet transitions in the case of zeolites having heavy cations. The polarity and acid-base behaviour of the zeolites also affect different photophysical processes.

4 Photophysical Processes in Organized Assemblies

In this Section, we will discuss how the dynamics of various photophysical processes are modified inside organized assemblies. Since the dynamics of the photophysical processes depends on the microscopic property (polarity, viscosity etc.) of the medium, the photophysical studies reveal information on the microscopic property of the organized assemblies.

Solvation Dynamics in Organized Assemblies

The solvation dynamics depends on the mobility of the solvent molecules in a medium. Due to the importance of water in biological systems we will focus our attention on relaxation properties of water in organized assemblies. The dielectric relaxation studies have already indicated that the water molecules present in biological environments are substantially slower compared to ordinary water. We will now show that the solvation dynamics studies, also reveal similar trends and reveal more direct information on mobility of water molecules in organized media.

Cyclodextrin

Cyclodextrins are water soluble cyclic polysaccharides which conatin a hydrophobic cavity of height 8 Å and diameter 5-8 Å in which organic molecules bind readily in aqueous medium. Fleming *et al.*[90] studied solvation dynamics of two laser dyes, coumarin 480 (C480) and coumarin 460 (C460) in γ-cyclodextrin (γ-CD) cavity. The marked blue shift of the emission spectra and the increase in fluorescence lifetimes of the two probes on addition of γ-CD to their aqueous solutions indicate that the probes are located inside the γ-CD cavity.[91] The initial component of solvation in γ-CD is found to be similar to that in bulk water (0.31 ps).[90] However, at longer times, the solvent response in γ-CD, reveal a component which is at least three orders of magnitude slower. Molecular dynamics calculations indicate that in the γ-CD cavity there are 13 water molecules for C480/γ-CD complexes and 16 in the case of C460.[90] Since these numbers resemble the number of water molecules present in the first solvent shell of the dyes in aqueous solutions, the response at short times for the C480/γ-CD complex should have been different from that for C460 due to the presence of fewer water molecules for the former. However, as the initial Gaussian component is same for the two dye molecules, it appears that the first solvent shell does not dominates the solvent response.[90]

Nandi and Bagchi[92] showed that the slow solvation dynamics in γ-CD may be explained if one assumes complete freezing of the translational motions of the solvent molecules inside the γ-CD cavity. They further showed that the slow part of the response contributes about 10% to the total response. It is proposed that the collective response of the solvent molecules, rather than the contribution from the different solvent shells, dominates the inertial component of solvation.

Microemulsion

The surfactant-coated water droplets in water-in-oil microemulsions serve as excellent model for the water molecules in confined environments. The emission spectra of certain solvent sensitive probes change markedly when it is transferred from bulk hydrocarbon to the water pool of a microemulsion. For example, absorption maximum of coumarin 480 (C480) in *n*-heptane and water are at 360 nm and 395 nm, respectively while the corresponding emission maxima are at 410 nm and 490 nm, respectively.[93] In a *n*-heptane solution of C-480 on addition of AOT and subsequently water, a very prominent shoulder appears at 480 nm (Fig. 8).[94] The 480 nm emission band and having excitation peak at 390 nm is assigned to the C480 molecules in the water pool of the microemulsion. Sarkar *et al.* studied the solvation dynamics of C480 in AOT/*n*-heptane/water microemulsions.[94] They observed distinct rise time in the nanosecond time scale at the red end of the emission spectra. This indicates nanosecond solvation dynamics in the microemulsions. They observed that in a small water pool (w_o=4, r_w=8Å) the solvation time is 8 ns while for a very large water pool (w_o=32, r_w= 64Å) the response is bimodal with a fast component of 1.7 ns and a slower component of 12 ns. For acrylodan-labelled human serum albumin in AOT microemulsion, using phase fluorimetry Bright *et al.* reported that the solvation time is about 8 ns for a small water pool (w_o=2) and 2 ns for a large water pool (w_o=8). For 4-aminophthalimide (4-AP), in a large water pool, the solvation dynamics is biexponential with an average solvation time of 1.9 ns.[96] In AOT microemulsions, the solvation time of 4-AP increases from 1.9 ns in H_2O to 2.3 ns in D_2O, which displays a 20% deuterium isotope effect. The appearance of a nearly 2 ns component in the large water pools indicates that even in the large water pools of the microemulsions the water molecules are about 6000 times slower compared to bulk water (solvation time 0.31 ps[90]).

A semi-quantitative explanation of the 2 ns component may be as follows. The static polarity or the dielectric constant of the water pool of the AOT microemulsions can be obtained from the position of the emission maximum of the probes (C480 and 4-AP).[94-96] For both the probes the water pool resembles an alcohol like environment with an effective dielectric constant ≈30-40. The dielectric relaxation time in such a water pool is about 10 ns.[58] If one makes a reasonable assumption that the infinite frequency dielectric constant of water in the water pool of the microemulsions is same as that of ordinary water i.e. 5, then the solvent relaxation time should be about 1.67 ns which is close to the observed solvation time in AOT microemulsions.

One might argue that the nanosecond dynamics observed in the water pool is not due to the slower water molecules but is because of the solvation by the Na^+ counter ions present in the water pool for the AOT microemulsions. Nanosecond solvation dynamics due to ions, in solutions as well as molten salts, is well documented in the literature.[97-99] Mandal *et al.*[100] studied the solvation dynamics of 4-AP in a microemulsion containing neutral surfactant triton X-100 where no ions are present in the water pool. The triton X-100 microemulsion also exhibits nanosecond solvation dynamics which suggests that the ionic solvation dynamics has little or no role in the solvation dynamics observed in the water pool.

Levinger *et al.* studied the solvation dynamics of a charged dye coumarin 343 (C343) in lecithin[101] and AOT microemulsions[102-103] using femtosecond upconversion. For lecthin microemulsions,[103] the solvent relaxation displays a very long component which does not become complete within 477 ps. This observation is similar to the nanosecond dynamics reported by Bright *et al.*[95] and Sarkar *et al.*[94] For C343 in AOT, Levinger *et al.* observed that the decay characteristics of the emission intensity at different wavelengths display considerable differences for sodium and ammonium counterions.[102] They however, did not present a complete analysis of this result in terms of dynamic Stokes shift and the decay of the solvent response function C(t). For Na-AOT, the solvation dynamics reported by Levinger *et al.*[103] for the charged probe C343 is faster than that reported by Bright *et al.*[95] and Sarkar *et al.*[94] It is obvious that due to its inherent negative charge, AOT repel the negatively charged C343 probe from its vicinity. Thus the C343 anion is expected to reside in the central region of the water pool. Neutral probes like C480 and 4-AP may stay both in the central region of the pool as well as in the peripheral region close to the AOT molecules. The discrepancy in the results in the case of AOT microemulsions, reported by Levinger *et al.* and those of Sarkar *et al.* and Bright *et al.* however, is too large to be explained in terms of different locations of the probes and merits further careful investigation.

Most recently, several groups studied solvation dynamics of nonaqueous solvents, such as, formamide,[103] acetonitrile and methanol[104] in AOT microemulsions. Using a picosecond setup, Shirota and Horie[104] demonstrated that in the AOT microemulsions the solvation dynamics of acetonitrile and methanol is non-exponential and 1000 times slower compared to those in the pure solvents. They attributed the non-exponenial decay to the inherent inhomogeneous nature of the solvent pools. Evidently, the static polarity and relaxation properties of the entrapped polar solvents vary quite strongly as a function of the distance from the ionic head group of the AOT surfactants. Within its nanosecond excited lifetime, the probe passes through different layers of solvents of different relaxation properties within the pool. This quite reasonably may give rise to a non-exponential decay.

Micelles

In aqueous micellar solutions, there are three possible locations of the probe, namely the bulk water, the "dry" micellar core and the Stern layer. Obviously the solvation time will be in the sub-picosecond time scale in the bulk water. In the dry hydrocarbon core of the micelle the probe is not expected to exhibit dynamic Stokes shift. However, if the probe stays in the Stern layer, its solvation dynamics may be quite different from that in the bulk water because the mobility of the water molecules may be considerably constrained in the Stern layer. Solvation dynamics in micelles has been studied using C480 and 4-AP as probes.[105-106] Emission properties of the probes in the micelles, are very different from those in water and in hydrocarbon. This shows that the probes reside neither in bulk water nor in core of the micelles and hence, are located in the Stern layer of the micelles. Sarkar *et al.*[105] and Datta *et al.*[106] studied solvation dynamics of C480 and 4-AP, respectively, in neutral (TX-100), cationic (CTAB) and anionic (SDS) micelles. It is observed that for SDS, CTAB, and TX-100, the average solvation times are respectively 180 ps, 470 ps and 1450 ps for C480[105] and 80, 270 and 720 ps for 4-AP.[106] The solvation times in micelles, differ only by a factor of 2 for the two probes. This suggests that the solvation dynamics in the Stern layer of the micelles does not depend very strongly on the probe. It is interesting to note that the time scale of solvation is similar to the intermediate range of dielectric relaxation times reported by Telgmann and Kaatze.[51] It is readily seen that the solvation dynamics in the Stern layer of the micelles is 3 orders of magnitude slower than that in bulk water (0.31 ps[90]), about 10 times faster than that in the water pool of the microemulsions,[94-96] and is slightly faster than the longest component of solvation dynamics in γ-CD.[90] The main candidates causing solvation in the Stern layer of the micelles, are the polar or ionic head groups of the surfactants, the counter ions (for SDS and CTAB) and the water molecules. Since the head groups are tethered to the long alkyl chains their mobility is considerably restricted. The dynamics of such long alkyl chains occurs in the 100 ns time scale[61] and hence, is too slow to account for the subnanosecond solvation dynamics observed in the micelles. The role of ionic solvation by the counter ions also appears to be minor because of the very similar time scale of the ionic (CTAB) and the neutral (TX-100) micelles.

Lipids

The state of solvation of a fluorescent probe, in the ground state, in the unilamellar and multilamellar vesicles is usually studied by the red edge excitation spectroscopy (REES).[67] The dynamics of the surfactant chain in the lipid bilayer is usually investigated using optical anisotropy and ESR.[61] However, the interesting issue of the dynamics of the water molecules inside the water pool of vesicles has been addressed only recently.[107] Datta *et al.*[107] studied C480 in sonicated unilamellar DMPC vesicles. The position of emission maximum of C480 in DMPC vesicles is once again different from that in bulk water and the hydrocarbon. This indicates the probe stays in the inner water pool of the vesicle. Datta *et al.*[107] observed that the solvation dynamics of C480 in DMPC vesicles is highly nonexponential with two components of 0.6 ns (40%) and 11 ns (60%). This result is very similar to the solvation dynamics of the same probe in the large water pools of AOT microemulsions.[94] Thus the nanosecond solvation dynamics in lipids can not be due to the chain dynamics of DMPC which occurs in the 100 ns time scale.[61] Since in the bulk water the solvation dynamics is much faster (0.31 ps[90]) the results reported by Datta *et al.*[107] demonstrates restricted motion of the water molecules in the inner water pool of the vesicles.

Polymer Hydrogels

Due to the bulk viscosity of the polymer solutions and particularly the semirigid hydrogels, one expects very slow relaxation of the water molecules in polymer matrices and polymer hydrogels. Contrary to this expectation, in the orthosilicate[108] and polyacrylamide[109] hydrogels, both solvation dynamics and rotational relaxation are found to occur in <50 ps time scale. The surprisingly fast solvation and rotational dynamics of small probe molecules in hydrogels may be attributed to the porous structure of the hydrogels, through which even large biomolecules pass through easily. Datta *et al.*[109] demonstrated that the microenvironment of 4-AP in polyacrylamide (PAA) hydrogel is quite heterogeneous. In the PAA hydrogel, there are broadly two kinds of environments. One of them is water like in which the 4-AP molecules exhibits emission maximum at 550 nm with lifetime 1.3 ns and the other is quite aprotic in which 4-AP emits at 470 nm with a 7.2 ns lifetime. The recent steady state anisotropy measurements by Claudia-Marchi *et al.*[110] demonstrates that for titania gels at the sol-gel transition point when the bulk viscosity increases abruptly, the emission anisotropy does not change perceptibly. Thus the microviscosity of the gel is very low in spite of the very high bulk viscosity. The NMR[111] and simulation[112] studies indicate that the diffusion coefficient of water molecules in polymer hydrogels is not appreciably slower compared to ordinary water and is smaller at most by a factor of 2 than that in ordinary water. Argaman and Huppert[113] studied solvation dynamics of coumarin 153 in polyethers and found very fast solvation times ranging from 50 fs to 100 ps. The fast solvation dynamics in polymer matrices is consistent with the dielectric relaxation studies[72] which shows that except the highly water soluble polymer, polyvinyl pyrolidone, dielectric relaxation times of most aqueous polymer solutions is faster than the 100 ps time scale.

Liquid Crystal

In search of the pseudonematic domains having long range order several groups have recently studied solvation dynamics in the nematic phase of the liquid crystals.[114-115] Rhodamine 700[114] and coumarin 503[115] exhibit biexponential solvation dynamics in liquid crystals. For coumarin 503 the slowest time constant decreases from 1670 ps at 311.5 K to 230 ps at 373 K. The solvation time is not affected by the nematic-isotropic phase transition. Thus, it appears that the local environment and not the long range order, controls the time dependent Stokes shift.

Zeolite and Nanoparticles

The solvation dynamics in microporous solids has been the subject of some recent studies. Sarkar *et al.*[116] showed that C480 exhibits wavelength dependent decays and time dependent Stokes shift in a solid host, faujasite zeolite 13X. They observed a highly non-exponential decay with an average solvation time of 8 ns. Interestingly the 8 ns time constant is very close to the nanosecond solvation dynamics ($\langle\tau\rangle=4.1$ ns) observed in molten salts.[97] In a faujasite zeolite the mobile components are the sodium ions and the probe dye molecule, itself. Since in a faujasite zeolite the encapsulated guest molecules hop from one cage to another in the nanosecond timescale,[89] the 8 ns relaxation time observed in zeolite may also arise as a result of the self-motion of the probe from one cage to another. The role of self-motion of solutes on the solvation dynamics has recently been discussed in detail by Biswas and Bagchi.[117] However, it is difficult to establish unequivocally whether the nanosecond dynamics observed in zeolite is due to ionic solvation or self-motion of the probe.

Pant and Levinger[118] studied solvation dynamics of C343 in a suspension of nanodimensional zirconia particles of radius 2 nm, in water-acetone mixture (95:5, v/v). They observed two subpicosecond components similar to those in bulk but having different amplitudes resulting in a relaxation time faster than that in bulk solution. They also showed that the maximum Stokes shift is three times smaller for the dye molecules adsorbed on the zirconia particles compared to those in bulk solution.

Proteins and DNA

One of the longstanding goals of biology is to understand the dynamics occurring in complex biomolecules such as proteins and DNA.[119-120] Several groups reported that the solvation dynamics of protein bound fluorophores is significantly slower compared to bulk water. Pierce and Boxer[121] and Bashkin *et al.*[122] reported that the solvation dynamics in the protein environments is non-exponential with a long component with time constant on the order of 10 ns. It is interesting to note that this time scale is very close to the nanosecond component of dielectric relaxation earlier observed for the aqueous protein solutions.[14-15,18]

The static and dynamic properties of DNA have been studied by the temperature dependent Stokes shift of an intercalated dye, acridine orange[123]. A large part of the Stokes shift of the intercalated dye in DNA, is found to be frozen out at low temperature, as in the solution. Thus, the interior of DNA is found to have the diffusive and viscous dynamic characteristics of a fluid, rather than the purely vibrational characteristics of a crystal. The results suggest that the probe dye molecule senses the movement of DNA and at high viscosity, the rate of DNA motion is limited by the rate of solvent motion.

Photoisomerisation and Microviscosities of Organized Assemblies

The friction imparted by several organized assemblies and interfaces to the photoisomerisation of organic molecules has been the subject of several recent studies. The rate of photoisomerisation of stilbene, in various organized assemblies is substantially slower compared to that in a homogeneous medium. Lifetime of *trans*-stilbene increases from 34 ps in aqueous methanol to 137 ps in aqueous solution of α-cyclodextrin (α-CD). This indicates that isomerisation of stilbene inside α-CD cavity is slower than that in aqueous methanol.[124] In the bigger β- or γ-CD cavity, fluorescence decays of *trans*-stilbene are biexponential with one component of 50 ps and another very slow component of several thousand picosecond. The slow component corresponds to a very rigid microenvironment.[124] In a zeolite, isomerisation of stilbene is retarded so much that its rate becomes comparable to the rate of intersystem crossing. This results in a strong phosphorescence.[125] Holmes *et al.* observed a biexponential decay for stilbene in a lipid and assigned this to the presence of two sites.[126] The isomerisation of 3,3'-diethyloxadicarbocyanine iodide (DODCI) and other cynaine dyes and malachite green (MG) has been studied at various interfaces, such as the air-water interface,[5] microemulsions,[127] micelles,[128] DNA and proteins.[129] The recent time resolved surface second harmonic generation (SSHG) experiments have demonstrated that for the air-water interface, the friction against the photoisomerisation is different for different probes.[5] While, for rod shaped DODCI, the isomerisation at the air-water interface is faster compared to that in the bulk water, for nearly planar malachite green, it is slower at the air-water interface.[5] In the water pool of a microemulsion, photoisomerisation of DODCI is nearly three times slower compared to ordinary water.[127] The photoisomerisation of DODCI is markedly slowed down at various micelle-water interfaces.[128] Compared to aqueous solution, in CTAB, SDS and TX-100 micelles, the rates of photoisomerisation of DODCI are respectively. 20, 7 and 8 times slower. It is pointed out earlier that at very high viscosity, the rate of photoisomerisation becomes inversely proportional to the viscosity of the medium (Smoluchowski limit). Assuming that the Smoluchowski limit and the same "slip/stick" boundary condition hold for the highly viscous solvent, *n*-decanol and the micelles and then, comparing the isomerisation rates of DODCI in the three micelles with that in *n*-decanol, the microviscosities of CTAB, SDS and TX-100 have been estimated to be 70.0±20, 24.5±2 and 26.0±2 cP, respectively.[128] Photoisomerisation of DODCI is also studied in aqueous solution in the presence of salmon sperm DNA and bovine serum albumin (BSA).[129] It is observed that the microenvironments of aqueous solutions of DNA and BSA behave like a highly viscous liquid and result in completely suppression of the isomerisation process.

Due to the very high local viscosity in the organized assemblies, the torsional motion of the TPM dyes is significantly hindered resulting in a dramatic increase in the quantum yield and lifetime of emission of the TPM dyes compared to aqueous solutions. Baptista and Indig[130] reported a 1000 fold increase in the quantum yield and lifetime of emission of TPM dyes on binding to a protein BSA. This suggests that the local viscosity of the protein is several orders of magnitude higher compared to that of water. Tamai *et al.*[131] studied the microviscosities of the polyacryamide gels using TPM leuco dyes. The microviscosity of the unswollen and the swollen gels has been esimated to about 20 cP and 10 cP respectively. This once again demonstrates that while the bulk viscosity of the semirigid gels is many thousand times higher than that of water, the microviscosity is only 10-20 times higher. This is consistent with the very fast solvation and rotational relaxation time in gels reported earlier.[108-109]

Proton Transfer Processes in Organized Assemblies

The pK_a of an acid and hydrogen ion concentration in an organized assembly often differ drastically from those in ordinary liquids. Measurement of the *p*H at a surface is one of the longstanding goals in chemistry. Using absorption spectra of bromophenol indicators, Mukherjee and Banerjee[132] estimated the *p*H and pK_a at the micelle-water interface. Eisenthal *et al.* used surface second harmonic generation to determine surface *p*H, pK_a and potential (ψ) at the air-water interface.[5] The results depend strongly on the nature of charge of the surfactants. For instance, if the surfactant is negatively charged (e.g. *p*-alkyl phenolate) the hydrogen ion concentration at the surface is greater than that in the bulk while the opposite is true for a cationic surfactant (e.g. *p*-alkyl anilinium).[5]

In AOT microemulsions, presence of the negatively charged head group causes a sharp gradient in *p*H/pOH over the nanometer sized water pool. Menger and Saito[133] reported that the acid-base property of *p*-nitrophenol (PNP) gets substantially modified in AOT microemulsions. While in bulk water, at *p*H=11.5, 95% of the PNP molecules remain in the anionic form, when an alkaline aqueous solution containing PNP is injected in the AOT microemulsion, no *p*-nitrophenolate anion is detected until the *p*H of the injected solution exceeds 11.5. On the basis of this, Menger and Saito concluded that the pK_a of PNP, in the AOT microemulsion, is greater than that in bulk water (7.14) by more than 4 units. However, it has been pointed out later that the local hydroxyl ion concentration near the negatively charged AOT head group, is substantially less than that in bulk water. Oldfield *et al.*[134] showed that if a negatively charged group is attached to PNP, the probe remains in the water pool of the AOT microemulsions and its acid-base property is similar to that in bulk water. Okazaki and Toriyama[135] studied the location of an organic acid at different *p*H in AOT microemulsion, using ESR spectroscopy. They observed that at low *p*H, when the molecule is in the neutral form, it stays close to the AOT-water interface, while at high *p*H the carboxylate anion is expelled from the AOT-water interface to the water pool.

The dynamics of the excited state proton transfer processes in organized assemblies are often quite different from those in ordinary solutions.[136] The sharp local variation of *p*H in the water pool of the AOT microemulsions affects the intermolecular proton transfer process quite strongly. Fendler *et al.*[137] studied excited state deprotonation of a tri-negatively charged probe, hydroxypyrene-trisulfonate in AOT microemulsions. They observed that while in the large pools the proton transfer process is similar to that in bulk water, it is quite different in the small water pools (w_0<7). They concluded that in the large water pool, due to the electrostatic repulsion from the negatively charged AOT ions, the negatively charged probe remains in the large water pools, far from the AOT anion and experiences an almost bulk water-like microenvironment. But in the small water pool, the very different local *p*H, near the AOT anions, renders the deprotonation/reprotonation behaviour quite different from that in ordinary aqueous solutions. In ordinary aqueous solutions emission of ethidium bromide (EB), EB is strongly quenched by the hydroxyl ions. However, in AOT microemulsion, the hydroxyl ion does not quench the EB emission at all even when a highly alkaline aqueous solution of EB (*p*H=12.6) is injected into the reverse micelle.[41] It is proposed that the anionic surfactant, AOT, strongly attracts the ethidium cation to the AOT-water interface, but expels the hydroxyl anion from the AOT-water interface to the water pool and hence, the hydroxyl anion can not access the ethidium cation.[41]

Fleming *et al.*[138] reported that the deprotonation rate of 1-naphthol is retarded 20 times inside cyclodextrin cavities, while deprotonation of protonated aminopyrene occurs nearly 3 times faster. Since in water-alcohol mixture, deprotonation rate for protonated aminopyrene, increases with alcohol concentration up to about 65-70% and decreases at higher alcohol concentrations,[32] the faster deprotonation of protonated aminopyrene, inside the cyclodextrin cavity, indicates that the polarity of the microenvironment is in between pure water and 65% alcohol. For 1-naphthol, the deprotonation rate monotonically decreases as the alcohol content increases.[34] The slower deprotonation rate of 1-naphthol in cyclodextrin[138] is consistent with this. Mandal *et al.*[139] reported dramatic reduction in the rate of excited state deprotonation of 1-naphthol in micelles, from 35 ps in bulk water to the nanosecond time scale. The retardation of the rate of proton transfer of 1-naphthol is manifested in the dramatic enhancement of the neutral emission at 360 nm. Along with this there is marked increase in the lifetime of the neutral emission at 360 nm and the rise time of the anion emission (460 nm), for CTAB, SDS and TX-100R. For cationic CTAB, the rise time of the anion emission (600 ± 100 ps) is similar to the lifetime of decay at 360 nm. However, for TX-100R and SDS, the rise time of the anion emission (at 460 nm) is found to be faster than the decay of the neutral emission (at 360 nm). This indicates that in TX-100R and SDS, there is no parental relation between the normal and the anion emission and they originate from the probe, 1-naphthol molecules, at distinctly different locations. This is consistent with the earlier observation,[34] that in alcohol-water mixtures at high alcohol content the rise time of the anion emission is faster than the decay time of the neutral form. For TX-100R and SDS, the rise times of the 460 nm band are 1.8±0.1 ns and 600±100 ps, respectively. The corresponding decay times at 360 nm are 2.5±0.1 ns and 1.8±0.1 ns, respectively.[139] The dramatic reduction in the rate of deprotonation of 1-naphthol in micelles is attributed to the non-availability of adequate number of water molecules to solvate the proton in the micellar environment. The ESPT process of 1-naphthol is also affected by lipids and found to report faithfully the transition temperature of the lipids.[140]

TICT and Micropolarity of the Organized Assemblies

Since the dynamics of the twisted intramolecular charge transfer (TICT) process is very sensitive to the polarity of the medium, the microscopic polarity of an organized medium may be determined from the rate of the TICT process. For TNS, which is nearly nonfluorescent in water ($\phi_f=10^{-3}$ and $\tau_f=60$ ps), the emission quantum yield and life time increases nearly 50 times on binding to cyclodextrins and more than 500 times on binding to a neutral micelle, triton-X 100 (TX).[43] Such a dramatic increase in the emission intensity and lifetime arises because of the marked reduction of the nonradiative TICT process inside the less polar microenvironment of the cyclodextrins and the micelle. Determination of the micropolarities of various organized assemblies using TICT probes, has been surveyed quite extensively in several recent reveiws.[43] Therefore, in this article we will focus only on some selected works not covered in the earlier reviews.

Inside the water pool of the microemulsions of the TICT process of several probes (ANS,[141] TNS,[142] nile red[143] etc.) is observed to be significantly retarded compared to bulk water and the lifetime of the probes increase from the picosecond time scale in water to several nanosecond in the water pool. The retardation of the TICT process inside the water pool of the microemulsion compared to ordinary water, is ascribed to the lower static polarity of the water pool compared to bulk water. The polarity or $E_T(30)$ of the pool is obtained from the observed rate of TICT and comparing them with the values obtained in homogeneous solutions. Karukstis *et al.* analyzed the emission spectra of PRODAN in microemulsions and showed that the PRODAN molecules at different sites within the microemulsions exhibit different emission spectra.[144] More recently, using picosecond total internal reflection, Bessho *et al.*[145] determined the emission lifetime of ANS at the water-heptane interface. The observed a nanosecond component in the decay of ANS at the water-heptane interface which indicates that the interface is considerably less polar than bulk water.

The polarity of the supercages of solid faujasite zeolites has been estimated using TICT probes. For this purpose, Ramamurthy *et al.*[146] used DMABN and Sarkar *et al.*[147] used nile red as the probe. Both the studies indicate that the polarity of the faujasite zeolite resembles that of 1:1 methanol-water mixture. Kim *et al.*[148] studied TICT of dimethyl-amino-benzoic acid (DMABA) in faujasite Y zeolites. In Y zeolites the lifetime of the TICT emission and the TICT/LE emission intensity ratio of DMABA are greater than those in polar solvents. This is attributed to hydrogen bonding between DMABA and the zeolites. Kim *et al.*[149] studied the effect of neutral SiO_2 colloids of diameters 300-400 Å in acetonitrile, on the dual emission of DMABA. For 10 μM DMABA, they found that up to a concentration of 0.3 μM SiO_2 the intensity of the TICT band increases while that of the normal band (LE) decreases. Intensity of the TICT emission decreases at SiO_2 concentrations above 0.3 μM. They attributed this to the formation of hydrogen bond between the SiO_2 particles and the DMABA molecule. At high SiO_2 concentrations due to submonolayer coverage of the silica particles the TICT emission decreases.

The internal cavity of the cyclic polysaccharide, cyclodextrin (CD) is highly nonpolar and hydrophobic and is known to retard the TICT process markedly when the probe gets encapsulated inside the cavity.[2,43] More recently, a linear polysaccharides dextrin has also been reported to provide a hydrophobic surface to which the probe TNS binds due to hydrophobic effect and as a result of lower local polarity, the TICT rate is retarded nearly 50 times[150]. The effect of salting in (urea, $LiClO_4$ etc.) and salting out (LiCl) agents on the hydrophobic binding of TNS with dextrin has been studied in detail. Interestingly another linear polysaccharide, dextran affect the emission properties of TNS, vary slightly. This is attributed to the difference in the stereochemistry of dextrin and dextran. For dextrin, one surface is highly polar with all the hydroxyl groups of the sugar pointing outward from it, while the other surface is completely devoid of hydroxyl group and hence, is nonpolar and hydrophobic. For dextran both the surfaces contain hydroxyl groups and hence, are polar.

Kim *et al.* studied effect of cyclodextrin (CD) on the emission properties of DMABA in aqueous solutions and reported that α-CD enhances the nonpolar (LE) emission and β-CD enhances the TICT emission[151]. Matsushita and Hikida[152] studied the effect of α-CD on the emission properties of p-dimethylamino acetophenone (DMACP) in aqueous solutions. DMACP does not give TICT emission in aqueous solutions. However on addition of α-CD both the LE and TICT emission of DMACP is enhanced. To explain the larger enhancement of the LE emission they proposed a 1:2 complex in which the DMACP molecule is completely enclosed by two α-CD molecules.

The extraordinary sensitivity of the TICT probe, TNS, has recently been exploited to probe the interaction of cyclodextrins (CD) and surfactants.[153] Study of such interactions is important due to the potential application of CD in targeted drug delivery, and particularly for understanding how CD affects cell membrane surfactants. The important issues are whether CD preserves the structure of the membranes and releases the drug encapsulated inside its cavity. Critical micellar concentration (cmc) of several ionic surfactants (alkyl sulfates, sulfonates and tetra-alkyl ammonium halides) as well as neutral surfactants (Triton X-100, Igepal etc.), have been reported to increase on addition of CD, while their aggregation numbers remain more or less unchanged.[154-157] The emission quantum yield of TNS in TX-100 micelles is nearly 10 times that of TNS bound to CD-s while the lifetime of the micelle bound TNS is about 5 times higher. On addition of TX-100 to an aqueous solution containing CD, the emission intensity of TNS initially exhibits a slight decrease and beyond a particular concentration of TX-100, the emission intensity and lifetime of TNS increase abruptly. The point of abrupt increase of emission intensity and lifetime of TNS, gives the apparent cmc of TX-100 in the presence of CD. The apparent cmc of TX-100 increases significantly on addition of β-CD. In 10 mM β-CD, the apparent cmc of TX-100 is 7.25 ±0.25 mM. This is 28±1 times the cmc of TX-100 in water.[240] However, in the presence of α-CD at similar concentrations, cmc of TX-100 remains more or less unaffected.[153] This indicates that TX-100 molecules bind very strongly with the large β-CD and very weakly with the small α-CD. This is in sharp contrast to the behaviour of the linear surfactants for which both α-CD and β-CD cause an increase in cmc. The dramatic difference in the interaction of TX-100 with α- and β-CD, may be attributed to the difference in size between α- and β-CD. Due to its large size the TX-100 molecule can not be inserted in the small α-CD cavity and thus addition of α-CD leaves the cmc of TX-100 unchanged. TX-100 however, is easily accommodated in the bigger β-CD cavity and thus is rendered unavailable for the formation of the micelles causing an increase in the cmc. The initial decrease in the emission intensity of TNS, at TX-100 concentrations below the apparent cmc, is ascribed to the competitive binding of TNS and TX-100 with β-CD. This causes displacement of TNS from the CD cavity by the TX-100 surfactant molecules. The binding constant of TX-100 with β-CD is estimated to be 9400 ±1300 L M^{-1}.

5 Conclusion

It is apparent that the dynamics of various photophysical processes are markedly modified in the organized assemblies and are thus sensitive probes to study the microscopic properties of the organized assemblies. Perhaps the most significant result is the observation that the water molecules in different organized and biological assemblies are significantly slower than ordinary water molecules. It is demonstrated that the local polarity, *p*H and viscosity in an organized media are markedly different from those in the ordinary solutions and often vary quite drastically over a small distance. Ultrafast lasers and the various sophisticated theoretical models which revolutionized chemical dynamics in ordinary liquids in the eighties, have been applied to study organized assemblies only recently and still the field is largely unexplored. Though the inherent complexity of the organized assemblies still eludes a complete and quantitative understanding of some of the questions there has been a significant improvement in our understanding of various issues. The enhanced understanding about the structure and function of organized assemblies should enable us to mimic the natural systems more closely.

6 Acknowledgements

The author would like to thank his students namely N Sarkar, K Das, S Das, A Datta, D Mandal and S K Pal. Special thanks are due to Professor B Bagchi for many stimulating and helpful discussions. Thanks are also due to the Department of Science and Technology and the Council of Scientific and Industrial Research (CSIR), Government of India for generous research grants.

References

1 *Photochemistry in Organized and Constrained Media* (Ed.(V Ramamurthy) VCH New York (1991)
2 V T D'Souza and K B Lipkowitcz *Chem Rev* **98** (1998) 1741; P Bortulos and S Monti *Adv Photochem* **21** (1995) 1; K A Konnors *Chem Rev* **97** (1997) 1325; G Wenz *Ange Chem Int Ed Engl* **34** (1994) 741; I M Warner *Anal Chem* **70** (1998) 477R
3 R Breslow *Chem Rev* **98** (1998) 1997; W Blokzijl and J B F N Engberts *Angew Chem Int Ed Engl* **32** (1993) 1545
4 R B Miranda and Y R Shen *J Phys Chem B* **103** (1999) 3292; I Benjamin *Annu Rev Phys Chem* **48** (1997) 401
5 K B Eisenthal *Chem Rev* **96** (1996) 1343
6 G R Fleming and M Cho *Annu Rev Phys Chem* **47** (1996) 109; R M Stratt *Acc Chem Res* **28** (1995) 201; P J Rossky and J D Simon *Nature* **369** (1994) 471
7 M L Horng, J A Gardecki and M Maroncelli *J Phys Chem A* **101** (1997) 1030
8 B Bagchi and R Biswas *Acc Chem Res* **31** (1998) 181; B Bagchi and N Gayathri A. *Adv Chem Phys* **89** (1998) 1
9 W Jarjeba, G C Walker, A E Johnson, N A Kahlow, and P F Barbara *J Phys Chem* **92** (1988) 7039; R Jimenez, G R Fleming, P V Kumar, M Maroncelli *Nature* **370** (1994) 263; C Silva, P K Walhout, K Yokoyama and P F Barbara *Phys Rev Lett* **80** (1998) 1086
10 N Nandi, S Roy and B Bagchi *J Chem Phys* **102** (1995) 1390; B J Schwartz and P J Rossky *J Chem Phys* **105** (1996) 6997
11 A J Benigno, E Ahmed and M Berg *J Chem Phys* **104** (1996) 7382
12 U Kaatze *Chem Phys Lett* **203** (1993) 1
13 L Zhang, H T Davies, D M Kroll and H S White *J Phys Chem* **99** (1995) 2878
14 R Pethig *Protein-Solvent Interactions* (Ed. R B Gregory) Marcel Dekker Inc. NY (1995) .265
15 S Mashimo, S Kuwabara, S Yagihara and K Higasi *J Phys Chem* **91** (1987) 6337
16 P S Belton *J Phys Chem* **99** (1995) 17061
17 V P Denisov, J Peters, H D Horlein and B Halle *Nature Struct Biol* **3** (1996) 505
18 N Nandi and B Bagchi *J Phys Chem B* **101** (1997) 10954; N Nandi and B Bagchi *J Phys Chem A* **102** (1998) 8217
19 S Fischer, C S Verma and R Hubbard *J Phys Chem B* **102** (1998) 1797
20 D H Waldeck *Chem Rev* **91** (1991) 415
21 S H Lin, M Groesbeck, I van der Hoef, P Verdegen, J Lugtenberg, R A Mathies *J Phys Chem B* **102** (1998) 2787
22 S Takeuchi and T Tahara *J Phys Chem A* **101** (1997) 3052
23 H A Kramers *Physica (The Hague)* **7** (1940) 284; P Hanggi, T Talkner and M Borkovec *Rev Mod Phys* **62** (1990) 251
24 B Bagchi and D W Oxtoby *J Chem Phys* **78** (1983) 2735; G Rothenberger, D K Negus and R M Hochstrasser *J Chem Phys* **79** (1983) 215
25 R M Bowman, D P Miller and K B Eisenthal *Chem Phys Lett* **155** (1989) 99
26 Y P Sun and J Saltiel *J Phys Chem* **93** (1989) 8310
27 J M Hicks, M T Vandersall, E V Sitzman, K B Eisenthal *Chem Phys Lett* **135** (1987) 413
28 S P Velsko and G R Fleming *Chem Phys* **65** (1982) 59
29 A Weller *Prog React Kinetics* **1** (1961) 188; J F Ireland and P A Wyatt *Prog Phys Org Chem* **12** (1976) 131
30 S K Kim, J J Breen, D M Willberg, L W Peng, A Heikal and A H Zewail *J Phys Chem* **99** (1995) 7421; A Douhal, F Lahmani and A H Zewail *Chem Phys* **207** (1996) 477
31 G W Robinson, P S Thistlewaite and J Lee *J Phys Chem* **90** (1986) 4224
32 E Pines and G R Fleming *J Phys Chem* **95** (1991) 10448
33 S P Webb, S W Yeh, L A Philips, M A Tolbert and J H Clark *J Am Chem Soc* **106** (1984) 7286
34 J Lee, G W Robinson, S P Webb, L A Philips and J H Clark *J Am Chem Soc* **108** (1986) 6538
35 J Lee, G W Robinson, S P Webb, L A Philips and J H Clark *J Am Chem Soc* **112** (1990) 1353
36 E Pines, D Huppert and N Agmon *J Chem Phys* **88** (1988) 5620
37 B H Robinson and G P Drobny *Ann Rev Biophys Biomol Struct* **24** (1995) 523; C V Kumar (ref. 1, p 783)
38 D P Millar, R J Robbins and A H Zewail *J Chem Phys* **76** (1982) 2080
39 J Ohmstead III and D R Kearns *Biochemistry* **16** (1977) 3647
40 M J Kamlet, J L M Abbouid and R W Taft *Prog Phys Org Chem* **13** (1981) 485; C Reichardt *Chem Rev* **94** (1994) 2319
41 S K Pal, D Mandal and K Bhattacharyya *J Phys Chem B* **102** (1998) 11017
42 Z R Grabowski *Pure Appl Chem* **65** (1993) 1751
43 K Bhattacharyya and M Chowdhury *Chem Rev* **93** (1993) 507
44 H J Kim and J T Hynes *J Photochem Photobiol A* **105** (1997) 337
45 A L Sobolewski, W Sudholt and W Domcke *J Phys Chem A* **102** (1998) 2716
46 T Ishida, Y Fujimura, T Fujiwara and O Kajimoto *Chem Phys Lett* **288** (1998) 433
47 J M Hicks, M T Vandersall, Z Babarogic and K B Eisenthal *Chem Phys Lett* **116** (1985) 18
48 Y Chang, P Chong and J D Simon *J Phys Chem* **99** (1995) 7382

49 D Attwood and A T Florence *Surfactant Systems* Chapman & Hall London (1983)

50 H H Paradies *J Phys Chem* **84** (1980) 599; S S Berr *J Phys Chem* **91** (1987) 4760; S S Berr, M J Coleman, R R M Jones and J S Johnson *J Phys Chem* **90** (1986) 5766; S S Berr, E Caponetti, R R M Jones, J S Johnson and L J Magid *J Phys Chem* **90** (1986) 5766

51 T Telgmann and U Kaatze *J Phys Chem A* **102** (1998) 7758 and 7766

52 Y C Jean and J H Ache *J Am Chem Soc* **100** (1978) 984 6320

53 J Eastoe, W K Young and B H Robinson *J Chem Soc Faraday Trans* **86** (1990) 2883

54 Y N Cao, H X Chen, G J Diebold, T Sun and M B Zimmt *J Phys Chem B* **101** (1997) 3005

55 A Amararene, M Gindre, J Y Le Huerou, C Nicot, W Urbach and M Waks *J Phys Chem B* **101** (1997) 10751

56 M B Temsamani, M Maeck, I El Hassani and H D Hurwitz *J Phys Chem B* **102** (1998) 3335; T De and A Maitra *Adv Coll Int Sci* **59** (1995) 95; T K Jain, M Varshney and A Maitra *J Phys Chem* **93** (1989) 7409

57 S P Moulik and B K Pal *Adv Coll Int Sci* **78** (1998) 99; K Mukherjee, D C Mukherjee and S P Moulik *Langmuir* **9** (1993) 1727

58 M D'Angelo, D Fioretto, G Onori, L Palmieri and A Santucci *Phys Rev E* **54** (1996) 993, 4620

59 D M Zhu, W Wu and Z A Schelly *J Phys Chem* **96** (1992) 2382, 712; H Caldaru, A Caragheorgheopal, M Dimonie, D Donescu, I Dragutan and N Marinescu *J Phys Chem* **96** (1992) 7109

60 R E Riter, J R Kimmel, E P Undiks and N Levinger *J Phys Chem B* **101** (1997) 8292

61 R Cassol, M T Ge, A Ferrarini and J H Freed *J Phys Chem B* **101** (1997) 8782

62 M M Sung-Suh and L Kevan *J Phys Chem A* **101** (1997) 1414

63 M Pasenkiewicz-Gierula, V Takaoka, H Miyagawa, K Kitamura and A Kusumi *J Phys Chem A* **101** (1997) 3677

64 R M Pearson and I Pascher *Nature* **81** (1979) 499

65 *Liposomes: A Practical Approach* (Ed. R C New) Oxford University Press England (1990)

66 J R Lakowicz and S Keating-Nakamoto *Biochemistry* **23** (1984) 3013

67 A P Demchenko and A S Ladokhin *Eur Biophys J* **15** (1988) 569; A Chattopadhyay and S Mukherjee *Biochemistry* **32** (1993) 3804

68 K H de Haas, C Blom, D van den Ende, M H G Devits, B Haveman and J Mellema *Langmuir* **13** (1997) 6658

69 A Srivastava and K B Eisenthal *Chem Phys Lett* **292** (1998) 345

70 E Kumacheva, Y Rharbi, R Mitchel, M A Winnik, L Guo, K C Tam and R D Jenkins *Langmuir* **13** (1997) 182

71 A R Eckert, T J Martin and S E Webber *J Phys Chem A* **101** (1997) 1646

72 N Shiyanishiki, S Yagihara, I Arita and S Mashimo *J Phys Chem B* **102**, (1998) 3249

73 R Olender and A Nitzan *J Chem Phys* **102** (1995) 7180

74 L Bromberg, A Y Grossberg, Y Suzuki and T Tanaka *J Chem Phys* **106** (1997) 2906; I Ohmine and T Tanaka *J Chem Phys* **77** (1982) 8725

75 Y B Zhang and Y X Zhang *Macromolecules* **29** (1996) 2494

76 A Chrambach and D Rodbard *Science* **172** (1971) 440

77 A M Mathur, S K Moorjani and A B Scranton *J Macromol Science -Rev Macromol Chem Phys* **C36** (1996) 405

78 V F Janas, F Rodriguez and C Cohen *Macromolecules* **13** (1980) 977

79 H Walderhans and B Nystrom *J Phys Chem B* **101** (1997) 1524; A K Lele, M M Hirve, M V Badiger and R A Mashelkar *Macromolecules* **30** (1997) 157

80 R M Dickson, D J Norris, Y L Tzeng and W E Moerner *Science* **274** (1996) 966

81 V Ramamurthy, D F Eaton and J V Casper *Acc Chem Res* **25** (1992) 299; V Ramamurthy (ref 1 p 303)

82 V Lachet, A Boutin, B Tavitian and A H Fuchs *J Phys Chem B* **102** (1998) 9224

83 P Demontis and G B Suffriti *Chem Rev* **97** (1997) 2845

84 B Smit and T L M Maesen *Nature* **374** (1995) 42

85 L Campana, A Selloni and A Goursot *J Phys Chem B* **101** (1997) 9932

86 W E Farneth and R J Gorte *Chem Rev* **95** (1995) 615

87 P A Anderson, A R Armstrong, A Porch, P P Edwards and L J Woodball *J Phys Chem B* **101** (1997) 9892

88 G Vitale, C F Mellot, M Bull and A K Cheetham *J Phys Chem B* **101** (1997) 4559

89 G Schrimp, B Tavitian and D Espinat *J Phys Chem* **99** (1995) 10932

90 S Vajda, R Jimenez, S J Rosenthal, V Fidler, G R Fleming and E W Castner Jr *J Chem Soc Faraday Trans* **91** (1995) 867

91 A Nag, T Chakrabarty and K Bhattacharyya *J Phys Chem* **94** (1990) 4203; W R Bergmark, A Davies, C York and G Jones II *J Phys Chem* **94** (1990) 4203

92 N Nandi and B Bagchi *J Phys Chem* **100** (1996) 13914

93 G Jones II, W P Jackson and C Y Choi *J Phys Chem* **89** (1985) 294

94 N Sarkar, K Das, S Das, A Datta and K Bhattacharyya *J Phys Chem* **100** (1996) 10523

95 J S Lundgren, M P Heitz and F V Bright *Anal Chem* **67** (1995) 3775

96 S Das, A Datta and K Bhattacharyya *J Phys Chem A* **101** (1997) 3299

97 E Bart, A Melstein and D Huppert *J Phys Chem* **99** (1995) 99, 9253

98 E Neria and A Nitzan *J Chem Phys* **100** (1994) 3855

99 A Chandra, D Wei and G N Pattey *J Chem Phys* **98** (1993) 4959

100 D Mandal, A Datta, S K Pal and K Bhattacharyya *J Phys Chem B* **102** (1998) 9070

101 D M Willard, R E Riter and N E Levinger *J Am Chem Soc* **120** (1998) 4151

102 R E Riter, E P Undiks and N E Levinger *J Am Chem Soc* **120** (1998) 6062

103 R E Riter, D M Willard and N E Levinger *J Phys Chem B* **102** (1998) 2705; R E Riter, E P Undiks, J R Kimel, D D Pant and N E Levinger *J Phys Chem B* **102** (1998) 7931

104 H Shirota and K Horie *J Phys Chem B* **103** (1999) 1437

105 N Sarkar, A Datta, S Das and K Bhattacharyya *J Phys Chem* **100** (1996) 15483

106 A Datta, D Mandal, S K Pal and K Bhattacharyya *J Mol Liq* **77** (1998) 121

107 A Datta, S K Pal, D Mandal and K Bhattacharyya *J Phys Chem B* **102** (1998) 6114

108 J D Jordan, R A Dunbar and F V Bright *Anal Chem* **67** (1995) 2436

109 A Datta, S Das, D Mandal, S K Pal and K Bhattacharyya *Langmuir* **13** (1997) 6922

110 M Claudia-Marchi, S A Bilmes and R Negri *Langmuir* **13** (1997) 3655

111 T P Hsu, D S Ma and C Cohen *Polymer* **24** (1983) 1273

112 P A Netz and T Dorfmuller *J Phys Chem B* **102** (1998) 4875

113 R Argaman and D Huppert *J Phys Chem A* **102** (1998) 6215

114 J Rau, C Ferrante, F W Deeg and C Brauchle *J Phys Chem B* **103** (1999) 931

115 G Saielli, A Polomeno, P L Nordio, P Bertolini, M Ricci and R Righini *J Chem Soc Faraday Trans* **94** (1998) 121

116 K Das, N Sarkar, S Das, A Datta and K Bhattacharyya *Chem Phys Lett* **249** (1998) 323

117 R Biswas and B Bagchi *J Phys Chem* **100** (1996) 4261

118 D Pant and N E Levinger *Chem Phys Lett* **292** (1996) 200

119 R B McGregor and G Weber *Nature* **319** (1986) 70

120 J R Lakowicz *Principles of Fluorescence Spectroscopy* Plenum Press New York (1983) Chap. 8

121 D W Pierce and S G Boxer *J Phys Chem* **96** (1992) 5560

122 J S Baskhin, G McLendon, S Mukamel and J Marohn *J Phys Chem* **94** (1990) 4757

123 E B Brauns, C J Murphy and M Berg *J Am Chem Soc* **120** (1998) 2449

124 G L Duveneck, E V Sitzmann, K B Eisenthal and N J Turro *J Phys Chem* **93** (1989) 7166

125 V Ramamurthy, J V Casper and D R Corbin *Tet Lett* **31** (1990) 1097

126 A S Holmes, D J S Birch, A Sanderson and G G Aloisi *Chem Phys Lett* **266** (1997) 309

127 A Datta, S K Pal, D Mandal and K Bhattacharyya *Chem Phys Lett* **278** (1997) 77

128 S K Pal, A Datta, D Mandal and K Bhattacharyya *Chem Phys Let* **288** (1998) 793

129 D Mandal, S K Pal, A Datta and K Bhattacharyya *Res Chem Intermediates* **25** (1999) 685

130 M S Baptista and J L Indig *J Phys Chem B* **102** (1998) 4678

131 N Tamai, M Ishikawa, N Kitamura and H Masuhara *Chem Phys Lett* **184** (1991) 398

132 P Mukerjee and K Banerjee *J Phys Chem* **68** (1964) 3567

133 F M Menger and G Saito *J Am Chem Soc* **100** (1978) 4376

134 C Oldfield, B H Robinson and R B Freedman *J Chem Soc Faraday Trans* **86** (1990) 833

135 M Okazaki and K Toriyama *J Phys Chem* **93** (1989) 5027

136 V Ramamurthy and D F Eaton *Acc Chem Res* **21** (1988) 300

137 M J Politi, O Brandt and J H Fendler *J Phys Chem* **89** (1985) 2345

138 J E Hansen, E Pines and G R Fleming *J Phys Chem* **96** (1992) 6904

139 D Mandal, S K Pal and K Bhattacharyya *J Phys Chem A* **102** (1998) 9710

140 J Sujatha and A K Mishra *Langmuir* **14** (1998) 2256

141 C H Cho, M Chung, J Lee, T Nguyen, S Singh, M Vedamuthu, S Yao, S Bzhu and G W Robinson *J Phys Chem* **99** (1995) 7806

142 D Mandal, S K Pal, A Datta and K Bhattacharyya *Analytical Sciences* **14** (1998) 199

143 A Datta, D Mandal, S K Pal and K Bhattacharyya *J Phys Chem B* **101** (1997) 10221

144 K K Karukstis, A Frazier, C L Loftus and A S Tuan *J Phys Chem B* **102** (1998) 8163

145 K Bessho, T Uchida, A Yamauchi, T Shiyoa and N Teramae *Chem Phys Lett* **264** (1997) 381

146 V Ramamurthy, D R Sanderson and D F Eaton *Photochem Photobiol* **56** (1992) 251

147 N Sarkar, K Das, D N Nath and K Bhattacharyya *Langmuir* **10** (1994) 326

148 Y Kim, B I Lee and M Yoon *Chem Phys Lett* **286** (1998) 466

149 Y Kim, H W Cheon, M Yoon, N W Song and D Kim *Chem Phys Lett* **264** (1997) 673

150 K Das, N Sarkar, S Das, K Bhattacharyya and D Balasubramanian *Langmuir* **11** (1995) 2410

151 Y H Kim, D W Cho, M Yoon and D Kim *J Phys Chem* **100** (1996) 15670

152 Y Matshushita and T Hikida *Chem Phys Lett* **290** (1998) 349

153 S K Pal, A Datta, D Mandal, S Das and K Bhattacharyya *J Chem Soc Faraday Trans* **94** (1998) 3471

154 G G Gaitano, A Crespo, A Compostizo and G Tardajos *J Phys Chem B* **101** (1997) 4413

155 D J Jobe, V C Reinsborough and S D Wetmore *Langmuir* **11** (1995) 2476

156 G Nelson and I M Warner *Carbohydrate Res* **192** (1989) 305

157 V K Smith, T T Ndou, A Munoz de la Pena, I M Warner *J Inclu Phenomena & Mol Recog* **10** (1991) 471

DYNAMICS OF PHOTOSYNTHETIC EXCITATION TRANSFER

VILLY SUNDSTRÖM* AND TÕNU PULLERITS

Department of Chemical Physics, Chemical Center, Lund University, P.O. Box 124, 221 00 Lund (Sweden)

Studies of structure and dynamics of photosynthetic light-harvesting pigment-protein complexes have recently seen great progress, and resulted in detailed understanding of the light-harvesting and light-conversion processes of photosynthesis. In this article, recent results have been reviewed and discussed on the elementary excitation transfer dynamics of the purple bacterial LH2 peripheral complex. When combining the information from the two LH2 structures that are now available with the experimental results obtained from a variety of ultrafast techniques, steady-state spectroscopy and computer simulations, a detailed understanding of the LH2 function is obtained. Dynamics of excitation transfer and trapping in the whole photosynthetic unit (PSU = LH2 + LH1 core + reaction center), interpreted with the help of models of the PSU obtained on the basis of the LH2 structure, allow us to suggest how the characteristic structural features of LH2 and LH1 have been designed to optimize the overall light-harvesting and trapping process in the PSU.

Key Words: Bacterial Photosynthesis; Antennae; Energy Transfer; Femtosecond Spectroscopy; Carotenoids

1 Introduction

The light-driven reactions of photosynthesis are the means by which nature converts solar energy into a stable electrochemical potential, which eventually is stored as chemical energy through a series of dark reactions. The light reactions occur in two closely coupled pigment systems; light energy is absorbed by a network of so-called antenna pigments bound to proteins and the excitation energy is very efficiently transported to the photochemical reaction center (RC) where the energy is converted into a stable trans-membrane charge separation through a sequence of electron transfer reactions[1-6]. Time-resolved picosecond measurements showed that this conversion process is typically finished within ~100 ps, explaining the high overall quantum yield (95%) of the process, known already in the early days of photosynthesis research[7]. In the photosynthetic purple bacteria to be discussed in this paper, the light-harvesting antenna generally consists of a core antenna, LH1, which for the bacteriochlorophyll (BChl) *a* containing species absorbs around 870-880 nm, while BChl *b* containing species exhibit major absorption around 1000 nm. An electron microscopy visualization of the photosynthetic membrane of the BChl *b* containing species *Rhodopseudomonas* (*Rps.*) *viridis* by Miller[8] showed for the first time how LH1 is arranged as a circle around the RC; the diameter of this RC-LH1 core was about 10-11 nm. In species with LH1 as the single antenna, the RC-LH1 forms a continuous network, through which ultrafast energy transfer occurs. In many BChl *a* containing species such as *Rhodobacter* (*Rb.*) *sphaeroides*, *Rhodopseudomonas* (*Rps.*) *acidophila* and *Rhodospirillum* (*Rs.*) *molischianum* a second peripheral light-harvesting complex, LH2, occurs, with major absorption bands at 800 and 850 nm (the exact position of the latter band depending amongst others on the degree of hydrogen bonding between the pigment and the protein[9,10]).

Both LH1 and LH2 have been studied extensively with biochemical techniques[11] and their genetics were developed[12]. This work established that the elementary building block of LH1 and LH2 is a pair of small polypeptides, called α and β, both containing a single transmembrane helix as the major structural element. Both α and β bind a single BChl molecule at a conserved histidine residue, positioned in the transmembrane helix, while in the case of LH2 the β-polypeptide binds a second BChl.

Earlier spectroscopic research using polarized light resulted in models of how the BChl *a* molecules in LH2 and LH1 were organized[13,14], and for

---

* E. Mail: Villy. Sundstrom @chem phys.lu.se
Fax: +46462224119

LH2 the model predicted fast energy transfer among the B850's and the B800's, while the B800→B850 energy transfer was estimated to be in the few ps range, consistent with the measured B800 fluorescence quantum yield. The carotenoids were positioned in such a way as to comply with the observed efficient energy transfer to the B800 and B850 BChls.

Time resolved studies using picosecond pulses were initiated in the '80s. Early experiments on LH1 and LH2 made use of the excitation annihilation effect and to explain the results, single site excited state lifetimes of much less than a picosecond had to be assumed[15]. Low intensity, high repetition rate pulses were applied later and either the spontaneous emission[16] or the time-resolved transmission[17] was detected. These experiments provided information about the overall dynamics and gave upper limits for many of the essential steps. Detailed studies of the most elementary ultrafast processes had to await experiments with shorter pulses (see below).

In this article, we would like to review recent femtosecond work on LH2 and LH1. We do not intend to provide a complete account of the literature on this subject, but rather using our own work as a starting point and making reference to a selection of other authors' work, we aim at presenting a picture of the function of LH2 and LH1. At the end, implications for the function of the whole photosynthetic unit (PSU) will be given. The structure of the article will follow that suggested by the structure of LH2: following a very brief introduction to the theory used to describe excitation dynamics we will discuss results on carotenoid to BChl energy transfer, B800 to B850 transfer, B800 intraband transfer, B850 intraband dynamics and finally we will briefly discuss the dynamics of the purple bacterial PSU and finish with some speculations.

2 The Structure of LH2 of *Rhodopseudomonas* acidophila and *Rhodospirillum* molischisanum

A major breakthrough in our understanding of the organization of the bacterial light-harvesting antenna and consequently of the process itself came with the discovery of the structure of the LH2 complex of *Rps. acidophila* by Cogdell and coworkers in 1995[18], followed by the LH2 structure of *Rs. molischianum* by Michel and Schulten and coworkers in 1996[19]. These structures revealed the 9- and 8-fold symmetric rings of $\alpha\beta$-heterodimers for *Rps. acidophila* and *Rs. molischianum*, respectively. Based on a low resolution electron density map and the analogy between LH2 and LH1, it is now generally believed that LH1 is a 16-fold symmetric ring of $\alpha\beta$-heterodimers, with the RC in its center[20].

Fig. 1 shows a schematic representation of the 2.5 Å LH2 structure of *Rps. acidophila* as obtained by Cogdell and coworkers[18]. The complex is a nonameric circular aggregate of $\alpha\beta$-heterodimers, with each subunit non-covalently binding three BChls and most likely one carotenoid. The aggregate is formed by two concentric rings of helical protein subunits with the α-polypeptides inside and the β's outside. The B850 ring is formed by the 9 pairs of BChls associated with the conserved histidines and is sandwiched between the concentric rings of α- and β-polypeptides, and the inter- and intra-subunit BChl-BChl center-to-center distances are very similar, about 9 Å. The 9 B800's are in a plane about 1.7 nm shifted towards the cytosolic side of the membrane and positioned between the β-helices. The B800-B800 center-to-center distance is about 21.2 Å. In the structure, only one carotenoid is well-resolved and a schematic view of its position relative to the B800 and B850 BChls is given in Fig. 2. The rhodopin glucoside molecule transverses the membrane, its polar head group is buried in a polar pocket at the cytosolic side of the membrane, it then passes the B800 BChl of the same subunit at close to van der Waals contact and finally the end of the carotenoid makes close non-bonding contacts with the α-B850 pigment in the next subunit.

The second known LH2 structure comes from *Rs. molischianum*[19] and is very closely related to that of LH2 of *Rps. acidophila*. The most conspicuous difference is that this LH2 is an $\alpha\beta$-octamer with 16 B850 BChls and 8 B800's. There are also some more subtle structural differences, of which the more pronounced are that in LH2 of *Rs. molischianum* the plane of the B800's is rotated by about 90 degrees compared to *Rps. acidophila* (resulting in a considerably weaker coupling between the B800 BChls), and that the B800 macrocycles are significantly tilted away by about 30 degrees from the membrane plane.

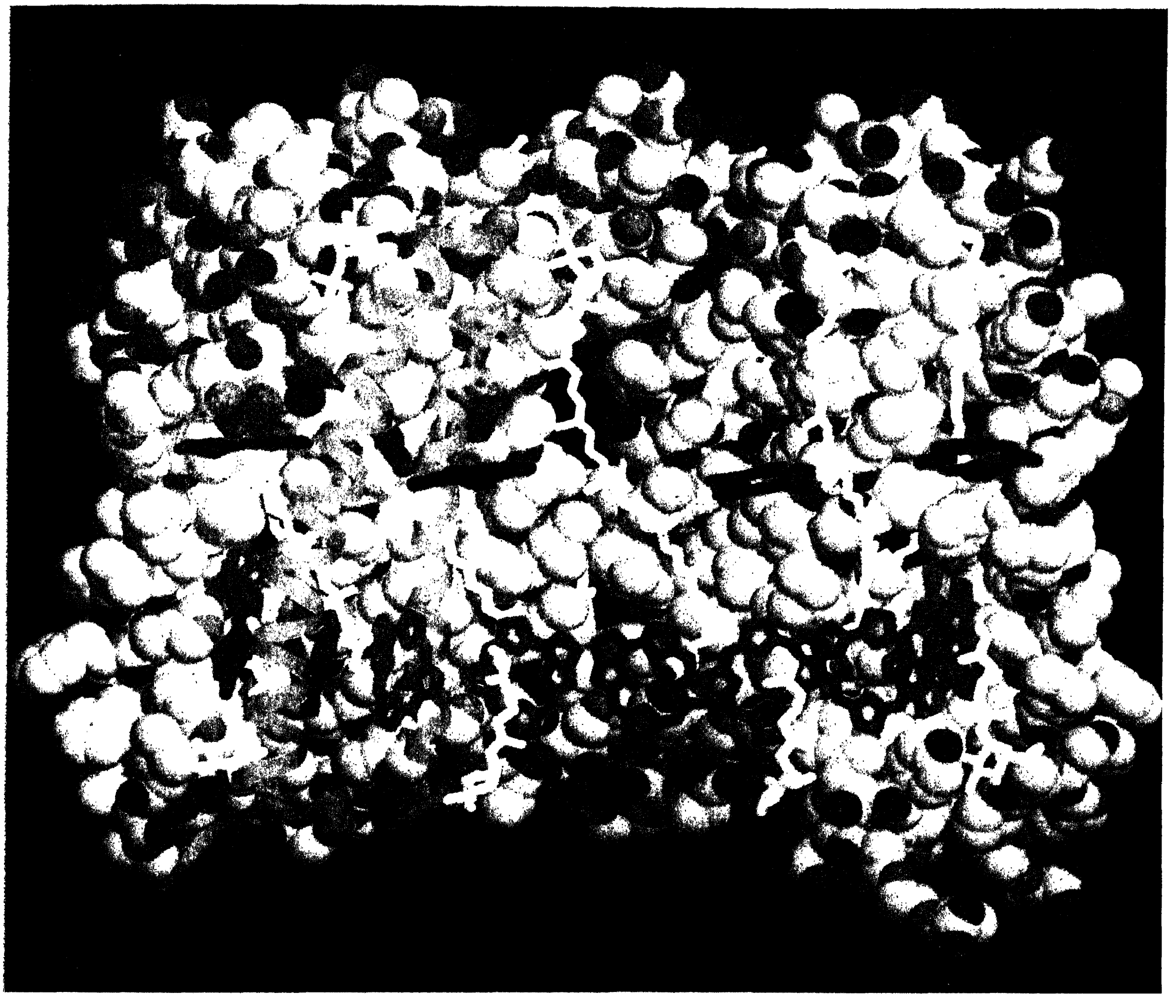

Fig. 1 Structure of the LH2 antenna from *Rps. acidophila*. The membrane plane is perpendicular to the plane of the figure and 2/3 of the LH2 protein is shown via space filled atoms of corresponding Van der Waals' radiuses. One $\alpha\beta$ polypeptide pair is represented via orange ribbons. For clarity we show only the porphyrin macrocycles of the BChl *a* molecules. The B800 BChl *a* molecules (blue bonds) are parallel to the membrane plane, whereas B850 molecules (green bonds) are perpendicular to the membrane plane. The carotenoid molecules are yellow. We point out that one of the carotenoid molecules is only partly resolved.

3 Theoretical Considerations for Energy Transfer and Spectroscopy of LH1 and LH2

Excitation transfer in photosynthetic antenna systems has usually been described as an incoherent Förster[21] hopping in a two-dimensional antenna array of pigment molecules[22-27]. It is hard to overestimate the physical insight obtained by this approach. At the same time a number of experimental facts do not fit into this picture, for example coherent nuclear motions in the antenna systems of photosynthetic purple bacteria[28-30] or the highly structured spectra of so-called Fenna-Matthews-Olson complexes[31]. The latter case, in particular, calls for the molecular exciton description[32] where an excitation is coherently delocalized over a number of pigment molecules and the absorption spectrum exhibits a prominent exciton band structure. Time evolution in the exciton picture occurs via phonon induced relaxation between

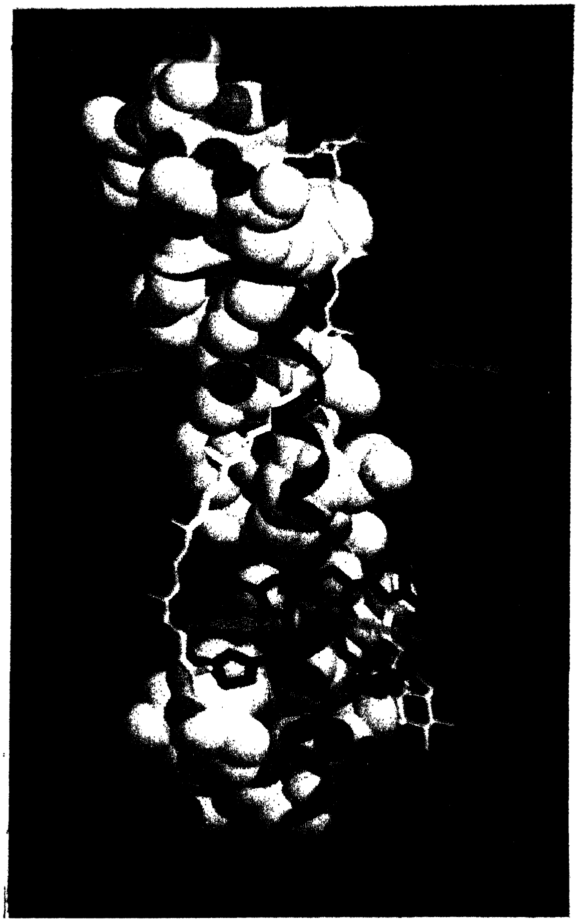

Fig. 2 Structure of one $\alpha\beta$ subunit of LH2 of *Rps. acidophila* as seen from inside of the LH2 ring. The B800, B850 and Crt molecules are blue, red and yellow, respectively. The direction of the Q_y transition dipole moments of the B800 and B850 BChl molecules are indicated with orange arrows.

exciton levels. These two descriptions, incoherent hopping and exciton relaxation, are the two qualitatively different limiting cases of the general process of excitation dynamics. What description should be chosen for a particular observation depends on the system properties and the experimental conditions. It may happen that the real situation is somewhere in between these two limiting cases, in which case the analyses is particularly challenging. The important factor deciding which processes occur, is the ratio of the coupling between electronic transitions (V) and the disorder (Δ). The disorder may be either static (spectral inhomogeneity) or dynamic (electron-phonon interaction). If V/Δ is much less than unity we are talking about very weak interactions and energy transfer is in the incoherent hopping limit. In the opposite case, if $V/\Delta \gg 1$, the interaction is very strong and the exciton picture is used. In both cases, the transfer rate can be calculated using first order perturbation theory leading to the Fermi Golden rule. In the hopping description, electronic coupling (V) acts as a perturbation; in exciton picture, electron phonon coupling (dynamic disorder) is the perturbation. The real experimental situation determines which part of the Hamiltonian should be taken as a perturbation and in which basis (excitonic or molecular) to think and work. In the exciton picture the excitation energy is delocalized over the interacting pigment molecules. However, the extent of delocalization is determined by the V/Δ ratio and in a real system exciton delocalization is generally smaller than the physical size of the molecular aggregate (the ring of BChl molecules in this case). The localization process may also have a dynamic part due to the dynamic contribution to the disorder Δ. The two processes, excitation hopping and exciton relaxation, coexist and they are both accounted for in a density matrix formulation of the dynamics. We are not going to further elaborate on the theoretical descriptions of these two modes of excitation dynamics, but refer to several original works as well as reviews[21,24,32,34-38,40-44]

4 Interactions and Energy Transfer Between Carotenoid and Bacteriochlorophyll Molecules of LH2

Carotenoid molecules in photosynthetic pigment-protein complexes in general have two major functions: photoprotection[45] against triplet states and singlet oxygen and light-harvesting[46-51]. Frequently, as is also suggested by the LH2 crystal structure, carotenoids have a structural function of stabilizing the pigment-protein of which they are a part. Here we will limit our discussion to the light-harvesting function, with the aim of revealing the mechanisms of energy transfer and pathways of energy flow between the carotenoid and BChl molecules of the LH2 complex. Due to their conjugated π-electron systems and electronic structure, carotenoid molecules are known to be very sensitive to electric fields[52-54]. Electrochromic band-shift measurements of carotenoid absorption spectra have therefore been extensively used to report on electron transfer processes and membrane organization. It was recently discovered that carotenoids also sense changes of local electric fields associated with optical excitation of nearby pigment molecules (BChls)[55]. We will briefly discuss how this property of carotenoids may be used to monitor excitation transfer dynamics in a LH complex. Several recent review articles have appeared on carotenoid light-harvesting[46-48,50,51] and we refer to them for an account of earlier work. Here we will discuss the most recent progress and status of the topic.

From the crystal structure of LH2 (Figs. 1 and 2), it is immediately apparent that carotenoid molecules, being very well integrated into the protein and coming within short distance of both the B800 and B850 BChl molecules, are ideally located for performing their two major functions. The closest distance from the carotenoid molecule to the central Mg atom of a BChl molecule is 9.3 Å for B800, 5.44 Å for the Mg atom of the α-B850 and 8.04 Å for the β-B850 Mg atom[56]. Several shorter, non-bonded contacts between Crt atoms and atoms of the BChl macrocycles (~3.5-5 Å), of potential importance for exchange interactions, are also observed in the structure.

An inspection of the crystal structure for Crt-BChl chromophore distances and orientations is quite informative as a starting point for a discussion on the mechanisms and channels of excitation transfer in LH2. In considering dipole-dipole interactions, the relative orientations of the transition dipole moments are important. From Fig. 2, it is seen that the Crt backbone (and thus the $S_0 \rightarrow S_2$ transition dipole) is essentially parallel with the B850 BChl $S_0 \rightarrow Q_x$ transition moment and perpendicular with all the other BChl (both B800 and B850) Q_y and Q_x transition dipoles. This suggests that Crt $S_2 \rightarrow$ B850 Q_x energy transfer could be quite efficient and proceed via the Förster mechanism, while all the other transfer channels from Crt S_2 should be considerably less efficient. The Crt S_2 state is known to decay very quickly (~200 fs)[57] via internal conversion to the optically forbidden S_1 ($2A_g^-$) state. So even with an efficient Crt $S_2 \rightarrow$ BChl Q_x transfer channel it is likely that some fraction of the energy would end up in the lowest excited Crt S_1 state. The dipole forbidden nature of this transition has triggered the suggestion that energy transfer from this state to the BChls does not occur via the Förster mechanism, but rather via electron exchange[46,58]. However, more recent calculations[59,60] suggest that even at these relative short distances, the Dexter exchange mechanism is very inefficient and that higher order Coulombic (quadrupole-dipole) and polarization interactions may, perhaps, account for a transfer channel from Crt S_1 to BChl, still with a reasonable rate (time constants on the time scale of tens of picoseconds)[60,61].

From recent femtosecond work many of these predictions appear to have been confirmed. Thus, transient absorption measurements on LH2 of *Rb. sphaeroides* by Trautman *et al.*[62] and by Shreve *et al.*[63] showed that following Crt excitation the B850 Q_y state was populated within 200 fs. Similar time resolved measurements by the same group on β-carotene showed that Crt $S_2 \rightarrow S_1$ internal conversion occurs on the same time scale (~200 fs)[57]. These two results suggested that in LH2 the Crt S_2 state may be deactivated by two competing channels, Crt $S_2 \rightarrow$ B850 and Crt $S_2 \rightarrow$ Crt $S_1 \rightarrow$ B850/B800 Q_y (Fig. 3). The relative contributions of the two channels would be determined by the ratio of the rates of the processes Crt $S_2 \rightarrow$ B850 and Crt $S_2 \rightarrow$ Crt S_1. These results have recently been further substantiated by transient absorption[64] and fluorescence upconversion[65,66] measurements. The picture that emerges (Fig. 3) is that fast (50-100 fs) energy transfer occurs from Crt S_2 to B850, presumably to the Q_x state. The relative rates of the two channels, Crt $S_2 \rightarrow$ B850 Q_x and Crt $S_2 \rightarrow$ Crt $S_1 \rightarrow$ B850/B800 determines how much of the energy that goes via this very fast channel and how much is transferred via the Crt $S_1 \rightarrow$ B850/B800 route. The transfer via this channel is probably considerably slower, on the few picosecond time scale, but still sufficiently fast for a reasonably efficient transfer from the Crt S_1 state (and competition with the radiationless decay of this state). Thus, it appears that nature has designed a very robust system with many possible pathways, the contribution of which in a particular complex is fine tuned by the exact nature of the pigments and the organization of the pigment molecules of the complex.

We conclude this section on carotenoids by

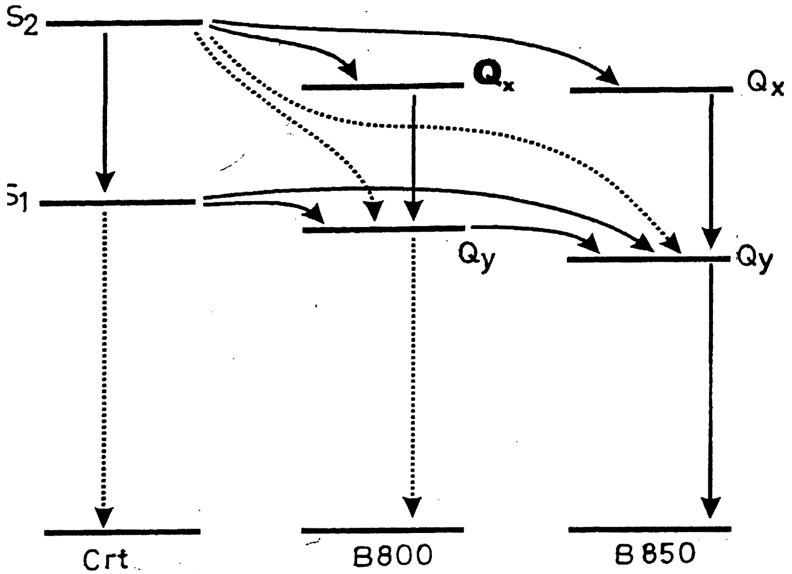

Fig. 3 Scheme of the energy levels together with excitation transfer and relaxation processes involved in LH2. Solid lines show the major and dotted lines the minor transfer/relaxation channels. We point out that the precise position of Crt S_1 energy level is not known.

briefly discussing some recent results of ultrafast carotenoid band shifts. Following excitation with a femtosecond pulse of the BChl Q_y bands of B800 and B850 of LH2 of *Rb. sphaeroides*, distinct changes in the carotenoid S_2 absorption spectrum between 430 and 530 nm were observed[55]. Femtosecond transient absorption spectra and kinetics were measured, revealing an ultrafast carotenoid response to the excited BChl pigments. The observed Crt response (Fig. 4) was interpreted as a Crt electrochromic response to the induced local electric fields from the photoexcited BChl B800 and B850 molecules. The change in dipole moment ($\Delta\mu_{B800}$ ~1D; $\Delta\mu_{B850}$ ~3D[67]) upon excitation creates an electric field change of the order of 10^8 V/cm at a distance of ~5Å from the BChl molecule, according to a simple point dipole approximation. Since the field strength falls off with a r^{-3} distance dependence, even at 20 Å from the excited BChl molecule the field strength is similar to the uniform trans-membrane fields used in Stark and ion gradient experiments of Crt electrochromic band shifts[68-70]. The two spectra in Fig. 4A measured at different times after excitation of B800 show that the response of the Crt to the local field is different when the excitation is located on B800 and B850, respectively. In the spectrum measured at 500 fs the excitation energy is primarily localized on B800, while at 10 ps energy transfer to B850 has occurred (with a time constant of 1.3 ps at 77K, see below); direct optical excitation of B850 gives a spectrum identical to the 10-ps spectrum with B800-excitation. A measurement of the kinetics of the Crt response (Fig. 4B) shows that the amplitude of the Crt response decays with a time constant exactly matching the B800 → B850 energy transfer. Thus, the Crt response is a direct sensor of the energy transfer between the BChl molecules. These results are indicative of a new property of carotenoids that is manifested as a unique ability to detect and report changes in their immediate environment, thereby serving as sensitive probes of local dynamics and structure. Extensions of this work to other LH2 and LH1 complexes[71] as well as to LHC2 from plants[72], now start to explore the generality of the observation as a probe of excitation dynamics and interactions in pigment-protein complexes.

5 B800 to B850 Energy Transfer

This transfer step is probably one of the best studied kinetic processes in bacterial light harvesting. Early time-resolved experiments found that excitation transfer from B800 to B850 in *Rb.*

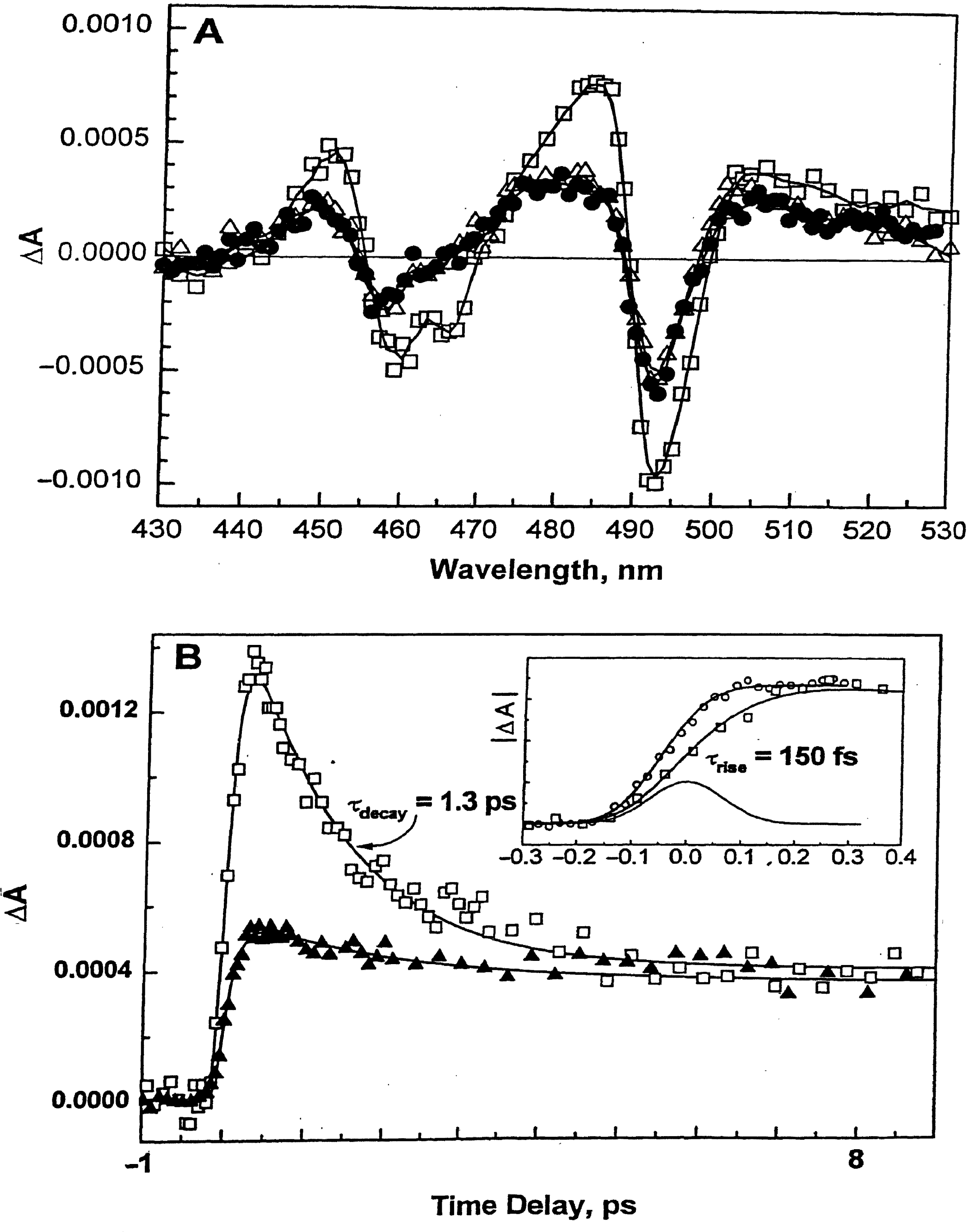

Fig. 4 (A) Carotenoid electrochromic shift spectrum measured at different times after excitation of the B800 pigment with a ~100 fs pulse. The spectra with open symbols were recorded 500 fs (squares) and 10 ps (triangles) after excitation in the B800 band at 795 nm. The spectrum with filled circles was recorded at ~2 ps after excitation in the B850 band at 865 nm. (B) Transient absorption kinetics recorded at 494 nm and 77 K; open squares, excitation at 795 nm and filled triangles excitation at 865 nm. Shown in the inset is a comparison of rises of the signal measured at 494 nm (open squares) and 530 nm (open circles). The signal measured at 530 nm is due to the excited state absorption of B800 and is therefore characterized by an instantaneous (pulse-limited) rise. Figure taken from ref.[55].

sphaeroides occurs on a picosecond or shorter time scale[17,73-76]. In subsequent work with sub-picosecond resolution, Shreve *et al.*[63] estimated the transfer step to be 0.7 ps at room temperature. This time constant has been confirmed a number of times with femtosecond time resolution[33,77-79]. A very similar rate for B800 to B850 transfer has also been found in two different LH2 complexes from *Rps. acidophila*[80,81]. For all species studied it was reported that the transfer time increases upon lowering the temperature, being 1.2 ps at 77 K[33,82] and 1.5 ps at 4 K[33] in *Rb. sphaeroides.* Fig. 5A shows the B800 → B850 transfer measured as the decay of the B800 ground state bleaching and stimulated emission at 4 K, 77 K and 300 K, while the kinetics in Fig. 5B illustrates the same process but now as the rise of the B850 bleach/stimulated emission. It is seen that the two different ways of measuring the B800 → B850 energy transfer gives perfectly matching time constants. Somewhat longer transfer times were extracted from hole burning measurements at 4 K[83,84].

The B800-B850 coupling of ~30 cm^{-1} suggests that the transfer occurs via the incoherent Förster transfer mechanism. It was realized that the spectral overlap where only 0-0 transitions of a donor and acceptor are involved is not large enough to explain the fast B800 to B850 transfer because of a relatively large energy gap and it was suggested that certain BChl *a* vibrational modes are involved in this step[84]. In order to examine this process in some detail, the B800 → B850 transfer was measured in a series of mutants with gradually blue-shifted B850[83,85] and B800[86] absorption bands. A single or double mutation of the tyrosine+13-tyrosine+14 motif of the α-polypeptide of LH2 of *Rb. sphaeroides* results in a shift of B850 to B839 and B826[9], respectively. In a similar way, mutation of βArg–10 blue-shifts the B800 band[86]. The experimentally observed variations of B800 → B850 transfer times with the energy gap between the donor and acceptor pigments of LH2 measured at 77 K was qualitatively reproduced by spectral overlap calculations[85-87]. Also the measured temperature dependence of the B800 → B850 transfer time could be accounted for with these calculations using the Förster transfer model. However, the above calculations did not provide an absolute value of the transfer rate. A more recent and quantitative Förster calculation of this energy transfer step[33,59] using reasonable values for the Franck-Condon factors of the vibrational modes of BChl *a*, which are essential to account for the spectral overlap between the B800 fluorescence and the

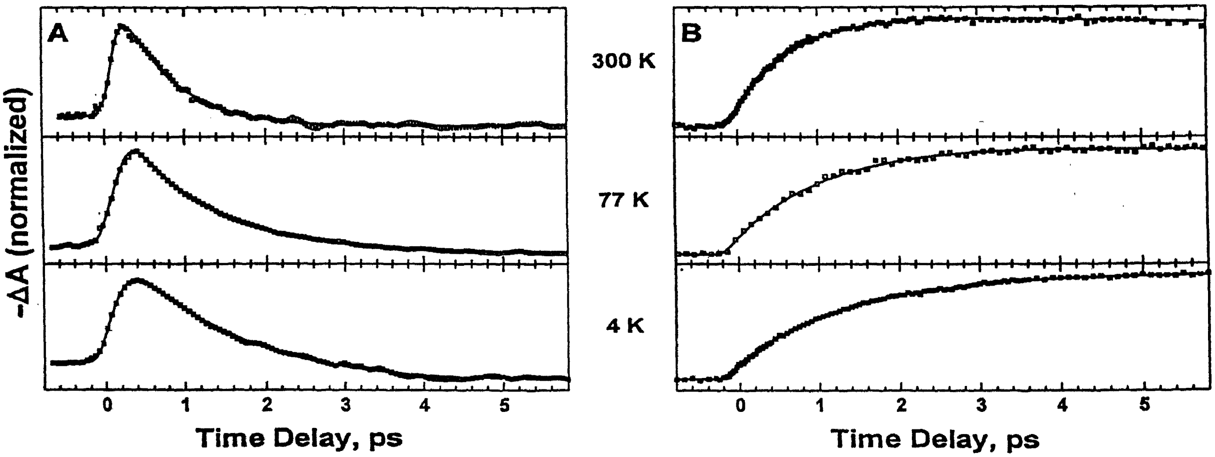

Fig. 5 (A) Two-color transient absorption signals in chromatophores of *Rb. sphaeroides* at three different temperatures. Pump and probe wavelengths are 795 and 800 nm, respectively. The kinetics were fit with a sum of three exponentials. The shortest time ~0.3 ps is the same in all curves and reflects the internal dynamics in B800. The second time constant was 0.7 ps at 300 K, 1.2 ps at 77 K and 1.5 ps at 4 K and it corresponds to B800 → B850 transfer. The third time constant is long and corresponds to the decay of the excitation in B850 (Taken from ref.33]). (B) B800 → B850 transfer measured as the rise of the B850 bleach/stimulated emission at the same three temperatures as in (A); excitation is at 800 nm and probing at 870 nm ?? The risetimes at each temperature match the 0.7, 1.2 and 1.5 ps decay times in (A) (Herek *et al.* unpublished)

B850 absorption, gave a B800 → B850 transfer time which is considerably longer than the measured one, suggesting that some additional channel may be operative in the B800 → B850 process. Based on hole burning experiments at high pressure[88] and Redfield theory calculations[89] it was suggested that this additional channel could be the interaction of the B800 excited state with the upper exciton band edge of B850. Indeed, several studies have suggested that the weakly-allowed higher edge of the B850 exciton band could be resonant with B800. For example, Wu *et al.*[88] found that the change of the cutoff between narrow and wide spectral holes burned into the B800 band correlated with the pressure shift of the B850 band relative to the B800 band, suggesting that an upper excitonic component of B850 is shifting under the B800 band. Pullerits *et al.*[33] analyzed the shape of the B800 absorption spectrum and concluded that it cannot be reproduced by the known spectral properties of BChl *a* suggesting that a considerable amount of the blue wing absorption of B800 originates from the B850 upper exciton component. Recent CD measurements on LH2 antenna complexes from a B800-less mutant of *Rb. sphaeroides* have provided direct evidence that a broad, relatively weak feature of the CD spectrum around 780 nm belongs to the upper exciton component of B850 BChls[90].

Thus, it appears that there are two qualitatively different contributions to the spectral overlap governing B800 to B850 transfer. First, there is a "normal" overlap mediated by phonons and vibrations; second, there is a direct transfer to the upper exciton component of B850 positioned somewhat to the blue of B800. In this picture the temperature dependence of the transfer in different species has different origin. In wild type *Rb. sphaeroides*, the energy gap between the donor and acceptor is substantially larger than kT, which implies that the vibronic part of the spectral overlap does not change with lowering temperature. At the same time, the overlap with the 780 nm upper excitonic component is reduced because of the narrowing of the B800 spectrum. In addition, at low temperature fast transfer among inhomogeneously distributed B800 molecules localizes the excitation on the red part of the B800 inhomogeneous distribution (see next section) which further slows down the upper exciton component induced transfer. At 4 K this transfer channel is probably inactive. If no other transfer channel is present, then the 0.7 ps and 1.5 ps transfer times at 300 K and 4 K in *Rb. sphaeroides* suggest that at room temperature half of the transfer occurs via the "normal" vibronic band Förster overlap whereas the other half involves the upper exciton level of the B850 band at 780 nm. On the other hand, in the B800-820 of *Rps. acidophila* the upper exciton component should be around 750 nm, which means that it no longer contributes to the B800-B820 spectral overlap even at room temperature. Since the energy gap between the bands is comparable to kT at room temperature, the spectral overlap of the phonon side bands reduces if the temperature is lowered, explaining the observed slowdown of the transfer from 0.75 ps at 300 K to 0.9 ps at 77 K[81].

Finally, we note that also higher order superexchange type coupling mediated by nearby chromophores, particularly carotenoid molecules, has been suggested as an additional possible transfer channel[33,61]. From the crystal structure of LH2 of *Rps. acidophila* it is evident that the carotenoid molecules are within very short distance from both the B800 and B850 BChl *a* molecules. Carotenoid S_2 state mediated B800-B850 coupling was recently assessed by Krueger *et al.*[59] using *ab initio* calculations. The authors found that the carotenoid S_2 state can only lead to a small additional coupling of 2-3 cm^{-1}. At the same time the authors have found a substantial mixing of the carotenoid and B850 orbitals, which could have a large influence on the B800-B850 coupling. Whether these types of higher order transfer processes are really functional in photosynthetic light harvesting remains to be seen.

6 Energy Transfer among the B800 Bacteriochlorophylls in LH2

From the structures of LH2 of *Rps. acidophila* and *Rs. molischianum* it is clear that the interaction between B800 pigments is sufficiently weak to avoid excitonic effects, while at the same time sufficiently strong to allow fast energy transfer, assuming a reasonable value for the overlap between B800 emission and B800 absorption[13,91-93]. Measurements of the B800 intraband energy transfer in native LH2 complexes presents several difficulties. The B800 excited state lifetime is very short due to the fast B800 → B850 transfer (see section 5); the B800 absorption band is relatively narrow, implying small spectral changes associated with transfer between the inhomogeneously broadened B800 pigment molecules, in particular when short and spectrally broad pulses are used. Nevertheless, spectrally resolved and polarization sensitive transient absorption measurements provided clear evidence of a fast intraband B800 transfer. Experimentally, several groups have reported the presence of an additional relaxation processes in the B800 band of LH2 besides the decay of the B800 excited state related to the B800 → B850 transfer. In general, the evidence was most clear at low temperatures and intraband excitation transfer and/or vibrational relaxation were suggested as possible kinetic processes. The earliest observation originates from the work of Kramer *et al.*[13], who based on steady-state fluorescence depolarization measurements estimated the rate of B800→B800 energy transfer to be about 500 fs, translating into a B800-B800 distance of about 21 Å, very similar to the 1995 crystallographic value[18].

Direct evidence for B800-B800 transfer in *Rb. sphaeroides* and *Rps. palustris* was first obtained at room temperature by Hess *et al.*[77] who observed in femtosecond pump-probe measurements a clear anisotropy decay with a time constant of about 1 ps. This time constant appeared to be too slow to explain the fluorescence depolarization by Kramer *et al.*[13] At the end of this section we provide a possible explanation to this discrepancy. These authors also observed a fast ~300 fs component in the isotropic decay of B800, which was assigned to energy transfer between almost parallel B800 molecules and possibly to vibrational relaxation.

Time-resolved experiments on a variety of LH2 systems largely confirmed the presence of a fast relaxation process in the B800 band at low temperatures[80,88,92,93]. In LH2 of *Rb. sphaeroides*, Hess *et al.* found a 300 fs relaxation channel in both isotropic and anisotropic decays (Fig. 6). The results were modelled as a hopping in a ring with an average pairwise nearest neighbour transfer time of 350 fs[93]. In the same LH2, Monshouwer *et al.* found that in the blue wing of the B800 absorption profile the major isotropic decay occurred with a 400-500 fs lifetime component, which matched a rise time in the red tail[82,92]. A very similar 400 fs intraband relaxation process was observed by Wu *et al.*[88] for B800 in LH2 of *Rps. acidophila* at 19 K and recently for the B800-820 LH2 from *Rps. acidophila* by Ma *et al.*[81] The latter authors also observed a very similar phase in the low temperature anisotropy decay, measured at the same probing wavelength. Also recent work by Wendling *et al.*[94] at 77 K on B800-850 LH2 of *Rps. acidophila* is fully consistent with a ~500 fs blue to red relaxation and an anisotropy decay with a closely related time constant. In the B800 band of LH2 of *Rs. molischianum*[94] studied at 77 K, both the blue-to-red isotropic decay and the absorption anisotropy decay occur in about 0.8-0.9 ps, a factor of 2 slower than observed in LH2 of *Rps. acidophila* and *Rb. sphaeroides*. The existence of a fast relaxation process in the B800 band at low temperature is supported also by hole burning experiments[95,96].

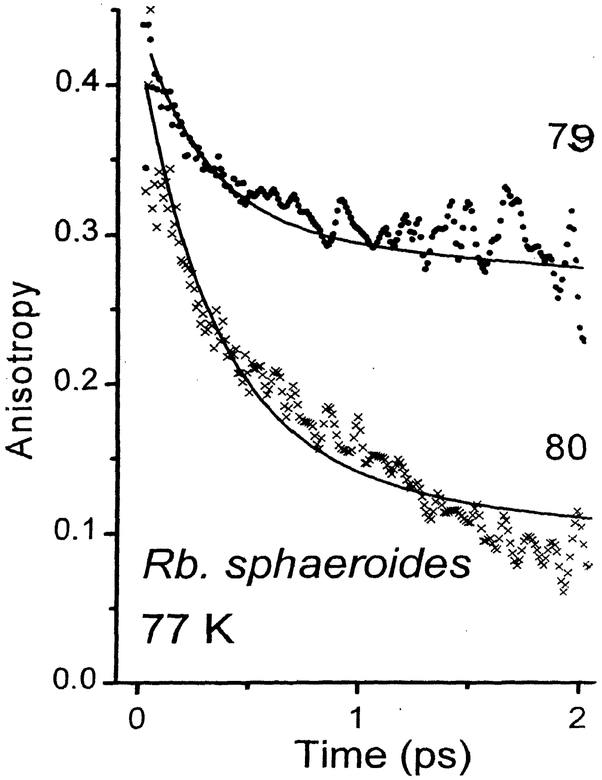

Fig. 6 Anisotropy decay of B800 of *Rb. sphaeroides* at 77 K. The solid curves represent the fit with a two-exponential decay with time constants 0.3 and 1.5 ps with amplitudes 0.12/0.2 and 0.08/0.1, respectively, and a constant level 0.2/0.1 at 790/800 nm. (Taken from ref. [93])

As mentioned above, at room temperature the rate of energy transfer among the B800's appears to slow down[77]. However, due to the fact that the time window available for the observation of the depolarization has significantly shortened at room temperature as a result of the faster B800→B850 energy transfer (see above) the depolarization times will be less precise and the results here are not as consistent as for low temperature. Ma *et al.*[80] report 300-400 fs anisotropy decays in the B800 band of LH2 (B800-850) of *Rps. acidophila* at room temperature, but the same group reports an anisotropy decay of more than 1 ps in the closely related B800-820 of the same purple bacterium[81]. This latter value is close to the value by Hess *et al.* for LH2 of *Rb. sphaeroides*[77] and that of Kennis at al. for LH2 (B800-850) of *Rps. acidophila*[97]. Photon echo and transient grating experiments on LH2 of *Rb. sphaeroides* by Joo *et al.*[78] have also been taken to reflect rather slow energy transfer among the B800's at room temperature.

In general, we believe that energy transfer within the B800 ring can be well understood on the basis of the Förster equation for energy transfer in the weak coupling limit. For LH2 of *Rps. acidophila*, the estimated nearest neighbour coupling is about 25 cm^{-1}, which is one order of magnitude less than the site inhomogeneity (about 150 cm^{-1}) and the electron-phonon coupling. Quantitative estimates of the rate of B800-B800 energy transfer systematically arrive at numbers in the range of a few hundred fs[33,59] up to 1 ps[88,92]. Since for the isotropic low temperature experiments the observed decay reflects the sum of all possible decay paths, *i.e.* for a blue B800 energy transfer to two neighbours plus downhill energy transfer to B850, a neighbour-to-neighbour transfer rate of 0.5–1 ps would be more than sufficient to account for the experimental observations.

Similarly, the anisotropy decay measurements at 77 K by Hess *et al.*[93] yielded an average nearest neighbour pairwise transfer time of 300-400 fs. The Förster equation correctly predicts the difference in the B800→B800 energy transfer rate between *Rps. acidophila* and *Rs. molischianum*, the latter being about two-fold slower due to the smaller dipole-dipole coupling. And perhaps most importantly, the temperature dependence of the Förster overlap integral can explain the decrease of the B800 to B800 transfer rate at room temperature. Calculations predict that due to the broadening of the homogeneous bands the transfer rate decreases between 77 K and room temperature[33,93].

7 Energy Transfer within the Strongly Coupled B850 Ring

Dynamics of the Excitation Transfer and Nature of the Excited State

From the published LH2 structures it is immediately clear that the BChl molecules in the B850 ring are strongly coupled and in fact both calculations and experiments show that the interaction between the BChls within a subunit and between BChls on adjacent subunits is of the order of 300 cm^{-1} [39,59,79,90,92,98]. There is now extensive evidence that the absorption bands of LH2 and LH1 are strongly inhomogeneously broadened[84,99,100-102], and non-linear spectroscopic experiments have shown that this is also true at room temperature[39,78,103-105]. Estimates in these papers for the amount of disorder range between 250 and 500 cm^{-1}, and these values are generally larger than the amount of excitonic coupling. Finally, electron-phonon/vibration coupling, which would be responsible for a dynamic localization of the excitation is estimated to be in the few hundred cm^{-1} range[107,108].

Since the mid-eighties, a multitude of time-resolved absorption, fluorescence and more recently non-linear spectroscopic experiments were performed on LH2, LH1 and more intact systems (for reviews of the earlier work see refs. 1-5). The general conclusion was that within a picosecond after excitation, the intracomplex energy transfer is more or less complete, requiring average single site lifetimes of a few hundred fs at most. In subsequent experiments aimed to time-resolve the B850 and B875 intraband dynamics, fast isotropic kinetics were measured within the B850/B875 band, exploiting the equilibration among an inhomogeneous spectral distribution of pigments exhibiting ultrafast energy transfer[30,39,103,108]. Alternatively, the intraband dynamics was studied by time resolved polarized spontaneous emission[79,104], or by polarized pump-probe experiments[30,39,108]. Recently, three-pulse stimulated photon echoes were obtained that measure all intraband spectral dynamics, including energy transfer[105,107].

The dynamic red-shift[30,108] and time resolved fluorescence depolarization[79] experiments resulted in very fast, 50 to a few hundred fs decay times. Modelling of these processes as a sequence of hopping events of localized excitations resulted in single site lifetimes of approx. 100 fs[30,79,103,104]. These models assumed the excitation to be localized to BChl dimers. From recent 3-pulse photon echo peak shift (3PPEPS) experiments on LH1 and LH2[107] and the LH1 subunit B820[105] it was similarly concluded that the excitation is localized to a small number of Bchls. It was suggested that on a time scale of less than 50 fs, due to fast fluctuations in the protein environment, the excitation becomes localized on a small part of the ring, possibly an $\alpha\beta$-BChl$_2$-heterodimer. In the peak shift decay, which is a direct measure of the transition frequency correlation function, this initial phase was followed both in LH1 and LH2 by an exponential phase that was interpreted as a loss of rephasing capability of the system due to energy transfer. For both light-harvesting complexes the homogeneous broadening was estimated to be 200 cm^{-1}, the inhomogeneous broadening 500 cm^{-1} and the hopping time to about 100 fs. This interpretation was supported by a 3PPEPS experiment on the LH1 subunit, B820, in which the 100 fs phase in the decay of the peakshift ascribed to energy transfer was no longer present and replaced by a non-decaying component arising from inhomogeneous broadening[107]. The similarity between the 3PPEPS of LH1 and B820, apart from the energy transfer phase was taken to suggest that in LH1 the elementary excitations are delocalized over small units, possibly dimers.

The room temperature polarized pump-probe experiments on LH1 and LH2 by Chachisvilis *et al.*[39,109] resulted in similar fast anisotropy decay times. For LH1, about 100 fs in the major absorption band and about 200 fs in the stimulated emission region; for LH2, 60 fs in the major absorption band and about 200 fs in the stimulated emission region. In an attempt to reconcile the isotropic and anisotropic decay times measured in LH2 it was concluded that a monomer-to-monomer hopping process was not consistent with the results and on the basis of this the authors suggested that the elementary excitation in LH1 and LH2 had a more collective nature. A very similar conclusion was drawn by Monshouwer *et al.* from isotropic and anisotropic decay experiments on LH1 of *Rps. viridis*[30].

Upon lowering the temperature, the inhomogeneous nature of the absorption band is strongly enhanced, resulting in multiexponential and wavelength dependent kinetics with phases ranging from the 100 fs region to the many picosecond time-domain[39,110], in qualitative agreement with theoretical predictions[111]. The experiments by Chachisvilis *et al.*[39] at cryogenic temperatures showed that excitation in the blue wing of the B850/B875 absorption still resulted in ultrafast downhill energy transfer. A very similar fast downhill energy transfer at 4 K was observed for *Heliobacterium chlorum*[112] and *Rps viridis* LH1[30]. The model developed for the spectral dynamics due to hopping energy transfer to some extent predicted the observed temperature dependence[110], assuming a model for the spectral properties of a single site as a function of temperature[113]. However, a close comparison of the isotropic and anisotropic kinetics measured at 4K through the band resulted in a similar discrepancy as mentioned-above at room temperature[39] and again led to the conclusion that the elementary excitation in LH1 and LH2 is not localized on a monomer.

At low temperature, a new dynamic feature was observed in LH2 at longer delays by Chachisvilis *et al.*[39] The stimulated emission/bleaching band broadens and splits into two bands in about 3 ps. The new band is located at about 870 nm and it continues to move further to the red and broadens on the tens of picoseconds time scale. Early 4.2 K steady state fluorescence measurements of a LH1-less mutant of *Rb. sphaeroides* showed an unusually large Stokes' shift[114], which was explained as an emission from a minor long-wavelength component of B850. On the other hand, recent time resolved data were interpreted as a stimulated emission from the lowest exciton component of a disordered ring of B850[115,116], whereas the slower phases of the dynamics were assigned to the transfer among inhomogeneously distributed rings[116]. The zero phonon hole action spectra have also been interpreted as indication that the lowest exciton component of B850 lies at 870 nm[91]. It is interesting to note that recent Stark hole burning measurements[117] have found a very small dipole moment change for this low exciton band. At the same time the polarizability change in B850 is rather large[67] leaving open the possibility to explain the slowly relaxing red emission as a polaron formation[118]. The fact that the effect is much less pronounced in LH1 suggests that it may be related to the tendency of LH2 to form very large aggregates[119,120] or to some LH2-specific impurity.

Localization of the Exciton in the Presence of Static and Dynamic Disorder

In the perfect exciton model the excitonic states of the LH2 ring are calculated by diagonalization of the exciton Hamiltonian, where all the site energies have been chosen to be identical. In such a model, the lowest excitonic state gains very little dipole strength, since all the dipoles are almost in the plane of the ring. By far the largest part of the dipole strength is collected in the next degenerate pair of excitonic states, the k = ±1 states, and all the other states contain no (or very little) dipole strength. In such a scheme, the low temperature radiative rate from the lowest level would be negligible and the state would not be fluorescent. Experiments with LH2 from *Rb. sphaeroides* and *Rps. capsulatus* have shown that this is not the case[37]. However, as mentioned above we know from hole burning and non-linear spectroscopy experiments, that in LH2 the site energies of the BChls are distributed in a Gaussian fashion, due to some small fluctuations in the pigment protein structure that modulate the transition frequency. If these fluctuations are 'static', i.e. they vary on a timescale much slower than the fluorescence (which of course is not really true, see below), then one can calculate the linear optical properties of the LH2 ring by averaging the outcome of the diagonalization procedure over all possible realizations of the energetic disorder. The temperature effect can be modelled by assuming that the excited state relaxation creates a Boltzmann distribution over the various exciton states. The result of such a calculation is that for increasing disorder (increasing Δ/V ratio) the previously forbidden exciton states gain dipole strength at the expense of the k=±1 states[6,35,39,40]. The calculation demonstrates that disorder in the site energies is an essential ingredient to understand the spectroscopy of LH2, and its major effect is that it destroys the 'delocalized exciton' picture that was advanced by some authors[18,98,121].

We saw how the static disorder destroys the perfect delocalization of the exciton states. It is clear that electron-phonon interaction (dynamic disorder), in general, further localizes the states. In order to study the effect of weak electron-phonon coupling on the initially created coherent superposition of exciton states, a function $C_n(t)$ was defined via density matrix in site representation as[40]

$$C_n(t) = \sum \left|\left\langle \rho_{i,j+n}(t) \right\rangle\right| \qquad \ldots (1)$$

The width of this function gives a convenient measure of delocalization. $C_n(t)$ was calculated for B850 molecules of LH2 for various parameter sets (Fig. 7 caption)[40]. Panel (A) of Fig. 7 corresponds to the ideal case without disorder. The symmetry of the exciton states of a ring gives $C_n(t)$ a sinusoidal form reflecting a fully coherent excitation, which does not change with time after the pump pulse is over. If we switch on the electron-phonon coupling (panel (B) in Fig. 7), we see that the initial coherence over the ring is not fully established since the dephasing and relaxation are effective already during the pulse. We observe how the system rapidly relaxes towards an equilibrium distribution which leads to an almost complete decay of $C_n(t)$ for larger n. We point out here that the equilibrium state reached in Fig. 7 does not imply that we have nonzero off-diagonal elements

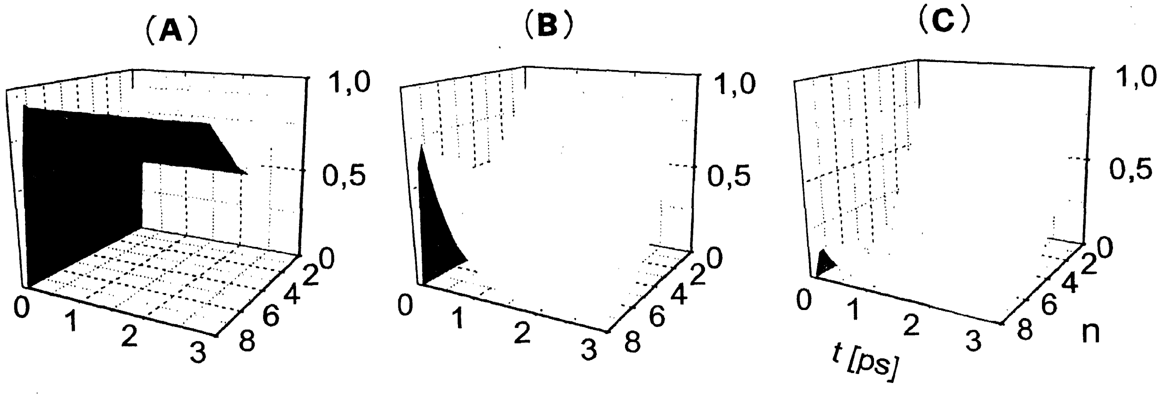

Fig. 7 The one-exciton coherences in the LH2 ring (B850) according to ref. 40. (A) a homogeneous system without electron-phonon interaction. (B) Homogeneous system with electron-phonon coupling 50 cm^{-1}, the spectral density has a maximum at 100 cm^{-1}, T = 280 K. (C) Electron phonon coupling as in (B) and spectral inhomogeneity with FWHM ~700 cm^{-1}. (Taken from ref. [40])

of the density matrix in the delocalized exciton basis. In fact we have an incoherent superposition of thermalized excitonic eigenstates. Finally, if we include both static and dynamic disorder we see that the long range coherence initially created by the laser pulse is further suppressed (panel (C) of Fig. 7). Comparison with the homogeneous case (middle panel) reveals that the final function is narrower if disorder is taken into account. This suggests that disorder plays a stronger localizing role than the electron-phonon interaction in B850. A similar conclusion was recently reached in a theoretical work based on the comparison of the superradiance in J-aggregates and in light-harvesting systems[122].

The behaviour of $C_n(t)$ reflects the dynamic exciton delocalization. If we take the full width at half maximum of $C_n(t)$ as the extent of exciton delocalization, we can estimate from the upper panel of Fig. 7, which corresponds to the parameters of the B850 ring of LH2, that the excitation is coherent over about 4 monomeric BChl molecules. As we will see below, a similar number has been suggested based on analyses of experimental results obtained with various methods: analyses of the absorption difference line shapes[39,123], superradiance[37], theoretical considerations[124] and the amount of induced absorption per absorbed photon[115]. At the same time, considerably larger values of the coherence size of the density matrix of B850 was reported by Mukamel and coworkers[125]. A careful comparison of used parameter values suggests that, at least a partial, reason for this discrepancy is the lower value of inhomogeneity used in ref.[125] as compared to refs.[35, 37, 39, 40].

One possibility to quantitatively assess the size of the exciton is based on the idea that the nonlinear optical properties of aggregates are sensitive to the delocalization length of the electronically excited states. For example, in a linear aggregate of two-level molecules one can calculate the exciton delocalization length from the approximate expression $\Delta\omega \approx 3\pi^2 V(N+1)^{-2}$, where $\Delta\omega$ is the difference between pump-pulse induced bleach (ground state to one-exciton transition) and pump-pulse induced absorption (one-exciton to two-exciton transition) maxima, V is the dipole-dipole interaction between nearest neighbours and N is the exciton delocalization length[126]. However, monomeric BChl *a* has a strong excited state absorption in the region of the Q_y transition[93, 127] and therefore B850 is much more realistically described as an aggregate of multilevel (not two-level) molecules where the one- to two-exciton transition has a significant intramolecular component where two photons double-excite a single molecule.

Simulations based on the model which includes monomeric doubly excited states and also accounts for the circular organization of the bacteriochlorophyll molecules of B850 suggested that the thermalized delocalization length (2 ps after excitation of B800) of the B850 exciton is 4±2 BChl molecules[109], the relatively large error limits allowing for the uncertainties in the dipole strength of the monomeric excited state absorption. In subsequent more detailed calculations, to fit experimental data of LH2 in the temperature range 296 - 4 K, spectral inhomogeneity of the BChl molecules was also included[39]. It was found that the quantitative value for the delocalization length depends significantly on the definition used. In this work the exciton delocalization length was defined as the FWHM of the ensemble averaged auto-correlation function of the lowest exciton state. It was found that the exciton is delocalized over four BChl *a* molecules of LH2 at ~1 ps after the excitation (Fig. 8)[39]. A recent calculation of the 1 ps room temperature and 77K pump-probe spectra measured for *Rps. viridis* resulted in a very similar estimate[128].

A second measure that has been considered is the amount of photobleaching of the major transition[129] or the amount of induced absorption per absorbed photon and surprisingly high numbers have been reported for the amplitude of the B850/B875 bleaching following excitation[130-132] or the amount of induced absorption[121]; these effects have generally been interpreted as arising from totally delocalized excitons. However, due to a multitude of effects, singlet-singlet and singlet triplet annihilation amongst them, these experiments have also been shown to be very sensitive to badly defined experimental conditions. Recently, Monshouwer and coworkers[133] attempted to measure quantitatively the amount of B850 bleaching per absorbed photon relative to the amount of bleaching in the LH1 dimeric subunit B820 and from this experiment it was concluded that the observed bleaching in LH2 corresponded with that expected for an excitation delocalized over about 4 BChls, a result very similar to the earlier B850

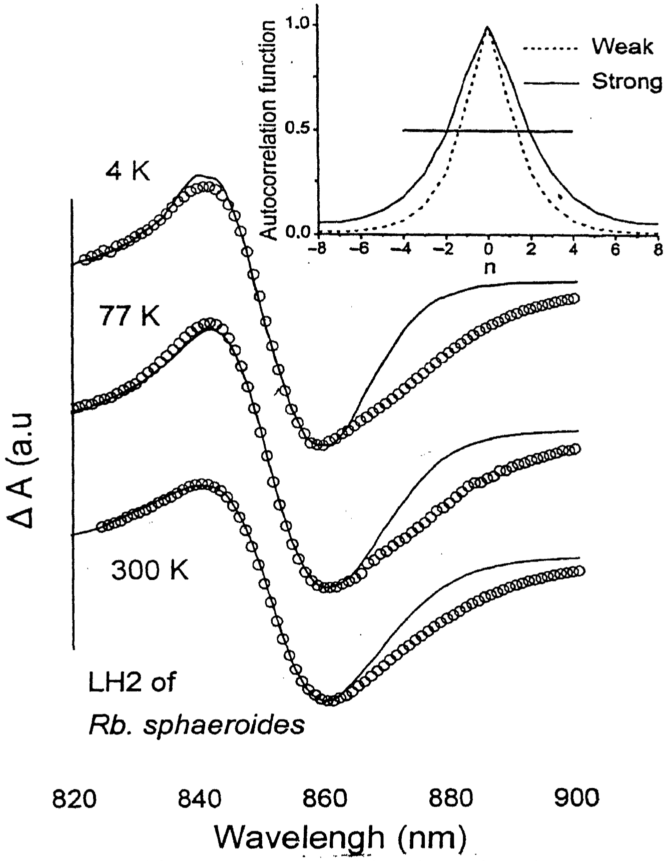

Fig. 8 Experimental (circles) and calculated (lines) transient absorption spectra of LH2 at three different temperatures. Experimental spectra are recorded 1.5 ps after excitation at 800 nm. Calculations are carried out with weak interaction ($V = 200\ \mathrm{cm}^{-1}$), FWHM of the inhomogeneous distribution is $550\ \mathrm{cm}^{-1}$, and homogeneous widths are 25, 50 and $75\ \mathrm{cm}^{-1}$ for 4, 77, and 300 K, respectively. In the inset, we present the autocorrelation function of the lowest state of B850 corresponding to the fits in case of strong ($V = 450\ \mathrm{cm}^{-1}$, solid) and weak ($V = 200\ \mathrm{cm}^{-1}$, dashed) interaction. (Taken from ref.[39])

absorption difference lineshape analyses[39,109] and to that obtained from simultaneously fitting the shape of the pump-probe spectra of B820 and B850[134].

A third measure of the delocalization length is given by the so-called superradiance, or better the radiative rate of LH2. At room temperature, the emitting dipole strength is about 2-3 times that of monomeric BChl *a*, and for LH2 is almost independent of temperature down to 4 K[37]. A calculation of the superradiance as a function of temperature reproduces these experimental observations if significant energetic disorder is assumed[109]. These experiments suggest a coherence length of a few BChl *a* as measured by the FWHM of the averaged exciton wavefunction and this corresponds nicely to the outcome of the pump-probe results discussed above. For LH1 at room temperature, the superradiance is very similar to that of B850, but upon lowering the temperature the emitting dipole strength increases suggesting that for LH1 disorder plays a somewhat less dominant role than for LH2.

Finally, for several systems including LH2 of *Rb. sphaeroides*[28,29,107], LH1 of *Rb. Sphaeroides*[28,29,104,106-108], LH1 of *R. rubrum*[29,106], LH1 of *Rps. viridis*[30] and B820[105,106,108,135] low frequency oscillatory phenomena have been observed in transient spectroscopic experiments following excitation with short (< 100 fs) pulses. In general these have been attributed to coherent nuclear motion in the excited state, possibly in combination with ground state wavepacket motion. The most surprising observation is that these nuclear coherences survive for several picoseconds, a time window in which many energy transfer steps have taken place and the excitation has spectrally "equilibrated". So far there is not a good model to explain this. Nevertheless, it may be clear that these observations are very difficult to reconcile with the traditional Förster model for energy transfer.

8 The PSU - Energy transfer over the Antenna Network and Trapping by the Reaction Center

As illustrated in Fig. 9, the LH2 peripheral antenna complex is just one part of the complete photosynthetic unit (PSU), the minimum pigment-protein unit capable of performing the primary photosynthetic processes. We will briefly describe the function of LH2 within this unit and we will also show how the different protein complexes cooperate to catch and transfer energy to the reaction center. The first step in moving the energy towards the reaction center after it has been absorbed by the LH2 complex, is a transfer to another LH2 (B850) or LH1 ring. Experimentally it is difficult to directly study LH2 ring-to-ring transfer (at least at ambient temperatures) since there are no (or very small) spectral changes associated with this process (all LH2 rings are virtually identical). Time resolved absorption and fluorescence anisotropy are not useful either, because the excitations are already depolarized (within the plane) through the rapid motion inside one ring and very little further depolarization occurs as a result of the ring-to-ring migration. However, LH2 → LH1 ring transfer is easily observable as a result of the differing absorption and fluorescence spectra of the two complexes. Since we do not expect the distances between LH2 rings and between LH2 and LH1 rings to be much different, and since the donor-acceptor spectral overlaps for B850 → B850 and B850 → LH1 energy transfer are quite similar (at least at room temperature when the spectra are broad), we can approximate all ring-to-ring transfer processes with that for LH2 (B850) → LH1.

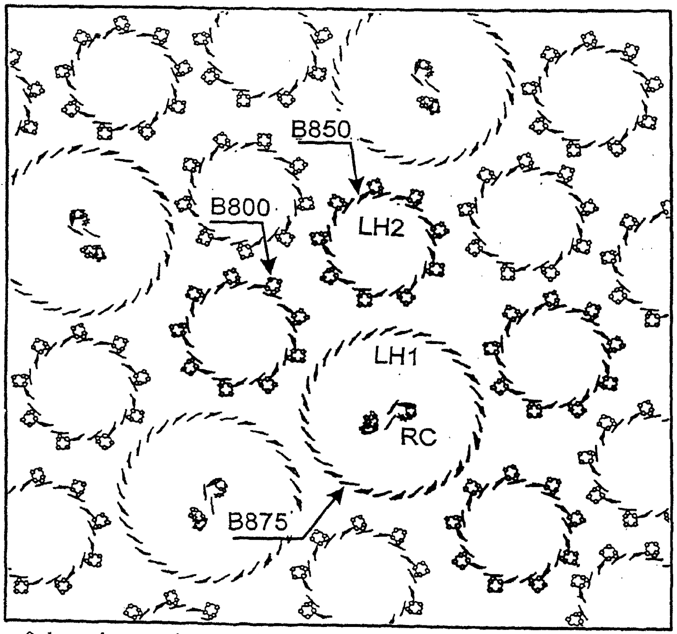

Fig. 9 Model of the primary photosynthetic machinery of purple bacteria based on the known structural data. Only bacteriochlorophyll molecules are shown. The highlighted five rings (four LH2s and one LH1+RC) correspond to a PSU which in this ratio satisfies the approximate 1:2:1 ratio of B800:B850:B875 band intensities in *Rb. sphaeroides*. The boundaries of PSUs are tentative and excitation transfer occurs between different PSUs which all together form large domains. The length of the side of the frame is about 330 Å.

The first results for this process appeared from absorption and fluorescence measurements with picosecond time resolution on several different species[2,75,136-140]. Due to the limited time resolution of these experiments and complex kinetics in intact pigment systems, the process was not clearly resolved in most cases. Nevertheless, these early results suggested that the LH2 → LH1 transfer step occurs on the time scale of 5-40 ps. In a femtosecond two-colour absorption measurement direct information was obtained on the LH2 → LH1 transfer step[141]. The build-up of LH1 excitations in *Rb. sphaeroides* at room temperature and 77 K was measured following excitation of B800, and the B850 → LH1 transfer step was found to occur with a time constant of ~3 ps at room temperature and ~5 ps at 77 K. From femtosecond transient absorption experiments similar to those of Hess *et al.*[141], Nagarajan and Parson[142] also concluded that LH2 → LH1 ring-to-ring transfer occurs with a ~5 ps time constant, and in addition they observed a slower phase (~25 ps) in the LH2 → LH1 process, which they ascribed to energy migration within the LH2 pool prior to transfer to LH1. Employing an effective Hamiltonian approach to calculate energy transfer rates between the light-harvesting complexes of a PSU modelled on the basis of the *Rs. molischianum* LH2 structure, Hu *et al.*[143] concluded that LH2 → LH2 and LH2 → LH1 ring-to-ring transfer occurs with the times ~7 and ~3 ps, respectively, in good agreement with the experimental results.

How the light-harvesting antenna makes contact with the reaction center and how energy is transferred into the reaction center (trapped) is an important aspect of the function of the whole photosynthetic unit. Information about this can be obtained by measuring the rate of energy transfer from LH1 to the special pair (P) electron donor in the reaction center, and from it estimating the distance between the LH1 molecules and the special pair. The description of the LH1 excited state is of crucial importance for the result; whether the excitation energy is delocalized over the whole LH1 ring or localized to only a few BChl molecules will obviously be important for interpreting the measurements. A transfer time of ~35 ps was obtained for this process by measuring the decay of LH1 excitations in the temperature range 77-177 K[144,145]. A similar result was obtained by Beekman *et al.*[146] by measuring the overall trapping time for a series of RC-mutants of *Rb. sphaeroides*, having modified charge separation times. From a measurement of core antenna fluorescence upon selective RC-excitation, Otte *et al.*[147] arrived at a similar conclusion. These results show that energy hopping from one ring to another within the PSU is fast as compared to the total ~60 ps lifetime of the excitations in the antenna[16,17,132] and the LH1 → RC energy transfer step[132,144-147]. This implies that energy transfer from the LH1 antenna to the special pair is the rate-limiting step of the overall energy trapping process. The trapping of excitation energy by photosynthetic reaction centers has often been discussed in terms of the "trap-limited" or "diffusion-limited" model and consequently we have termed this new situation "transfer-to-trap-limited" excitation dynamics[111,146,148-151].

From the model of the PSU (Fig. 9), it appears that this slow rate of LH1 → RC energy transfer is a direct consequence of the size of the reaction center protein, which prevents a shorter antenna-special pair distance. It is interesting to speculate about whether this long LH1 - P distance is of any functional importance. A trivial reason is that the distance is just determined by the physical size of the RC proteins, i.e. by the size of the RC required to fulfill its function. Another, more interesting reason to have a large distance between the LH1 BChls and the special pair of the reaction center, could be that the oxidized primary donor (P^+) is a very reactive species. With a too small LH1 – P distance, the antenna BChls could be oxidized by P^+, which would lead to very efficient quenching of the excitation energy within the LH1 antenna. This idea has previously been suggested for the RC of photosystem 2 of green plants for which the oxidized primary donor $P680^+$ has an extremely oxidizing potential. Hence, whatever the reason for the long LH1-P distance is, the organism is faced with the problem of maximizing the LH1 → P energy transfer rate in order to optimize trapping efficiency. The circular arrangement of the LH1-core antenna, where all the antenna pigments can transfer energy to the special pair of the RC with approximately the same rate is obviously one means to increase LH1 → P transfer efficiency. If, for instance, there would only be 4-6 entries into the RC from the LH1 antenna, as was often suggested in the lattice models[152] used before the advent of the crystal structures of LH2 and LH1, the LH1 → P transfer would be many times slower and the trapping efficiency markedly lower than the observed ~95%. In addition, we conjecture that the exciton delocalization discussed in Sections 3 and 7 is another part of this optimization. It can be estimated that for a LH1 exciton of delocalization length of ~4 BChl monomer units, the coupling to the special pair will be approximately four-fold the coupling between a monomeric BChl and P. A four-fold longer trapping time (i.e. 200-250 ps) would decrease the overall trapping efficiency from the observed ~95% to ~80%. These two factors taken together may therefore increase the trapping rate by as much as a factor of ten, as compared with the situation of a core antenna consisting of weakly coupled pigments having only a few entries into the RC. Thus we propose that the ring-like organization of the LH1 core antenna and its strongly coupled BChl molecules, with the centrally positioned reaction center, is essential for the high trapping efficiency in these organisms.

9 Acknowledgements

The authors would like to thank their coworkers of the Department of Chemical Physics, Lund University.Lund, Sweden. The authors are also thankful to Prof. Rienk van Grondelle for many productive discussions. Financial support is acknowledged from the Swedish NFR, the K & A. Wallenberg Foundation, the Crafoord Foundation and the European Union (Contract Nos: SCI-CT92-0796; ERBCHBGCT930361; ERBFMGECT950020).

References

1 R van Grondelle *Biochim Bioplys Acta* **811** (1985) 147

2 R van Grondelle, J P Dekker, T Gillbro and V Sundström *Biochim Biophys Acta* **1** (1994) 1187

3 T Pullerits and V Sundström *Accounts Chem Res* **29** (1996) 381

4 G R Fleming and R van Grondelle *Cur Opin Struct Bio* **7** (1997) 738

5 V Sundström and R van Grondelle In *Anoxygenic Photosynthetic Bacteria* (Eds. R E Blankenship, M T Madigan and C E Bauer) Kluwer Academic Publishers Dordrecht (1995) 349

6 V Sundström, T Pullerits, R van Grondelle *J Phys Chem* (Submitted)

7 L N M Duysens *Doctoral Thesis* State University of Utrecht The Netherlands (1953)

8 K R Miller *Nature* **53** (1982) 300

9 G J S Fowler, R W Visschers, G G Grief, R van Grondelle and C N Hunter *Nature* **355** (1992) 848

10 J D Olsen, G D Sockalingum, B Robert and C N Hunter *Proc Natl Acad Sci* USA **91** (1994) 7124

11 H Zuber and R J Cogdell In *Anoxygenic Photosynthetic Bacteria* (Eds. R E Blankenship, M T Madigan and C E Bauer) Kluwer Academic Publishers Dordrecht (1995) 315

12 C N Hunter In *Anoxygenic Photosynthetic Bacteria* (Eds. R E Blankenship, M T Madigan and C E Bauer) Kluwer Academic Publishers Dordrecht (1995) 473

13 H J M Kramer, R van Grondelle, C N Hunter, W H J Westerhuis and J Amesz *Biochim Biophys Acta* **765** (1984) 156

14 H van der Laan, C De Caro, Th Schmidt, R W Visschers, R van Grondelle, G J S Fowler, C N Hunter and S Völker *Chem Phys Lett* **212** (1993) 569

15 J G C Bakker, R van Grondelle, W T F den Hollander *Biochim Biophys Acta* **725** (1983) 508

16 A Yu Borisov, A M Freberg, V I Godik, K K Rebane and K K Timpmann *Biochim Biophys Acta* **807** (1985) 221

17 V Sundström, R van Grondelle, H Bergström, E Åkesson and T Gillbro *Biochim Biophys Acta* **851** (1986) 431

18 G McDermott, S M Prince, A A Freer, A M Hawthornthwaite-Lawless, M Z Papiz, R J Cogdell and N W Isaacs *Nature* **374** (1995) 517

19 J Koepke, X Hu, C Muenke, K Schulten and H Michel *Structure* **4** (1996) 581

20 S Karrasch, P A Bullough and R Ghosh *EMBO J* **14** (1995) 631

21 Th Fröster *Naturwissenschaften* **33** (1946) 166

22 G W Robinson *Brookhaven Symp Biol* **19** (1967) 16

23 R M Pearlstein *Brookhaven Symp Biol* **19** (1967) 8

24 L L Shipman *Photochem Photobiol* **31** (1980) 157

25 Z G Fetisova, A Yu Borisov and M V Fok *J Theor Biol* **112** (1985) 41

26 J M Jean, C-K Chan, G R Fleming and T G Owe *Biophys J* **56** (1989) 1203

27 T Pullerits and A Freberg *Biophys J* **63** (1992) 879

28 M Chachisvilis, T Pullerits, M R Jones, C N Hunter and V Sundström *Chem Phys Lett* **224** (1994) 345

29 M Chachisvilis, H Fidder, T Pullerits and V Sundström *J Raman Spectroscopy* **26** (1995) 513

30 R Monshouwer, A Baltuska, F van Mourik and R van Grondelle *J Phys Chem A* **102** (1998) 4360

31 R E Fenna and B W Matthews *Nature* **258** (1975) 573

32 A S Davydov *Theory of Molecular Excitons* Plenum New York (1971)

33 T Pullerits, S Hesss, J L Herek and V Sundström *J Phys Chem* **101** (1997) 10560

34 T S Rahman, R S Knox and V M Kenkre *Chem Phys* **44** (1979) 197

35 O Kühn, T Renger, V May, J Voigt, T Pullerits and V Sundström *Trends in Photochem Photobiol* **4** (1997) 213

36 P D Laible, R S Knox and T G Owens *J Phys Chem B* **102** (1998) 1641

37 R Monshouwer, M Abrahamsson, F van Mourik and R van Grondelle R *J. Phys. Chem B.* **101** (1997) 7241

38 H Fidder, J Knoester and D A Wiersma *J Chem Phys* **95** (1991) 7880

39 M Chachisvilis, O Kühn, T Pullerits and V Sundström *J Phys Chem B* **101** (1997) 7275

40 O Kühn and V Sundström *J Chem Phys* **107** (1997) 4154

41 D L Dexter *J Chem Phys* **21** (1953) 836

42 G D Scholes, R D Harcourt and K P Ghiggino *J Chem Phys* **102** (1995) 9574

43 R G Alden, E Johnson, V Nagarajan, W W Parson, C j Law and R G Cogdell *J Phys Chem B* **101** (1997) 4667

44 A G Redfield *Adv Magn Reson* **1** (1965) 1

45 D Sieferman-Harms *Physiol Plant* **69** (1987) 561

46 R J Cogdell and H A Frank *Biochim Biophys Acta* **895** (1987) 63

47 Y Koyama *J Photochem Photobiol* 9 (1991) 265

48 H A Frank and R J Cogdell In *Carotenoids in Photosynthesis* (Eds. A Young and G Britton) Chapman & Hall London (1993) 252

49 H A Frank and R L Christensen In *Anoxygenic Photosynthetic Bacteria* (Eds. R E Blankenship, M T Madigan and C E Bauer) Kluwer Academic Publishers Amsterdam (1995) 373

50 H A Frank and R J Cogdell *Photochem Photobiol* **63** (1996) 257

51 Y Koyama, M Kuki, P O Andersson, T Gillbro *Photochem Photobiol* **63** (1996) 243

52 D E Fleischman and R K Clayton *Photochem Photobiol* **8** (1968) 287

53 N G Holmes and A R Crofts *Biochim Biophys Acta* **459** (1977) 492

54 N G Holmes, C N Hunter, R A Niederman and A R Crofts *FEBS Lett* **115 (1980)** 43

55 J L Herek, T Polivka, T Pullerits, G J S Fowler, C N Hunter and V Sundström *Biochem* **37** (1998) 7057

56 A Freer, S Prince, K Sauer, M Papiz, A Hawthornthwaite-Lawless, G McDermott, R Cogdell and N W Isaacs *Structure* **4** (1996) 449

57 A P Shreve, J K Trautman, T G Owens and A C Albrecht *Chem Phys Lett* **178** (1991) 86

58 M R Wasielewski, D M Tiede and H A Frank In *Ultrafast Phenomena* (Eds. G R Fleming and A E Siegman) Springer-Verlag Berlin (1986) 388

59 B P Krueger, G D Scholes and G R Fleming *J Phys Chem B* (In press)

60 H Nagae, T Kikitani, T Katoh and M Mimuro *J Chem Phys* **98** (1993) 8012

61 G D Scholes, R D Harcourt and G R Fleming *J Phys Chem B* **101** (1997) 7302

62 J K Trautman, A P Shreve, C A Violette, H A Frank, T G Owens and A C Albrecht *Proc Natl Acad Sci* USA **87** (1990) 215

63 A P Shreve, J K Trautman, H A Frank, T G Owens and A C Albrecht *Biochem Biophys Acta* **1058** (1991) 280

64 P O Andersson, R J Cogdell and T Gillbro *Chem Phys* **210** (1996) 195

65 M Ricci, S E Bradforth, R Jimenez and G R Fleming *Chem Phys Lett* **259** (1996) 381

66 B P Krueger, G D Scholes, R Jimenez and G R Fleming *J Phys Chem B* **102** (1998) 2284

67 L M P Beekman, R N Frese, G J S Fowler, R Picorel, R J Cogdell, I H M Stokkum, C N Hunter and R van Grondelle *J Phys Chem B* **101** (1997) 7293

68 J B Jackson and A R Crofts *FEBS Lett* **4** (1969) 185

69 W Crielaard, R W Visschers, G J S Fowler, R van Grondelle, K J Hellingwerf and C N Hunter *Biochim Biophys Acta* **1183** (1994) 473

70 D S Gottfried, M A Steffen and S G Boxer *Science* **251** (1991) 662

71 J L Herek, T Polivka, T Pullerits, R J Cogdell, C N Hunter and V Sundström *Xith Internl Cong Photosynth* Budapest Hungary (1998)

72 C C Gradinaru, I H M van Stokkum, R van Grondelle and H van Amerongen *Xith Internl Cong Photosynthe* Budapest Hungary

73 R van Grondelle, H Bergström, V Sundström and T Gillbro *Biochim Biophys Acta* **894** (1987) 313

74 H Bergström, R van Grondelle and V Sundström *FEBS Lett* **250** (1989) 503

75 A Breiberg, V I Godik, T Pullerits and K Timpmann *Biochim Biophys Acta* 973 (1989) 93

76 A Freberg, V I Godik, T Pullerits and K Timpmann *Chem Phys* **128** (1988) 227

77 S Hess, F Feldchtein, A Babin, I Nurgaleev, T Pullerits, A Sergeev and V Sundström *Chem Phys Lett* **216** (1993) 247

78 T Joo, Y Jia, J Y Yu, D M Jonas and G R Fleming *J Phys Chem* **100** (1996) 2399

79 R Jimenez, S N Dikshit, S E Bradforth and G R Fleming *J Phys Chem* **100** (1996) 6825

80 Y -Z Ma, R J Cogdell and T Gillbro *J Phys Chem B* **101** (1997) 1087

81 Y -Z Ma, R J Cogdell and T Gillbro *J Phys Chem B* **102** (1998) 881

82 R Monshouwer, I Zarate de Ortiz, F van Mourik and R van Grondelle *Chem Phys Lett* **246** (1995) 341

83 H Van der Laan, Th Schmidt, R W Visschers, K J Visscher, R van Grondelle and S Volker *Chem Phys Lett* **170** (1990) 231

84 N R S Reddy, G J Small, M Seibert and R Picorel *Chem Phys Lett* 181 (1991) 391

85 S Hess, K J Visscher, T Pullerits, V Sundström, G J S Fowler and C N Hunter *Biochem* **33** (1994) 8300

86 G J S Fowler, S Hess, T Pullerits, V Sundström and C N Hunter *Biochem* **36** (1997) 11282

87 S V Kolaczkowski, J M Hayes and G J Small *J Phys Chem* **98** (1994) 13418

88 H -M Wu, S Savikhin, N R S Reddy, R Jankowiak, R J Cogdell and G J Small *J Phys Chem* **100** (1996) 12022

89 O Kuhn and V Sundström *J Phys Chem B* **101** (1997) 3432

90 M H C Koolhaas, R N Frese, G J S Fowler, T S Bibby, S Geogakopoulou, G van der Zwan, C N Hunter and R van Grondelle *Biochem* **14** (1998) 4693

91 H -M Wu, M Ratsen, R Jankowiak, R J Cogdell and G J Small *J Phys Chem B* **101** (1997) 7641

92 R Monshouwer and R van Grondelle *Biochim Biophy Acta* **1275** (1996) 70

93 S Hess, E Åkesson, R J Cogdell, T Pulleritis and V Sundström *Biophys J* 69 (1995) 2211

94 M Wendling, J M Salverda, F van Mourik and R van Grondelle (In preparation)

95 C De Caro, R W Visschers, R van Grondelle and S Volker *J Phys Chem* **98** (1994) 10584

96 N R S Reddy, R J Cogdell, L Zhao and G J Small *Photochem Photobiol* **57** (1993) 35

97 J T M Kennis, A M Streltsov, S I E Vulto, T J Aartsma, T Nozawa and J Amesz *J Phys Chem* **101** (1997) 7827

98 K Sauer, R J Cogdell, S M Prince, A A Freer, N W Isaacs and H Scheer *Photochem Photobiol* **64** (1996) 564

99 K Timpmann, A Freiberg and V I Godik *Chem Phys Lett* **182** (1991) 617

100 T Pullerits and A Freiberg *Chem Phys* **149** (1991) 182 617

101 F Van Mourik, R W Visschers and R van Grondelle *Chem Phys Lett* **193** (1992) 1

102 R W Visschers, F van Mourik, R Monshouwer and R van Grondelle *Biochim Biophys Acta* **1141** (1993) 238

103 H M Visser, O J G Somsen, F van Mourik, S Lin, I H M van Stokkum and R van Grondelle *Biophys J* **69** (1995) 1083

104 S E Bradforth, R Jimenez, F van Mourik, R van Grondelle and G R Fleming *J Phys Chem* **99** (1995) 16179

105 J -Y Yu, Y Nagasawa, R van Grondelle and G R Fleming *Chem Phys Lett* **280** (1997) 404

106 M Chachisvilis and V Sundström *Chem Phys Lett* **262** (1996) 165

107 R Jimenez, F van Mourik, J -Y Yu and G R Fleming *Phys Chem B* **101** (1997) 7350

108 R Kumble, S Palese, R W Visschers, P L Dutton and R M Hochstrasser *Chem Phys Lett* **261** (1996) 396

109 T Pullerits, M Chachisvilis and V Sundström *J Phys Chem* **100** (1996) 10787

110 H M Viser, O J G Somsen, F van Mourik and R van Grondelle *J Phys Chem* **100** (1996) 18859

111 O J G Somsen, F van Mourik, R van Grondelle and L Valkunas *Biophys J* **66** (1994) 1580

112 U Liebl, J -L Lambry, J -L Martin and M H Vos *Biochem* **36** (1997) 5912

113 T Pullerits, R Monshouwer, F van Mourik and R van Grondelle *Chem Phys* **194** (1995) 395

114 R J Van Dorssen, C N Hunter, R van Grondelle, A H Korenhof and J Amesz *Biochim Biophys Acta* **932** (1988) 179

115 J T M Kennis, A M Streltsov, H Permentier, T J Aartsma and J Amesz *J Phys Chem B* **101** (1997) 8369

116 A Freiberg, J A Jackson, S Lin and N W Woodbury *J Phys Chem A* **102** (1998) 4372

117 M Rätsep, H -M We, J M Hayes, R E Blankenship, R J Cogdell and G J Small *J Phys Chem B* **102** (1998) 4035

118 T Pullerits, T Polivska, J L Herek and V Sundström *Xith Internl Cong Phosynthesis* Budapest Hungary

119 R van Grondelle, C N Hunter, J G C Bakker and H J M Kramer *Biochim Biophys Acta* **723** (1994) 30

120 M Vos, R J van Dorssen, J Amesz, R van Grondelle and C N Hunter *Biochim Biophys Acta* **933** (1988) 132

121 D Leupold, H Stiel, K Teuchner, F Nowak, W Sandner, B Ücker and H Scheer *Phys Rev Lett* **77** (1996) 4675

122 E O Potma and D A Wiersma *J Phys Chem* **108** (1998) 4894

123 T Pullerits, M Chachisvilis and V Sundström In *Photosynthesis from Light to Biosphere* (Ed. P Mathus) Kluwer Academic Publishers Dordrecht **1** (1995) 107

124 J A Leegwater *J Phys Chem* **100** (1996) 14403

125 T Meier, V Chernyak and S Mukarmel *J Phys Chem* **101** (1997) 7332

126 M Van Burgel, V Nagarajan and W W Parson *J Am Chem Soc* **102** (1995) 20

127 M Becker, V Nagarajan and W W Parson *J Am Chem Soc* **113** (1991) 6840

128 V I Novoderezhkin, R Monshouwer and R van Grondelle (In preparation)

129 V I Novoderezhkin and A P Razjivin *FEBS Lett* **368** (1995) 370

130 W Xiao, S Lin, A K W Taguchi and N W Woodbury *Biochem* **33** (1994) 8312

131 I A Abdourakhmanov, R Danielius and A P Razjivin *FEBS Lett* **245** (1989) 47

132 J T M Kennis, T J Aartsma and J Amesz *Biochim Biophys Acta* **188** (1994) 278

133 R Monshouwer *Doctoral Thesis* Free University of Amsterdam The Netherlands (1998)

134 V I Novoderezhkin, R Monshouwer and R van Grondelle *J Phys Chem B* (Submitted)

135 W M Diffey, B J Homoelle, M D Edington and W F Beck *J Phys Chem B* **102** (1998) 2776

136 F G Zhang, T Gillbro, R van Grondelle and V Sundström *Biophys J* **61** (1992) 694

137 M Müller, G Drews and A Holzwarth *Biochim Biophys Acta* **1142** (1993) 49

138 J T M Kennis, T J Aartsma and J Amesz *J Chem Phys* **194** (1993) 285

139 H Kramer, G Deinum, A T Gardiner, R J Cogdell, C Francke, T J Aartsma and J Amesz *Biochim Biophys Acta* **1231** (1995) 33

140 F G Zhang, R van Grondelle and V Sundström *Biophys J* **61** (1992) 911

141 S Hess, M Chachisvilis, K Timpmann, M R Jones, C N Hunter and V Sundstrom *Proc Natl Acad Sci* USA **92** (1995) 12333

142 V Nagarajan and W W Parson *Biochem* **36** (1997) 2300

143 X Hu, T Ritz, A Damjanovic and K Schulten *J Phys Chem B* **101** (1997) 3854

144 H Bergström, R van Grondelle and V Sundström *FEBS Lett* **250** (1989) 503

145 K J Visscher, V Sundström, H Bergström and R van Grondelle *Photosynth Res* **22** (1989) 211

146 L M P Beekman, F van Mourik, M R Jones, H M Visseer, C N Hunter and R van Grondelle *Biochem* **33** (1994) 3143

147 S C M Otte, F A M Kleinherenbrink and J Amesz *Biochim Biophys Acta* **1143** (1993) 84

148 O J G Somsen, L Valkunas and R van Grondelle *Biophys J* **70** (1996) 669

149 K Timpmann, F G Zhang, A Freiberg and V Sundström *Biochim Biophys Acta* **1183** (1993) 185

150 K Timpmann, A Freberg and V Sundström *Chem Phys* **194** (1995) 275

151 R van Grondelle and V Sundström In *The Chlorophylls* (Ed. H Scheer) CRC Press Boca Raton USA (1993) 403

152 R M Pearlstein *Photochem Photobiol* **35** (1982) 835

PHOTO AND RADIATION CHEMISTRY OF QUINONES

TULSI MUKHERJEE

Radiation Chemistry & Chemical Dynamics Division, Bhabha Atomic Research Centre, Trombay,
Mumbai 400 085 (India)

Quinones form a key group of organic compounds having tremendous importance in the areas of chemotherapy of cancer (with antitumour antibiotics) and textile dyes (with anthraquinone dyes). With the advancement in the study of fast reaction techniques, notably time-resolved fluorescence, laser flash photolysis and pulse radiolysis techniques, significant mechanistic studies have been done to understand the behaviour of excited states and free radicals generated from quinones. The present review gives an oversight on the photo- and radiation chemistry of quinones with special emphasis on the studies made during the last three decades.

Key Words: **Photochemistry; Radiation Chemistry; Quinones; Naphthoquinones; Anthraquinones; Fluorescence; Laser Flash Photolysis; Pulse Radiolysis**

Introduction

Quinones, having at least two carbonyl groups in the para-position of a ring represent an important class of versatile organic compounds endowed with rich and fascinating chemistry[1-4]. Quinones have evoked strong interest as a separate class of compounds during the second half of the present century.

The spectroscopic and photochemical properties of substituted naphthoquinones and anthraquinones have been the subject of diverse and extensive investigation because of their structural relationships to a variety of derivatives of biological, pharmaceutical and commercial importance[1-4].

The most important biological processes like respiration and photosynthesis incorporate isoprenoid quinones as the integral part of the electron and energy transport chains in mitochondria and chloroplast[1-4]. Quinones are also often responsible for the photoinduced (mostly by UV light) damages of a number of living organisms, as the quinone moieties are the most likely targets of radiation[5].

Since 1955, the National Cancer Institute (USA) has screened over 2000 potential drugs for antitumour activity[6,7]. Out of these, majority are quinones. Many potential drugs have been identified. A considerable amount of research has gone into elucidating the molecular mechanism of action of these antitumour quinones. While several mechanisms are possible, a single mechanism may not fully explain all of the cytotoxic effects.

One of the objectives of the NCI and other studies elsewhere has been to determine if there are any structure-activity relationships within the major structural groups ranging from simplest benzoquinones to the complex multiple heteroatom quinones.

There is currently a great amount of interest in the synthesis and mode of action of anthracycline antibiotics, e.g. adriamycin (doxorubicin), daunomycin (daunorubicin), AZQ, BZQ, AZT, mitoxantrone etc[8,9]. One research school believes that these compounds intercalate with DNA with the amino-sugar residue probably playing a key role in stabilising the complex, while the quinonoid moiety may be responsible for the anticancer activity, possibly by virtue of its ability to act as an electron transfer agent. Some of the antibiotics mentioned above are shown in Fig. 1. It can be seen that the only apparent similarity in these structures is that all of them contain a quinone group. The number of such compounds that has been studied by advanced techniques of pulse radiolysis and flash photolysis is increasing rapidly

**E-mail* : mukherji@magnum.barc.ernet.in;
Fax: (022) 550 5151; 551 9613.

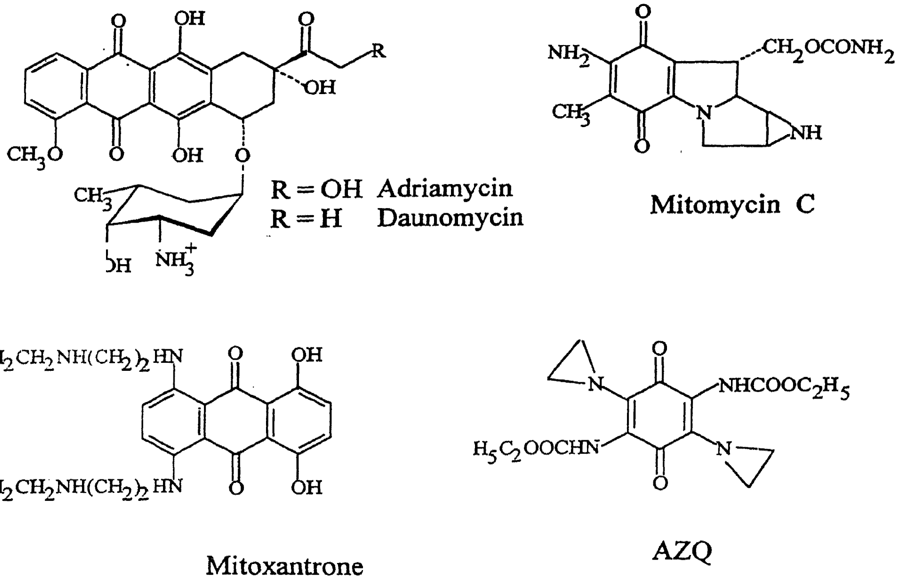

Fig. 1 Structures of few anti-tumour drugs with central quinonoid moiety

over nearly last three decades. Around the main objectives cited above, a large number of studies[10-17] have been made on the structure properties relationships.

Many of the hydroxy- and amino- substituted anthraquinones are widely used as commercial vat dyes for both natural and synthetic fibres[18-21]. In particular, the hydroxy-substituted derivatives are of importance because of their very high light stabilities on poly(ethylene tetraphthalate) (PET) fibres, and at the same time, their capacity to initiate dye-sensitised degradation of the textile fibre, i.e. textile photo-tendering[22,23]. Experimental evidence indicates that the photoactive state of the dye is the lowest triplet (T_1) state. Those dyes where T_1 state is an (n, π^*) state are much better sensitisers than those where it is a (π, π^*) state. A fundamental question that arises is: can the light fastness properties of anthraquinone dyes be correlated with the emission characteristics of the dye? For a better understanding of the above phenomena, it is very essential to have a complete understanding of the rates of the photophysical processes following absorption of light.

Of late, photochemical hole burning (PHB), a kind of photobleaching which utilises a site-selective photoinduced reaction to form a persistent hole in an inhomogeneously broadened absorption band by laser light irradiation[24-27], has assumed great significance *vis-a-vis* quinones. The hole formation and its observation is a tandem two photon process, which is different from ordinary one photon absorption spectroscopy. PHB has great implications[28,29] in molecular spectroscopy, optical data storage and ultra- narrow optical filters. Quinizarin has been shown as an important PHB material to produce a large number of multiple holes at high density. For all these a detailed knowledge of the photophysical and photochemical processes after laser irradiation and properties of the excited states are essential.

During the last 32 years, a number of excellent monographs[1-4,10-17] have appeared in the literature on the subject topic, the first being in 1967 and the last being in 1999. While efforts will be made to minimise overlap, a certain extent of commonality will be inevitable, as a vast amount of research in the subject area has been credited to this author's school at Manchester (U.K.) and BARC (India).

In the present article, an effort is made to capture the essence of some recent studies in quinones and also point out some future prospects.

Characteristics of Excited States

As a result of absorption of light, several excited states may be produced, depending on the

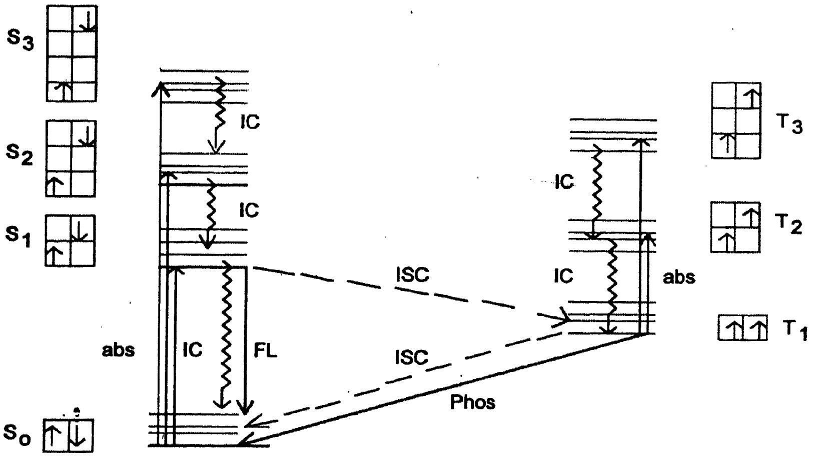

Fig. 2 Typical Jablonski diagram of a quinone showing different photophysical transitions.

characteristics of the substrate and the solvent. A typical Jablonski diagram (Fig. 2) illustrates the various optical and non-radiative transitions that may occur in a quinone molecule.

An excited state is usually characterised by its three important properties: Energy (E), lifetime (τ) and quantum yield (ϕ). Quinones, in general, absorb photons of characteristic energy and get excited to the S_1/S_n states. Fast photophysical processes ensure that the fluorescence quantum yield from the S_1-state is virtually zero, while the T_1-state is significantly populated. A large number of molecules in the excited T_1 state gets deactivated to the ground state by phosphorescence. T_1-T_n absorption may be easily characterised. Suitable substitution in the molecule results in increase in fluorescence quantum yield and change in the T_1-T_n absorption characteristics. Laser flash photolysis technique has been utilised for characterising the T_1-T_n absorption process, while steady-state and time-resolved fluorescence techniques are utilised to characterise the S_1-state.

Light Induced Processes in Quinones

The first light induced process in quinone, the photodimerisation of thymoquinone, was reported[30] in 1857. The next report, oxidation reactions of quinones, was published[31] in 1901, after 44 years! During the next 50 years, many qualitative works on quinones were published[32]. Significant progress in the chromatographic and spectroscopic techniques, especially, the discovery of flash photolysis and pulse radiolysis techniques[14,15], enabled a much more systematic and quantitative investigations of the light induced processes in quinones than those described in a few previous excellent review articles[16,17].

Light induced reactions of quinones[16] may be either intermolecular or intramolecular. The former usually involves reaction of the excited quinone with the ground state of a substrate such as another quinone, an olefin, a hydrogen donor, etc. The intramolecular reaction is usually between the excited quinonoid moiety with an appropriate part of an attached side chain, e.g. simplest methyl groups in duroquinone to the poly-isoprenoid systems found in many naturally occurring quinones.

In hexane solutions, 1,4-naphthoquinone (NQ) exhibits λ_{max} at 246, 330 and 425 nm with extinction coefficients of 24×10^3, 3.2×10^3 and 50 $dm^3 mol^{-1}cm^{-1}$, respectively[33]. Obviously the first two are due to π-π^* transition and the third one due to n-π^* transition (all singlet-singlet absorption). An extremely weak n-π^* singlet-triplet absorption may be seen at 491 nm in heptane[34].

On the other hand, the electronic absorption spectrum of 9,10-anthraquinone (AQ) shows a weak absorption beginning at ~424 nm, arising from excitation to pair of closely spaced $^1(n, \pi^*)$ states, S_1 and S_2, having orbital symmetries B_{1u} and A_u, respectively[35,36]. This band is formally orbital symmetry forbidden. Three π-π^* transitions at 325 and 252 nm (both *Y*-polarised) and 272 nm (*z*-polarised) have been characterised[37-39].

For both quinones, the intersystem crossing efficiency ϕ ($S_1 \rightarrow T_n$) has been shown to be very high[40], ϕ_{ISC}=0.8 (NQ) and 0.9 (AQ). The ϕ_p for AQ=0.44[41] in EPA at 77K, with ~zero ϕ_{fl}. The triplet T_1 energies for NQ and AQ have been determined as 58 and 63 kCal mol^{-1}, respectively and have been shown to be extremely solvent-dependent[41-46]. For AQ, T_1 has been identified as a ^3B (n,π^*) state and T_2 as a ^3A_u state just 410 cm^{-1} above T_1[47]. Phosphorescence emission from T_1 is shown to be predominantly *Z*-polarized[48]. This emission is formally spin and orbital symmetry forbidden. As a result a number of papers[47,49-52] have focussed on this aspect. There have been a large number of other investigations on related areas. A detailed discussion is beyond the scope of this review.

Substitution of electron donating groups (-OH, -NH$_2$, -OMe etc.) into one of the benzenoid rings of NQ and AQ markedly alter the photophysical properties[53-58]. Firstly, due to substitution of the electron donating groups in 1 or 2-positions of the benzenoid rings, a strong visible absorption band appears in their absorption spectra with a weakening of the absorption at ~325 nm. The visible band is shown to arise from a $^1(\pi,\pi^*)$ transition of charge-transfer (CT) character, the λ_{max} depending on the position and electron donating power of the substituent group. Particularly in the 1-position, an intramolecular hydrogen bonding may occur between the carbonyl oxygen and the hydrogen on the substituent. This may prevent intramolecular photoreduction by hydrogen donors. Hydroxy and amino-substituted NQ and AQ show lack of phosphorescence at 77K but are weakly fluorescent. Armed with advanced techniques of laser flash photolysis[11,14] and time-resolved fluorescence[59-61] techniques, this author's school has exhaustively studied the photophysics of a large number of substituted quinones[62-72].

Spectroscopy and Photodynamics of the S_1 State

The first electronic excited (S_1) state of quinones is responsible for many photophysical characteristics. Intramolecular hydrogen bonding can have a profound effect on the geometric, electronic, vibrational and photodynamical radiationless transition properties of molecules in their excited states. An important manifestation of hydrogen bonding has been shown to be an enhanced $S_1 \rightarrow S_0$ internal conversion rate[57] which can occur by several mechanisms.

It has been demonstrated[56,57] that electron donating substituents (OH, NH$_2$, etc) to the anthraquinone core cause rapid internal conversion rate enhanced by both intra- and intermolecular hydrogen bonds. This behaviour has been explained by invoking stretching vibrations of the hydrogen in the hydrogen bond as radiationless decay accepting modes for the $S_1 \rightarrow S_0$ process, due to significant vibrational anharmonicity[73]. In extreme cases excited state intra or intermolecular proton transfer, leading to adiabatic irreversible excited state rearrangement has been observed to play an important role in the nonradiative dissipation of the excitation energy. While the excited state intramolecular proton transfer (ESIPT) has been a favoured topic, existence of an intramolecular hydrogen bond in substituted quinones, e.g. 1-aminoanthraquinone[56], 1,5-diaminoanthraquinone[57] and 1,4-dihydroxy anthraquinone (quinizarin) does not necessarily ensure ESIPT due to the energy barrier between the two possible tautomeric forms. Another possible mechanism for efficient radiationless deactivation has been shown to be the intermolecular interaction involving charge transfer (CT)[77,78] and the role of protic solvents[79]. In an extensive study on the photodynamics of naphthazarin (5,8-dihydroxy-1,4-naphthoquinone) and several disubstituted (with OH and NH$_2$) anthraquinones, it has been conclusively established that the nonradiative internal conversion process via the hydrogen bond stretching vibrations in different possible intra and intermolecular modes is the major deactivation pathway in such quinones. For hydroxy-substituted quinones, the hydrogen bond is much stronger in comparison to that with other substituents. As a result, the interaction with proton donating or accepting solvents is very insignificant. Except quinizarin (1,4-dihydroxy-9,10-anthraquinone), other dihydroxy derivatives undergo ESIPT process which is responsible for very high rate constant for the radiationless process. In benzene, compared to other nonpolar solvents like cyclohexane, higher rate constant has been attributed to the formation of quinone-benzene excited state charge transfer complex.

Table I

Fluorescence characteristics of naphthazarin, quinizarin, 1,4-diamino-9,10-anthraquinone (1,4-DAAQ) and 1-amino-4-hydroxy-9, 10- anthraquinone (1,4-AHAQ) and their deuterated derivatives. Solvent: cyclohexane (adapted from ref. [55])

Quinones	ϕ_f	τ_f, ns	k_R,$10^7 s^{-1}$	k_{NR},$10^8 s^{-1}$
Naphthazarin	0.008	0.22	3.7	45.1
D-Naphthazarin	0.022	1.21	1.8	8.1
Quinizarin	0.140	2.38	5.9	3.6
D- Quinizarin	0.320	7.69	4.2	0.9
1,4-DAAQ	0.037	0.93	4.0	10.4
D-1,4- DAAQ	0.180	5.11	3.6	1.6
1,4-AHAQ	0.083	1.58	5.3	5.8
D-1,4-AHAQ	0.250	6.60	3.8	1.1
Methoxy-quinizarin	0.068	1.30	5.2	7.2
1,8-DHAQ	0.010	0.09[a]	11	110

[a] τ_f (deuterated) 0.14 ns

In elucidating the photodynamic mechanism in substituted quinones, deuterium isotope effect has been of immense help, as shown in Table I. All the quinones are very weakly fluorescent (except quinizarin) with single exponential fluorescence decay independent of excitation and emission wavelength. On deuteration, there is significant increase in ϕ_f and increase in τ_f, but decrease in k_R and k_{NR} values. These observations, coupled with small Stokes' shift demonstrate that these quinones do not undergo ESIPT reaction (except naphthazarin). Hence, fluorescence emission occurs from the excited keto form of the quinones. It has been also shown that the effect of deuteration (and also, temperature) is more prominent in case of amino substituted quinones where more number of intermolecular hydrogen bonds with solvents are possible.

However, in the case of 1,8-dihydroxy-9,10-anthraquinone, where the nature of hydrogen bonding is different, a biexponential fluorescence decay has been observed, independent of excitation and emission wavelengths. Quantum yields in polar solvents, e.g. acetonitrile and ethanol, are nearly double of that in cyclohexane. This trend is reverse in comparison to that in other hydroxy and amino-substituted quinones. The effect of deuteration on ϕ_f and τ_f was not very significant. The existence of two hydrogen bonded forms in keto-enol type of equilibrium (ESIPT process) in the excited state had to be invoked to explain the observations. Fig. 3 depicts the Lippincott-

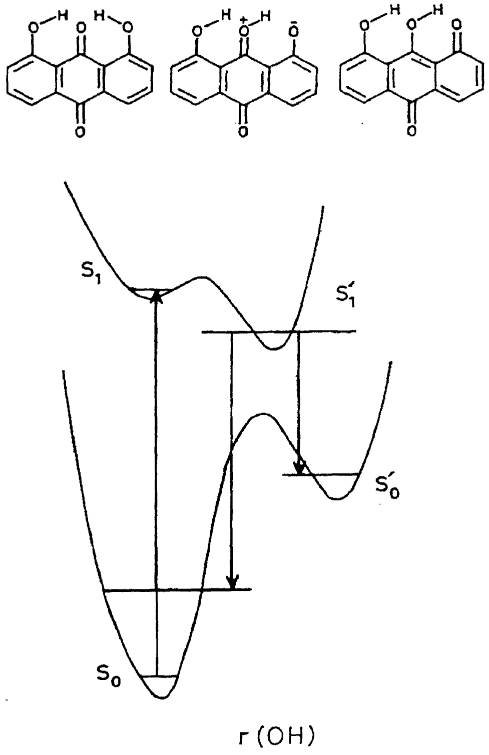

Fig. 3 Potential energy curves (not to scale) along the OH coordinate of the transferring protons for 1,8-dihydroxy-9,10-anthraquinone. The structures show the normal form (left), the proton transfer form (right) and the charged structure in the S_1 state (middle) (Reproduced from ref. [55] with permission)

Table II

Photophysical parameters for substituted naphtho- and anthraquinones

Quinone	Solvent	$\varepsilon_{T\text{-}T}$(10^4 $dm^3mol^{-1}cm^{-1}$) λ_{max} (nm)	ϕ_T	Ref.
Juglone	Cyclohexane	2.34(280),5.70(325),3.05(770)	0.24	63
	Acetonitrile	2.00(280), 4.89(325)	0.22	
	Methanol	1.96(280), 5.06(325),2.98(370)	0.21	
	Isopropanol	1.92(280),3.62(325)	0.18	
Naphthazarin	Cyclohexane	2.75(280);2.35(335);1.62(380); 0.98(415), 1.22(440)	0.24	64
	Methanol	1.40(280);0.90(330), 0.72(360), 0.63(380),0.64(405),0.63(435)	0.34	
	Isopropanol	1.33(265);0.89(310), 0.94(330), 0.78(365), 0.69(408);0.63(440)	0.30	
Quinizarin	Cyclohexane	1.68(360)	0.11	95
	Isopropanol	2.20(360)	0.09	
1,4-AHAQ	Cyclohexane	1.92(360)	0.06	95
	Isopropanol	2.50(360)	0.06	
1,4-DAAQ	Cyclohexane	1.00(360)	0.06	
	Isopropanol	1.60(360)	0.06	
1,5-DHAQ	Cyclohexane	1.5(330)	0.12	96
	Acetonitrile	0.8 (580)	0.07	
	Isopropanol	2.1 (330)	0.09	
1,5-DAAQ	Acetonitrile	1.7 (540)	0.40	96
	Isopropanol	2.4 (540)	0.18	
1,8-DHAQ	Cyclohexane	1.4 (320)	0.33	96
	Acetonitrile	1.0 (600)	0.16	
	Isopropanol	2.1 (320)	0.15	
Methoxy-quinizarin	Cyclohexane	1.69 (320)	0.17	72
	Acetonitrile	0.7 (600)	0.24	
	Isopropanol	2.20 (320)	0.12	

Schroeder type potential energy curves as suggested by Smulvich *et al.*[80]

Several authors have studied the absorption and fluorescence characteristics of mono-substituted[56,81] and 2,6-disubstituted[57] anthraquinones in benzene (assumed as non-interacting with the quinone excited state) and ethanol (a hydrogen bond forming solvent). These authors tried to find out the quantitative contribution of the intra- and intermolecular hydrogen bonding on the photophysical parameters of these quinones, especially their nonradiative decay rate constants. However, we demonstrated that benzene forms CT-type exciplexes with S_1-states of these quinones. A comparison of fluorescence lifetimes in cyclohexane, carbon tetrachloride, benzene and toluene shows that for 1-AAQ, τ_f decrease from cyclohexane or CCl_4 to benzene to toluene (as in the case of 1,4-disubstituted hydroxy and amino quinones). On the other hand, for

2-AAQ and 2,6-DAAQ, τ_f values increased by about two times in benzene and toluene compared to those in cyclohexane or CCl_4 with ~15 times increase in ϕ_f. This suggests that S_1 states of these two quinones also interact strongly with benzene, probably via exciplex formation.

Intermolecular complexation with solvent has been demonstrated[71] for 6,11-dihydroxynaphthacene-5, 12-dione.

In some cases, e.g. 1,4-AHAQ, 1,4-DAAQ and 1,4-DHAQ, the fluorescence spectra in benzene exhibit significant red shift with concomitant decrease in ϕ_f and τ_f (compared to values in cyclohexane). Steady-state Stern-Volmer analysis gave a k_q ~10^8 dm^3 $mol^{-1}s^{-1}$. However, dynamic quenching in cyclohexane solution, i.e. quenching of τ_f, did not conform to the *S-V* plots. A plot of $(1/\tau_f^q - 1/\tau_f)^{-1}$ vs 1/[quencher], where τ_f^q and τ_f are the lifetime values in the presence and the absence of the quencher, gave a straight line[66,69], (Fig. 4) indicating exciplex formation. Similar or comparable results were obtained with a large number of hydrocarbon[66,69] and amine[70] quenchers.

Study of an important molecular electronic property, namely, the directions of the electronic transition moments and the rotational dynamics of the molecules in solution, has always attracted photophysicists. Linear and circular dichrographic studies of some anthracycline drugs were reported earlier[82]. Anisotropic rotational behaviour[83] of the anthracycline model-quinizarin, was exhaustively studied[67] with different excitation wavelengths and at different temperatures.

Nanosecond Laser Flash Photolysis

Excited triplet states are often implicated as the reactive intermediates responsible for photochemical change, due to longer lifetime due to the spin-forbidden nature of the transitions involved[84]. Phototendering and fading of anthraquinonoid dyes are believed to involve the triplet excited states. Spectroscopy of the triplet states, especially the *T-T* transition (Fig. 2) causing *T-T* absorption spectra, triplet quantum yield (ϕ_T) and interaction of the triplets with the solvent, etc. are best studied by employing the technique of nanosecond laser flash photolysis coupled with kinetic spectrophotometry technique[14,85-88]. As most substituted quinones have favourable absorption parameters in the wavelengths of excimer lasers, the latter have been used as excitation light source in all our studies and many others. The *T-T* absorption spectra are determined by following the change in absorbance as a function of wavelength and correcting for the depletion of the parent quinone[14].

A transient species may be identified as a triplet

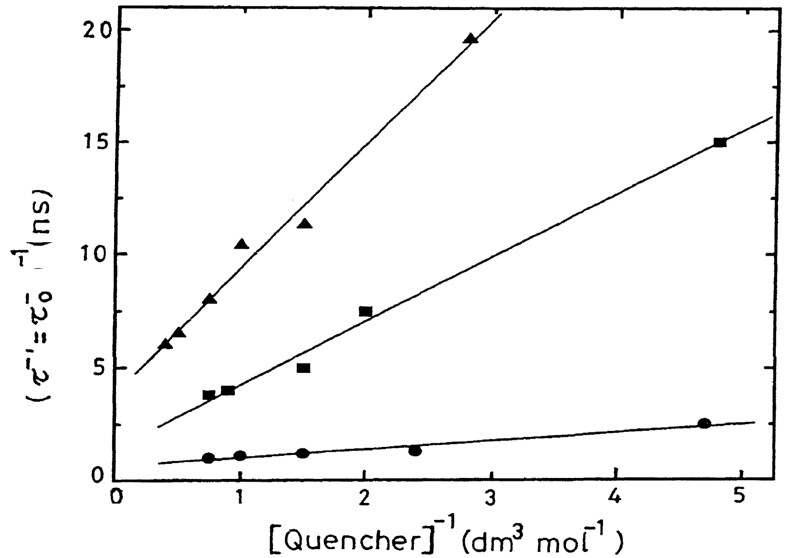

Fig. 4 Plot of $(\tau^{-1}-\tau_0^{-1})^{-1}$ versus $[\text{Quencher}]^{-1}$ for the dynamic fluorescence quenching of quinizarin by (▲) benzene, (■) toluene and (●) para-xylene in cyclohexane (Reproduced from ref. [66] with permission)

state by many considerations, namely, sensitised production by triplet-triplet energy transfer, sensitisation of another triplet, reactivity with oxygen, etc. For this purpose, the triplet state of β-carotene is particularly useful, since it has very low triplet energy level (E_T=75 k J mol^{-1})[89], so that most other triplets (E_T >75 k J mol^{-1}) can sensitise it, producing an intense *T-T* absorption at 520 nm (ε_T=240,000 dm^3 mol^{-1} cm^{-1}). These triplets cannot be produced directly due to very low intersystem-crossing efficiency. By choosing a suitable donor or acceptor, the triplet energy levels of substituted quinones have been determined[90,91]. By choosing a nonpolar solvent like cyclohexane and acetonitrile, quinones form only triplet states[92-96], while in polar solvents having extractable hydrogen atoms, e.g. methanol, ethanol, isopropanol, etc., triplet states abstract H-atoms to form semiquinone radicals[63-65,68,92,97]. Apart from known photochemical excitation techniques, irradiation of quinone solutions in nonpolar solvents give rise to triplet states of quinones via the geminate recombination of initially formed ion pairs.

The extinction coefficient for the *T-T* absorption can be measured by at least seven techniques[89]. Out of these only two are most widely used. (i) Energy transfer method, initially used for pulse radiolysis method[97], and later extended to the laser flash photolysis technique[98,99]. The general principle of this method has been described by Amouyal *et al.*[99] and is beyond the scope of this review due to lack of space. (ii) Singlet depletion method[100], applied to wavelength regions where *T-T* absorption is negligible compared to the ground state absorption. After a laser pulse is given, change in absorbance may be given as

$$\Delta A=(\varepsilon_T-\varepsilon_S).[^3Q].l \qquad \ldots (1)$$

where, ε_T and ε_S are the extinction coefficients of the triplet and the ground states, respectively,[^3Q] is the concentration of the triplet state and l is the optical path length. Rearranging equation (1),

$$\varepsilon_{\mathrm{T}} = \varepsilon_{\mathrm{S}} + \cdot \; {}_{[^3Q]} \quad \text{for } l = 1 \text{ cm} \qquad \ldots (2)$$

Hence, once ^3Q is known by determining. the extinction coefficient at an appropriate wavelength, it is possible to construct a true *T-T* absorption spectrum. Typical examples of difference and true *T-T* absorption spectra are shown in Fig. 5. A comparable semiquinone spectra obtained from laser flash photolysis of quinizarin in isopropanol is shown in Fig. 6.

Pulse radiolysis and laser flash photolysis are two complementary techniques, capable of giving

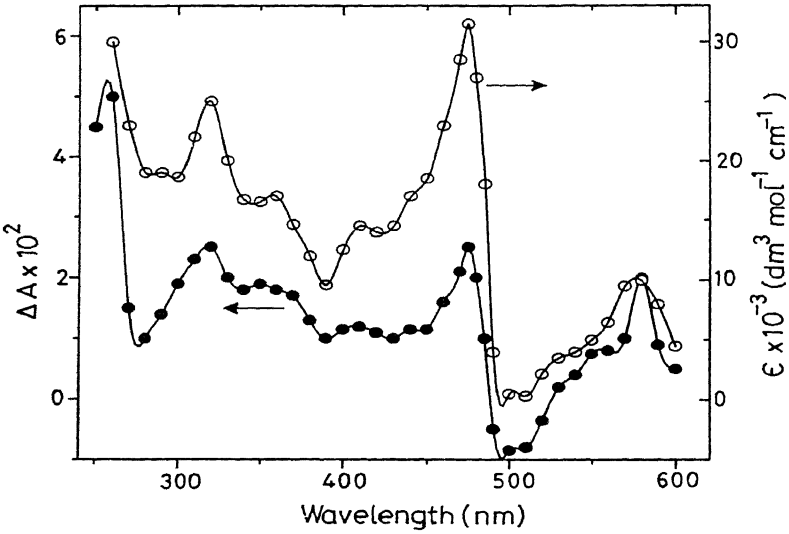

Fig. 5 Difference (-●-●-) and corrected (-○-○-) absorption spectra for the T-T transition in quinizarin in cyclohexane by 248 nm laser excitation (Reproduced from ref. [95] with permission)

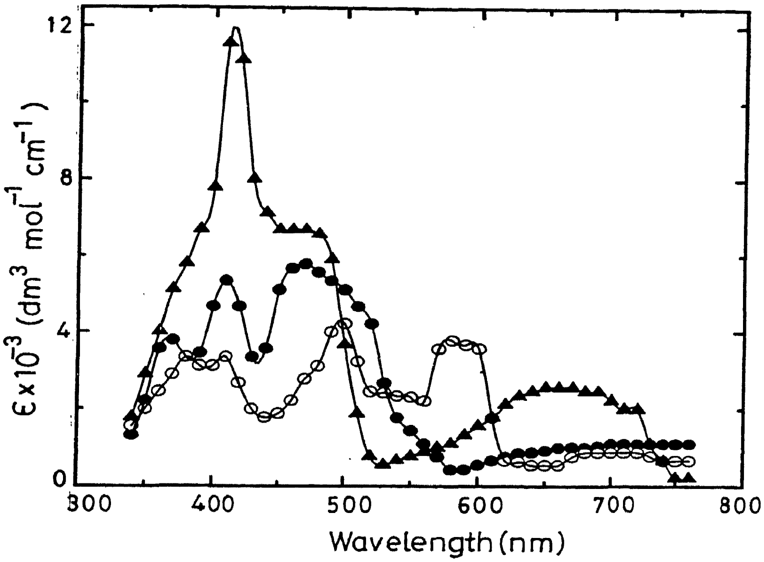

Fig. 6 Corrected absorption spectra of the neutral semiquinone radicals of quinizarin (-▲-▲-), AHAQ (-●-●-) and DAAQ (-O-O-), produced by 248 nm laser excitation in isopropanol (Reproduced from ref. [95] with permission)

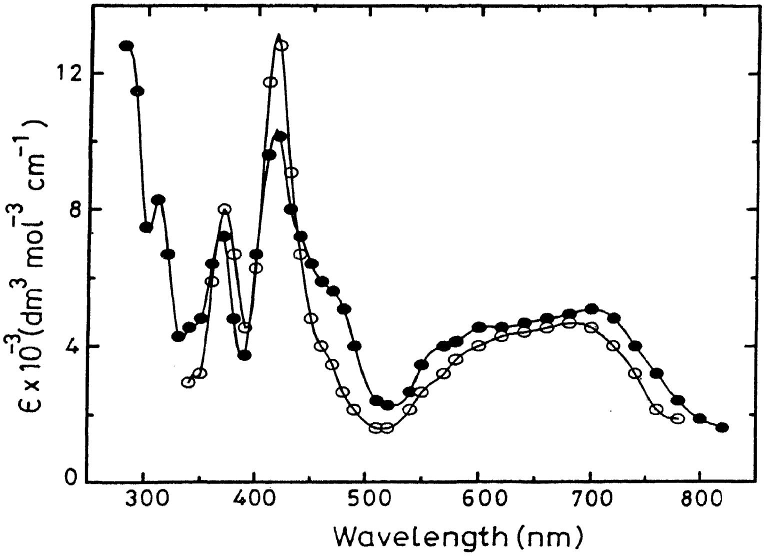

Fig. 7 Corrected semiquinone absorption spectra of 5-methoxyquinizarin in isopropanol, as obtained from pulse radiolysis (-O-O-) and from 248 nm laser flash photolysis (-●-●-). (Reproduced from ref. [68] with permission)

similar information. Fig. 7 shows two corrected absorption spectra of 5-methoxyquinizarin in isopropanol as obtained by these two techniques. Marginal differences in the two spectra probably arise due to small uncertainties in the yield value.

A general equation for measuring the quantum yield of triplet formation may be given as:

$$\phi_T(Q) = \phi_T(R)\frac{A_T(Q)}{A_T(R)}\cdot\frac{\varepsilon_T(R)}{\varepsilon_T(Q)}\cdot\frac{A_G(R)}{A_G(Q)} \quad \ldots (3)$$

where T and G (subscripts) denote triplet and ground states, respectively. R denotes a reference, e.g. biphenyl ($\lambda_{T\text{-}T}$=361.5 nm, $\varepsilon_{T\text{-}T}$=4.28×10^4 dm^3 mol^{-1}cm^{-1} and ϕ_T =0.84)[99].

Table II gives data on T-T absorption on a number of amino and hydroxy substituted naphtho and anthraquinones.[93-96] The obvious inference that can be drawn is that the introduction of hydroxy and amino substitution into the non-quinonoid phenyl rings drastically alters the spectroscopic properties of the triplet state. Although ϕ_T for unsubstituted quinones is close to unity, substitution dramatically reduces the value. While the major path of deactivation of the triplet states of the unsubstituted parents is by phosphorescence emission, no phosphorescence could be detected for the hydroxy- and amino-substituted quinones, where the major deactivation path must be $T_1 \rightarrow S_0$ radiationless reverse intersystem crossing process (Fig. 2), which may be due to photo-enolisation of the excited state through intramolecular proton transfer[55]. Also of interest is the observation that the triplet energy levels of these substituted quinones are lowered to a great extent compared to those in the unsubstituted quinones. The combination of the unusual spectroscopic properties of the triplet states, namely, very low ϕ_T, and very short lifetime due to fast deactivation through radiationless processes, may probably be responsible for the colour fastness of the anthraquinonoid dyes.

Unlike in the case of quinizarin where no long-lived transients are observed in cyclohexane and acetonitrile, such transients are formed in the case of methoxy-quinizarin[68], 1, 4-AHAQ[65] and 1, 4-DAAQ[65]. This must be due to stronger intramolecular hydrogen bonding in quinizarin, as such hydrogen bonds would be considerably weakened by introduction of a methoxy group in the 5-position or by replacing one or both OH with NH_2.

In many cases where direct photo-generation of the triplet states of quinones is not very facile, pulse radiolysis offers a viable route, e.g. ubiquinone[99,102]. By choosing either a suitable donor or acceptor, as the case may be, and energy transfer method described by Bensasson and Land[103], the triplet characteristics may be determined[63-65,68,92,97,104-107].

Anthracycline antibiotics and their derivatives have been shown to photosensitise the formation of singlet oxygen via their triplet state[106]

Formation of Semiquinones in Aqueous Solutions

Quinones are capable of reacting with a large number of radiation-produced primary species like e_{aq}^-, H-atom and OH•.[10,14,15] While e_{aq}^- and H• may reduce quinones by one-electron reduction process to the semiquinone, OH• may either add to the ring or some suitable substituent position and give rise to one-electron oxidation to some form of transient. Formation of semiquinones by γ-radiolysis has been discussed in detail in earlier monographs[107-110] and will not be included here. Pulse radiolysis kinetic spectrophotometry technique has opened up new scope for detailed studies[10-15,111,112] on semiquinones. Pulse radiolytic formation of one-electron reduced transients may be summarised as follows:

$$H_2O \rightsquigarrow e_{aq}^-, H^\bullet, OH^\bullet, H_2, H_2O \qquad \ldots(4)$$

$$Q + e_{aq}^- \longrightarrow Q \qquad \ldots(5)$$

$$Q + H^\bullet \longrightarrow QH^\bullet \rightleftharpoons Q^{\bullet-} + H^+ \qquad \ldots(6)$$

In aqueous solutions containing sodium formate, the reaction may be:

$$HCOO^- + OH^\bullet\,(H)^\bullet \longrightarrow CO_2^{\bullet-} + H_2O\,(H_2) \qquad \ldots(7)$$

$$Q + CO_2^{\bullet-} \longrightarrow Q^{\bullet-} + CO_2 \qquad \ldots(8)$$

As reaction (5) also takes place, yield of $Q^{\bullet-}$ increases in this case.

In aqueous alcoholic solutions containing either methanol or isopropanol, following reactions take place.

$$CH_3OH + OH^\bullet(H)^\bullet \longrightarrow {}^\bullet CH_2OH + H_2O\,(H_2) \qquad \ldots(9)$$

$$(CH_3)_2CHOH + OH^\bullet\,(H^\bullet) \longrightarrow (CH_3)_2C^\bullet OH + H_2O(H_2) \qquad \ldots(10)$$

$$Q + {}^\bullet CH_2OH \xrightarrow{H_2O} Q^{\bullet-} + H_2CO + H^+ \qquad \ldots(11)$$

$$Q + (CH_3)_2C^\bullet OH \longrightarrow Q^{\bullet-} + (CH_3)_2CO + H^+ \qquad \ldots(12)$$

Higher alcohols may also be used. However, more branched radicals, e.g. $^{\bullet}CH_2(CH_3)_2COH$ (formed by reactions of $OH^{\bullet}$/ $H^{\bullet}$ with tert-butanol) are normally unreactive.

Semiquinones are also formed photolytically from quinones by abstraction of a hydrogen atom from the solvent by the triplet state of the quinone.

$$Q^*+(CH_3)_2CHOH \longrightarrow QH^{\bullet}+(CH_3)_2C^{\bullet}OH \quad \ldots (13)$$

The organic radical formed may give more semiquinone by reaction (9). Excited quinones may also abstract electrons from suitable donors.

$$Q^*+OH^- \longrightarrow Q^{\bullet -}+OH^{\bullet} \quad \ldots (14)$$

Quinones may also be reduced by excited states of other molecules by electron transfer reaction

$$Q+Chl^* \longrightarrow Chl^{\bullet +}+Q^{\bullet -} \quad \ldots (15)$$

Semiquinones can also be formed from hydroquinones by photoionisation.

$$QH^{\bullet}+e^-_{aq}+H^+ \quad \ldots (16)$$

Excited dye molecule (D^*) can oxidise hydroquinone (QH_2) to the semiquinone.

$$D^*+QH_2 \longrightarrow DH^{\bullet}+QH^{\bullet} \quad \ldots (17)$$

In most cases, an aqueous solution of the quinone has been used for radiation chemical studies. However, the reaction sequence depends entirely on the added scavengers, e.g. sodium formate, methanol, isopropanol, tertiary butanol or others. This author's groups have extensively used a relatively novel solvent system comprising of a mixture of isopropanol (5 mol dm^{-3}) and acetone (1 mol dm^{-3}) in water (32.5 mol dm^{-3}). The advantage of this system, over and above solubilizing insoluble (in water) quinones, lies in the chemistry involved[113,114].

In the aqueous-organic mixed solvent system (MS), reactions (18) and (19) predominate, followed by reaction (12).

$$e^-_{aq}+(CH_3)_2CO \longrightarrow (CH_3)_2CO^- \quad \ldots (18)$$

$$(CH_3)_2CO^-+H_2O \rightarrow (CH_3)_2C^{\bullet}OH+OH^- \quad \ldots (19)$$

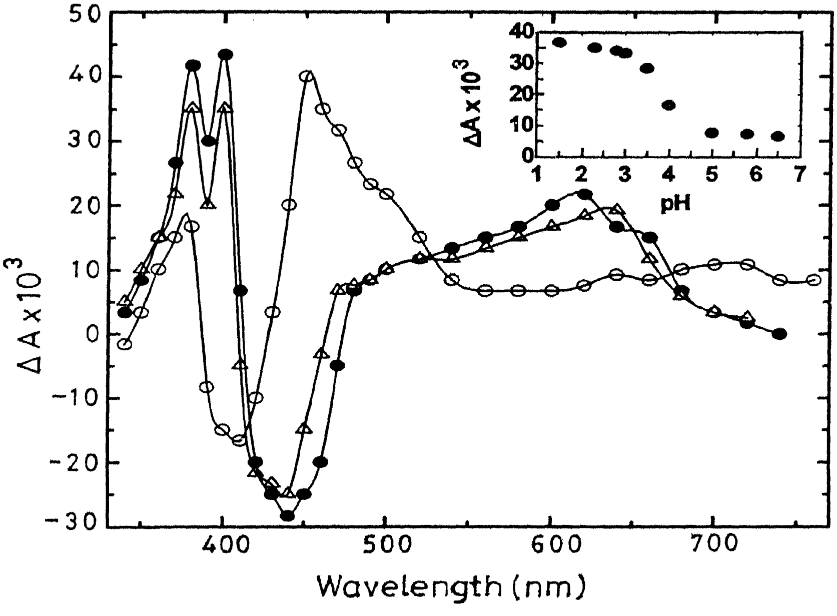

Fig. 8 Semiquinone-quinone difference spectra for 1,8-dihydroxy-9,10-anthraquinone in aqueous isopropanol-acetone mixed solvent at *p*H 1.3 (●) and 6.5 (O) and also in pure isopropanol (Δ). Dose 9.4 Gy. *Inset*: Variation of ΔA with pH at 380 nm. Circles are the experimental points and the solid curves is calculated according to eq. (24). (Reproduced from ref. [125] with permission)

Characteristics of Semiquinones

Optical Absorption Characteristics

Study of physical chemistry of semiquinones relies heavily on knowledge of optical absorption characteristics of the radicals, namely, absorption maxima and extinction coefficients. As radiation dose can be calculated fairly accurately, the yield of radicals can be easily estimated. From the observed absorbance at a given dose, extinction coefficient of the semiquinone can be calculated.

The observed absorbance (ΔA) after an electron pulse is given to the solution containing quinone

Table III

Comparison of spectroscopic characteristics and pK(1) of quinones.

Quinone	λ_{max}, nm (ε, 10^3 dm^3 mol^{-1} cm^{-1}) QH$^{\bullet}$	Q$^{\bullet -}$	pK(1) of QH$^{\bullet}$	Ref
Benzoquinone (BQ)	415(4.7)^{a}, 410 (3.8)^{b}	425(6.9)^{a}, 430 (3.6)^{b}	4.0^{a},4.7^{b}	10^{a}, 115^{b}
1,4-Naphthoquinone(NQ)	370 (7.2)^{a}, 370 (8.1)^{b}	390(12.5)^{a},375 (7.8)^{b}	4.1^{a},4.3^{b}	115^{b},10^{a} 116^{b}
2,3-Dimethyl-NQ^{a}	380(7.3)	400(11.4)	4.25	10
2-Hydroxy-NQ (Lawsone)^{a}	370 (5.9)	390 (6.3)	4.7	10,116
5-Hydroxy-NQ (Juglone)^{a}	370 (12.6)	385 (12.2)	3.65	116,117
5,8-Dihydroxy-NQ (Naphthazarin)^{a}	380 (11.8), 760 (2.7)	380 (10.5) 425 (8.9), 720 (1.7)	2.7	116,118
9,10-Anthraquinone (AQ)	375 (9.8)^{a,c} 380 (8.9)^{b}	395(7.0)^{a,c},480(6.5)^{a,c} 385 (6.7)^{b}, 490 (5.2)^{b}	5.3^{a} 4.4^{b}	115^{b},10^{a}, 116,119
AQ-1-sulphonate ^{a,c}	385 (10.7)	400 (7.2), 500 (7.2)	5.4	119,120
AQ-2-sulphonate ^{a,c}	390 (11.2)	400 (7.3), 500 (7.3)	3.25	119,121
AQ-1,5-disulphonate ^{a}	385 (8.4)	390 (5.6), 500 (5.7)	6.1	119
AQ-2,6-disulphonate ^{a}	388 (9.5)	396 (6.4), 515 (8.3)	3.0	119
1-Amino-AQ ^{b}	400 (10.5) 470 (2.9),650 (2.0)	390 (6.7) 480 (10.3), 740 (2.0)	5.8	122
1-Hydroxy-AQ ^{b}	390 (10.5) 520 (1.1),620 (1.4)	390 (8.1) 445 (7.9), 730 (1.7)	4.6	122
1-Amino-4-hydroxy-AQ ^{b}	410 (6.8) 490 (4.7),700 (2.5)	390 (6.3) 500 (13.1), 740 (3.4)	6.3	123
1,4-Diamino-AQ ^{b}	390 (6.5) 490 (8.0),720 (2.2)	385 (6.0) 510 (14.4), 740 (3.3)	7.9	123
1,4-Dihydroxy-AQ (Quinizarin) ^{b}	410 (11.6) 680 (3.0),720 (2.7)	388 (5.8) 475 (13.7), 720 (1.8)	3.3	113,124
Quinizarin 2-sulphonate ^{a}	425 (12.4) 680 (3.0)	390 (6.4), 475 (17.2) 700 (2.6), 780 (2.3)	2.2	124
Quinizarin 6-sulphonate ^{a}	420^{b} (12.4) 680 (3.0)	390 (6.4), 475 (17.2) 700 (2.6), 780 (2.3)	2.2	124
5-Methoxy-quinizarin ^{b}	370 (6.6), 420 (12.1)	375 (6.5), 480 (16.9)	3.65	122
1,5-Dihydroxy -AQ ^{b}	410 (12.4) 620 (2.2)	390 (8.0), 440 (13.0), 720 (1.4)	3.65	125
1,8-Dihydroxy-AQ^{b}	400 (15.8) 620 (3.4)	380 (8.5) 450 (14.7), 720 (1.8)	3.95	125
1-Chloro-AQ^{b}	380 (8.9)	390 (5.0), 500 (5.4)	4.2	126
1,5-Dichloro-AQ ^{b}	380 (8.0)	390 (4.7), 520 (4.8)		126
1,8-Dichloro-AQ ^{b}	375 (9.9)	390 (5.1), 530 (6.0)	3.9	126
2-Hydroxy-AQ ^{b}	380 (6.6)	400 (6.6), 450 (4.4)	4.7	127
2,6-Dihydroxy-AQ ^{b}	390 (11.0)	410 (9.0), 450 (4.5)	5.4	127
Adriamycin/Daunomycin^{a}	420 (13.2) 720 (4.2)	380 (5.0) 480 (14.8), 720 (3.4)	2.8	128
5,12-Naphthacene quinone ^{b}	390	390 (3.3), 460 (2.6)	6.0	115

^{a} : 10^{-1} mol dm^{-3} sodium formate in water; **b:** 5 mol dm^{-3} isopropanol+1 mol dm^{-3} acetone in water; **c:** corrected ε-values [119].

and a suitable additive, will constitute a difference absorption spectrum given by:

$$\Delta A = (\varepsilon_{\text{semiquinone}} - \varepsilon_{\text{quinone}}) \cdot \Delta C_{\text{quinone}} \cdot l \qquad \ldots (20)$$

where, l=optical path length, $\Delta C_{\text{quinone}}$ is the amount of quinone converted into the semiquinone and ε terms are the respective molar extinction coefficients.

Depletion will occur in the wavelength region where the parent quinone absorbs more strongly than its semiquinone (Fig. 8). As $\varepsilon_{\text{quinone}}$ is known at all wavelengths, and $\Delta C_{\text{quinone}}$ can be easily calculated at a given dose (as G-value is known under different experimental conditions), $\varepsilon_{\text{semiquinone}}$ can be calculated at any given wavelength by using eq. (20).

$$\varepsilon_{\text{semiquinone}} = \varepsilon_{\text{quinone}} + \frac{\Delta A_{\text{obs}} \times (G\varepsilon)_{\text{dosimeter}}}{A_{\text{dosimeter}} \times G_{\text{semiquinone}}} \qquad \ldots (21)$$

A plot of $\varepsilon_{\text{semiquinone}}$ vs λ will constitute a corrected absorption spectrum of the radical (Fig. 9). Numerous studies have been made and corrected absorption spectra of the semiquinones have been determined (Table III).

A close examination of Table III reveals few interesting trends. For example, most neutral semiquinones generated from naphthoquinone and anthraquinone derivatives absorb strongly around 370-390 nm region, while their anions absorb at longer wavelength with higher extinction coefficients. Except for naphthoquinone and 2-hydroxynaphthoquinone, they all have extinction coefficient in the vicinity of 12,000 $dm^3\ mol^{-1}\ cm^{-1}$. In the case of dihydroxy-substituted quinones a weak and broad absorption band is observed at 700-760 nm region. Unsubstituted or sulphonated anthrasemiquinone radical anions have two distinct absorption peaks around 400 and 500 nm with comparable extinction coefficients. For other substituted anthrasemiquinones, on the other hand, extinction coefficients of these two bands, widely differ. Dihydroxy-anthrasemiquinone derivatives show weak absorption bands (extinction coefficient ~6,000 $dm^{-3}\ mol^{-1}\ cm^{-1}$) around 380-390 nm and stronger absorption bands (extinction coefficient ~13,000-17,000 $dm^3\ mol^{-1}\ cm^{-1}$) around 475 nm. The exact nature of the red band is still a matter of intense speculation. The effect of matrix (i.e. change of solvent) on the absorption characteristics has been very minimal in general, showing that in most cases intramolecular stabilisation is predominant.

A close scrutiny at the formation of semiquinone from quinone shows that the parent quinone structure changes to aromatic in the semiquinone. All UV-visible absorptions are thus considered as due to π-π^* transitions. As the shift in $\lambda_{\max}$ between the neutral semiquinone and its anion is usually small, it is safely assumed that the orbitals involved in the absorption process are not significantly affected by protonation. Similar arguments hold good for substituted quinones, where the effect of ring substitution on $\lambda_{\max}$ has been seen to be very small (see Table IV). However, for -OH substitution, the effect is more prominent due to stronger intramolecular hydrogen bonding[72].

Some people have argued[129] that semiquinones may exist in an associated form (Q.... $Q^{\bullet -}$). This is possible in specific cases if the parent quinone is aggregated. In dilute aqueous solutions, however, the probability of dimerisation is indeed very small and can be neglected.

Acid-Base Dissociation Constants

Semiquinone radical anions can undergo protonation steps to form neutral semiquinone or in very strongly acidic solution, a semiquinone cation radical. On the other hand, semiquinone radical anions containing ionisable H can undergo deprotonation to form dianion, trianion or even polyanion. An example may be given by the case of naphthazarin (5, 8-dihydroxy-1, 4-naphthoquinone) (NzH_2)[118] where 5 different states of protonation of the semiquinone radicals are possible.

$$NzH_2 \xrightarrow{\text{reduction}} NzH_2^{\bullet -}\ \text{(anion)} \qquad \ldots(22)$$

$$NzH_4^{\bullet} \xrightarrow{pK(-1)} NzH_3^{\bullet} \xrightarrow{pK(1)} NzH_2^{\bullet} \xrightarrow{pK(2)} NzH^{\bullet 2-} \xrightarrow{pK(3)} Nz^{\bullet 3-}. \qquad .(23)$$

Studies on pK(-1) are rare[130]. It is probably believed that in very strong acidic solutions, semiquinone radicals can remain in the cationic form. Except some ESR studies, very little research has been oriented to this direction. Irradiation of *p*-benzoquinone in a $CFCl_3$ matrix at 77K and subsequent ESR studies[131] established a symmetric σ-radical cation. *In situ* UV photolysis of *p*-benzoquinone in CF_3COOH at room temperature apperntly gave a symmetric ~~π-cation radical~~[132,133].

Mayer and Kraslukianis[130] did pulse radiolysis of *p*-benzoquinone, 1,4-naphthoquinone, naphthazarin, 9,10-anthraquinone and quinizarin, in freon 113 (CF_2Cl-$CFCl_2$) solution at room temperature. Blue shifted UV-visible absorption spectra were assigned to the radical cations. High formation rate constants (~10^{10} dm^3 mol^{-1} s^{-1}) have been reported. The value of pK(1) is the most important parameter as pK(2) and pK(3) are normally measurable in very strongly alkaline solutions only[118].

As the absorption spectra of neutral and anionic semiquinones differ considerably, it has been possible to estimate pK(1) and in many cases, even pK(2), by choosing appropriate wavelengths and a modified Henderson's eq. (24):

$$A_{obs} = \frac{A_{QH_3^{\bullet}}}{1+10^{pK(1)-pH}+10^{pK(1)+pK(2)-2pH}} \quad \frac{A_{QH_2^{\bullet-}}}{1+10^{pH-pK(1)}+10^{pK(2)-pH}} \cdot \frac{A_{QH_2^{\bullet-}}}{1+10^{2pH-pK(1)-pK(2)}+10^{pH-pK(2)}} \qquad \ldots (24)$$

A representative plot of ΔA vs *p*H is shown in Fig. 8 (inset). However, whereever such intramolecular stabilisation effect is not present, the pK(1) value goes up, e.g. 9,10-anthraquinone-1, 5-disulphonate; 1, 4-diamino-9, 10-anthraquinone; 1-amino-4-hydroxy-9,10-anthraquinone 5,12-naphthacene quinone, etc.

In case of benzo-semiquinone the pK(1) value is 4.1 is aqueous solution[10] and 4.7 in the aqueous-organic mixed solvent[115]. However, in case of substituted quinones, especially OH-substituted quinones, the anion gets extra stabilised due to the intramolecular H-bonding. As a result, pK(1) values are lower, as shown in Table III.

Charge on the Semiquinone

Conventional ionic salt effect studies in absence of any buffer often gives indication of the net charge at near neutral *p*H[118]. However, we have shown that ionic salt effect studies, together with pulsed conductance studies and electron spin resonance spectroscopy can identify the ionic charge on the molecule without any doubt[134,135]. Once charge on a species at a given *p*H is known, charge at other *p*H values can be ascertained by knowing the *p*K values of the transient.

To test this hypothesis, Mukherjee *et al.* Demonstrated the efficacy of the techniques by

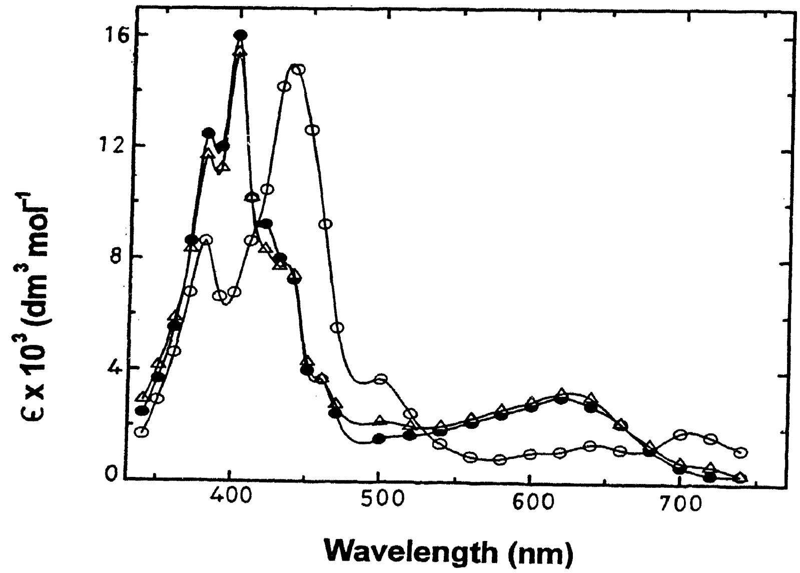

Fig. 9 Semiquinone absorption spectra for 1,8-DHAQ, based on Fig. [8] (Reproduced from ref. [125] with permission)

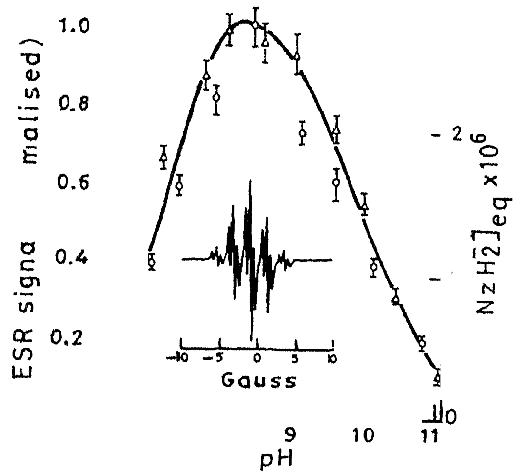

Fig. 10 Normalised ESR signal (O) and naphthazarin semiquinone concentration at equilibrium as obtained from pulse radiolysis (Δ), as a function of *p*H. *Inset*: ESR spectrum of the semiquinone (Reproduced from ref. [135] with permission)

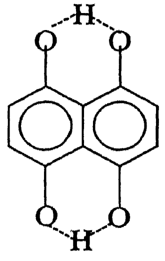

Fig. 10(b)

comparing the yield of the semiquinone derived from naphthazarin with the normalised ESR signal. Not only an extremely good correlation was obtained (Fig. 10), but the chemical structure of the semiquinone, with the odd electron delocalised over the entire structure, could also be established[134,135].

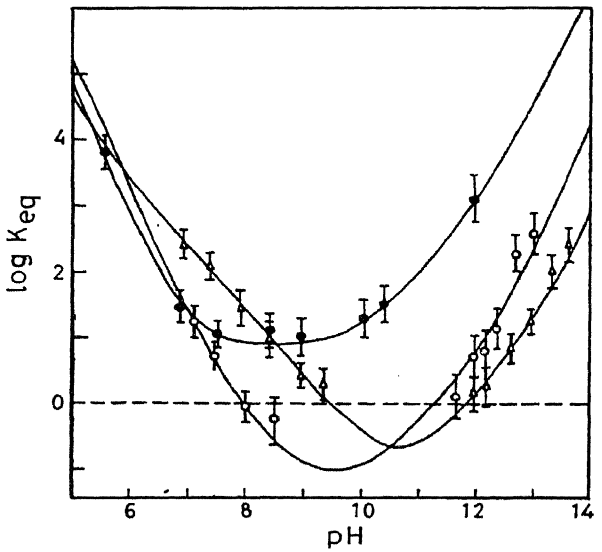

Fig. 11 Variation of log K_{aq} with *p*H for (O) sodium quinizarin 2-sulphonate, (●) quinizarin and (Δ) 5-methoxy quinizarin in aqueous isopropanol acetone mixed solvent. Solid lines represent theoretical best fit on experimental parent and semiquinone pK_a and assumed hydroquinone pK_a values (Reproduced from ref. [113] with permission)

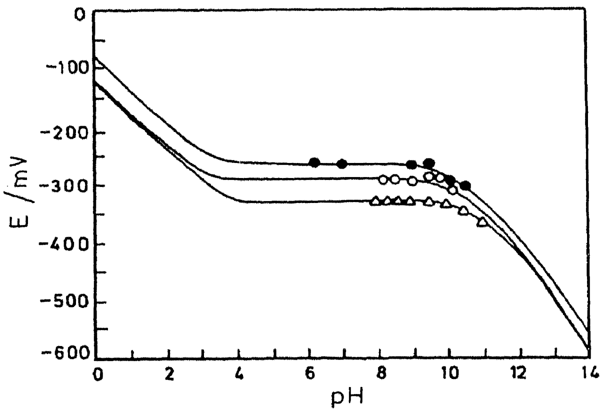

Fig. 12 *p*H-dependence of one-electron reduction potential in mixed solvent, (O) sodium quinizarin 2-sulphonate, (●) quinizarin and (Δ) 5-methoxyquinizarin. Solid lines give theoretical best fit (Reproduced from ref. [113] with permission)

Rate Constants for Formation of Semiquinones

Quinones are electron attracting type of molecules and can be reduced by a large variety of reducing radicals. Typically, rate constants for formation of semiquinones due to reactions with e^-_{aq} (or, e^-_{solv}) are virtually diffusion-controlled and fall around (1-5)×10^{10} dm^3 mol^{-1} s^{-1} (see Table IV). These rate constants are normally directly calculated from a Δ*A* vs *t* plot at ~720 nm, representing decay of e^-_{aq}, and correcting for the matrix. Alternatively, competition kinetics with another solute may also be used. In the presence of

Table IV

Formation rate constants of transients formed by one-electron reduction of some representative quinones[e]
(k in 10^9 dm^3 mol^{-1} s^{-1})

Quinone	e_{aq}^- (pH)	$CO_2^{\cdot -}$ (pH)	$(CH_3)_2C^{\cdot}OH$ (pH)	$H^{\cdot}$ (pH)	Ref
Benzoquinone (BQ)	i	i	5.0 (2.5) 2.3 (8.0), 3.0^c	i	115
1,4-Naphtho-quinone (NQ)	i	i	1.7 (2.5) 2.6 (7.0), 2.3^c	i	115, 116
2-Hydroxy-NQ (Lawsone)	i	i	3.9(1.8),1.0(6.7) 1.3 (10.3) 2.3 (13.0),1.0^c	i	116
5-Hydroxy-NQ (Juglone) [a]	28(6.4),21(10.5)	4.4 (1.2) 3.8(6.4),1.3(10.5)	3.1(2.0),2.9(7.0) 1.7 (10.4) 1.4 (13.0),3.1^c	2(1.2)	116, 117
5,8-Dihydroxy-NQ (Naphthazarin) [a]	31.0 (5.8) 24.0(9.2),22(13)	5.1 (5.8) 2.2(9.2),1.4(13)	1.5(1.3),2.0(5.2) 1.5 (7.0),1.5(11)	8.9 (1.2)	116, 118
9,10-Anthra-quinone (AQ)[d]	i	i	2.7(2.0),1.8(8.0) 1.6 (12.0),1.9^c	i	115, 116, 119
1-Amino-AQ [b]	i	i	3.0(2.0),3.2(8.0) 2.8 (12.0),0.9^c	i	122
1-Hydroxy-AQ [b]	i	i	3.2(2.0),2.8(8.0) 1.5 (12.0),2.0(b)	i	122
2-Hydroxy-AQ [b]	8.0 (11.0)	1.0 (11.0)	1.3(1.5),1.3(7.0) 0.9 (13.0),1.3^c	-----	127
1,4-Diamino-AQ	i	i	0.9 (5.5)	i	123
1-Amino-4-hydroxy-AQ [b]	50.0(11),53(~14)	1.1(11),1.3(~14)	1.6 (8.8)	----	123
1,4-Dihydroxy-AQ (Quinizarin)f Methoxy quinizarin (QZOMe)	i	i	3.3(1.2),3.2(5.4) 1.5(10.4) 1.8(~14)	i	113, 124
1,5-Dihydroxy -AQ	45.0(11.0) 53.0(~14)	1.0 (11.0) 0.27 (~14)	2.2 (---)	-----	125
1,8-Dihydroxy-AQ	34.0(11.0) 38.0(~14)	1.7 (11.0) 0.37 (~14)	2.0 (---)	-----	125
2,6-Dihydroxy-AQ	14.0(11.0)	1.0 (11.0)	2.3(1.5),1.2(7.0) 0.7 (13.0),0.7^c	-----	127
AQ-1,5-disulphonate	17.0 (8.4)	10.0 (8.4)	-----	2.4 (2.0)	119
AQ-2,6- disulphonate	10.0 (7.0)	0.8 (7.0)	-----	3.0 (1.4)	119
QZ 2-sulphonate (QZ- 6-sulphonate)	27.0 (6.5) 18.0(11.7)	3.1 (1.1),3.2 (5.7) 1 (10.4),0.2 (~14)	-----	----	124
1-Chloro-AQ	i	i	2.5(2.0),2.4(9.0)1.6^c	i	126
1,5-Dichloro-AQ	i	i	2.2(2.0),2.0(9.0) 1.7^c	i	126
1,8-Dichloro-AQ	i	i	2.9(2.0),2.6(9.0) 2.2^c	i	126
5,12-Naphtha-cenequinone	i	i	3.1(2.0),1.7(8.0) 2.1^c	i	115
Adriamycin	25.0 (6.5) 15.0(11.5)	3.5 (1.1),3.4 (6.5) 0.18 (11.5)	-----	2.9 (1.1)	128

c : pure isopropanol

d : k with CH_2OH 2.1x10^8 dm^{3}mol^{-1}s^{-1}[136] (in alkaline methanol solution)

e : excludes those reported in reference [112]

f : k with CH_2OH (acidic solution)=7.5 x 10^8 dm^3 mol^{-1}s^{-1} [137].

i : insoluble in water

substituents, the electron affinity of the molecule changes. However, it has been difficult to have a direct correlation between e_{aq}^{-} rate constants and substitution effects. A few general (but not universal) observations are as follows:

a) In alkaline solutions *k* values are lower, obviously due to the Coulombic repulsion between the negative charges on the two reactants. However, the difference in *k*-values is not very significant. A number of specific examples have been discussed in reference[13]. Others are observable in Table IV.

b) Where a negatively charged substituent is attached to the molecule (say, SO_3^-), the rate constant increases with substitution, due to the electron withdrawing ability of the $-SO_3^-$ group from the aromatic ring, stabilising the formed radical anion.

c) Reducing agents other than e_{aq}^{-} always react much slower, by an order of magnitude. Same trend as in (a) above is observed in such cases too.

d) Neutral radicals (e.g. $(CH_3)_2C^{\bullet}OH$) react at a slower rate than the anionic radicals ($CO_2^{\bullet -}$, $CH_2O^{\bullet -}$).

e) At acidic *p*H, rate constants for H atom reactions are much higher than bulkier radicals like $^{\bullet}COOH$, $^{\bullet}CH_2OH$ etc.).

Disproportionation Reactions of Semiquinones

In de-oxygenated aqueous solutions, semiquinone normally undergo a bimolecular disproportionation reaction, forming the parent quinone and two- electron reduced hydroquinone.

$$2\ \text{Semiquinone} \longrightarrow \text{Quinone+Hydroquinone} \qquad \ldots (25)$$

Typical rate constants fall in the range of 10^8-10^9 $dm^3mol^{-1}s^{-1}$. However, in cases where substituents are present, an equilibrium of the type of reaction (26) has been observed over a range of intermediate *p*H values.

$$2\ \text{Semiquinone} \rightleftharpoons \text{Quinone+ Hydroquinone} \qquad \ldots (26)$$

Especially in the case of hydroxy-substituted naphthoquinones[117,118] and anthraquinones[113,124] such equilibrium was seen to lie heavily to the left, showing exceptional stability of the semiquinones.

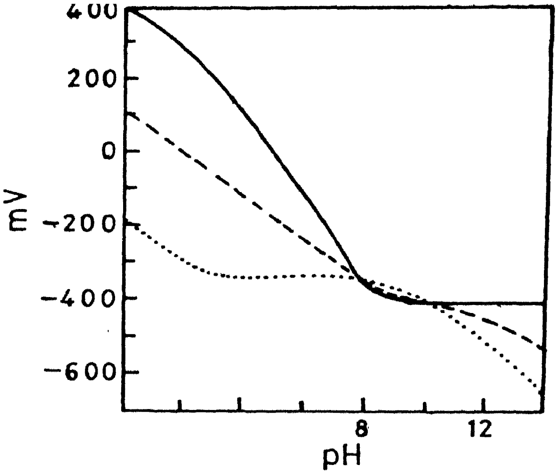

Fig. 13 Variation of E^1 (....), E^2 (—) and E^m (----) of adriamycin (and daunomycin) with pH (Reproduced from ref. [141] with permission)

It was conclusively established that this was due to the nearness of the E^1 (one-electron reduction potential), E^2 (second one-electron reduction potential) and E^m (two-electron reduction potential) values of the quinone and their characteristic change as a function of *p*H as a consequence of the *p*K values of the species (quinones, semiquinones and hydroquinones) involved.

Mukherjee *et al.* attempted[113,128] to quantify the observed stability of semiquinones as a function of *p*H, by correlating the K_{eq} values with *p*K values of the species involved and their redox characteristics (Fig. 13). Excellent agreement between experimental data and theoretical calculation was achieved.

One-Electron Reduction Potentials

The reduction potentials for semiquinones are those for formation from the parent quinones, i.e. the one-electron reduction potential of the parent quinone, E $(Q/Q^{\bullet -})$, and for reduction to hydroquinone, i.e. the second one-electron reduction potential, $E(Q^{\bullet -}/Q^{2-})$ for addition of the second electron to the quinone. These reduction potentials depend on *p*H as Q, $Q^{\bullet -}$ and Q^{2-} can all be protonated.

Pulse radiolysis has been established as possibly the "cleanest" method for determining these potentials[15,138]. After the anionic form of a semiquinone has been formed at low concentration by the action of an appropriate electron-donating reducing agent, it is possible to establish an equilibrium of the type

$$Q^{\bullet -}+R \qquad\qquad Q+R^{\bullet -} \qquad \ldots (27)$$

with a reference redox couple $R/R^{\bullet -}$ under ideal chemical conditions, before $Q^{\bullet -}$ can disappear by disproportionation or other chemical reactions. Measurement of equilibrium optical absorbance can then give the equilibrium constant K for the reaction (27). If the reduction potential $E(R/R^{\bullet -})$ is known, the value of $E(Q/Q^{\bullet -})$ at 25°C vs NHE can easily be derived as

$$E^1(Q/Q^{\bullet -})=E^1(R/R^{\bullet -})-59.16 \log K \qquad \ldots (28)$$

where all E values are in mV. The reduction potential $E(Q^{\bullet -}/Q^{2-})$ is obtained from:

$$E^2(Q^{\bullet -}/Q^{2-})=2E^m(Q/Q^{2-})-E^1(Q/Q^{\bullet -}) \qquad \ldots (29)$$

where $E^m(Q/Q^{2-})$ is the known two-electron potential of the quinone.

It is imperative to have an accurate E^1 value for the reference from the literature[138]. Care has to be taken about solvent also, as Mukherjee *et al.* have demonstrated[114]. For example, the $E^1(MV^{2+}/MV^{+})$ is -450 mV in aqueous system while it is-330 mV in isopropanol-acetone-aqueous (mixed) solvent. Over last two decades a large number of E^1 values have been determined accurately by this simple method. Some chosen values are shown in Table V. When only a single ionisation of the

Table V

Redox potentials of several quinone/semiquinones systems

Quinone	E^1_7 mV	E^2_7 mV	E^m_7 mV	Ref
Benzoquinone (BQ)[b]	-30	-	-	115
1,4-Naphthoquinone (NQ)[b]	-200	-	-	115
NQ-2-sulphonate	-60	+300	+120	
2,3-Dimethyl-NQ	-240	-	-	139
2-Hydroxy-NQ[b]	-350	-	-	116
5-Hydroxy-NQ	-95[a],-125[b]	+157 (pH 2)[a]	+69 (pH 2)[a]	116, 117
5,8-Dihydroxy-NQ	-109[a], -115[b]	-15[a]	-62[a]	116, 118
9,10-Anthraquinone (AQ)	-266[a], -445[b]	-	-	115
AQ-1-sulphonate[a]	-415	-	-	119, 120
AQ-2-sulphonate[a]	-380	-76	-228	119-121
AQ-1,5-disulphonate[a]	-418	-283	-350	119
AQ-2,6-disulphonate[a]	-215	-	-	119
1-Amino-AQ[b]	-435	-	-	122
1-Hydroxy-AQ[b]	-385	-	-	122
1-Amino-4-hydroxy-AQ[b]	-408[b]	-348[b]	-388[b]	123
1,4-Diamino -AQ[b]	-410	-329	-380	123
1,4-Dihydroxy-AQ (quinizarin)[b]	-249[b], (-326)	-188	-229	113, 124
Quinizarin 2-sulphonate [a]	-270[a], -298[b]	-246	-258	124
Quinizarin 6-sulphonate [a]	-249[a]	-213	-231	124
5-Methoxyquinizarin [b]	-333	-192	-263	113
1,5-Dihydroxy-AQ[b]	-326, -306[b]	-273	-300	125
1,8-Dihydroxy-AQ[b]	-298 (pH 7),-377 (pH 11)	-345, -325[b]	-415, -380	125
1-Chloro-AQ[b]	-360	-	-	126
1,5-Dichloro-AQ[b]	-370	-	-	126
1,8-Dichloro-AQ[b]	-410	-	-	126
2-Hydroxy-AQ[b]	-440	-	-	127
2,6-Dihydroxy-AQ[b]	-400	-	-	127
Adriamycin/Daunomycin[a]	-341	-260	-300	140, 141
Mitomycin C	-310[a]			142
AZQ	-70[a]			6
bzq	-376[A]			6
5,12-Naphthacene quinone[b]	-380			115

(Abbreviations as in Table I)

semiquinone is considered, $E^1(Q/Q^{\bullet-})$ is related to pH as:

$$E^1(Q/Q^{\bullet-})=E^1(Q/Q^{\bullet-})_7+59.16 \log (K+[H^+])/(K+10^{-7}) \quad \ldots (30)$$

where K is the ionisation constant. Thus in the pH-independent region ($pH > pK$), the redox process is the simple addition of an electron, whereas in the acidic region, it also involves addition of a proton (i.e. $Q+H^++e^-_{aq} \rightarrow QH^\cdot$). More complex correlation between E^1 and pH has been done and experimentally verified [140,141].

Anthracyclines and their Model Quinones

First One-Electron Step

The most basic chemical structural model for anthracyclines adriamycin (doxorubicin) and daunomycin (daunorubicin) was considered to be the strongly intramolecularly hydrogen-bonded naphthazarin (5,8-dihydroxy-1,4-naphthoquinone). It is usually customary to study the way in which such simple quinones form radicals in order to gain insight into the way more complex quinones might produce toxic and other effects. This is more so as the radical centres in the complex molecules are usually located in these simpler models. Treatment of naphthazarin will also demonstrate how various data may be compiled and compared.

In aqueous solution, naphthazarin (NzH_2) can exist in the fully protonated form (NzH_2), anionic form (NzH^-) or dianionic form (Nz^{2-}) depending on the pH.

$$NzH_2 \overset{pK=7.85}{\rightleftharpoons} NzH^- \xrightarrow{pK=10.7} Nz^{2-} \quad \ldots (31)$$

Pulse radiolytic one-electron reduction of naphthazarin in aqueous formate/formic acid solution[118] leads to various protonated forms of the semiquinone. Change in absorbance at chosen wavelengths of the semiquinone absorption spectra, plotted as a function of pH, allowed three of the four forms to be identified, with pK values of 2.7 and >13.8. The charge on the semiquinone at pH~5 was confirmed to be -1, based on ionic strength effect on the disproportionation rate. The radical at this pH was thus assigned the structure $NzH_2^{\bullet-}$. The transition $NzH_3^\cdot \rightarrow NzH_2^{\bullet-}$ was assigned the pK=2.7. The reduction in pK value by 1.4 units over that of simple 1,4-naphthoquinone was easily attributed to the strong intramolecular hydrogen bonding in $NH_2^{\bullet-}$. Pulsed conductance and ESR studies further confirmed structural assignments[134,135]. It may be mentioned here that the stability of the $NzH_2^{\bullet-}$ form of naphthazarin semiquinone over a pH range of 11.1 units is the best known example of stabilisation due to intramolecular hydrogen bonding.

The ESR studies also established that the $pK \geq 13.8$ could be assigned to the transition $NzH_2^{\bullet-} \rightarrow NzH^{\bullet 2-}$, and that the structure of the semiquinone was a strongly intramolecularly hydrogen-bonded highly symmetric structure where the unpaired electron is delocalised over the entire ring structure. The one-electron reduction potential (E^1) values were calculated at several pH values using several redox standards. From these measurements, E^1_7 =–109 mV vs NHE at 25°C was established. A E^1 vs pH plot shows a region independent of pH, i.e. no proton involved in the reduction process, confirming the above structural assignments.

Second One-Electron Step

In many cases, semiquinones are present at appreciable concentrations in solutions containing quinones and the corresponding hydroquinone. In the case of naphthazarin, the $NzH_2^{\bullet-}$ form was found to be extremely stable in weak alkaline solutions unlike at the two extremes of the pH range when the disproportionation of the semiquinone was complete. The reaction (26) was studied over the entire pH range 1-14. Within pH ~6 to 11, the disproportionation was incomplete and the semiquinone was stable over hundreds of milliseconds at least. The equilibrium concentration of the semiquinone was measured and the equilibrium constant K_{eq} was calculated. Such stability constants were related to the one-electron reduction potentials for the quinone and the semiquinone (at 25°C) via the expression:

$$E^1(\text{Quinone/Semiquinone})–E^2(\text{Semiquinone/Hydroquinone})=–59.16 \log K_{eq} \quad \ldots (32)$$

The two one-electron reduction potentials are related in turn to the two-electron reduction potential of the quinone (equation),

$$E^1(\text{Quinone/Semiquinone})+E^2(\text{Semiquinone/Hydroquinone})=2E^m(\text{Quinone/Hydroquinone}) \quad \ldots (33)$$

Extremely good correlation was obtained among measured and calculated physical parameters, establishing a complete chemistry of naphthazarin semiquinones. The hydroquinones were actually formed *in-situ* in the cell in the pulse radiolysis set-up, by giving a large number of electron pulses to the solution and measuring the absorbance immediately[143]. The close proximity of E^1, E^2 and E^m vs *p*H over a small *p*H range gives physicochemical explanation about the exceptional stability of naphthazarin semiquinones.

Quinone Antitumour Drugs

Physiological enzyme based reduction of quinone antitumour drugs caused by xanthine oxidase, cytochrome P450 reductase etc.[114], leads to the formation of semiquinone and hydroquinone forms. Pulse radiolysis can generate and characterise these intermediates and products[11,14,15].

Clinically most successful antitumour drug, adriamycin undergoes redox cycling reactions producing also some toxic side effects. When adriamycin is reduced by one-electron reducing enzymes, the daunosamine moiety is liberated. As in Mitomycin C,[145] it was believed that the process occurred at the semiquinone stage.

These anthracyclines are much complex molecules and a larger number of combination of pK values leads to several states of overlapping protonation over a narrow *p*H range[146]. A large number of protonation, namely $^+HAdH_2$, AdH_2, $^+HAdH^-$, AdH^-, Ad^{2-} etc (Ad=adriamycin core without two ionisable H) are possible with *p*K values like 8.22, 9.01, 9.36, 10.1 and 13.2. Closeness of these *p*K values makes study with anthracyclines a very complex proposition. In the above formulation, fully protonated adriamycin was represented as $^+HAdH_2$ where the first H refers to the amino-sugar NH_2 and the other two to those on the hydroquinone.

Pulse radiolysis of aqueous solution of adriamycin under reducing conditions leads to semiquinone radicals in their various protonated forms[128,140,141,147,148]. In the acidic region, a semiquinone pK of 2.9 fit the data. Daunomycin semiquinone showed the same pK within experimental error.

The one-electron reduction potential of adriamycin and daunomycin was estimated as a function of *p*H[141] as in the case of naphthazarin. Within experimental error limit, E^1 of both anthracyclines were treated as identical. Around *p*H 7, E^1 was independent of *p*H, showing that the one-electron reduction process does not involve either an uptake or liberation of a proton around this pH. A number of experiments confirm that the reduction process in this region is :

$$^+HAdH_2 + e_{aq}^- \longrightarrow {}^+HAdH_2^{\bullet -} \qquad \ldots (34)$$

The pK of 2.9 thus corresponds to

$$^+HAdH_3^{\bullet} \qquad\qquad {}^+HAdH_2^{\bullet -} + H^+ \qquad \ldots (35)$$

We could get a best fit of E^1 vs *p*H at *p*H>7 only when a pK=9.2 for the $(NH_3^+ \rightarrow NH_2 + H^+)$ ionisation at the sugar moiety of the semiquinone was implicated. A lot of experiments gave a $E^1_7 = -341$ mV vs NHE at 25°C for the two anthracyclines. Later on, similar values were reported for other structurally related anthracycline derivatives.

Analogous to the naphthazarin semiquinone, the initial absorption decays in a second-order manner due to disproportionation reaction of the semiquinone. The equilibrium was much more to the semiquinone. Over a narrow range E^1, E^2 and E^m values are very close, demonstrating exceptional stability. However, in this case, deglycosylation of the initially formed hydroquinone to form the quinone methide tautomer, wherein the absorption characteristics are virtually indistinguishable, was established. There has been no evidence for the liberation of daunosamine at the semiquinone stage. For these drugs, however, the presence of the equilibrium (26) even at neutral pH indicates that loss from semiquinone and hydroquinone will be indistinguishable. The rate constant of deglycosylation reaction was established as 1.1 s^{-1} and the rate constant for the quinone method to 7-deoxy-adriamycinone (having similar absorption characteristics as that of the parent quinone) reaction was 1.5 x 10^{-2} s^{-1}, at *p*H 7[149].

Two-Electron Reduction

Land *et al.*[143] have shown how pulse radiolysis can be used to generate 2-electron reduced species from parent quinones. A significant difference in behaviour of reduced naphtho- and anthraquinones was established during our subsequent studies. Naphthoquinones generated corresponding hydroquinones by complete 2-electron reduction. The fully reduced species readily reacted with ozygen to generate the parent quinone, e.g. naphthazarin.

$NzH_2 \xrightarrow{2e^-_{aq}} NzH_2^{2-}$
(dianionic form of the hydroquinone) ... (36)

Depending on pK values, neutral or anionic forms of the hydroquinone are formed. Then,

Hydroquinone Quinone ... (37)

This reaction is quite slow in the case of naphthazarin. However, it becomes faster when oxygen is bubbled, or, in alkaline solutions. Same reaction in the case of anthraquinone and higher derivatives gives rise to a reduced species which does not react with oxygen, or, reacts infinitesimally slowly. It was inferred that the reduced species could not be a normal hydroquinone. Several studies led to the proposal that a dihydroquinone type of molecule is generated.

Reactivity with Oxygen

When an electron pulse is given to a solution with contains known quantity of oxygen, initially both semiquinone and $O_2^{\bullet-}$ (superoxide radical) may be produced depending on the relative concentrations and rate constants. However, in all cases studied so far, the following reaction

$\text{Quinone}+O_2^{\bullet-} \rightleftharpoons \text{Semiquinone}+O_2$ .... (38)

occur, with equilibrium, if any, established within a few hundred microseconds. The exact course of reaction depends entirely on the relative one-electron reduction potential of $O_2/O_2^{\bullet-}$ system (E^1 =-155 mV at 25°C vs NHE, when oxygen concentration is expressed in mol dm^{-3} unit) and $Q/Q^{\bullet-}$ system (see Table V for some representative values).

A close look on Table V will show that naphthoquinones may be reduced to their semiquinones with $O_2^{\bullet-}$ as $E(O_2/O_2^{\bullet-}) < E(Q/Q^{\bullet-})$. On the other hand, $O_2^{\bullet-}$ radicals are preferentially formed by the reaction of anthrasemiquinones with O_2 as $E(Q/Q^{\bullet-}) < E(O_2/O_2^{\bullet-})$.
The rate constant for the important reaction

$O_2^{\bullet-}+\text{Adriamycin} \rightleftharpoons O_2+$
Adriamycin semiquinone ... (39)

could be determined pulse radiolytically as 3.5 x 10^8 dm^3 $mol^{-1}s^{-1}$. If one assumes $E^1(O_2/O_2^{\bullet-})=-155$ mV and E^1 (adriamycin/adriamycin semiquinone)= –341 mV, one can calculate the equilibrium constant as 7.04×10^{-4} at *p*H 7. In the acidic *p*H, upto *p*H ~5, the K value does not change much. At *p*H <5, $HO_2^{\bullet}$ forms from $O_2^{\bullet-}$. At *p*H>7, the equilibrium is even more to the left. This consideration clearly shows that superoxide radicals are formed by reaction of the semiquinone with O_2, a finding of great biomedical significance.

Presence of oxygen in the vicinity of enzymatically produced anthracycline semiquinones leads to predominant formation of $O_2^{\bullet-}$, sometime leading to concomitant $OH^{\bullet}$ formation, causing cardiotoxicity and cytotoxicity. The equilibrium reaction eq. (39) may be used in calculating $E^1(Q/Q^{\bullet-})$ system by either measuring equilibrium concentrations or by measuring rate constants. Results are in agreement with the Marcus theory of electron transfer reactions.

Radiation Chemistry of Orthoquinones

Most of radiation chemical studies on quinones involve 1,4- or para-quinones. Recently, ortho-quinones have assumed renewed significance in melanoma-related studies[150]. It was interesting to note that limited stability of anisyl-3,4-quinone[151] prompted the authors to prepare anisyl-3,4-semiquinone by one-electron oxidation of anisyl - 3,4-hydroquinone, and not by one-electron reduction of the quinone. The transient absorption spectrum showed a maximum at ~320 nm and a smaller maximum at ~400 nm ($k=4.7\times10^9$ dm^3 $mol^{-1}s^{-1}$). This semiquinone was shown to form an equilibrium involving the parent quinone, O_2 and $O_2^{\bullet-}$. The favoured direction is $O_2^{\bullet-}$ reducing the quinone to its semiquinone. Calculations led to $E^1\geq+77$ mV. The authors set a limit of $E^1>>+100$ mV. The corresponding E^1_7 for the structurally related but unstable 1,2-benzoquinone[10] was estimated to be +210 mV pulse radiolytically. Such studies have physiological significance in explaining the cytotoxicity mechanism associated with the administration of 4-hydroxyanisole in the treatment of malignant melanoma.

Oxidation of Quinones

As the hydroxyl radical ($OH^{\bullet}$) is a non-selective oxidising agent, it is normally converted into some secondary radical by using a suitable chemical.

$$e_{aq}^- + N_2O \xrightarrow{H_2O} N_2 + OH^\bullet + OH^- \quad (40)$$

$$OH^\bullet + N_3^- \longrightarrow N_3^\bullet + OH^- \quad \ldots (41)$$

N_3^- may be replaced by halides, thiocyanate etc. e.g.

$$OH^\bullet + 2Br^- \longrightarrow Br_2^{\bullet -} + OH^- \quad \ldots (42)$$

Simple quinones undergo $OH^\bullet$ addition to the ring as oxidation reaction. On the other hand, hydroxy-substituted quinones can undergo additional oxidation reaction at the –OH site, first by addition to form cyclohexadienyl type radical, followed by water elimination to form semi-oxidised quinone as free radicals[152]. Such oxidation reactions of 1,4-dihydroxyquinones assumes special significance in view of these compounds being the central functional chromophoric centre of the quinonoid antitumour drugs, e.g. one-electron oxidation of adriamycin has been implicated by ESR studies[153]. However, such oxidation reactions are more complex than one-electron oxidation of juglone[116], of dihydroxy-anthraquinones and their sulphonate derivatives[125,154] which have been characterised by using $OH^\bullet$ and other more selective oxidants $N_3^\bullet$, $Br_2^{\bullet -}$, $SO_4^{\bullet -}$, $^\bullet CH_2CHO$ ($^\bullet CHCHO^-$), etc. As in the case of one-electron reduced species, one can measure the difference absorption spectrum (Fig. 14) and corrected spectrum (Fig. 15) for the one-electron oxidised substrate. Rate constants for the formation

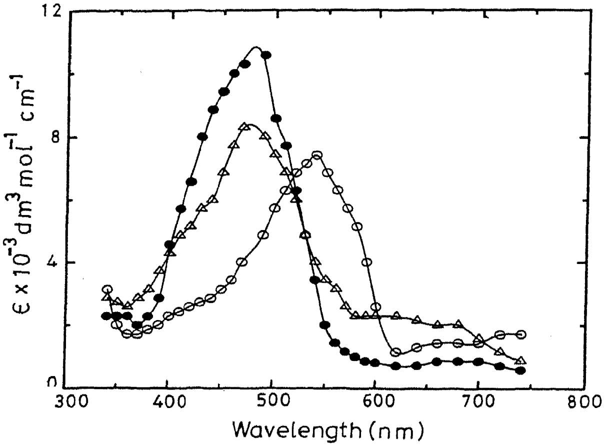

Fig. 15 Corrected absorption spectra of the one-electron oxidised quinones as in Fig. [14] (Reproduced from ref. [154] with permission)

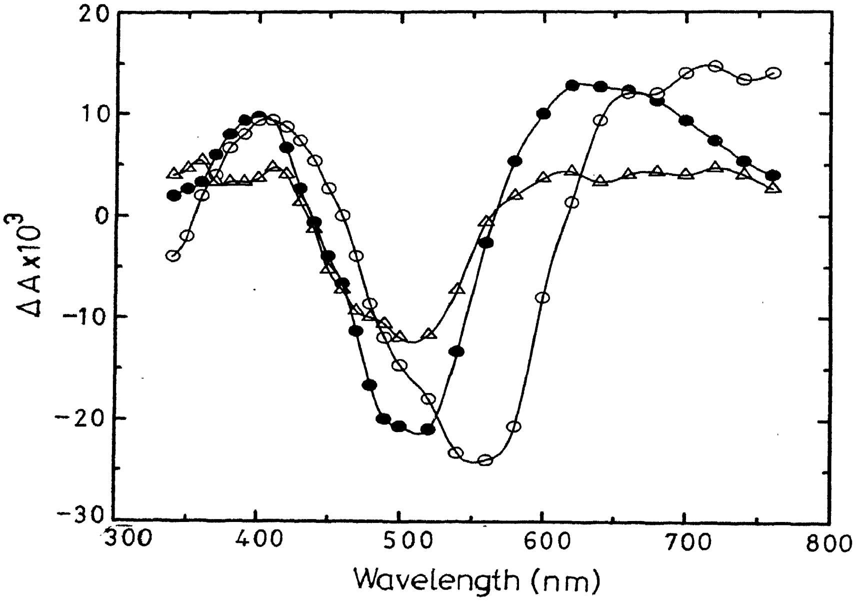

Fig. 14 Difference absorption spectra of the one-electron oxidised quinizarin (O), 1,5-dihydroxy-9,10-anthraquinone (Δ) and 1,8-dihydroxy -9,10-anthraquinone (●) at *p*H 11. Oxidant: NaN_3. Dose 9,4 Gy (Reproduced from ref. [154] with permission)

Table VI

Comparison of spectroscopic characteristics and pK of one-electron oxidised quinones in aqueous solution

Quinone	λ_{max}, nm (ε, $10^3 dm^3 mol^{-1} cm^{-1}$)		pK	Ref
	neutral	anionic		
2-Hydroxy-NQ(Lawsone)	340(3.4), 450(2.8)	-		116
5-Hydroxy-NQ (Juglone)	420(2.8), 540(3.1)	-		116
5,8-Dihydroxy-NQ	390(3.2), 500(4.8)	440(3.4)	<3.5	152
(Naphthazarin)	~800(broad) (0.7)	770(4.5), 870(3.9)		
1,4-Dihydroxy-AQ (Quinizarin)	i	390(3.0, 540(7.0)	i	154
1,5-Dihydroxy-AQ	i	472(10.5)	i	154
1,8-Dihydroxy-AQ	i	482(8.3)	i	154
Quinizarin 2-sulphonate	465(8.0)	390(2.9), 610(7.0)	8.0	154
Quinizarin 6-sulphonate	468(7.4)	420(4.0), 600(5.8)	7.9	154

i: Very poor solubility of the quinone at pH <10.5. No measurements

Table VII

Formation rate constants of transients formed by one-electron oxidation of some representative quinones (k in 10^9 dm^3 mol^{-1} s^{-1}) in aqueous solution

Quinone	$OH^{\cdot}$ (pH)	$N_3^{\cdot}$ (pH)	$O^{\cdot-}$ (pH)	Ref
2-Hydroxy-NQ	11.0 (7.5)	6.0 (7.0)	7.4 (12.5)	116
5-Hydroxy-NQ	2.6 (10.4)	3.9 (10.4)	1.3 (13.0)	116
5,8-Dihydroxy-NQ	3.4 (5.3),6.7 (9.2)	0.5 (5.8) 4.0 (9.1),4.8 (~13)	1.0(~13.0)	152
1,4-Dihydroxy-AQ(Quinizarin)	13.0(11.0)	6.5(11),7.0(~14)	3.7 (~14)	154
1,5-Dihydroxy -AQ	41.0 (11.0)	12 (11),14 (~14)	14.0 (~14)	154
1,8-Dihydroxy-AQ	21.0 (11.0)	10 (11),10 (~14)	5.0 (~14)	154
Quinizarin 2-sulphonate	9.7 (11.0)	1.4 (6.0) 4.4 (11),4.4 (~14)	1.7 (~14)	154
Quinizarin 6-sulphonate	11.0) (11.0)	1.3 (6.0) 5.6 (11),5.7 (~14)	1.5 (~14)	154

reactions are within the range 10^9-10^{10} $dm^3mol^{-1}s^{-1}$. It may be noted that, unlike in the case of reduced semiquinones, quinonoid character is retained in the semi-oxidised quinones. Some representative spectroscopic data are given in Table VI while rate constants are given in Table VII.

Mukherjee *et al.* have shown[152] that the decay of naphthazarin proceeds by a complicated mechanism not fully understood in spite of extensive studies. At low dose condition, there was no visible change in the concentration of naphthazarin. The pK of the semi-oxidised naphthazarin was shown as <4. The most interesting observation was the evidence for the disproportionation[136] proceeding to an equilibrium level in favour of the semiquinone[137]. Possibility of dimerisation of the one-electron oxidised species was not fully explored.

Contrary to the naphthazarin case, dihydroxyanthraquinones form semi-oxidised quinones which undergo simple bimolecular disproportionation to the diquinone and parent quinone[154]. The pK for semi-oxidised anthraquinone derivatives was measured and shown to be around ~8.

The third aromatic ring in the anthraquinone derivatives possibly renders all secondary reactions very slow in comparison with the timescale for radical decay.

Future Prospects

It is amazing that quinones have sustained interest of radiation chemists for over three decades. The basic radiation chemistry of simple quinones and their simple derivatives is now well-understood. Therefore, efforts have to be diverted to complex derivatives of quinones, as the characteristics of the parent as well as the semiquinones will depend heavily on the perturbing groups/rings present. The accumulated data will give a clear insight into the perturbation effect of the overall substitution.

In the present scenario of protection of product development rights, it is expected that a large number of new products, based on the basic anthracycline structure will be developed for anti-tumour trials. While basic radiation chemistry may not differ significantly from what we already know, it will be very interesting to know how the redox properties change with new structures[155]. The most important characteristics for either anti-tumour action or toxicity is the redox potential values. We should be able to put substituents at will to have a desired redox potential of the substrate. This is extremely important from research point of view. However, no concerted effort has been directed to this goal.

A large number of studies are expected towards understanding the chemistry of the metabolites derived from complex biological quinones. Right now the field is barren, mainly because the facility of pulse radiolysis is not available openly to scientists the world over.

In the basic research areas, very wide scope exists towards understanding the characteristics of the excited S_1/T_1 states and their reactivities. Quinones, by virtue of their electronegativity, form and ideal partners for electron transfer. A number of studies have begun where quinone moiety is bridged with another moiety through methylene bridges, e.g. prophyrin-quinone bridged systems[156,157]. Presently, only basic data may be collected on excitation and electron transfer. In few years' time, such systems may find wide application in photodynamic therapy, where light will be absorbed by the prophyrin, electron transfer will take place and the semiquinone developed will participate in the anti-tumour activity.

In a biological environment, the redox properties of the quinone/semiquinone system will be profoundly affected by solvation as well as by complexation with other surrounding molecules, and also by availability of large number of free and bound protons. Semiquinones are capable of complexing with quinones, other semiquinones, as well as hydroquinones. They can also complex with metal ions[158,159]. Even in the simplest case of Cu^{2+}/benzosemiquinone system, the latter substitute for a water molecule in the co-ordination sphere of the metal ion. Although the reduction potential of benzoquinone is +99 mV and that of Cu^{2+} is +153 mV, no rapid inner-sphere electron transfer is seen.

Micellar systems and microemulsions provide useful biological models for specific studies. We have demonstrated the generation of a large number of semiquinones in cationic, anionic and neutral micelles by simple light irradiation. It will be interesting to study chemistry of the semiquinones of water-insoluble complex biologically important quinones dissolved in micelles and microemulsions.

In short, there is ample scope for furtherance of knowledge of photo and radiation chemistry of quinones.

Acknowledgements

The author is grateful to Jyoti Pandya for meticulous typing of the manuscript and M C Rath for assistance in getting the figures done. The author also wishes to express his deep gratitude to his co-authors, both at Paterson Institute, Manchester and in BARC, Mumbai.

References

1 *The Chemistry of Functional Groups, The Chemistry of the Quinonoid Compounds* (Eds: S Patai and Z Rappoport) Wiley New York **2** (1988)

2 *The Chemistry of the Quinonoid Compounds* (Ed: S Patai) Wiley London (1974) **Parts 1 & 2**

3 R H Thompson *Naturally Occurring Quinones* Chapman and Hall London **3** (1987)

4 R A Morton (Ed) *Biochemistry of Quinones* Academic Press New York (1965)

5 D Geed, B J Hales and G Porter *Proc Royal Soc A* **334** (1973) 505

6 J Butler and B M Hoey *Br J Cancer* **55** (suppl-III) (1987) 53

7 J S Driscoll, G F Hazard, H B Wood and A Goldin *Cancer Chem Rep* **2** (1974) 1

8 F Arcamone *Doxorubicin Anticancer Antibiotics,*

Medicinal Chemistry Monograph Vol 17 Academic Press New York (1981)
9 M S El-Khadem (Ed) *Anthracycline Antibiotics* Academic Press New York (1982)
10 A J Swallow *Functions of Quinones in Energy Conserving Systems* (Ed: B J Trumpower) Academic Press New York (1982) 59
11 R Bensasson, E J Land and T J Truscott *Excited States and Free Radicals in Biology and Medicine* Oxford University Press Oxford (1993) Ch 11
12 P Neta *The Chemistry of the Quinonoid Compounds* (Ed: S Patai and Z Rappoport) John Wiley New York **2** (1989) 879
13 J Mayer (Ed) *Properties and Reactions of Radiation Induced Transients: Selected Topics* Polish Scientific Publishers PWN Warszawa (1999) 205
14 R Bensasson, E J Land and T J Truscott *Flash Photolysis and Pulse Radiolysis* Oxford University Press Oxford (1983)
15 *The Study of Fast Processes and Transient Species by Electron Pulse Radiolysis* (Eds: J H Baxendale and F Busi) Reidel Dordrecht (1982)
16 J M Bruce *The Chemistry of the Quinonoid Compounds* (Ed: S Patai) John Wiley London (1974) Part 1 Ch 9 p 465
17 J M Bruce *Quart Rev* **21** (1967) 405
18 Colour Index 4th edition *Society of Dyers and Colour* Bradford U K (1992)
19 C G Giles and R S Sinclair *J Soc Dyers and Colour* **88** (1972) 109; **89** (1973) 56
20 G S Egerton and A G Roach *J Soc Dyers and Colour* **74** (1958) 401 & 408
21 G S Egerton and O N E N Assaad *J Soc Dyers and Colour* **83** (1967) 45 & 409
22 J F McKellar *Radiat Res Rev* **3** (1971) 141
23 M W Rembold and H E A Kramer *J Soc Dyers Colour* **94** (1978) 12; **96** (1980) 122
24 A A Gorokhovski, K K Kaarh and L A Rebane *JETP Lett* **20** (1974) 216
25 B M Kharlamov, R I Personov and L A Bykovskaya *Opt Commun* **12** (1974) 191
26 L A Rebane, A A Gorokhovski and J V Kikas *Appl Phys* **B 29** (1984) 235
27 J Friedrich and D Haarer *Angew Chem (Intl Ed Engl)* **23** (1984) 113
28 W E Moerner *J Mol Electron* **1** (1985) 55
29 M Mailer *Appl Phys* **B 41** (1986) 73
30 A Lallemond *Ann Chim Phys* **49** (1948) 1857
31 G Ciamician and O Silber *Ber* **34** (1901) 1530
32 A Schonberg and A Mustafa *Chem Rev* **40** (1947) 181
33 A Kuboyama, R Yamazaki, S Yabe and Y Uchara *Bull Chem Soc Japan* **42** (1969) 10
34 W Herre and P Weis *Spectrochim Acta(A)* **29** (1973) 205
35 P Galaup, J Megel and H P Trommsdorff *Chem Phys Lett* **41** (1976) 397
36 E Kanezki, N Nishi and M Kinoshita *Bull Chem Soc Japan* **52** (1979) 2836
37 H R Drott and H R Dearman *J Chem Phys* **47** (1967) 1896
38 J D Scott and W H Watson *J Chem Phys* **49** (1968) 4246
39 N V Platonova, K R Popov and L V Smirnov *Opt Spectrosc* **26** (1969) 197
40 A A Lamola and G S Hammond *J Chem Phys* **43** (1965) 2129
41 C A Parker and G S Hatchard *Analyst (London)* **87** (1962) 664
42 G D Baruch, S N Singh and R S Singh *Bull Chem Soc Japan* **42** (1969) 3572
43 S N Singh and R S Singh *Indian J Pure Appl Phys* **5** (1967) 342 & 394
44 W G Herkstroeter, A A Lamola and G S Hammond *J Am Chem Soc* **86** (1964) 4537
45 M Kasha *Radiat Res Suppl* **2** (1960) 243
46 A Kuboyama and S Yabe *Bull Chem Soc Japan* **40** (1967) 2475
47 K E Drabe, H Veenvliet and D A Wiersma *Chem Phys Lett* **35** (1975) 469
48 H H Dearman, N Sundarachari and D Uklu *J Chem Phys* **45** (1966) 4563
49 T Murao and T Azumi *J Chem Phys* **70** (1979) 4460; **72** (1980) 4401
50 S Khalil and L Goodman *J Phys Chem* **80** (1976) 470
51 K K Lehmann, J Smolarek, O S Khalil and L Goodman *J Phys Chem* **83** (1979) 1200
52 N S Strokach, D N Shigorin and B N Kolokolov *Opt Spectrosc* **43** (1977) 514
53 D K Palit *Ph D Thesis* University of Bombay Bombay (1989)
54 H Pal *Ph D Thesis* University of Bombay Bombay (1991)
55 D K Palit, H Pal, T Mukherjee and J P Mittal *J Chem Soc Faraday Trans* **86** (1990) 3861
56 H Inoue, M Hida, N Nakashima and K Yoshihara *J Phys Chem* **86** (1982) 3184
57 S R Folm and P F Barbara *J Phys Chem* **89** (1985) 4489
58 P F Barbara, P K Walsh and L F Brus *J Phys Chem* **93** (1989) 29
59 J R Lakowicz *Principles of Fluorescence Spectroscopy Plenum Press* New York (1983)
60 D V O'Connor and D Phillips *Time Correlated Single Photon Counting* Academic Press New York (1984)
61 J N Demas *Excited State Lifetimes Measurements Academic Press* New York (1983)
62 D K Palit, T Mukherjee and J P Mittal *J Indian Chem Soc* **LXIII** (1986) 35
63 D K Palit, H Pal, T Mukherjee and J P Mittal *J Photochem* **37** (1987) 95
64 D K Palit, H Pal, T Mukherjee and J P Mittal *J Photochem Photobiol A:Chem* **43** (1988) 59
65 D K Palit, H Pal, T Mukherjee and J P Mittal *J Photochem Photobiol A:Chem* **52** (1990) 375
66 H Pal, D K Palit, T Mukherjee and J P Mittal *Chem Phys Lett* **173** (1990) 354
67 D K Palit, H Pal, T Mukherjee and J P Mittal *Chem Phys* **126** (1988) 441
68 H Pal, D K Palit, T Mukherjee and J P Mittal *Indian J Chem* **31A** (1992) 811
69 H Pal, D K Palit, T Mukherjee and J P Mittal *J Chem Soc Faraday Trans* **89** (1993) 683
70 H N Ghosh, H Pal, D K Palit, T Mukherjee and J P Mittal *J Photochem Photobiol A:Chem* **73** (1993) 17

71 M C Rath and T Mukherjee *J Chem Soc Faraday Trans* **93** (1997) 3331

72 T Mukherjee and J M Bruce *Indian J Chem* **33A** (1994) 386

73 P Avouris, W M Gilbert and M A El Sayed *Chem Rev* **77** (1977) 793

74 T P Carter, M.H. Van Benthen and G D Gillespie *J Phy Chem* **87** (1983) 1891

75 T P Carter, G D Gillespie and M A Connolly *J Phys Chem* **86** (1982) 192

76 G Smulerich, A Amirav, U Evan and J Jortner *Chem Phys* **73** (1982)

77 N Ideda, T Okada and N Mataga *Chem Phys Lett* **69** (1980) 251

78 N Mataga *Molecular Association* (Eds: H Ratajczak and J W Orville-Thomas) Wiley Chichester **2** (1981) p 509

79 L A Hallidy and M R Topp *Chem Phys Lett* **48** (1977) 40; *J Phys Chem* **82** (1978) 2273 & 2415

80 G Smulevich and P Foggi *J Chem Phys* **87** (1987) 5664

81 J Ritter, H U Borst, T Lindner, M Hauser, S Brosig, K Bredereck, U E Steiner, D Kuhn, J Keleman and H E A Kramer *K Photochem Photobiol A: Chem* **41** (1988) 227

82 B Samori, A Rosai, I D Pellarno, G Marconi, L Valentini, B Gioria and A Vigavani *J Chem Soc Perkin Trans II* (1987) 1419

83 M D Barkley, A A Kowalczyk and L Brand *J Chem Phys* **75** (1981) 3581

84 J B Birks *Photophysics of Aromatic Molecules* Wiley London (1970)

85 H Labhart and W Heizelmann In: *Organic Molecular Photophysics* (Ed: J B Birks) Wiley New York (1973)

86 R Bensasson and E J Land *Photochemical and Photobiological Reviews* **3** (1978) 163

87 P J Wagner and G S Hammond *Advances in Photochemistry* Vol **5** (Eds: W A Noyes, G S Hammond and J N Pitts) *Interscience* New York (1968)

88 S P McGlynn, T Azumi, M Kinoshita *Molecular Spectroscopy of the Triplet State* Prentice Hall New Jersey (1969)

89 E J Land and A J Swallow *Arch Biochem Biophys* **145** (1971) 365

90 G Porter and F Wilkinson *Proc Royal Soc* **A 264** (1961) 1

91 I Carmichael and C L Hug *J Phys Chem Ref Data* **15** (1986) 1

92 D K Palit, T Mukherjee and J P Mittal *J Indian Chem Soc* **63** (1986) 35

93 D K Palit, H Pal, T Mukherjee and J P Mittal *J Photochem* **37** (1987) 95

94 D K Palit, H Pal, T Mukherjee and J P Mittal *J Photochem Photobiol A:Chem* **43** (1988) 59

95 D K Palit, H Pal, T Mukherjee and J P Mittal *J Photochem Photobiol A:Chem* **52** (1990) 375

96 H Pal, D K Palit, T Mukherjee and J P Mittal *J Photochem Photobiol A:Chem* **62** (1991) 183

97 E J Land *Proc Royal Soc (London)* Ser **A 305** (1968) 457

98 J T Richards and J K Thomas *Trans Faraday Soc* **66** (1970) 621

99 E Amouyal, R Bensasson and E J Land *Photochem Photobiol* **30** (1974) 415

100 H Labhart Helv *Chem Acta* **47** (1964) 2279

101 R Bensasson, C Chachaty, E J Land and C Salet *Photochem Photobiol* **16** (1972) 27

102 R Bensasson and E J Land *Trans Faraday Soc* **67** (1971) 1904

103 B E Hulme, E J Land and G O Phillips *J Chem Soc Faraday Trans 1* **68** (1972) 2003

104 E J Land, E McAlpine, R S Sinclair and T G Truscott *J Chem Soc Faraday Trans 1* **72** (1976) 2091

105 A Andreoni, E J Land, V Malatesa, A J McLean and T G Truscott *Biochim Biophys Acta* **990** (1989) 190

106 T Nakayama, K Ushida, K Hamanoue, M Washio, S Tagawa and Y Tabata *J Chem Soc Faraday Trans* **86** (1990) 95

107 J H Fendler and E J Fendler *The Chemistry of the Quinonoid Compounds* (Ed: S Patai) *(Part 1)* John New York (1974) p 539

108 J Perkowski and J Mayer *J Radioanal Nucl Chem* **132** (1989) 269

109 J Perkowski and J Mayer *J Radioanal Nucl Chem* **172** (1993) 19

110 J Perkowski and J Mayer *J Radioanal Nucl Chem* **173** (1993) 339

111 T Mukherjee *Atomic Molecular and Cluster Physics* (Ed: S A Ahmad) *Narosa* New Delhi (1997) p 299

112 A J Swallow *Prog Reaction Kin* **9** (1978) 238

113 T Mukherjee, A J Swallow, P M Guyan and J M Bruce *J Chem Soc Faraday Trans* **86** (1990) 1483

114 H Pal and T Mukherjee *J Indian Chem Soc* **70** (1993) 409

115 M C Rath and T Mukherjee *Radiat Phys Chem* **49** (1997) 29

116 M C Rath, H Pal and T Mukherjee *J Chem Soc Faraday Trans* **92** (1996) 1891

117 T Mukherjee *Radiat Phys Chem* **29** (1987) 455

118 E J Land, T Mukherjee, A J Swallow and J M Bruce *J Chem Soc Faraday Trans* 1 **79** (1983) 391

119 H Pal, D K Palit, T Mukherjee and J P Mittal *Radiat Phys Chem* **37** (1991) 227

120 B E Hulme, E J Land and G O Phillips *J Chem Soc Faraday Trans I* **68** (1972) 1992

121 D Meisel and P Neta *J Am Chem Soc* **97** (1975) 5198

122 H Pal, T Mukherjee and J P Mittal *Radiat Phys Chem* **44** (1994) 603

123 H Pal, D K Palit, T Mukherjee and J P Mittal *Radiat Phys Chem* **40** (1992) 529

124 T Mukherjee, E J Land, A J Swallow, P M Guyan and J M Bruce *J Chem Soc Faraday Trans 1* **84** (1988) 2855

125 H Pal, D K Palit, T Mukherjee and J P Mittal *J Chem Soc Faraday Trans* **87** (1991) 1109

126 M C Rath, H Pal and T Mukherjee *Radiat Phys Chem* **47** (1996) 221

127 H Pal, T Mukherjee and J P Mittal *J Chem Soc Faraday Trans* **90** (1994) 711

128 E J Land, T Mukherjee, A J Swallow and J M Bruce *British J Cancer* **51** (1985) 515

129 E Mc Alpine, R S Sinclair, T G Truscott and E J Land *J Chem Soc Faraday Trans I* **74** (1978) 597

130 J Mayer and R Krasluklanis *J Chem Soc Faraday Trans* **87** (1991) 2943

131 H Chandra, L Portwood and M C R Symons *J Chem Soc Faraday Trans I* **85** (1989) 1801

132 M C Depew, Z -L Liu and J K S Wan *J Am Chem Soc* **105** (1983) 2480

133 Z -L Liu, L -M Wu and Y -C Liu *Magn Reson Chem* **26** (1988) 577

134 N J F Dodd and T Mukherjee *Biochemical Pharmacology* **33** (1984) 379

135 T Mukherjee, B Cercek, N J F Dodd and A J Swallow *Radiat Phys Chem* **30** (1987) 271

136 J Mayer and R Krasiukianis *Radiat Phys Chem* **36** (1990) 169

137 J Mayer and R Krasiukianis *Radiat Phys Chem* **37** (1990) 273

138 P Wardman *J Phys Chem Ref Data* **18** (1989) 1637

139 K B Patel and R L Willson *J Chem Soc Faraday Trans* **69** (1973) 814

140 E J Land, T Mukherjee, A J Swallow and J M Bruce *Archives Biochem Biophys* **225** (1983) 116

141 T Mukherjee, E J Land, A J Swallow and J M Bruce *Archives Biochem Biophys* **272** (1989) 450

142 J Butler and B M Hoey *Free Rad Biol Med* **2** (1986) 77

143 E J Land, T Mukherjee, A J Swallow and J M Bruce *J Chem Soc Faraday Trans 1* **79** (1983) 405

144 S S Pan, P A Andrewsm, C J Glover and N R Bachur *J Biol Chem* **259** (1984) 959

145 B Hoey, J Butler and A J Swallow *Biochem* **27** (1988) 2608

146 R J Sturgeon and S G Schulman *J Pharm Sci* **66** (1977) 958

147 B A Sringen and G Powis *Arch Biochem Biophys* **209** (1981) 209

148 C Houee-Levin, M Gardes-Albert, C Ferradini, M Faraggi and M Klapper *FEBS Lett* **179** (1985) 46

149 J S Lea, F A P Rushton E J Land and A J Swallow *Free Rad Res Comms* **8** (1990) 241

150 C Lambert, J N Chacon, M R Chedekel, E J Land, P A Riley, A Thompson and T G Truscott *Biochim Biophys Acta* **993** (1989) 12

151 C J Cooksey, E J Land, P A Riley, T Sarna and T G Truscott *Free Rad Res Comms* **4** (1987) 131

152 T Mukherjee, E J Land, A J Swallow, J M Bruce, P C Beaumont and B Parsons *J Chem Soc Faraday Trans 1* **84** (1988) 3423

153 D D Pietronigro, J E Mc Guinness, M J Koren, R Gippa, M L Seligman and H B Demopoulos *Physiol Chem Phys* **11** (1979) 405

154 H Pal, D K Palit, T Mukherjee and J P Mittal *J Chem Soc Faraday Trans* **88** (1992) 681

155 M C Rath, R T Pardasani, P Pardasani, S Muktawat, R Ghosh and T Mukherjee (to be published)

156 G Bhaskar Maiya (Private Comm)

157 E J Land, D Lexa, R V Liddell and G A Nemeth *J Phys Chem* **91** (1987) 4831

158 S Das, P C Mandal, M C Rath and T Mukherjee *Res Chem Intermed* **25** (1999) 351

159 S Das, P C Mandal, M C Rath and T Mukherjee *Radiat Res* (1999) (in print)

MAGNETIC FIELD EFFECT IN CHEMISTRY—THE INDIAN SCENARIO

SAMITA BASU*, MINTU HALDAR† AND MIHIR CHOWDHURY†

Nuclear Chemistry Division, Saha Institute of Nuclear Physics, 1/AF, Bidhannagar, Calcutta 700 064, (India)

†*Department of Physical Chemistry, Indian Association for the Cultivation of Science,*
Jadavpur, Calcutta 700 032 (India)

In the last three decades it has been conclusively established that a small magnetic field, even though energetically insignificant, may substantially influence the dynamics of reactions in which a radical pair (RP) is formed as an intermediate. The basic concepts of Radical Pair Mechanism have been elaborated. Illustrations have been provided with photochemical reactions of singlet and triplet RPs investigated in Indian laboratories.

Key Words: Magnetic Field Effect in Chemistry; Spin Chemistry; Radical Pair Mechanism; Radical Reactions; Exciplex Luminescence; Flash Photolysis.

Introduction

Amongst the short-lived intermediates of chemical reactions, radicals have drawn considerable attention owing to their ubiquity and high reactivity. A determination of the nature of the intermediate and their spatial dynamics is not enough for understanding chemical and biological reactions involving radical pairs (RP) or radical ion pairs (RIP); a knowledge of the time-evolution of the spin states of the RP/RIP is essential. Chemical reactions of RPs are dependent on the spin state. In the elementary act of bond-breaking and bond-forming the electron spin angular momentum of the RP has to be conserved in the absence of compensatory changes in other types of angular momentum. Various types of *magnetic interactions* are able to change the electron spin state of reactive RP/RIP intermediates and thus transform the non-reactive radicals into the reactive ones. Even though the contribution of magnetic interaction to chemical energy is vanishingly small, one can still exercise considerable control over the dynamics of geminate recombination of RP by switching a magnetic field on and off, which in turn opens or closes certain spin channels. This combined evolution of spin and spatial separation of a RP/RIP in the presence or absence of a magnetic field has received considerable attention these days[1-12] and has been baptized by a new name 'spin-chemistry'. This brief overview discusses some selected aspects of spin-chemistry and highlights the contributions from Indian scientists.

Historical Perspective

Physical Chemists, as match-makers between Physics and Chemistry, have always considered it their prerogative to investigate the influence of different forms of energy on chemical reactions. The roles played by heat, electricity, and light had been well-recognised for a long time. It was natural, therefore for scientists to ask the question — can magnetic field affect a chemical reaction? Towards the end of the nineteenth century and the beginning of the twentieth century a number of exploratory experiments were attempted even though there was no sound theoretical justification for MFE. The first report of MFE on non-magnetic materials was in 1908 by Rosenthal[13], who observed that the hydrolysis of starch was influenced by field; but it was quickly refuted by

---

*E.Mail:*PCMC@Mahendra. iacs.res.in

Ceigelsky[14]. Reports came in sporadically, but all these suffered from two defects. First, these effects were extremely small and second, irreproducible. The field remained factually controversial and conceptually illusory for a long time. Early experimentalists craved for some new light from fellow theoretical scientists.

Bhatnagar *et al.* in 1929 tried to explain the magnetic field effect on certain redox reactions by adding a Zeeman energy term to Free Energy of activation and the Thermodynamic Free Energy of a reaction[15]. Simple calculation, however, showed that even for paramagnetic ions the magnetic perturbation energy at the accessible laboratory field of 10 KG is 3×10^4 times smaller than the thermal energy. It is obvious, therefore , that one needs to go a little deeper into chemical bond formation to explain the relationship between magnetic field and chemical reaction.

During the mid twenties earth-shaking discoveries occurred in Physics, and the ripples generated thereof rocked chemistry too. First, there was the discovery of electron spin which explained the magnetic behaviour of atoms with unpaired electrons. Second, Heitler-London treatment of the simplest chemical bond, namely H_2 molecule, showed that the spins of an electron pair need to be opposite for bond formation. If the spins of two electrons in two interacting atoms be the same, a repulsive state results. Thus, mere collision between two H atoms is not enough to form a bond; their spins should also be appropriately oriented. In other words, the pre - exponential factor Z in the Arrhenius rate expression (Rate=Z exp $(-E^{\neq}/RT)$) should be dependent on the spin orientation. The current explanation of magnetic field effect (MFE) on a radical pair recombination process focuses precisely on this term (instead of the energy - sensitive exponential term proposed by Bhatnagar).

Wigner in 1933 first gave a concrete model for MFE on catalysed ortho-para conversion of H_2 molecule[16]. If a *o*-H_2 molecule (nuclear spins parallel) sits on the surface of a ferromagnetic substance with its axis perpendicular to the surface, the two spins on the two atoms experience different fields; their frequencies (ω) of precessional motion around the axis (i.e., $\omega = g\beta H$, where g is the Lande *g*-factor, β the Bohr magneton and H the external magnetic field) become different, leading to a rapid conversion to the para-form with anti-parallel spin orientation. This explanation of Wigner did not have appreciable effect on magneto-chemists until the chemically induced dynamic nuclear polarisation (CIDNP) was discovered accidentally in the end-sixties. The idea that non-equilibrium nuclear spin (as also an external field) could affect the rate of chemical recombination of a RP gained momentum and a number of precise well-thought-out experiments were performed since end-seventies.

The so-called RP/RIP mechanism lying at the heart of CIDNP/CIDEP phenomena turned out to be the most valuable key for systematically tracing out magnetic field effects on chemical kinetics and kinetically-controlled yields[7]. During the last three decades magnetic field effects have been studied extensively for various kinds of photochemical and biological reactions such as photoinduced electron and hydrogen abstraction, photodecom-position, photosubstitution, photoisomerization and photosynthesis. In conjunction with the experimental studies, theoretical concepts of magnetic field effects on chemical reactions have been developed by a number of workers, as summarised in several reviews and books[1-12].

Theoretical Consideration

According to the classical transition state theory the rate constant of a chemical reaction is given by $k = k_{el}\nu_n \exp[-\Delta G^{\neq}/k_B T]$, where ν_n is the frequency of passage (nuclear motion) through the transition state at the intersection point of the potential energy surfaces of the reactants and the product, $\Delta G^{\neq}$ the free energy of activation, k_B the Boltzmann constant, T the temperature in Kelvin and k_{el} the electronic transmission coefficient which is a measure of the averaged transition probability per passage through the intersection region. A substantial magnetic field effect on chemical reaction might indeed be possible if the k_{el} could be affected by changing the number of degrees of freedom accessible to a chemical system. Two types of chemical reactions can be distinguished according to the degree of electronic coupling between reactant and product states. For an adiabatic reaction, where there is substantial coupling, i.e $k_{el} \approx 1$, any significant magnetic field effect might be excluded. For non-adiabatic reactions which involve very weak electronic coupling, i.e., $k_{el} << 1$, the magnetic field effect could be significant, if potential energy surfaces of different spin multiplicities are involved in the crossing. Such an explanation has often been invoked for magnetic field effect on emission intensity in vapour phase, such as that from I_2, CS_2, NO_2, carbonyl compounds, SO_2 and alkali metals[11].

The above suggestion that the vapour phase MFE originates from nearly forbidden transitions between degenerate states of different multiplicities at the crossing point of potential energy surface (PES) is transferable to the condensed phase in somewhat modified form; for instance, the potential energy curves of ^{3}RP and ^{1}RP nearly merge for distances greater than 10Å, and a magnetic field can then easily activate or deactivate the transition between the two curves at distances where the two states are degenerate. This mechanism known as Radical Pair Mechanism (RPM) consists of following steps:

(a) Excitation of a molecule to the singlet state, from which the molecule may or may not deactivate to the triplet state by spin-orbit coupling (SOC)-induced intersystem crossing (ISC) process.

(b) Generation of a RP (or RIP) in a definite spin-correlated state which, depending on the spin-parentage, could be a singlet, or a triplet (triply degenerate) or a coherent mixture of the two. In photochemical reactions, it is possible to transmit the spin-multiplicity of the precursor to the RP generated by bond cleavage or electron transfer or H-transfer, because all these processes are much faster than the spin flipping process.

(c) The two radical partners then separate from each other through thermal motion until their coupling (i.e., exchange integral, J) becomes zero which makes all four states of RPs/RIPs nearly degenerate.

(d) At this stage a magnetic field (internal or external) could change the relative spin orientation of the partners of the RPs when the two components of the RP remain for considerable time as a geminate pair within the cage formed by the surrounding solvent molecules.

(e) Finally, a bond is formed at the time of re-encounter which is termed as geminate recombination. If SOC-induced triplet recombination is small, the cage products could originate only from singlet RPs/RIPs. The triplet RP can not recombine (unless SOC has mixed it with the singlet state) and therefore escape from the cage as separated radicals or free ions to form escape products. Therefore, the ratio of cage to escape product is determined by the spin state at the time of combination. If the RPs/RIPs are generated initially in the singlet state, a reduction (or enhancement) in the ISC rate by a magnetic field brings about an increase (or decrease) of the cage product and a decrease (or increase) of the escape product. The reverse is the case when the RPs/RIPs are formed initially in the triplet state.

The overall dynamics is complicated since various processes like spin evolution, diffusional motion, non-radiative decays and chemical combination mutually influence each other. In order to understand the dynamic behaviour of the RP, a stochastic Liouville equation[7] needs to be solved. The Liouville equation approach, though intellectually satisfying, is hardly followed by chemists for explaining experimentally observed intricacies. A reaction rate approach is more pragmatic, though empirical in nature. Following kinetic framework (Scheme 1) is convenient for

DETAILS OF INTERSYSTEM CROSSING PROCESS

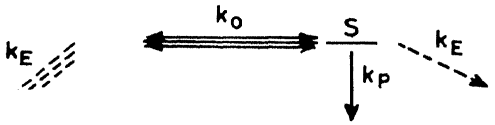

IN ABSENCE OF EXTERNAL MAGNETIC FIELD

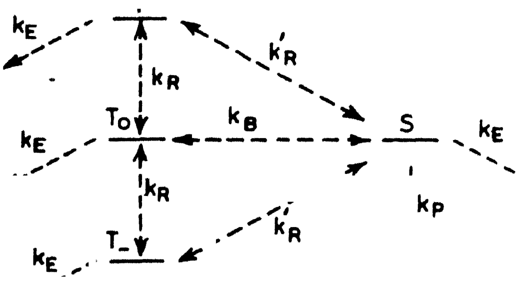

IN PRESENCE OF A SUFFICIENTLY LARGE FIELD

Scheme 1

discussion of observed trends of MFE on dynamics. Magnetic field sensitive rates are k_B, k_R and k_R', while k_0, k_E, k_S, and k_T are independent of field. Although the main focus of our discussion is the field-sensitive pathways which cause ISC within the RP, the field-insensitive ones are almost equally important in determining the overall magnitude of MFE and the dynamical behaviour of a RP.

Before a discussion of the individual rate processes, let us represent diagrammatically singlet and triplet states of a RP. According to Fig. 1 the

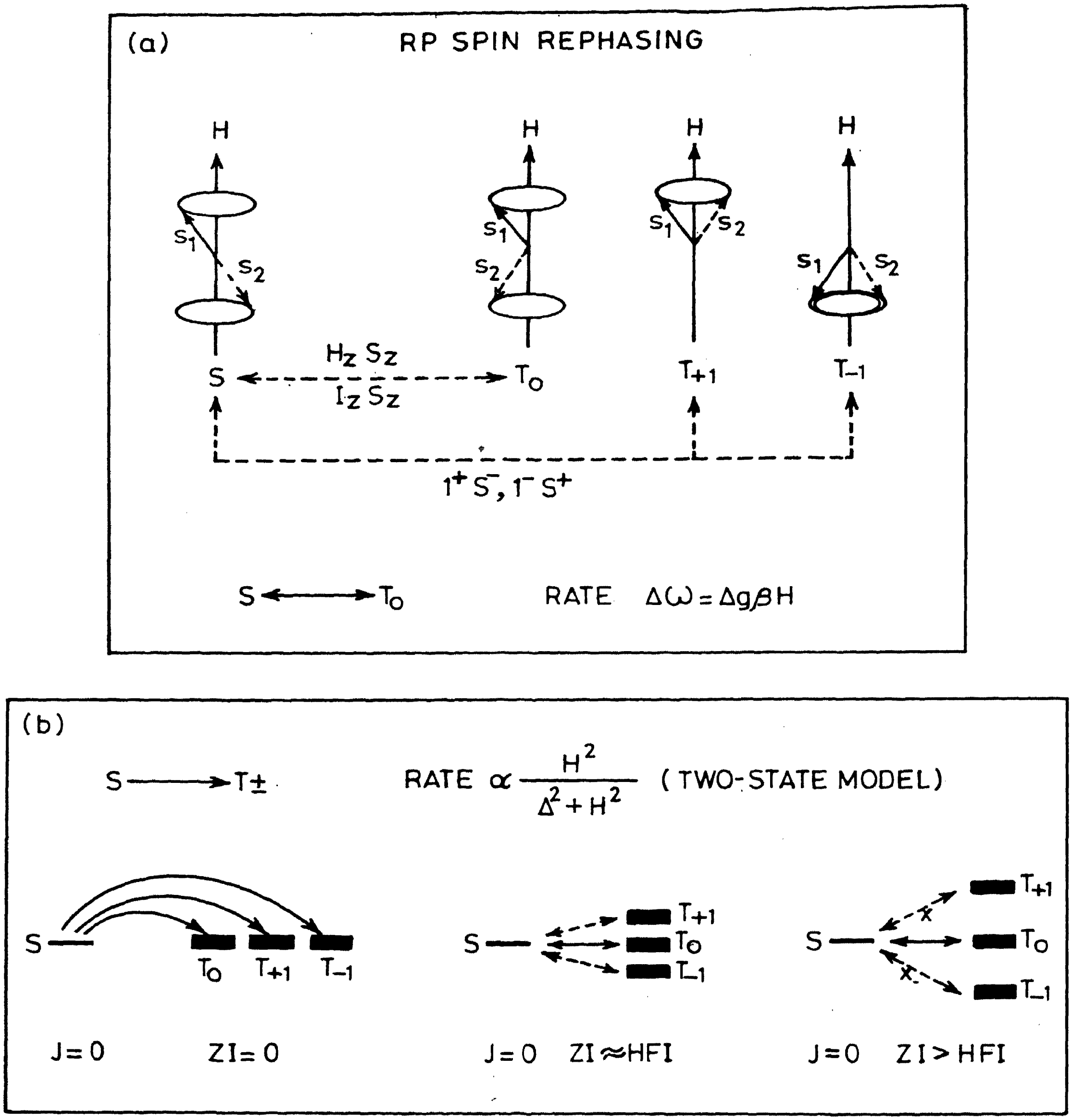

Fig. 1 A diagramatic representation of the singlet to triplet evolution within a radical pair, (a) shows that $S \leftrightarrow T_0$ spin evolution takes place by the interaction of the externally applied magnetic field and/or by the interaction of the component of nuclear moment and the component of spin moment in the z-direction, whereas, $S \leftrightarrow T_\pm$ spin evolution takes place by the interaction of the components of the nuclear and the spin moments which are perpendicular to z-axis, (b) shows how the increasing Zeeman interaction (ZI) (i.e., increasing magnetic field) suppresses the $S \leftrightarrow T$ evolution by gradually blocking the $S \leftrightarrow T_\pm$ channels.

individual electron spin motions are confined to cones described along the axis of quantization (suppose it to be the laboratory z-axis), nearly upward for α-spin and nearly downward for β-spin. The result of the vectorial sum of two electron spins could be either 1 or 0. The first results in three degenerate triplet (T) states with spin orientations T_+ ($\alpha\alpha$), T_0 (½ ($\alpha\beta+\beta\alpha$)) and T ($\beta\beta$), which have the resultants nearly parallel, perpendicular and antiparallel to the z-axis respectively; and the second in a singlet (S) state with spin function (½($\alpha\beta-\beta\alpha$)). Note that in the three triplet states the magnitudes of resultant vectors remain same, only their orientations with respect to the z-axis are different . The precessional motions of the two spin vectors in S and T_0 states differ in phase which is responsible for the difference in the length of the resultant vector. In brief, a spin-rephasing is necessary for the S↔T_0 transition while a spin-flipping is required for T_0, S↔$T_\pm$ transitions.

Let us now discuss the role of the field in determining the magnitude of each of the individual rates in Scheme 1.

(a) S↔T_0 Transition Rate, k_B

If the distance between the component radicals of the RP/RIP is such that the coupling between the two spin vectors is negligible, i.e., $J \approx 0$, the two vectors s_1 and s_2 precess independently around the applied field (H) in the z-direction with frequencies $\omega_i = g_i \beta_e H$, where g_i is the Lande g-factor for the i-th radical and β_e the Bohr magneton for electron. The difference in precessional frequencies ($\Delta\omega$) of the two component spin vectors, which is proportional to the difference of g-factors (Δg) of the radicals, causes the relative spin orientation appropriate for S to evolve into a spin orientation corresponding to T_0. However, by this mechanism S↔$T_\pm$ transition rates are not affected by an external magnetic field. For organic c-centered radicals Δg is of the order of 0.001[4], and it follows that k_B is of the order of 10^9 in a field of 10 Tesla. If there are heavy atoms in the molecule, particularly if the heavy atom is close to the unpaired electron centre, the Δg-controlled k_B could be larger. The important point to note is that this rate is proportional to the magnetic field, by adjusting which it is possible to make k_B greater or less than other competing reaction rates such as k_S and k_E.

(b) Zero Field S↔T_0, $T_\pm$ Rate, k_o

The value of k_0 is important for MFE in as much as it determines the ratio of the rate at the field B to the rate at zero field. The k_o is partially determined by the hyperfine interaction between the nuclear spins and electron spins. The zero-field precessional motion occurs around the direction of I_N. If I_N is assumed to remain constant in the first approximation, the total ensemble may be treated as a combination of three sub-ensembles precessing around the three orthogonal laboratory axes; the precessional motion around the Z-component of I_N cause S↔T_o transition, while similar motions around the component along the x-axis or the y-axis cause S↔$T_\pm$ transitions. Actually however, both I_N and electron spin vectors precess around their resultant vector and there occurs flip-flop change of magnetic quantum numbers of electronic and nuclear spins during the angular momentum exchange process. Two qualitative points that emerge from the consideration of the compensation of the electron spin angular momentum by the nuclear spin angular momentum are (1) k_0 must be sensitive to isotope substitution and (2) the external field has to compete with the internal field (discussed in the next section).

(c) S, T_0 ↔$T_\pm$ Transition Rates k_R, k_R'

(i) *Non-Degeneracy Effect*: First, we have to note that each level splits up in a group of closely spaced levels due to interaction with nuclear spin levels. Second, unlike the S↔T_0 case, the degeneracy of the energy-exchanging levels is not maintained as the field is increased. The extent of any two-level transition is governed by the expression $H_{ij}^2/(\Delta_{ij}^2 + H_{ij}^2)$, where ($\Delta_{ij}$ is the separation between the two levels i and j and H_{ij} is the transition matrix coupling the two levels. Thus, the transition rate decreases as the separation is increased. The Zeeman interaction removes the degeneracy between (S, T_0) and ($T_\pm$). The k_R decreases sharply at low-fields, and as soon as the Zeeman splitting exceeds the hyperfine splittings, the k_R, k_R' become nearly constant.

(ii) *Tumbling Effect*: The question might be asked, is there any other factor that might overcome the energy separation factor? One possibility is the field-induced coupling between the two states. The couplings between S and T± increase with field but it is too feeble to counter the Zeeman splitting effect. More effective however, is the change of relaxation rates, k_R due to the tumbling motion of the anisotropic radical in a magnetic field. Expressions for field dependence of k_R, k_R' due to anisotropies in hyperfine interaction, dipole-dipole interaction between the two radicals, and g-tensor are shown below.[17]

(a) Spin-Lattice Ralaxation Rate [$k_{rel}(\delta hf)$] due to Hyperfine Anisotropy:

$$\frac{1}{k_{rel}(\delta hf)} = \frac{1}{\gamma^2 H_{loc}^2 \;\; \tau_c(\delta hf)} \; \vdots \; \frac{\tau_c(\delta hf)}{H_{loc}} \text{-} H_{ex}^2 \quad \ldots(1)$$

where γ is the magnetogyric ratio of the electron, H_{loc} the locally fluctuating field for the electron, and $\tau_c(\delta hf)$ the correlation time due to δhf interaction. It is obvious from eq. (1) that the spin-lattice relaxation rate [$k_{rel}(\delta hf)$] decreases in proportion to the square of the applied magnetic field.

(b) Spin-Lattice Relaxation Rate due to Inter-Radical Dipole-Dipole Interaction of Biradicals

$$\frac{1}{k_{rel}(dd)} \quad \frac{1}{\gamma^2 H_{dd}^2 \tau_c'} \;'\; \frac{H_{ex}^2 \tau_c'}{H_{dd}} \quad \ldots(2)$$

where H_{dd} is the locally fluctuating magnetic field due to *dd* interaction between the two radicals, and τ_c' the rotational correlation time for the same. Here too, with increase of magnetic field spin-lattice relaxation rate [$k_{rel}(dd)$] induced by dipole-dipole interaction decreases. The field-dependence due to both causes are similar, namely these two anisotropies cause a decrease in the rates k_R, and k_R' at low, but not too low. At still higher fields the contribution of $\delta(hfc)$ and (dd) terms become negligible, and the contribution of δg-anisotropy becomes predominant.

(c) Spin-Lattice Relaxation Rate [$k_{rel}(\delta g)$] Induced by g Anisotropy

$$\frac{1}{k_{rel}(\delta g)} = \frac{10\hbar^2\gamma^2\tau_c(\delta g)}{\delta g^2\beta^2} + \frac{10\hbar}{\delta g^2\beta^2\tau_c(\delta g)H_{,}} \quad \ldots(3)$$

where $\delta g^2 = g_1^2 + g_2^2 + g_3^2 - 3[(g_1+g_2+g_3)/3]^2$ (g_1, g_2, g_3 are g values for the principal axis of the g tensor of a radical), β the electron Bohr magneton and $\tau_c(\delta g)$ the correlation time due to δg interaction. From eq. (3) it follows that the spin-lattice relaxation rate [$k_{rel}(\delta g)$] increases at first as the external field square, but eventually saturates out.

Summarising, the field dependence of S↔T± is complex and may be discussed only for different ranges of the field. At very low fields of the order of 0.05T, a sharp decrease in rate occurs, caused by a competition between Zeeman interaction and Hyperfine interaction. In the field range of 0.05 - 2T the S→T± rates further decrease due to anisotropy in HFC and dipole-dipole interaction. At still higher fields these contributions become negligible and there occurs an increase in the relaxation rate due to g anisotropy (Fig. 2).

(d) The Rates of Recombination, k_S and k_T

The rates of recombination in singlet and triplet states, though field insensitive, have significant roles to play in determining the extent of MFE and dynamics. For example, if the two are equal, the field-sensitive rate of the ISC can not cause any variation of the yield with field. One of the ways by which k_T could be comparable with respect to k_S is by spin-orbit coupling (SOC). In heavy atoms SOC intermixes singlet and triplet states to produce S′ and T′ states and as a consequence, equalizes k_S' and k_T'. The MFE is therefore felt less in these systems.

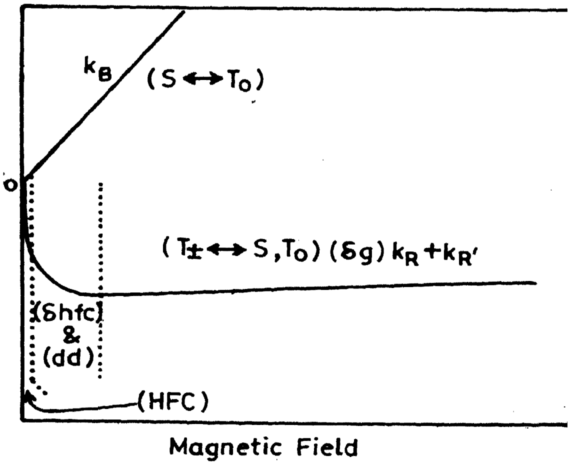

Fig. 2 Schematic diagram for the variation of rates with field.

(e) The cage - Escape Rate k_E

The cage - escape rate is very important in determining the extent of MFE. The evolution of spin is a comparatively slow process in many RPs at low fields. If the escape rate is large as it is in non-viscous neat solvents, there will be hardly any spin evolution during the short residence time of the radicals, and MFE will be small. In order to increase the residence time and have appreciate MFE, following ideas have been tried—

(a) Increase the viscosity and decrease the temperature of the solvent.
(b) Try oppositely charged radicals in a solvent of low dielectric constant.
(c) Chain the radicals by flexible bridges such as $(CH_2)_n$ so that escape is nearly impossible.
(d) Incorporate the RP in a micelle. For radicals with low solubility in water and high solubility in organic hydrocarbon, the surface of the micelle serves as a good reflecting boundary.

RP Decay Dynamics

It is difficult to extract all the kinetic parameters of the scheme from the experimental data. However, the rate expressions, may be simplified by making some pragmatic assumptions. It has been deduced that for triplet precursor the rates could be expressed as follows[11]:

$$H = 0T,\ [R] = I_0 \exp(-k_0 t) \qquad \ldots (4)$$

$$H >> 0T,\ H \approx H_L,\ [R] = I_f \exp(-k_f t) + I_s \exp(-k_s t) \qquad \ldots (5)$$

where $[R]$ is the total radical pair concentration in all the four sublevels, i.e.

$$[R] = [S] + [T_+] + [T_-] + [T_0]$$

For $k_B >> k_P >>$ other rates, k_f and k_S can be represented as follows,

$$k_f = k_p/2 + k_S$$

$$k_S = k_R + k_R + k_E \qquad \ldots (6)$$

If $k_p >> k_B >>$ other rates, the expressions changes to,

$$k_f = k_B + k_S$$

$$k_S = k_R + k_R' + k_E \qquad \ldots (7)$$

Experimental Techniques

We shall concentrate here only on two techniques - fluorescence and transient absorption (laser flash photolysis). For triplet-born non-fluorescent RP, we adopt the latter technique and for singlet-born fluorescent RP the former one.

The MFE on non-luminescent transients, e.g., triplets, free ions, radicals, etc, can be monitored using laser flash photolysis kinetic spectrometer and a steady or pulsed magnetic field[17-21]. Dutta *et al.* set up a laser flash photolysis system, where the third or fourth harmonic of a Nd:YAG laser was used as the pump and white light from a pulsed Xe-lamp served as the probe. An off-axial arrangement of the two beams was employed to facilitate placement of a tiny steady electromagnet. A sensitive differential amplifier was employed to amplify the signal changes. The analog signal was digitized with the help of a transient digitizer and subsequently stored in an IBM PC-AT micro computer.[18] Aich *et al.* used transverse arrangement where the pump and the probe are oriented at right angles to each other; a hole through the core of the electromagnet allowed the passage of pumping laser beam[20]. For high field studies, Misra *et al.* have employed a synchronised pulsed home-built electromagnet, where the pulsed current is provided by discharge of capacitors through an air-core coil (Kapitza's technique), the pulsed duration being about 7.8 ms. A Xe lamp is triggered about 1.8 ms after the trigger of the capacitor discharge unit (i.e. at the commencement of the plateau region of the magnetic field profile). The laser is triggered at the flat portion of the lamp profile and the transient absorption followed by oscilloscope as usual[19].

The MFE on time-integrated exciplex luminescence being small, a sensitive apparatus is needed for study. Nath and Chowdhury employed a sinusoidally varying magnetic field and locked in the fluorescence (φ) – detecting photomultiplier output with magnetic field at twice the frequency[22,23]. Very recently using a full-wave phase-locked detection system the signal-to-noise ratio of the system has been increased remarkably.

to 1000:1[24]. The field-induced change $\Delta\varphi$ (proportional to the defector a.c output) is normalised by dividing by φ (proportional to the d.c component of PM response) and plotted against wavelength, λ, to obtain magnetic-field-modulated-luminescence spectra (MFMLS) of the exciplex.

The observation of time evolution of the MFE on exciplex luminescence is possible by normal time-correlated-single-photon-counting technique if the MFE is large. The low S/N ratio is inherent in the technique, but long term fluctuation can be taken care of by dividing the collection time equally and alternately between MF in the ON and the OFF position[25].

Results and Discussion

A Triplet-Born RP

A1 Benzilketyl-SDS Radical Pair[18,19,26,27]*:*

Benzil (Bz), a typical aromatic ketone, has two vicinal keto groups, any one of which can abstract H-atom from suitable H-donors. Surfactants can act as H-atom donors and at the same time can provide micellar environment. The latter confines the RP, reduces k_E and increases geminate recombination probability, thereby making it easier to observe MFE on the T↔S ISC process. The escaped radical yield, as measured by the value of A(t) after a long time, and the lifetime of the RP estimated from the slow component (k_S) of a the bi-exponential decay increase drastically on application of a small field and then reach saturation. This is a clear signature of HFC-controlled intersystem crossing discussed before, that is to say, the k'_R decreases drastically as ZI exceeds HF width of levels. Interesting things happen at very high fields (≈ 10T) to which Misra *et al.* have recently extended their work. After 4T, the radical yield and the lifetime decrease again (Figs. 3, 4(a) and 4(b)). This reduction in MFE is due to increase of k_R and k'_R with field, rapid relaxation being caused by the tumbling of a molecule with anisotropic g-tensor in the magnetic field. The increase in the k_R and k'_R partially opens up the blocked $T_\pm \leftrightarrow S$ channels and hence decreases MFE. The same result can be obtained by using fields provided by a neighbouring paramagnetic ion such as Cu^{++}. The effect of the Cu^{++} ion may be viewed as due to the exchange interaction of the Cu^{++} with the RP as a whole or with one of the radicals. The coupled spin moments of the RP (or radicals) and the Cu^{++} precesses around the resultant vector causing a spin relaxation by changing the orientation of the RP spin vector (Figs. 5(a) & (b)). It is also possible

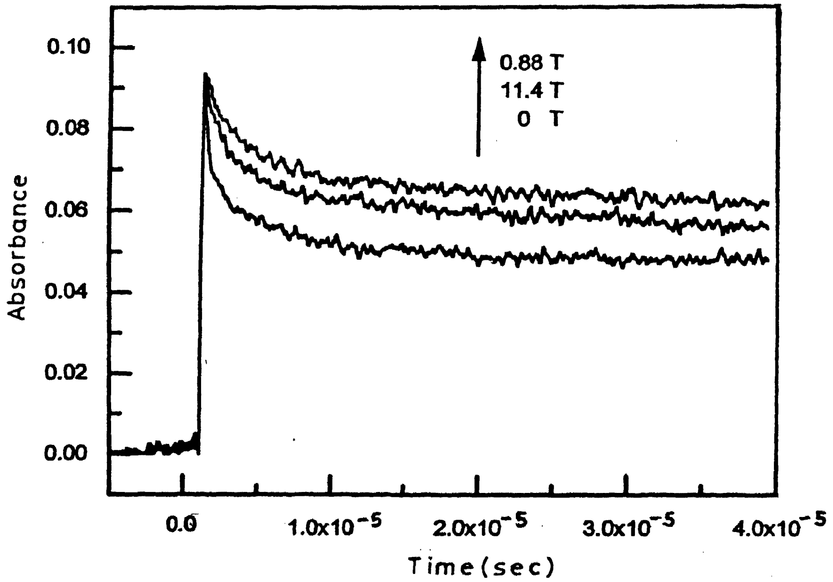

Fig. 3 MFE on the decay profile of benzilketyl:SDS radical pair (370 nm) in SDS micellar solution.

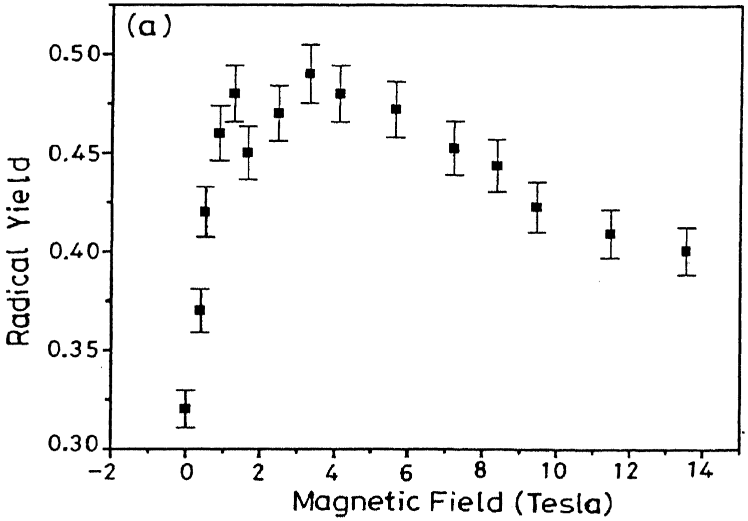

Fig. 4 (a) Plot of radical yield (benzilketyl) vs. magnetic field (benzil, SDS in water)

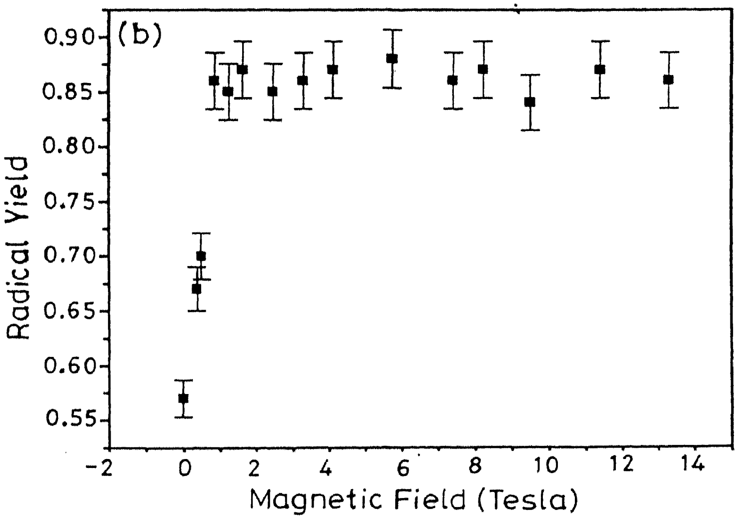

Fig. 4 (b) Plot of radical yield (benzilketyl) vs. magnetic field (benzil, SDS in 10.2 v/v water:dioxane mixture).

to demonstrate the effect of escape rate on the overall MFE of this system. If the size of the micelle is decreased by adding a little dioxane, the escape rate should increase and the MFE decrease. The overall shape of the yield vs. field curve is sensitive to the size of the micelle (Figs. 4(a) & (b)). The inversion effect is prominent at low escape rate, but not for increased escape rate in a small-sized micelle. A better way of manipulating k_E is by chaining flexibly the two radicals; the MFE increases considerably, and the inversion effect also becomes more prominent.

A2 $(C_{60})_n$ /Pyrene RP[28]

The molecule C_{60} does not have a magnetic nucleus and is therefore devoid of HFC. Due to spherical shape there ought not to be any anisotropy either. This should allow one to concentrate on the effect of an external field on the $S \leftrightarrow T_0$ transition. Recently, Haldar *et al.* detected a

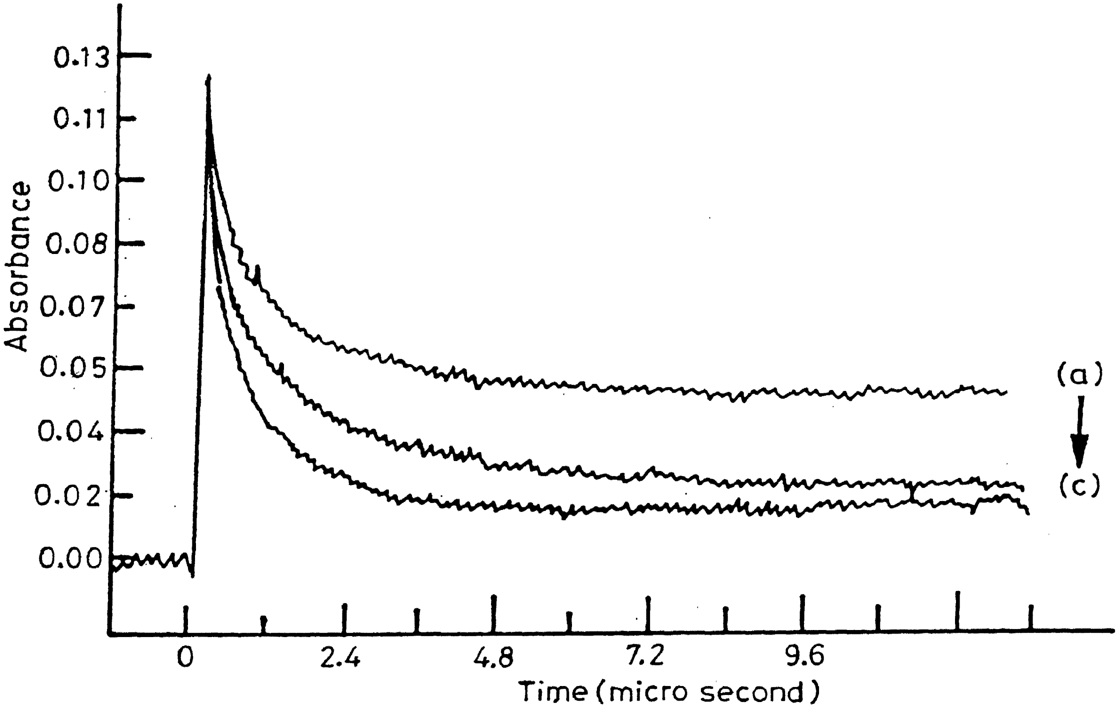

Fig. 5 (a) Effect of $CuCl_2$ on the transient decay at 370 nm. Concentration of Cu^{2+} are (a) 0.0 M; (b) 3.0 M; (c) 5.0 mM.

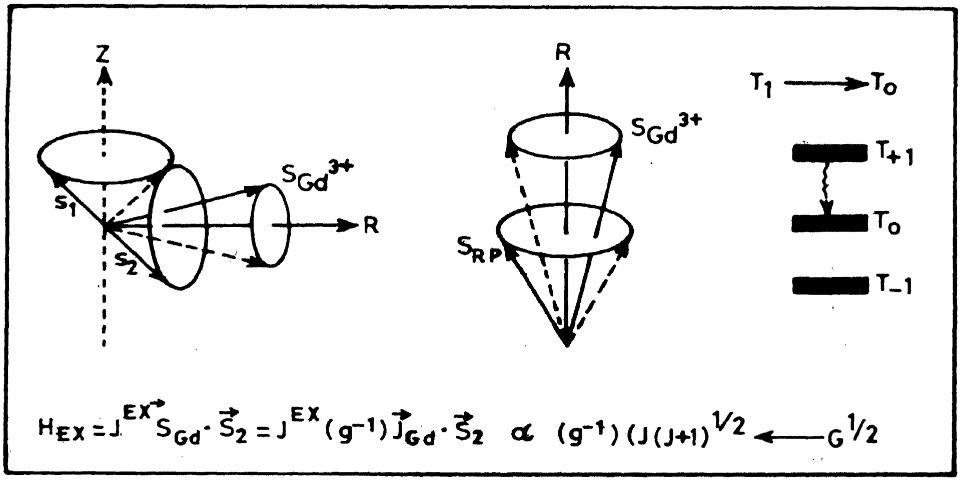
Z
S_1
S_2
S_{Gd}^{3+}
R
R
S_{Gd}^{3+}
S_{RP}
$T_1 \longrightarrow T_0$
T_{+1}
T_0
T_{-1}
$H_{EX} = J^{EX} \vec{S}_{Gd} \cdot \vec{S}_2 = J^{EX} (g-1) \vec{J}_{Gd} \cdot \vec{S}_2 \propto (g-1)(J(J+1))^{1/2} \longleftarrow G^{1/2}$

Fig. 5 (b) Rotation of the spin vector of one of the radicals due to coupling with the spin moment of the paramagnetic ion (Gd^{3+} or Cu^{2+}).

MFE at high fields on the Pyrene-C_{60} RP system in a fluorinated micellar environment. The RP decay time as measured by the slow component ($1/k_S$) decreases with field, while the opposite is observed for most other organic triplet RPs. Lack of HFC in $(C_{60})_n$ and small HFC in P_y^+ are responsible for such observations (Fig. 6). The high-field dependence of the MFE corresponds to the relaxation mechanism. The overall relaxation rate of a RP contains sum of contributions from two ions. If we assume that the contribution by the C_{60} is negligible because of its isotropicity, the

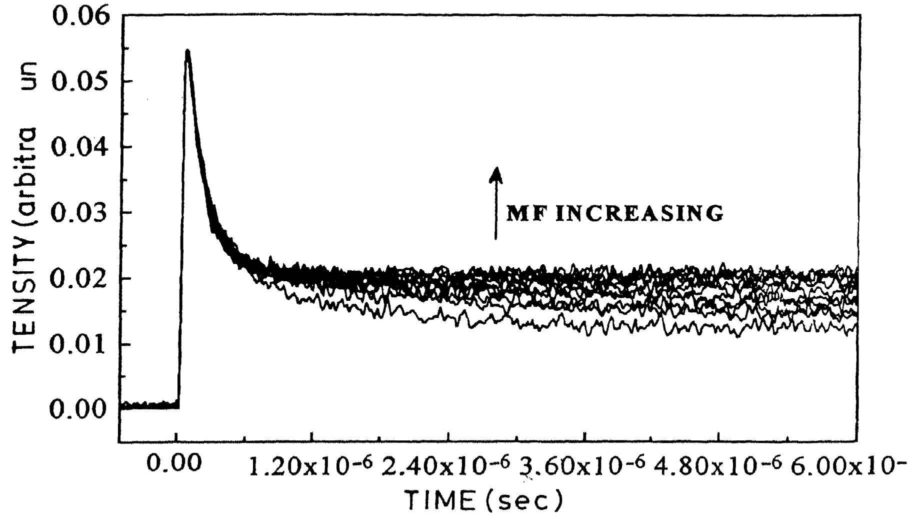

Fig. 6 Decay of the transient species obtained at 980 nm in presence of varying external fields.

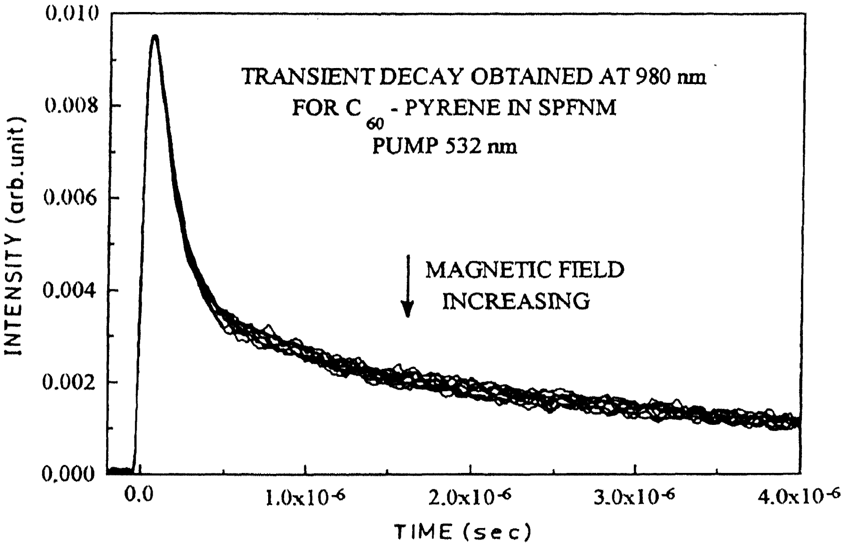

Fig. 7 Typical decay of the transient obtained at 370 nm in presence of various external fields for benzophenone tetracarboxylate ketyl radical in aqueous CTAB solution.

contribution of the other ion, namely P_y^+ can be found out. Thus it could be the starting point for separation of individual ionic contributions of RIPs to MFE.

A3 Benzephone Tetracarboxylate/CTAB Radical Ion Pair[17]

Confinement is the root cause for micellar enhancement of cage-time and hence the degree of spin evolution. For uncharged organic RP, the solubility of radicals in water is far less than in the hydrocarbon core of the micelle, and hence the micelle reduces the escape rate. On the other hand, ionic radicals, which are soluble in water, exhibit practically no MFE in micellar medium. However, Haldar *et al.* have shown that highly charged radicals can be trapped in the Stern Layers at the micellar surface and thus not allowed to escape fast into water in which it is soluble. The field-dependence of the decay rates (Fig.7) show that at low fields HFC (both isotropic and anisotropic) mechanisms are active.

A4 [Ru(bpy)$_2$ H$_3$ Pzbzim]$^{2+}$/N,N′-Methylviologen Radical Ion Pair in Sodium Laurate (SL) Micelle[29]

This is an example where inorganic radicals are involved. The Δg of such a RP ought to be high. So should by the g anisotropy. Thus one might expect higher $S \leftrightarrow T_0$ dephasing rates and $T_\pm \leftrightarrow S_0$, T_0 relaxation rates at comparatively low fields. Fig. 8 shows the effect of external magnetic fields on the transient absorption at 620 nm (corresponding to MV^+ radical cation) in SL micellar solution. It has been found that the escaped radical yield increases with increasing magnetic field beyond 3T, but in the range 0-3T there is practically negligible MFE. The $S \leftrightarrow T$ ISC in such RP is principally dictated by the Δg-mechanism. Since this RP of mixed parentage is predominantly singlet in origin, the overall MFE is small. The Δg-induced ISC is proportional to the external magnetic field, and does not show any saturation

A5 Fluorescence and DABCO[30] *: MFE in Viscous Homogeneous Solution*

The study of MFE on RPs generated by electron transfer in the triplet state was carried out by Periaswamy *et al.*, with diazabicyclo-octane (DABCO) and fluorenone as electron donor and acceptor, respectively, in propylene carbonate as solvent. As expected, in homogenous low viscous media, the MFE on the escape radical yield was only 1.6% at 343K. This, however, increased to 2.4% at η=45.3 cP at 223K. The effect saturated at 270 Gauss indicating the dominance of HFC mechanism.

A6 Application of MFE in Secondary Reaction of ^{3}RP

Turro *et al.*[4] made in interesting application of MFE on triplet-born RP. He used DBK at low concentrations as photo-initiator in the emulsion polymerisation of styrene and applied a low external magnetic-field to slow down the Triplet-Singlet conversion rate of the RP photo-generated from ^{3}DBK. The rate of polymerisation and the molecular weight of the polymer grew dramatically on application of a small field. The effect of MFE on the photo-initiated polymerisation process has been re-examined by Mandal and co-workers[31,32] who followed the course of polymerisation reaction with time in great detail. Polymerization was conducted at fixed photoinitiator concentration but at various irradiation intensities and at either 0G or 1000G magnetic field. Their results show that the field shortens the polymer particle nucleation period to a small extent. The small field-effect on steady state rate of

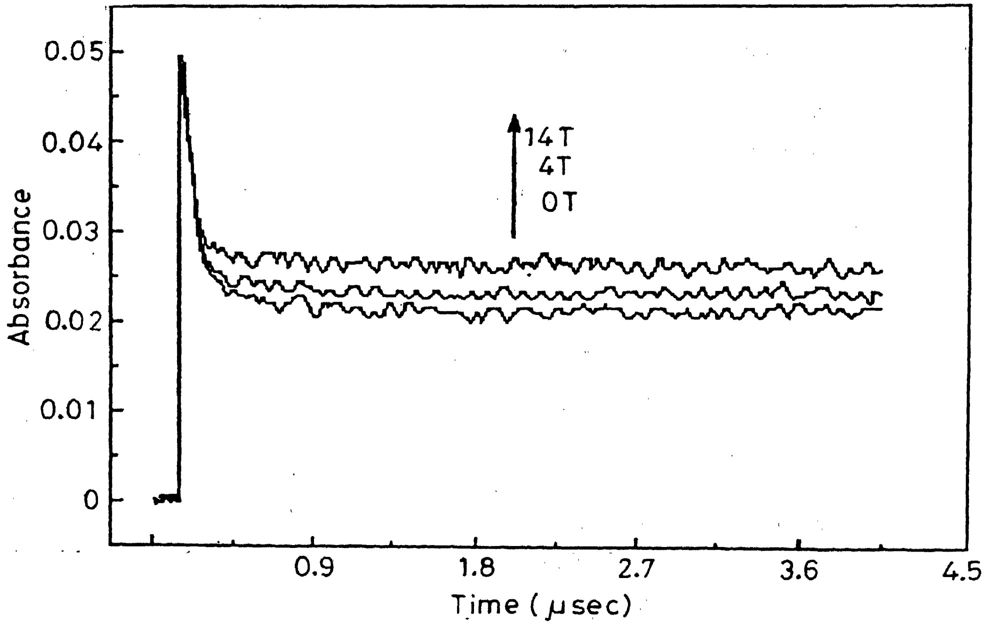

Fig. 8 Effect of external magnetic field on the transient decay profile at 620 nm of methyl viologen radical cation (MV^+) in sodium laurate solution.

polymerization is best noticed at low light intensities (i.e. low radical generation rates). A field effect on molecular weight is observed when the conversion is low (≈5%) i.e. at the particle nucleation stage. However, molecular weight increases greatly with conversion both with and without field, and the field effect on molecular weight, if any, is masked by the conversion effect when the polymerization is well within the steady rate period or at the limiting conversion stage (Fig. 9).

B Singlet-Born RP

RPs and RIPs are generated as transients in three main groups of chemical reactions - H-atom transfer, homolytic bond cleavage and electron-transfer. These processes, however, have to compete with fast radiative and non-radiative energy relaxation processes of the concerned excited state. Homolytic bond cleavage requires a repulsive PES with respect to the bond length as variable co-ordinate. This requirement is met by many organic molecules in their triplet states, but not in their singlet states. Similarly, a H-atom transfer can hardly occur within the short span of singlet lifetime. For it requires the presence of hetero-atomic groups in donor-acceptor molecules, which frequently increase competing de-energising ISC/IC rates of the lowest singlet state, and make the extent of H- atom transfer in the singlet state insignificant. The electron transfer between a donor and an acceptor, on the other hand, is a fast long-distance process, and can compete effectively with other processes of the S_1 State. The photon-induced electron transfer (PET) is, therefore, a very common way of generating singlet-born RIP. Because of the generation of charged species by electron-transfer, solvent molecules get intimately associated with the generated RP and it becomes necessary to distinguish between contact ion pairs (CIP), solvent-shared ion pairs (SSIP) and uncorrelated solvated free radicals. The contact pairs with various extents of charge separation depending on the solvent are called exciplex, some of which are frequently fluorescent. This view of the genesis of the exciplex via electron transfer is particularly appropriate for polar solvents. The interdependence of spin and spatial motions make detailed calculations of MFE on exciplex luminescence virtually impossible. Nevertheless, qualitative predictions are possible.

B1 Field Variation of MFE Exciples Luminescence

The yield of CIP could be measured by the steady state fluorescence intensity, and the magnetic field induced % change of intensity could be interpreted as a MARY spectrum[22,23]. At very low fields (<10G) the exciplex fluorescence intensity remains constant, then increases steadily, and after about 100/200 Gauss becomes constant again. This feature is a clear signature of the HFC mechanism. In zero field, a S-born ^{1}RP is converted to T_0 $T_{\pm'}$ (three types of ^{3}RPs) at equal rates by the magnetic nuclei present in the radical

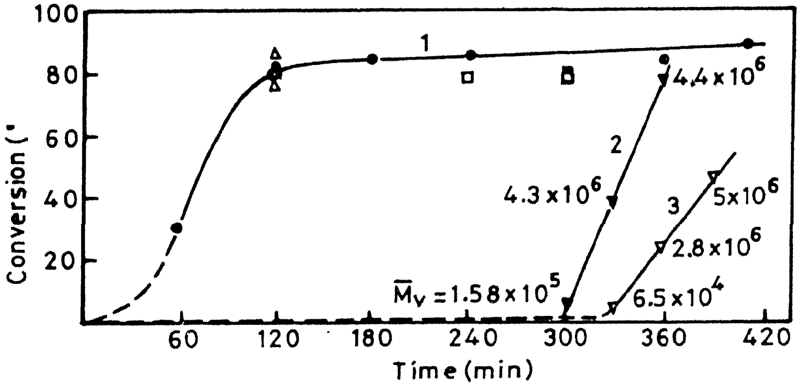

Fig. 9 % conversion vs time curves of EP of styrene using DBK as photoinitiator at different light intensities at 30°. Filled symbols refer to polymerization in presence of magnetic field of 1000 G and open symbols to that for 0 G. Light intensity is varied by changing K_2CrO_4 concentration in filter solution. The K_2CrO_4 concentrations are Δ, 0.027 gm/l; O, 0.09 gm/l; □, 0.137 gm/l; ∇, 0.18 gm/l. M_v, data at various conversions are indicated.

partners As explained before, when an external field is applied, the $S \leftrightarrow T_{\pm'}$ rates become nearly zero due to Zeeman splitting. The blockage of the two channels however, is not complete - because of relaxation of spins due to $\delta_{hfc,}$ δ_{dd} and δg. For the field range 0-500 Gauss, the field-induced change in relaxation rate or the Δg-effect is negligible. For the field range 0.5-10 KG the Δg induced change becomes perceptible by the short-lived ^{1}RP, but the rate being a two-way reversible rate, a quasi-equilibrium between S and T_0 is soon reached. At still higher fields the relaxation rate decreases. This change, as explained earlier, is perceptible for a long-lived triplet-born ^{3}RP, but not for a short-lived ^{1}RP. The δg-induced relaxation rate regularly increases with field. This should cause a partial opening of the blocked $S \leftrightarrow T_\pm$ channels and hence there ought to be a decrease of intensity with field. Although inversion of MFE has been reported for triplet-born RPs, it is yet to be reported for exciplex luminescence.

At very low fields, in linked RP systems the MFE, is opposite in sign; that is, a decrease in exciplex intensity, instead of an increase, is observed. This has been attributed to the presence of non-zero exchange integral. Suppose, the S and T_0 is non-degenerate in zero external field. On application of a field, $T_\pm$ shift in energy, and one of these may become degenerate with S at a certain field; this degeneracy causes the ISC to increase, leading to a decrease in exciplex intensity. This explanation has found support from the observation that shorter the distance between the donor and the linked acceptor, more prominent is the minimum and higher the field at which the minimum appears. In unlinked systems the average donor-acceptor distance is large and hence, instead of a discernible minimum the intensity remains almost constant for fields of 1-10 Gauss.

It is meaningful to correlate the quantity $B_{1/2}$, the field for which MFE is half the saturation value, with the average hyperfine constant of the radicals. The $B_{1/2}$ value is the measure of HFI present in the system. Weller[33] proposed the following approximate relation for calculation of $B_{1/2}$ of a RP from hfi in the individual radicals

$$B_{1/2}=2(B_1^{\,2}+B_2^{\,2})/(B_1+B_2) \qquad \ldots (8)$$

where the B_i values are related with the hyperfine coupling constant a_{iN} and nuclear spin I_N by the equation

$$B_i=[a_{iN}^{\,2} I_N(I_N+1)]^{1/2} \qquad \ldots (9)$$

MFE have been studied on different exciplex systems as shown in Table I. A comment on the $B_{1/2}$ value of the An-PFN exciplex may be pertinent: In the case of An-PFN exciplex, the experimentally obtained $B_{1/2}$ value is much higher (> 125 Gauss) compared to the theoretically calculated one. Despite higher hfi for F-atom, the calculated value for the planar aromatic fluoro-derivative, PFN comes out low due to high symmetry of the molecule. The calculated value increases if the molecule is assumed to have a distorted non-planar structure in the excited state. The experimentally obtained higher value of $B_{1/2}$ has been associated by Misra *et al.* to a floppy motion of the PFN radical anion[44].

B 2.1 Solvent Dielectric Dependence of MFE

The frequency of re-encounter and the degree of spin evolution are dependent on the PES, which in turn is dependent on the properties of the solvent. For radical ions pairs, the Coulombic cage is strongly modified by the solvent dielectric constant (ε). In a very low ε medium the cage is too strong to permit excursion by RP partners to distances that allow spin-evolution. For high ε medium the cage is too open, and the high escape rate reduces MFE. Thus the maximum MFE is obtained at medium ε. This is borne out by studies on different exciplexes, *viz,* Py-DMA[22,23,34-37], CNP-AN[38-40], DPH-DMA[41], Pypolystyrene-DMA[50-52], etc. In aprotic solvents, the maximum MFE was obtained for solvent mixtures having ε between 14 and 18 in most cases. In alcoholic media the ε_{max} gets shifted to much higher value (ε_{max}.=28 for Py-DMA, ε_{max}.=38 for CNP-AN and ε_{max}.=26 for Py – diethylaniline[54]). The PES (Fig. 10) influences the MFE. In this schematic diagram A, C and E represent contact ion pair (CIP) or exciplex, solvent separated ion pair (SSIP) and free ions respectively while B is the transition state for the interconversion between CIP and SSIP. With the increase in ε, the energy barrier between B and C rises in height while the barrier between B and A and the slope of the path C to E decrease. Therefore, in more polar solvents, free ion

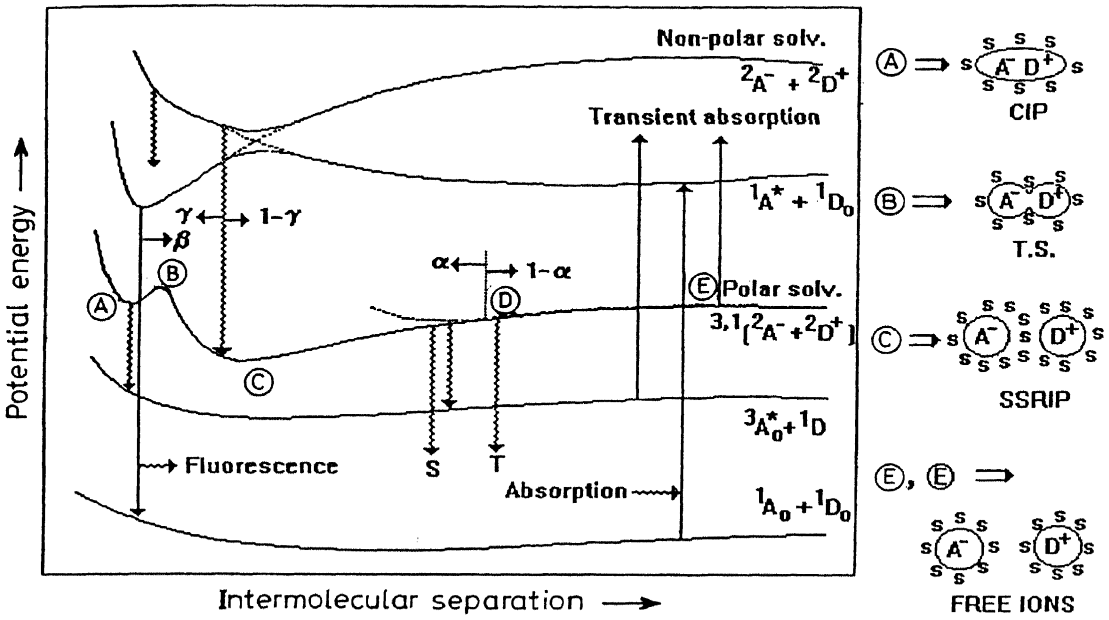

Fig. 10 A schematic diagram of exciplex system both in polar and non-polar media.

formation is favoured at the expense of SSIP which predominates over CIP. At the co-ordinate D, where J≈0, S→T transition takes place. The ion pairs existing in the singlet state can either form free ions or return to C (SSIP), fraction of which crosses the barrier between B and C to produce A (CIP). An external magnetic field lifts the degeneracy between the S and $T_\pm$ resulting in an increasing population of singlet RIPs. In a highly polar medium, most of the singlet ion pairs produce free ions while in a nonpolar solvent only a few RIPs can reach D. A medium of intermediate polarity balances all the energy terms, so that the major fractions of RIPs follow the return path (D→C→B→A) appearing as an increase in luminescence. The behaviour of alcohols in reducing MFE is fairly unique. The enhanced luminescence (φ) and longer lifetime in alcohols as compared to isodielectric mixtures of aprotic solvents indicate that the alcohols are better cages. Effectively, the alcohols form a relatively stronger hydrogen bonded cage which limits the diffusional excursion and interfere with spin evolution through exchange effects. However, an alternative explanation could be that, in alcoholic media, the HFIs are presumably reduced due to rapid hopping of hydrogen atoms. However, D-substitution in solvent has little effect. Finally, it may be mentioned that Nath *et al.*[34] used an empirical expression for spin evolution on the basis of Schulten's numerical calculation for a typical exciplex system and combined it with analytical solution of Smoluchowski's equation under a force field, and deduced an expression for ϕ and $\Delta\phi/\phi$ which reproduced the shape of experimental curves.

If the polarity of the solvent is the parameter to control the dynamics of the RIPs, MFE ought to maximise at a particular ε irrespective of the exciplex system. However, it does not happen for all exciplex systems. The exciplex between ECZ and DCB or PMC and DCB show maximum field effect at the dielectric constant 9 and 12[45]. The exciplex DPH-DCB also shows considerable increase in luminescence in presence of a magnetic field of the order of 60G around $\varepsilon \approx 10$ in THF-DMF and $\varepsilon \approx 11$ in THF-ACN[49]. This lower value of ϵ_{max} is ascribed to lesser extent of charge-transfer in this exciplex. Aich and Basu[45] proposed that the extent of charge-transfer (δ) in the CIP has a significant role to play in determining ε_{max}. The values of oxidation potential signify that the δ-values are in following order PMC-DCB>DPH-

Table I

MFE on exciplex systems

Sl. No.	Exciplex Systems	in typical protic and aprotic solvents at corresponding (ε_{max})		$B_{½}$ (Gauss)	
		Aprotic	Protic	Experimental	Calculated
1.	Pyrene – N,N- dimethyl aniline (Py-DMA)[22,23,34-37]	9.0 (14.0) 13.5 (15.0)[!]	2.0 (29.0)	55	54.8
2.	9-Cyano-phenanthrene–*trans*-anethole (CNP-AN)[38-40]	4.5 (18.0)	0.8 (33.0)	35	34.1
3.	1,6-Diphenylhexa- 1,3,5-triene – DMA (DPH-DMA)[41]	3.2 (16.0)	-	104	54.3
4.	1,4- Diphenyl-butdiene – DMA (DPB-DMA)[42]	5.4 (16.0)	-	114	
5.	Anthracene – DMA (An-DMA)[43]	7.0 (15.0)	-	73	
6.	An – julolidine (An-JL)[43]	2.0 (15.0)	-	73	
7.	An – 1-phenyl piperidine (An-IPP)[43]	7.0 (15.0)	-	62	
8.	An – perfluoro naphthalene (An-PFN)[44]	3.2 (14.5)	-	>125	35.3 – 71.8 – 175
9.	N-Ethylcarbazole – 1,4- dicyanobenzene (ECZ-DCB)[20,24,45-47]	1.37 (9.0)	-	32	30
10.	1,4,5,8,9- Pentamethyl carbazole – DCB (PMC-DCB)[45,48]	0.025 (12.0)	-	43	-
11.	DPH-DCB[49]	0.18 (10.5) at 530 nm & 0.7% (10.5) at 600 nm	-	17	20
12.	Py-polystyrene-DMA[50-52]	9% (14.0)		55	

Calculated by UHF-INDO method.[53]

! After thoroughly drying the solvent mixture

DCB>ECZ-DCB. Indeed, the ϵ_{max} decreases in the above order. (Table I).

The diffusion-based explanation of maximum MFE at an intermediate ε is not consistent with the observation by Werner *et al.* that in the linked system Py $(CH_2)_n$ DMA the nature of the MFE vs. ε curve is very similar to the unlinked system Py/DMA[55]. Based on this observation the last group of investigators have suggested that the polarity of the solvent affects the rate of back-electron-transfer, which is responsible for the maximisation of MFE at an intermediate dielectric constant. Obviously, contradictory facts and explanations need to be further looked into.

B 2.2 Solvent Microheterogeneity Effects on MFE

Although the variation of the magnitude of $\Delta\phi/\phi\%$ for a particular exciplex system in different binary solvent mixture is very similar, i.e., ε_{max} value remains almost the same irrespective of the solvent mixtures, the magnitude itself shows a large variation at ε_{max} for different solvent mixtures[36]. Recently Petrov *et al.*[56,57] found that a mixture of highly polar DMSO and non-polar benzene yields a still higher value of $\Delta\phi/\phi$ at the same ε_{max}. They explained the results on the basis of microheterogeneity created by preferential solvation wherein the SSIPs are trapped in the energy surface and thus get a longer time for spin evolution before the radical ions could combine to form the luminescent CIPs. To explore this idea further, Bera *et al.*[36,37] chose one of the solvent components as water which has ε greater than DMSO while the other non-polar component was chosen as dioxane or tetrahydrofuran (THF) which could be mixed with water in all proportions. In contradiction to the commonly held view that MFE on exciplex emission is destroyed in aprotic solvent mixtures, they observed a MFE which is appreciable but less than that of benzene-DMSO mixtures used by Petrov *et.al.* Since dioxane is less polar than THF, dioxane/water mixture should exhibit more microheterogeneity than THF/water; however, the order of MFE observed is opposite to that expected from the microheterogeneity concept. Moreover, if there were preferential solvation by the polar component, the non-polar component should not have mattered. It does not explain the experimental result that MFE is halved on replacing THF by dioxane. Bera *et al.* have tried to influence the miscibility of the two components by adding ionic salts-both of type "salting in", e.g., $LiClO_4$, and "salting out", e.g., Nacl, NaBr, Na_2S, Na_2SO_4 and $MgSO_4$. However, MFE does not depend on the nature of salts. They also tried to modulate the solvent microheterogeneity either by adding a solvent which dissolves in both the poorly miscible ones, such as acetone in benzene/DMSO, or by varying the medium temperature, but could not find any appreciable effect on MFE[36]. It was also found by Aich and Basu that for some exciplex systems, the MFE is greater for neat solvents than polar-nonpolar mixed solvents of the same ε[45]. Petrov *et al.*'s model therefore, fails to systemize the pattern of MFE in mixed solvents. Werner and Staerk's model[55], which is fairly successful in correlating MFE and lifetime of RIPs in linked systems, fails to explain trends of MFE in unlinked systems. Obviously, the complexity of the interdependent spin and spatial motion in an yet-to-be-understood solvent environment stands in the way of proposing an acceptable model.

In view of the success of micellar cages in studying triplet RPs, it is worthwhile to search for similar micellar enhancement of MFE on exciplex luminescence. However, all attempts yielded negative results. Being nonpolar in nature the An-PFN system might have possibilities in this regard[44]. Misra *et al.* have chosen a C_9 fluorinated micelle, which solubilises PFN better. Though the steady-state emission spectrum shows a distinct broad C-T emission band around 430 nm, appreciable change in exciplex luminescence in the presence of MF could not be observed. The low dielectric constant (8.0) in the interior of the micelle might be responsible for this negative result. Aich *et al.* tried to detect MFE on exciplex luminescence of ECZ-DCB in SDS micellar media[20]. The magnitude of MFE is very small in homogeneous media of medium ε; it is further quenched in micellar medium and could not be observed.

B3 MFE:Time-Resolved Exciplex Emission

Time-resolved investigation of MFE on exciplex luminescence from Py-DMA and CNP-AN systems were carried out by Nath *et al.* and Basu *et al.* respectively[25,58,59]. They found that, in both the systems, the magnetic field modulated luminescence, $\Delta\phi$, reached a maximum in about tens of nanoseconds (ns) and then decayed while $\Delta\phi/\phi$ reached saturation in about 60 ns. The curves were fitted with an expression obtained by coupling Hong and Nooandi's analytical solution of Smoluchowski's diffusion equation with the simplified assumption that the spin evolution is linear upto a limiting time and then remains steady. Basu *et al.* carried out time-resolved studies in the presence and absence of magnetic field with long chain Py-polystyrene-DMA and compared the results with those of free Py-DMA system[50]. It was found that inspite of the fact that the lifetime of the polymer linked exciplex is much longer than that of the unlinked exciplex, the MFE is quite similar in both the cases. This was ascribed to saturation of the spin evolution after 10ns. One advantage of the chosen polymer was that the growth of the exciplex emission being slow, MFE could be studied directly on the growth process. It was observed that MFEs on the growth and the decay processes are nearly equal, which implies a reversible CIP-SSIP equilibrium.

B4 MFE on Polymer Linked Exciplex

Generally, the dependence of luminescence yield on magnetic field shows a fairly marked difference between linked and unlinked systems. The most extensive studies on linked systems were carried out by Werner and Staerk[55], Staerk *et al.*[60] and Tanimoto *et al.*[61]. The enhancement of exciplex fluorescence intensity, even upto 50%, was reported in a magnetic field less than 0.1 tesla. They found that the exciplex fluorescence yield is sensitive to the number of methylene links; longer the chain length, the smaller the value of J and consequently greater the spin evolution. Finally, for much larger n, RIPs behave as if they are free. The last observation comes from studies by Dutta *et al.* on a polystyrene polymer (M_n=4770) containing Py as one end group and DMA as the other[50-52]. They found a few differences. Unlike the unlinked system case, in pure acetone $\Delta\phi/\phi$ is higher than that in a mixed solvent (THF/DMF) of the same ε. The results have been interpreted on the basis that coil extension and dielectric constant dependent diffusion compete with each other, resulting in the observed solvent composition dependent behaviour. Later, they reported MFE behaviour of Py-PS-DMA in isodielectric mixtures of THF/DMF and benzene (Bz)/dimethylsulphoxide (DMSO) and compared the observations with that of unlinked Py-DMA system. In Bz –DMSO, instead of enhancement of MFE as observed in Py-DMA system by Petrov *et al.*, a significant reduction of MFE occurs. These studies demonstrate the importance of the solvent-dependent polymer backbone conformation. In both the solvent mixtures, the normal luminescence, ϕ exhibits a shift in wavelength, indicating the presence of multiple conformations of different magnetic sensitivities. Time-resolved spectra at different time intervals also support this conclusion.

B.5 Effect of Concentration of Donors and Other Species

B.5.1 Concentration of donor

With increase in concentration of the non-luminescent component of the exciplex the value of $B_{½}$ becomes greater. It is proposed that in the presence of excess quencher concentration the electron hops between neutral molecules and corresponding ionic free radical, which interferes with the spin evolution rate. The proposed mechanism has similarity with ZENO effect. One can also look at it in the following way. The fast electron exchange causes broadening of the energy of the individual spin state and the magnetic field has to overcome this broadening in order to suppress the $S \rightarrow T_{\pm}$ evolution completely. Thus saturation occurs at higher fields at higher concentrations. For some observations one has to look beyond the hopping theory for $B_{½}$ increase. Instead of adding the same donor (D) , DMA, to the mixture with Py, another donor(D'), N,N-dimehyltoluidine (DMT), with the same HFI as D was added, the increase in $B_{½}$ was identical, although the hopping rate is expected to be lower in the mixed donor (DMA+DMT) case than in the singlet donor (DMA or DMT) case. Also, lifetime variation by addition of quenchers did not change $B_{½}$. Recently, it has been found that the experimental $B_{½}$ values for ECZ-DCB[45], PMC-DCB[45] and DPH-DCB[49] systems remain almost the same for different concentrations of DCB. However, it should be noted in these exciplex systems, ECZ, PMC or DPH molecules mainly contribute to HFI. Since the quencher, DCB, has very little contribution to HFI (B_I=4.6G), the insensitivity of $B_{1/2}$ to DCB concentration do not necessarily imply the absence of electron hopping between $DCB^{-\bullet}$ and DCB. Tanimoto *et al.*[61] noted that even linked Ph-DMA systems behave similar to unlinked systems with respect to increase in concentration of free donors. He suggested 'structural changes in the exciplex' as one of the causes. Anisotropic dipolar interaction could be another reason for higher value of $B_{½}$, particularly for the DPH-DMA system[41].

B.5.2 Effects of Concentration of Paramagnetic Ions

A paramagnetic ion may couple with any of the two ion-radicals in the RIP. A coupled system causes a precession of the angular momentum vectors around the resultant vector. If a paramagnetic ion is present in the neighbourhood of the RIP and preferentially couples with the radical of opposite charge, the relative orientation of the two spin vectors of the RIP could change (Fig. 5(b)). Indeed, it was observed that the MFE on exciplex luminescence decreases linearly with the concentration of lanthanum acetylacetonates.

The quenching power is proportional to the spin-only moment of the Ln^{3+} ion, and not to its total momentum. In other words, the curve representing the quenching power vs. number of f-electrons peaks at Gd^{3+}. This anomalous observation was explained by Basu *et al.*[35,40] using a spin-exchange hamiltonian.

B.6 Anisotropic Magnetic Field Effect

The occurrence of anisotropic MFE requires restricted rotational diffusion of RIPs. The first example of anisotropic MFE was obtained during investigation of the photosynthetic reaction centre (PRC) suspended in viscous glycerol. Boxer *et al.*[2] showed in their study on PRC that the quantum yield of triplet (ϕ_T) in quinone depleted PRC is dependent on their orientation in the magnetic field. More recent examples of anisotropic field effect are DPH-DMA[41] and DPH-DCB[49] exciplex systems where the rotational motions of RIPs have been restricted by increasing the medium viscosity with a polymeric substance. It was observed by Basu *et al.* that the $\Delta\phi/\phi\%$ is dependent, albeit to a small extent, on the direction of polarisation of the exciting light with respect to the axis of the magnetic field. The anisotropy vanishes in a non-viscous medium. In the high field region, quantum yield anisotropy is mainly caused by the anisotropy of the g-tensors in the RIP. For the field strength $0<H<1$ KG the dominating terms are dipole - dipole and nuclear hyperfine interactions. For the DPH-DMA and DPH-DCB exciplexes the determining factor for the observed anisotropicity in MFE seems to be the anisotropic dipolar interaction[62] rather than the HFI. The extent of anisotropy is observed to be somewhat higher for the DPH-DCB than that for DPH-DMA. The anisotropy experiments were carried out near the dielectric maxima. ($\varepsilon_{max}=10$ for DPH-DCB and 15 for DPH-DMA). The more polar medium used for DPH-DMA might have stabilised the individual radical ions dissipating their charges and consequently reducing the anisotropic dipole-dipole interactions[49].

B.7 MFE and the Nature/Conformation/ Composition of the Compex

The wavelength dependence of MFE allows one to distinguish between excimer and exciplex on the one hand, and between exciplex and triplex on the other. Sometimes the MFE-spectrum does throw light on 1:2 complex (i.e triplex) formation. This may be illustrated with the DPH/DCB system which forms both 1:1 and 1:2 complexes. The DPH-DCB system[49] shows unusual variation of $\Delta\phi/\phi$ with wavelength (Fig.11). The field effect exhibits a maximum at 530nm, but dips at 540 nm before steadily rising upto 600nm. This signifies formation of two types of complex of different magnetic sensitivities.

It is possible, in principle, for the rotational angular momentum to compensate for a change in

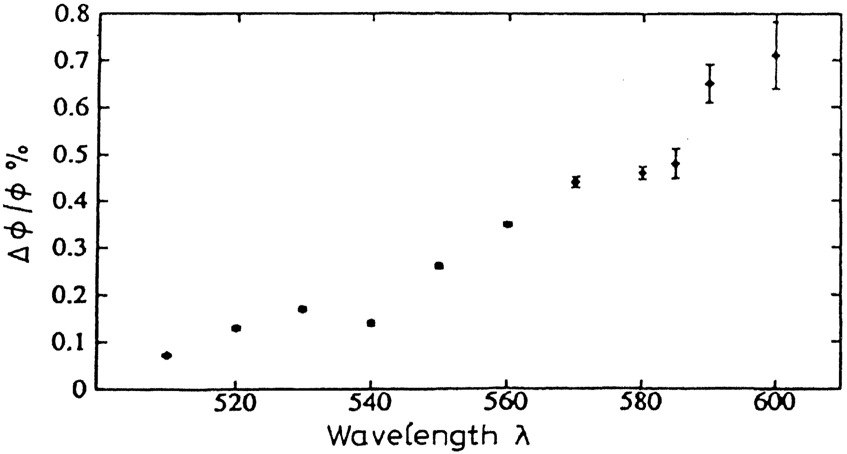

Fig. 11 Wavelength (λ in nm) dependence of percentage magnetic field effect ($\Delta\phi\phi\%$) for DPH–DCB exciplex in THF–DMF at $\epsilon\approx10.5$, [DPH]=0.1 mM, and [DCB]=40 mM. The magnetic field applied was 60 G.

the spin angular momentum, thus rotation might play a role in the ISC process and hence, in MFE. Bera *et al.*[43] undertook a comparative study of three exciplex systems, An-DMA, An-IPP and An-JL in order to observe the influence of conformation of an exciplex, or more correctly, that of the donor in the exciplex. In DMA both methyl-group and amino-group rotations around the corresponding σ-bonds are possible, and the amino group may take any suitable orientation with respect to the phenyl ring. In 1PP the methyl group rotation is prevented by connecting the two methyl groups with each other by a saturated hydrocarbon chain, but the amino group rotation may still occur. In JL, both methyl-group and amino-group rotations are restricted by joining the two methyl groups with the phenyl ring by two saturated hydrocarbon chains. The evidence of the influence of structure appears in $B_{\frac{1}{2}}$ values. The experimental $B_{\frac{1}{2}}$ values of both An-DMA and An-JL cpomplexes are around 73±2 Gauss. However, $B_{\frac{1}{2}}$ for An-1PP exciplex is around 62±2 Gauss which is smaller than that for others. This difference in $B_{\frac{1}{2}}$ for An-1PP could be due either to slower rate of electron exchange between 1PP radical cation and neutral 1PP or to difference in HFIs in these donor radicals caused by geometry. On the other hand, the $\Delta\phi/\phi\%$ values of An-DMA and An-1PP are almost the same, which for the complex, An-JL, is much less, inspite of the fact that the maximization of MFE occurs around ε=15 in aprotic solvents for all the complexes. Naturally, HFI (as measured by $B_{\frac{1}{2}}$) can not explain the observed differences. The lower ionization potential value and hence the larger radius of capture of JL causes a greater distance between the partners of RIPs at the time of their generation, which might explain the lower ϕ value of An-JL compared to An-DMA. Lifetime seems to be another factor that needs to be taken into account for explaining the differences in both ϕ and $\Delta\phi/\phi$ values between An-JL and An-DMA. It is also possible that the internal rotation of the (CH_3) – group gets coupled with the spin motion in case of DMA and thereby increases the ISC rate and hence, MFE. In brief, the conformation of a donor may effect the MFE for multitude of reasons, but no single cause could be pin-pointed.

To observe whether it is possible to alter the primary ET reaction pathway by changing the substituents on D or A molecules, a comparative study has been carried out with a set of four D-A systems that consist of two derivatives of carbazole, i.e. ECZ and PMC as donor molecules and a pair of cyanobenzenes, i.e. DCB and 1,2,4,5-tetracyanobenzene(TCNB) as acceptor molecules[45,48]. From the variation of the transient absorption decay rate constant in absence and in presence of a low magnetic field, it was possible to assess the spin state of the parent RP/RIP from which the transients originated. In the case of ECZ-DCB system the formation of RIP occurs initially in the singlet state. A field causes acceleration of decay of RP (as measured by transient absorption) and a simultaneous enhancement of exciplex luminescence. In contrast, if ECZ is replaced by PMC which has a greater number of substituents, the yield of triplet DCB is increased in the presence of MF, and at the same time there occurs slight increase in exciplex luminescence on application of a field. In this case, therefore, it is necessary to assume the production of RP via both singlet and triplet states. In case of ECZ-TCNB and PMC-TCNB, exciplex luminescence could not be observed, but the yield of the radical $TCNB^{\bullet-}$ is markedly enhanced in presence of a MF. This leads to the conclusion of triplet parentage of the RP.

Concluding Remarks

Magnetic field effect in chemistry has come a long way from the faltering steps with which it started. It is now a matured science with well-established facts backed by reliable theories. Given the complexity of coupled spin and spatial dynamics in heterogeneous condensed phase mixtures, the plurality of explanations and consequent ambiguities that remain in a few cases are not unexpected. New experiments by microwave, NMR and EPR techniques are being done to unravel the finer details of the spin evolution process, interpretation of which offers new challenges to theoreticians. The level of our present understanding is perhaps enough to go ahead and apply our knowledge to biology where mechanisms other than the radical pair mechanism may operate. There already has been good progress in the understanding of MFE on photosynthetic reaction centre and enzymatic reactions (such as that of B_{12}-coenzymes, Horseradish peroxidase and metalloflavoenzymes). The coming decade is expected to witness more. It is hoped that through multi-prong experimentation it will be possible to differentiate between fictitious and authentic claims of magneto-biology.

References

1 P W Atkins and T P Lambert *Ann Rep Prog Chem* **A 72** (1975) 67

2 S G Boxer, C E D Chidsey and M G Roelofs *Ann Rev Phys Chem* **34** (1983) 389

3 A L Buchachenko *Prog React Kinet* **13** (1984) 163

4 I R Gould, N J Turro and M B Zimmt *Adv Phys Org Chem* **1** (1984) 20

5 K M Salikhov, Y N Molin, R Z Sagdeev and A L Buchachenko *Spin Polarisation and Magnetic Field Effects in Radical Reaction* Elsevier Amsterdam (1984)

6 S Basu, D N Nath and M Chowdhury *Proc Indian Natl Sci Acad* **54A** (1988) 830

7 U E Steiner and T Ulrich *Chem Rev* **89** (1988) 51

8 U E Steiner and H F Wolff *Photochemistry and Photophysics* (Eds F F Sabek and G W Scott) CRC Press Boca Raton F L (1991)

9 M Chowdhury, R Dutta, S Basu and D Nath *J Mol Liq* **57** (1993) 195

10 K Bhattacharyya and M Chowdhury *Chem Rev* **93** (1993) 507

11 S Nagakura, H Hayashi and T Azumi (Eds)"Dynamic Spin Chemistry" Kodansha Tokyo and John Wiley & Sons, INC New York (1998)

12 M Chowdhury *J Indian Chem Soc* **76** (1999) 1

13 I Rosenthal *Sitzer Akad Wiss Berlin* **1** (1908) 20

14 R Cegielsky *Ber Phys Yer* **15** (1908) 566

15 S S Bhatnagar, K N Mathur and R N Kapur *Phil Mag* **8** (1929) 457

16 E Wigner *Z Phys Chem B* **23** (1933) 28

17 M Halder and M Chowdhury *Chem Phys Letts* (1999) (in press)

18 R Dutta and M Chowdhury *J Photochem Photobiol A* **55** (1990) 197

19 A Misra, R Dutta, D N Nath, S Sinha and M Chowdhury *J Photochem Photobiol A* **96** (1996) 155

20 S Aich and S Basu *J Chem Soc Faraday Trans* **91** (1995) 1593

21 S Aich, C Raha and S Basu *J Chem Soc Faraday Trans* **93** (1997) 2991

22 D N Nath and M Chowdhury *Indian J Pure and Apply Phys* **22** (1984) 687

23 D N Nath and M Chowdhury *Chem Phys Letts* **109** (1984) 13

24 S Aich, S Basu and D N Nath *J Photo Chem Photobiol A* **109** (1997) 95

25 S Basu, D N Nath and M Chowdhury *Chem Phys Letts* **161** (1989) 449

26 A Misra, R Dutta and M Chowdhury *Chem Phys Letts* **243** (1995) 308

27 A Misra, M Halder, R Dutta and M Chowdhury *Chem Phys Letts* **305** (1999) 63

Acknowledgement

The authors gratefully acknowledge financial support from CSIR (Grant no. 01/1348/95/EMR II) and DST (National Laser Programme).

28 M Halder, A Misra, A Banerjee and M Chowdhury *J Photochem.Photobiol. A* (1999) (in press)

29 A Misra, M Halder, M Chowdhury *Res in Chem Int* (1999) (in press)

30 N Periaswamy and H Linschitz *Chem Phys Letts* **64** (1979) 281

31 M Nazimuddin, A R Das, B M Mandal and S N Bhattacharyya *Eur Polym J* **837** (1990)

32 S K Ghosh, M Nazimuddin and B M Mandal *Makromol Chem Rapid Commun* **13** (1992) 383

33 A Weller, F Nolting and H Staerk *Chem Phys Letts* **96** (1983) 24

34 D N Nath and M Chowdhury *Pramana* **34** (1990) 51

35 S Basu, L Kundu and M Chowdhury *Chem Phys Letts* **141** (1987) 115

36 P K Bera, D Nath and M Chowdhury *J Phy chem A* **101** (1997) 384

37 P K Bera, D Nath and M Chowdhury, *J Phys Chem* **102** (1998) 7889

38 S Basu, D N Nath and M Chowdhury *J Chem Soc Faraday Trans I* **83** (1987) 1325

39 D N Nath, S Basu and M Chowdhury *J Chem Phys* **91** (1989) 5857

40 S Basu, D N Nath and M Chowdhury *J I Lumin* **4041** (1988) 252

41 R Dutta, S Basu and M Chowdhury *Chem Phys Letts* **182** 429

42 R Dutta, Ph.D. thesis (1991) Jadavpur University, Calcutta

43 P K Bera, A Misra, D Nath, S Sinha and M Chowdhury *J Photochen Photobiol A* **95** (1996) 127

44 A Misra, R Dutta, M Haldar and M Chowdhury *Chem Phys Letts* **28** (1997) 254

45 S Aich and S Basu *J Phys Chem A* **102** (1998) 722

46 S Aich and S Basu *Photochem Photobiol* (1999) (in press)

47 S Aich, T Sengupta, S Bhattacharyya and S Basu *J Pol Sc Pant A* (1999) (in press)

48 S Aich and S Basu *Chem Phys Letts* **281** (1997) 247

49 T Sengupta, S aich and S Basu *J Phys Chem B* **103** (1999) 3784

50 S Basu, D N Nath, M Chowdhury and M A Winnik *Chem Phys* **162** (1992) 145

51 R Dutta, D N Nath, M Chowdhury and M A Winnik *J Photochem Photobiol A* **84** (1994) 265

52 R Dutta, M Chowdhury and M A Winnik *Polymer* **36** (1995) 4445

53 S Basu *Proc Natl Acad Sci* **103** (1991) 557

54 N Kh Petrov, A L Shushin and E L Framkerich *Chem Phys Letts* **82** (1981) 339

55 U Werner and H Staerk *J Phys Chem* **99** (1995) 248

56 (a) N Kh Petrov, V N Borisenko, A V Starostin and M V Alfimov *J Phys Chem* **96** (1992) 2901

(b) N Kh Petrov, A Weissner, T Fiebig and H Staerk *Chem Phys Letts* **241** (1995) 127

57 N Kh Petrov, V N Borisenko and M V Alfimov *J Chem Soc Faraday Trans* **90** (1994) 109

58 D N Nath, S Basu and M Chowdhury *J Indian Chem Soc* **LX111** (1986) 56

59 S Basu, T Chakraborty and M Chowdhury *J Ind Chem Soc* **66** (1989) 599

60 H Staerk, W Kirhnle, R Treichel and A Weller *Chem Phys Letts* **118** (1985) 19

61 (a) Y Tanimoto, K Hasegawa, N Okada, M Itoh, K Iwai, K Sugioka, F Takemura, R Nakagaki and S Nagakura *J Phys Chem* **93** (1989) 3586

(b) H Cao, K Miyata, T Tamura, Y Fujiwara, A Katsuki, C –H Tung and Y Tanimoto *J Phys Chem A* **101** (1997) 407 and references therein

(c) H Cao, Y Fujiwara, T Haino, Y Fukazawa, C –H Tung and Y Tanimoto *Bull Chem Soc Jpn* **69** (1996) 2801

62 J Tang and J R Norris *Chem Phys Letts* **92** (1982) 136

PHOTOIONIZATION STUDIES IN AQUEOUS MICELLAR SOLUTIONS

A V SAPRE

Radiation Chemistry & Chemical Dynamics Division, Bhabha Atomic Research Centre,
Trombay, Mumbai 400 085 (India)

Micellar environments offer several exciting possibilities of photoinduced chemical reactions. The present article deals with photoionization processes with special reference to the photoionization of phenothiazine and its derivatives. These molecules are widely being used as drugs and in photoredox type of reactions due to their facile oxidation behaviour for achieving charge separation in organized media. Wavelength dependent photoionization and observed laser intensity dependent effects are discussed. Observations on two sites of solvation for electron solvation on photoionization of phenothiazine in non-ionic micellar solutions are elaborated. Implications of these results have been discussed.

Key Words: Micellar Solutions; Photoionization; Electron Solvation; Laser Flash Photolysis; Phenothiazine

Introduction

In the past six decades or so after the concept of micelles was emerged[1], the world of micelles has really widened and expanded. With the availability of sufficiently pure surfactants and new experimental techniques, the physicochemical characterization of various types of micelles has been accomplished to a good degree. These systems are less complicated than the real biological systems like enzymes or biomembranes but show essential features of such systems and have been used as good models for biomembranes and enzyme catalysis[2,3].

Photochemical studies in micellar systems received attention after the attempts to harness solar energy by chemical means began nearly two decades ago[2-4]. Solar photons are used to generate either an electronically excited state of suitable donor (acceptor) which transfers an electron to another suitable acceptor (donor) to create an ion pair or using a suitable substrate having low ionization potential, ions are created by photoionization. The ions can then be collected by suitable electrode system to obtain photocurrent. Micelles are recognized as good means of compartmentalizing solutes and increase the ion yield by preventing the back electron transfer/recombination of the ion-pair.

For details of the micellar systems the reader is referred to some excellent books and review articles on the topic[2-6]. However, for the understanding of the present work a brief summary is given. Long chain organic molecules having hydrophobic tails and hydrophilic head groups aggregate in aqueous solutions above a certain concentration called the critical micellar concentration (CMC) to give aggregates called micelles. Typical such molecules are

Anionic	Sodium dodecyl sulphate	$Na^{+}\,^{-}O_3SO\,C_{12}H_{25}$
Cationic	Hexadecyl trimethyl ammonium chloride	$CH_3(CH_2)_{15}N(CH_3)_3^{+}\,Cl^{-}$
Non-ionic	TritonX-165	$i\text{-}C_8H_{17}\text{-}C_6H_4\text{-}(OCH_2CH_2)_{16}\text{-}OH$

These aggregates have non-polar cores surrounded by polar shell of head groups called Stern layer. For non-ionic micelles the shell is

Fax: 91-22-5505151
E-Mail:cdscd@magnum.barc.ernet.in

thick and is called palisade layer. The Stern layer is further surrounded by ionic atmosphere of counter ions and water molecules called Gouy-Chapman layer, before the bulk water is reached.

By changing the concentrations and other conditions, various micellar structures are possible. At low surfactant concentrations nearly spherical micelles are formed which change over to cylindrical, bilayer micelles as the concentration is increased. In organic non-polar media inverted micelles with polar core and non-polar bulk are formed. In the presence of a co-surfactant e.g. an alcohol, optically clear microemulsions are formed. These structures are depicted in Fig. 1[2,3]. In the present article, mainly the photoreactions in normal micelles are considered.

Micelles offer microenvironments that are quite different from the bulk solution phase. Solutes solubilized in micelles experience microscopic parameters that differ drastically from the bulk solvent. Within a few nanometer distance the microscopic dielectric constant varies from 2 to 80 for aqueous solutions and microviscosities change by an order of magnitude. These factors give rise to some fascinating dimensions to photoinduced processes, both chemical and physical, that take place in micelles. Some of these are summarized in Table I. Some fascinating studies on the dynamics of photophysical processes are described by Kankan Bhattacharyya in another article of this issue[7-9]. Effect of Micellar cage and the hyperfine coupling (HFC) on the recombination reactions showed isotope effect for nuclei having nucl moments. This has lead to isotope enrichment in compounds containing nuclei e.g. C-13, S-33, Ge-73[10-13]. Effects of micellar environment on the photoproducts, regioselectivity have been investigated in details[14-17]. Normally, it is difficult to observe phosphorescence at room temperature due to fast quenching of triplet states and hence transparent glassy matrices at low temperature are required for this purpose. However, by using micelles to reduce concentration quenching and non-radiative processes, in combination with external heavy atom effect, phosphorescence can be seen at room temperature[18-19]. This technique has become popular as an analytical tool[20-21]. Micelle environments can also be used to induct asymmetric synthesis (e.g. menadione in sodium cholate micelles)[22] and catalyze U(IV)-U(VI) exchange reactions. Our experiments showed

Table I

Fascinating aspects of photoprocesses in micellar systems

Micellar cage effect, Magnetic isotope effect, photochemical isotope separation [10-12]
Room temperature phosphorescence [18-21]
Photochemistry in restricted geometries, control of photoproducts [13-17]
Reactions with reduced dimensionality[24].
Slowing down of Solvation dynamics[7-9]
Inter/intramolecular H atom transfer reactions[13-17]
Possibilities of asymmetric induction[22]
Photoionization, Charge separation[25]
Host-Micelle Quenching[26-27]

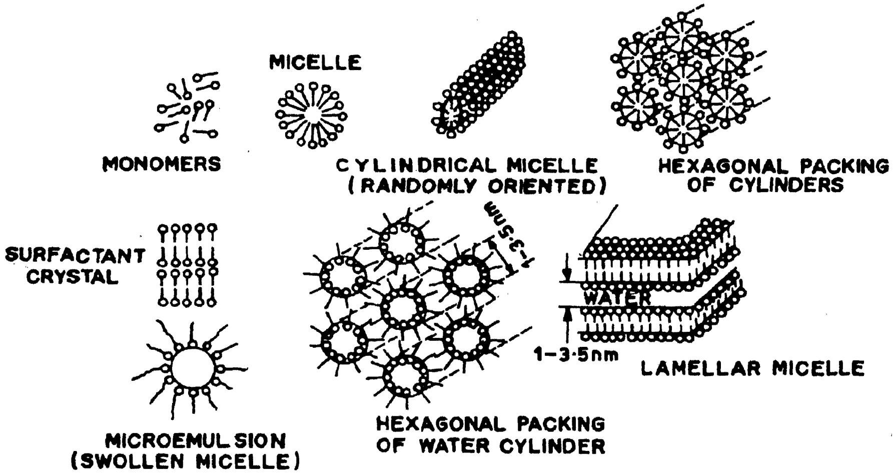

Fig. 1 Structures of various types of micelles formed in solutions

nearly 4-5 times of rate enhancement for such reaction in micelles. The surfactant-uranium complexes formed in such environments have been characterized by standard techniques[23]. Micellar environments have been seen to reduce dimensionality for radical reactions taking place at the micellar surface, thus increasing their rates by an order of magnitude[24]. Studies on photoionization and photoinduced charge separation are being widely carried out[25]. Quenching of excited states by host micelles is also an exciting aspect of micellar photochemistry[26-27].

Following absorption of light which takes place in femtosecond time scale, several processes take place in the micellar media. Typical time scales for such reactions[28] have been given in Table II. In the present article dynamics of photoionization reactions, an important aspect of micellar photochemistry is discussed. Work done in our laboratory and some aspects of work done in other laboratories have been discussed.

Table II

Time scale of micellar photoevents

Event	Time scale
Thermal/Normal Reactions	S
Triplet life-times, phosphorescence	mS-S
Break-up of micelles	0.1-10 mS
Quenching of triplets, Exit rates of solutes	1-100μS
Monomer exchange	100nS-1μS
Quenching of singlet states, Electron transfer Fast Surface reactions	1-10 nS
Fluorescence Depolarization	100pS-1 nS
Exciplex electron transfer, proton transfer	10 pS
Photoexcitation, Photoionization	10 fS

(m: milli, μ: micro, n: nano, p: pico, f: femto, S: second)
Adapted from reference 28

Experimental Techniques

A schematic diagram of the picosecond flash photolysis apparatus used in the present work is given in Fig. 2. Briefly third (355nm,35ps, 5mJ) and fourth (266nm,35ps,1.5mJ) harmonic output from an active-passively mode-locked Nd-YAG laser (10Hz) were used for excitation of the solutions[29-30]. The transients produced were monitored by their transient absorption using a white light continuum (400-950 nm) produced by focusing the residual fundamental (1064 nm) on to a cell of H_2O-D_2O mixture. Solutions were flowed through a 1 cm path-length cell so that a fresh solution is exposed to the laser pulses. The delay between pump-probe pulses was adjusted with 1 M length optical delay line. The probe beam was split into two by a beam splitter (50:50) to generate a reference and an analyzing beam, both were then passed through a spectrograph and recorded with a dual diode array based optical multichannel analyzer and the signals were processed on a PC. Transient absorption studies in the nano and microsecond time region were carried out using the same excitation source with a tungsten lamp, monochromator, photomultiplier (Hamamatsu R-928) and a digital oscilloscope (Tektronix-TDS-

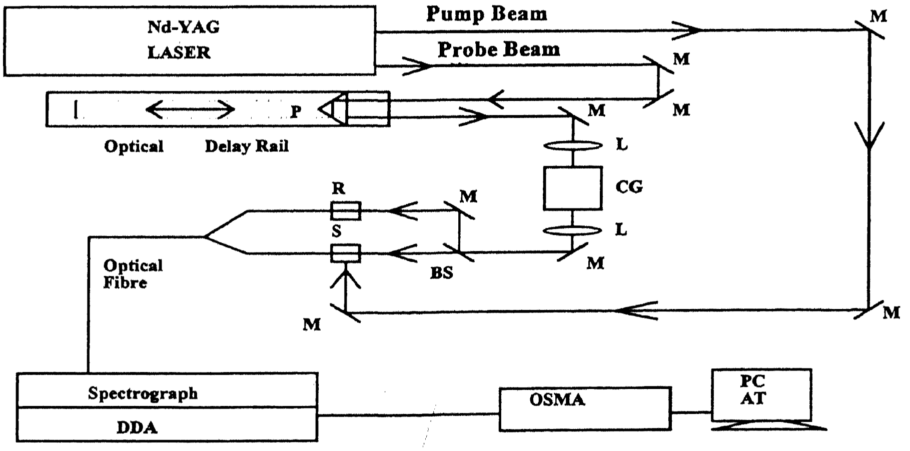

Fig 2 Schematic diagram of Pico-second laser flash photolysis, M, mirror; L, planocovex lens; P, prism; CG, continuum generator; BS, beam splitter; R, reference cell; S, sample cell, DDA, duel diode array; OSMA, optical spectroscopic multichannel analyser.

520) combination. Some experiments were carried out on laser kinetic spectrometer (Applied Photophysics Model K-347) using 248nm pulses from an excimer laser.

Photoionization

Photoionization is one of the most important photoprocess studied in micellar solutions in which the excited state donates an electron to the solvent.

$$P + h\nu \rightarrow P^{*} \rightarrow (P^{+} - e^{-}) \rightarrow P^{+} + e_{s}^{-} \qquad \ldots (1)$$

where: P: ionizable probe molecule, e_s^-: solvated electron, P^+: cation radical. In non-polar solvents, the electron is not stabilized by the solvent and hence the recombination of the ion-pair is a major process leading to poor yields of the ions. In polar solvents the ion yields are increased and in the ionic micelles the recombination is prevented, thus increasing the ion-yields. Pyrene, perylene, tetramethylbenzidine (TMB), N,N,N'N'-tetramethylphenelenediamine (TMPD), phenothiazine (PTH) are commonly used probes for the photoionization process. For the former three aromatic probes the photoionization is a biphotonic process[31-34]. The amine probes have low ionization potentials and the ionization quite often is a monophotonic process[32-33]. In general, degradation of DNA, amino acids and other cellular components by excitation in the spectral region <300nm involves a distinct possibility of photoionization[35]. Involvement of ionization processes by excitation in the region >300nm is important from the point of view of phototoxic effects on the skin, eyes etc. due to the possibility of monophotonic ionization of the substrates. These have direct applications in photomedicine and related areas. Photoionization induced by UV-A radiation in the phototherapy/psoralens has been recognized as an important process[36]. The increasing use of excimer (248 & 193nm) and other UV laser radiations in medicine and surgery has necessitated investigations on the photoeffects of deep UV radiations and photoionization is one of the most important such effect[34]. Photoionization is also important for the action of some conductive coating agents[37]. We have chosen PTH as a probe to study photoionization in organic and aqueous micellar media and some studies were carried out on the surfactant Triton X-100 and some of its anologues are described here.

Photoionization of Phenothiazine

Phenothiazine (PTH) and its derivatives are being widely used as psychotropic drugs[38]. However, their use is known to induce photoallergic and phototoxic effects of eye and skin when the patients are exposed to sunlight. The structure of PTH is given below.

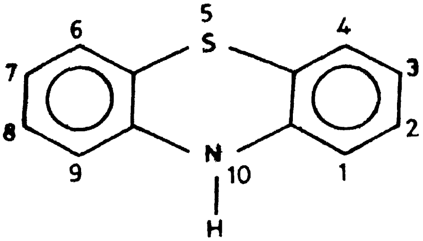

PTH derivatives have been studied as electron donors in electron transfer reactions due to their low ionization potentials[39]. Presence of two heteroatoms in PTH's adds to a total number π electron >4n + 2. The resulting non-pairing of bonding and antibonding orbitals facilitates ionization[40]. Besides the facile formation of the cation radical by removal of an electron from highest occupied molecular orbital (HOMO) in the ground state, PTH and its derivatives exhibit excellent photoredox properties that are important for the utilization of solar energy[41]. The crystal structure of PTH shows that the molecule is folded along the N-S axis with the two planes containing the phenyl rings having a dihedral angle of 158.5[42,43]. The amount of folding increases for larger substituents like 10 substituted ones and chlorpromazine has a dihedral angle of 139.4° The PTH molecule opens up on the formation of the radical cation and the dihedral angle increases to 172° in PTH^+. Recent resonance Raman studies indicate that neutral PTH molecule has a non-linear structure with dihedral angle of ~153° and the radical cation has a planar/near-planar structure with ~180° dihedral angle[44]. Photoelectron spectroscopy studies indicate that increase of the dihedral angle gives a better overlap between the ring C and N atoms as well as the ring C and S atoms. The work further suggests that the amine part of the PTH is pyramidal in the neutral ground state and planar in the radical cation ground state.

The photoelectron spectra of PTH and its derivatives show that the first ionization potential is N centered (7.26 eV for PTH) and the second one is S-centered[39]. The good electron donating properties of PTH have been used in the study of photoinduced electron transfer and back electron transfer in fullerene C-60-PTH charge transfer complexes and dissociative electron transfer from photoexcited PTH and 10-methyl PTH to chloroalkanes by us[45,46].

The early work cited above on PTH in micellar solutions of SDS showed that monophotonic ionization occurs on excitation with 347.1nm laser pulses[32]. Phototoxic effects could arise due to such a process by exposure to UV A radiation($\lambda >$ 300nm) in the sunlight. Although early work showed that the solvated electron yield depends linearly on the laser intensity, biphotonic ionization is also reported in micellar media[47]. It is not clear whether the biphotonic ionization proceeds via singlet or triplet state for a given excitation wavelength. Iwaoka and Kondo[48] observed the formation of chlorpromazine (CPZ) cation radical in the flash photolysis. Navaratnam and coworkers[49] directly observed and identified the excited triplet states of PMZ and CPZ, their cation radicals and solvated electrons produced by photoionization. Observation of linear change of the optical density due to solvated electron with increase in flash intensity led them to conclude that the ionization is monophotonic for both the molecules. Motten *et al.*[47] reported the detection of e_s^- by ESR only for the excitation of CPZ to S_2 state. No e_s^- was observed for S_1 excitation and photolysis of promazine (PMZ) yielded no evidence for e_s^- whether the excitation was in S_1 or S_2 state. Smith and McGimpsy[34] have studied one and two colour photochemistry of PTH in acetonitrile and reported that ionization takes place via singlet manifold to give cation radical of PTH, in competition to intersystem crossing and bond cleavage. For PMZ and CPZ Garcia *et al.*[50] found that the ionization proceeds via excited singlet state at 355nm excitation in alcohol. Turro *et al.* have found that PTH^+ formation is mainly monophotonic with minor contributions from biphotonic processes, while triplet yield increases with 0.8 power of light intensity[51]. Hence, the mechanism of photoionization of PTH and its derivatives like PMZ, CPZ is not clear. The effect of alkyl chain length on the photoionization of N-substituted and sulphonated alkyl PTH derivatives in anionic alkyl sulphate and cationic trimethyl ammonium bromide micelles has also been studied[52-53]. Guo *et al.*[54] have also studied the laser flash photolysis of PTH and its N-alkyl derivatives in acetonitrile at 248nm and photoionization is reported. We carried out laser flash photolysis experiments on PTH in cyclohexane, methanol and in aqueous micellar solutions of SDS and Triton X-100 by excitation at 355 and 266nm[29] in the picosecond time domain. The excitation with $\lambda >$ 300nm produces S_1 while that with $\lambda < 300$nm produces S_2 singlet excited states. These wavelength dependent experiments showed interesting features which are described below.

The singlet-singlet (S_1-S_n) absorption spectrum of PTH in cyclohexane was found to have a maximum at 650nm and a decay time of 900 ps which matches with the fluorescence life-time of PTH. In representative polar, protic solvent, methanol; on 355nm excitation both the singlet excited state of PTH (λmax=650nm) and the cation radical PTH^+ (λ_{max}=520 nm) are seen (Fig. 3) showing that the ionization and excitation processes occur simultaneously (Scheme I).

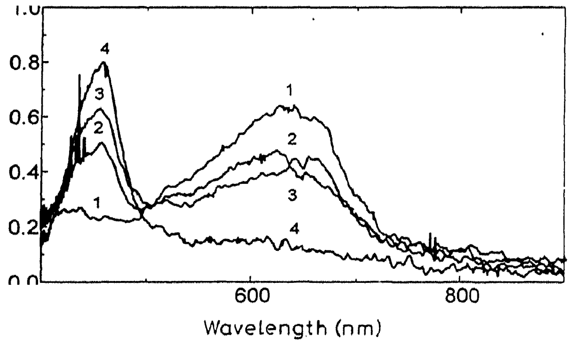

Fig. 3 Transient absorption spectra obtained on excitation of PTH in methanol by 355nm laser light. (1) 0ps, (2) 330 ps, (3) 730 ps, (4) 4 ns and after the laser pulse.

$PTH + h\nu \rightarrow PTH^* (S_1) \rightarrow PTH (S_0)$ Internal Conversion (IC) ... (2)

$\rightarrow PTH^+ + e_s^-$ Ionization from singlet state ... (3)

$\rightarrow PTH^* (T_1)$ Intersystem Crossing (ISC) ... (4)

$\downarrow \rightarrow PTH^+ + e_s^-$ Ionization from triplet state ... (5)

$\rightarrow (PTH^+ + e_s^-) \rightarrow PTH^+ + e_s^-$ Ion Escape ... (6)

$\rightarrow PTH^* (T_1)$ Recombination ... (7)

Scheme 1

Early steps of intramicellar charge separation/photoionization can be described as follows

$$\underset{\mathrm{I}}{(\mathrm{PTH})_m} \xrightarrow{h\nu} \underset{\mathrm{II}}{\mathrm{PTH}_m^*} \rightarrow \underset{\mathrm{III}}{[\mathrm{PTH}^+ \ldots e^-]_m} \rightarrow \underset{\mathrm{IV}}{(\mathrm{PTH}^+)_m} + \underset{\mathrm{V}}{e_{qf}^-} \quad \ldots (8)$$

$$\underset{\mathrm{V}}{e_{qf}^-} \rightarrow \underset{\mathrm{VI}}{e^-_{presol}} \rightarrow n(H_2O)\text{- i.e. } \underset{\mathrm{VII}}{e_s^-} \quad \ldots (9)$$

where m denotes the micellized species. The electron ejection from the excited state of PTH (II) can be visualized as passing through a micellized ion-pair (III), from which a quasi-free electron (V) escapes in to the bulk medium leaving behind the micellized cation radical of PTH (IV). The quasi-free electron (e_{qf}^-) solvates in the medium and two distinct species have been identified. The partially solvated electron e^-_{presol} (VI) absorbs in the infrared region of the spectrum ~ 1250nm which undergoes further solvation to give e_s^- (VII) and in water it has well characterized absorption spectrum with λ_{max} at 720nm. The photoionization and solvation steps were studied by Gauduel and coworkers[55-57] and found that the rise time for the presolvated species is 250 fS and for the fully solvated species it is 270fS in SDS micelles. The rise time of the e_{presol}^- species includes ejection of electron from the non-polar core of the micelle, thermalization and its trapping in the aqueous phase. For this the electron has to pass through the hydrocarbon chains of the SDS micelle and overcome the potential barrier of the interfacial Stern layer. When compared with the rise time of e^-_{presol} with that in neat water, (110fS), it is clear that its rate of formation is slowed down in aqueous micellar phase. Once the electron gets trapped in shallow traps, the final stabilization of this species to give fully solvated species occurs in a single step with time constant of 270fS. It was found that following fast charge separation in the SDS micelle, the yield of geminate recombination of the ion-pair is small, which is the determining factor for the initial photoionization yield (Φe^-). The Φe^- is a parameter that includes primary ionization cross section (σ_{ip}) and an electron escape probability (W)[58]. Thus

$$\Phi e^- = \sigma_{ip} \times W \quad \ldots (10)$$

Either or both the terms could be affected by the variation of the surface electric potential of the micelle (ψ). It is thus of primary interest to study the effect of ψ on the photoionization and electron transfer processes in the early time scales.

The results in methanol (Fig. 3) show that the S_1 state undergoes ISC to triplet (T_1) having absorption peak at 460nm as the time delay increases. The peaks due to the PTH^+ is seen at 520nm. After the decay of singlet state beyond 6ns, the residual absorption of e_s^- is seen at 630nm . When PTH solubilized in SDS and Triton-X-100 solutions is excited with 355 nm laser pulses, transient absorptions due to cation radical (PTH^+), singlet state and solvated electron (e_s^-) are seen. The yield of photoionization increases in the micellar solutions as compared to methanol. The transient absorption spectra obtained in these two micellar solutions are given in Figs. 4 & 5 at different delay times. It is seen from the figures that, at zero delay the cation radical, singlet and the

Table III

Quantum Yields of excited species and solvated electrons produced on photoexcitation of PTH by 355 and 266nm laser pulses.

Solvent	$f(S_1)$	$\phi(T_1)$	$\phi(e_s^-)$
Cyclohexane	0.8	0.64 (0.41)	
Methanol	0.8	0.44 (0.33)	0.1 (0.12)
Decanol		0.45	
Triton X-100		0.38	0.22
Brij-58		0.36	0.25
SDS	0.9	0.34 (0.3)	0.32 (0.35)

Relative errors ± 0.05 in ϕ, Values in brackets are for 266nm excitation.

$f(S_1) = \phi(S_1)$ 266nm ext/$\phi(S_1)$ 355nm ext : (The ratio of singlet state yields at the two wavelengths of excitation)

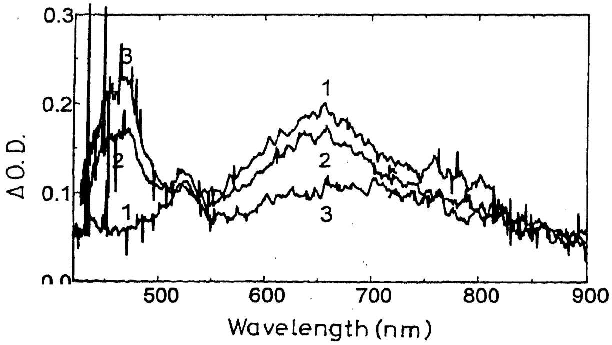

Fig. 4 Transient absorption spectra obtained on excitation of PTH in SDS micellar solution by 355nm laser light. (1) 0 ps, (2) 850 ps (3) 6. ns after the laser pulse.

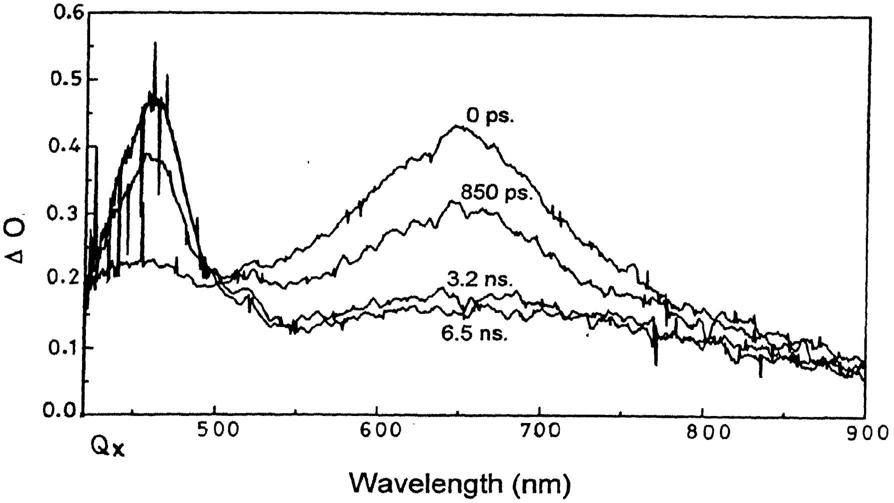

Fig. 5 Transient absorption spectra obtained on excitation of PTH in Triton X-100 micellar solution by 355nm laser light. (A) 0 ps, (B) 850 ps, (C) 3.2 ns, (D) 6.5 ns after the laser pulse.

e_s^- are the species present. After a delay of 6 ns, absorption due to the triplet state generated from ISC from singlet and ion-recombination is seen. As compared to methanol the ionization yields are more in micellar solutions and the singlet yields are correspondingly less. It is also seen that the e_s^- yields are more in anionic SDS micelle than in the non-ionic Triton X-100 or Brij-58. This is attributed to the negative charge on the anionic micelle which repels e_s^- out of the micellar phase to water. When PTH is excited with 266nm pulses, it was found that the electron yields are higher. The data on the yields is given in Table III. The data shows that ionization probability is more when S_2 state of PTH is excited.

Laser Intensity Effects

The mechanism of photoionization of PTH seems to be controversial and not very clear. Hence, laser intensity dependence studies were carried out. On the basis of linear dependence of e_s^- yields on the laser intensity (I_t) Alkaitis *et al.*[32] have shown that the ionization process is monophotonic in SDS solutions. However, both mono and biphotonic processes have been reported in the literature. Smith and McGimpsy[34] have found that the ionization of PTH in acetonitrile proceeds by a stepwise biphotonic process via singlet manifold. Photoionization of PTH derivatives chlorpromazine (CPZ) and promazine (PMZ) was found to be monophotonic by Navaratnam *et al.*[49]. However, Buetner *et al.*[59] observed that the photoionization of CPZ is a stepwise biphotonic process at $\lambda >$ 300nm. But the ionization for both the drugs studied was monophotonic at 266 nm. Using computer simulation of the intramolecular kinetics they have demonstrated that estimated triplet lifetime is sufficiently long (23 nS at room temperature) to account for the monophotonic ionization observed by other workers. These authors conclude that photoionization of PZ and CPZ is not an important mechanism for the observed phototoxic and photoallergic effects of these drugs in sunlight. Formalism of the photoionization and simple mathematical treatments of the mechanisms of the photoionization have been discused for some other molecules[60-61]. Garcia *et al.*[50] have found that singlet state of CPZ and PMZ is involved in the ionization process in methanolic and aqueous solutions. Turro *et al.* found that the formation of PTH^+ is a largely monophotonic process, with small contribution from the biphotonic process[51]. For the triplet the exponent is 0.8 (see eq. 12) which is consistent with reaction 5. We have studied the laser intensity effects with the aim of monitoring the singlet and the e_s^- yields.

It was ensured that the quantitative criterion for saturation given by Lacish *et al.*[62] is satisfied (eq. 11).

$$\sigma(I_t) < 1 \qquad \ldots(11)$$

where s is the cross section of PTH at the wavelength of photolysis and I_t is the photon flux in photons/cm^2 .Typical values of σ (I_t) used range from 0.05 to 0.16 for 266 and 355 nm laser pulses. The exact procedure for arriving at the yields is described in ref. 29. At moderate laser intensities the optical density (OD) or concentration of a transient chemical species is described as a function of laser intensity (I_t) by

$$OD = k\, I_t^{\,n} : \qquad \ldots (12)$$

where k is a constant related to specific experimental conditions and n is photonicity of the process. The value of n can be determined from the logarithmic plot of above eq. (13).

$$\log (OD) = \log k + n \log (I_t) \qquad \ldots (13)$$

From the slopes of the plots the value of n, the photonicity, was determined for both 266 and 355nm excitations in different solutions and is given in Table IV. Fig. 6 shows typical plots for log(I_t) vs log(OD) for 355 and 266nm excitations in methanol.

It can be concluded the the photoionization processs in SDS by 266nm excitation to S_2 level proceeds by a monophotonic process, while that at 355nm in SDS occurs through a complicated route involving both mono- and biphotonic processes. It can be expected that vibrationally excited molecules in the S_1 state contribute to the monophotonic ionization process. In methanol it is found that the ionization process proceeds by a biphotonic path. The effect of laser intensity on the yield of singlet state of PTH and e_s^- was observed at 355nm excitation. The results are given in Table V which clearly show that e_s^- are generated at the expense of the singlet state.

Table IV

Photonicity of the ionization process

Solution	Methanol		SDS in water	
Excitation λ nm	266	355	266	355
n value (slope)	0.97	1.7	0.95	1.48

The gas phase ionization potential IP_G usually gets reduced in liquid phase (IP_L) and these two are related by following equation:

$$IP_G = IP_L + P + V \qquad \ldots (14)$$

where P and V are polarization energy of the positive ion and ground-state conduction band potential (electron affinity) in liquid, respectively[63-65]. The P can be given by Born equation

$$P = e^2/2r\, [1 - (1/\varepsilon)] \qquad \ldots (15)$$

Table V

Effect of laser intensity on the yields of singlet state of PTH and e_s^- on excitation at 355nm in methanol

Laser Intensity I (Photons/cm ^{2}) × 10^{-16}	Φ (S_1)	Φ (e_s^-)
0.51	1.0	—
1.22	0.72	0.07
1.84	0.70	0.10
2.1	0.62	0.14
2.6	0.46	0.18

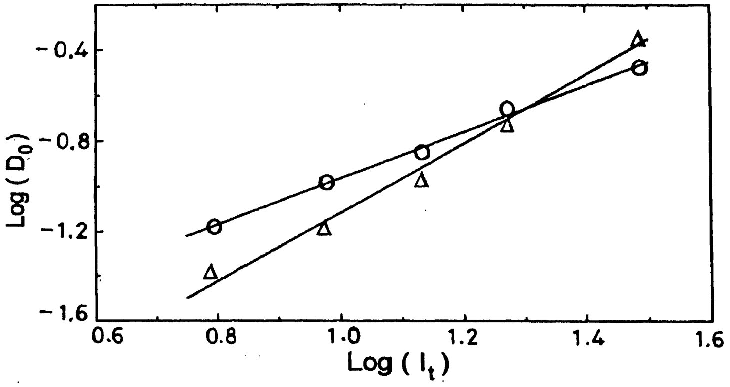

Fig. 6 Log(D_O) at 720nm vs Log(I_t) (laser intensity) for PTH (-O-) 266 nm excitation (*B*, -Δ-) 355nm excitation in SDS micellar solution.

where e is the electronic charge, r- the solute radius and ε- is the dielectric constant of the medium. Since both P and V are negative quantities, usually, $IP_G > IP_L$. For PTH the ionization potential in non-polar solvents (IP_D) is known to be 6.96 eV [66] and since values of P and V are negligible in non-polar media, IP_D can be equated to IP_G . r is usually obtained from molar volumes (M) using

$$r = [\ 3M/4\ \pi \rho\ N\ ]^{1/3} \qquad \ldots (16)$$

where N: Avogadro Number and ρ is the density. For the molecules where the molar volume is not known partial molar addition method given by Edwards[67] can be used. Using the above equation IP_L for PTH is calculated to be 3.96eV (~315nm) in methanol and 3.51eV in micellar solutions used. The estimated IP is lower by 3eV in methanol and 3.4eV in aqeous micellar solutions of SDS. The above calculations indicate that monophotonic ionization is not possible by 355nm (3.49eV) excitation in methanol. However, 266nm (4.66eV) photolysis of PTH in methanol supports monophotonic ionization in methanol and micellar media. The mixed mono and biphotonic process can be visualized as occurring via singlet excited state as a biphotonic process and via vibrationally excited states in the excited singlet state as a monophotonic process. These processes can be described by following schemes. Scheme 1 depicts monophotonic ionization by 266 nm light while Scheme 2 depicts the mixed mono and biphotonic ionization in SDS micellar solutions. Scheme 3 shows biphotonic ionization in methanol solutions by 355nm excitation.

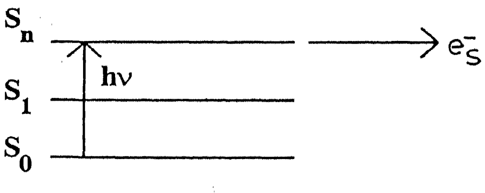

Scheme 1

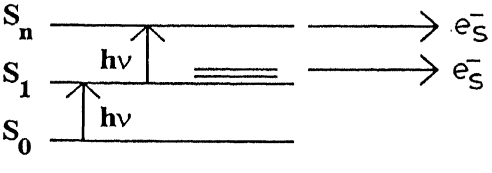

Scheme 2

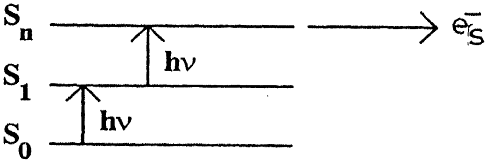

Scheme 3

Photoionization was also seen in non-ionic surfactant micelle Triton X-165 on excitation of the phenoxy chromophore with 248nm excimer laser pulses[68]. The photoionization was found to be monophotonic. Using eqs. 12, 13 with IP_L= 8.3eV (for a similar molecule o-cresol) and micellar radius 3.5nm, as Tx-165 is a large molecule, it was found that the ionization threshold is calculated to be ~ 6eV (i.e. 190nm). Hence, the observed monophotonic ionization can be explained by taking an effective radius of 0.2 nm which works out to be the size of the phenoxy chromophore. Hence, it seems that the size of the chromophore than the entire length of the molecule matters for the ionization behaviour. Similar results have been obtained by Bernas and coworkers[63-65]. For simple molecules like indole, the photoionization threshold was found to be 4.35 eV. Taking IP_G to be 7.9 eV, a large P value (-2.35 eV) is obtained for aqueous indole which corresponds to r value of 1.4 A°, much smaller than the the value of 3.36 eV obtained from molar volume. It was concluded that, r could be the dimension of positive charge localized on the N atom that participated in the photoionization. P is also affected by the solvent dielectric constant. Whether static or high frequency (optical) dielectric constant is to be used depends on the solvent relaxation during electron ejection. Despite large number of studies role of solvent, nature of molecule undergoing photoionization and the hole generated is not clear.

ESR and Related Studies

Turro and coworkers[51] have studied the time resolved and Fourier Transform (TRESR, FTESR respectively) of PTH solubilized in SDS micelles and in ethanol. A broad resonance due to PTH cation radical (g = 2.0053) with poorly resolved hyperfine structure and that due to e_s^- in water (g =

2.0005) was obtained on photolysis at 355nm in SDS micelles. Both these resonances were seen completely in emission. Similar results were obtained for 266 and 308 nm irradiation. The signal observed in the photolysis of PTH in ethanol is seen as absorption and is better resolved than that in SDS solutions. The spin polarization carried by e_s^- is transferred to a stable nitroxide free radical (pyrrolidinyloxyl derivative: $N^{\cdot}$) and the process is found to be faster by 5 times than the reaction of e_s^- with $N^{\cdot}$. The differences are attributed to the spin state factors and differences in the reactivities of radicals for spin exchange processes. Both ϕ e_s^- and ϕ PTH^+ were found to be less in alcohols as compared to that in SDS micelles. These results show that radical pair mechanism (RPM) does not play a role in the photoionization. The development of RPM polarization requires that the radical pair survives for a few nS. Since escape is fast, e_s^- escapes in pS time scales and therefore the absence of RPM is not surprising. It seems that spin polarization is carried over to the ^{3}PTH and triplet polarization is strong.

The effect of alkyl chain length on the photoionization of N-alkyl phenothiazines and sulphonated alkyl phenothiazines in anionic sulphete micelles (chain lengths C-10, C-12, C-14) and cationic alkyl trimethyl ammonium bromide micelles (chain length C-10, C-12, C-14) have been studied by Kevan and coworkers[52,53] using ESR and electron spin modulation techniques. It was found that the location of PTH moiety with respect to micelle-water interface together with cation-water interface is the major factor controlling the photoionization effects.

Dual Sites of Electron Solvation

If an electron is created inside the core of the micelle, due to the non-polar nature of the micellar core the electron will diffuse out to the bulk aqueous phase and get solvated. Most of the early work was done with ionic micelles where the ionic effects are very strong and the Stern layer is thin. However, the non-ionic micelles have thick palisade layers and the charge effects are absent. Hence, it would be interesting to see the solvation behaviour of electron generated inside the micellar core which diffuses out in to the bulk water. The energy of the photogenerated electron is normally ~0.1-5eV and their thermalization lengths are in the range of few nm. Since the thickness of the palisade layer of the same order, the possibility of electron solvation in the relatively polar palisade layer exists. To look into this exciting possibility, micellar solutions of non-ionic surfactant Triton X-165 (Tx) were photolyzed by 248 nm pulses from an excimer laser[68] and transient absorption spectra were recorded on photoionization. The absorption spectrum at 1 μS showed two absorption peaks at 630nm and 720nm. These were found to be due to two solvated species of electrons ejected by photoionization. Concomitantly, cation radical of Tx was also seen at 480nm. These two species were attributed to the electron solvated in the thick palisade layer of the non-ionic micelle (630nm) and solvated in bulk aqueous phase. Such spectra were also obtained in other Tritons of different chain lengths namely Tx-45 (Cn=5),100 (Cn=9.5),114 (Cn=7.5), 305 (Cn=30), 405 (Cn=40), 705 (Cn=70) where Cn is the number of carbon atoms in the polyoxyethylene chain of the Triton. The ratio of the two peaks changed when the chain length of the Tx was increased. The ratio of OD630nm/OD720nm decreased on increasing the chain length which is expected as the escape of the electrons in the bulk water is retarded when the surfactant chain length increases. The results were confirmed by excitation of PTH probe solubilized in another non-ionic micelle-Brij-35. Picosecond studies showed that the thermalization and solvation processes are complete in < 1ns and the duel sites appear in ~ 10ns time[69]. A typical time resolved spectra of these species is given in Fig 7 .

The reactions that take place on the photoionization can be summarised as follows:

$$\mathrm{PTH} + h\nu \rightarrow \mathrm{PTH}^* (\mathrm{S}_1) \rightarrow \phi (\mathrm{S}) = 0.75 \qquad ..\ (2)$$

$$\rightarrow \mathrm{PTH}^+ + e^- \rightarrow \phi (\mathrm{S}) = 0.25 \qquad ..\ (3)$$

$$\rightarrow \mathrm{PTH}^* (\mathrm{T}_1) \rightarrow .\phi (\mathrm{T}) = (.45) \qquad ..\ (4)$$

$$e^- \rightarrow e_m^- \quad k_{18} = ? \quad (\mathrm{dm^3 mol^{-1}\ s^{-1}}) \qquad (18)$$

$$\mathrm{PTH}^+ + e_m^- \rightarrow \mathrm{PTH}^* (\mathrm{T}_1)$$

$$k_6 = 5\times 10^{10}\ \mathrm{dm^3 mol^{-1}\ s^{-1}} \qquad ..\ (6)$$

$$e_m^- \rightarrow e_s^- \quad k_{19} = ?\ (\mathrm{dm^3 mol^{-1}\ s^{-1}}) \qquad (19)$$

Here e_m^- represents the electron solvated in

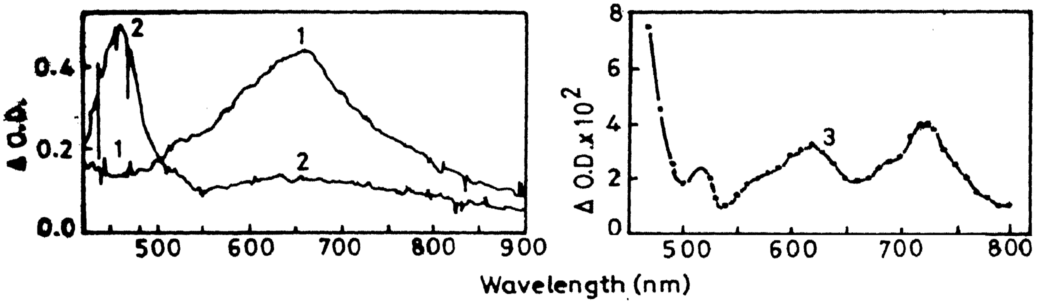

Fig. 7 Transient absorption spectra produced on laser flash photolysis of N_2 flushed solutions of PTH in Triton X-165 : 1). immediately (delay - 0 ps) and 2): 4000 ps after the 35 ps, 355 nm laser pulse. 3: immediately after XeF (351 nm) excimer laser pulse

palisade layer of the micelle and the unknown rate parameters are the solvation time for the quasi-free/dry electron to solvate in the palisade layer to give e_m^- and the time for e_m^- to diffuse out in bulk water to become e_s^-. The rate constants for these reactions 18 and 19 (k_{18} and k_{19}) are not known. To obtain these rate constants numerical simulations were carried out[70]. The above 6 equations lead to various coupled differential equations, the solutions of which were used to generate the evolution profile of the concentrations of the above transient species. The initial concentrations of the excited species are fixed as per experimental conditions and other rate constants and three quantum yields are known. With some reasonable assumptions the simulated curves were fitted with experimentally observed decays by changing k_{18} and k_{19}. For this purpose the numerical integrations were done for 10nS with a step of 10 pS. By comparing the concentration profile of the transients with the simulated ones the solvation times have been estimated to be 10pS ($1/k_{18}$) and 400pS ($1/k_{19}$) respectively[70].

These studies were extended to liquid crystalline regions of Tx-100 and water and the two sites of solvation were also seen in these solutions[71]. For this purpose electrons were generated by high energy electron irradiation in pulse radiolysis experiments. In the liquid crystalline region 40-70% Tx-100 the two transient absorption peaks at 630nm and 720nm due to e_m^- and e_s^- are seen. The reactivities of these two electron species towards solutes solubilized in aqueous phase (e.g. nitrate ions) and in micellar phase (e.g. pyrene) were found to be different. The electron solvated in palisade layer (e_m^-) reacts more efficiently with pyrene while the electron solvated in water (e_s^-) reacts more efficiently towards nitrate ions. Such selective reactivities the electron species with the substrates solubilized in different compartments of the microheterogenous media are of immense interest for understanding the radiation damage in biological systems.

Conclusion

Micellar systems offer wide variety of environments for chemical reactions. In this article photoionization processes using phenothiazine molecule and its derivatives as probe are described. Work carried out in our laboratory on photoionization of phenothiazine in aqueous micellar solutions has been reviewed. The wavelength dependence of the photoionization process and its fluence dependence has been described. Mechanism for observed photoionization processes in methanol and micellar media is given. For wavelengths >300nm ionization is a minor process photoinduced processes and in the sunlight the process can be neglected. Continuously tunable wavelength dependent experiments are required to understand such effects. Results on the observation of dual sites of solvation for the photogenerated electrons in non-ionic micellar media have been summarised.

Acknowledgements

Contributions from Dr H N Ghosh and Dr D K. Palit in the experimental work are gratefully acknowledged. The author is also thankful to Dr J P Mittal Guest Editor of this issue and Director, Chemistry & Isotope Group, BARC, for encouragement and stimulated discussions.

References

1 G S Hartley *Quart Revs Chem Soc* **2** (1948) 152

2 J H Fendler and E J Fendler *Catalysis in Micellar and Macromolecular Systems* Academic Press N Y 1975

3 K Kalyansundaram *Photochemistry in Microheterogeneous Systems* Academic Press Orlando USA 1987

4 J H Fendler *Accts Chem Res* **13** (1980) 7

5 B Lindman and H Wennerstrom *Topics in Current Chemistry* **87** (1980) 1

6 V Ramamurthy (Ed) *Photochemistry in Organized and Constrained Environments* VCH Publishers NY (1991)

7 Kankan Bhattacharyya *PINSA-A* **66A** (2) 2000

8 N Sarkar, K Das, A Datta and K Bhattacharyya *J Phys Chem* **100** (1996) 10523

9 S Das A, Datta and K Bhattacharyya *J Phys Chem A* **101** (1997) 3299

10 N J Turro, B Krautler and D R Anderson *J Am Chem Soc* **101** (1979) 7435

11 N J Turro, M-F Chow, C-J Chung, Y Tanimoto and G C Weed *J Am Chem Soc* **103** (1981) 4574

12 A I Buchachenko *Chem Revs* **95** (1995) 2507

13 M Wasaka, H Hayashi, K Ohara and T Takada *J Am Chem Soc* **120** (1998) 3227

14 N J Turro and W R Cherry *J Am Chem Soc* **100** (1978) 7431

15 N J Turro and J Mattey *J Am Chem Soc* **103** (1981) 4200

16 B H Baretz and N J Turro *J Am Chem Soc* **105** (1983) 1309

17 N J Turro, K C Lin and M-F Chow *Photochem Photobiol* **26** (1977)413

18 R Humphrey-Barker, Y Moroi and M Graetzel *Chem Phys Lett* **58** (1978) 207

19 K Kalyansundaram and J K Thomas *Chem Phys Lett* **51** (1977) 501

20 L J Kline Love and M Skrilec *Anal Chem* **53**(1981)

21 L J Kline Love, J G Harbarta and M Scrilec *Anal Chem* **53** (1981)437

22 A V Sapre, K V S Rama Rao and K N Rao *Proc 7 Inte Conf Radi Res Amsterdam* (1983) p A-2-22

23 R A Singh, A V Sapre, S R Dharwadkar and K V S Rama Rao *Thermochim Acta* **131** (1988) 79

24 A J Frank, M Graetzel and J J Kovak *J Am Chem Soc* **98** (1976) 3317

25 A Bernas, D Grand and S Hauteclouque in *Excess Electrons in Dielectric Media* (Ed C Ferradini and J P Jay-Gerin) CRC Press Boca Raton Fl USA (1991)

26 A V Sapre, K V S Rama Rao and K N Rao *J Phys Chem* **84** (1980) 2287

27 D K Palit, A V Sapre and J P Mittal *Chem Phys Lett* **269** (1997) 286

28 J K Thomas, F Grieser and M Wong *Ber Bunsenges Phys Chem* **82** (1978) 937

29 H N Ghosh, D K Palit, A V Sapre and J P Mittal *J Phys Chem B* **101** (1997) 2315

30 D K Palit, A V Sapre and J P Mittal *Indian J Chem A & B* (1992) F-46

31 J K Thomas and P Piciulo *J Am Chem Soc* **100** (1978) 3239

32 S A Alkaitis, G Beck and M Gratzel *J Am Chem Soc* **92** (1975) 5723

33 S A Alkaitis and M Gratzel *J Am Chem Soc* **98** (1976) 3589

34 G A Smith and W Grant McGimpsy *J Phys Chem* **98** (1994) 2923

35 H Groerner *J Photochem Photobiol B Biology* **26** (1994)117

36 P D Wood and L T Johnson *Photochem Photobiol* **65** (1997) 642

37 R Noufi A J Frank and A J Nozik *J Am Chem Soc* **103** (1981) 1847

38 R R Gupta Ed *Phenothiazines and 1 4- Benzothiazines: Chemical & Biomedical Aspects* Elsevier Amsterdam (1988)

39 N L Domelsmith, L L Munchausen and K N Houk *J Am Chem Soc* **99** (1977) 6506

40 B R Henry and M Kasha *J Chem Phys* **47** (1967) 3319

41 M Hu and L Kevan *J Phys Chem* **94** (1990) 5348

42 J J H McDowell *Acta Cryst* **B32** (1976) 5

43 J D Bell J F Blout O V Briscoe and H C Freeman *Chem Commun* (1968) 1656

44 D Pan and D L Phillips *J Phys Chem A* **103** (1999) 4737

45 H N Ghosh, D K Palit, A V Sapre and J P Mittal *Chem Phys Lett* **265** (1997) 365

46 S Nath, H Pal, D K Palit, A V Sapre and J P Mittal *J Phys Chem A* **102** (1998) 5822

47 A G Motten G R Buetner and C F Chignell *Photochem Photobiol* **42** (1985) 9

48 T Iwaoka and M Kondo *Bull Chem Soc Japan* **47** (1974) 980

49 S Navaratnam, B J Parsons, G O Phillips and A K Davis *J Chem Soc Faraday Trans* **74** (1977) 1811

50 C Garcia, G A Smith, W Grant McGimpsey, I Kochevar and R W Redmond *J Am Chem Soc* **117** (1995) 10871

51 N J Turro, I V Khudyakov and H V Willigen *J Am Chem Soc* **117** (1995) 12273 1811

52 Y S Kang, P Bagliani, H I D McManus and L Kevan *J Phys Chem* **95** (1991) 7944

53 Y S Kang and L Kevan *J Phys Chem* **98** (1994) 2498

54 Q X Guo, Z X Liang, B Liu, S D Yao and Y C Liu *J Photochem Photobiol A: Chemistry* **93** (1996)27

55 Y Gauduel, S Pommeret, N Yamada, A Migus and A Antonetti *J Am Chem Soc* **111** (1989) 49741

56 Y Gaude,l S Berrod, A Migus, N yamada amd A Antonetti Bio*chemistry* **27** (1988) 2509

57 A Migus, Y Guaduel, J L Martin and A Antonetti *Phys Revs Lett* **58** (1987) 1559

58 Y Gauduel, S Pommeret, A Migus and A Antonetti *Radiat Phys Chem* **34** (1989) 5

59 G R Buetner, R D Hall, C F Chignell and A G Motten *Photochem Photobiol* **49** (1989) 249

60 G Grabner, G Kohler, J Zelner and N Getoff *Photochem Photobiol* **26** (1977) 449

61 A C Bhasikuttan, A V Sapre, K V S Rama, Rao and J P Mittal *Photochem Photobiol* **62** (1995) 245

62 U Lacish, A Shafferman and G Stein *J Chem Phys* **64** (1976) 4205

63 D A Bernas, A Grand and E Amouyal *Chem Phys* **44** (1979) 73

64 E Amouyal, A Bernas and D Grand *Photochem Photobiol* **29** (1979) 1077

65 D Grand, S Hautecloque, A Bernas and A Petit *J Phys Chem* **87** (1983) 5236

66 A Fulton and L E Lyons *Aust J Chem* **21** (1968) 873

67 J T Edwards *J Chem Ed* 47 (1970) 261

68 H N Ghosh, D K Palit, A V Sapre, K V S Rama Rao and J P Mittal *Photochem Photobiol* **59** (1994) 405

69 H N Ghosh, D K Palit, A V Sapre, K V S Rama Rao and J P Mittal *Chem Phys Lett* **203** (1993) 5

70 H N Ghosh, A V Sapre and K V S Rama Rao *Chem Phys Lett* **255** (1996) 49

71 H N Ghosh, A V Sapre and J P Mittal *Radiat Phys Chem* **49** (1997) 107

PHOTOPHYSICAL PROPERTIES OF TWO INFRARED LASER DYES-IR-144 AND IR-140: A PICOSECOND LASER FLASH PHOTOLYSIS STUDY

JYOTIRMAYEE MOHANTY, DIPAK K PALIT* AND JAI P MITTAL@

Radiation Chemistry and Chemical Dynamics Division,
Bhabha Atomic Research Centre, Trombay, Mumbai - 400 085 (India)

The photophysical properties of two important tricarbocyanine dyes, IR-140 and IR-144, have been investigated in aqueous and organic solvents, binary solvent mixtures as well as in organised media. The fluorescence quantum yields, the life times and the radiative and nonradiative rates of the S_1 state have been determined by steady state and time resolved fluorescence and absorption techniques. The fluorescence characteristics of these weakly fluorescent dyes (fluorescence efficiencies are less than 10%) are seen to be very sensitive to the $E_T(30)$ values (parameter indicative of solvent polarity and hydrogen bond donating ability) of the solvents. Linear free energy plots of the nonradiative rates (k_{nr}) and the $E_T(30)$ values of the solvents showed a linear relationship with larger solvent $E_T(30)$ values yielding larger nonradiative rates. However, the radiative and nonradiative rates for both the dyes showed negligible dependence on solvent viscosity, indicating that photoisomerization reaction is not a major contributing pathway for the relaxation of the excited singlet state. Inspection of the ground state absorption spectra and particle size measurements indicated extensive aggregation of IR-144 in aqueous and aqueous-organic mixed solvents, while IR-140 showed little evidence of aggregation. Strong overlapping of the ESA spectra with the gain spectra of these dyes clearly explains the sensitiveness of the dye laser emission spectra on the concentration of the dyes. The dyes also show excitation wavelength dependent anisotropy which should be the responsible factor for depolarisation of the dye laser emission with excitation at shorter wavelengths, say 337 or 532 nm.

Key Words: **Infrared Laser Dyes-IR-144 & IR-140; Absorption & Emission Characteristics; Solvent Effects; Excited State Absorption; Stimulated Emission; Excited State Absorption Anisotropy**

1 Introduction

The growing interest in the applications of near-infrared (NIR) dyes in chemistry[1] and biology[2] has motivated a large amount of research in the last few decades. Recently, Soper *et al*[3] have shown that NIR dyes have better single molecule detection efficiency over the visible dyes due to low background fluorescence arising from the fluorescent impurities[4]. However, the major difficulties associated with the utilization of the NIR dyes are the low fluorescence quantum yields, short fluorescence lifetimes and solvent sensitive photophysical properties, e.g. many of these dyes undergo extensive ground state aggregation in aqueous solution, further reducing the fluorescence efficiency[5,6]. Another difficulty is the availability of limited number of fluorochromes with high fluorescence efficiencies appropriate for this region[3].

Among the dyes of this class the two most important and efficient ones are IR-144 and IR-140 for which lasing action has been achieved in 800-950 nm region. For the operation of NIR dye lasers with high average power, a major limitations has been the choice and availability of an optical pump source[7-9]. The frequency - doubled Nd : YAG laser has been shown to be an ideal optical pump for yellow-to red emitting laser dyes combining high peak power pulses with high pulse repetition rates[10]. However, optical pumping of the dyes, IR-144 and IR-140, at 532 nm occurs by pumping excited states of the dye molecule lying outside of the principal absorption band of the molecule[11]. As

---

*Author for correspondence:
@Also associated as Hony Professor with the Jawaharlal Nehru Centre for Advanced Scientific Research, Bangalore.
e mail: dkpalit@apsara.barc.ernet.in
Fax: 91-22-5505151 / 5519613

a consequence, the optimum dye concentrations necessary to ensure adequate absorption of the 532 nm pump radiation are very high, resulting in the shift in the maxima of the lasing wavelength[4]. This effect is caused by self absorption which quenches lasing at the primary peak in the fluorescence band and causes the laser to oscillate near a strong secondary or tertiary vibronic peak[7]. Another consequence of pumping these dyes at 532 nm is that the molecules are excited either to the upper vibrational levels of the first excited singlet state (S_1) or the second excited singlet state (S_2). Pumping excited states higher than S_1 has been found to alter the state of polarization of the dye laser emission. Detailed investigations of IR-144 and IR-140, have shown that the polarization of the dye emission relative to that of 532 nm pump radiatition is only 10-15%[12-14]. This depolarization has been explained due to molecular rotational relaxation of the pump-polarization induced anisotropy of the dye molecules as the latter relax from highly excited singlet levels to the lower levels of S_1 from where the laser action commences[12]. Also experimental evidence has been obtained regarding strong nonlinear absorption due to excited state absorption (ESA) at 532 nm pump wavelength and quenching of the dye laser emission at 1064 nm for the dye IR-140[12,13]. ESA can be a severe limiting factor in power scaling of the dye lasers [14-17].

Although several attempts have been made to characterize the lasing properties of these IR-dyes[11-17], less attention has been paid to characterize the detailed photophysical properties of these dyes. Detailed knowledge of the photophysical properties of the dyes in different kinds of media or environment is essential to judge their suitability in sensitive applications based on their fluorescence properties. Quantitative information regarding the various energy degradation pathways for the excited dye molecule and the role of the different chromophoric groups in energy relaxation mechanism will help in designing and synthesizing new and more efficient dyes for specific applications. In this article, the authors like to present the results of their detailed study on the excited state absorption and emission characterstics of IR-140 and IR-144 in different solvents.

2 Experimental Details

IR-140 and IR-144 dyes, the structure of which has

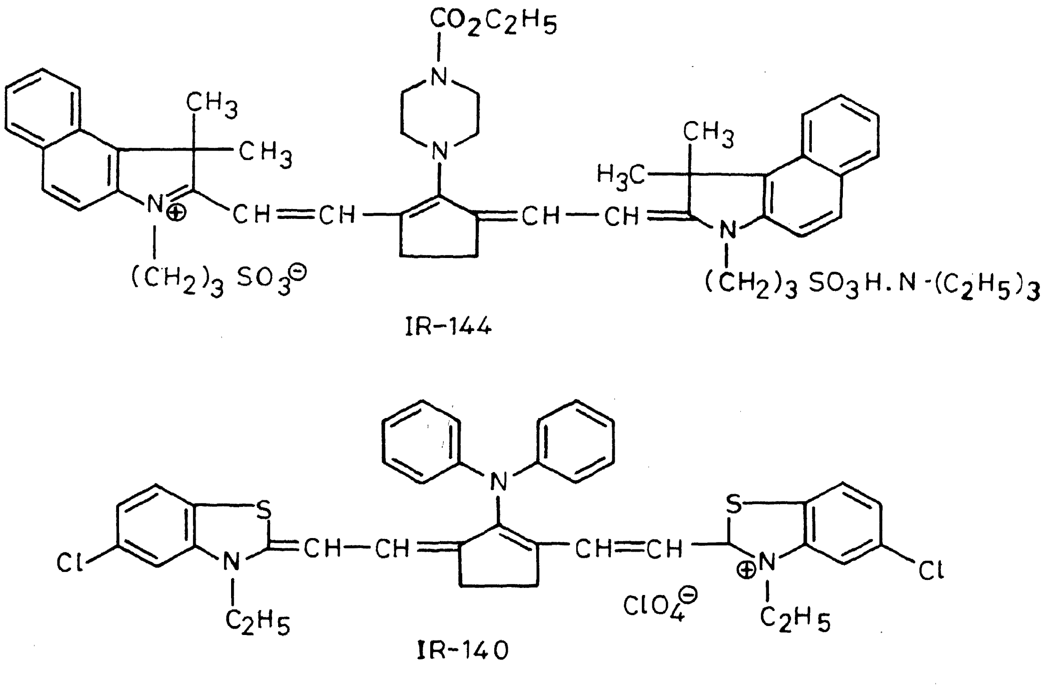

Scheme 1

been presented in Scheme I, have been procured from Exciton Inc., USA and have been used without further purification. Sodium dodecyl sulfate (SDS) and triton X-100 (Tx-100) were obtained from Fluka. All the solvents were of spectroscopic grade and used as received. Nanopure water was used for preparing aqueous solutions.

Steady state absorption spectra were acquired on a Shimadzu model UV-160 A double beam spectrophotometer. For recording the steady state fluorescence spectra, the Raman line at 766 nm, generated by focussing the 35 psec laser pulse at 532 nm into carbon tetrachloride (CCl_4) liquid of 5 cm path length, was used for excitation (the fundamental and the other lines generated were separated from the 766 nm line by using a Schott lower cut-off filter at 645 nm.) of the sample kept in a quartz cell of 10 mm path length and the fluorescence light emitted were detected in the transverse direction by using an optical multichannel analyser (Spectroscopy Instruments, Germany) consisting of a spectrograph, a dual diode array and a controller connected to a PC AT. Spectra thus obtained were corrected for the wavelength dependent reflectivity of the grating of the spectrograph and also the wavelength dependent sensitivity of the diode arrays by multiplying with a correction factor obtained by comparing the experimental fluorescence curve of IR-140 in ethylene glycol (EG) with that of the standard one reported in the literature[18]. For determination of the fluorescence quantum yield, the optical densities (OD's) of all the dye solutions were kept constant (OD $\sim 0.3 \pm 0.02$) at 766 nm and the areas under the corrected fluorescence curves were compared with that of IR-140 in EG-dimethyl sulfoxide (DMSO) (1:1) mixture for which the quantum yield is already reported[18]. However, corrections were made for variations of the ground state optical densities of the solutions and refractive indices of the different solvents. For fluorescence anisotropy measurements pure vertically polarised excitation light at 766 nm was obtained by using a cubic beam splitter as a reflector and the polarisation direction of the emitted fluorescence light was selected by using a dichroic sheet polariser (Oriel, Cat. No. 27306).

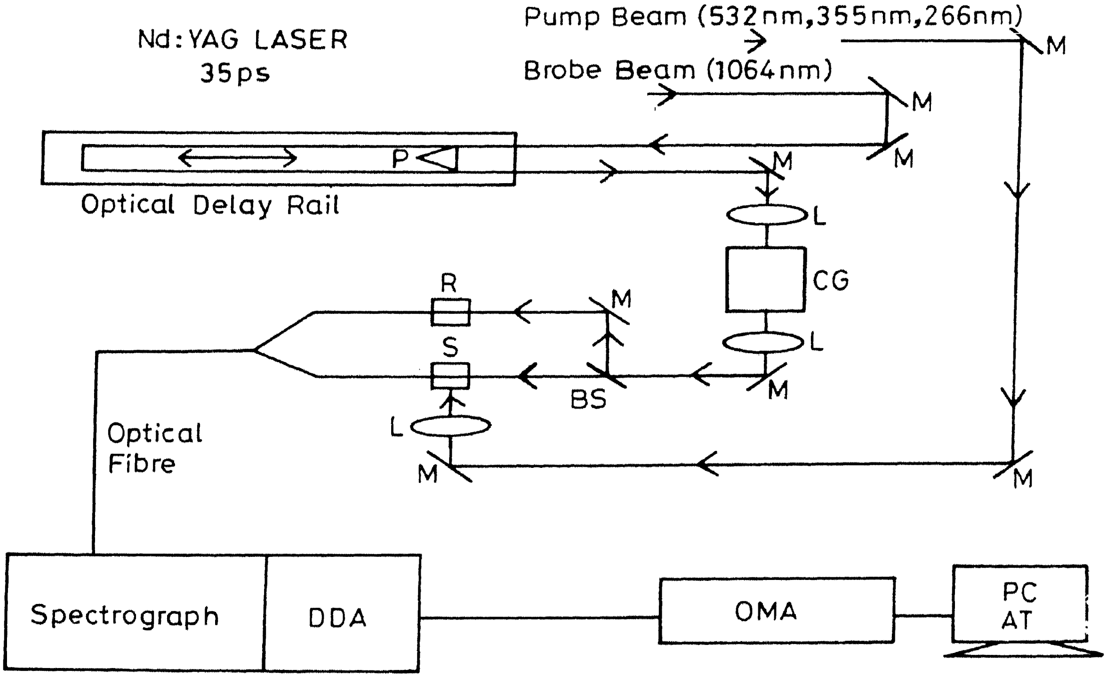

Fig. 1 Block diagram of the picosecond laser flash photolysis set up.
Schematic Diagram of Pico-Second Laser Flash Photolysis: M-Mirror; L-Planoconvex Lens; P-Prism; CG-Continuum Generator (450-900 nm); BS-Beam Splitter; R-Reference Cell; S-Sample Cell, DDA-Dual Diode Array; OSMA-Optical Multichannel Analyser

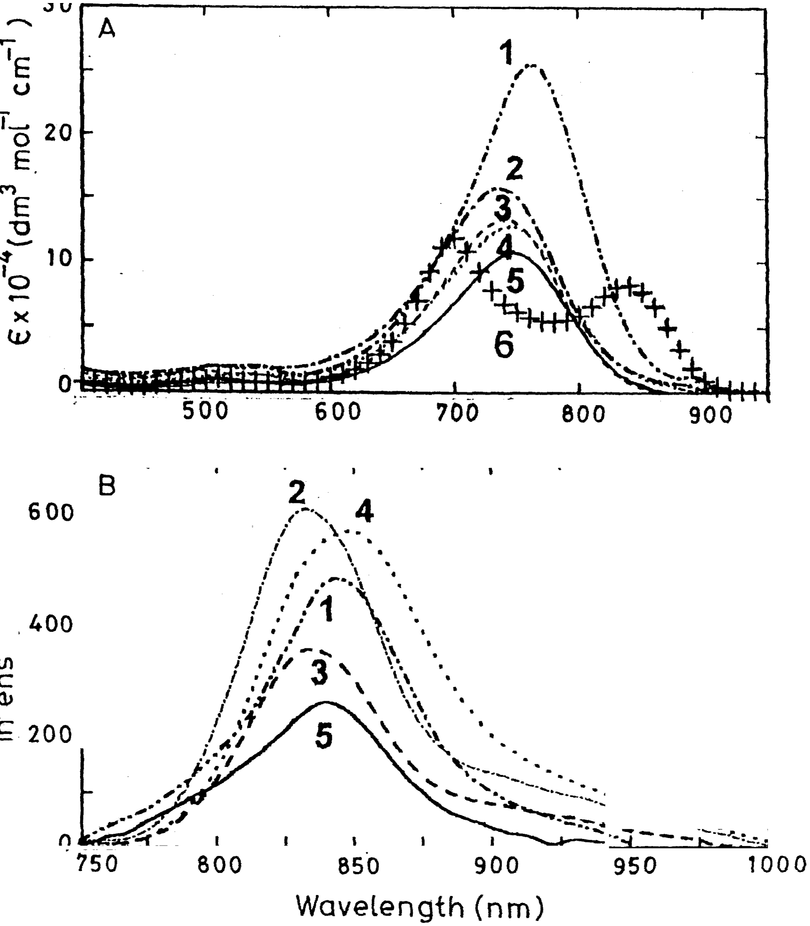

ig. 2 Steady state absorption (A) and fluorescence (B) spectra (λ_{ex} = 766 nm) of IR-144 dye in (1) DCE, (2) ACN, (3) MeOH, (4) DMSO, (5) EG and (6) H_2O.

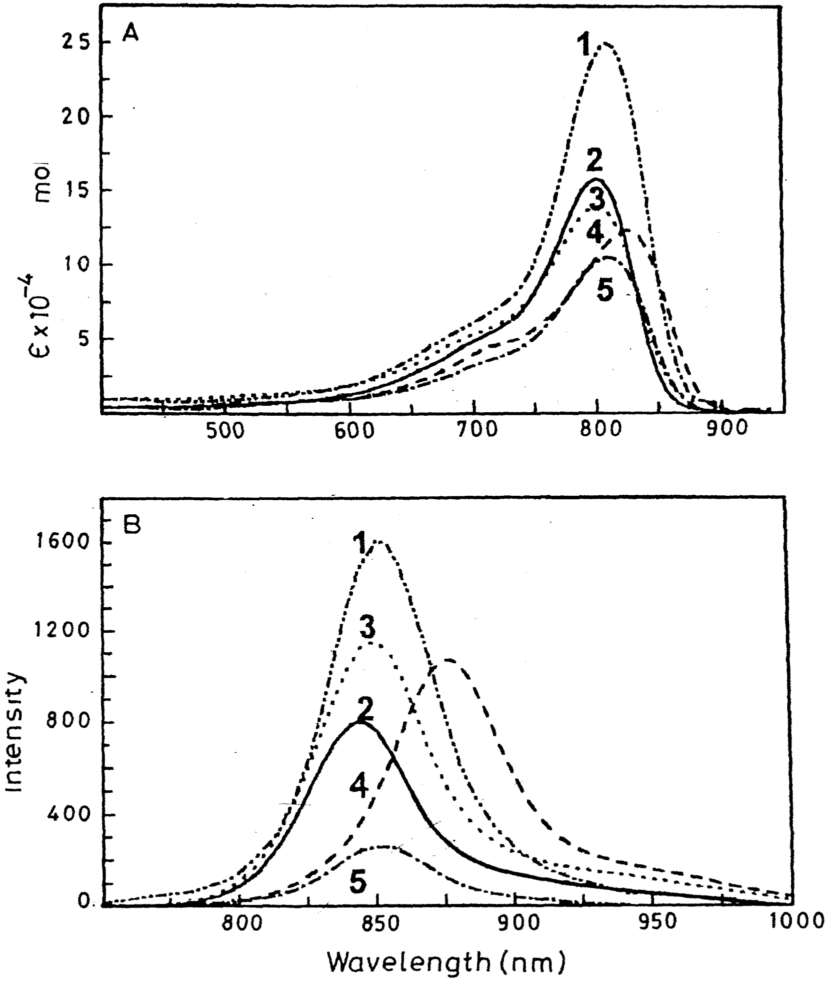

Fig. 3 Steady state absorption (A) and fluorescence (B) spectra (λ_{ex} = 766 nm) of IR-140 dye in (1) DCE, (2) MeOH, (3) ACN, (4) DMSO and (5) EG.

Volume average sizes of the particles of the aggregated dye molecules were measured using a particle size analyzer, the working of which is based on the principle of dynamical light scattering (Brookhaven Instruments model BI-900).

The picosecond transient absorption spectrometer, block diagram of which has been shown in Fig. 1, has been described in detail elsewhere[19,20]. Briefly, the second harmonic (532 nm, 5 mJ) or Raman shifted 766 nm (~ 0.5 mJ) light pulses of 35 ps duration from an active-passive mode locked Nd:YAG laser (Continuum model YG-501-10) were used for excitation. A white light continuum in the wavelength range (400-930 nm) generated by focusing the residual fundamental light (1064 nm, 20 mJ) on to a cell of 10 cm length containing H_2O:D_2O (1:1) mixture was used as the probe to record the absorption spectra of the transient using the optical multichannel analyser. A single axis linear motion stage of 1 m length was used to delay the probe light upto 6 nsec.

3 Results and Discussion

The electronic absorption and fluorescence spectra of IR-140 and IR-144 have been presented in Figs. 2 & 3 respectively. Important photophysical parameters of these dyes in different kinds of media studied here have been presented in Table I, which shows that the fluorescence quantum yields are correlated better with the $E_T(30)$ scale of the solvents rather than mere the polarity scale based upon dielectric constant of the solvent[3,21,22]. As the $E_T(30)$ values of the solvents increase, the quantum yields of fluorescence decrease. While IR-140 dye is insoluble in aqueous solution, IR-144 dye is sparingly soluble. The absorption spectrum of IR-144 in aqueous solution shows two distinct bands at 670 and 840 nm, which are different from the single band shown in nonaqueous solvents or even in micellar solutions. These two peaks can be associated with H and J-aggregates of the dye, respectively[5,23-26]. Such aggregates have also been seen in methanol (MeOH):H_2O (above 80% of V:V of MeOH) and DMSO:H_2O (above 70% of V:V of DMSO) mixtures. The phenomena of aggregation have been confirmed by the measurement of the particle sizes. The volume average sizes of the particles are 212, 448 and 1633 nm in H_2O, MeOH/H_2O and DMSO/H_2O media, respectively. IR-144 dye has been seen to be nonfluorescent in aqueous solution. The solubility of both the dyes was seen to increase due to addition of the

Table I
Photophysical properties of IR-144 and IR-140 in different solvents

Dye	Solvents	$E_T(30)$ (Kcal - mol^{-1})	λ_{max}^{abs} (nm)	λ_{max}^{em} (nm)	ϕ_f ± 0.005	τ_{S1} ps ± 50ps	k_r, $10^7 sec^{-1}$	k_{nr}, $10^9 sec^{-1}$
IR-144	DCE	41.3	763	845	0.04	850	4.7	1.1
	DMSO	45.1	745	850	0.05	800	6.3	1.2
	ACN	45.6	738	832	0.04	730	5.5	1.3
	MeOH	55.4	740	835	0.02	450	4.4	2.2
	EG	56.3	750	842	0.02	440	4.5	2.2
	Glycerin	57.0	750	835	0.02	440	4.5	2.2
	MeOH-H_2O(1:1)	58.3	740	836	0.01	220	4.6	4.5
	H_2O	63.1	670, 840	—	—	< 50	—	very high
	Tx-100	53.0	765	839	0.02	350	5.7	2.8
	SDS	57.5	755	839	0.01	300	3.3	3.3
IR-140	DCE	41.3	810	852	0.08	1270	6.3	0.7
	DMSO	45.1	830	875	0.06	830	7.2	1.1
	ACN	45.6	800	850	0.06	1180	5.1	0.8
	MeOH	55.4	800	845	0.04	320	12.5	3.0
	EG	56.3	810	852	0.04	240	20.0	4.0
	MeOH-H_2O(2:1)	60.3	800	843	0.02	250	8.0	3.9
	Tx-100	53.0	825	845	0.02	500	4.0	2.1

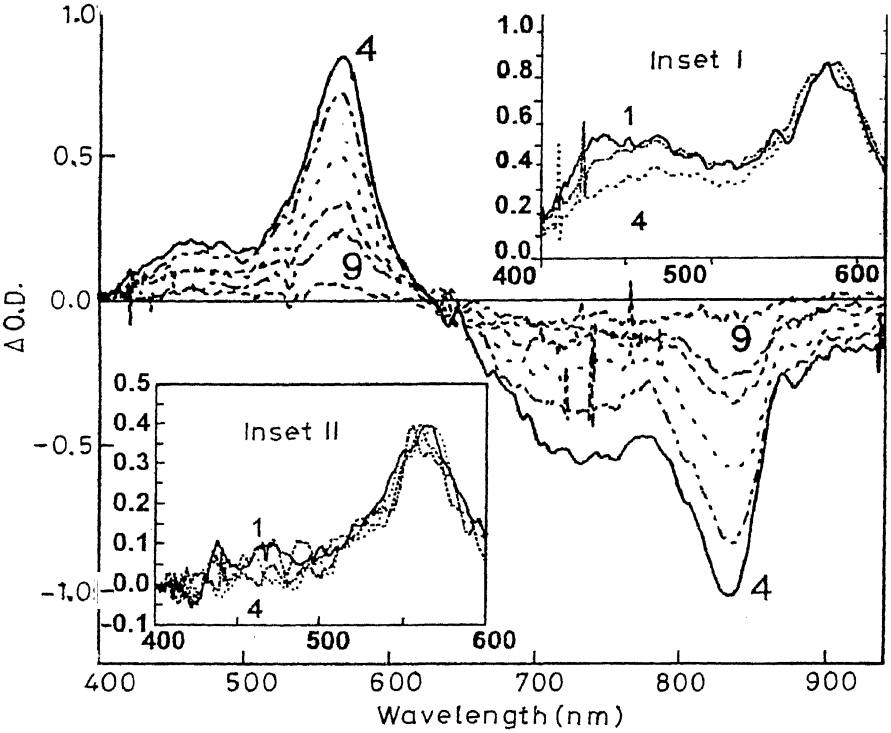

Fig. 4 Time resolved transient absorption spectra of IR-144 in ACN by 532 nm laser light. Time delays (ps): (1) -26, (2) -19, (3) -13, (4) 0, (5) 200, (6) 600, (7) 1000, (8) 1200 and (9) 2600 [Inset I and Inset II: Normalised transient absorption spectra earlier than 0 ps time delays at 570 nm with λ_{ex} = 532 nm and 766 nm, respectively].

surfactants above their critical micellar concentration in the aqueous solutions. Both dyes showed a single absorption band in micellar solutions similar to those observed in nonaqueous solutions. Also, in case of IR-144 dye the fluorescence yields were significantly higher in both SDS and Tx-100 micelles as compared to that in neat H_2O in which it is nonfluorescent[3,27]. These observations indicate that the dyes get solubilized in the palisade layers of the micelles and aggregation is prevented. However, both dyes were not soluble in aqueous solutions of cationic surfactant solution e.g. cetyltrimethyl ammonium chloride.

Fig. 4 shows the time resolved absorption spectra of the transients produced on laser flash photolysis of IR-144 in acetonitrile (ACN) on excitation at 532 nm. The transient absorption spectrum observed immediately after the 35 ps laser pulse (i.e. at 0 ps) shows four distinct features-two positive absorption bands with maxima at ca 450 and 580 nm and two negative absorption bands with the peaks at ca 720 and 840 nm. Among the two negative absorption bands one with maximum at ca 720 nm is due to bleaching of the ground state of the dye on excitation to S_1 or S_2 state since the wavelength maximum matches nearly with that of the ground state absorption spectrum. The other negative absorption band with peak maximum at ca 840 nm can be assigned to the stimulated emission by the probe light as the peak maximum is near to that of the steady state fluorescence spectrum. The absorbance values monitored at 550 and 840 nm after the zero picosec delay, were seen to decay with the same rate indicating that they originate from the same state, i.e. S_1 or the fluorescent state. The lifetime of the S_1 state as determined from the average values of these decay rates is given in Table I. The inset I of Fig. 4 shows the time evolution of the transient absorption spectra, in the 400-600 nm region recorded at time delays earlier than the zero psec i.e. within the width of the pump laser pulse. The different spectra, with the absorbance values normalised at 580 nm, clearly show the presence of another transient with absorption peak at ca 435 nm which decays with a very fast rate. Although, it has not been possible to measure the decay rate or the lifetime of this transient species quantitatively using our spectrometer, its presence is evident from the spectral evolution and it can be assigned due to the S_2 state generated by 532 nm excitation or due to the relaxation of the higher vibrational states in the S_1 state produced due to internal conversion process from the initially excited S_2 state. To distinguish between these two possibilities, the dye was excited in its primary absorption band at 766 nm where excitation only to S_1 state is possible and the transient absorptions were monitored in the same region. Under these conditions, the very fast relaxation process for the 435 nm absorption band was not seen (inset II of Fig. 4). Hence, it becomes obvious that the transient absorption spectra recorded in times earlier than zero psec delay due to 532 nm excitation is due to $S_2 \rightarrow S_n$ absorption. S_2 state decays very fast in subpicosec time scale to the S_1 state. The nature of the absorption spectra of the transients in other solvents remain more or less similiar and the lifetimes of the S_1 state in these solvents has been given in Table I. However, in viscous solvents like EG and glycerin, the stimulated emission peak shows a gradual red shift with increase in time delay. For example in EG the emission maximum shifts from 835 nm to 842 nm which are the peak maxima recorded at zero and 3 ns delay, respectively, (Fig. 5) and in glycerin this shift is from 819 to 834 nm. The steady state fluorescence maxima observed in EG and glycerin are at 842 nm and 835 nm, respectively. Hence, this shift of maxima of the stimulated emission band with time in more viscous solvents can be assigned to the formation of a new transient, for example excited state intramolecular charge transfer species[28] or new conformers via rotations of single or double bonds, which have been observed for other cyanine dyes[28,29]. Przhonska *et al.*[28] investigated the photophysical processes in indopentamethinecyanine dyes and showed that the S_1 state of these dyes can undergo two important processes which are *cis-trans* isomerization and twisted intramolecular charge transfer (TICT). In polar solvent TICT is the main process and the contribution of the isomerization process is only a few percent. However, we are unable to furnish further evidences in favour of these processes because we have been unable to resolve the multicomponents in the transient absorption decays. Probably, study of the wavelength dependence of the fluorescence decay will be able to provide more information regarding this.

The transient absorption spectra of IR-140 in different solvents recorded immediately after the laser pulse also show the similiar features as has been described for IR-144 in the previous

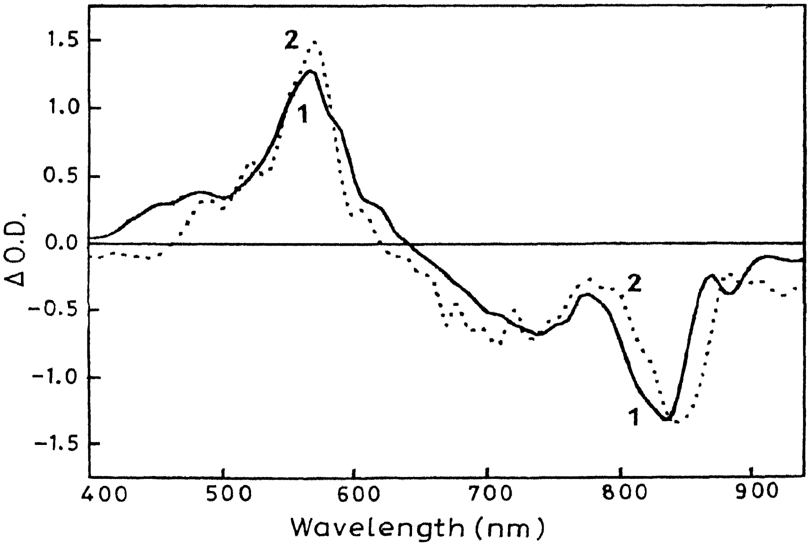

Fig. 5 Normalised transient absorption spectra of IR-144 in ethylene glycol ($\lambda_{ex} = 532$ nm) at 855nm.Time delays (ps): (1) 0, (2) 3000.

paragraph. Fig. 5 shows the representative time resolved spectra of the transient produced on laser flash photolysis of IR-140 in DMSO solution. The lifetimes of the excited singlet state of IR-140 in various solvents as determined from the decay of the transient absorption from the flash photolysis experiments are given in Table I. The life time of IR-140 in EG (240 ps) is in good agreement with those already reported[18,30]. Although no appreciable shift of the maxima of the band due to stimulated emission has been observed in ACN, DMSO and methanol, about 10-12 nm shift has been observed in viscous solvents, say EG and glycerin-methanol mixture.

Table I reveals that the lifetimes of both dyes have a good correlation with the $E_T(30)$ values of the solvents. Lifetime decreases as the $E_T(30)$ value increases. However, in the presence of water the lifetimes in methanol were found to show large decrease as the percentage of water was increased. For IR-144, the lifetime decreased from 440 ps in neat methanol to 220 ps in 1:1 (V:V) methanol water mixture and in neat water the dye was nonfluorescent. The singlet lifetime in water could be estimated to be less than 50 ps from transient absorption measurements. In the case of IR-140 also the lifetime decreased from 320 ps in neat methanol to 250 ps in 2:1 (V:V) methanol : H_2O mixture. However, this dye is insoluble in H_2O and no measurements could be made in this solvent. Very low solubility and ultrashort lifetime of the S_1 state of IR-144 in water can be attributed due to aggregation of the dye molecules. The effect of viscosity (η) of the medium on the lifetimes of the singlet state associated with these dyes also can be seen from the Table I. The lifetimes do not change significantly in the three alcoholic solvents, methanol (η=0.345 cp), EG (19.9 cp) and glycerin (954 cp).

The radiative (k_r) and nonradiative (k_{nr}) decay

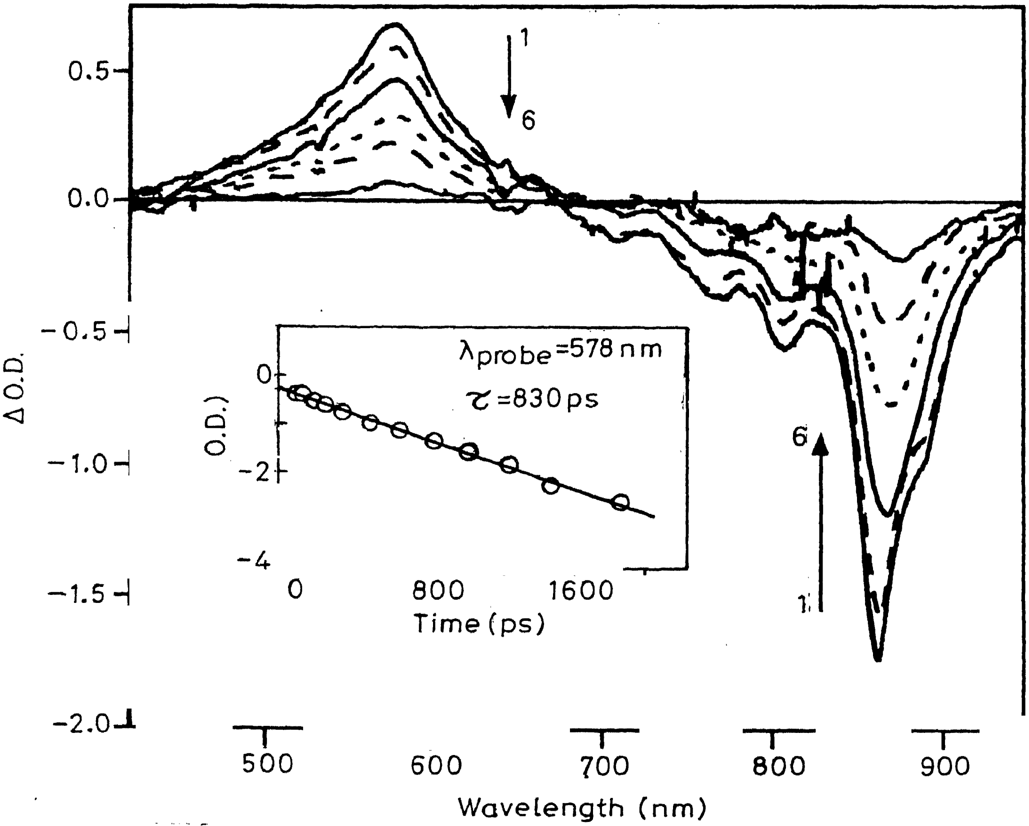

Fig. 6 Transient absorption spectra of IR-140 in DMSO (λ_{ex} = 532 nm). Time delays (ps): (1) 0, (2) 150, (3) 400, (4) 800, (5) 1200 and (5) 1800. Inset shows the first order plot of the decay of the transient absorption monitored at 578 nm.

rates for a quasi two-level system can be calculated from fluorescence quantum yield (ϕ_f) and singlet state (S_1) lifetime using the relations:

$$k_r = \phi_f / \tau_f \qquad \dots (1)$$

and

$$k_{nr} = (1-\phi_f)/\tau_f \qquad \dots (2)$$

The values of k_r and k_{nr} determined for the two dyes in different solvents are also presented in Table I. k_r values of both the dyes are seen to be in the range of 4-8 × 10^7 s^{-1} and are not sensitive to the solvent characteristics. However, the k_{nr} values show around three-fold and four-fold increase due to increase in $E_T(30)$ values from 41.3 (dichloroethane, DCE) to 58.3 (MeOH : H_2O :: 1:1) and 60.3 (MeOH : H_2O :: 2:1), for IR-144 and IR-140, respectively. The k_{nr} values for these dyes showed only small changes in alcohol series but larger changes were observed in the methanol-water binary solvents. Soper *et al.*[3] suggested that the nonradiative rates which represents a sum of rates associated with different processes depopulating the excited singlet state (S_1) can be represented in many tricarbocyanine polymethine dyes by the expression

$$k_{nr} = k_{isc} + k_p + k_{ic} + k_{sd} \qquad \dots. (3)$$

Where k_{isc} is the rate of intersystem crossing to the triplet manifold, k_p is the rate of photoisomerization, k_{ic} represents the rate of internal conversion and k_{sd} is the solvent - dependent nonradiative rate. Our transient absorption studies suggest that the k_{isc} is insignificant because the ground state bleach recovery rate and the S_1 state decay rate is comparable and also neither triplet absorption is observed nor bleaching due to $S_0 \rightarrow S_1$ absorption survived after the complete decay of the singlet state (Figs. 4, 5 and 6). Also the S_1 state decay rate has been seen to be unaffected in presence of heavy atom (iodine). Hence, the yield of formation of the triplet (ϕ_{isc}) and hence k_{isc} can be neglected. The k_{ic} can be time dependent due to conformational changes occurring during the excited state life time of the molecule and affect the rate of internal conversion. The rate of photoisomerization, k_p, as well as the time dependent internal conversion rate, k_{ic} are expected to exhibit solvent viscosity dependence, due to changes in molecular configuration in the excited state.

Comparing the τ_1, k_r and k_{nr} values of both the dyes in alcoholic solvents, namely, methanol, EG and glycerin (GY), it becomes evident that these parameters are nearly independent of viscosity and hence the possibility of occurrence of large conformational changes, or photoisomerization in the excited state can be excluded. Besides, it has been established that in tricarbocyanine dyes, the activation energy for *cis-trans* photoisomerization is reasonably high, due to the presence of steric hindrance between the heteroaromatic fragments of these dyes[31].

In order to understand the importance of the parameter k_{sd}, the rate of solvent dependent nonradiative process, which is a characteristic associated with the solvent, linear free energy relationships were constructed from the ln(k_{nr}) *vs.* different solvent parameters. The slope of this plot should be representative of the nonradiative pathway to a particular property of the solvent. For these two dyes we observed that the k_{nr} values could be better correlated with E_T (30) parameters of the solvents and the correlation plots have been given in Fig. 7. E_T (30) value of a solvent can be correlated with the polarizability as well as the hydrogen bond donating ability of the solvents. The large deviation of the value of k_{nr} in case of IR-144 in methanol-water (1:1) mixed solvent from linearity (Fig. 7A) is due to formation of

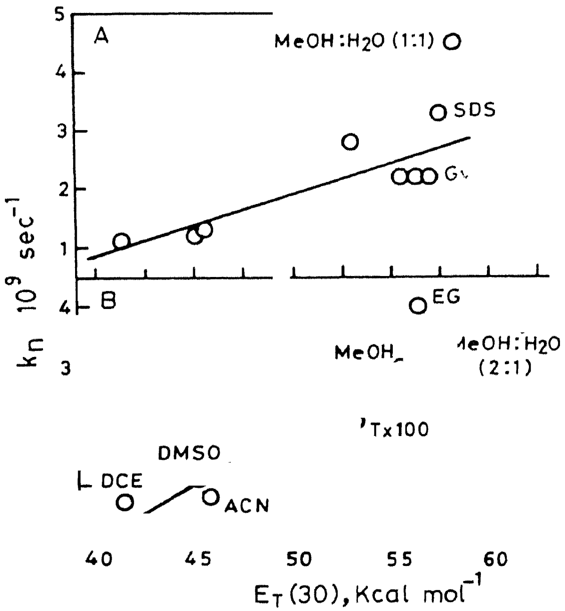

Fig. 7 Linear free energy plots of k_{nr} versus solvent E_T (30) values in different solvents for IR-144 (A) and IR-140 (B).

aggregates in presence of water. The linear relationship of k_{nr} with $E_T(30)$ values of the solvents indicate the involvement of the intramolecular charge transfer character of the fluorescing state.

Extinction coefficients for $S_1 \rightarrow S_n$ absorption for both the dyes in three important solvents ACN, DMSO and MeOH at 550 nm (at this wavelength the ground state absorption coefficients of both the dyes are very low, only a few thousands) were determined via the calculation of the concentration of the S_1 state species of the dye by comparing with the concentration of the benzophenone triplet[32,33] in ACN at 525 nm ($\varepsilon_{525nm} = 6500 \pm 400$ dm^3 mol^{-1} cm^{-1}) and C_{60} triplet[19] in benzene at 740 nm ($\varepsilon_{740nm} = 14{,}000$ dm^3 mol^{-1} cm^{-1}) produced due to excitation on 355 and 532 nm, respectively, in similiar experimental conditions. In this process we have assumed that all the numbers of the excited state species produced at higher excited electronic states due to excitation on 355 or 532 nm find their way to the S_1 state. Hence knowing the concentration of the S_1 state species and the ground state absorption coefficients at different wavelengths, the excited state absorption (ESA) spectra were correlated for ground state bleaching effect. Also it was necessary to correct the ESA spectra for the overlapping of the stimulated emission spectra. For this purpose we made the assumption that at the experimental conditions of recording the ESA spectra and fluorescence spectra (for example, excitation wavelength 766 nm, 2 mm thin samples of O.D. 0.5) the stimulated emission spectra should be very nearly same as the fluorescence spectra and hence ESA spectra were corrected for the overlapping effect of the stimulated emission on them. The corrected ESA spectra for these dyes have been presented in Fig. 8. Strong overlapping of the ESA spectra with the stimulated emission spectra, particularly for IR-

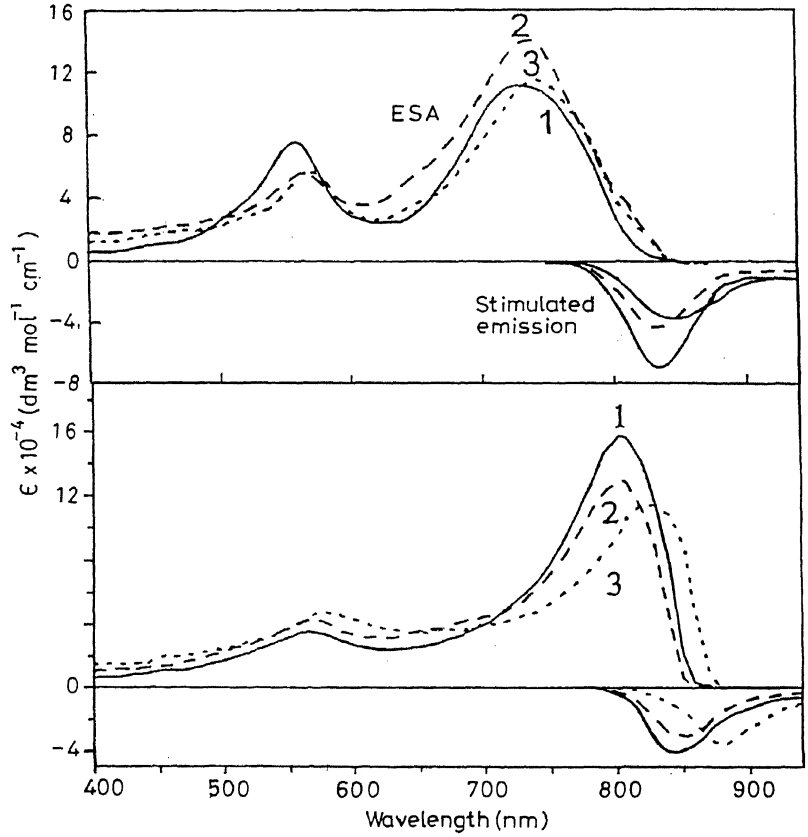

Fig. 8 Corrected ESA and stimulated emission spectra of IR-144 (A) and IR-140 (B) in (1) MeOH, (2) ACN and (3) DMSO.

140, clearly indicates the sensitiveness of the gain spectra on the concentration of the dye as reported earlier[14-17].

Fig. 9 shows the excited state absorption anisotropy spectra of these two dyes in DMSO obtained from transient absorption measurements observed immediately after the ps laser pulse of 766 nm. In both the cases the anisotropy values are constant in the wavelength range 500-800 nm ($r_0 = 0.18$ and 0.26 for IR-144 and IR-140 respectively) which are in agreement with the values obtained from steady state fluorescence anisotropy measurements at 800 nm. The rotational correlation times determined from the anisotropy decay obtained from excited state absorption measurements at 546 nm in ACN and DMSO are given in Table II. Rotational correlation times could not be measured with sufficient accuracy in

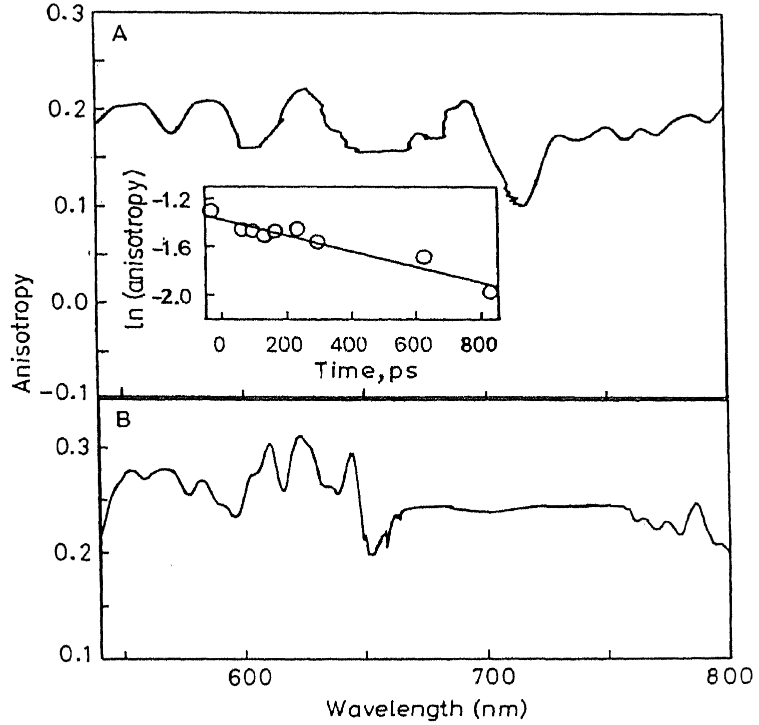

Fig. 9 Absorption anisotropy spectra of IR-144 (A) and IR-140 (B) in DMSO ($\lambda_{ex} = 766$ nm). Inset shows the first order plot of the anisotropy decay.

Table II

Anisotropy measurement, $\lambda_{ex} = 766$ nm

Dye	Solvents	η, cp	R_0^a	τ_R (Ave.)
IR-144	Glycerol	954.0	0.25 ± 0.02	—^{b}
	DMSO	1.996	0.20 ± 0.02	1.6 ns ± 0.2 ns
	Acetonitrile	0.345	0.20 ± 0.02	220 ps ± 50 ps
IR-140	Ethylene glycol	19.9	0.28 ± 0.02	—^{b}
	DMSO	1.996	0.25 ± 0.02	1.0 ns ± 0.2 ns
	Acetonitrile	0.345	0.25 ± 0.02	200 ps ± 5 ps

a) In case of IR 144, the value of R_0 is the average one of the measurements from excited state absorption (500 nm - 800 nm) and steady state fluorescence at 800 nm, for IR 140 the value of R_0 has been obtained from excited state absorption measurements only.

b) $\tau_R >> \tau_f$, hence could not be determined

EG and glycerin because of their large values compared to the life times of the corresponding excited state. It is interesting to note that due to excitation on 532 or 355 nm (which causes the transitions $S_0 \rightarrow S_2$ and $S_0 \rightarrow S_3$, respectively) the anisotropy values obtained are nearly zero in both the excited state absorption as well as in the steady state fluorescence measurements in case of both the dyes. These observations confirm the earlier observations that the polarization of the dye laser emission due to excitation on 355 nm or 532 nm is only 10-15% with respect to the pump polarization[12-14]. As the rotational correlation time in DMSO, the solvent which is normally used in case of these IR-dyes, is longer than the lifetime of the emissive state. Rotational relaxation of the dye can not be the responsible factor for depolarization of the dye laser emission. The following arguments can be the possible explanation for this fact. The direction of the emission dipole of the dyes can be calculated from the eq. (4).

$$r_0 = 0.2\,(3\cos^2\delta - 1) \qquad \dots (4)$$

where δ is the angle between the directions of the absorption and emission dipole moments. Using the value of r_0 (~0.25 for both the dyes) the angle between the directions of the emission dipole moment and $S_0 \rightarrow S_1$ absorption dipole moment is about 30°. The transition dipole moment for the $S_0 \rightarrow S_1$ absorption possibly lie along the long axis of the molecule. The zero anisotropy values for the $S_0 \rightarrow S_2$ (532 nm) or S_3 (355 nm) transition suggest that these dipole moment directions lie along the short axis (i.e. perpendicular to the long axis) of the dye molecule. Because in this case the δ value can be calculated from the eq. (4) assuming zero anisotropy value, is about 55°. Excitation wavelength dependence anisotropy of the molecules has already been reported in the literature by many groups[34,35].

In conclusion, we have investigated the fluorescence and excited state absorption properties of the two imporant laser dyes IR-144 and IR-140 in different organic and aqueous solutions including micelles. From the photophysical properties being reported here it becomes evident that apart from the most commonly used solvent DMSO which is hazardous for health other solvents with low $E_T(30)$ values should give equivalent efficiency as compared to the former one. In aqueous and aqueous - organic solvents, the poor solubility and poor fluorescence efficiency of IR-144 has been attributed to the aggregation. Although no evidence has been obtained in favour of aggregation of IR-140 in aqueous solution, the solubility and efficiency of the dye laser emission of IR-140 are equally affected. ESA spectra are strongly overlapped with the gain spectra of the dyes and hence the dye laser performance is expected to be strong function of dye concentration as well as pumping intensity. Anisotropy study has revealed that with pump excitation at 337 or 532 nm, the dye laser polarization is scrumbled by pumping at 766 nm (say Ti-sapphire laser will produce more polarization in pure dye laser emission).

References

1 (a) T Imasaka, A Yoshitake and N Ishibashi *Anal Chem* **56** (1984) 1077; (b) T Imasaka, A Yoshitake, K Hirata, Y Kawabata and N Ishibashi *Anal Chem* **57** (1984) 947; (c) K Sauda, T Imasaka and N Ishibashi *Anal Chem* **58** (1986) 353; (d) T Imasaka, A A Tsukamoto and N Ishibashi *Anal Chem* **61** (1989) 2285; (e) T Imasaka and N Ishibashi *Anal Chem* **62** (1990) 363A; (f) M A Roberson, D A Wilberforce, D Norris and G Patonay *Anal Lett* **23** (1990) 719; (g) G Patonay and M D Antoine *Anal Chem* **63** (1991) 321A; (h) G Patonay, M D Antoine, S Devanathan and L Strekowski *Appl Spectrosc* **45** (1991) 457; (i) J Y Zen and G Patonay *Anal Chem* **63** (1991) 2934; (j) T Higashijima, T Fuchigami, T Imasaka and N Ishibashi *Anal Chem* **64** (1992) 711

2 (a) D Wolf *Biochemistry* **24** (1985) 582; (b) B Packard and D Wolf *Biochemistry* **24** (1985) 5176

3 S A Soper and Q L Mattingly *J Am Chem Soc* **116** (1994) 3744

4 B M Pierce and R R Birge *IEEE J Quant Electron* QE **18** (1982) 1164

5 W West and S Pearce *J Phys Chem* **69** (1965) 1894

6 S Makio, N Kanamaru and J Tanaka *J Bull Chem Soc Jpn* **53** (1980) 3120

7 Y Miyazoe and M Maeda *Appl Phys Lett* **12** (1968) 206

8 C D Decker and F K Tittel *Opt Commun* **7** (1973) 155

P E Oetinger Jr and C F Dewey *IEEE J Quant Electron QE* **12** (1976) 95

10 E O Ammann and C D Decker *J Falk IEEE J Quant Electron* QE **10** (1974) 463

11 K Kato *IEEE J Quant Electron* QE **12** (1976) 442

12 C D Decker *App Phys Lett* **27** (1995) 607

13 D E Evans, J Puric and M L Yeoman *Appl Phys Lett* **25** (1974) 151

14 I Wieder *Appl Phys Lett* **21** (1974) 318

5 J Shah and R F Leheny *Appl Phys Lett* **24** (1974) 562

16 R F Leheny and J Shah *IEEE J Quant Electron* QE **11** (1975) 70

17 C Lin and A Dienes *Opt Commun* **9** (1974) 21

18 P Sperber, W Spangler, B Meier and A Penzkofer *Opt Quant Electron* **20** (1988) 395

19 D K Palit, A V Sapre, J P Mittal and C N R Rao *Chem Phys Lett* **195** (1992) 1

20 H N Ghosh, H Pal, A V Sapre and J P Mittal *J Am Chem Soc* **115** (1993) 11722

21 C Reichardt *Angew Chem* **18** (1979) 98

22 C Reichardt (Ed) *Molecular Interaction* John Wiley & Sons, New York (1982) pp 241

23 (a) A S Davidov (Ed) *Theory of Molecular Excitons* Mc Graw Hill, New York (1962); (b) M Kasha, H R Rawls and M A El-Bayoumi (Eds); *Molecular Spectroscopy* Butterworths London (1995)

24 (a) F C Spano, J R Kuklinski and S Mukamel *Phys Rev Lett* **65** (1990) 211; (b) A A Muenter, D V Brumbaugh, J Apolito, L A Horn, F C Spano and S Mukamel *J Phys Chem* **96** (1992) 2783

25 (a) H Fidder, J Terpstra and D A Wiersma *J Chem Phys* **94** (1991) 6895; (b) S De Boer and D A Wiersma *Chem Phys Lett* **165** (1990) 45

26 W J Harrison, D L Mateer and G J T Tiddy *J Phys Chem* **100** (1996) 2310

27 S A Soper Jr, B L Legendre and J Huang *Chem Phys Lett* **237** (1995) 339

28 O Przhonska, Y Slominsky, A Kachkovsky, U Stakl, M Senoner and S Dahne (Ed. A Tramer) *Fast Elementary Processes in Chemical and Biological Systems* AIP Press (1996) p 197

29 I Martini and G V Hartland *Chem Phys Lett* **258** (1996) 180

30 F Ganikhanov, J -M Hsieh and Ci-Ling Pan *Opt Commun* **114** (1995) 289

31 V Kuzmin and A Darmanyan *Chem Phys Lett* **54** (1978) 159

32 I Carmichael and G L Hug *J Phys Chem Ref Data* **15** (1985) 1

33 S L Murov, I Carmichael and G L Hug (Eds) *Handbook of Photochemistry* Marcel Dekker Inc (1993)

34 D K Palit, H Pal, T Mukherjee and J P Mittal *Chem Phys* **126** (1988) 441

35 M D Barkley, A A Kowlczyk and L Brand *J Chem Phys* **75** (1981) 3581